Some Remarks on the Photophysics of Nitrogen Dioxide

Iain Wilkinson

School of Chemistry

University of Leeds

A thesis submitted for the degree of

Doctor of Philosophy

30th Sepetember 2009

The candidate confirms that the work submitted is his own, except where work which has formed part of jointly-authored publications has been included. The contribution of the candidate and the other authors to this work has been explicitly indicated below. The candidate confirms that appropriate credit has been given within the thesis where reference has been made to the work of others.

This thesis is dedicated to my mother. The example she has set and her unwavering support and belief in me is ever inspiring.

Acknowledgements

Most of the research described in this thesis is my own work but I would like to acknowledge the contributions of others. The article presented in Appendix A was published in the Journal of Chemical Physics and describes the imaging studies and the interpretation of these experiments that are presented in Chapter 4. The article and thesis chapter were principally written by myself where I took advice about corrections from my supervisor and journal referees. Similarly, the article presented in Appendix B was published in the Journal of Chemical Physics and describes the imaging studies and the interpretation of these experiments presented in Chapter 5. Again the article and thesis chapter were principally written by myself where advice was taken about corrections from my supervisor, Dr Marcelo de Miranda and the journal referees. However, it should be stated that the angular momentum theory presented in Chapter 5 and the paper shown in Appendix B as well as the supplementary material to the paper (Appendix C) were written almost exclusively by Dr de Miranda.

Appendices D and E have been published in the Journal of Chemical Physics and Chemical Physics Letters respectively. They describe a range of experiments which were performed to understand the relaxation and ionisation dynamics of azulene after excitation to its S_2, S_3 and S_4 states and the influence of the relaxation processes on its ionisation behaviour. The majority of the work was performed by Dr Valérie Blanchet, Dr Kevin Raffael, Dr Giorgio Turri, Dr Béatrice Chatel and Professor Bertrand Girard with my supervisor Professor Benjamin J. Whitaker at the Laboratoire Collisions Agrégats Réactivité at the Université Paul Sabatier in Toulouse. However, some complimentary experiments were performed in Leeds by

Dr Ivan Anton Garcia and me using an earlier version of the spectrometer described in Chapter 3. My contribution to the work was to record single-colour velocity map images of the photoelectrons ejected by azulene on irradiation with nanosecond and femtosecond laser pulses at excitation energies of ~3.10 eV and ~4.66 eV and ~3.20 eV and ~4.81 eV respectively with Dr Anton Garcia. We also measured ~100 ps pump-probe ion and electron decay transients using different laser polarisation combinations and selected electron images with 180 fs femtosecond temporal resolution. These measurements were made using pump photon excitation energies of ~4.81 eV and using a two-photon probe field with a photon energy of 3.20 eV.

I would not have been able to perform the work presented in this thesis without the help and support I have received from a great number of people during the last four years or so. I feel enormously fortunate to have been given the opportunity to work under the supervision of Professor Ben Whitaker both during my MChem project and my PhD. Ben has been unbelievably patient, approachable and supportive during my time at Leeds and I owe him more than I can articulate. His high standards, passion for science and extensive scientific knowledge have made my time at Leeds challenging, stimulating and rewarding and some of the best years of my life so far. Most of all I would like to thank him for the passion he has given me for science and research. It has been an honour to work with Ben and I hope I can now count him not just as a teacher and drinking partner but also as a friend. I wish him every success in the future and hope to carry on working with him for many years to come.

I would also like to thank Dr Ivan Anton Garcia who also played a large role in giving me a love for research science. Ivan's careful and considered approach to science and his ability to convey the meaning and importance of the measurements we made together was inspiring. A lot of what I have achieved to produce this thesis has been due to the excellent training he gave me during his brief time in Leeds. Furthermore, Ivan really pushed me to think for myself and solve my own problems, in this respect I owe

him a great deal. I feel enormously privileged to have worked and spent time with him and more so to count him as a good friend.

I would also like to express my gratitude to Dr Panagiotis Kapetanopoulos who has been a pillar of support, particularly helpful with any electrical or mechanical problems and a great friend. Similarly I would like to thank Dr Nick Form for his help and support and uncompromising patience. Despite the extra amplitude shaping that my hands applied frequently to his coherent control experiments he never lost his temper and we still remained friends. I would also like to thank Dr Jean-Benoit Hamard who as an extended member of the research group provided a great deal of entertainment and fun in what could at times be a dreary basement. I would also like to express my appreciation to Dr Kate Furneaux and Tamsin Malkin for their evening food offerings without which, many of the late nights which were required to record what turned out to be important experimental data would not have been possible.

I would like to express my gratitude to Dr Marcelo de Miranda for all of his help throughout my research degree. Despite him having no affiliation with my research until the last year or so of my degree he has been ever accommodating and has spent many hours of his free time breaking down seemingly complicated scientific ideas and bringing some clarity where before there was only confusion. I would also like to thank Dr Valérie Blanchet who has been enormously supportive at every available opportunity. Her passion for science and the intensity with which she approaches it are both inspiring and unrivaled. My thanks also go to Dr Mark Blitz and Dr Andrew Goddard who as members of the atmospheric research groups had no obligations whatsoever to give me all of the invaluable help and support that they so freely gave.

I would also like to express my thanks to Mr Dave Fogarty for all of his help over the last 8 years. His belief in me, his extensive help with computer related problems and his advice have been invaluable. I am also really grateful for the opportunities he gave me in the teaching laboratory where I found demonstrating to the undergraduates valuable and extremely

rewarding. My thanks also go to Mr John Dixon and Mr Matthew Broadbent from the mechanical workshops particularly for the machining of the electrostatic lens assembly and its adjustment mount as well as Mr John Spence and Mr Geoffrey Taylor from the electrical workshops and Mr Mike Holmes and the IT staff.

Finally I would like to thank my family and friends, especially my parents and my step dad Peter. They in particular have been enormously supportive and have frequently made significant sacrifices to get me where I am today. I could not have achieved this without them.

Abstract

A high kinetic energy resolution velocity map imaging spectrometer has been designed and constructed to perform energy- and time-resolved photoion or photoelectron imaging experiments. When coupled with fast detector gating the instrument allowed direct current slice ion imaging experiments to be performed. Alternatively crush imaging experiments could be performed with better mass resolution and greater signal intensities.

The main body of the thesis focuses on the application of this spectrometer to the study of the ultraviolet fragmentation of nitrogen dioxide. A combination of direct current slice imaging, crush velocity map imaging and photofragment resonantly enhanced multiphoton ionisation spectroscopy experiments have been performed to understand the fragmentation dynamics. At an excitation energy of ~5.49 eV $O(^3P_J)$ fragments were formed preferentially in coincidence with NO $(1)^2\Pi_\Omega$ fragments in v=1 with a bimodal rotational distribution. $O(^1D_2)$ fragments were observed to be formed preferentially with vibrationally excited NO $(1)^2\Pi_\Omega$ (v=1) with a bimodal rotational distribution. In addition the polarisation of the $O(^1D_2)$ fragments was extracted and the orbital angular momentum alignment of these fragments was found to be essentially independent of kinetic energy release. The results were interpreted in terms of the topology of the electronically excited states of nitrogen dioxide.

In a separate set of experiments the visible/ultraviolet decomposition dynamics of nitrogen dioxide were studied. Internally excited NO $(1)^2\Pi_\Omega$ fragments were observed to be formed and were probed using state-selective multiphoton ionisation schemes. Direct measurements of atomic oxygen fragments suggest that these fragments are produced via one or more high-lying neutral electronic states. In the case of ground state oxygen atoms, fragmentation results in the preferential production of highly vibrationally excited neutral NO co-fragments. $O(^1S_0)$ fragments were also observed and interpreted to be produced in coincidence with NO $(1)^2\Pi_\Omega$ fragments. The relevance of these results to the interpretation of recent time-resolved experiments was discussed.

Abbreviations

VMI	Velocity Map Imaging
3D	Three-Dimensional
NO_2	Nitrogen Dioxide
DC	Direct Current
REMPI	Resonantly Enhanced Multi-Photon Ionisation
N_2O_4	Dinitrogen Tetroxide
PES	Potential Energy Surface
MCSCF	Multi-Configurational Self-Consistent Field
NIST	National Institute of Standards and Technology (of America)
LIF	Laser Induced Fluorescence
MPI	MultiPhoton Ionisation
GAMESS	General Atomic and Molecular Electronic Structure System
MRCI	Multi-Reference Configuration Interaction
VUV	Vacuum UltraViolet
ZEKE	Zero Electron Kinetic Energy
PEPICO	PhotoElectron-PhotoIon COincidence
TOF	Time-Of-Flight
Nd:YAG	Neodymium doped Yttrium Aluminium Garnet
FWHM	Full-Width Half-Maximum
OPO	Optical Parametric Oscillator
NOPA	Non-collinear Optical Parametric Amplifier
UV	Ultra Violet
CF	ConFlat
MCP	MicroChannel-Plate
CCD	Charged Couple Device
GPIB	General Purpose Interface Bus
2D	Two-Dimensional
MS	Mass Spectrometer
DOF	Distance-Of-Flight
amu	atomic mass units
BASEX	BAsis Set EXpansion
POP	Polar Onion Peeling
HeNe	Helium Neon

TTL	Transistor-transistor logic
CPA	Chirped Pulse Amplification
PEM	PhotoElastic Modulator
BNC	Bayonet Neill-Concelman
1D	One-Dimensional
TR FTIR	Time-Resolved Fourier Transform Infra-Red
RRKM	Rice-Ramsperger-Kassel-Marcus
DMI	Dissociative Multiphoton Ionisation
ATI	Above Threshold Ionisation

Contents

List of Figures

Chapter 1

Introduction

Since the development of the velocity map imaging (VMI) technique in 1997 (1) it has been widely adopted and applied to the detailed study of a large number of gas-phase decomposition and scattering processes. The ability of this powerful detection technique to measure the full product velocity profile with single quantum state specificity in single experiments has delivered fascinating insights into the nature of microscopic chemical and physical interactions. The importance and prevalence of the technique in gas-phase reaction dynamics studies can be attributed to the large amount of information it can yield and its wide range of applications in both the time and frequency domains. Using VMI, dissociation and ionisation dynamics of neutral and charged species are now routinely studied in great detail giving insights into the flow of charge and energy in molecular systems (10; 11; 12; 13; 14; 15; 16; 17; 18; 19; 20; 21; 22; 23; 24). Additionally, extensions of the technique to three-dimensional (3D) or coincidence imaging experiments have allowed three (and in some cases four or five) body fragmentation processes to be similarly investigated with these correlated measurements providing information about the fragmentation processes in the molecular frame of reference (25; 26; 27; 28).

The VMI technique has also been applied to inelastic and reactive scattering processes to provide a deep understanding of microscopic energy transfer (29; 30; 31; 32; 33; 34) and canonical chemical processes (35; 36; 37; 38). In addition the wealth of information provided by this multidimensional detection technique has been used to provide perspicacity into time-resolved coherent control experiments of atomic and molecular systems (39; 40; 41; 42). In recent years the scope of the VMI technique has

been further broadened through the detailed study of the ionisation behaviour of seeded and unseeded solvent clusters (43; 44; 45; 46; 47; 48). These experiments represent a bridge between the gas and solution phases but the technique is not just limited to the study of fluids as the recent application of the technique to study the photochemistry of surfaces demonstrates (49).

In this thesis the application of the VMI technique to the comprehensive study of the photodissociation dynamics of nitrogen dioxide (NO_2) is reported. An outline of the thesis follows. The spectroscopy and decomposition behaviour of NO_2 at excitation energies between 1 and 20 eV is summarised in Chapter 2. This chapter aims to provide background information for Chapters 4, 5 and 6 which make up the main body of work in this thesis.

In Chapter 3 different approaches to VMI experiments are discussed and the VMI spectrometer that was constructed and optimised in order to carry out the work reported in Chapters 4, 5 and 6 is described. Firstly, an overview of the spectrometer is given followed by a discussion of some of the electrodes that have been used by others in order to project photoproduct distributions onto position sensitive detectors in charged particle imaging experiments. Different approaches to extracting velocity distributions, translational anisotropy parameters and alignment and orientation moments from velocity map images are then discussed. This involves an overview of various methods for extracting dynamical parameters from crush velocity map images and also methods for exclusively measuring the central slice of photoproduct Newton spheres. The operation of the lens assembly which has been implemented in the Leeds VMI spectrometer to perform energy-resolved (nanosecond time scale) and time-resolved (femtosecond time scale) photodissociation and photoionisation experiments is then described. Finally, the procedures used to perform the experiments that are reported in this thesis are detailed.

Chapter 4 describes experiments that were carried out in order to probe the photodissociation dynamics of nitrogen dioxide above the second dissociation limit at photolysis energies close to 5.49 eV (~226 nm). Here, the $O(^3P_J)$ + NO $(1)^2\Pi_\Omega$ adiabatic product channel was examined using direct current (DC) slice VMI (36; 50) of the $O(^3P_J)$ and NO $(1)^2\Pi_\Omega$ fragments. Mass-resolved REMPI spectroscopy and crush VMI were also used to probe directly the rovibrational population distributions of the NO $(1)^2\Pi_\Omega$ fragments. In addition possible interference from the dissociation of dinitrogen

tetroxide (N_2O_4) was examined by investigating the effect of the sample temperature on the $O(^3P_J)$ fragment energy distributions. In these experiments the $O(^3P_J)$ + NO $(1)^2\Pi_\Omega$ dissociation channel was found to favour the production of vibrationally cold, highly rotationally excited NO $(1)^2\Pi_\Omega$ products with all three oxygen spin-orbit components. Other minor dissociation channels which produce $O(^3P_J)$ atoms were also identified. At the end of the chapter the significance of these dissociation channels is discussed and a reinterpretation of previous studies of NO_2 dissociation on excitation to the $(3)^2A'$ state is presented.

Chapter 5 describes DC slice and crush VMI experiments that were also undertaken to probe the photodissociation dynamics of nitrogen dioxide above the second dissociation limit. Here the $O(^1D_2)$ + NO $(1)^2\Pi_\Omega$ diabatic product channel was examined at similar excitation energies. Using one- and two-colour imaging experiments to observe the velocity distributions of state selected NO fragments and O atoms respectively it was possible to build a detailed picture of the dissociation dynamics. By combining the information obtained from VMI studies with mass-resolved REMPI spectroscopy it was possible to interpret and fully assign the features in the NO images. From the two-colour images of the $O(^1D_2)$ photofragments recorded with different polarisation combinations of the pump and probe laser fields the orbital angular momentum alignment in the atomic fragment could be extracted. It was found that the entire $O(^1D_2)$ photofragment distribution was similarly aligned with most of the population in the $M_J=\pm1$ magnetic sub-levels. Here, the similarity of the fragment polarisations was interpreted as a signature of all of the $O(^1D_2)$ atoms being formed via the same avoided crossing. At the photolysis energies considered here the NO fragments were formed preferentially in v=1 where these vibrationally excited fragments were observed to exhibit a bimodal rotational distribution. This is in contrast to the unimodal rotational profile of the NO fragments in v=0. These observations are discussed in terms of the calculated topology of the adiabatic potential energy surfaces. By considering these findings and the results presented in Chapter 4 the vibrational inversion and rotational bimodality of the v=1 fragments resulting from the diabatic dissociation channel are attributed to the symmetric stretch and bending motion generated on excitation to the $(3)^2A'$ state.

Chapter 6 describes nanosecond experiments that have been performed in order to study the visible/ultraviolet decomposition dynamics of nitrogen dioxide. These stud-

ies complement the results of recent time-resolved experiments. Here, NO^+ fragment distributions have been studied in detail using the VMI technique in order to highlight multi-excitation pathway, multi-dissociation channel fragmentation behaviour. Here, neutral ground state internally excited NO fragments were observed to be the dominant photoproducts. These fragments were inferred to be formed via a number of optical pathways and were observed to be probed via state-selective multiphoton ionisation schemes. Experiments that were performed to image the $O(^3P_J)$ fragments directly following multiphoton fragmentation suggested that the diatomic co-fragments for this decomposition channel were formed with ~30 vibrational quanta of internal excitation. Analysis of the ground electronic state atomic spin-orbit distribution suggested a high degree of non-adiabaticity between the different atomic spin-orbit asymptotes. Direct observation of $O(^1S_0)$ atoms confirmed that multiple dissociation limits were accessed following visible-ultraviolet excitation of NO_2. The results suggested that the majority of the photofragments were formed via a number of high-lying electronic states that produced neutral fragments which were subsequently ionised.

Some conclusions from the work are presented in Chapter 7 along with some future work that would be required to probe some unanswered questions that arise from this thesis. The appendices include a number of published manuscripts that detail the majority of the work reported in the experimental chapters as well as a detailed description of the angular momentum treatment that was adapted by Marcelo de Miranda in order to extract dynamical parameters from the $O(^1D_2)$ images reported in Chapter 5. Additionally published manuscripts describing some time-resolved experiments concerning the photoionisation dynamics of azulene that were carried out both in Leeds and Toulouse are included.

Chapter 2

The Spectroscopy of NO_2

2.1 Nitrogen dioxide

The photodissociation of NO_2 has been extensively studied for more than half a century. This deceptively complex triatomic molecule is known to be important in the chemistry of combustion (51) and the atmosphere (52) and has been an important subject of study in the development of reaction dynamics (53; 54). The spectroscopy of NO_2 is complicated by its open-shell electronic structure which gives rise to highly coupled electronic states and non-adiabatic decomposition dynamics that are particularly apparent when the low-lying adiabatic potentials are excited. The study of this behaviour has resulted in an extensive body of literature. Some of the detailed investigations that have been undertaken in both the energy (4; 55; 56; 57; 58) and the time domain (59; 60; 61; 62; 63) are highlighted. It is also noted that although the majority of the photolysis studies focus on fragmentation via the first dissociation limit, thorough single- and multiphoton fragmentation experiments have also been carried out above higher dissociation thresholds (5; 7; 8; 28; 64; 65; 66; 67; 68; 69; 70; 71).

The valence configuration of NO_2 consists of 17 electrons that result in a ground electronic state with doublet spin multiplicity and a bent nuclear configuration that was discussed by Mulliken (72) and Walsh (73). This electronic configuration, labelled the $(1)^2A_1$ state in C_{2v} symmetry, is shown below in Table 2.1. The dominant electronic configurations associated with the Franck-Condon regions of some of the low-lying excited valence states of NO_2 are also shown. The dominant electronic configurations of some of the higher energy valence states are shown in Table 2.2.

State / C_{2v}	Coefficient	$3a_1$	$2b_2$	$4a_1$	$5a_1$	$3b_2$	$1b_1$	$4b_2$	$1a_2$	$6a_1$	$2b_1$	$7a_1$	$5b_2$	n←$(1)^2A_1$
$(1)^2A_1$	0.9210112	↑↓	↑↓	↑↓	↑↓	↑↓	↑↓	↑↓	↑↓	↑				N/A
$(1)^2B_1$	0.9144082	↑↓	↑↓	↑↓	↑↓	↑↓	↑↓	↑↓	↑↓		↑			$2b_1(\uparrow)$←$6a_1(\uparrow)$
$(1)^2B_2$	0.8836805	↑↓	↑↓	↑↓	↑↓	↑↓	↑↓	↑	↑↓	↑↓				$6a_1(\downarrow)$←$4b_2(\downarrow)$
	-0.2316846	↑↓	↑↓	↑↓	↑↓	↑↓	↑↓	↑↓	↓	↑	↑			$2b_1(\uparrow)$←$1a_2(\uparrow)$
$(1)^2A_2$	0.9254254	↑↓	↑↓	↑↓	↑↓	↑↓	↑↓	↑↓	↑	↑↓				$6a_1(\downarrow)$←$1a_2(\downarrow)$
$(2)^2A_2$	0.7231020	↑↓	↑↓	↑↓	↑↓	↑↓	↑↓	↑	↑↓	↑	↓			$2b_1(\downarrow)$←$4b_2(\downarrow)$
	-0.5415803	↑↓	↑↓	↑↓	↑↓	↑↓	↑↓	↓	↑↓	↑	↑			$2b_1(\uparrow)$←$4b_2(\uparrow)$
$(2)^2B_2$	0.7505094	↑↓	↑↓	↑↓	↑↓	↑↓	↑↓	↑↓	↑	↓	↑			$6a_1(\downarrow)$←$1a_2(\downarrow)$, $2b_1(\downarrow)$←$6a_1(\downarrow)$
	0.4057011	↑↓	↑↓	↑↓	↑↓	↑↓	↑↓	↑↓	↓	↑	↑			$2b_1(\uparrow)$←$1a_2(\uparrow)$
	0.3448084	↑↓	↑↓	↑↓	↑↓	↑↓	↑↓	↑↓	↑	↑	↓			$2b_1(\downarrow)$←$1a_2(\downarrow)$
$(3)^2A_2$	0.6842351	↑↓	↑↓	↑↓	↑↓	↑↓	↑↓	↑	↑↓	↓	↑			$6a_1(\downarrow)$←$4b_2(\downarrow)$, $2b_1(\uparrow)$←$6a_1(\uparrow)$
	0.4530760	↑↓	↑↓	↑↓	↑↓	↑↓	↑↓	↓	↑↓	↑	↑			$2b_1(\uparrow)$←$4b_2(\uparrow)$
	0.2991941	↑↓	↑↓	↑↓	↑↓	↑↓	↑↓	↑↓	↑		↑↓			$2b_1(\downarrow)$←$1a_2(\downarrow)$, $2b_1(\uparrow)$←$6a_1(\uparrow)$
	0.2311586	↑↓	↑↓	↑↓	↑↓	↑↓	↑↓	↑	↑↓	↑	↓			$2b_1(\downarrow)$←$4b_2(\downarrow)$

Table 2.1: Electronic configurations of some of the ground and low-lying electronically excited states of NO_2. The electronic configurations are represented by the α (↑) and β (↓) spin state populations of the 12 valence molecular orbitals that are labelled according to their C_{2v} symmetries. The configurations and their coefficients were calculated using the General Atomic and Molecular Electronic Structure System (GAMESS) US software package (74) by performing multi-configurational self consistent field (MCSCF) calculations with a 6-311G basis set and by restricting the nuclear framework to C_{2v} symmetry. The coefficient is the expectation value of the relevant electronic configuration at the equilibrium geometry of the electronic ground state, the square of this coefficient gives the fractional parentage of the configuration for the electronic state. The states are presented in the order of increasing vertical excitation energy as determined by the MCSCF calculations. The n←$(1)^2A_1$ column shows the change in the ground state electronic configuration to produce the relevant excited state.

The effects of the valence molecular orbital populations on the nuclear framework of NO_2 are seen throughout the low energy absorption spectrum. For the majority of the nuclear coordinate space, an independent electron or Hartree-Fock picture of the electronic structure provides a qualitative description of these effects. In the $(1)^2A_1$ state. the highest energy, free-radical $6a_1$ electron is antibonding and is stabilised by reduced bond angles. Conversely, the second highest energy $4b_2$ molecular orbital electrons are stabilised by increased bond angles. In the electronic ground state the high energy of the $6a_1$ electron with respect to the $4b_2$ electron pair therefore results in an equilibrium bond angle of 134.25° (75).

After electronic transitions involving the $6a_1$ and/or $4b_2$ valence electrons, the change in population of these molecular orbitals results in significant changes in the equilibrium nuclear geometry and bending mode excitation in the electronically excited states. In comparison, the remaining valence electrons are relatively non-bonding with respect to bond angle and tend to preserve the bent nuclear geometry after excitation. This results in intense and narrow peaks in the absorption profile with little evidence of bending mode vibrational progressions. The signatures of some of the different valence transitions of NO_2 are discussed in the following pages along with some of what is known about the relaxation, decomposition and ionisation dynamics occurring after excitation at total energies between 1 and 20 eV.

2.2 Valence-valence transitions

Evidence for the vibronic coupling between the low-lying electronic states of NO_2 is seen in the first electronic (1.86–4.96 eV or 667–250 nm) absorption band (76; 77) (see Fig. 2.1) where the complex vibrational progressions are indicative of the mixed character of the excited state potential energy surfaces (PES). Throughout this absorption band the $(1)^2B_2$ adiabatic state carries the majority of the oscillator strength [0.01670 at 3.33 eV (78)] from the ground state potential (54; 79; 80) where the excitation is principally attributed to the $6a_1 \leftarrow 4b_2$ transition. This photoexcited state effectively mixes with the ground $(1)^2A_1$ state due to a low-lying conical intersection between the two PES at bond angles close to 108°, bond lengths close to 126 pm and an energy close to 1.2 eV (81; 82; 83; 84; 85; 86; 87). Transitions to the $(1)^2B_1$ state are also electric dipole allowed, although the oscillator strength for this $2b_1 \leftarrow 6a_1$ excitation

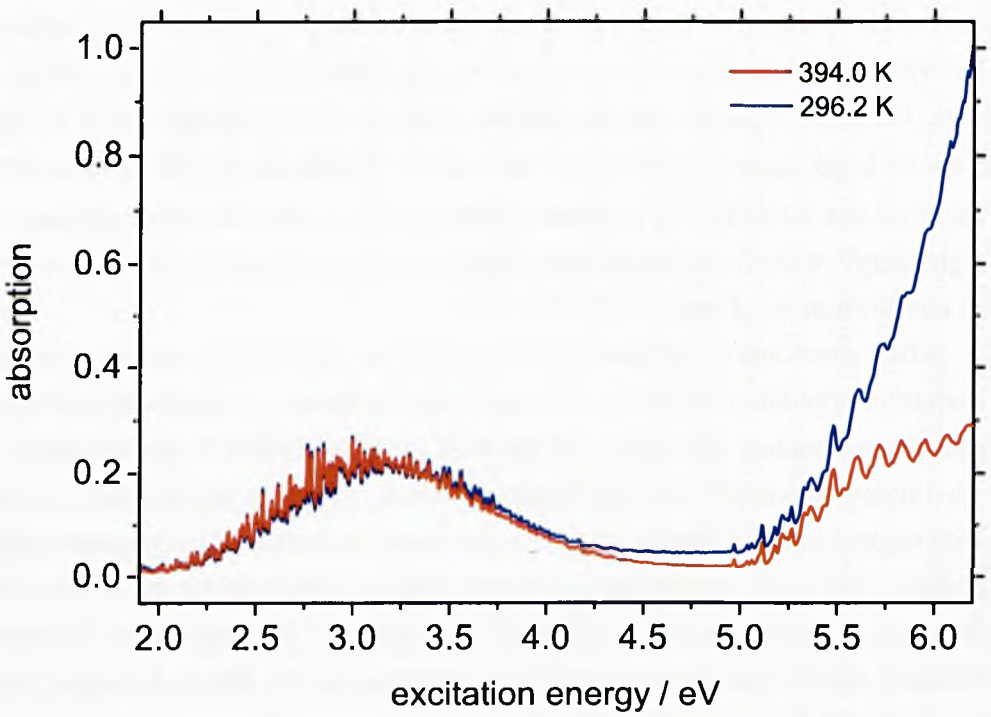

Figure 2.1: The optical absorption spectrum of NO_2 recorded at 296.2 and 394.0 K. The spectra were recorded using a dual beam Perkin-Elmer Lambda 900 UV/Visible spectrometer operating with a 0.20 nm data interval and a slit width of 0.1 nm between 200 and 650 nm. The wavelength scale has been converted to an electron volt scale (~1.9–6.2 eV) so that it is consistent with the energy units used throughout this thesis. The spectra were recorded using a 100 mm path length quartz absorption cell. The cell had a total volume of $\sim 1.6\times10^{-4}$ m^3 and contained a 1:3:10 mixture of NO_2 (Air Products Ltd.), O_2 (BOC Gases) and He (BOC gases) respectively at a total pressure of 200 mbar. The absorption cell was heated using a variac and heating tape combination where a thermocouple with 0.05 K accuracy was used to monitor the sample temperature. The effect of increased temperature is seen in the absorption profile. The UV absorption cross-section is observed to decrease as the $2NO_2 \rightleftharpoons N_2O_4$ equilibrium is pushed towards the monomer. The influence of this equilibrium on experiments that measure the UV decomposition dynamics of NO_2 is discussed in Chapter 4.

is calculated to be significantly lower (0.004924 at 1.75 eV) (78). Transitions to this excited state increase the complexity of the absorption profile due to direct excitation processes and also because of the Renner-Teller interaction (75) that occurs between the excited state and the $(1)^2A_1$ ground state. In addition, further perturbations arrise from the mixing of all of these states with the $(1)^2A_2$ potential that occurs through the spin-orbit interaction (88; 89).

At excitation energies in excess of 3.11 554 6(6) eV (55), fragmentation is known to occur to produce NO $(1)^2\Pi_{\frac{1}{2}}$ in coincidence with $O(^3P_2)$ atoms. The thresholds for NO $(1)^2\Pi_{\frac{3}{2}}$, $O(^3P_1)$ and $O(^3P_0)$ products occur 14.856 meV (90), 19.623 meV (91) and 28.141 meV (91) higher in energy respectively. Although the fragmentation dynamics via these dissociation limits are rather complex, the fragmentation is generally thought to occur via a reduction in bond angle as the nuclear framework relaxes from the Franck-Condon region of the $(1)^2B_2$ photoexcited state. This allows ultrafast internal conversion to occur to the unbound adiabatic ground state potential as the nuclear configuration of the conical intersection is accessed within 10 fs of excitation. Asymmetric stretch motion then results in barrierless fragmentation on the ground electronic surface with the majority of the excited state population being depleted after a number of non-adiabatic curve crossings and re-crossings within 100 fs (83). Support for this mechanism is provided by *ab-initio* studies (82; 83; 92) and also by experimental observables like the stepwise change in dissociation timescale with excitation energy (58; 59; 60; 61; 93). Excitation energy dependent photoproduct rovibrational and angular distribution measurements provide further support with rotationally excited/rotationally bimodal product state distributions and variations in the anisotropy parameter suggesting parent bending mode excitation is important during the dissociative process (56; 94; 95; 96).

The effects of electronic coupling between higher energy excited states are seen in the second electronic absorption band (4.97–6.42 eV or ~248–193 nm) (76; 77) where excitation from the ground electronic state has an average oscillator strength of ~0.006 (77; 97). This absorption feature is made up of a broad continuum feature with an overlying diffuse vibrational progression that has recently been attributed to symmetric stretch motion in the excited state (8). The absorption feature has been predominantly attributed to excitation of one of the $1a_2$ electrons to the $2b_1$ molecular orbital in order to produce the short-lived [41.0±1.6 ps at the origin, sub-100 fs

less than 100 meV above this level (98; 99)] $(2)^2B_2$ adiabatic state. Although multi-configurational self-consistent field (MCSCF) calculations highlight a similar contribution of multi-electron excitation configurations (see Table 2.1). Following excitation to this state, non-adiabatic interactions are known to have a significant effect on the decomposition process (8; 64; 65). This is principally displayed by the approximately equal yields of $O(^3P_J)$ and $O(^1D_2)$ fragments on excitation above the NO $(1)^2\Pi_{\frac{1}{2}}$ + $O(^1D_2)$ dissociation limit (5.082 91 eV) (7; 99; 100; 101). Although the decomposition via this photoexcited state has not been studied as extensively as that occurring via the $(1)^2B_2$ state, it is thought that the single-photon fragmentation occurs with differing degrees of bending and symmetric stretch excitation via at least two adiabatic surfaces. This results in multimodal diatomic photoproduct distributions which are dominated by internally excited fragments (4; 5; 6; 7; 64; 65).

Multiphoton excitation processes to the $(2)^2B_2$ state have also been studied. The laser induced fluorescence (LIF) behaviour of the low-lying vibrational levels of this state were studied by Tsukiyama *et al.* using direct single and two photon resonant excitation pathways (102). The multiphoton scheme was achieved using two unfocused, tunable dye lasers, the first to excite a rovibrational level of the $(1)^2B_2$ manifold and the second to further excite the molecules to the $(2)^2B_2$ potential (102). The multiphoton excitation scheme and the resulting visible fluorescence signals highlight the optical coupling between the low-lying levels of the $(1)^2B_2$ state and certain rovibrational levels of the $(1)^2B_2$ potential.

A number of multiphoton ionisation (MPI) experiments have been carried by Grant and co-workers where they attributed NO fragment ion signals to a resonantly enhanced two photon excitation process to the short-lived $(2)^2B_2$ state (67; 68; 69; 70). Initial experiments were carried out with a single laser that was tuned between 2.38 and 2.95 eV in order to excite NO_2 molecules under different conditions (70). In these experiments high laser intensities (in excess of 1×10^{10} W cm^{-2}) were used in order to drive multiphoton processes with the single laser field. Between 2.35 and 2.53 eV an excitation energy dependent variation in NO_2^+ and NO^+ yield was observed where the parent ion signal was attributed to a four photon (1+2+1) REMPI process. At slightly higher excitation energies (in excess of 2.58 eV) the NO_2^+ yield dropped significantly while a concomitant increase in the NO^+ yield was observed. This fragment ion signal was interpreted as a signature of a resonantly enhanced two photon pump process via

the $(1)^2B_2$ and $(2)^2B_2$ potentials that resulted in dissociation. The nascent diatomic fragments were said to be subsequently ionised in a (2+2) REMPI process. The NO photoproduct distributions that resulted from this excitation scheme were later analysed by some of the same researchers (69). These studies highlighted the production of NO $(1)^2\Pi_\Omega$ fragments with both $O(^3P_J)$ and $O(^1D_2)$ atoms. A subsequent publication compared these results with the single-photon photoproduct distributions formed on excitation to the $(2)^2B_2$ state (103). The single and two photon distributions were observed to be markedly different.

The multiphoton studies of the fragmentation occurring via the $(2)^2B_2$ state were later extended by Grant and co-workers by incorporating a separate probe laser to ionise the diatomic photofragments (67). This allowed the yields of individual NO quantum states to be probed as a function of the photolysis energy. Principally the researchers probed different rotational states of vibrationally cold diatomic photoproducts over a pump energy range that spanned the two-photon threshold for fragmentation via the respective NO $(1)\ ^2\Pi_\Omega$, $\mathbf{v''}$, $\mathbf{J''}$ + $O(^1D_2)$ dissociation limit. The onset of ion production from different NO $(1)\ ^2\Pi_\Omega$ $\mathbf{v''}$=0 rotational states was consistent with the proposed two photon process. Separate measurements of the photoproduct distribution at fixed photolysis energies [within 12.4 meV of the $O(^1D_2)$ dissociation limit] highlighted that fragment rotational state and Λ-doublet population distributions were a sensitive function of photolysis energy. These observations were attributed to the effects of parent molecules being excited from different initial rotational states to sets of intermediate NO_2 resonances in the $(1)^2B_2$ manifold on their way to dissociation. Additional measurements were performed in order to estimate the yields of the diatomic photofragments formed in internally excited states via the two-photon NO $(1)\ ^2\Pi_\Omega$ + $O(^3P_J)$ dissociation limit. This allowed the researchers to estimate a two-photon $O(^1D_2)$:$O(^3P_J)$ product ratio of 1:4 which is in contrast to the single-photon 1:1 ratio.

State / C_{2v}	Coefficient	$3a_1$	$2b_2$	$4a_1$	$5a_1$	$3b_2$	$1b_1$	$4b_2$	$1a_2$	$6a_1$	$2b_1$	$7a_1$	$5b_2$	n←$(1)^2A_1$
$(2)^2A_1$	0.8183922	↑↓	↑↓	↑↓	↑↓	↑	↑↓	↑↓	↑↓	↑↓				$6a_1(\downarrow)\leftarrow 3b_2(\downarrow)$
	0.2287032	↑↓	↑↓	↑↓	↑↓	↑↓	↑↓	↑	↑	↑↓	↓			$(2b_1, 6a_1)(\downarrow)\leftarrow(4b_2, 1a_2)(\downarrow)$
	0.2236218	↑↓	↑↓	↑↓	↑↓	↑↓	↑↓	↑	↓	↑↓	↑			$6a_1(\downarrow)\leftarrow 4b_2(\downarrow)$, $2b_1(\uparrow)\leftarrow 1a_2(\uparrow)$
	-0.2054070	↑↓	↑↓	↑↓	↑↓	↑↓	↓	↑↓	↑↓	↑	↑			$2b_1(\uparrow)\leftarrow 1b_1(\uparrow)$
$(3)^2B_2$	0.6281004	↑↓	↑↓	↑↓	↑	↑↓	↑↓	↑↓	↑↓	↑↓				$6a_1(\downarrow)\leftarrow 5a_1(\downarrow)$
	0.4789246	↑↓	↑↓	↑↓	↑↓	↑↓	↑↓	↑↓	↑	↑	↓			$2b_1(\downarrow)\leftarrow 1a_2(\downarrow)$
	-0.3938530	↑↓	↑↓	↑↓	↑↓	↑↓	↑↓	↑↓	↓	↑	↑			$2b_1(\uparrow)\leftarrow 1a_2(\uparrow)$
$(3)^2A_1$	0.5589386	↑↓	↑↓	↑↓	↑↓	↑↓	↑↓	↓	↑	↑↓	↑			$6a_1(\downarrow)\leftarrow 1a_2(\downarrow)$, $2b_1(\uparrow)\leftarrow 4b_2(\uparrow)$
	0.4982711	↑↓	↑↓	↑↓	↑↓	↑↓	↑	↑↓	↑↓	↓	↑			$6a_1(\downarrow)\leftarrow 2b_1(\downarrow)$, $2b_1(\uparrow)\leftarrow 6a_1(\uparrow)$
	0.2926956	↑↓	↑↓	↑↓	↑↓	↑↓	↑↓	↑	↓	↑↓	↑			$6a_1(\downarrow)\leftarrow 4b_2(\downarrow)$, $2b_1(\uparrow)\leftarrow 1a_2(\uparrow)$
	0.2672229	↑↓	↑↓	↑↓	↑↓	↑↓	↓	↑↓	↑↓	↑	↑			$2b_1(\uparrow)\leftarrow 1b_1(\uparrow)$
	-0.2662430	↑↓	↑↓	↑↓	↑↓	↑↓	↑↓	↑	↑	↑↓	↓			$(2b_1, 6a_1)(\downarrow)\leftarrow(4b_2, 1a_2)(\downarrow)$
	0.2310481	↑↓	↑↓	↑↓	↑↓	↑↓	↑	↑↓	↑↓	↑	↓			$2b_1(\downarrow)\leftarrow 1b_1(\downarrow)$
$(2)^2B_1$	0.7554151	↑↓	↑↓	↑↓	↑↓	↑↓	↑	↑↓	↑↓	↑↓				$6a_1(\downarrow)\leftarrow 1b_1(\downarrow)$
	0.5118800	↑↓	↑↓	↑↓	↑↓	↑↓	↑↓	↑↓	↑	↑↓	↑			$2b_1(\uparrow)\leftarrow 1a_2(\uparrow)$, $6a_1(\uparrow)\leftarrow 1a_2(\downarrow)$

Table 2.2: As Table 2.1 but for some of the higher energy valence states of NO_2

Grant and co-workers went on to to study the diatomic photoproduct alignment just above the two-photon NO (1) $^2\Pi_\Omega$ + O($^1D_2$) dissociation limit at excitation energies close to 2.58 eV (68). This was achieved by measuring the intensity ratio of ion signals from fragment rotational states using a probe laser field that was linearly polarised parallel or perpendicular to the linearly polarised pump laser. In order to validate the measurements, the experiments were performed by probing two different rotational branches. Additionally measurements were taken at three different pump photon energies where it was found that the results were consistent over the probed energy range of 745 meV. The researchers observed a rotational state dependent ion yield ratio that was most consistent with a $\cos^4\theta$ photoproduct angular distribution for both rotational branches (where θ=0 when the fragment recoil direction is parallel to the pump laser polarisation vector). This is consistent with their proposed dissociative mechanism of excitation to the $(1)^2B_2$ state followed by the absorption of another pump photon to the $(2)^2B_2$ potential. Based on the rotational constants of NO_2 in the electronically excited state (75) (see Table 2.3) and the lifetime of the $(2)^2B_2$ state after single-photon excitation (98; 99), the reduction of the photofragment translational anisotropy from a pure $\cos^4\theta$ distribution was attributed to a small degree of excited state mixing at the level of the first photon. Unfortunately, for the discussion that follows in Chapter 6, these researchers did not report the pump laser intensities used to perform their two-laser photoproduct distribution measurements.

Single- and multiphoton experiments have been carried out in order to probe higher energy neutral states of NO_2. Below the vertical ionisation potential [~11.23 eV (104)], the majority of these resonances are attributed to Rydberg states. Of these states, those converging on the linear ground $(1)^1\Sigma^+$ [or $(1)^1A_1$ in C_{2v} symmetry] electronic state of the cation have received the most attention due to their accessibility in the laboratory; although other excited valence states (8; 77; 97; 105) and Rydberg series that converge on excited ion states also exist (77; 106; 107). A strong series of overlapping absorption bands are observed between 6.4 and 9.5 eV in the electron impact spectra recorded by Edqvist and co-workers (106) and Au and Brion (77). Nakayama *et al.* detected the same absorption profile with higher resolution using single-photon optical spectroscopy (97). The observed absorption bands have been interpreted as signatures of the vertical $5b_2 \leftarrow 6a_1$ valence-valence transition and the

vertical $3s\sigma \leftarrow 6a_1$, $3p\sigma \leftarrow 6a_1$ and $3p\pi \leftarrow 6a_1$ Rydberg transitions by a number research groups. Nakayama *et al.* attributed the absorption feature between 8.27 and 9.18 eV (which peaks close to 8.67 eV) to the $5b_2 \leftarrow 6a_1$ valence-valence transition although this transition was later correlated with the 6.4–7.8 eV absorption band by Au and Brion. The latter assignment appears to be supported by the agreement between the experimentally determined (77; 97) and calculated (108) oscillator strengths for this transition. The valence nature of the transition is consistent with the onset of the (4) and $(5)^2A'$ states [which on the basis of Tables 2.1 and 2.2 are thought to correspond to the $(2)^2A_1$ and $(3)^2B_2$ states in C_{2v} symmetry] observed in the high-level electronic structure calculations of Schinke *et al.* at excitation energies close to 7.1 eV (8; 109). However, it is noted that the electronic configurations reported in Tables 2.1 and 2.2 do not support the importance of the aforementioned $5b_2 \leftarrow 6a_1$ electronic transition at these excitation energies. Despite this, in agreement with Schinke and co-workers, a number of optically bright $^2A'$ valence state configurations are calculated to lie within this energy region. Regardless of the electronic parentage of this state, at least one experiment seems to have probed its fragmentation behaviour (110). LIF measurements of the nascent NO $(1)^2\Pi_\Omega$ fragments produced after single-photon excitation to the high energy tail of this absorption band, at excitation energies of ~7.867 eV, have shown that highly internally excited ground state NO fragments ($\mathbf{v''}$=4–21, $\mathbf{N}_{peak}$~60) are produced in coincidence with $O(^3P_J)$ atoms. Although these experiments were carried out well above the NO $(1)^2\Pi_{\frac{1}{2}}$ + $O(^1D_2)$ and NO $(1)^2\Pi_{\frac{1}{2}}$ + $O(^1S_0)$ [7.305 291 eV (55; 111)] dissociation limits (see Table 2.4), negligible yields of the electronically excited atoms were reported to be produced.

State	T_0 / eV	ω_1 / eV	ω_2 / eV	ω_3 / eV
$(1)^2A_1$	0	0.16362 (75)	0.092945 (75)	0.20046 (75)
$(1)^2B_2$	1.2068 (84)	0.1570 (112)	0.9243 (112)	0.09606 (112)
$(1)^2B_1$	1.82796 (113)		0.0572 (113)	
$(2)^2A''$ $[(1)^2A_2]$	2.0128 (88)		0.0915 (89)	0.0159 (89)
$(2)^2B_2$	4.9749708 (99; 114)	0.1433 (115)	0.06502 (115)	0.04420 (115)

State	A / meV	B / meV	C / meV	α / °	r_0 / pm
$(1)^2A_1$	0.510284 (116)	0.0537727 (116)	0.0508883 (116)	134.25 (114)	119.34 (75)
$(1)^2B_2$	0.973 (79)	0.0559 (79)	0.0488 (79)	101.3	128.1
$(1)^2B_1$				180 (113)	123 (r_e) (113)
$(2)^2A''$ $[(1)^2A_2]$				109.4 (88)	149.7/117.1 (109)
$(2)^2B_2$	0.510284 (114)	0.0500078 (114)	0.0453094 (114)	120.8 (114)	131.4 (114)

Table 2.3: Spectroscopic constants and equilibrium geometries of some of the spectroscopically important valence states of NO_2

2.3 Rydberg series and the ion states of NO_2

The remaining bands in the 6.4–9.5 eV region of the NO_2 absorption spectrum have been assigned to the three lowest-lying Rydberg series. The 7.8–8.2 eV electron impact band, that peaks close to 8.0 eV, has been attributed to the $3s\sigma \leftarrow 6a_1$ transition by Au and Brion (77) whereas Edqvist and co-workers (106) assigned the entire profile between 6.4 and 8.2 eV to this feature, neglecting to attribute any of the observed absorption profile to valence-valence transitions (106). Ritchie and Walsh measured the optical absorption profile of NO_2 between 7.2 and 9.2 eV where they observed a weak feature at 8.0 eV and significantly stronger absorption features at higher excitation energies. The higher energy features were attributed to the $np\sigma\ ^2\Sigma_u^+$ Rydberg series with a dominant peak at ~8.6 eV. This feature was assigned to vibrationally excited levels of the n=3 state and the series as a whole was interpreted as converging on the ground state of the cation. As the ground parent ion state of NO_2 is linear (73), the maximum in the absorption profile occurs with a large degree of bending mode excitation (v_2'=10 or 11) where the Rydberg bands appear diffuse. Edqvist and co-workers assigned the electron impact feature at ~8.6 eV to the same Rydberg series suggesting a quantum defect value of 0.74 in good agreement with its low principal quantum number, p orbital assignment. Later studies by Grant and co-workers used multiphoton excitation processes to probe the same Rydberg series by monitoring the parent ionisation occurring after resonant transitions through the $(1)^2B_2$ first excited state and the low-lying $3p$ Rydberg levels (103; 117; 118; 119; 120). After single-photon excitation to the $(1)^2B_2$ manifold, the interconversion that occurred to vibrationally excited levels of the $(1)^2A_1$ state resulted in many nuclear geometries being sampled. This provided access to low-lying vibrational levels of the linear Rydberg series which have poor Franck-Condon overlap for single-photon transitions from the bent electronic ground state. By further exciting the vibrationally excited molecules using a second pump field, Grant and co-workers were able to observe signatures of different rovibrational levels of the $3p\sigma\ ^2\Sigma_u^+$ and $3p\pi\ ^2\Pi_u^+$ intermediate states by ionising them with a third laser. These experiments allowed the researchers to isolate the electronic origins of these states at 6.8995 eV and 7.1898 eV respectively (118). Later experiments by the same research group focused on excitation to vibrationally excited levels of the $3p\sigma\ ^2\Sigma_u^+$ state (119) allowing them to determine accurate values for the rotational and vibrational constants

Product 1	Product 2	Threshold / eV
NO $(1)^2\Pi_{\frac{1}{2}}$	$O(^3P_2)$	3.115546
O_2 $(1)^3\Sigma_g^-$	$N(^4S_{\frac{3}{2}})$	4.5302*
NO $(1)^2\Pi_{\frac{1}{2}}$	$O(^1D_2)$	5.08291
O_2 $(1)^1\Delta_g$	$N(^4S_{\frac{3}{2}})$	5.5060*
O_2 $(1)^1\Sigma_g^+$	$N(^4S_{\frac{3}{2}})$	6.1570*
O_2 $(1)^3\Sigma_g^-$	$N(^2D_{\frac{5}{2}})$	6.9138*
NO $(1)^2\Pi_{\frac{1}{2}}$	$O(^1S_0)$	7.30529
O_2 $(1)^1\Delta_g$	$N(^2D_{\frac{5}{2}})$	7.8895*

Table 2.4: NO_2 dissociation thresholds that lead to neutral fragments and are energetically accessible between 3 and 8 eV. The thresholds are calculated using the NO($1\ ^2\Pi_{\frac{1}{2}}$) + $O(^3P_2)$ dissociation limit measured by Jost and co-workers (55), enthalpies of formation of $NO_2(1^2A_1)$ and $N(^4S_{\frac{3}{2}})$ (121), atomic excited state energies from the National Institute of Standards and Technology (NIST) atomic spectral database (91) and the relevant diatomic spectroscopic constants compiled by Huber and Herzberg (90). For the thresholds marked with a * the standard enthalpy of reaction has been converted to a dissociation energy by assuming that all of the relavant species behave like ideal gases.

of the Rydberg series (see Table 2.6) and to discover Fermi resonances in the Rydberg manifold. The experimental determinations were supported by coupled cluster calculations using a diffuse basis set, the results of which were found to be in good agreement with their experimental results. Signatures of the overlapping $3p\sigma\ ^2\Sigma_u^+$ and $3p\pi\ ^2\Pi_u^+$ Rydberg series were also seen in the electron impact experiments of Au and Brion with the peak of the vertical absorption band occurring at ~8.7 eV. These Rydberg series are observed to dominate the absorption profile up to an excitation energy of 9.5 eV (77; 97).

The Rydberg series converging on the ground cation state have been theoretically studied by Petsalakis *et al.* (122). These researchers used *ab initio* multi-reference configuration interaction (MRCI) calculations with single and double substitutions to calculate the linear and bent PES of the ns←$6a_1$, np←$6a_1$ and nd←$6a_1$ Rydberg series. These calculations highlighted the valence-Rydberg interactions that generally

Product 1	Product 2	Threshold / eV
$O_2\ (1)^3\Sigma_g^-$	$N(^2P_{\frac{1}{2}})$	8.1058*
$O_2\ (1)^1\Sigma_g^+$	$N(^2D_{\frac{5}{2}})$	8.5405*
$O_2\ (1)^1\Sigma_u^+$	$N(^4S_{\frac{3}{2}})$	8.5800*
$NO\ (1)^2\Sigma^+$	$O(^3P_2)$	8.59587
$NO\ (2)^2\Pi_{\frac{1}{2}}$	$O(^3P_2)$	8.754568
$O_2\ (1)^3\Delta_u$	$N(^4S_{\frac{3}{2}})$	8.7857*
$O_2\ (1)^3\Sigma_u^+$	$N(^4S_{\frac{3}{2}})$	8.8706*
$O_2\ (1)^1\Delta_g$	$N(^2P_{\frac{1}{2}})$	9.0815*
$NO\ (3)^2\Pi_{\frac{1}{2}}$	$O(^3P_2)$	9.60875
$NO\ (2)^2\Sigma^+$	$O(^3P_2)$	9.72298
$O_2\ (1)^1\Sigma_g^+$	$N(^2P_{\frac{1}{2}})$	9.7326*
$NO\ (1)^2\Sigma^+$	$O(^1D_2)$	10.56324
$NO\ (2)^2\Pi_{\frac{1}{2}}$	$O(^1D_2)$	10.72193
$O_2\ (2)^3\Sigma_u$	$N(^4S_{\frac{3}{2}})$	10.6499*
$O_2\ (1)^1\Sigma_u^+$	$N(^2D_{\frac{5}{2}})$	10.9636*
$O_2\ (1)^3\Delta_u$	$N(^2D_{\frac{5}{2}})$	11.1693*
$O_2\ (1)^3\Sigma_u^+$	$N(^2D_{\frac{5}{2}})$	11.2541*
$NO\ (3)^2\Pi_{\frac{1}{2}}$	$O(^1D_2)$	11.57612
$NO\ (2)^2\Sigma^+$	$O(^1D_2)$	11.69034
$O_2\ (1)^1\Sigma_u^+$	$N(^2P_{\frac{1}{2}})$	12.1556*
$O_2\ (1)^3\Delta_u$	$N(^2P_{\frac{1}{2}})$	12.3613*
$O_2\ (1)^3\Sigma_u^+$	$N(^2P_{\frac{1}{2}})$	12.4461*
$NO\ (1)^2\Sigma^+$	$O(^1S_0)$	12.78562
$NO\ (2)^2\Pi_{\frac{1}{2}}$	$O(^1S_0)$	12.94431
$O_2\ (2)^3\Sigma_u$	$N(^2D_{\frac{5}{2}})$	13.0334*
$NO\ (3)^2\Pi_{\frac{1}{2}}$	$O(^1S_0)$	13.79850
$NO\ (2)^2\Sigma^+$	$O(^1S_0)$	13.91272

Table 2.5: NO_2 dissociation thresholds that lead to neutral fragments and are energetically accessible between 8 and 14 eV. The thresholds are calculated using the $NO(1\ ^2\Pi_{\frac{1}{2}}) + O(^3P_2)$ dissociation limit measured by Jost and co-workers (55), the enthalpies of formation of $NO_2(1^2A_1)$ and $N(^4S_{\frac{3}{2}})$ (121), atomic excited state energies from the NIST atomic spectral database (91) and the relevant diatomic spectroscopic constants compiled by Huber and Herzberg (90). For the thresholds marked with a * the standard enthalpy of reaction was converted to a dissociation energy by assuming that all of the relavant species behave like ideal gases.

occur at linear geometries and extended N–O bond lengths. Avoided crossings between Rydberg and valence states were also observed to occur at bent geometries for the states of $^2B_2$ and $^2A_2$ symmetry. Interestingly, close to the excitation energies associated with the vertical excitation to the low-lying levels of the studied Rydberg series, the fourth and fifth dissociation limits of NO_2 are reached at 8.59587 eV (55; 90) and 8.75457 eV (55; 90) respectively. These limits mark the energetic thresholds for production of NO $(1)^2\Sigma^+$ + $O(^3P_J)$ and NO $(2)^2\Pi_{\frac{1}{2}}$) + $O(^3P_J)$ products respectively. Therefore, the interaction of populated Rydberg levels with valence sates correlating with these limits will likely result in electronically excited diatomic fragments being produced in coincidence with ground state oxygen atoms. A process that appears to have been observed in the single-photon LIF experiments of Welge at excitation energies of 9.574, 10.03 and 10.64 eV (123). The dominance of these Rydberg levels in the absorption spectrum at these excitation energies and the observation of fluorescence signatures of rotationally excited NO $(1)^2\Sigma^+$ v'=0 and NO $(2)^2\Pi_\Omega$ v'=0, 1, 2 and 3 fragments provide support for these Rydberg-valence avoided crossings. Further support comes from the time-resolved multiphoton experiments of Lopez-Martens *et al.* (124), Schmidt *et al.* (125), Eppink *et al.* (126), Form *et al.* (14) and Vredenborg *et al.* (28) who observed signatures of NO $(1)^2\Sigma^+$ fragments after three photon excitation at excitation energies between 2.95 and 3.14 eV. Similar experiments at higher excitation energies (3.30 eV) observed signatures of the NO $(3)^2\Pi_\Omega$ products formed after three photon excitation where the energetic threshold for NO $(3)^2\Pi_\Omega$ + $O(^3P_J)$ fragmentation occurs at 9.60875 eV (25).

n	Rydberg Orbital	Initial Orbital	Ion State	δ	T_0 / eV	ω_1 / eV	ω_2 / eV	ω_3 / eV	Differential Oscillator Strength / eV^{-1}
3	$s\sigma$	$6a_1$	$(1)^1A_1$	1.10 (106)	8.0 (77)				0.14 (77; 97)
3	$p\sigma$	$6a_1$	$(1)^1A_1$	0.74 (106)	6.8995 (118)	0.17371 (119)	0.07702 (119)		0.14 (77; 97)
3	$p\pi$	$6a_1$	$(1)^1A_1$		7.1898 (118)	0.175 (127)	0.075 (127)		0.14 (77; 97)
3	$s\sigma$	$4b_2$	$(1)^3B_2$	0.98 (106)	9.51 (106)		0.075 (106; 128)		0.39 (77; 97)
4				0.98 (106)	11.35 (106)		0.08 (106)		0.14 (77; 97)
5				0.98 (106)	12.00 (106)		0.08 (106)		0.13 (77)
3	$p\sigma$	$4b_2$	$(1)^3B_2$	0.70 (106)	10.46 (106)				0.07 (77)
3	$d\sigma$	$4b_2$	$(1)^3B_2$	0.35 (106)	10.92 (106)		0.069 (97; 128; 129)		0.16 (77)
3	$s\sigma$	$4b_2$	$(1)^1B_2$	0.98 (106)	11.11 (106)		0.07 (97)		0.14 (77)
3	$p\sigma$	$1a_2$	$(1)^3A_2$	0.78 (106)	10.85 (97; 106; 128; 129)				0.16 (77)
3	$p\sigma$	$1a_2$	$(1)^1A_2$	0.79 (106)	11.267 (97; 106)				0.14 (77)
3	$s\sigma$	$1b_1$	$(1)^3B_1$	~1 (106)	14.7 (106)				0.27 (77)
3	$s\sigma$	$1b_1$	$(1)^1B_1$	~1 (106)	14.7 (106)				0.27 (77)
3	$s\sigma$	$5a_1$	$(1)^3A_1$	~1 (106)	14.7 (106)				0.27 (77)
3	$s\sigma$	$5a_1$	$(2)^1A_1$	~1 (106)	17.4 (106)				0.27 (77)
3	$s\sigma$	$3b_2$	$(2)^3B_2$	1.02 (106; 107)	15.382 (77; 106; 107; 129)				0.25 (77)
4				0.94 (106)	17.408 (106; 107; 129)				0.36 (77)
5				0.94 (107)	18.034 (106; 107; 129)				0.40 (77)
3	$p\pi$	$3b_2$	$(2)^3B_2$	0.68 (106; 107)	16.327 (77; 106; 107; 129)				0.28 (77)

continues on next page

n	Rydberg Orbital	Initial Orbital	Ion State	δ	T_0 / eV	ω_1 / eV	ω_2 / eV	ω_3 / eV	Differential Oscillator Strength / eV^{-1}
4				0.65 (106; 107)	17.647 (106; 107; 129)				0.27 (77)
5				0.64 (106; 107)	18.145 (106; 107; 129)				0.32 (77)
6				0.59 (107)	18.395 (107)				0.42 (77)
7				0.52 (107)	18.536 (107)				0.39 (77)
3	$d\sigma$	$3b_2$	$(2)^3B_2$	0.14 (107)	17.190 (77; 107; 129)	0.135 (107)			0.36 (77)
4				0.15 (107)	17.943 (77; 107; 129)	0.136 (107)			0.40 (77)
5				0.16 (107)	18.279 (77; 107; 129)	0.138 (107)			0.39 (77)
6				0.16 (107)	18.461 (77; 107; 129)	0.131 (107)			0.43 (77)
7				0.06 (107)	18.577 (107)	0.143 (107)			0.39 (77)
8				0.06 (107)	18.644 (107)	0.137 (107)			0.38 (77)
9				0.07 (107)	18.689 (107)	0.138 (107)			0.38 (77)
10				0.08 (107)	18.722 (107)	0.137 (107)			0.37 (77)
11				0.08 (107)	18.746 (107)	0.138 (107)			0.37 (77)
12				0.07 (107)	18.764 (107)	0.141 (107)			0.37 (77)
13				0.07 (107)	18.779 (107)				0.36 (77)
14				0.06 (107)	18.790 (107)				0.34 (77)
15				0.13 (107)	18.798 (107)				0.33 (77)
3	$d\pi$	$3b_2$	$(2)^3B_2$	0.18, 0.08 (106; 107)	17.268 (106; 107; 129)	0.137 (107)			0.38 (77)
4				0.18, 0.08 (106; 107)	17.973 (106; 107; 129)				0.40 (77)
5				0.18, 0.08 (106; 107)	18.298 (106; 107; 129)				0.39 (77)

continues on next page

n	Rydberg Orbital	Initial Orbital	Ion State	δ	T_0 / eV	ω_1 / eV	ω_2 / eV	ω_3 / eV	Differential Oscillator Strength / eV^{-1}
3	$d\delta$	$3b_2$	$(2)^3B_2$	0.02 (107)	17.326 (107)	0.134 (107)			0.36 (77)
4				0.01 (107)	18.005 (107)	0.137 (107)			0.40 (77)
5				0.01 (107)	18.314 (107)	0.132 (107)			0.39 (77)
6				0.01 (107)	18.48 (107)	0.141 (107)			0.31 (77)
3	$s\sigma$	$4a_1$	$(2)^3A_1$	0.96 (106)	17.98 (106)				0.40 (77)
4				0.97 (107)	19.774 eV (107)				0.40 (77)
3	$p\sigma$	$4a_1$	$(2)^3A_1$	0.73, 0.80 (106; 107)	18.63, 18.505 (106; 107)				0.38 (77)
4				0.77 (107)	19.956 (107)				0.37 (77)
3	$p\pi$	$4a_1$	$(2)^3A_1$	0.66 (107)	18.786 (107)				0.38 (77)
3	$d\sigma$	$4a_1$	$(2)^3A_1$	0.34 (107)	19.339 (107)				0.33 (77)
3	$d\pi$	$4a_1$	$(2)^3A_1$	0.25 (107)	19.467 (107)				0.34 (77)
3	$d\delta$	$4a_1$	$(2)^3A_1$	0.16 (107)	19.581 (107)				0.34 (77)

Table 2.6: Spectroscopic constants of some of the low-lying Rydberg states of NO_2

The first ionisation potential of NO_2 corresponds to the removal of the $6a_1$ electron (71; 127) and is reached just above 9.5 eV (117; 130). However, poor Franck-Condon factors for single-photon excitation experiments prohibit NO_2^+ from being produced with appreciable yields in vacuum ultraviolet (VUV) experiments at excitation energies below 11 eV. For this reason, Grant and co-workers used a multiphoton excitation scheme, similar to that used to detect signatures of the $3p\sigma\ ^2\Sigma_u^+$ and $3p\pi\ ^2\Pi_u^+$ Rydberg states, in order to accurately determine the adiabatic ionisation potential of NO_2 (9.586±0.002 eV) (117). The same research group later used this excitation scheme in order to excite specific high-lying Rydberg states that converge on vibrationally excited levels of the ground $(1)^1A_1$ cation state (131; 132; 133; 134; 135; 136; 137; 138; 139). Using a variety of detection techniques, these experiments allowed the researchers to study the mode specific vibronic autoionisation behaviour of NO_2 just above the adiabatic ionisation potential and to discover Fermi resonances in the first ionisation continuum.

Close to and above the first ionisation limit, intense signatures of Rydberg series that converge on electronically excited ion states are observed in the absorption profile. The overlapping vibrational progressions of these Rydberg series and the ion continua to which they converge characterise the absorption spectrum of NO_2 between 9.5 and 20 eV (77; 97; 106; 107). In this excitation range, seven or more ion states can be accessed. Here the density of ion states is due to the doublet ground state structure of neutral NO_2. This allows two different ion states with similar electronic symmetries to be formed as spin-up or spin-down electrons are stripped from doubly occupied valence molecular orbitals. Due to the degeneracy of the triplet ion states, these ion states are (statistically) expected to have three times the photoionisation cross section of their singlet counterparts. On a similar basis, the Rydberg series converging on the triplet ion states are expected to have absorption cross-sections which are three times the size of the Rydberg series that converge on the singlet ion. As outlined in the introduction, the majority of the valence electrons are non-bonding with respect to bond angle. This results in significantly larger Franck-Condon factors for ionisation from the neutral ground state to the excited ion states with respect to ionisation via the cation ground state. These effects are principally responsible for the profiles of the VUV absorption and photoelectron spectra of NO_2.

Edqvist and co-workers used a combination of VUV photoelectron spectroscopy using the He(I) and He(II) emission lines and electron impact energy depletion spectroscopy to detect neutral Rydberg states between 5 and 20 eV and connect them with specific ion states (106). They detected a Rydberg series close to 9.66 eV that was attributed $3s\sigma \leftarrow 4b_2$ transition. As expected, this series displays an extensive bending progression, due to the excitation of one of the bending angle sensitive $4b_2$ electrons. Based on the vibrational spacing of this progression (0.08 eV on average) and the ionisation profile of this band, Edqvist and co-workers suggested that this series converged on the $(1)^3B_2$ ion state that is observed at an energy of 12.86 eV and shared a similar vibrational profile in the photoelectron spectrum. The same Rydberg vibrational progression was also observed in the optical absorption spectra of Price and Simpson (128), Nakayama *et al.* (97) and Tanaka and Jursa (129) as well as in the electron impact work of Au and Brion (77). Additionally, the n=4 progression of the Rydberg series was seen by Tanaka and Jursa as a broad maximum at 11.55 eV. This feature along with the n=5 transition was observed in both electron impact studies and allowed Edqvist and co-workers to assign a quantum defect value to the series of 0.98. The photoelectron spectroscopy work of Brundle and Neuman (140) and Baltzer *et al.* (127) and the pulsed field ionisation zero electron kinetic energy (ZEKE) synchrotron studies of Jarvis *et al.* (71) support the existence of a bent excited ion state at 12.862 eV with a bending vibrational frequency of ν_2=79.2 meV. This state is now known to be the first excited ion state of NO_2.

Other Rydberg series converging on the $(1)^3B_2$ state of the cation have been detected. Edqvist and co-workers assigned a weak feature at 10.46 eV to the $3p\sigma \leftarrow 4b_2$ transition (106). At higher excitation energies Price and Simpson (128) observed a bending progression (peaking close to 10.92 eV) that was subsequently observed by Nakayama *et al.* (97) and Tanaka and Jursa (129). The progression, with a spacing of 0.07 eV, was not observed in the electron impact spectrum of Edqvist and co-workers suggesting this series has a lower absorption cross-section than the $ns\sigma$ series. Despite this, Edqvist *et al.*, assuming that the transition was indeed Rydberg in nature, attributed the band to the $3d\sigma \leftarrow 4b_2$ transition after calculating a quantum defect value of 0.35 for the series. Another vibrational progression was observed by Nakayama *et al.* at an excitation energy close to 10.73 eV where the spacing of the bands was also

State	T_0 / eV	ν_1 / eV	ν_2 / eV	ν_3 / eV	r_{NO} / pm	α / °
$(1)^1A_1$	9.586	0.175	0.077	0.29465	112.1	180
$(1)^3B_2$	12.815		0.0793		121.0	121.17
$(1)^3A_2$	13.593	0.169	0.0847		121.8	129.00
$(1)^1A_2$	14.067	0.120	0.0763 (71), 0.0833 (127)	0.183	121.6	129.74
$(1)^1B_2$	14.441	0.128	0.0718	0.1854	121.7	125.26
$(1)^3A_1$	17.068	0.128			129.3	132.48
$(1)^3B_1$	17.199	0.126			129.2	93.42
?	18.466	0.1738	0.117	0.2547		
$(2)^3B_2$	18.860	0.138	0.0838	0.208		
$(2)^1B_2$	18.945	0.1336				

Table 2.7: Spectroscopic constants of the low-lying ion states of NO_2. The data were taken from the high resolution single photon ionisation work of Jarvis *et al.* (71) and Baltzer *et al.* (127). Where the assignment of the cation states differ between the two studies, the assignments of Baltzer *et al.* are presented due to the support provided by the two-hole-one-particle configuration interaction calculations of Schirmer *et al.* (141). It is also noted that these assignments are more consistent with the triplet states having greater ionisation cross-sections than their singlet counterparts; as outlined in the main body of the text. Averages of the T_0 and vibrational energy values are reported where the two sources report values that are relatively close in energy, otherwise both values are given with appropriate references. The feature in the photoelectron spectrum at 18.466 eV was interpreted as a signature of the $(1)^3A_1$ ion state by Jarvis and co workers. As this state has been assigned by Baltzer *et al.* to the feature at 17.068 eV, its spectral signatures are reported without a state assignment. The geometries of the cation states are taken from the multi-reference-configuration interaction calculations of Hirst (142).

found to be 0.07 eV. A similar progression was observed in the photoelectron spectrum of Edqvist and co-workers at 14.45 eV that was attributed to the $(1)^1B_2$ cation state in agreement with the photoelectron studies of Brundle and Neuman (140), Katsumata *et al.* (104), Baltzer and co-workers (127) and Jarvis and co-workers (who observed the fourth excited ion state at an excitation energy of 14.442 eV with a bending quantum of 71.4 meV) (71). By correlating the Rydberg and ion state progressions, a quantum defect value of 0.98 was calculated allowing the Rydberg transition to be attributed to the $3s\sigma \leftarrow 4b_2$ transition.

The He(I) photoelectron spectra of Brundle and Neuman (140), Edqvist co-workers (106) and Baltzer *et al.* (127) and the ZEKE spectrum of Jarvis *et al.* (71) show a diffuse and short bending progression close to 13.593 eV. This feature has been attributed to the removal of the $1a_2$ valence electron to produce the $(1)^3A_2$ ion state (see Table 2.8). A similar profile was observed in the absorption spectra of Price and Simpson (128), Nakayama and co-workers (97) and Tanaka and Jursa (129) and the electron impact work of Edqvist and co-workers and Au and Brion (77) at an excitation energy close to 10.85 eV. Based on this correlation, a quantum defect value of 0.78 has been calculated which is in good agreement with the assignment of the 10.85 eV feature to the $3p\sigma \leftarrow 1a_2$ transition. The corresponding transition to the $(1)^1A_2$ ion state (~14.067 eV (71; 127)) has been attributed to the feature observed by Nakayama *et al.* at an excitation energy of 11.267 eV due to the similar profiles of the Rydberg and ion features.

State / C_{2v}	Coefficient	$3a_1$	$2b_2$	$4a_1$	$5a_1$	$3b_2$	$1b_1$	$4b_2$	$1a_2$	$6a_1$	$2b_1$	$7a_1$	$5b_2$	Ionised Electron	Associated Valence Transition
$(1)^1A_1$	0.8827756	↑↓	↑↓	↑↓	↑↓	↑↓	↑↓	↑↓	↑↓					$6a_1(\uparrow)$	
$(1)^3B_2$	0.9003350	↑↓	↑↓	↑↓	↑↓	↑↓	↑↓	↑	↑↓	↑				$4b_2(\uparrow)$	
$(1)^3A_2$	0.8939891	↑↓	↑↓	↑↓	↑↓	↑↓	↑↓	↑↓	↑	↑				$1a_2(\downarrow)$	
$(1)^1A_2$	0.6162080	↑↓	↑↓	↑↓	↑↓	↑↓	↑↓	↑↓	↑	↓				$1a_2(\downarrow)$	
	0.6162080	↑↓	↑↓	↑↓	↑↓	↑↓	↑↓	↑↓	↓	↑				$1a_2(\uparrow)$	
$(1)^1B_2$	0.5373277	↑↓	↑↓	↑↓	↑↓	↑↓	↑↓	↑	↑↓	↓				$4b_2(\downarrow)$	
	0.5373277	↑↓	↑↓	↑↓	↑↓	↑↓	↑↓	↓	↑↓	↑				$4b_2(\uparrow)$	
	0.2743539	↑↓	↑↓	↑↓	↑↓	↑↓	↑↓	↑↓	↑		↓			$6a_1(\uparrow)$	$2b_1(\downarrow) \leftarrow 1a_2(\downarrow)$
	0.2743539	↑↓	↑↓	↑↓	↑↓	↑↓	↑↓	↑↓	↓		↑			$6a_1(\uparrow)$	$2b_1(\uparrow) \leftarrow 1a_2(\uparrow)$

Table 2.8: Ground and excited electronic configurations of NO_2^+ that can be accessed from the neutral ground state after excitation at energies between 9.586 and 15 eV. The electronic configurations are represented by the α ($\uparrow$) and β ($\downarrow$) spin state populations of the 12 valence molecular orbitals that are labelled according to their C_{2v} symmetries. The configurations and their coefficients were calculated using the General Atomic and Molecular Electronic Structure System (GAMESS) US software package (74) by performing multi-configurational self consistent field (MCSCF) calculations with a 6-311G basis set and by restricting the nuclear framework to C_{2v} symmetry. The coefficient is the expectation value of the relevant electronic configuration, the square of this coefficient gives the fractional parentage of the configuration for the electronic state. Where possible the ionised electron is identified. The Associated Valence Transition column shows any changes, other than the removal of the ionised electron, to the electronic configuration of the neutral ground state in order to produce the relevant electronic state. The ion states are tabulated in energy order according to the experiments of Baltzer *et al.* (127) and the calculations of Hirst (142).

State / C_{2v}	Coefficient	$3a_1$	$2b_2$	$4a_1$	$5a_1$	$3b_2$	$1b_1$	$4b_2$	$1a_2$	$6a_1$	$2b_1$	$7a_1$	$5b_2$	Ionised Electron	Associated Valence Transition
$(1)^3B_1$	0.8520285	↑↓	↑↓	↑↓	↑↓	↑↓	↑↓	↑	↑	↑↓				$4b_2(\downarrow)/1a_2(\downarrow)$	$6a_1(\downarrow)\leftarrow 1a_2(\downarrow)/4b_2(\downarrow)$
	-0.2703242	↑↓	↑↓	↑↓	↑↓	↑↓	↑	↑↓	↑↓	↑				$1b_1(\downarrow)$	
$(1)^1B_1$	0.4712970	↑↓	↑↓	↑↓	↑↓	↑↓	↑↓	↑	↓	↑↓				$1a_2(\uparrow)$	$6a_1(\downarrow)\leftarrow 4b_2(\downarrow)$
	0.4712970	↑↓	↑↓	↑↓	↑↓	↑↓	↑↓	↓	↑	↑↓				$1a_2(\downarrow)$	$6a_1(\uparrow)\leftarrow 4b_2(\uparrow)$
	0.4088601	↑↓	↑↓	↑↓	↑↓	↑↓	↑	↑↓	↑↓	↓				$1b_1(\downarrow)$	
	0.4088601	↑↓	↑↓	↑↓	↑↓	↑↓	↓	↑↓	↑↓	↑				$1b_1(\downarrow)$	
$(1)^3A_1$	0.7046462	↑↓	↑↓	↑↓	↑	↑↓	↑↓	↑↓	↑↓	↑				$5a_1(\downarrow)$	
	-0.3596288	↑↓	↑↓	↑↓	↑↓	↑↓	↑↓	↑	↓	↑	↑			$4b_2(\downarrow)$	$2b_1(\uparrow)\leftarrow 1a_2(\uparrow)$
	-0.3129415	↑↓	↑↓	↑	↑↓	↑↓	↑↓	↑↓	↑↓	↑				$4a_1(\downarrow)$	
	0.2062259	↑↓	↑↓	↑↓	↑↓	↑↓	↑↓	↑	↑	↑	↓			$4b_2(\downarrow)/1a_2(\downarrow)$	$2b_1(\downarrow)\leftarrow 1a_2(\downarrow)/4b_2(\downarrow)$
$(2)^3B_2$	0.8829158	↑↓	↑↓	↑↓	↑↓	↑↓	↑↓	↑↓	↑		↑			$1a_2(\downarrow)$	$2b_1(\uparrow)\leftarrow 6a_1(\uparrow)$
$(2)^1B_2$	0.4066790	↑↓	↑↓	↑↓	↑↓	↑↓	↑↓	↑↓	↑		↓			$6a_1(\uparrow)$	$2b_1(\downarrow)\leftarrow 1a_2(\downarrow)$
	0.4066790	↑↓	↑↓	↑↓	↑↓	↑↓	↑↓	↑↓	↓		↑			$6a_1(\uparrow)$	$2b_1(\uparrow)\leftarrow 1a_2(\uparrow)$
	-0.3821337	↑↓	↑↓	↑↓	↑↓	↑	↑↓	↑↓	↑↓	↓				$3b_2(\downarrow)$	
	-0.3821337	↑↓	↑↓	↑↓	↑↓	↓	↑↓	↑↓	↑↓	↑				$3b_2(\uparrow)$	
	-0.2133670	↑↓	↑↓	↑↓	↑↓	↑↓	↑↓	↑	↑↓	↓				$4b_2(\downarrow)$	
	-0.2133670	↑↓	↑↓	↑↓	↑↓	↑↓	↑↓	↓	↑↓	↑				$4b_2(\uparrow)$	

Table 2.9: As Table 2.8 but for the ion states with origins between 15 and 20 eV (see Table 2.7).

Signatures of Rydberg series converging on the higher-lying excited states of the triatomic cation should result from the promotion of the $1b_1$ [correlating with the $(1)^3B_1$ ion state at 17.068 eV or the $(1)^1B_1$ ion state at 17.199 eV (127)] and $5a_1$ [correlating with the $(1)^3A_1$ ion state at 17.068 eV and the $(2)^1B_2$ ion state at 18.945 eV (71; 127)] valence electrons. A broad intense feature has been observed in the electron impact spectra of Edqvist and co-workers (106) and Au and Brion (77) that peaked close to 14.3 eV. This feature was attributed to the $3p \leftarrow 1b_1$ and $3s\sigma \leftarrow 5a_1$ transitions by Au and Brion, although spectrally resolved signatures of these Rydberg states have yet to be identified. At excitation energies between 14.3 and 18.5 eV Rydberg series corresponding to the excitation of the $3b_2$ valence electron and converging on the $(2)^3B_2$ ion state [with a T_0 of ~18.860 eV (71; 107; 127; 129)] are said to dominate the absorption profile (77; 106; 107; 129). These Rydberg series were originally studied by Tanaka and Jursa (129) where they observed four series with different quantum defects. Using the profile of the strong $(2)^3B_2$ photoelectron band (71; 106; 127; 140), signatures of the different $nl\lambda \leftarrow 3b_2$ states have been assigned to peaks occurring between 15.382 eV and the ionisation limit (107) (see Table 2.6). Many of these Rydberg series display vibrational progressions with ~0.135 eV spacings which corresponds to the $(2)^3B_2$ state symmetric stretch harmonic frequency (71; 127). The common ionisation limit of all these series allows quantum defect values for the different series to be reliably determined, facilitating the assignment of the orbital angular momentum and its projection for each series. At slightly higher excitation energies, the Rydberg series corresponding to the $4a_1$ valence electron-Rydberg transitions begin. These states converge on the $(2)^3A_1$ and $(2)^1A_1$ cation states and are observed to dominate the remainder of the 1–20 eV absorption spectrum of NO_2 between 18.8 and 20 eV (77; 107; 127).

2.4 Ion pair formation and dissociative ionisation

Above the first ionisation potential of NO_2, a variety of ion or ion-pair states can be accessed. As most of these states lie above the energetic thresholds for ionic fragmentation, the majority yield charged photofragments. These fragmentation processes are observed to be highly state-specific with different ionic states, and in some cases different vibrational levels within ionic states, exhibiting quite different dissociative be-

haviour (143). The important ionic dissociative processes occurring in NO_2 between 10 and 20 eV are outlined below.

Absorption to autoionising Rydberg levels and the electronic ground state of the cation dominate the NO_2 absorption profile between 9.586 and 12.5 eV. For this reason parent ions are observed to dominate the ion spectrum throughout this energy range (77; 143). Despite this, fragment ions are still formed; albeit with significantly smaller yields. As the ground ion state has been observed to be stable after single-photon excitation between 9.586 and 12.5 eV (143), this implies that fragmentation must be due to excitation to different electronic states. Evidence for such absorption processes is seen in the electron impact experiments of Au and Brion (77) and the VUV experiments of Nakayama *et al.* (97). Au and Brion observed the formation of NO^+ ions close to 10.5 eV while an ion threshold was observed at 10.83 eV in the total ion yield measurements of Nakayama *et al.* As the energetic threshold for dissociative ionisation [to produce NO^+ $(1)\ ^2\Sigma^+$ in coincidence with $O(^3P_J)$] occurs at 12.37975 eV (55; 90) (see Table 2.10), these fragments must be formed via a dissociative ion-pair state. Based on the lowest dissociation limit of NO_2 (55), the lowest ionisation potential of NO (90) and the electron affinity of ground state atomic oxygen (144), NO^+ $(1)^2\Sigma^+$ can be formed in coincidence with $O^-(^2P_{\frac{3}{2}})$ at an excitation energy of 10.9186 eV. Considering the energy resolutions of these experiments and the sample gas temperatures, this energy is in good agreement with the observed thresholds.

As mentioned in the previous paragraph, dissociative ionisation is energetically feasible above 12.37975 eV. However, the stability of the electronic ground state, which is known to correlate with the NO^+ $(1)^2\Sigma^+ + O(^1D_2)$ dissociation limit (142), prevents this process from occurring in single-photon and electron impact experiments at excitation energies below the onset of first electronically excited state of the cation (71; 77; 127; 143). Excitation to this $(1)^3B_2$ electronic state occurs at energies in excess of 12.75 eV (127). After excitation at energies spanning the (0 0 0) or (5 0 0) vibrational levels, the lifetime of the state is observed to reduce from 150 μs to <150 ns (143). Over the same excitation energy range NO^+ $(1)^2\Sigma^+$ fragment ion yields are observed to increase from 0 to 100%. The calculations of Hirst indicate that the $(1)^3B_2$ state correlates, adiabatically, with the NO^+ $(1)^2\Sigma^+ + O(^3P_J)$ dissociation limit (142). The metastability of the ion state is then attributed to the ~0.8 eV barrier

that occurs in the potential between the photoexcited potential well and the dissociative asymptote.

Excitation to the $(1)^3A_2$ ion state becomes energetically feasible close to 13.593 eV (71; 127). The photoelectron signature of this electronic state is markedly linewidth broadened (71; 106; 127; 140) which has resulted in estimates of a sub-100 fs excited state lifetime (71; 127). The short lifetime of the state can be understood in terms of its shallow potential minimum (~0.1 eV) and its correlation with the NO^+ $(1)^2\Sigma^+ + O(^3P_J)$ dissociation limit (142). This is supported by the photoion-photoelectron coincidence (PEPICO) spectra of Eland and co-workers (143). These researchers highlighted that NO^+ $(1)^2\Sigma^+$ ions were formed exclusively following excitation to this electronic state and that on energetic grounds they must have been formed with $O(^3P_J)$ atoms. For this channel, the diatomic fragments were observed to be formed with translational energies that were close to the energetic limit.

The fourth photoelectron band opens at an excitation energy of 14.067 eV and is attributed to the production of NO_2^+ in its $(1)^1A_2$ state. Excitation to the ground vibrational level of this state has been observed to produce both NO_2^+ and NO^+ ions by Eland and Karlsson who measured photoproduct yields of 30% and 70% respectively and inferred an excited state lifetime of ~0.8 μs (143). On excitation with a single quantum of symmetric stretch the fragment ion yield was observed to increase to 100% with a concurrent decrease in excited state lifetime that is inferred to be less than 150 ns at this level. The calculations of Hirst highlight the correlation of this state with the NO^+ $(1)^2\Sigma^+ + O(^1D_2)$ dissociation limit, where this fragmentation threshold is known to occur at an energy of 14.3471 eV (142). The potential was calculated to be bound with a ~0.9 eV barrier to fragmentation to produce $O(^1D_2)$ fragments. Considering the extent of the vibrational progression in the photoelectron band, this suggests that these electronically excited fragments are not formed with appreciable yields after single-photon excitation to this state. The NO^+ fragments that were observed by Eland and Karlsson must therefore be produced via a non-adiabatic transition. The calculations of Hirst suggest that the fragments may be produced via an intersystem crossing to the repulsive $(1)^3B_1$ surface.

The onset of the $(1)^1B_2$ state [14.441 eV (71; 127)] occurs just above the threshold for NO^+ $(1)\ ^2\Sigma^+ + O(^1D_2)$ production. This photoelectron band displays extensive vibrational structure and 100% of the observed ion signal is found to be due to

NO^+ $(1)^2\Sigma^+$ fragments. Eland and Karlsson measured these fragments and estimated an excited state lifetime of less than 70 ns (143). Of the diatomic fragments, 25% are formed with little kinetic energy and were inferred to dissociate via the $O(^1D_2)$ channel, while the remaining fragments must be formed concomitantly with $O(^3P_J)$ atoms. The kinetic energy of both groups of fragments were observed to take up the majority of the excess energy for the fragmentation, suggesting little rovibrational excitation in the diatomic ions. The calculations of Hirst rationalise the lifetime of the ion state in terms of the calculated potential (142). The state correlates adiabatically with the $O(^1D_2)$ limit and is calculated to be bound with a deep well depth and a ~1.0 eV barrier to fragmentation. It therefore seems unlikely that the NO^+ $(1)^2\Sigma^+$ fragments observed by Eland and Karlsson can be produced in coincidence with $O(^1D_2)$. Hirst suggests that an intersystem crossing process to the $(1)^3B_1$ surface is responsible for the production of NO^+ $(1)^2\Sigma^+$ with $O(^3P_J)$ atoms in this case.

Assigning the ion states to particular electronic configurations becomes increasingly difficult above 17 eV due to the broad profiles in the photoelectron spectrum associated with the increasing importance of electron correlation and multiple electronic configurations in describing the excited state potentials (141; 142) (see Table 2.7). This is reflected in the differing assignments of the same photoelectron spectra recorded by Jarvis *et al.* (71) and Baltzer *et al.* (127) who ascribe the photoelectron bands close to 17.07 and 17.20 eV to the $(1)^3B_1$ and $(1)^1B_1$ states and the $(1)^3A_1$ and $(1)^3B_1$ states respectively. Additionally, and in contrast to Baltzer *et al.*, Jarvis and co-workers suggest that excitation to the $(1)^3A_1$ state occurs at an excitation energy above 18.466 eV. As the triplet states are expected to display more intense photoelectron signatures and considering the support provided by the calculations of Schirmer *et al.* (141), the assignment of the 17.07 and 17.20 eV features to the $(1)^3A_1$ and $(1)^3B_1$ sates seems the more reasonable. The assignment of the $(1)^3A_1$ feature is in agreement with the calculations of Hirst (142). However, it is noted that these calculations place the $(1)^3B_1$ state at significantly lower energies and place the $(2)^1A_1$ and $(1)^1B_1$ photoelectron bands within the energy range associated with the strong 17.07 and 17.20 eV photoelectron bands. Despite the uncertainty about the electronic structure associated with these features, the spectra and the symmetric stretch frequencies measured by Jarvis *et al.* and Baltzer *et al.* are in good agreement.

Just below the excitation energies associated with the 17.07–17.20 eV photoelectron bands, a number of dissociative ionisation pathways become energetically accessible (see Table 2.10). At 16.5695 eV dissociative ionisation can occur to form NO^+ $(1)^2\Sigma^+$ fragments in coincidence with $O(^1S_0)$ atoms. At similar excitation energies dissociative ionisation to produce O_2^+ $(1)^2\Pi_g$ with $N(^4S_{\frac{3}{2}})$ atoms (~16.5999 eV) and $O^+(^4S_{\frac{3}{2}})$ atoms with NO $(1)^2\Pi_{\frac{3}{2}}$ fragments (~16.73361 eV) can occur. At the onset of the 17.07 eV photoelectron feature, NO^+ ions dominate the ion spectra with little (77) or no (143) signals observed from parent ions. The dominance of the diatomic fragments is observed at excitation energies between 17.07 and 18.80 eV where the kinetic energy release distribution is observed to be complex with a primary peak close to 2.0 eV and subsidiary maxima at 0.2 and 4.0 eV. As NO^+ fragments can be formed via three different dissociation limits it is tempting to attribute these features to fragments formed via the three different oxygen atom limits. However, without independent measurements of the kinetic energy release of these fragments this cannot be confirmed. Eland and Karlsson attribute the primary peak and the majority of the distribution to slightly vibrationally excited NO^+ fragments formed in coincidence with $O(^1D_2)$ atoms.

Above 17.4 eV, after excitation to the same photoelectron bands, O^+ fragments are observed in the experiments of Eland and Karlsson (143). At the onset of this signal, a yield of 3% is recorded where the O^+ fragments are formed with a kinetic energy that is close to 0.6 eV, indicating that the majority of the the available excess energy is partitioned into translation. The O^+ yield is observed to increase to 14% between 17.4 and 18.1 eV with a slight increase to 15% between 18.1 and 18.8 eV. Here, the kinetic energy release of the fragments was observed to peak close to 0.6 eV across the bands. As the onset of O^+ formation occurs just above the origin of the ~17.2 eV band, it has been suggested that excitation to this cation state is responsible for the O^+ fragments.

Between 18.75 and 20.00 eV, three more dissociative ionisation pathways open to produce NO^+ $(1)^3\Sigma^+$ with $O(^3P_2)$, O_2^+ $(1)^2\Pi_g$ with $N(^2D_{\frac{5}{2}})$ and $N^+(^3P_0)$ with O_2 $(1)^3\Sigma_g^-$ (see Table 2.10). At 18.860 eV a strong electronic transition opens to what is thought to be the $(2)^3B_2$ state (71; 127; 140). Another transition to the $(2)^1B_2$ ion state has also been suggested to occur close to 19 eV by Jarvis and co-workers (71). At excitation energies between 18.9 and 19.4 eV, Eland and Karlsson measured NO^+ and O^+ ions with equal yields of 48% each while O_2^+ fragments were observed with a yield of 4%

Product 1	Product 2	Product 3	Threshold / eV
$NO^+ (1)^1\Pi^+$	$O^-(^2P_{\frac{3}{2}})$		10.9186
$NO^+ (1)^1\Pi^+$	$O(^3P_2)$	e^-	12.3797
$NO^+ (1)^1\Pi^+$	$O(^1D_2)$	e^-	14.3471
$NO^+ (1)^1\Pi^+$	$O(^1S_0)$	e^-	16.5695
$O_2^+ (1)^2\Pi_g$	$N(^4S_{\frac{3}{2}})$	e^-	16.5999
$NO\ (1)^2\Pi_{\frac{1}{2}}$	$O^+(^4S_{\frac{3}{2}})$	e^-	16.7336
$NO^+ (1)^3\Sigma^+$	$O^-(^2P_{\frac{3}{2}})$		17.3222
$NO^+ (1)^3\Sigma^+$	$O(^3P_2)$	e^-	18.7834
$O_2^+ (1)^2\Pi_g$	$N^+(^2D_{\frac{5}{2}})$	e^-	18.9835
$O_2\ (1)^3\Sigma_g^-$	$N^+(^3P_0)$	e^-	19.0644

Table 2.10: NO_2 Dissociation thresholds that lead to ionic fragments and are energetically accessible below 20 eV. The thresholds are calculated using the NO $(1)^2\Pi_{\frac{1}{2}}$ + $O(^3P_2)$ dissociation limit measured by Jost and co-workers (55), enthalpies of formation of NO_2 $(1)^2A_1$ and $N(^4S_{\frac{3}{2}})$ (121), atomic excited state energies and ionisation energies from the NIST atomic spectral database (91) and the relevant diatomic spectroscopic constants (including the ionisation potentials) compiled by Huber and Herzberg (90).

over a relatively narrow excitation window between 18.95 and 19.05 eV (143). At similar excitation energies, Shibuya *et al.* (145) observed NO^+ and O^+ fragments with yields of ~60% and 40% respectively while Au and Brion (77) detected NO^+, O^+ and O_2^+ ions. In the experiments of Eland and Karlsson the diatomic oxygen fragments were observed to be formed with little translational energy, and were therefore attributed to the O_2^+ $(1)^2\Pi_g$ with $N(^2D_{\frac{5}{2}})$ dissociative ionisation limit. The NO^+ and O^+ kinetic energy distributions were observed to be broad across the 18.75–20.00 eV excitation range.

2.5 Summary

The spectroscopy and decomposition behaviour of NO_2 is generally complex and state specific. Between 1.2 and 6.4 eV the absorption spectrum is dominated by valence-

valence transitions to highly coupled electronic potentials. After excitation between 3.12 and 4.96 eV excitation principally occurs to the $(1)^2B_2$ state which is strongly coupled to the $(1)^2A_1$ ground state and to a lesser extent the $(1)^2B_1$ and $(1)^2A_2$ manifolds. Dissociation via the $(1)^2B_2$ state is observed to occur on a sub-picosecond timescale at excitation energies between 3.19 and 4.96 eV. Photoproduct distributions are observed to be markedly non-statistical throughout this range.

At excitation energies between 4.97 and 6.42 eV excitation to the $(2)^2B_2$ dominates. Excitation to this state produces NO $(1)^2\Pi_\Omega$ fragments in coincidence with $O(^3P_J)$ and $O(^1D_2)$ atoms on a sub-100 fs timescale at excitation energies above 5.1 eV. Approximately equal yields are measured for single-photon excitation to this state, greater yields of $O(^3P_J)$ fragments are observed in multiphoton excitation processes to the same final state. The photoproduct distributions produced via this state have been observed to peak with internally excited diatomic fragments via both dissociation limits.

At excitation energies in excess of 6.4 eV the absorption spectrum is thought to be dominated by signatures of Rydberg states; although many other excited valence states are calculated to occur. The Rydberg series that converge on the ground state have been calculated to strongly interact with valence sates in this region. This is thought to result in fragmentation to produce oxygen atoms in coincidence with electronically excited NO fragments. Although few studies of the fragmentation behaviour of NO_2 have been performed between 6.4 eV and the first ionisation potential, many dissociation limits are expected to occur within this excitation range. If populated, the valence states which correlate with these different asymptotes would be expected to produce a variety of electronically excited photofragments that have yet to be observed.

The adiabatic ionisation potential of NO_2 is reached at 9.586 eV but the ground state of the cation is known to correlate with electronically excited fragments and is observed to be stable with respect to excitation from its origin up to 12.5 eV. This has allowed the autoionisation behaviour of high-lying, vibrationally excited Rydberg states to be studied. Higher energy excitation can populate electronically excited cation states which are observed to fragment in state specific manners. The signatures of the fragmentation dynamics via these ion states has been helpful in interpreting signatures of competing multiphoton excitation processes in time-resolved experiments (28).

Chapter 3

Construction and Optimisation of a High Resolution Crush and Direct Current Slice Velocity Map Imaging Spectrometer

3.1 The Leeds VMI spectrometer

The VMI spectrometer that is described in the following pages and was used to carry out the experiments reported in the following chapters is shown in Fig. 3.1 and schematically in Fig. 3.2. It consisted of two differentially pumped chambers, the first for the generation and collimation of a supersonic expansion and the second for optical ion and electron generation with subsequent mass and velocity resolved detection. The two chambers were separated by a skimmer with a 1 mm diameter orifice (Beam Dynamics Inc.) and could be isolated using a gate valve. For the discussion that follows the time-of-flight (TOF) axis of the spectrometer is defined as the x-axis (horizontal axis in Fig. 3.6), the laser propagation axis is defined as the y-axis (the axis going into the page in Fig. 3.6) and the imaging plane is denoted as the (y, z)-plane (where the z-axis is the vertical axis in Fig. 3.6).

The molecular beam chamber of the spectrometer was pumped by a Pfeiffer TMH 1001P turbo molecular pump backed by an Edwards E2M40 rotary pump to achieve a (uncalibrated) base pressure of 5×10^{-8} mbar that was measured using an ion gauge

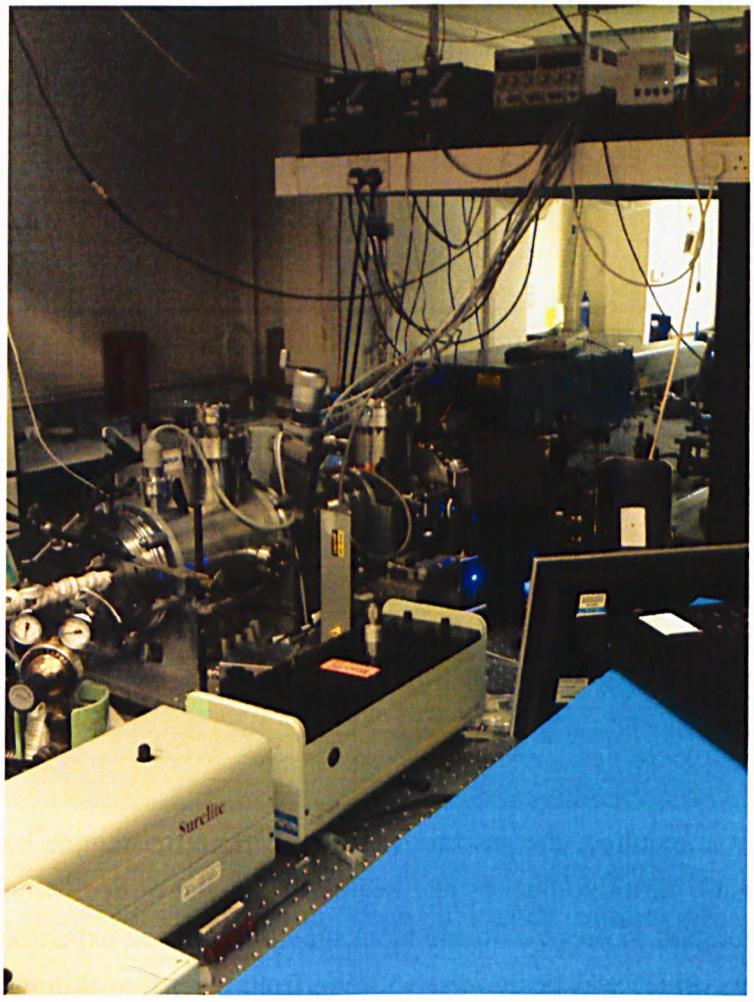

Figure 3.1: The Leeds VMI spectrometer

(MKS hot cathode with a MKS 959 hot cathode controller). In the experiments described in this thesis, pulsed or continuous molecular beams were produced using a Parker Series 9 pulsed valve (General Valve, 500 μm orrifice) with Iota One driver unit (Parker-Hannifen Corporation) or a 50 μm pinhole respectively. The expansion conditions were tailored to particular experiments. In all cases, molecular beams were generated by seeding a small amount of sample in a helium carrier gas. Gas phase species (and liquid phase species with appreciable room temperature vapour pressures) were premixed in a sample cylinder whereas solid phase and liquid phase species with low room temperature vapour pressures were introduced to the carrier gas *in situ*. Where

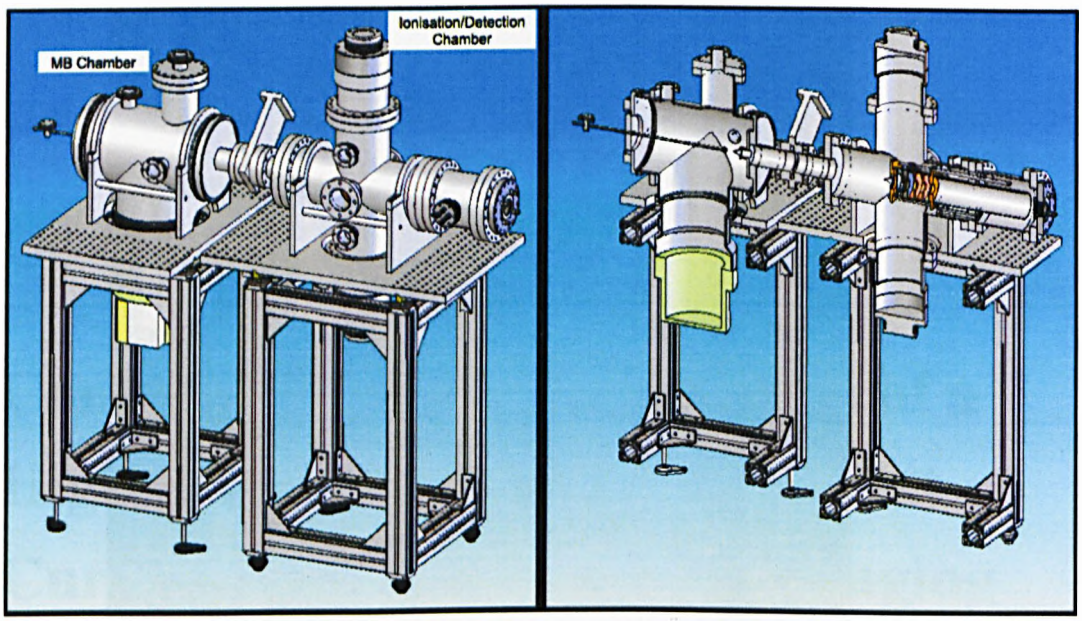

Figure 3.2: SolidWorks schematic (left) and cut through schematic (right) of the Leeds VMI spectrometer

heating was required, the gas line was heated from the sample holder to the nozzle orifice using cartridge heaters and heating tapes, the orifice being held at the highest temperature to prevent nozzle blockage. In all of the experiments reported here, the nozzle orifice was positioned ~50 mm from the 1 mm skimmer used to separate the two chambers and collimate the supersonic expansion. The vacuum windows in the molecular beam chamber allow reagent molecules to be generated photochemically from precursor molecules present in the expansion mixture. By photolysing these molecules close to the molecular beam nozzle orifice the translational velocity spread of the resulting reagent molecules can be minimised and the reagent molecules can be rotationally cooled (although this is not further discussed here).

The photolysis/ionisation/detection chamber was pumped by one or two Leybold Turbovac 361 turbo molecular pumps which were backed by the same Edwards E2M40 rotary pump that was used to back the turbo pump of the expansion chamber. This resulted in an (uncalibrated) ambient pressure of 5×10^{-9} mbar that was measured using another ion gauge (MKS hot cathode with a MKS 919 hot cathode controller). To

Figure 3.3: Electrostatic lens components. All components were machined from 316 stainless steel except for the mounting flange (304 grade stainless steel) and the ruby ball spacers.

prevent the measurement of ions or electrons from the ion gauge, this ion gauge was switched off during experiments. The ion/electron VMI electrostatic lens could be mounted along the axis of the molecular beam propagation direction or perpendicular to this axis. In the experiments reported here the ion optics were mounted on-axis to minimise the effect of the transverse velocity of the molecular beam pulse, allowing the highest possible kinetic energy resolution to be achieved. The electrostatic lens components are shown in Fig. 3.3 and the assembly is shown in Fig. 3.4. The assembly is shown schematically in Figs. 3.5 and 3.6.

The lens was constructed from 316 (A4) stainless steel electrodes separated by 2 mm using insulating ruby balls with 3 mm diameter (Swiss Jewel Company) as spac-

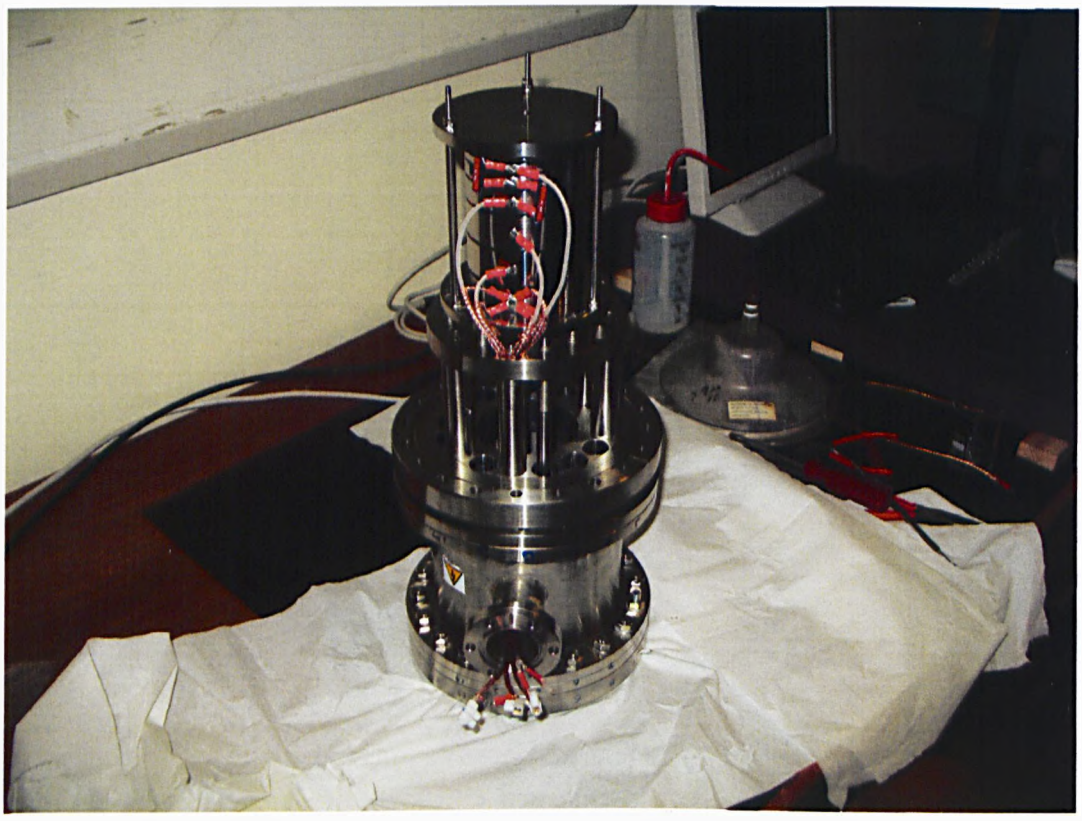

Figure 3.4: Electrostatic lens assembly (the second skimmer and the mu-metal shielding tube are not shown).

ers. Photoions and electrons were created along the axis that defines the centre of the laser port electrode apertures using a variety of light sources (sse Fig. 3.5). Nanosecond neodymium doped yttrium aluminium garnet (Nd:YAG) lasers [Continuum Inc. Surelite SLII-10 or SLIII-10, ~4–7 ns pulse length at full-width half-maximum (FWHM), ~0.124 meV bandwidth FWHM, 10 Hz repetition rate] and their harmonics have been used either directly as photolysis sources or to generate tunable pump or probe radiation using dye lasers (Sirah Laser- und Plasmatechnik GmbH Cobra Stretch with 1800 lines mm^{-1} gratings, ~0.02 meV bandwidth FWHM) or a broadband optical parametric oscillator (OPO) system (Continuum Inc. Surelite OPO, ~9 meV bandwidth FWHM). Alternatively ultrashort laser pulses from a commercial titanium:sapphire chirped pulse regenerative amplifier (146) system have been used where the system

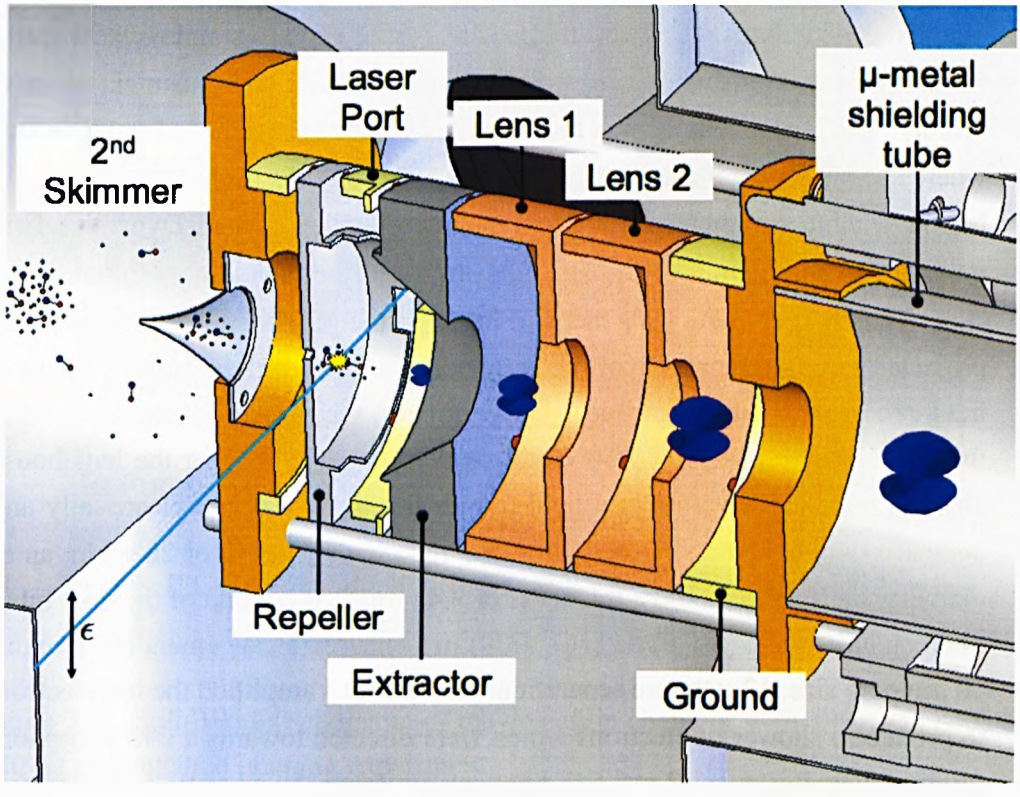

Figure 3.5: SolidWorks cut-through schematic of the lens assembly with a cartoon of the molecular beam skimming process, the dissociation/ionisation process and the projection of the photoion/photoelectron distribution towards the detector face. In all experiments the laser beams enter the electrodes along the spectrometer y-axis and through the 10×10 mm apertures in the laser port electrode.

was pumped by a continuous Nd:YAG laser and seeded by a silica erbium doped fiber ring oscillator (147) (Clark-MXR Inc. CPA 2010, 775 nm, ~150 fs pulse length FWHM, ~12 meV bandwidth FWHM, ~1 kHz repetition rate). The fundamental light was used to generate harmonics or to pump commercial non-collinear optical parametric amplifier (NOPA) systems (148; 149) (Clark-MXR Inc. NOPA or Light Conversion Ltd. TOPAS White). The harmonics and tunable NOPA outputs (450-750 nm, ~15-50 fs pulse length FWHM, 260–140 meV bandwidth FWHM) were used either directly or frequency doubled or mixed to generate ultraviolet (UV) pump or probe pulses.

The VMI electrodes were mounted on an earthed housing which was connected to

a double sided conflat (CF) 150 flange via a set of six 316 stainless steel springs and three adjustment pins which allow translational and angular adjustment of the lens assembly. The lens assembly was held together using three threaded stainless steel rods where the nuts were locked in place using Araldite glue. In the experiments reported here a second skimmer with a 2 mm orifice diameter (Beam Dynamics Inc.) was mounted on the bottom of the lens housing to further spatially collimate the expansion. The charged particles generated between the repeller and extractor plates were projected through the centre of the extractor, lens and earth electrodes by the electric field generated by the electrodes. Depending on the polarity of the electrodes either the photoions or photoelectrons could be detected. On leaving the lens housing the charged particles travelled in a field free drift tube which was electrically and magnetically shielded by an earthed mu-metal tube with a length of 283 mm, an external diameter of 76.20 mm and a thickness of 3.48 mm. At the end of the drift tube a dual microchannel-plate (MCP) detector (150) in a chevron arrangement (40 mm diameter, 10 μm pore size, 12 μm pore separation, Photek Ltd.) amplified the ion/electron signal to produce a shower of electrons which were directed towards a P43 phosphor screen (40 mm diameter, $\tau_{\frac{1}{2}}$=1.2 ms, 548 nm peak emission, 50 cd sr W^{-1} efficiency, Photek Ltd.). The resulting phosphorescence was recorded with a LaVision Imager 3 charged couple device (CCD) camera with a 2.8–12 mm focal length, 1.4 f-number lens and operating with a variable repetition rate. The resulting image frames were analysed using an event counting macro (that was written by André Eppink) and then averaged and post processed on a personal computer using the DaVis software package (version 6.3, LaVision GmbH). Alternatively the total or mass resolved ion or the total electron signal could be recorded by observing the current reduction at the phosphor screen. This was achieved using fixed MCP voltages and monitoring the alternating current component of the voltage at the phosphor screen. Here, a capacitor and inductor in the phosphor screen power supply line was used and the voltage reduction between them was recorded in time using an oscilloscope (LeCroy Waverunner 6100). The resulting signals could then be averaged and saved to a file using a general purpose interface bus (GPIB) connection from the oscilloscope to a personal computer. This allowed TOF or mass gated REMPI spectra to be recorded.

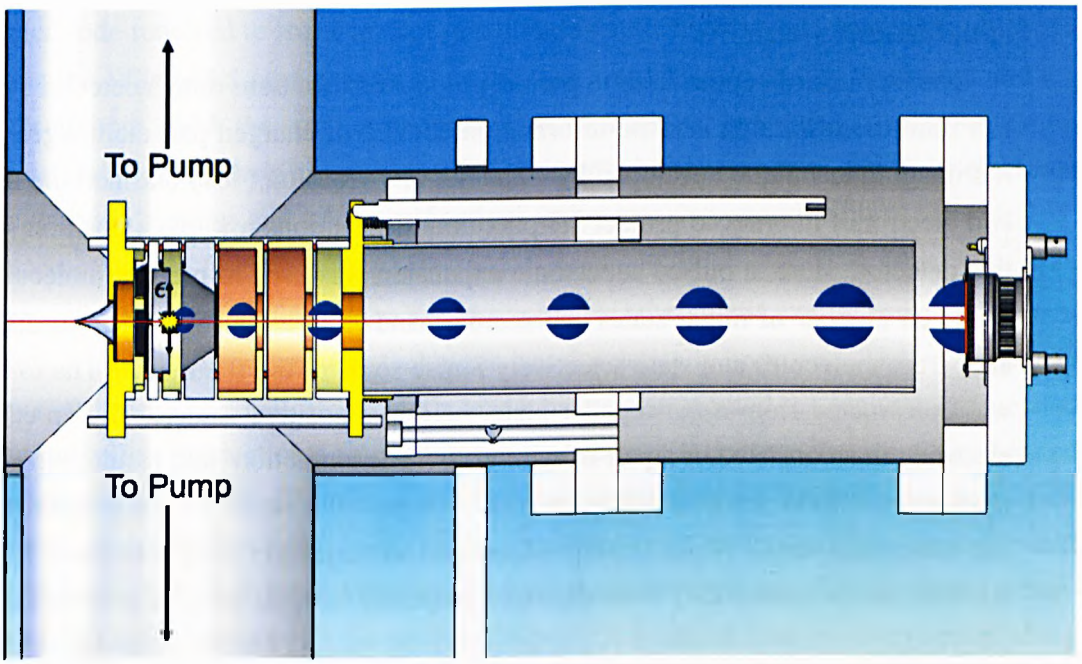

Figure 3.6: SolidWorks schematic of the detection chamber with a cartoon depicting a direct current slice imaging experiment.

3.2 Electrostatic lenses and VMI optimisation

3.2.1 Product imaging and velocity map imaging

Product imaging methods are used in order to measure 3D electronic, atomic or molecular distributions in order to understand state-resolved decomposition/reaction dynamics in detail. These measurements are usually achieved using the electric field generated by two or more electrodes to project a charged particle distribution onto a two-dimensional (2D) position sensitive detector. The arrival time of the charged species can then be related to their mass and the radial and angular profiles can be related to the fragment kinetic energies and the decomposition/reaction dynamics respectively. The mass, kinetic energy and angular resolution of these experiments is determined by the distribution of the reagents over initial or photoexcited quantum states, the energy spread associated with an ionisation process, the construction and operating voltages of the electrodes used to project the distribution and the spatial and temporal resolution

of the detector system.

The ion/electron optics used to project product distributions onto a detector system can limit the resolution and the information content of charged particle images. The ion imaging technique developed by Chandler and Houston (151) outlined the use of two electrodes in order to project 3D photoion distributions towards a position sensitive detector. Here, a pulsed supersonic expansion was used to prepare molecules in a limited number of initial states and narrow bandwidth lasers were used to dissociate parent molecules and state selectively ionise some of the fragments. The ion lens was constructed from a flat repeller plate, held at a positive voltage, and an earthed electrode that consisted of a pair of wire grids. The extraction field resulted in a negative electric field gradient along the TOF axis and flat lines of equipotential along the orthogonal axes. When photoproducts and subsequently photoions were formed between the two plates they were therefore projected through the wire grids and onto a 2D position sensitive detector. A phosphor screen was positioned behind the detector in order to convert the amplified electrical signal to visible photons which were photographed using a conventional camera. The radius of the resulting image was related to the product of the fragment velocity and the ion TOF. Hence the velocity profiles, and thus the internal state, and angular distributions of the photofragments could be examined to provide insight into the mechanism of the photofragmentation process. A few years later apparatus was developed that allowed photoelectron distributions to be studied in a similar way (152).

Unfortunately in the ion and electron imaging experiments referred to above, the radial resolution was limited by the size of the ion/electron production volume and the distortion of the ion/electron trajectories as they passed close to the grid electrodes (153). In order to limit the severity of the grid distortions, fine mesh grids had to be used which limited the charged particle throughput and thus the ion/electron signal. Like the kinetic energy, the mass resolution of the ion imaging technique was also limited by the ion production volume and was further degraded by the turnaround time associated with products formed with their velocity vectors pointing away from the detector. Although it was well known at this stage how the mass resolution of the technique could be improved [using the space focusing approach adopted by Wiley and McLaren in their TOF-mass spectrometer (MS) in 1955 (154)], the extra grid

electrode required to focus ions of given mass with a higher mass resolution (<1% using the Wiley-McLaren approach) resulted in lower kinetic energy resolution and ion throughput. With the conflicting requirements of kinetic energy/angular, mass resolution and signal intensity, compromises were sought between two and three electrode extraction systems and grid specifications in ion imaging experiments (155; 156; 157; 158; 159; 160; 161; 162; 163; 164; 165).

With the introduction of the VMI technique (1) the kinetic energy and angular resolution limit of the ion imaging technique was dramatically improved. The improvement was the result of a new electrostatic lens which circumvented the problems associated with the ion production volume and the ion/electron trajectory distortions associated with grid electrodes. By using a flat repeller plate in conjunction with two open aperture extraction electrodes, grids could be removed from the lens assembly which could increase ion throughput to 100% and remove the distortions associated with the extraction grids. Furthermore the lens assembly produced curved lines of equipotential along the TOF axis of the lens assembly, which allowed charged particles to be focused in the two transverse directions; where these directions can be used to define the (y, z)-plane. It was theoretically and experimentally demonstrated that when the three electrodes (repeller, extractor and earth) were held at a particular voltage ratio, charged particles could be focused at different radii at the detector face according to their velocity in the (y, z)-plane. This mapping of the fragment velocity to detector radius was found to be linear, the effect was found to be essentially independent of the mass to charge ratio of the particle and, over a limited range, the position of formation in the (y, z)-plane. This focusing regime was termed VMI.

An ion trajectory simulation is shown schematically in Fig. 3.7 where the simulation was performed using the SimIon 7 (Scientific Instrument Services Inc.) ion and electron optic simulation software. The ion lens used in the simulation is based on the design outlined in the original VMI paper (1). It incorporated a circular repeller plate with a diameter of 80 mm, a thickness of 3 mm and a 4 mm hole for the introduction of a molecular beam along the TOF axis, or what is also defined here as the x-axis, of the spectrometer. The extractor electrode also had an external diameter of 80 mm and a thickness of 3 mm. This electrode was separated from the repeller electrode by 20 mm along the x-axis and incorporated a 28 mm aperture. The third, earth, electrode

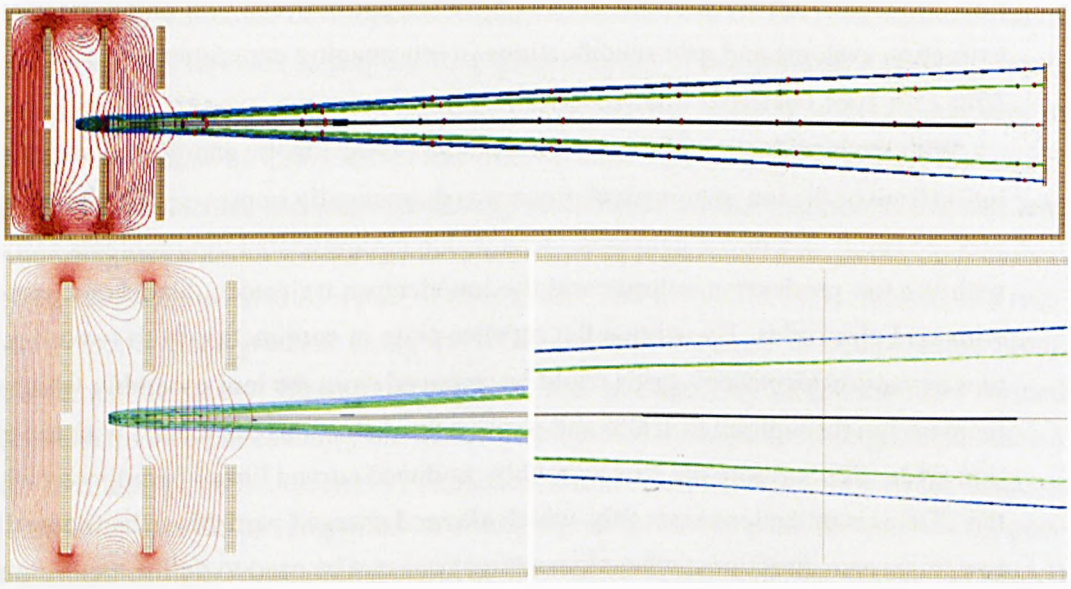

Figure 3.7: Simlon 7 simulation of atomic oxygen ion trajectories caused by a set of electrodes based on the design of Eppink and Parker (1). The electrodes have a 80 mm diameter and the extractor and earth electrodes have a 28 mm aperture. The electrodes are 2 mm thick and are separated by 20 mm. The distance between the ion formation points and the detector face is fixed at 410 mm resulting in a drift tube length of 372 mm. Oxygen ions are generated with 1.5 eV of kinetic energy and are ejected at 0, 45 , 90, 135, 180, 225, 270 and 315°. Ions are formed in the center of the repeller and extractor plates as well as 1 mm above and below this point in order to demonstrate the re-centring effect of the VMI electrodes. The red dots on the ion traces represent the ion positions separated by 500 ns time increments. Here a repeller voltage of 1000 V is simulated and an extractor voltage of 732 V is used. This extractor to repeller voltage ratio results in the preferential velocity focusing of the oxygen ions initially ejected at angles of 90 and 270°.

was displaced from the extractor by 20 mm along the x-axis and had identical dimensions to the extractor electrode. When ions or electrons were formed in the centre of the repeller and extractor electrodes in the x-dimension, an extractor-repeller voltage ratio, $\frac{V_E}{V_R}$, of 0.732–0.735 results in velocity map imaging at a planar detector face for a field-free drift distance of 372 mm and repeller voltages, V_R, between 500 and 5000 V. The simulation shown in Fig. 3.7 displays the ion trajectories when a repeller voltage of 1000 V is implemented with an extractor voltage, V_E, of 732 V to achieve velocity focusing of the oxygen ions. Here the drift distance is defined as the minimum separation of the earth electrode to the front face of the detector. The total ion/electron distance of flight, DOF, is therefore 410 mm. The trajectories shown in Fig. 3.7 display atomic oxygen ions formed with kinetic energies of 1.5 eV and initially traveling at 0, 45, 90, 135, 180, 225, 270 and 315° with respect to the x-axis where direct travel towards the detector face is defined by an angle of 0°. Ions are formed in the centre of the (y, z)-plane (i.e. at the point in the plane defined by the axis of symmetry of the lens assembly) and also 1 mm above and below this point along the y-axis (which is defined as the vertical direction in Fig 3.7 but is the axis going into the page in Fig. 3.6). This y-displacement simulates the largest dimension of the ionisation volume associated with the molecular beam source (i.e. the molecular beam diameter). The displacement of the ion generation points is shown in the bottom left panel of Fig. 3.7. The red lines around the electrodes represent lines of equipotential and the red dots on the ion trajectories show the ion positions at 500 ns increments.

The simulations in Fig. 3.7 highlight a number of important aspects of the lens assembly. Firstly the curved red lines of equipotential highlight the focusing effect of the cylindrically symmetric electrodes in the (y, z)-plane. The field gradient along the x-axis then shows the extraction effect and the ability of the assembly to turnaround charged particles (of low enough momentum) which are initially traveling away from the detector. The blue, green and black lines illustrate different ion trajectories. The blue lines represent the paths of oxygen ions which are formed with initial recoil angles of 90 and 270° and at different positions along the y-axis of the spectrometer. The green lines represent the paths of ions formed with initial recoil angles of 45, 135, 225 and 315° at different ion creation points along the y-axis. The black lines represent similar trajectories of ions formed with initial recoil angles of 0 and 180°. Charged particles formed at different positions along the y-axis with different initial recoil angles [but

the same velocity in the (y, z)-plane] are focused over a narrow detector radius, this re-centring effect of the lens assembly is partially responsible for the increase in energy and angular resolution with respect to the ion imaging technique (1). It is noted that the spherical and chromatic aberration associated with this lens assembly is precisely what allows the electrodes to achieve VMI. However, these aberrations also cause a few unwanted effects.

In all of the simulations shown here, the extractor electrode potential has been adjusted to optimally focus charged particles striking the detector face at maximum radii (corresponding to fragments that were ejected at 90 and 270° with maximum kinetic energy). In Fig. 3.7, the repeller electrode potential was set to 1000 V and the extractor potential was set to 732 V. This results in relatively tight focusing at the maximum radius, however, the bottom right panel of Fig. 3.7 shows that the charged particles with lower velocities in the (y, z)-plane are not focused as tightly at the detector. In fact oxygen ions (or any other charged particles) with lower velocities in the (y, z)-plane reach a focus beyond the detector face, resulting in lower velocity resolution for these particles. In a similar way, charged particles with greater velocities in the (y, z)-plane would reach a focus before the detector face. The VMI lens is optimally focused at a single radius only, the spherical and chromatic aberration which is responsible for this focusing regime results in a focal curve in the TOF direction (as shown in the bottom right panel of Fig. 3.7). Furthermore a particular $\frac{V_E}{V_R}$ optimally focuses charged particles formed at a single point in the x-dimension between the repeller and extractor plate only. In practice the ionisation volume has a finite width along the TOF direction (usually between 30 and 8000 μm depending on the probe beam profile, focus and wavelength). At the VMI voltage ratio, this cannot be compensated for and the effect reduces the achievable kinetic energy resolution using this type of electrostatic lens (see Fig. 3.9).

The negative electric field gradient between the repeller and extractor electrodes allows ions or electrons which are initially traveling away from the detector to be turned around. The magnitude of this field gradient affects the compression of the photofragment Newton spheres along the TOF axis. A large field gradient increases the mass resolution of the spectrometer, however, this resolution is always less than that of a Wiley-McLaren mass spectrometer with equivalent drift tube length [unless a reflectron is implemented between the electrodes and the position sensitive detector (166)].

The reduction of mass resolution with the VMI lens in comparison to a three electrode ion imaging instrument is a consequence of the fact that VMI and space focusing (154) cannot be simultaneously achieved. Despite this, moderate mass resolution can be achieved using the VMI technique [1 atomic mass unit (amu) in 50 using a standard VMI lens operating at relatively low repeller voltages and a 400 mm drift tube].

3.2.2 Image inversion and slice imaging

Since the introduction of the VMI technique a number of different methods have been used in order to extract the velocity and angular profiles of the projected ion or electron distributions. In the original ion imaging and VMI experiments the inverse Abel transform was used in order to reconstruct the meridional slice of the 3D scattering distribution from its 2D projection (167; 168). This analytic inversion method relies on a small ratio between the initial and final kinetic energy of the photofragments in order to process the image line-by-line and is only applicable to distributions of charged particles that had an axis of cylindrical symmetry in the imaging plane. Additionally the method is notoriously sensitive to noise and most numerical approaches proposed for implementing the Abel inversion have a built in smoothing mechanism to reduce this problem. The Fourier-Hankel algorithm is one such approach that is routinely used to solve the inverse Abel integral. However, the transform still magnifies image noise and results in its accumulation toward the image centre line. This can introduce artefacts that were not present in the raw image, particularly when noisy images are back transformed. Alternative analytic approaches like the back-projection or onion-peeling method (169; 170; 171) make similar assumptions to those of the inverse Abel methods when they are practically applied to velocity map image reconstruction. These methods also accumulate noise at the image centre line but under certain circumstances also over-subtract the contribution of faster fragments, an effect that is accentuated by noisy images (172).

Alternative methods have been implemented that address some of the limitations of the aforementioned inversion methods. The iterative inversion method developed by Vrakking approaches the inversion problem by calculating the projection of an assumed 3D particle distribution and comparing the result to the experimental projection (173). This is a so called forward convolution approach. Based on the similarity

between the projection of the test distribution and the experimental image, the assumed 3D distribution is adjusted. This process is then iterated until an acceptable level of agreement is observed between the test projection and the experimental data. Initial guesses for 3D distribution can be made using the similarity between the radial profiles of the 3D distribution and the experimental 2D projection or the initial 3D distribution can be obtained by inverse Abel transforming the data. As the method describes all data in polar rather than Cartesian co-ordinates, the noise associated with the inversion is projected towards a central spot in the image as opposed to the image centre-line.

A similar approach to that detailed above has been developed by Dribinski and co-workers who expanded the 2D image projection over a set of basis functions that are projections of Gaussian like functions (174). In this case the inverse Abel transforms of the basis functions are analytically known and the resulting basis function coefficients then contain the necessary information to reconstruct the 3D particle distribution. This approach is referred to as the Basis Set Expansion or more commonly just the BASEX method. As the method is carried out in Cartesian co-ordinates, experimental noise is accumulated at the image centre-line affecting the angular distribution fidelity, although to a lesser degree than the Hankel method.

Of the various algorithms considered above, the BASEX method was found to outperform the other inversion methods in the majority of a range of image inversion tests (175). However, since these tests were performed a number of improved implementations of the tested inversion techniques have been reported. The BASEX method has been adapted and re-written to carry out the inversion in polar co-ordinates (172). Here, the image noise is concentrated at the image centre and notable improvements in inversion speed are demonstrated resulting in this method, referred to as pBASEX, being widely adopted. A similar polar co-ordinate formulation of the onion-peeling method has been reported by Zhao *et al.* (176) where the inversion speed of this polar onion peeling (POP) method was subsequently increased by Roberts *et al.* (177). These researchers used the ideas employed in the BASEX method by using a basis set of radial distribution functions in order to efficiently calculate the 2D projections that are used for the onion peeling subtraction. The researchers report similar reconstruction accuracy and speeds to those of the pBASEX approach. Alternative iterative inversion methods have also been proposed by Renth and co-workers (178). Here

the inversion accuracy was increased further by applying physically meaningful constraints to the inversion process and by considering noise statistics. These methods also implemented a cross validation procedure using different halves or quadrants of the image. This allowed the inversion algorithms to be terminated after the optimum number of iterations. These modern inversion methods are reported to produce highly accurate radial and angular profiles which are effected by image noise to a much lesser degree than the inverse Abel methods originally implemented in ion imaging and VMI experiments.

Although efficient and reportedly accurate methods of reconstructing the meridional slice of an axisymmetric projected 3D distribution are now available, the extension of these methods to reconstruct non-axisymmetric distributions is in general not possible. Situations predominantly arise in crossed molecular beam experiments where the reaction product distributions do not possess an axis of cylindrical symmetry but the loss of symmetry can also occur when photoproduct distributions are measured. In the latter case axial symmetry can be lost when linear pump and probe laser polarisations are crossed. In photodissociation experiments involving randomly oriented gas phase molecules this loss of symmetry is the result of photofragments being produced with a polarised distribution of angular momentum vectors. If the photoproduct distribution is probed via an intermediate resonance, this provides sensitivity to this polarisation; photofragments whose angular momentum vectors are aligned preferentially with respect to the probe laser polarisation will be more efficiently probed. In this way the angular profile of velocity map image features will be modulated according to the recoil vector of the probed fragments, the alignment of the fragment angular momentum vectors, the probe laser polarisation vector and the sensitivity of the probe transition to the alignment effects. Due to these sensitivities where crossed laser polarisations are used to probe aligned photoproduct distributions, the probe light-fragment interactions can result in the loss of axial symmetry in the resulting ion or photoelectron cloud. If we were able to reconstruct the 3D charged particle distribution generated using different laser polarisation combinations or directly measure the central slices of these distributions, and provided we knew the identity of the intermediate resonance in the probe step, we would have enough information in order to obtain not only the photoproduct energy distribution and the translational anisotropy parameters of the image features but also the molecular-frame alignment parameters that describe the fragment

angular momentum polarisation. These molecular-frame polarisation moments would then give us detailed information about decomposition process and are a sensitive way of probing short-lived optically dark potentials in an energy resolved (nanosecond) experiment.

There are a number of different methods which can be used in conjunction with velocity map imaging to extract dynamical parameters from the projections of non-axially symmetric charged particle distributions. Since the earliest crossed-molecular beam imaging experiments forward convolution approaches have been used in order to obtain product speed and angular distributions (29; 30; 31; 32; 33). Here, a trial differential cross-section is taken and the resulting 2D projection of the products generated by such a cross-section is simulated by forward convolution. The simulated projection is then compared with the experimental image and the initial trial cross-section is refined. The process is then iterated until good agreement is reached between the trial cross-section and the experimental image. A similar approach can be applied to obtain the speed, translational angular and angular momentum alignment and/or orientation distributions from the photoproducts of a unimolecular decomposition process when a set of laser polarisation dependent images are recorded. This type of approach has been applied to extract alignment or orientation moments (as well as the photofragment velocity and angular distributions) from velocity map images by a number of research groups (179; 180; 181; 182). Alternative methods of extracting these dynamical parameters include the Fourier moment analysis developed by Bass and co-workers (183). Here, iterative fitting to the projected images is used to evulse alignment, orientation and translational anisotropy parameters from sets of projected images. An interesting, yet experimentally intensive method, has also been recently demonstrated by Wollenhaupt *et al.* (40). Here, many laser polarisation combinations were used in order to tomographically reconstruct the highly complex photoelectron distributions that were generated using polarisation shaped laser pulses from many 2D projections. It is also noted that the onion-peeling methods of Winterhalter *et al.* (170) and an adapted version of the pBASEX method (172) could be applied to invert images produced from non-axisymmetric charged particle distributions. However, to the author's knowledge these methods have yet to be applied to VMI experiments where cylindrically asymmetric charged particle distributions have been measured.

A different approach to extracting dynamical parameters from charged particle distributions is to directly and exclusively detect the meridional slice of a product distribution. For an axially symmetric photoproduct distribution and within the limit of an infinitely narrow slice width, this equatorial slice is equivalent to the inverted image obtained from one of the analytic inversion algorithms discussed above. In the slicing experiment the approximation is made that the finite slice width is narrow enough that it is a good representation of an infinitely narrow slice of the photoproducts. Where this is a good approximation high kinetic energy resolutions can be achieved with the concomitant measurement of accurate angular distributions (184; 185; 186). As reconstruction algorithms often introduce artificial noise, and in some cases artefacts, to the radial and angular profiles of velocity map images, good slice image data can yield superior kinetic energy resolution and angular distribution fidelity with respect to analytically inverted crush images. For cylindrically symmetric photoproduct distributions slice imaging techniques yield the full translational energy and anisotropy information of the photoproduct distribution directly, obviating the need for reconstruction procedures. In the case of aligned or oriented photoproduct distributions, images can be recorded without symmetry restrictions. Alignment or orientation moments, translational anisotropy parameters and photoproduct energy distributions can then be obtained by fitting to the angular profiles of the slice image features.

A number of different methods have been proposed to slice photoproduct distributions. By delaying the ionisation laser and positioning it down the TOF axis with respect to the photolysis light field, Tonokura and Suzuki outlined how the central slice of a photofragment distribution could be selectively ionised by focusing the probe pulse into a laser sheet (187). Here the slice resolution was determined by the pump-probe delay/probe laser position along the TOF axis, the fragment kinetic energy release and the probe laser pulse duration. Favourable aspects of this optical slicing technique are the narrow slice width (which is limited by the laser focus along the spectrometer TOF axis and the ionising laser pulse width) and that the spatially separated fragments are ionised, reducing space charge and transition saturation effects. However, the high laser pulse fluences that are generally required to drive REMPI processes are often difficult to realise over the laser sheet. Additionally it is difficult to achieve a homogeneous and reproducible probe laser fluence across the sheet. Therefore, two alternative selective ionisation schemes have been proposed to achieve

optical slice imaging (50; 184) which under certain circumstances improve ionisation efficiency/uniformity and reproducibility.

Alternative slicing techniques have been developed in order to selectively detect the central slice of the entire charged particle distribution. Gebhardt and co-workers used a set of pulsed extraction electrodes in order to temporally stretch photoion distributions along the TOF axis (188). The electrodes were made up of a repeller and earthed extractor grid in order to accelerate the ion distribution towards the detector face and a three element Einzel lens that was used to achieve VMI. Here the extraction field on the repeller was pulsed with the potential on the central Einzel lens electrode. This allowed the photofragments to expand under field-free conditions before being extracted and velocity focused by the switched electrodes. By gating the voltage at the detector at the correct temporal delay, the central slice of the expanded ion distribution could then be detected exclusively. A similar approach was implemented by Cruse and Softley who applied the technique to Rydberg tagged molecules which were field ionised by the pulsed electrodes (189). As REMPI or direct ionisation schemes are not always possible, this approach extended the range of systems that could be studied using this pulsed extraction slice imaging technique. A strength of the pulsed extraction technique over other slice imaging methods is that any neutral photofragment distribution can be effectively sliced with easily achievable detector gate widths provided a big enough extraction delay can be achieved and a suitable ionisation scheme is available. However, the grid electrode and the electrode pulsing used in the technique lead to distortions of the photoion distribution, compromising the kinetic energy and angular resolution of the VMI technique. For this reason Chestakov *et al.* applied a similar delayed extraction scheme using a conventional VMI lens (184), thus removing the grid distortions. In this case both the repeller and extractor electrodes had to be pulsed. However, in these experiments the fidelity of the VMI was still limited by the electrical ringing and finite switching time associated with the electrode pulsing.

As alternatives to the slicing methods discussed above, two slicing schemes were proposed to temporally stretch the arrival time of charged particle distributions at the detector face without using grid electrodes or pulsed extraction fields. Both of these schemes rely on static electric fields where the extraction field gradients were significantly reduced with respect to those employed in Eppink and Parkers original VMI experiments (1). Townsend *et al.* increased the charged particle TOF spread by adding

an extra open aperture electrode to the conventional VMI electrode stack (50). This allowed the electric field strength between the repeller and extractor electrodes to be reduced where the velocity focusing was then achieved by adjusting the voltage of another open aperture electrode. Here the expansion of the ion cloud was associated with the increase in turnaround time of photoions originally travelling away from the detector face. Provided the extraction field strength was low enough, these photoions could not catch up with the fragments initially travelling towards the detector. By pulsing the imaging detector voltage, this allowed the central slice of the photoion distribution to be selectively detected. Subsequent experiments in the same research group incorporated a fourth open aperture electrode to further increase the spread of the Newton spheres and reduce the effective slice width (185). The extraction scheme was termed DC slice imaging.

Using the same principles as those implemented by Townsend *et al.*, a more elaborate 29 electrode stack was implemented by Lin and co-workers in order to stretch photoion Newton spheres along the TOF axis (36). With these electrodes two regions of weak and highly homogeneous extraction field were produced. Here, the weak extraction field resulted in an extensive spread in ion TOF and the transition between the two electric field regions allowed velocity focusing to be achieved. Additionally the weak field strengths and the field homogenety result in a low sensitivity to the ion formation point along the TOF axis and good velocity focusing for a large range of ion generation points in the transverse directions. These aspects of this lens system were particularly useful when it was applied to crossed molecular beam imaging experiments. However, for obvious reasons, the four electrode scheme, or a five electrode variant, of the DC slice imaging technique has usually been implemented in photodissociation studies.

A number of points should be made about the slicing schemes described above. As the aim of these experiments is to selectively detect the central slice of the charged particle distribution, the vast majority of the experimental signal is purposefully neglected. This signal reduction becomes increasingly severe when slicing experiments are performed with narrower gate widths. In experiments where the equitorial slice of the distribution corresponds to an azimuthal angle that is orthogonal to the favoured recoil direction or where the measured slice corresponds to a portion of the product Newton sphere that was inefficiently ionised due to fragment polarisation, the loss of

signal is further compounded. Where signal strengths are low these effects will prohibit the use of slicing techniques.

In slice images the ratio of the slice to total Newton sphere width inherently reduces as the image radius or fragment kinetic energy decreases. This results in a systematic reduction of kinetic energy resolution and accuracy of the kinetic energy intensity profile and angular distribution with image radius. These effects may be expected to be particularly problematic when the alignment or orientation of photoproducts are studied as a function of kinetic energy, as in this case the alignment moments associated with image features at different radii will be sampled to different degrees. Unfortunately, however, the influence of these effects on the dynamical parameters obtained from slice images is yet to be quantitatively studied. All that can be stated presently is that provided temporally short detector gates are used and the fragments with minimum kinetic energy are sufficiently stretched along the TOF axis, errors in the dynamical parameters will be minimal and the slice images can be treated in the same manner as inverted crush images. In situations where the slice to Newton sphere width ratio is large, energy and angular distributions should be corrected (15), although, simple correction schemes for distributions with kinetic energy dependent anisotropy parameters are yet to be developed. These corrections could be made using the forward convolution approaches outlined above, but in this case implementation of these methods nullifies the principle benefits of the slice imaging approach. For this reason, where photofragment distributions cannot be thinly sliced, projection and reconstruction approaches are more favourable due to the greater signal intensities.

DC slicing experiments are attractive variants of the slice imaging methods due to the relative ease of implementation and the similarity of the apparatus required to perform them and crush VMI experiments. An additional benefit of the DC slicing technique is that the weak extraction field results in stable extraction conditions and a reduced velocity focusing sensitivity to the ion generation position along the TOF axis. However, the method also has some significant limitations that must be considered so that these experiments can be performed effectively. As the amplification efficiency of the MCP detectors used in charged particle imaging experiments increase with the momentum of the detected species along the TOF axis, the electron signals that the detectors produce are notably reduced when weak field charged particle extraction is used instead of the higher extraction fields commonly employed in conventional VMI

experiments. Furthermore, the expansion of photoproduct distributions along the TOF axis is facilitated by the momentum of the photoproducts. This means that heavy photofragments formed with large kinetic energies can have large TOF spreads and can be effectively sliced using relatively large detector gate widths and commonly implemented flight tube lengths. In contrast light species and/or those formed with low kinetic energies are more problematic. Hydrogen atoms with low kinetic energies are difficult to slice effectively and so far nobody has been able to apply the technique (or any other slicing scheme) to a distribution of photoelectrons. Although a number of procedures can be used to slice slow and/or light photoproduct distributions at fixed laser excitation energies (using reduced repeller voltages, extended TOF tubes and short gate widths), these approaches either result in a significant loss of signal or may result in photoproduct distributions which expand too much to be completely detected. For these reasons compromises often have to be made between kinetic energy resolution/angular distribution fidelity and signal levels so that good signal-to-noise levels are maintained. With the strengths and limitations of the DC slice imaging method in mind it is desirable to be able to carry out crush velocity map imaging experiments with subsequent image inversion and slice ion imaging experiments for high kinetic energy resolution detection or the detection of non-axially symmetric photoion distributions using a single spectrometer. In this way imaging experiments can be tailored to solve particular problems.

3.2.3 The Leeds electrostatic lens assembly

The electrostatic lens assembly that was constructed for the Leeds VMI spectrometer is based on the designs of Yonekura *et al.* (31) and Wrede *et al.* (190). Whereas the three lens VMI electrodes proposed by Eppink and Parker (1) allow VMI to be achieved at a single voltage ratio, the six electrodes incorporated in this lens system allowed VMI to be achieved over a range of voltage ratios. This allowed the ion/electron extraction conditions to be tailored to particular experiments and was exactly what allowed the spectrometer to function effectively in both crush and slicing modes.

In order to optimise the operation of the lens, extensive ion and electron trajectory simulations were performed so that different extraction voltage schemes could be developed. Through a variety of simulations it was found that extractor to repeller voltage

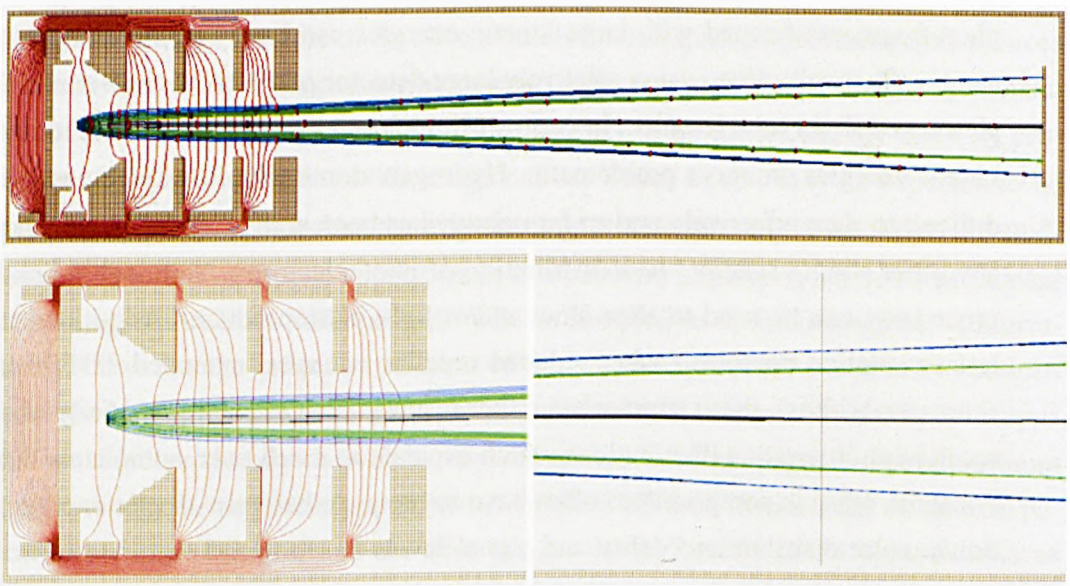

Figure 3.8: SimIon 7 simulation of atomic oxygen ion trajectories caused by the Leeds VMI electrode set. Here, oxygen ions are generated with 1.5 eV of kinetic energy and are ejected at 0, 45 , 90, 135, 180, 225, 270 and 315°. Ions are formed in the center of the laser port electrode aperture as well as 1 mm above and below this point in order to demonstrate the re-centring effect of the VMI electrodes. The red dots on the ion traces represent the ion positions separated by 500 ns time increments. A repeller voltage of 1000 V is simulated with a laser port electrode voltage of 930 V, an extractor voltage of 860 V and lens 1 and lens 2 voltages of $\frac{2}{3}$ and $\frac{1}{3}$ of the extractor voltage respectively. This corresponds to Voltage Scheme 1 referred to in the text. The relatively high extractor to repeller voltage ratio of the lens system, 0.86, with respect to that of the Eppink and Parker lens, 0.73 (see Fig. 3.7), results in a weaker extraction electric field that increases the turnaround time of ions formed with velocity vectors initially pointing away from the detector. Velocity focusing is then achieved by the lensing effect of the two electrodes further down the spectrometer TOF axis. An increased TOF and spread in ion arrival time is observed at the detector with respect to the lens shown in Fig. 3.7.

ratios between 0.74 and 0.88 could be implemented at repeller voltages between 500 and 5000 V while retaining VMI conditions. Here, the lens electrodes were adjusted to different voltages that depended on the extractor-repeller voltage ratio in order to velocity focus the charged particle distributions at the detector. It was found that good velocity focusing could be achieved for the aforementioned extractor-repeller voltage ratios for a range of fragment masses and kinetic energies. In the simulations, trajectories of charged particles with masses between 9.109×10^{-31} and 2.107×10^{-25} kg (e^- and I^+ respectively) and kinetic energies between 0 and 4 eV were considered. It is also noted that $\frac{V_E}{V_R}$ ratios that are greater than 0.88 could be implemented for the lens assembly, however, under these conditions tight velocity focusing could only be achieved over limited repeller voltages.

A number of restrictions were applied to the lens voltages for the trajectory simulations. Firstly, all voltages were constrained to have the same polarity to minimise the number of power supplies required in real experiments. Secondly the electrode voltages were limited so that the voltage difference between consecutive lenses in the assembly were less than 2500 V to prevent electrical discharge. Finally the laser port voltage was always set at $(\frac{(V_R-V_E)}{2} + V_E)$ in order to produce a stable and homogeneous initial extraction field.

Through the trajectory simulations, it was found that for fragments formed with a single velocity the tightest velocity focusing at the detector face was achieved for $\frac{V_E}{V_R}$=0.86–0.88. These voltage ratios also result in the largest spread in arrival time of the fragments at the detector. As the TOF spread produced for $\frac{V_E}{V_R}$=0.86 was sufficient for the majority of ion slicing experiments and the detector signal would be largest for this ratio, an electrode voltage scheme was adopted using a ratio that was close to this. In this scheme the lens 1 and lens 2 voltages were fixed at $\frac{2}{3}$ and $\frac{1}{3}$ of the extractor voltage respectively in order to velocity focus the photofragments. Here the focus of the lens assembly was adjusted by changing the voltage of the extractor electrode (and therefore the voltages of lenses 1 and 2) at a fixed repeller voltage. This corresponds to Voltage Scheme 1 that was used to generate the ion trajectory simulation shown in Fig. 3.8.

The simulation shown in Fig. 3.8 displays the trajectories of oxygen ions formed under similar conditions to those presented for the Eppink and Parker lens in Fig. 3.7 (1.5 eV kinetic energy, ejection at angles of 0, 45, 90, 135, 180, 225, 270 and 315° and

ion generation at three points vertically separated by 1 mm and in between the extractor and repeller electrodes). Here the ions were generated in the centre of the laser port electrode aperture resulting in a total DOF of 410 mm (c.f. the simulation shown in Fig. 3.7) and a field-free DOF of 317 mm. In this case a repeller voltage of 1000 V is simulated with a laser port electrode voltage of 930 V, an extractor voltage of 860 V and lens 1 and lens 2 voltages that were fixed at ~573 and ~287 V respectively. In this simulation the red electric field contours (lines of equipotential) have been set to the same separations as those shown in Fig. 3.7. Comparison between Fig. 3.7 and Fig. 3.8 therefore highlights the reduced electric field gradient achieved using the Leeds VMI electrodes and this voltage scheme with respect to the Eppink and Parker VMI lens.

For situations where experimental signals were limited or where better mass resolution was required, a second voltage scheme was adopted for the Leeds VMI lens assembly which used a $\frac{V_E}{V_R}$ value of 0.75. In this case lens 1 and 2 were held at voltages that were close $\frac{V_E}{45}$ and $\frac{V_E}{90}$ respectively in order to achieve velocity focusing. Here the focusing was achieved by adjusting the lens voltages only and $\frac{V_E}{V_R}$ was fixed at a value of 0.75. Due to the low lens electrode voltages, this scheme is similar to an Eppink and Parker extraction scheme except in this case adjusting the focus of the lens assembly has little effect on the TOF of the fragments and for an equivalent DOF the lens electrode voltages result in a slight reduction in image size. The electrode voltage ratios outlined here will be referred to as Voltage Scheme 2.

Practically the voltage schemes described above were realised using two high-voltage divider circuits with outputs for the repeller, extractor, lens 1 and lens 2 electrodes. By carrying out the majority of the voltage division outside of the imaging chamber, the different voltage schemes could easily be exchanged or altered while maintaining the vacuum of the imaging chamber. The external voltage dividers were powered using a pair of medium high voltage (MHV), 5 kV, 25 W power supplies (Stanford Research Systems PS350/5000 V-25 W) and voltage division was achieved using high precision, high voltage resistors. The power supplies were capable of producing output voltages between 0 and 5000 V with 1 V precision. This was taken into account in the trajectory simulations. In all cases the divided voltages were stabilised using 220 pF capacitors. The outputs of the voltage dividers were connected to a four pin MHV vacuum feedthrough using 50 Ω coaxial cable. Similar cable was used inside

the imaging chamber to pass the respective voltages to the electrodes. Here, the cables were wired on the outside of the earthed mu-metal shielding tube. The electrical shielding of all four coaxial cables were connected to each other as well as the lens assembly housing which was earthed through the detection chamber. The laser port electrode was connected to both the extractor and repeller electrodes via 5 GΩ high precision, high power (2 W) resistors in the vacuum chamber. This set the laser port potential half way between the repeller and extractor voltages in all experiments.

In order to simulate the function of the lens assembly a number of aspects of its operation needed to be considered. Firstly in order to perform slice velocity map imaging while retaining the option of good mass resolution and higher signal strengths in crush velocity map imaging experiments the lens needed to be able to achieve good velocity focusing at a range of extractor-repeller voltage ratios. For the two types of experiment the lens assembly had to produce a good spread in ion arrival time or good Newton sphere compression along the TOF axis with relatively low flight times respectively. This function of the Leeds lens assembly is demonstrated in Fig. 3.9. As the velocity focusing in VMI experiments not only depends on the electrode voltage ratios but also on the ionisation volume and for a particular fragment kinetic energy the absolute electrode voltages these effects should be simulated. Furthermore, as in crush velocity map imaging experiments the entire photoproduct Newton sphere is detected the uniformity of the velocity focusing for different parts of the Newton sphere should be examined. Where possible differences in the velocity focus for different parts of the Newton sphere should be minimised as they will result in biased image reconstruction. An additional consideration is how the velocity focusing changes with the kinetic energy release of the fragments as this will effect the kinetic energy resolution of both slice and crush velocity map images. In order to simulate some these effects the changes in velocity focusing for different parts of the ion Newton spheres are plotted in Figs. 3.10, 3.11 and 3.12 for different repeller voltages and ionising laser beam diameters. Similarly the changes in velocity focusing for ions that were initially ejected in the imaging plane are shown Figs 3.13, 3.14 and 3.15 for different repeller voltages and ionising laser beam diameters.

All of the simulation results shown here were carried out using singularly charged particles with masses corresponding to those of atomic oxygen. The effects of simulating different charged particle masses were found to display the same trends with

repeller voltage and kinetic energy as those presented by Townsend *et al.* (50). For this reason the results of simulations using different masses are not shown here. The simulations for the oxygen ions are found to be representative of the trends observed for all of the other simulated ion masses. In all cases results are reported for the Eppink and Parker electrodes operating under VMI conditions and the Leeds electrodes operating under VMI conditions using the two extraction voltage schemes. The total x-axis DOF from ion generation to the detector face was on average 410 mm for both lens assemblies where in general the DOF for individual ions vary depending on the simulated x-axis width of the ionisation volume. In all of the simulations the lenses were optimally focused for ion trajectories resulting in features with the maximum radius at the detector face. This type of focusing is favourable despite the reduction of image focus for features closer to the centre of the detector. Here the linear mapping of velocity to detector radius results in features that are separated by a given energy gap having the greatest spatial separation at low detector radii. It is therefore preferable to achieve better velocity focusing at higher detector radii where features are necessarily more congested. The details of different sets of simulations are given below and the results are summarised at the end of this section.

The top panel of Fig. 3.9 shows how the ion TOF changes using an Eppink and Parker lens assembly and the Leeds lens assembly using the two proposed extraction ratios with repeller voltages between 500 and 5000 V. The bottom panel of Fig. 3.9 shows the change in the temporal Newton sphere width or TOF spread for different repeller voltages under the same conditions. Here, all simulations consider ions that were ejected at angles of 0, 45, 90, 135, 180, 225, 270 and 315° with a kinetic energy of 1.5 eV. For the Eppink and Parker lens simulations the ion generation points were positioned in the centre of the extractor and repeller plates and 1 mm above and below this point along the spectrometer y-axis. For the simulations of the Leeds electrode stack, the ion generation points were in the centre of the laser port electrode aperture and 1 mm above and below this point along the spectrometer y-axis. These results show the increase in TOF with reduced repeller voltage and, by comparison of the results for Voltage Scheme 1 and 2, show how the change in TOF due to a reduced extractor-repeller voltage ratio is a significantly smaller effect than that arising from the reduction of the repeller voltage. As expected the results also show how increases in the extractor-repeller voltage ratio results in a significant increase in the spread in

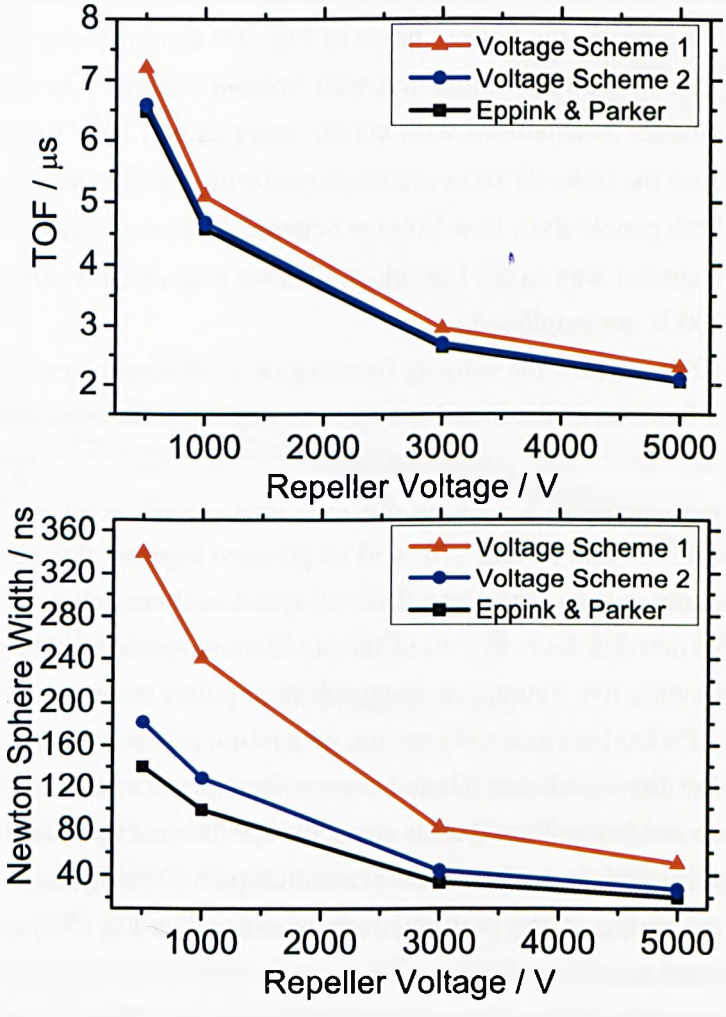

Figure 3.9: Results from simulations of atomic oxygen ion trajectories caused by the Eppink and Parker and Leeds VMI electrode sets. In the case of the Leeds electrodes the effects of two different extraction voltage schemes are shown. This simulation considers ions that were ejected at angles of 0, 45, 90, 135, 180, 225, 270 and 315° with kinetic energies of 1.5 eV. For the Eppink and Parker lens assembly the ion generation points were positioned in the centre of the extractor and repeller plates and 1 mm above and below this point along the spectrometer y-axis. For the simulations of the Leeds electrode stack, the ion generation points were in the centre of the port electrode aperture and 1 mm above and below this point. In the top panel the average TOF is plotted as a function of repeller voltage for the different lens assemblies and extraction voltage schemes. In the bottom panel the variation in the spread of the ion TOF with different repeller voltages for the same electrodes and voltage schemes is shown.

arrival time of the ions and that this effect is non-linearly increased by reduced repeller voltages. Specifically the bottom panel of Fig. 3.9 demonstrates how the Leeds VMI electrodes can be used in conjunction with Voltage Scheme 1 to effectively slice oxygen photoproduct distributions with kinetic energies of 1.5 eV or more when detector gate widths on the order of 10 ns are employed with repeller voltages of <3000 V. Additionally both panels show how Voltage Scheme 2 allows the Leeds VMI electrodes to behave in a similar way to the Eppink and Parker lens when repeller voltages between 500 and 5000 V are employed.

Fig. 3.10 shows how the velocity focusing of the different lenses and voltage schemes change as a function of the initial ion ejection angle. These simulations considers oxygen ions that were initially ejected at angles of 0, 45, 90, 135, 180, 225, 270 and 315° with a kinetic energy of 1.5 eV. In this case ions ejected at angles of 0 and 180°, 45, 135, 225 and 315° and 90 and 270° will be grouped together due to their similar velocity components in the (y, z)-plane that will result in them being projected to a similar radius at the detector face. For all of the simulations carried out to produce this figure and the following five figures, six ion generation points were used. In this case, for the Eppink and Parker lens assembly the ion generation points were positioned 100 μm before and after the equidistant plane between the extractor and repeller plates and also 1 mm above and below these points along the spectrometer y-axis. For the simulations of the Leeds electrode stack, the ion generation points were positioned 100 μm before and after the centre of the port electrode aperture (see Fig. 3.5) along the TOF axis and also 1 mm above and below these points along the spectrometer y-axis. Here the 200 μm separation of ion generation points along the TOF axis represents the finite diameter of the ionising laser beam at its interaction point with the molecular beam. For this and the following figures the velocity focusing of the lens assemblies is represented by the maximum difference between the radii at which fragments with similar initial kinetic energies in the (y, z)-plane strike the detector face. This quantity is referred to as the focal spread. In Fig. 3.10 the focal spread is plotted against the average radius at which fragments with similar initial kinetic energies in the (y, z)-plane strike the detector face when a repeller voltage of 3000 V is simulated. The figure shows that fairly similar velocity focusing is achieved for the different lens assemblies and operating voltages. For all three lens configurations the velocity focusing is observed to get progressively worse as fragments with lower initial velocities in the (y, z)-plane

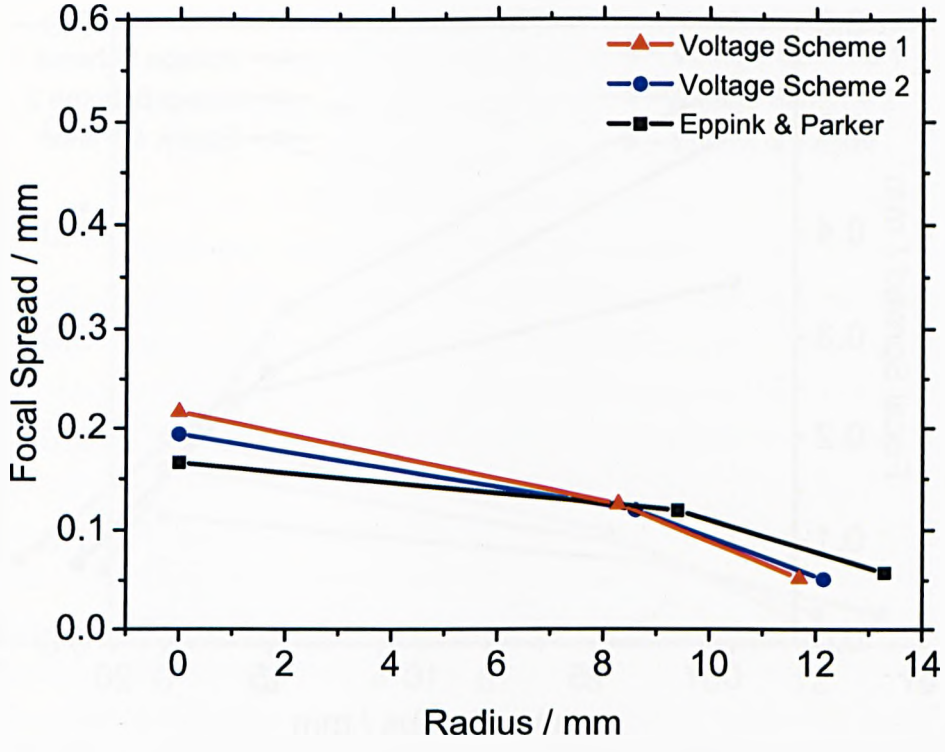

Figure 3.10: Results from trajectory simulations of atomic oxygen ions caused by the Eppink and Parker and Leeds VMI electrode sets. This simulation considers ions that were ejected at angles of 0, 45, 90, 135, 180, 225, 270 and 315°. Six ion generation points were used for all of the simulations. For the Eppink and Parker lens assembly the ion generation points were positioned 100 μm before and after the plane which was equidistant from extractor and repeller plates and also 1 mm above and below these points along the spectrometer y-axis. For the Simulations of the Leeds electrode stack, the ion generation points were positioned 100 μm before and after the centre of the port electrode aperture (see Fig. 3.5) along the TOF axis and also 1 mm above and below these points along the spectrometer y-axis for both of the simulated extraction voltage ratios. These ion generation points simulate the finite width of the ionising laser beam across the molecular beam (in this case the laser beam is taken to have a diameter of 200 μm) and the largest dimension of the ionisation volume, i.e. the molecular beam diameter. Ions were simulated with kinetic energies of 1.5 eV and using repeller voltages of 3000 V. The velocity focus or focal spread is defined as the maximum radial distance between fragments formed with ejection angles that lead to similar radii at the detector face. The figure shows how the velocity focus or focal spread changes with the average detector radius for the fragments formed with ejection angles that are velocity focused to similar radii. In all cases observed here the focal spread increases for ions with lower initial kinetic energies in the (y, z)-imaging plane.

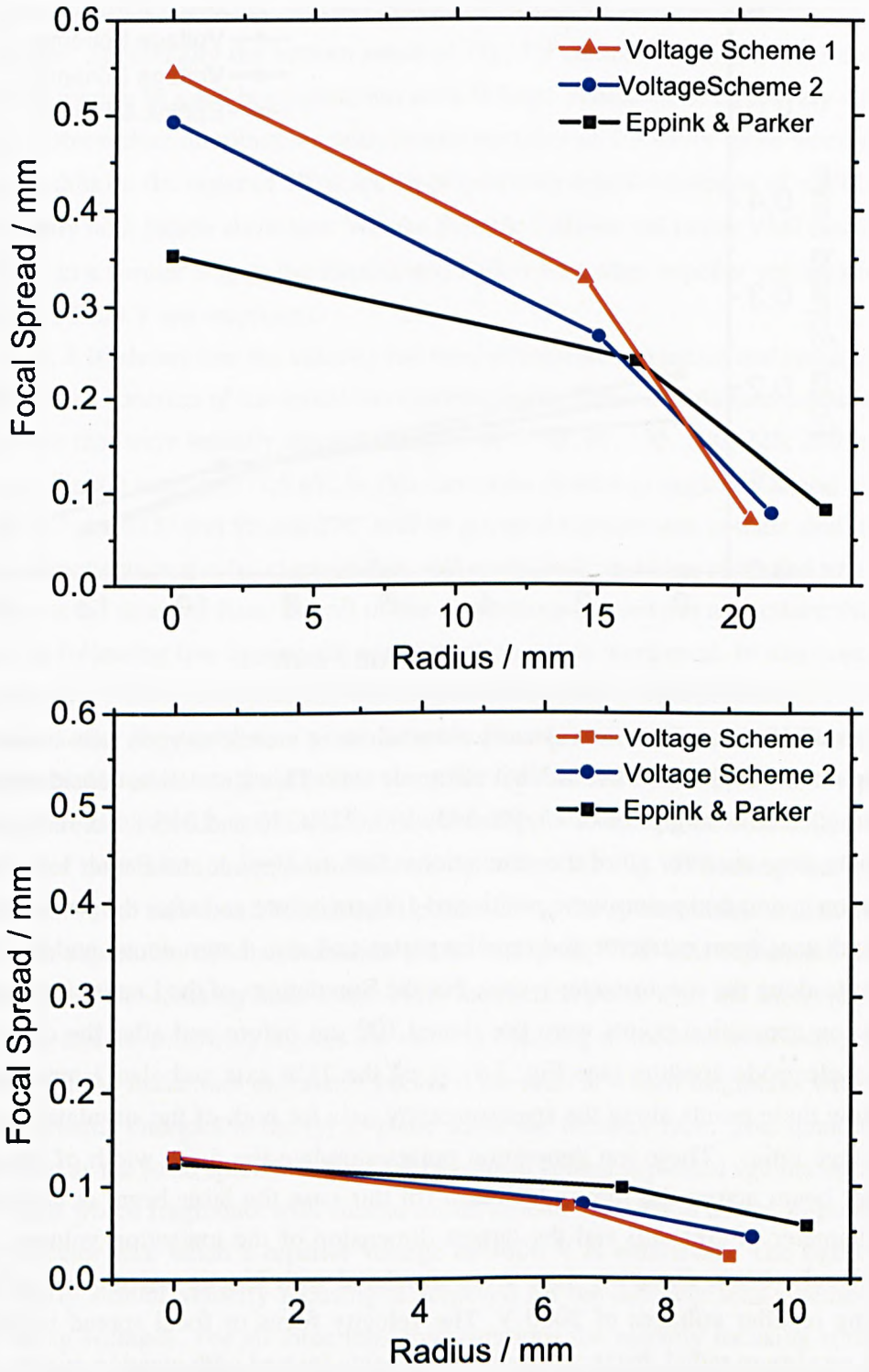

Figure 3.11: As Fig. 3.10 but for repeller voltages of 1000 V (top) and 5000 V (bottom).

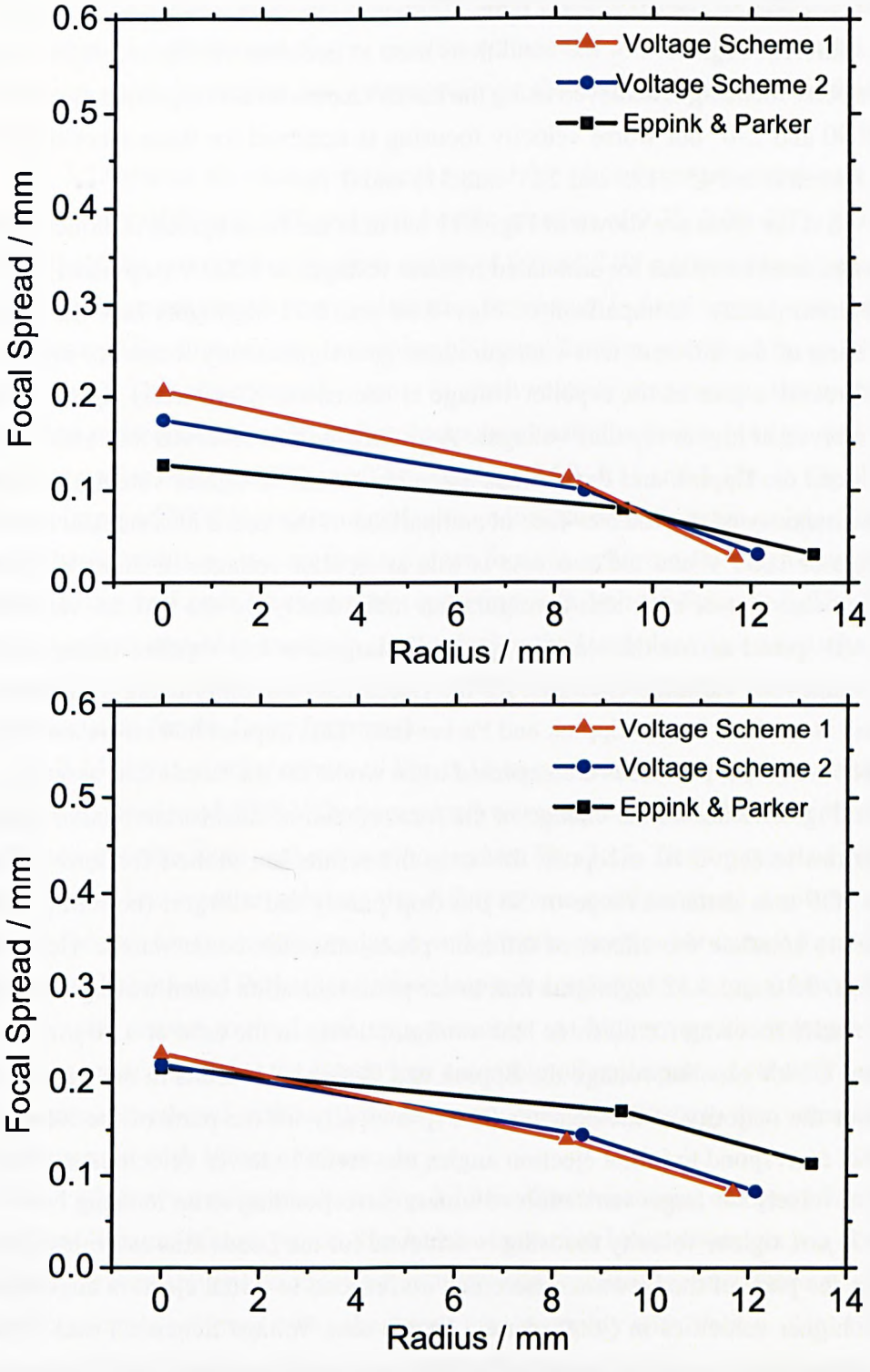

Figure 3.12: As Fig. 3.10 but for ionising beam diameters of 50 μm (top) and 400μm (bottom).

are considered. Here different parts of the photoproduct Newton spheres are focused to different degrees. For the conditions used to generate this figure, slightly improved velocity focusing is achieved using the Leeds electrodes for fragments ejected at angles of 90 and 270° but worse velocity focusing is achieved for those ejected with angles between 0 and 45°, 135 and 225° and 315 and 0°.

Similar plots are shown in Fig. 3.11 but here the focal spread is plotted against average detector radius for simulated repeller voltages of 1000 V (top panel) and 5000 V (bottom panel). Comparison of Figs. 3.10 and 3.11 highlights how the velocity focusing of the different lens configurations gets significantly worse for ions ejected at all recoil angles as the repeller voltage is decreased. Conversely tighter focusing is observed at higher repeller voltages. Additionally it is observed that under these conditions the Eppink and Parker lens assembly results in tighter velocity focusing over the majority of the detector face in comparison to the Leeds lens stack at repeller voltages of 1000 V and the converse is true at repeller voltages of 5000 V. Considering the behaviour of each lens configuration individually we see that the variation in the focal spread across the Newton spheres is largest at low repeller voltages. At these voltages the variation is largest for the Leeds lens assembly using Voltage Scheme 1 and is smallest for the Eppink and Parker lens. This implies that errors associated with reconstruction processes are expected to be worse for the Leeds lens assembly.

Fig. 3.12 shows the change in the focal spread of ions formed under similar conditions to Fig. 3.10 except in this case the results are plotted for ions formed over a TOF axis distance range of 50 μm (top panel) and 400 μm (bottom panel) in order to simulate the effects of different photoionisation beam waists. Comparison of Figs. 3.10 and 3.12 highlights that lower photoionisation beam waists result in tighter velocity focusing for all three lens configurations. In the case of a 50 μm beam waist and a 3 kV repeller voltage the Eppink and Parker lens results in the tightest focusing over the majority of the detector face [principally for the parts of the Newton sphere that correspond to initial ejection angles that result in lower velocities in (y, z)-plane]. Conversely for larger ionisation volumes, corresponding to an ionising beam waist of 400 μm, tighter velocity focusing is achieved for the Leeds lens assembly [principally for the parts of the Newton sphere that correspond to initial ejection angles that result in higher velocities in (y, z)-plane]. In this case Voltage Scheme 1 and 2 give fairly similar results and the tighter velocity focusing with respect to the Eppink and Parker

lens assembly is attributed to the conical extractor plate in the Leeds assembly and the extra lenses. As mentioned above, repeller voltages of 3 kV with laser beam waists of 200 μm result in similar foci (averaged over the detector face) for all three lens assemblies.

Fig. 3.13 shows the change in focal spread for photoions generated with initial ejection angles of 90 and 270° and with kinetic energies of 0.25, 0.50, 0.75. 1.00, 1.25 and 1.50 eV. By considering ejection angles of 90 and 270° exclusively the change in focus with fragment kinetic energy simulates the change in focal spread with fragment kinetic energy for slice images (assuming all image features are sliced by an infinitely narrow gate). This effect equally occurs in crush velocity map images but in this case there is an additional reduction in focus associated with the fragments that are initially ejected at angles other than 90 and 270° (see Figs 3.10, 3.11 and 3.12). In Fig. 3.13 repeller voltages of 3000 V are simulated with an ionisation laser beam waist of 200 μm. Under these conditions we see that a tighter focus is achieved for fragments that are focused using the Leeds lens assembly operating with Voltage Scheme 1. The Eppink and Parker lens assembly results in similar foci to the Leeds lens assembly when Voltage Scheme 2 is implemented, although the latter lens configuration results in slightly tighter focusing for the faster fragments.

Fig. 3.14 shows similar results to Fig. 3.13 except in this case repeller voltages of 1000 V (top panel) and 5000 V (bottom panel) were implemented. All other simulation conditions were the same as those used to produce Fig. 3.13. The top panel of Fig. 3.14 shows that at low repeller voltages the different lens configurations result in similar velocity focuses for fragments produced with kinetic energies between 0.5 and 1.5 eV but that the Eppink and Parker lens offers improved velocity focusing at lower kinetic energies with respect to the Leeds lens assembly. At higher repeller voltages (5 kV, bottom panel of Fig. 3.14) the Leeds lens assembly offers improved velocity focusing for fragments produced with any kinetic energy, this is particularly true when the lens is implemented with Voltage Scheme 1.

Fig. 3.15 shows similar results to Fig. 3.13 but for ionisation volumes of 50 μm (top panel) and 400 μm (bottom panel). For narrow ionisation beam diameters it is observed that all three lens configurations result in fairly similar focal spreads although slightly better focusing is achieved using the Leeds lens assembly with Voltage Scheme 1 for fragments with higher kinetic energies. For larger ionisation beam waists significantly

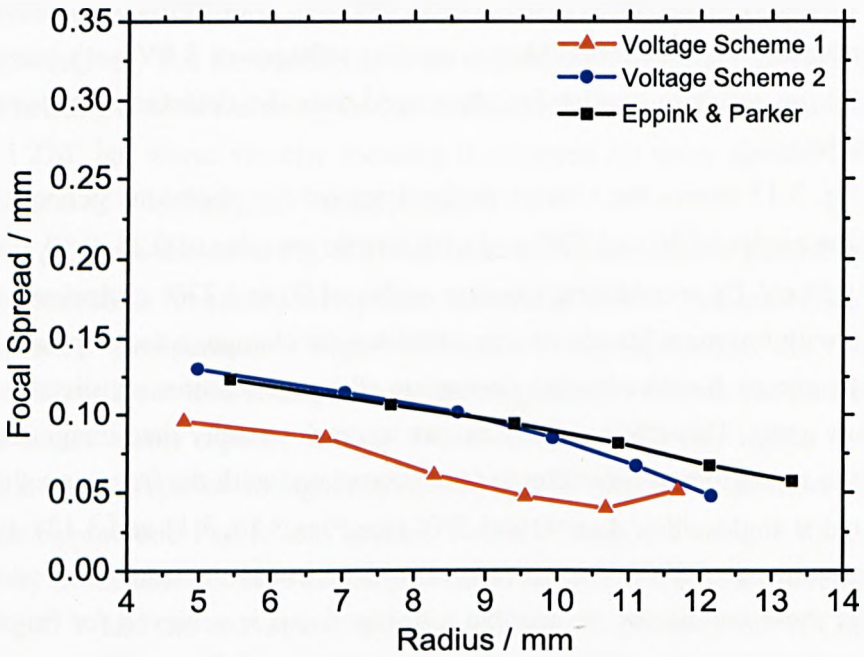

Figure 3.13: Results from trajectory simulations of atomic oxygen ions caused by the Eppink and Parker and Leeds VMI electrode set. This simulation considers ions that were ejected at angles of 90 and 270° exclusively, these ions represent those preferentially detected in a slice imaging experiment. For all simulations six ion generation points were simulated. For the Eppink and Parker lens assembly the ion generation points were positioned 100 μm before and after the centre of the extractor and repeller plates along the TOF axis and also 1 mm above and below these points along the spectrometer y-axis. For the simulations of the Leeds electrode stack, the ion generation points were positioned 100 μm before and after the centre of the port electrode aperture along the TOF axis and also 1 mm above and below these points for both of the simulated extraction voltage ratios. These ion generation points simulate the finite width of the ionising laser beam (in this case taken to have a diameter of 200 μm) and the largest dimension of the ionisation volume, the molecular beam diameter. Ions were simulated with kinetic energies of 0.25, 0.50, 0.75. 1.0, 1.25 and 1.50 eV to simulate the change in the velocity focus of fragments produced with partner fragments in a range of quantum states. The simulations were carried out using repeller voltages of 3000 V. The figure shows the variation in the velocity focus (defined as the maximum radial distance between fragments formed with the same kinetic energy when they reach the detector face) against the average detector radius for the fragments formed with each kinetic energy.

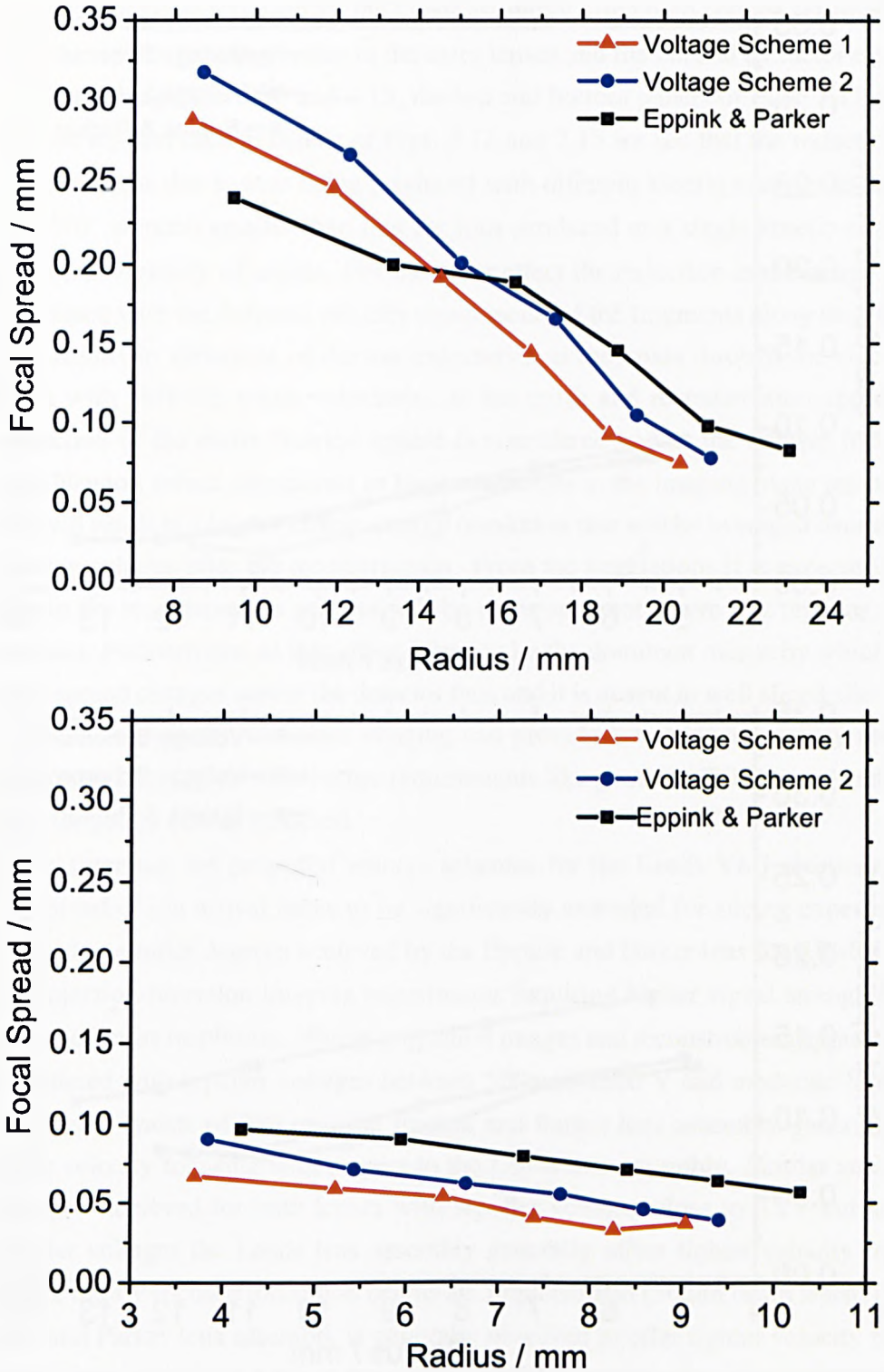

Figure 3.14: As Fig. 3.13 but for repeller voltages of 1000 V (top) and 5000 V (bottom).

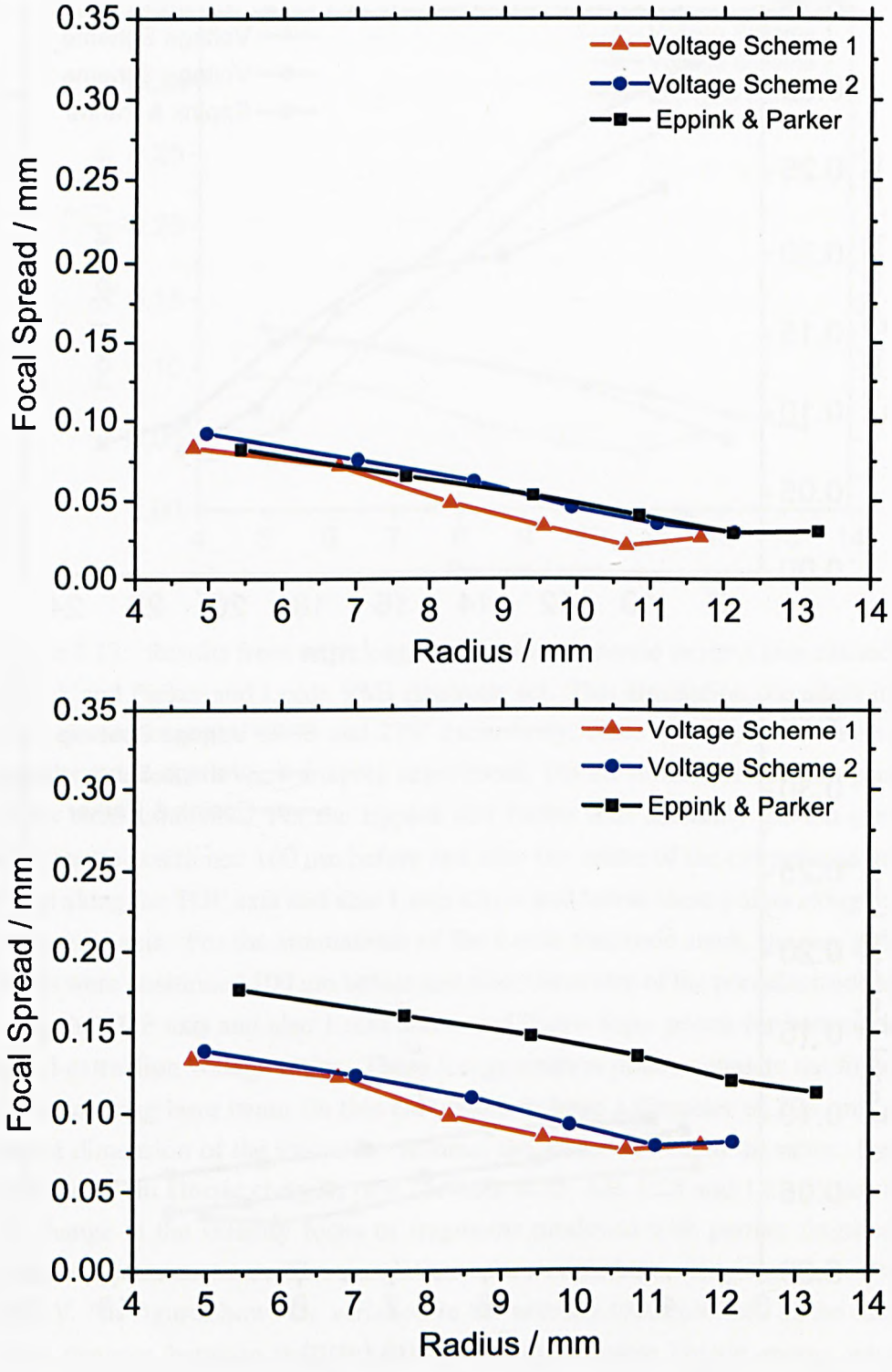

Figure 3.15: As Fig. 3.13 but for ionisation laser diameters of 50 μm (top) and 400 μm (bottom).

tighter focuses are achieved for the Leeds assembly using both voltage schemes. In this case the tighter focusing is due to the extra lenses and the conical extractor electrode.

Comparing Figs. 3.10 and 3.13, the top and bottom panels of Figs. 3.11 and 3.14 and the top and bottom panels of Figs. 3.12 and 3.15 we see that the reduction in the velocity focus due to ions being produced with different kinetic energies at angles 90 and 270° is much smaller than that for ions produced at a single kinetic energy and ejected at a variety of angles. For the latter effect the reduction in the image focus is associated with the different velocity components of the fragments along the TOF axis. This results in variations of the ion trajectories as they pass through the electrostatic fields with different x-axis velocities. In the crush and reconstruction approach the projection of the entire Newton sphere is considered and as the relative focusing of each Newton sphere diminishes as lower velocities in the imaging plane are projected this will result in a loss of kinetic energy resolution that will be averaged over all of the Newton spheres after the reconstruction. From the simulations it is expected that the bias in the reconstruction process will be more apparent where low repeller voltages are used. Furthermore, as this effect seems to be the dominant means by which the ion focal spread changes across the detector face and it is absent in well sliced slice images it would be expected that slice imaging can provide better kinetic energy resolution than crush imaging provided other requirements like good ion TOF spread and narrow detector gating can be achieved.

In summary the proposed voltage schemes for the Leeds VMI electrodes allow the spread of ion arrival times to be significantly extended for slicing experiments or crushed to similar degrees achieved by the Eppink and Parker lens for REMPI spectra or projection-inversion imaging experiments requiring higher signal strengths and/or increased mass resolution. Where projection images and reconstruction approaches are considered with repeller voltages between 500 and 2500 V and moderate laser beam foci (beam waists of 200 μm) the Eppink and Parker lens assembly generally offers better velocity focusing with respect to the Leeds lens assembly. Similar velocity focusing is achieved for both lenses with repeller voltages close to 3 kV but at higher repeller voltages the Leeds lens assembly generally offers tighter velocity focusing. Where tightly focused ionisation beams are implemented (50 μm beam waists) the Eppink and Parker lens assembly is generally observed to offer tighter velocity focusing at repeller voltages of 3 kV or less. For loosely focused ionising laser beams (waists

of the order of 400 μm or greater) the velocity focusing of the Leeds lens assembly is generally observed to be tighter than that of the Eppink and Parker lens arrangement for repeller voltages of 3 kV and above.

Where the meridional slice of the photoproducts is considered alone the Leeds lens assembly is found to offer tight velocity focusing for fragments formed with a range of kinetic energies under the majority of conditions. Indeed the velocity focusing is found to be significantly better than that achieved using the Eppink and Parker lens stack in all but one of the conditions presented here. As the Leeds lens system is capable of producing a good spread of ion arrival times and tight velocity focusing of the meridional photoproduct slice it is therefore expected that the lens set should allow photoproduct distributions to be measured with high kinetic energy resolution when slice images of photoproducts with appreciable initial momenta are measured.

Generally it is observed that the relative change in focus across the detector face is greatest for the Leeds lens assembly. This is denoted by the increased gradients of the lines connecting the simulation points in the figures with respect to those of the Eppink and Parker lens assembly. This effect usually results in the tightest velocity focus being achieved using the Leeds lens assembly with Voltage Scheme 1 but in unfavourable cases also results in diminished velocity focusing with respect to the Eppink and Parker lens over the majority of the detector face. It is also noted that in all cases the increased focal spread towards the centre of the imaging detector is greatest when the entire Newton sphere is recorded. This effect is observed to be more significant for the Leeds lens assembly and is expected to result in slight biases to the dynamical parameters extracted from crush images using reconstruction techniques. In contrast the increase in focal spread for fragments ejected parallel to the detector face and formed with different kinetic energies is found to be significantly less. As the reduction in image focusing associated with fragments that are ejected at angles that deviate significantly from 90 and 270° are absent in well sliced slice images these observations give some justification as to why slice imaging can offer increased kinetic energy resolution with respect to crush and reconstruction experiments.

3.3 Experimental procedures

3.3.1 Electrode and skimmer alignment

A procedure has been developed in order to optimise the alignment of the electrostatic lens assembly so that photoions are projected onto the centre of the detector face. This procedure was necessary when the assembly was removed and reattached to the chamber or when the assembly needed to be translated along the TOF axis.

Firstly, both chambers were brought up to atmospheric pressure and the camera and detector were removed. During the procedure the detector was placed on a vacuum line which maintained a pressure of 1×10^{-6} mbar. With the detector back under high-vacuum, the position of the laser port electrode was then set along the spectrometer TOF axis using the three adjustment pins on the lens assembly. The angular alignment of the electrode stack was then achieved using a helium-neon (HeNe) laser. Here, the beam was directed through the centre of the hole in the DN160-DN100 reducing flange that housed the detector and centred on the hole in the repeller plate using a pair of adjustable mirrors. As the HeNe beam profile was larger than the 2.5 mm repeller hole, the specular back reflection from the polished repeller electrode could be directed back along the beam path using the adjustment pins on the lens assembly. Care was taken not to translate the lens during this step. The laser beam was then re-centred in the reducing flange and the hole in the repeller electrode and the back reflection was optimised using the lens assembly adjustment pins so that it travelled back along the HeNe beam line. This process was repeated until the laser beam alignment converged so that it was centred in the flange and the repeller hole and the back reflection was directed back along the laser beam path.

With the laser beam passing through the centre of the repeller electrode, and therefore the second skimmer which was mounted on the lens assembly, the first skimmer which separated the molecular beam and the detection chamber was adjusted to maximise the light that passed through its aperture. With the first skimmer fixed, the molecular beam nozzle could then be translated so that the nozzle orifice was centred in the laser beam. The detector could then be reattached to the ionisation chamber and the chambers could be pumped to low pressure. The nozzle position could then be optimised using a parent ion signal. This alignment procedure resulted in photoion

distributions striking the centre of the detector face enabling velocity map images to be recorded with maximum resolution.

3.3.2 Stray fields and electron centring

Although the procedure outlined above effectively centred the photoion distributions, the photoelectron distributions were observed to strike the detector face off-centre. This prevented photoelectron images from being expanded at the detector face (by using lower repeller voltages) in order to maximise the kinetic energy resolution. As the electric field-free drift tube was effectively shielded by the mu-metal tube, this was attributed to the effects of a stray magnetic field (likely from nuclear magnetic resonance spectrometers) around the laser-molecular beam interaction region and the lens assembly which was not magnetically shielded.

To combat the effect of this stray field, two Helmholtz coil sets were produced using 0.8 mm diameter lacquered copper wire. This approach was advocated in the first electron imaging experiments (152). All coils were made up of 22 turns of wire and had a diameter of 152 mm. The vertical coils were produced by wrapping the wire around the outside of the top and bottom arms of the detection chamber cross piece. This resulted in a coil separation of ~160 mm. The horizontal coils were produced using two plastic frames which were positioned around the optical arms of the detection chamber. This resulted in a coil separation of ~168 mm. The coils were connected so that current would flow through both coils in the same direction. The pairs of coils were then connected to different channels of a 30 A triple output adjustable power supply (TTi El 302Tv). This created a uniform and tunable magnetic field in the centre of the electrodes that could be adjusted to centre the projected electron distributions on the detector face. Currents between 2 and 4 A on each coil pair were commonly used to re-centre the distributions. Re-centred photoelectron images recorded using the Helmholtz coils were observed to be perfectly circular within the resolution of the 640×480 pixel camera system. Photoelectron kinetic energy distributions and angular distributions that were obtained from velocity map images recorded with and without the Helmholtz coils were found to be identical.

3.3.3 Synchronisation

Experiments could be synchronised using one or two digital pulse/delay generators (Berkeley Nucleonics Corporation BN565 and a Stanford Research Systems DG535). Where possible, one of the delay generators would operate using its internal trigger at a repetition rate of 10 Hz (BN565) and, if necessary, the second delay generator (DG535) could be externally triggered from one of the outputs of the first delay generator. Where the pulsed molecular beam valve was implemented a single delay generator channel would trigger the Iota One molecular beam driver unit to open the gas valve for a time that was partially determined by the temporal width of the transistor-transistor logic (TTL) electrical pulse (typically 150 μs). Typical experiments involving nanosecond lasers would involve Nd:YAG lasers operating in an external trigger mode where one delay generator channel would be used to fire the Nd:YAG flashlamp and a second would trigger the Nd:YAG Q-switch. This allowed the Nd:YAG laser timing and its output energy to be controlled independently. Typical photolysis laser delays of 750 μs were required in order to probe the correct part of a molecular beam pulse. In order to monitor the ion current at the phosphor so that TOF and/or REMPI spectra could be recorded the digital oscilloscope would be triggered by another delay generator channel. Photodiodes were also connected to the oscilloscope in order to monitor laser intensities for signal normalisation. Another delay channel was used to trigger the camera acquisition where the camera acquisition time was controlled in the DaVis acquisition software (20 ms). Where necessary another delay channel was used to trigger the pulser unit that was used to detect ions of a given mass or to slice ion distributions. Here, the electrical pulse width was controlled by switches on the gating unit and the electrical pulse length could be adjusted between 7 and 135 ns (FWHM).

In the time-resolved experiments reported in the appendices the timing of the chirped pulse amplification (CPA) laser system could not be altered. For this reason the CPA was used as the master clock in these experiments. An experimental repetition rate of ~1024 Hz was therefore fixed which where necessary had to be pulse divided (using the BN565). As the pulsed molecular beam valve could be driven at a maximum repetition rate of 25 Hz a continuous nozzle was used for these experiments. The LaVision camera could be driven at a maximum repetition rate of 30 Hz with a maximum

exposure time of ~1 ms. As the maximum exposure time of the camera (at any acquisition rate) was 100 ms, an aqcuisition rate of 10 Hz was used with an exposure time of 70 ms. Here the signal from ~717 laser shots was integrated at the CCD chip (preventing the use of any centroiding software). Future time-resolved experiments will be carried out with a newly purchased CCD camera system (Prosilica 1380) which will allow a camera aqcuisition time on the order of seconds thus reducing the experimental duty cycle.

In the alignment experiments reported in Chapter 5 the master clock for the experiment had to be the photoelastic modulator (PEM) used to rotate the probe laser polarisation. Here the driving frequency of the PEM (100 000 Hz) was frequency divided using a delay generator (BN565) to the maximum repetition rate of the Nd:YAG lasers (10 Hz). The sinusoidal output of the PEM was used to externally trigger the delay generator which was set to trigger at a custom voltage that gave stable and reproducible triggering. The temporal delay of the flash lamp of the Nd:YAG laser that was used to pump the probe dye laser was tuned in order to produce maximum or minimum modulation of the polarisation vector. The optimisation was achieved by spatially separating the vertical and horizontal polarisation components of the dye laser beam using a Rochon prism (Optics For Research PUR-10-2) and maximising/minimising the intensity of the rotated laser polarisation using a photodiode and oscilloscope. The temporal delays of the pump laser, molecular beam valve, the camera and the detector pulser were adjusted around the optimum probe laser delay in order to synchronise the experiment. In these experiments the images recorded with different pump and probe laser polarisation combinations were recorded in separate acquisitions where the probe laser polarisation was flipped by shifting all delays by half the modulation cycle of the PEM.

3.3.4 Molecular beam optimisation

In the experiments reported in this thesis, the pulsed molecular beam valve was operated at a repetition rate of 10 Hz and was used in conjunction with PPS poppets. Although the softer teflon poppets were found to provide a longer term seal of the molecular beam valve, the PPS poppets were preferred for reasons outlined below.

Molecular beam poppets were routinely changed, in accord with the manufacturers instructions, so that the rotational cooling and the density of the gas pulses were kept at an optimum. Here, the optimum valve tension was achieved outside of the chamber by applying the same pressure differential to the nozzle as would be used in an experiment. The valve was tightened up to the shims while the solenoid was energised and the poppet and armature held back. The valve was then pulsed using an electrical pulse length of 150 μs and the nozzle was untightened by a sixteenth of a turn. This procedure was found to reproducibly result in rotationally cold and temporally short molecular beam pulses.

A backing gas of 2% NO in helium at a stagnation pressure of ~1 bar was used to align the molecular beam nozzle and assess the rotational temperature and temporal duration of the gas pulses after every poppet change. NO neutrals were ionised via a (1+1) REMPI process through the (0, 0) $(1)^2\Sigma^+ \leftarrow (1)^2\Pi_\Omega$ band at excitation energies close to 5.49 eV using a dye laser with a Coumarin 2 or Coumarin 46 dye in an ethanol solvent. The unfocused laser beam was tuned to a strong rotational line and was passed through the centre of the laser port electrode along the y-axis of the spectrometer. The molecular beam nozzle position was then adjusted in order to maximise the NO ion signal at the detector face. The molecular beam timing was then adjusted by changing the delay of the laser pulse with respect to the molecular beam valve driver unit pulse. This allowed the temporal profile of the gas pulse to be measured. Temporal durations of 200–250 μs were usually observed. By measuring the ion signal as the REMPI laser was scanned, rotational profiles consistent with temperatures of <10 K were measured. In the experiments reported in this thesis, pump lasers were delayed so that they crossed the molecular beam axis ~80 μs into the molecular beam pulse. At this delay the rotational cooling and signal intensity was found to be optimum.

Where teflon poppets were used the pulse duration and rotational temperature associated with the supersonic expansion were observed to increase above 250 μs and from <10–30 K respectively after ~20 hours of operation. In contrast the PPS poppets were observed to retain short pulse lengths and cold rotational distributions for ~100 hours of operation after which the valve seal was frequently lost or the pulse lengths and NO rotational temperatures were found to increase significantly. In order to assess the molecular beam conditions the pulse duration was measured at the beginning of each day. Provided the pulse duration had not changed from the previous day, the rotational

profile of NO was only measured every few days. If changes in the gas pulse lengths were observed the rotational profile was measured more often. Poppets were routinely changed when pulse durations in excess of 250 μs and/or rotational temperatures in excess of 15 K were observed.

For the continuous molecular beam used in the femtosecond experiments the molecular beam nozzle was usually aligned using trace quantities of azulene (seeded from the room temperature vapour pressure) in He. The ion signal generated by a (1+1) REMPI process using the third harmonic of the CPA (~258 nm) was used to optimise the nozzle position. Typical energies of 250 nJ were used. To carry out photoelectron imaging experiments using ultrashort UV laser pulses it was necessary to keep the gas pressure in the ionisation chamber to a minimum. For this reason helium backing gas pressures of less than 200 mbar were used resulting in typical uncalibrated molecular beam chamber pressure readings of 5×10^{-6} mbar and uncalibrated ionisation chamber pressure readings of 5×10^{-8} mbar. In this case careful regulation of the 1 bar (minimum) helium flow from the cylinder was achieved using needle valves in the molecular beam gas line.

3.3.5 Electrode voltage optimisation

The VMI electrodes that have been discussed in the previous pages were held at particular voltages using the two tuneable MHV power supplies. The outputs of the power supplies were connected to one of two different voltage divider circuits on the outside of the detector chamber. Using Voltage Scheme 1 (by connecting voltage divider 1 to the power supplies and the chamber), the voltage of the first power supply corresponded to the repeller voltage which could be varied between 0 and 5000 V. The focus of the lens assembly could be adjusted by changing the voltage of the second power supply. This voltage corresponded to the voltage of the extractor electrode and simultaneously adjusted the voltages of lenses 1 and 2. Using Voltage Scheme 2 (by connecting voltage divider 2 to the power supplies and the chamber), the voltage of the first power supply corresponded to the repeller voltage and the extractor voltage was held at $\frac{3}{4}V_R$. In this case, the voltage of the second power supply corresponded to the voltage of lens 1 multiplied by a factor of 45. Adjustment of this power supply resulted in the simultaneous variation of the voltages of lenses 1 and 2. Again variation of the

voltage of the second power supply was used to tune the lens focusing. Although this was not necessary in any of the experiments reported here, the resistors in the voltage dividers could be altered easily in order to produce better mass resolution, a reduction of image size or an increase in the spread of ion arrival time for a particularly demanding experiment.

For imaging experiments the focusing of the imaging electrodes were optimised each day. Initially NO ion signals from a 2% NO in He gas mixture were focused by monitoring the ion spot size at the detector using the CCD camera output. To record images of photofragments the lens focusing was tailored to a particular set of experiments. The repeller electrode voltage was adjusted so that the ion or electron image filled as much of the detector face as possible while still maintaining low laser fluences and good signal-to-noise ratios. The extractor electrode voltage was then adjusted so that a strong image feature with a velocity which was close to the maximum measured was optimally focused by eye by monitoring the CCD camera output. When the focusing was close to optimum it was then adjusted by recording 1000 laser shot (or greater if signals were particulalry weak) velocity map images with different extractor voltages. This allowed the optimum lens focusing to be achieved with an extractor voltage precision of 1 V.

Where strong signals were present in the REMPI spectra of low or zero kinetic energy species the lens focus was usually detuned to spread the ion or electron signal out over a greater detector area. This allowed higher detector voltages to be used to provide better signal to noise for the detection of the weaker signals in the REMPI profile.

3.3.6 Mass gating and slice imaging

In the experiments reported here a custom gating unit was used in order to measure ions with a given mass exclusively or to selectively detect portions of the photoion Newton spheres. The gating unit was capable of producing electrical pulses with temporal widths of 7–135 ns and temporal profiles that can be approximated by Gaussians at short pulse lengths and top hat functions for longer pulse lengths. The temporal duration of the electrical pulse was set on the detector gating unit and could be monitored via a bayonet Neill-Concelman (BNC) connector output using an oscilloscope. The

voltages of the electrical pulses could be adjusted between 1 and 1000 V where the voltage was set at the detector power supply. The gating unit was applied to the far side of the second MCP to minimise any electric field in the field-free region of the spectrometer. It is noted that although the minimum electrical pulse width was close to 7 ns, the temporal width of the detector on-time could be significantly less. This is illustrated in Fig. 3.16 which shows the response of a 25 mm dual MCP detector that had been gated using a similar gating unit to that used in the experiments documented here and was illuminated with a picosecond laser pulse.

In order to produce Fig. 3.16 the voltages of the MCPs were set to give strong (un-gated) signals from the illuminating laser pulse. The voltage of the second MCP was then reduced by close to 1000 V so that no signal was observed from the detector. The remaining voltage on the second MCP was then defined as the MCP offset and a voltage of 1000 V was applied to the gating unit. In this way a signal was only detected when the pulser unit increased the second MCP voltage to levels where the UV photons could be detected. With the voltages set, the temporal delay of the gating pulse was swept over the delay of the laser pulse. This resulted in a mapping of the minimum temporal detector response which for the 25 mm detector was found to have a FWHM of 3.5 ns. The difference between the temporal response of the detector and the electrical gating pulse width was due to the fact that only the peak of the electrical pulse resulted in detection of the UV photons. This fact coupled with the quasi-exponential gain increase of MCP detectors with detector voltage results in a significantly shorter detector gate than the driving electrical pulse. Here, it is noted that a detector response of 3.5 ns could not be achieved using the detector with 40 mm diameter employed in the Leeds spectrometer due to its larger capacitance. However, pulse widths of the order of just less than 6 ns are expected to be achieved using the 40 mm detector under optimum conditions. This provides adequately narrow pulses for the majority of ion slice imaging experiments.

In order to selectively measure fragments of a given mass the gating unit voltage and pulse width needed to be set. This was usually achieved by monitoring the TOF spectrum before the gating unit was switched on and measuring the time delay between the probe laser and the arrival time of ions of given mass at the detector face. This delay was easily measured on an oscilloscope which displayed the voltage drop at the detector phosphor and the output of a photodiode that was used to monitor the probe

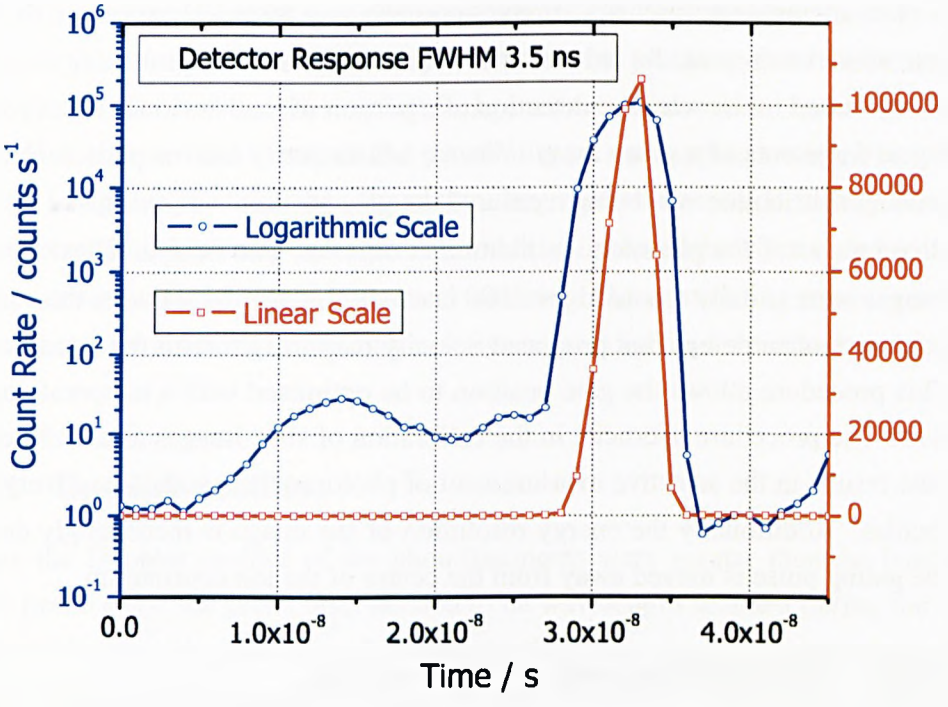

Figure 3.16: Temporal profile of the response of a 25 mm diameter dual MCP detector when it was gated by a similar gating unit as was used in the experiments reported in this thesis and was illuminated with a UV picosecond laser pulse. Here the temporal profile was recorded by sweeping the gate pulse across the temporal delay associated with the picosecond laser pulse. The figure is courtesy of Photek Ltd. and was kindly provided for use in this thesis to demonstrate the gating unit performance.

laser pulse. The mass gate could then be set by maximising the gate pulse width and reducing the voltage of the second MCP until all of the image signal disappeared. The pulser unit delay could then be set on the delay generator according to the TOF measurement and the pulser voltage would be increased to a value that corresponds to slightly more than the voltage removed from the second MCP. The gate width was then, if necessary, reduced and the mass gate delay tuned to only detect ions of given mass. It is noted that care had to be taken if crush velocity map images or REMPI spectra were recorded in this way. The entire distribution of the ions of given mass had to be detected so as not to bias the data.

For slicing experiments a similar approach was taken. However, in this case the gate width was repeatedly reduced while optimising the ion signal using the gate delay. This resulted in the selective detection of a portion of ion Newton spheres corresponding to fragments of a given mass. When a satisfactorily narrow portion of the photoproduct distribution was being measured the gate position was optimised by recording slice images of the photoion distribution at different gate delays. These optimisation images were usually recorded for 2000 laser shots. The images were then analysed in order to isolate delays that produced velocity map images with the maximum radius. This procedure allows the gate position to be optimised with a temporal precision of 2 ns. The procedure is crucial in the calibration of slice images as an off-centre mass gate results in the selective measurement of photoproducts with deceptively small velocities. Additionally the energy resolution of the image is increasingly degraded as the gating pulse is moved away from the centre of the ion distribution.

3.3.7 Thresholding and event counting

In order to maximise the signal to noise levels in the imaging experiments, signal thresholding was used to remove the contributions of camera and detector noise from the image frames. Threshold values were set by optimising detector voltages to provide the highest photoion/electron signal using low laser fluences and while keeping detector noise to a minimum. To assess the correct threshold value for each set of experiments, images were recorded with different threshold values and the value which gave the best compromise between signal intensity and signal-to-noise level was chosen. For experiments carried out with laser repetition rates that allowed image frames associated with single laser shots to be individually captured and analysed (10 Hz) an event counting (191) and centroiding routine was implemented in order to increase image resolution. In this case the signal intensity in each 3×3 camera pixel grid was measured and counted as an event if the intensity exceeded the threshold value. The centroiding procedure then found the centres of these image events and placed this information in a new image buffer where the image intensity was set to one at the centre of mass of each event and zero everywhere else. Similar events were added to the image buffer after the image frame associated with each laser shot was analysed. In setting the threshold value for these experiments thresholds were chosen so that each

laser shot produced at least one event. Care was also taken to keep the laser energy low enough so that less than 100 events were detected per laser shot in order to avoid space charge effects in the laser-molecular beam interaction volume and at the detector face. This also worked to reduce the probability of overlapping events which would bias the image acquisition when the centroiding routine was used. Ideally the acquisition detected at least one event per laser shot with the probe laser switched on and zero otherwise. The thresholding, event counting and centroiding routines were all implemented as a macro in the DaVis software package and were written by André Eppink.

3.3.8 Doppler profiles

Where the Doppler profiles of the photofragments were greater than the bandwidth of the probe laser, the probe laser needed to be wavelength scanned during the image or spectral acquisition process. For images, this was achieved by repeatedly scanning the dye laser wavelength from red to blue (where the laser scan is more reproducible) across the Doppler profile using a simple LabVIEW (National Instruments) script (Doppler scan.vi) on the image acquisition computer. The Sirah LabVIEW virtual instrument library was used to communicate with the dye laser through an RS232 connection.

3.3.9 REMPI spectra

Mass-resolved REMPI spectra were recorded by integrating individual ion peaks in the TOF mass spectrum on an oscilloscope. Alternatively REMPI spectra of the entire photoion or photoelectron distribution could be recorded by integrating the entire TOF trace. Care was taken in order to slightly defocus the imaging electrodes before the TOF integration was set up in order to prevent detector damage due to intense low kinetic energy features that may occur within the REMPI profile. The lens defocusing also allowed the detector gain to be increased so that the signal to noise levels of weak REMPI features could be increased. The probe laser scans were achieved using another simple LabVIEW program (Sirah_Scan_Scope_v2.0.vi) which used the Sirah LabVIEW virtual instrument library to scan the laser from an initial wavelength to a final wavelength in user defined steps that occur when the program allowed the scan

to continue. Photodiodes were used in order to monitor the pump and probe laser intensities on the oscilloscope, by measuring the area under the photodiode peaks as a function of the laser wavelength the REMPI spectra could be normalised for laser power variations. The TOF integration conditions as well as the integration conditions of the photodiode outputs could be set in the LabVIEW program which allowed scans to be repeated. The oscilloscope acquisition was synchronised to each laser shot and so that the acquisition only took place after the laser had moved to its acquisition point. The synchronisation was achieved using a GPIB connection from the personal computer running the LabVIEW script to the oscilloscope where both the oscilloscope and the probe laser were triggered from the same delay generator. Signal averaging was achieved on the oscilloscope by setting a user defined number of laser shots. After each acquisition, the laser wavelength, the (averaged) signal intensity and the (averaged) photodiode signals were written to a user defined text file.

3.3.10 Data processing

Velocity map images could be processed using the DaVis software package with an image processing macro ('Program JPV') that was written by Jean-Paul Visticot or the LabVIEW based image analysis software, 'Analyse.exe', that was written by Lionel Poisson. Due to the extra features associated with 'Analyse.exe' this software was usually used. Here, image centres were found with a precision of half a camera pixel using ring overlays on the images. All images were found to be perfectly round within the limiting resolution of the 640×480 pixel CCD camera. The ion or electron images were then processed with and without symmeterisation in order to observe any spurious affects associated with the symmeterisation process. The effects of the symmeterisation would be expected to have the largest effect on the image angular distributions and could lead to artefacts such as higher order alignment moments in alignment experiments. In all of the experiments reported here the angular distributions of the image features did not gain any extra features through the symmeterisation process. For this reason symmeterised images and the data extracted from these images are reported in this thesis.

In the case of crush velocity map images the 2D projection of the 3D distribution was reconstructed, assuming that the 3D distribution possessed an axis of cylindrical

symmetry, using the Hankel transform (167) algorithm that is implemented in both image processing packages. Here the 3D distribution was reconstructed by taking the inverse Hankel transform of the Fourier transform of each row of the projected image. This allows the 3D spatial distribution of the ions/electrons to be built up in a series of horizontal slices. The radial and angular information can then be extracted from the 3D distribution by exclusively considering the infinitesimally narrow slice at the centre of the distribution along the TOF axis.

In slice imaging experiments the central slice, which was directly recorded in these cases, was assumed to be infinitesimally narrow. Deviations from this assumption will lead to errors in the measurement of the photofragment energy distribution and angular profiles. In all of the experiments reported here (symmeterised) slice images and inverted crush images were treated in the same way. In order to produce photoproduct energy distributions the pixels in the images were multiplied by an $r\sin\theta$ Jacobian term and the resulting images were integrated with respect to angle to produce one-dimensional (1D) functions in energy space. The radial co-ordinate was then calibrated in energy by squaring the image radius (in units of pixels) and multiplying the result by a calibration factor with units of eV pixel^{-2}. The procedure for obtaining the calibration factor is outlined below. Energy distributions were obtained from 'Analyse.exe' by using the 'Direct Integration' option in the 'Radial evolution' tab and exporting the resulting profile to a text file. The energy calibration was then carried out using the Origin Data Analysis and Graphing Software package (OriginLab).

Angular distributions were obtained by integrating image features with respect to radius to produce an angular profile of the image feature at angles between 0 and 2π. This was achieved in 'Analyse.exe' by using the 'Angular evolution' tab and setting the laser polarisation direction and the minimum and maximum image radius for the angular profile. The resulting angular distribution was exported as a text file and imported into Origin in order to fit to the angular distributions using sets of Legendre polynomials and to obtain anisotropy parameters.

The VMI extraction conditions and hence the energy distributions could be calibrated by recording single laser velocity map images (either crush or DC slice) of the single and two-photon dissociation of molecular oxygen at excitation energies of 5.49439 eV. Here $O(^3P_2)$ fragments were ionised in a (2+1) REMPI process by scanning the Doppler profile of the atomic fragments. High laser pulse energies (~1.5 mJ

pulse^{-1} with a 250 mm focal length lens and a neat expansion of O_2) were required in order to drive the single photon forbidden absorption process to the Herzberg continuum and the two-photon process to produce $O(^3P_2)$ fragments with higher kinetic energies in coincidence with $O(^1D_2)$ and $O(^3P_J)$ fragments. Similar results to those of Buijsse *et al.* were obtained (192). These researchers have studied the decomposition process in detail which is now thought to be well understood. Alternatively crush velocity map images of the photoelectrons from NO $(1)^2\Pi_\Omega$ were measured via a (1+1) REMPI process at an excitation energy close to 5.49 eV in order to calibrate the spectrometer. In this case a strong rotational line of the (0, 0) $(1)^2\Sigma^+ \leftarrow (1)^2\Pi_\Omega$ band was selected as an intermediate resonance on the way to ionisation. In some of the experiments reported in Chapter 6 dye laser photon energies between 4.77 and 5.08 eV were employed to probe the visible-UV fragmentation behaviour of NO_2. In these experiments the laser dye that was used to generate these photon energies prevented the extraction conditions from being calibrated using O_2 fragmentation or kinetically and vibrationally cold NO $(1)^2\Pi_\Omega$ ionisation. The dissociation of molecular bromine via its $(1)^1\Pi_u$ state was therefore used to calibrate the electrostatic lens conditions. Using an excitation energy of ~2.952 eV, the resulting $Br(^2P_{\frac{3}{2}})$ fragments were ionised and projected towards the detector face using a (2+1) REMPI process at an excitation energy of 4.84010 eV. This ionisation scheme incorporated the $4s^22p^45p^1$ $Br(^2S_{\frac{1}{2}})$ state for the intermediate resonance that facilitated single photon ionisation to the three spin-orbit levels of the $4s^22p^4\ ^3P_J$ state and the $4s^22p^4\ ^1D_2$ state of the Br^+ cation. Similar results to those reported by Cooper *et al.* were obtained in these calibration experiments (193). For the relevant experiments reported in Chapter 6 the $Br(^2P_{\frac{3}{2}})$ images allowed the extraction conditions to be accurately calibrated as the optical beam lines did not need to be adjusted for the calibration.

The energies of the first and second dissociation limits of molecular oxygen [5.115 and 7.082 eV (90; 91)], the first dissociation limit of molecular bromine [1.9701 eV (90)] and the first ionisation potential of NO $(1)^2\Pi_\Omega$ [9.2642 eV (194; 195)] are well known. Additionally the vacuum photolysis/photoionisation wavelengths used in the fragmentation of O_2 and the ionisation of NO $(1)^2\Pi_\Omega$ could be accurately calibrated from the energy of the well-known two-photon resonance employed in the (2+1) ionisation of $O(^3P_2)$ (91) that occurs at the centre of the Doppler profile of the oxygen dissociation experiment and close to the excitation energy employed for NO $(1)^2\Pi_\Omega$ ionisiation.

Similarly the well-known resonance employed in the (2+1) REMPI scheme outlined above for $Br(^2P_{\frac{3}{2}})$ atom detection allowed the ionisation wavelength in these experiments to be accurately calibrated but in this case the photolysis wavelength had to be calibrated using a fibre-coupled spectrophotometer (Ocean Optics Inc. HR4000CG-UV-NIR). This allowed the kinetic energies of the measured photofragments to be accurately calculated and subsequently assigned to peaks in the photofragment distributions. By dividing the assigned kinetic energy (in units of eV) by the square of the image radius corresponding to the centres of the assigned image features, a calibration factor was obtained. Provided the VMI conditions were met in the experiment, this calibration factor should be the same across the entire detector face (1).

The consistency of the calibration factors have been carefully checked for both photoelectron and photoion images. By imaging $O(^3P_2)$ fragments from O_2 and the photoelectrons from NO $(1)^2\Pi_\Omega$ on the same day (i.e. with the same laser focus, laser-molecular beam interaction volume and electrode potentials) four different calibration factors can be obtained at four different detector radii. In these experiments fragments with kinetic energies of 1.897, 1.953 and 2.937 eV and 1.697 eV for the three $O(^3P_2)$ ion partner fragments (1 photon $O(^3P_J)$, 2 photon $O(^1D_2)$ and 2 photon $O(^3P_J)$ respectively) and the electrons from NO $(1)^2\Pi_\Omega$ **v**=0 **N**=0 (probed via the $(1)^2\Sigma^+ \leftarrow (1)^2\Pi_\Omega$ R_1 rotational branch) were expected respectively. At a repeller voltage of 3001 V and an extractor voltage of 2614 V (using Voltage Scheme 1), the four image features were observed at radii of 49±0.5, 158±0.5 and 192±0.5 and 148±0.5 pixels respectively. This results in four respective calibration factors of 7.901×10^{-5}, 7.824×10^{-5}, 7.997×10^{-5} and 7.746×10^{-5} eV pixel^{-2} and an average calibration factor of 7.859×10^{-5} eV pixel^{-2} with a 1% standard deviation.

REMPI spectra were processed by normalising the intensity profiles according to the photodiode signals recorded with the spectra. These REMPI profiles were purposefully recorded over relatively narrow excitation energy windows (corresponding to a maximum of 2.5 nm tuning range close to 225 nm) to minimise laser power variations due to the laser dye curves. REMPI spectra with laser power variations of less than 10% were selectively processed. (1+1) REMPI spectra of NO $(1)^2\Pi_\Omega$ were divided by the laser power whereas (2+1) REMPI spectra of $O(^3P_J)$ fragments were normalised by the square of the laser power to compensate for the change in excitation efficiency

to the intermediate resonance in the probe step. Here the pump transition for the fragmentation and the ionisaton of fragments from the intermediate ionisation resonance were assumed to be independent of laser power within the 10% laser power variation.

Chapter 4

Photodissociation of NO_2 in the $(3)^2A'$ State: The $O(^3P_J)$ Channel

4.1 Introduction

The absorption spectrum of NO_2 displays two broad features at excitation energies between 1.77 and 6.20 eV (~700 and 200 nm) (76; 77; 196; 197). The first absorption feature (1.77–4.96 eV or 700–250 nm) displays a complex vibrational progression and has been principally attributed to excitation to the $(2)^2A'$ state. After excitation to this electronic state above 3.115546(6) eV (55), fragmentation is known to occur via the first dissociation limit. This fragmentation process was studied in detail by Busch and Wilson in 1972 in their original photofragment ion studies (53; 54). This pioneering work paved the way for many other photodissociation studies of NO_2 and investigations of the energy partitioning after fragmentation of other chemical species but was also particularly important in the development of the VMI technique (175) that has been used to carry out the majority of original experiments reported in this thesis.

$$NO_2\ (1)^2A' \rightarrow NO\ (1)^2\Pi_{\frac{1}{2}};0,0 + O(^3P_2) \quad E \geq 3.11555\ eV$$

$$NO_2\ (1)^2A' \rightarrow NO\ (1)^2\Pi_{\frac{1}{2}};0,0 + O(^3P_1) \quad E \geq 3.13517\ eV$$

$$NO_2\ (1)^2A' \rightarrow NO\ (1)^2\Pi_{\frac{1}{2}};0,0 + O(^3P_0) \quad E \geq 3.14369\ eV$$

$$NO_2\ (1)^2A' \rightarrow NO\ (1)^2\Pi_{\frac{3}{2}};0,0 + O(^3P_2) \quad E \geq 3.13040\ eV$$

$$NO_2\ (1)^2A' \rightarrow NO\ (1)^2\Pi_{\frac{3}{2}};0,0 + O(^3P_1) \quad E \geq 3.15003\ eV$$

$$NO_2\ (1)^2A' \rightarrow NO\ (1)^2\Pi_{\frac{3}{2}};0,0 + O(^3P_0) \qquad E \geq 3.15854\ eV$$

The rise of the second electronic absorption band of NO_2 is assigned to the opening of the $(3)^2A' \leftarrow (1)^2A'$ transition at 4.97498 eV (99). At these excitation energies the effects of the NO_2/N_2O_4 equilibrium becomes important (76; 198). At excitation energies above 4.96 eV (~250 nm), the absorption cross-section of N_2O_4 rises sharply, with the N_2O_4 to NO_2 absorption cross-section ratio increasing from 1×10^{-21} cm^2 $molecule^{-1}$ at 3.10 eV (~400 nm) to 1×10^{-17} cm^2 $molecule^{-1}$ close to 6.20 eV (76; 77). The ultraviolet photolysis of N_2O_4 has been noted to produce electronically and vibrationally excited NO_2 as well as NO $(1)^2\Pi_\Omega$ and $O(^3P_J)$ products, making it difficult to separate the decomposition product channels of the two species. (4; 199; 200) The equilibrium results in ~81% of NO_2 existing in its dimeric form at room temperature and atmospheric pressure (STP). The obvious implication is that photodissociation studies at excitation energies above 4.96 eV require careful reagent preparation, N_2O_4 correction factors and/or experimental methods which allow the NO_2 and N_2O_4 photoproducts to be distinguished.

The second electronic absorption band of NO_2 is made up of a broad continuum structure with a superimposed vibrational comb. This absorption band shows a much simpler vibronic structure than the visible/near UV band and was partially analysed by Harris and King (201). The symmetry of the excited state was later assigned as $^2A'$ or $^2B_2$ (in C_s or C_{2v} notation) when the band was further studied by Ritchie *et al.* (202) The transition principally corresponds to the $2b_1 \leftarrow 1a_2$ valence electron excitation (72; 73; 105) and carries an average differential oscillator strength of 0.0068 eV^{-1} (77; 97). At its origin the $(3)^2A'$ state is known to be predissociative with a lifetime of 41.0±1.6 ps (98; 99) and is calculated to be weakly bound with a shallow potential well in the asymmetric stretching coordinate in the adiabatic representation (8). For an overview of the topography of the $(3)^2A'$ surface and other relevant electronic states, the recent results of Schinke and co-workers are recommended (8).

At higher excitation energies, 5.082909 eV, dissociation to produce NO in coincidence with electronically excited oxygen can occur (55; 91),

$$NO_2\ (1)^2A' \rightarrow NO\ (1)^2\Pi_{\frac{1}{2}};0,0 + O(^1D_2) \qquad E \geq 5.08291\ eV$$

$$NO_2\ (1)^2A' \rightarrow NO\ (1)^2\Pi_{\frac{3}{2}};0,0 + O(^1D_2) \qquad E \geq 5.09777\ eV$$

The O($^1D_2$) yield is found to remain relatively constant, between 40 and 50%, upon direct excitation to the (3)^{2}A′ state above this energetic threshold (7; 98; 99; 100; 101). Although full dynamical calculations on accurate potential energy surfaces are required to understand the details of the branching ratio into the two channels (8), the significant O(^3P_J) yield can be rationalized by the correlation of the (3)^{2}A′ manifold with the NO (1)$^2\Pi_\Omega$ + O(^3P_J) dissociation channel via the asymmetric stretch in the adiabatic representation. The O($^1D_2$) yield is then explained by the proximity of the adiabatic (4)^{2}A′ surface [also labelled (2)^{2}A$_1$ at C_{2v} geometries] that correlates with the NO (1)$^2\Pi_\Omega$ + O($^1D_2$) dissociation channel along the asymmetric stretch coordinate. This view is supported by the experimental results of Tsuji *et al.* (98) and Uselman and Lee (99) who observed that asymmetric stretch excitation in the (3)^{2}A′ state promoted the predissociation and also dramatically increased the O($^1D_2$) yield close to the (3)^{2}A′ origin. On excitation to the (3)^{2}A′ state with two vibrational quanta in the asymmetric stretch, the excited state lifetime is inferred to decrease below 100 fs (98; 99). No further significant decrease in lifetime is inferred at higher excitation energies throughout the rest of the vibrational manifold.

A number of experiments have been carried out to measure the energy partitioning of the dissociation over a range of excitation energies. The spin-orbit branching ratios (uncorrected for degeneracy and line-strength factors) of the ground state oxygen photoproducts have been measured by Rubahn *et al.* at excitation energies close to 5.49 eV (~226 nm) (203). Here they obtained O($^3P_2$):O($^3P_1$):O($^3P_0$) branching ratios of 1.00:0.71:0.25, 1.00:0.68:0.27 and 1.00:0.50:017 in a thermal sample, a neat supersonic expansion and a seeded supersonic expansion of NO_2 respectively using LIF. Miyawaki *et al.* (204) carried out similar measurements at excitation energies of 5.826 eV (212.9 nm) in a molecular beam and determined a branching ratio of 1.00:0.35:0.08, suggesting that there is a weak wavelength dependence to the measured O(^3P_J) distribution between 5.49 and 5.83 eV. It is noteworthy that for excitation below the (3)^{2}A′ band origin, that is to the continuum of the (2)^{2}A′ potential energy surface, both groups recorded similar spin-orbit ratios.

The production of NO (1)$^2\Pi_\Omega$ in coincidence with O(^3P_J) has been studied close to the (3)^{2}A′ origin, below the O($^1D_2$) threshold, by a number of researchers. McKendrick *et al.* (205) measured NO fragments in both v=2 and 6 at a photolysis energy of 4.989 eV (248.5 nm). Slanger *et al.* (206) later repeated this experiment but probing

other vibrational levels (v=4-8) with a separate probe laser using LIF. They observed a marked vibrational inversion with the population distribution peaking at v=7. McFarlene *et al.* (2) used a REMPI detection scheme to probe the whole vibrational distribution at the same photolysis wavelength. These experiments observed a bimodal vibrational distribution peaking at v=0 with a subsidiary maximum at v=5 [although the peak at v=0 has been questioned in the literature (3)]. Non-statistical NO fragment rotational profiles were also observed. More recently, Morrell *et al.* carried out a further study at excitation energies close to 4.99 eV using time-resolved Fourier transform infra-red (TR FTIR) spectroscopy to measure the NO fragment fluorescence in v=2–8 (207). The measured vibrational distribution was in qualitative agreement with McFarlene *et al.*; peaking at v=5.

At slightly higher excitation energies and above the threshold for $O(^1D_2)$ production the $O(^3P_J)$ product channel has been studied using the VMI technique by Ahmed *et al.* (3) and separately by Brouard *et al.* (4) Ahmed and co-workers measured the kinetic energy distribution of the unaligned $O(^3P_0)$ fragment in a single laser experiment at an excitation energy of 5.4804 eV (226.23 nm). Here the $O(^3P_0)$ distribution was interpreted to peak in coincidence with NO $(1)^2\Pi_\Omega$ fragments in v=4 or 5 with an average translational anisotropy parameter of 1.32. Additionally, images of the NO $(1)^2\Pi_\Omega$ fragments were recorded using REMPI to ionize the fragments via the $(1)^2\Sigma^+ \leftarrow (1)^2\Pi_\Omega$ (0, 0), (1, 1) and (2, 2) transitions. It was determined that the rotational profiles of the NO produced in coincidence with $O(^1D_2)$ and $O(^3P_J)$ were markedly different.

The Brouard group imaged all three spin-orbit components of the ground state oxygen fragment distribution in a single-laser experiment at excitation energies close to 5.49 eV. The kinetic energy profiles of the oxygen fragments were found to be bimodal and to depend strongly on the partial pressure of the NO_2 in the sample mixture. The signal strength of the slow component was found to be particularly sensitive to the NO_2 partial pressure although the kinetic energy spread of the fast component was also observed to narrow as the NO_2 partial pressure was reduced. The slow component was attributed to the dissociation of N_2O_4 at 5.49 eV to produce NO_2 with both NO and $O(^3P_J)$. (207; 208) The broadening of the fast component was attributed to the photolysis of N_2O_4 to produce translationally hot NO_2 fragments (200; 209; 210) which were subsequently photolysed to produce $O(^3P_J)$. The $O(^3P_J)$ images recorded at low

NO_2 partial pressures were ascribed to the photolysis of NO_2 alone with the $O(^3P_0)$ kinetic energy distribution obtained at low partial pressure being narrower than that measured by Ahmed *et al.* It was, therefore, suggested that the distribution obtained by Ahmed *et al.* contained interference from the photolysis of N_2O_4 contaminant. Brouard *et al.* interpreted their low pressure data as being due to $O(^3P_0)$ fragments produced in coincidence with NO $(1)^2\Pi_\Omega$ in v=4-6. The translational anisotropy of the total $O(^3P_0)$ distribution was determined to be 1.0. The analysis of the $O(^3P_2)$ and $O(^3P_1)$ images may have been affected by orbital angular momentum alignment effects and as a result the anisotropies of these images were not reported. Despite the efforts of the Brouard group to minimize the N_2O_4 content of their supersonic expansion, the slow component of the signal was still dominant in the $O(^3P_2)$ distributions that they measured.

At an excitation energy of 5.826 eV the photodynamics of the dissociation have been studied by Ahmed *et al.* (5) and by Richter *et al.* (211) Ahmed *et al.* used VMI in order to measure the orbital angular momentum alignment of the $O(^3P_2)$ and $O(^3P_1)$ photofragments and also recorded images of the unaligned $O(^3P_0)$ fragment. At this excitation energy, the alignment of the $O(^3P_2)$ fragment was found to be negligible, in contrast, the $O(^3P_1)$ fragment was found to display appreciable orbital alignment. The $O(^3P_1)$ kinetic energy release spectrum displayed a bimodal distribution, peaking at a translational energy consistent with the co-production of NO $(1)^2\Pi_\Omega$ in v=4. A subsidiary maximum at low kinetic energy was assigned to the production of $O(^3P_1)$ in coincidence with NO $(1)^2\Pi_\Omega$ in v=10 or 11. The spin-orbit branching ratios were noted to be markedly different for the fast and slow $O(^3P_J)$ fragments. The TOF mass spectrometry $O(^3P_2)$ experiments of Richter *et al.* agree qualitatively with the measurements of Ahmed *et al.*, also suggesting a bimodal fragment distribution with a peak close to the kinetic energy associated with NO molecules in v=4.

At higher excitation energies, Coroiu *et al.* used the VMI technique to probe the $O(^3P_J)$ fragment distribution close to 6.20 eV in a single laser experiment (6). A bimodal velocity distribution was observed for all three spin-orbit components. In each case the distribution peaked at speeds consistent with the production of highly vibrationally excited NO fragments, in v=13 or 14. A secondary peak was interpreted to be due to NO $(1)^2\Pi_\Omega$ in a vibrational level close to 7. As with the results obtained at lower excitation energies, potential angular momentum alignment of the $O(^3P_2)$ and $O(^3P_1)$

may have effected the measured kinetic energy profiles and translational anisotropies. However the fast component of the unaligned $O(^3P_0)$ fragment anisotropy was measured to be ~1.00, in accord with the results of Brouard *et al.* close to 5.49 eV. The anisotropy of the slow component was measured to be 0.55 implying dissociation taking place on a longer timescale and/or via a more bent geometry.

The TR FTIR experiments of Hancock and Morrison at photolysis energies of 6.42 eV (193 nm) also suggest a bimodal vibrational distribution of the $O(^3P_J)$ fragments (7). By recording the fluorescence of the NO fragments produced in coincidence with both ground and electronically excited state oxygen atoms, the overall vibrational distribution was measured. The primary peak in the distribution occurs with NO in v=5, which may be due to either the $O(^3P_J)$ or $O(^1D_2)$ dissociation channel. Above v=6, NO can only be formed in coincidence with $O(^3P_J)$ fragments. The vibrational populations between v=7 and 16 displayed bimodal structure, peaking at v=7 [and perhaps below with a contribution from the $O(^1D_2)$ co-fragments] with an ancillary maximum at v=14. An interesting aspect of these experiments is that their time-resolved nature should have identified any contributions from the dissociation of N_2O_4. The absence of these contributions seems to suggest that the $O(^3P_J)$ dissociation is genuinely vibrationally bimodal; at least at excitation energies of 6.42 eV.

In summary, the literature regarding the energy partitioning in the dissociation of NO_2 from the $(3)^2A'$ state does not paint an entirely consistent picture. At photolysis energies close to 4.989 eV, the $O(^3P_J)$ distribution has been measured to peak with NO $(1)^2\Pi_\Omega$ in v=0 with a subsidiary maximum somewhere between v=5 and 7 (2; 205; 206; 207). At 5.49 eV the distribution is interpreted as peaking somewhere between v=4 and 6 (3; 4). At slightly higher excitation energies, 5.83 eV, a bimodal distribution is measured with a major peak at a kinetic energy consistent with the production of NO $(1)^2\Pi_\Omega$ fragments in v=4 with an ancillary maximum consistent with production in v=10 or 11 (5). At excitation energies close to 6.20 eV, the kinetic energy of the $O(^3P_J)$ fragments are consistent with production in coincidence with NO $(1)^2\Pi_\Omega$ in v=7 and v=13 or 14 (6). At still higher excitation energies, the NO $(1)^2\Pi_\Omega$ distribution is found to peak at v=7 or less with a small peak at v=14 in the NO $(1)^2\Pi_\Omega$ + $O(^3P_J)$ distribution (7). The energy partitioning determined by all of these studies is summarized in Fig. 4.1. The most probable internal energy of the photofragments

is plotted against the initial excess energy in the $(3)^2A'$ state for the high and low energy channels respectively. The error bars represent the half-width half-maxima of the reported internal energy profiles in each study. In the study of Hancock and Morrison (7) only a vibrational profile was reported (represented by open triangles in the figure). However the calculations of Schinke *et al.* (8) allow the expected rotational energy in the low (internal) energy channel to be estimated. Accordingly Hancock and Morrisons datum with an additional 695 meV of internal rotational energy (solid black triangle) has also been reported.

The dissociation dynamics at excitation energies close to 5.49 eV are particularly interesting. This is the only excitation energy at which a bimodal $O(^3P_J)$ energy distribution has been attributed to N_2O_4 photolysis. The two imaging studies carried out close to this excitation wavelength measured $O(^3P_J)$ distributions with similar profiles (3; 4). However, these studies differ substantially in the determined kinetic energies of the peaks of the $O(^3P_J)$ fragment distributions. Here experiments are described at photolysis energies close to 5.49 eV using the DC slice imaging detection technique (50). Substantially higher energy resolution of the $O(^3P_J)$ kinetic energy release spectra was achieved than has been obtained previously. These experiments were coupled with detection of the NO co-fragments in order to understand the energy partitioning of the dissociation and the mechanism in more detail. The results of these experiments allowed some previous observations to be reappraised critically and provide a new interpretation of the photodissociation dynamics of the $(3)^2A'$ state of NO_2 that is in accord with recent theoretical work (8). The chapter is organized in the conventional experimental, results, discussion format.

4.2 Experimental

In the experiments reported here, DC slice (50) and crush (1) velocity map imaging have been employed in conjunction with mass resolved REMPI spectroscopy in order to probe the nitric oxide and atomic oxygen photoproducts of nitrogen dioxide photolysis at excitation energies close to 5.49 eV using the VMI spectrometer presented in Chapter 3. Reagent molecules were prepared in a pulsed supersonic expansion of 2% NO_2 (Air Products Ltd.) purified by reaction with 5% O_2 (BOC gases) in a seed gas of He (BOC gases). The supersonic expansion was created by a heated pulsed valve

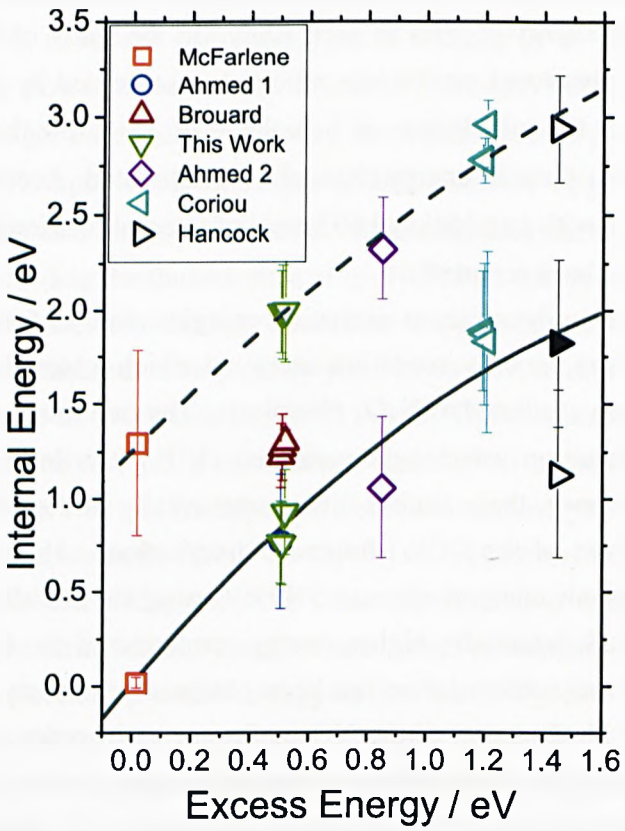

Figure 4.1: Peak internal energy of the NO $(1)^2\Pi_\Omega$ fragments produced in coincidence with $O(^3P_J)$ for two different dissociation channels (high internal energy, low internal energy) at different excess energies in the $(3)^2A'$ state. The figure compares previous studies; McFarlene (2), Ahmed (1) (3), Brouard (4), Ahmed (2) (5), Coroiu (6) and Hancock (7); with this work. The error bars represent the half-width half-maximum of the internal energy distributions reported in these studies. In the experiments of Hancock and Morrison (7) only vibrational profiles were recorded. In this case the rotational energy corresponding to N~57 has been added to the most probable vibrational energy for the low internal energy channel (to give a total internal energy of ~1.82 eV). This rotational energy is in accord with this work at excitation energies close to 5.49 eV and also the theoretical results of Schinke *et al.* (8) This point is drawn as a filled triangle. The lines drawn through the points are quadratic least squares fits but are merely a guide to the eye and have no physical significance. The solid line links data for the channel producing fast O atoms. The dashed line links data for the channel producing slow O atoms.

(General Valve) with a 500 μm orifice and a backing pressure of ~1 bar. For all of the experiments other than the temperature studies, the nozzle was held at 393 K in order to push the NO_2/N_2O_4 equilibrium to 99.9% in favor of the monomer. The expansion chamber was held at a (uncalibrated) pressure between 1-8$\times10^{-6}$ mbar throughout the experiments. The rotational temperature of the molecular beam was determined to be ~20 K from the rotational profile of NO contaminant in the NO_2 expansion. The detection chamber was held at a (uncalibrated) pressure close to 1×10^{-8} mbar throughout these experiments.

The frequency tripled output of a Nd:YAG laser (Continuum Surelite III-10) was used to pump a dye laser (Sirah Cobra Stretch) operating with a Coumarin 2 (Exciton) and, separately, a Coumarin 47 dye (Exciton) to span the required excitation wavelengths. The fundamental was frequency doubled to produce pulses with maximum energies between 2.5 and 3.0 mJ pulses at a repetition rate of 10 Hz at excitation energies between 5.25 and 5.69 eV (236 and 218 nm) with a temporal profile of 4 ns at FWHM. During the experiments, the laser energy was maintained between 50 and 500 μJ and was focused 2 mm beyond the molecular beam jet with a 250 mm fused silica lens. The single laser pulse photodissociated and ionized the photofragments via (1+1) or (2+1) REMPI processes for the nitric oxide and oxygen fragments respectively.

In these experiments the detector was gated to detect ions of a given mass, and for slicing experiments to detect the central part of one of the photoproduct distributions. In the slicing experiments, the detector on-time was maintained below 20 ns (usually less than 10 ns) using a custom built power supply (Photek Ltd.). Images were captured using a 640×480 pixel CCD camera (LaVision Imager 3) and were averaged and processed using the DaVis software package (LaVision) and an event counting macro. Crush velocity map images were post-processed using the Hankel/Abel transform to reconstruct the photoproduct distributions after the projection (167; 168; 175). To generate kinetic energy distributions, all velocity map images (crush and slice) were treated by multiplying the image pixels by the relevant $r\sin\theta$ Jacobian term and integrating the resulting intensity distributions with respect to angle produce 1D functions in energy space. The 1D profiles were then calibrated in energy using NO photoionisation or O_2 photodissociation, the mechanisms and energetics of which are well understood. In the case of slice images, this treatment assumes an infinitely narrow slice

of the photoproduct distribution. Although this is an approximation, the treatment has previously been used to accurately reproduce photoproduct energy and angular distributions from slice images (provided a narrow enough slice of the distribution is measured) (12; 15; 188; 212; 213; 214; 215).

4.3 Results

DC slice images of the three $O(^3P_J)$ fragment spin-orbit distributions were recorded using a single laser, scanning the Doppler profiles of the fragments in order to probe the entire distributions. In these experiments, the pulse energies were maintained close to 250 μJ pulse^{-1}. The resulting images are shown in Fig. 4.2 (panels a, b and c). The corresponding calibrated kinetic energy release spectra are shown in the same figure (panels d, e and f). The kinetic energy resolved spin-orbit branching ratio was determined in separate experiments in which the three images were recorded on the same day under identical conditions (nozzle temperature 393 K, backing pressure 1 bar). The relative signal intensity ratio of the $O(^3P_J)$ fragments with kinetic energies between 0.50 and 1.55 eV was determined to be 1.00:0.71:0.15 for the $O(^3P_2)$, $O(^3P_1)$ and $O(^3P_0)$ fragments respectively. The image intensities in Fig. 4.2 have been normalized to this ratio. This normalization allowed the spin-orbit intensity ratio of the slower fragments to be extracted. For the fragments with kinetic energies between 0 and 0.5 eV this was determined to be 1.00:0.47:0.11.

The kinetic energy distributions of the atomic oxygen fragments are highly structured. The $O(^3P_1)$ and $O(^3P_0)$ fragment distributions peak at kinetic energies of 1.03 and 1.04 eV respectively. The $O(^3P_2)$ distribution shows two major peaks at 0.95 and 1.05 eV. Further experiments were performed to probe the NO $(1)^2\Pi_\Omega$ fragments directly. In these experiments, the NO fragments were probed state specifically via a (1+1) REMPI scheme on the $(1)^2\Sigma^+ \leftarrow (1)^2\Pi_\Omega$ (also referred to as A←X) transitions. These experiments probe the NO fragments produced in coincidence with $O(^3P_J)$ and $O(^1D_2)$ fragments since both product channels are open at excitation energies in excess of 5.083 eV (243.9 nm). Spectra were collected by recording the total mass-resolved (by time-of-flight) NO^+ signal arriving at the phosphor screen while scanning the excitation/probe wavelength. The spectra of the (0, 0), (1, 1) and (2, 2) bands so recorded were in good agreement with those obtained by Im and Bernstein (216) and Grant and

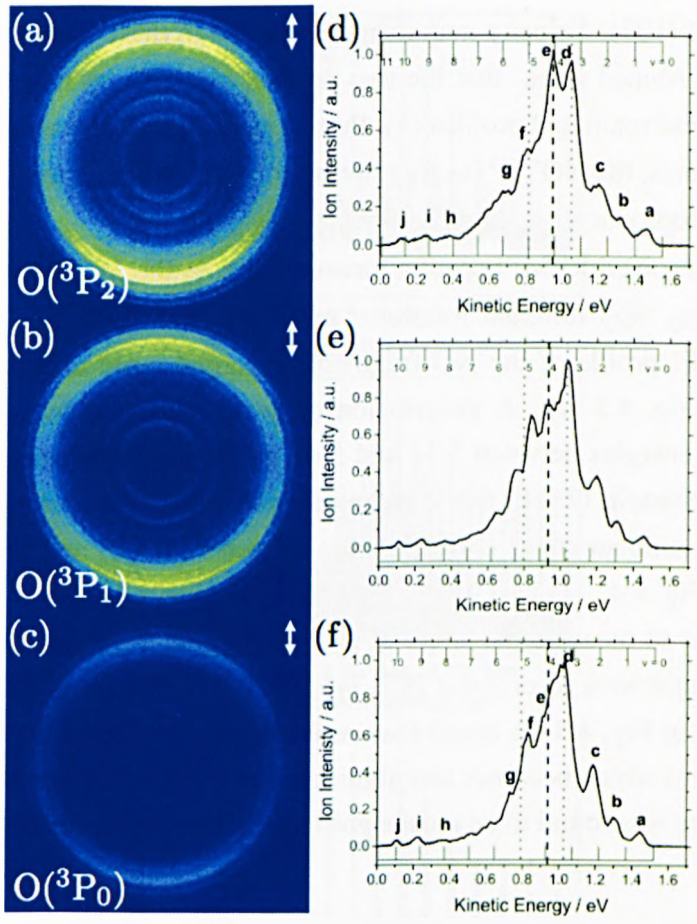

Figure 4.2: DC slice velocity map images of the $O(^3P_2)$, $O(^3P_1)$ and $O(^3P_0)$ fragments, respectively (a), (b) and (c), recorded using a single laser for both photolysis of the parent NO_2 molecule and photoionization of the O fragment. The laser, which is polarized vertically to the image plane, is scanned over an energy range of approximately 39 meV around each ionization resonance in order to ensure that the entire Doppler profile of the O fragments is evenly sampled. Each image is recorded for ~150 000 laser shots. Panel (d) shows the $O(^3P_2)$ translational energy distribution produced from the photodissociation of NO_2 via the $(3)^2A'$ state with associated peak labels as discussed in the text. The distribution is simply obtained by multiplying each image pixel by the appropriate Jacobian, $r\sin\theta$, and integrating the corresponding image (Fig. 4.2(a)) with respect to angle. The resulting 1D profiles were then calibrated against a known kinetic energy release spectrum, usually of O atoms from the ~5.49 eV photodissociation of O_2, recorded immediately prior or post the image acquisition with exactly the same extraction voltages and laser/molecular beam intersection point. Panels (e) and (f) show the photofragment distributions as in (d) but for the $O(^3P_1)$ and $O(^3P_0)$ fragments respectively.

co-workers (103). Velocity map images recorded in these bands confirmed the observations of Ahmed *et al.* that the two product channels produce NO fragments with very different rotational profiles (3). Furthermore, for all of the probed rotational lines in these bands, the NO $(1)^2\Pi_\Omega$ fragments produced in coincidence with $O(^3P_J)$ are the minor photoproducts.

Mass-resolved REMPI spectra measured across the excitation region of the (2, 3) band display very different rotational profiles to the (0, 0), (1, 1) and (2, 2) bands. The REMPI profile of the NO fragments recorded close to the (2, 3) band head is shown in Fig. 4.3 (a). A progression of peaks separated by ~4.6 meV occurs for excitation energies between 5.34 and 5.41 eV in good agreement with the results of Im and Bernstein (216). Some representative velocity map ion images recorded in different rotational states corresponding to peaks (a), (b) and (c) in Fig. 4.3 (a) are shown in Fig. 4.4.

In order to measure the effect of N_2O_4 on the $O(^3P_J)$ kinetic energy distributions, $O(^3P_J)$ images were recorded at 295, 345 and 393 K. The resulting energy distributions are shown in Fig. 4.5. A broad feature is observed in the $O(^3P_2)$ distributions at low temperatures which becomes less significant as the temperature is increased to 393 K. This feature was found to be most significant in the $O(^3P_2)$ distribution.

4.4 Discussion

4.4.1 $O(^3P_J)$ spin-orbit branching ratios

The atomic photofragment signal intensities and the associated kinetic energy distributions and translational anisotropies will be affected by orbital angular momentum alignment effects. In a one-laser one-colour experiment it is impossible to quantify these effects, although the $O(^3P_0)$ fragment is intrinsically unaligned. Ahmed *et al.* have measured the orbital angular momentum alignment of the $O(^3P_1)$ and $O(^3P_2)$ fragments at 5.82 eV (5). Here, it is assumed that the electronic orbital angular momentum alignment does not change significantly between 5.83 and 5.49 eV. With this in mind, the results of Ahmed *et al.* suggest that the fast component (0.5-1.55 eV) of the $O(^3P_2)$ distribution (Fig. 4.3) is not significantly aligned. This means that the observed intensity ratio of the $O(^3P_2)$ to $O(^3P_0)$ images should give a good measure of the true

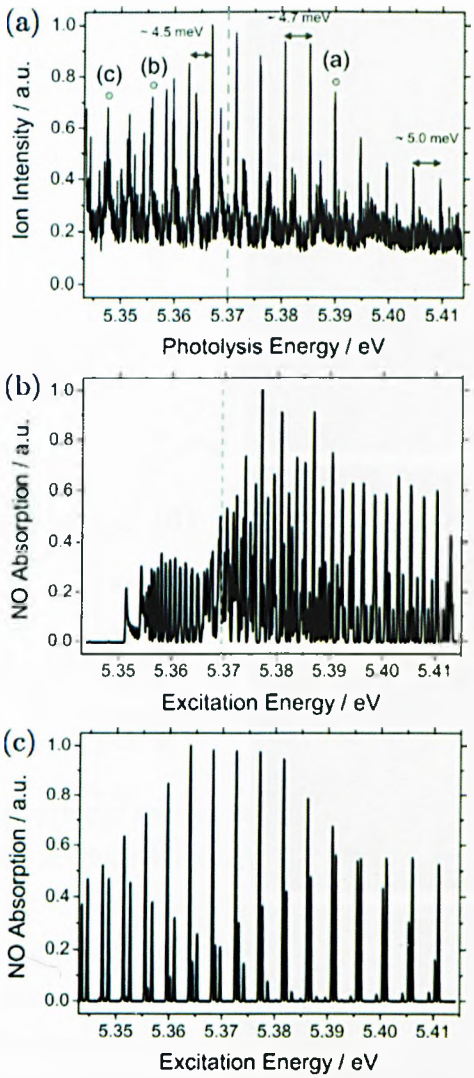

Figure 4.3: Panel (a) mass-resolved (time-of-flight) REMPI excitation spectrum of NO(1 $^2\Pi_\Omega$) recorded at single photon excitation energies spanning the range of the (2, 3) $(1)^2\Sigma^+ \leftarrow (1)^2\Pi_\Omega$ transition. Peak separations are noted to be around 4.6 meV. The expected position of the (2, 3) band head is superimposed on the spectrum as a dashed vertical line at ~5.37193 eV. The lines in the spectrum marked a, b, and c correspond to the excitation energies used to record the images presented in Fig. 4.4. Panels (b) and (c) show simulated NO absorption spectra for the NO $(1)^2\Sigma^+ \leftarrow (1)^2\Pi_\Omega$ transition using the LIFBASE spectral simulation software package (9). Panel (b) shows the absorption of NO fragments produced in **v**=3 with a peak in a statistical rotational distribution at **N**=21, while (c) shows the absorption of NO fragments produced in **v**=1 with a sharp rotational profile peaking at **N**=57 with a FWHM corresponding to the energy spread of 10 rotational levels.

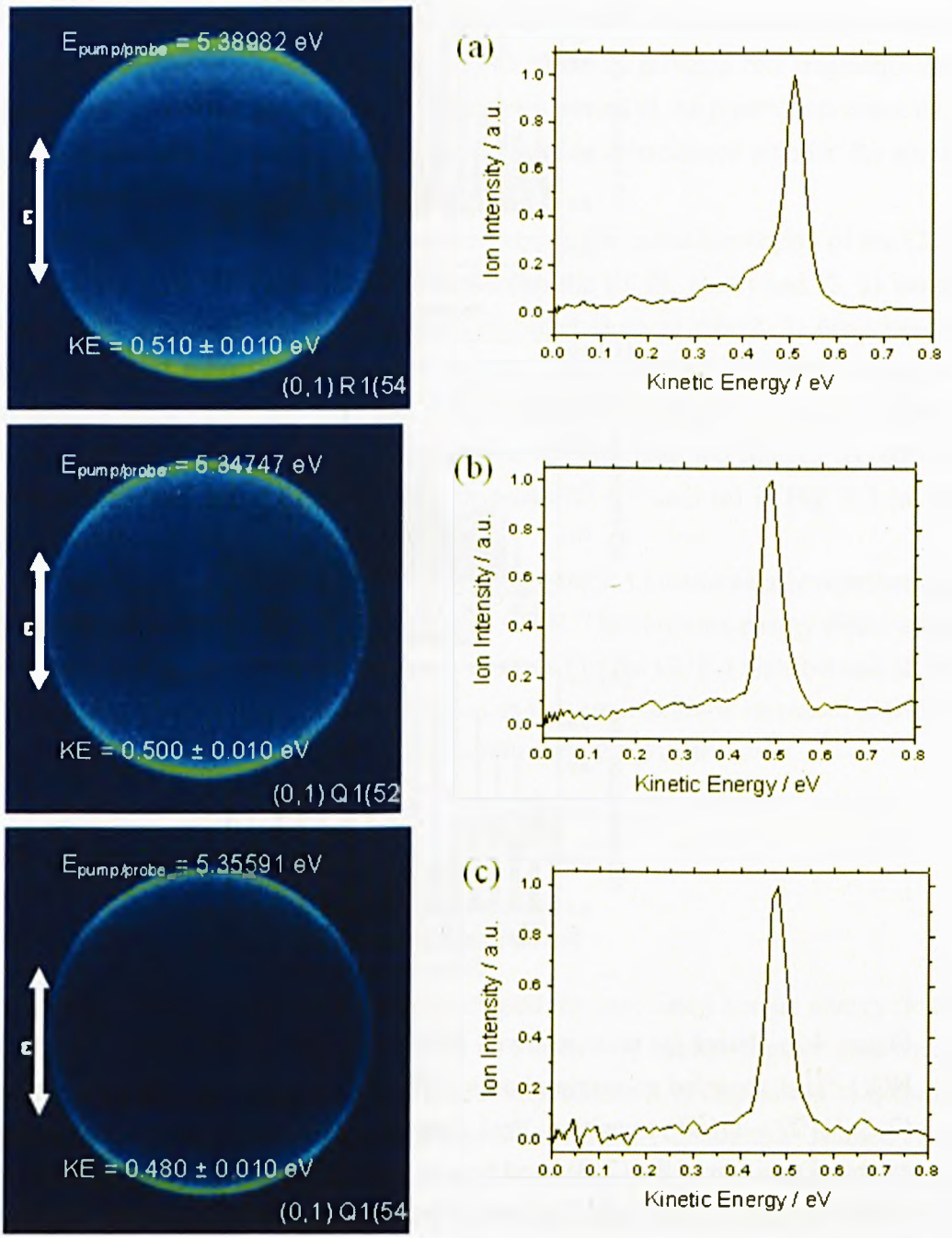

Figure 4.4: Representative velocity map images and corresponding kinetic energy release spectra of NO fragments formed at excitation energies close to 5.29 eV (a, b and c in Fig. 4.3). The kinetic energy release of these fragments is too high for the fragments to be rotationally hot NO $(1)^2\Pi_\Omega$ radicals in v=3. These NO fragments must be formed in the 2, 1 or 0 vibrational states. See text for discussion.

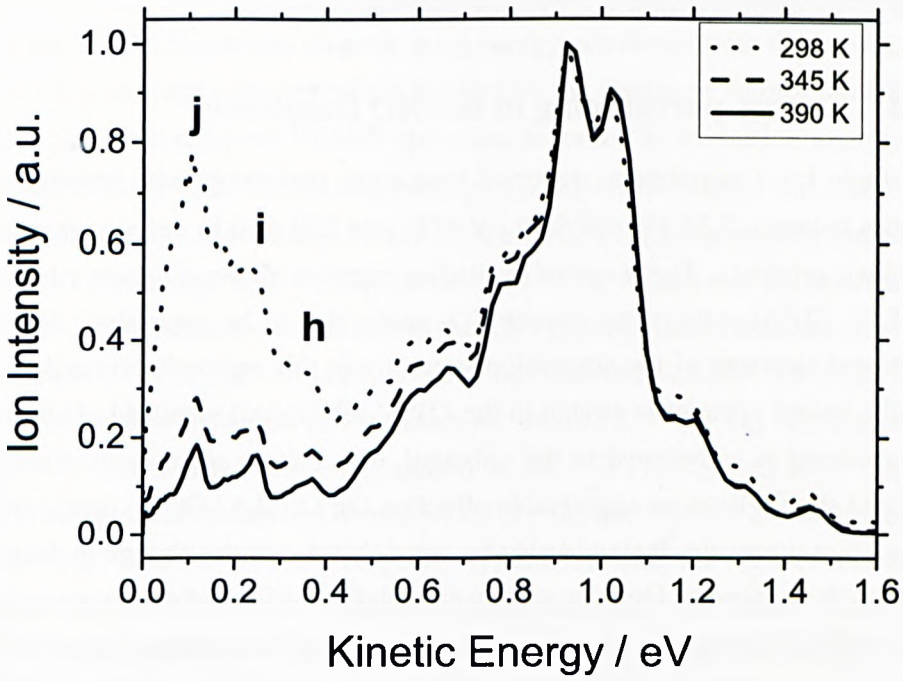

Figure 4.5: $O(^3P_2)$ energy release spectra recorded at a backing pressure of 1 bar and nozzle temperatures of 295 K (dotted line), 345 K (dashed line) and 393 K (solid line).

spin-orbit branching ratio. In contrast, because the $O(^3P_1)$ photoproducts are most probably aligned, their measured intensity must be considered as a lower bound. With this caveat, the spin-orbit intensity ratio of the fast $O(^3P_J)$ fragments is determined to be 1.00:0.71:0.15 at a sample temperature of 393 K; in slight disagreement with the results of Rubahn *et al.* (203) Normalizing the ratio with respect to the two photon line strengths and the state degeneracies highlights the preference of the dissociation for the production of $O(^3P_1)$ photoproducts, which is markedly non-statistical [in agreement with the results of Rubahn *et al.*]. The spin-orbit intensity ratio of the slow $O(^3P_J)$ fragments (0-0.5 eV of kinetic energy) was found to be quite different; favoring dissociation to produce $O(^3P_2)$ photoproducts. A branching ratio of 1.00:0.47:0.11 (uncorrected for degeneracy and line strength factors) is obtained at a sample temperature of 393 K, although the orbital angular momentum alignment effects mean that the $O(^3P_1)$, and possibly the $O(^3P_2)$, signals are lower bounds of the real intensities. De-

spite this, the difference in the spin-orbit branching ratio must reflect real differences in the dissociation dynamics of the slow and fast fragments.

4.4.2 Energy partitioning in the NO fragments

The single laser experiments reported here were performed with varying excitation energies between 5.34 eV and 5.64 eV (232 and 220 nm) in order to probe different photolysis products. The range of excitation energies allows different vibrational levels of the $(3)^2A'$ state of the parent NO_2 molecules to be populated. However, the vibrational structure of the absorption spectrum in this region is primarily associated with the bound symmetric stretch in the $(3)^2A'$ vibrational manifold. This stretch can be considered as orthogonal to the unbound, dissociative asymmetric stretch coordinate, and should have no appreciable effect on the $O(^1D_2)$ / $O(^3P_J)$ branching ratio or dissociation timescale. It should also be noted that due to the change in the photolysis wavelength required to Doppler scan over each $O(^3P_J)$ ionization resonance, structure due to individual rotational levels in the NO co-fragment cannot be resolved in these single laser experiments. Despite this, the energy distributions of all three $O(^3P_J)$ spin-orbit components are highly structured [Figs. 4.2 (d)-(f)].

Focusing on the intrinsically unaligned $O(^3P_0)$ distribution [Fig. 4.2 (f)], the majority of the oxygen atoms are formed with kinetic energies between 1.55 and 0.50 eV. This part of the distribution can be split into at least seven distinct peaks (labeled a-g). The maximum of the distribution occurs at a kinetic energy consistent with the production of $O(^3P_0)$ in coincidence with NO $(1)^2\Pi_{\frac{1}{2}}$ in **v**=3 and **N**~21. This is in good agreement with the results of Ahmed *et al.* (3) when the vibrational comb in their paper is corrected so that **v**=0 is positioned at a total photofragment kinetic energy consistent with dissociation via the NO $(1)^2\Pi_{\frac{1}{2}}$ + $O(^3P_0)$ limit (~2.379 eV). With the correction to the results of Ahmed *et al.*, the peak in their and the distributions reported here are in slight disagreement with Brouard *et al.* who claim that the peak of the distribution is consistent with NO $(1)^2\Pi_\Omega$ production in **v**=4-6. Considering the reported high kinetic energy peaks of the $O(^3P_J)$ distributions observed at 4.99, 5.82 and 6.20 eV (consistent with maxima at **v**=0, **v**=4 and **v**=7) a distribution peaking at **v**=3 for a photolysis energy of 5.49 eV appears to be consistent with the majority of

the previous results (see Fig. 4.1) and it is concluded that the differences between the reported energy distributions must be due to errors in the calibration of the ion images.

If the O(^3P_J) fragments do peak at an energy consistent with the production of the NO $(1)^2\Pi_\Omega$ co-fragments in v=3 (as implied by the results of Ahmed *et al.* (3) and this work), the mass-resolved REMPI spectrum recorded at excitation energies between 5.41 and 5.34 eV [229 to 232 nm, see Fig. 4.3 (a)] should reveal the rotational profile of these fragments. Between 5.41 and 5.34 eV NO $(1)^2\Pi_\Omega$ fragments can only be produced in coincidence with O($^1D_2$) in v=0 or 1. This means that the spectral signature of the v=3 fragments would be due to the O(^3P_J) dissociation channel only. Rotationally cold NO $(1)^2\Pi_{\frac{1}{2}}$ in v=3 is expected to be observed at 5.3692 eV (230.92 nm) due to the reasonable transition probabilities for the $(1)^2\Sigma^+\leftarrow(1)^2\Pi_\Omega$ (2, 3) transition (see Table 4.1) and assumed large population of the NO $(1)^2\Pi_\Omega$ v=3 level (based on the O(^3P_J) energy distributions). Given the NO $(1)^2\Pi_\Omega$ and NO $(1)^2\Sigma^+$ rotational constants (1.7049 cm^{-1} and 1.9956 cm^{-1} respectively) and knowing the higher order terms in the Dunham expansion, (90; 217) and the origin of the NO $(1)^2\Pi^+$ state at 5.45105 eV (90), intense peaks in the v=3 rotational profile would be expected to occur at an excitation energy of ~5.3838 eV (230.29 nm) with prominent rotational lines separated by ~1.5 meV. Examination of the REMPI spectrum in Fig. 4.3 (a) reveals no such features. Instead a broad rotational progression with average peak spacing of ~4.6 meV is visible. Clearly the observed rotational profile does not originate at 5.3692 eV [the $(1)^2\Sigma^+\leftarrow(1)^2\Pi_\Omega$ (2, 3) band origin, shown as a dashed vertical line in the figure] and the NO co-fragment associated with the peak of the O($^3P_0$) kinetic energy release spectrum cannot be in v=3. This remark is confirmed with the presentation of a simulated absorption profile, obtained using the LIFBASE program (9), of NO fragments in v=3 with a statistical rotational profile peaking at N~21 in Fig. 4.3 (b).

It has already been noted that the recorded REMPI spectrum is in agreement with the spectrum observed by Im and Bernstein between 5.23 and 5.46 eV (216). They attributed the signal to a multiphoton dissociation process but an alternative interpretation is presented here. Several representative single-laser mass-resolved velocity map images of the NO fragment recorded between 5.34 and 5.43 eV are shown in Fig. 4.4. These images have been recorded for the peaks marked a, b and c in the REMPI spectrum [Fig. 4.3(a)]. Analysis of the kinetic energies of these fragments indicates that if they were from NO in v=3, the probed states would span rotational states between

$(1)^2\Sigma^+ \leftarrow (1)^2\Pi_\Omega$ Vibrational Band	Band Head / eV	Transition Probability
(3, 3)	5.65147	6.186×10^{-4}
(2, 2)	5.59478	2.624×10^{-3}
(1, 1)	5.53765	1.610×10^{-3}
(0, 0)	5.47989	2.389×10^{-3}
(3, 4)	5.42924	1.807×10^{-3}
(2, 3)	5.36921	1.178×10^{-3}
(1, 2)	5.30850	1.671×10^{-5}
(0, 1)	5.24723	4.909×10^{-3}

Table 4.1: Transition probabilities and excitation energies for selected vibrational bands in the $(1\ ^2\Sigma^+)\leftarrow(1)\ ^2\Pi_\Omega$ absorption spectrum of NO. The data are taken from constants published in the LIFBASE spectral simulation program (9).

N=18 and **N**=33. This would result in peak separations between 1.2 and 2.5 meV in the REMPI spectrum, which are not observed. Furthermore, comparison of the photolysis/probe wavelengths used to obtain the images with the NO $(1)^2\Sigma^+\leftarrow(1)^2\Pi_\Omega$ (2, 3) absorption lines in LIFBASE (9) indicates that the NO fragments with 18-30 quanta of rotational energy could not be probed by the applied laser field. In order to produce a rotational profile with peak separations of the order of 4.6 meV fragments with significantly higher rotational energies are required, corresponding to NO fragments occupying rotational levels with quantum numbers around 57, or ~700 meV of rotational excitation.

The requirement for rotational excitation in the 700 meV range and the kinetic energy release observed in Fig. 4.4 is only consistent with NO fragments in the vibrational range of **v**=0 to 2. Considering the ionization stage of the experiment, summing the photon energy and the maximum vibrational energy of the NO $(1)^2\Pi_\Omega$ fragments (**v**=2), an energy between 5.92 and 5.99 eV can be accessed over the excitation range of Fig. 4.3 (a) at the one photon level. This means that the NO $(1)^2\Pi_\Omega$ fragments could only be probed via the $(1)^2\Sigma^+$ (A) or the $(2)^2\Pi_\Omega$ (B) intermediate state (with term energies of 5.45105 and 5.69256 eV respectively) (90) in a (1+1) REMPI process. It is also noted that ionization of the NO $(2)^2\Pi_\Omega$ state to the ground cation state is forbidden within a Koopmans type picture of the (1+1) ionization process (218). This is consis-

tent with experimental studies in which the NO $(2)^2\Pi_\Omega$ state fluorescence is observed without any competition from ionization. There are no intermediate resonances at the two photon level for a (2+1) ionization process of the NO fragments. Therefore one must conclude that the carrier of the spectrum in Fig. 4.3(a) must be NO $(1)^2\Pi_\Omega$ fragments in v=0, 1 or 2 probed via a (1+1) REMPI process using the NO $(1)^2\Sigma^+$ state as an intermediate resonance.

Because of the shorter bond length of the NO $(1)^2\Sigma^+$ state with respect to the NO $(1)^2\Pi_\Omega$ state (106.37 and 115.08 pm respectively) (90), the rotational bands of the $(1)^2\Sigma^+\leftarrow(1)^2\Pi_\Omega$ transitions are shaded to the blue. It is therefore expected that the absorption lines of rotationally excited NO fragments, which are probed via the NO $(1)^2\Sigma^+$ state, will occur at higher excitation energies than the vibrational band head. With the constraints on the populated vibrational levels of the NO $(1)^2\Pi_\Omega$ fragments imposed by the energetics, there are only two vibrational bands which may be probed in Figs. 4.3(a) and 4.4; the (1, 2) and (0, 1) bands. The line spacing and line intensities observed in Fig. 4.3(a) imply a rotational profile which peaks in a rotational level close to 57. For the $(1)^2\Sigma^+\leftarrow(1)^2\Pi_\Omega$ transition, the 57^{th} rotational level in the Q branch should occur ~113 meV to the blue of the (1, 2) and (0, 1) band heads. Based on the information in Table 4.1 , it is expected that the $Q_1(57)$ rotational line of the (1, 2) and (0, 1) vibrational bands will occur at 5.425 and 5.368 eV respectively. The spectrum shown in Fig. 4.3(a) is therefore attributed to highly rotationally excited NO $(1)^2\Pi_\Omega$ fragments produced in v=1.

The assignment is confirmed by comparison of Fig. 4.3(a) with simulations of the NO $(1)^2\Sigma^+\leftarrow(1)^2\Pi_\Omega$ absorption spectrum using LIFBASE as shown in Fig. 4.3(c). The simulated line positions match the observed positions for NO $(1)^2\Pi_\Omega$ populations in v=1. A non-statistical rotational distribution spanning N=52 to 65 and peaking close to N=60 simulates the intensity profile of the NO fragments; although exact agreement was not sought and is not expected since LIFBASE is only capable of simulating an absorption spectrum and not a REMPI spectrum. The rotational energies of the imaged NO fragments can be calculated from their kinetic energies assuming that the fragments have one quanta of vibrational excitation. The measured kinetic energies of the NO fragments (Fig. 4.4) are consistent with production in v=1 with rotational quantum numbers between 49 and 58.

In the light of this new rovibrational assignment, the NO $(1)^2\Pi_\Omega$ fragments probed by Im and Bernsteins experiment between 5.23 and 5.46 eV (216) correspond to the entire rotational distribution of the $(1)^2\Sigma^+\leftarrow(1)^2\Pi_\Omega$ (0, 1) vibrational band (216). Despite these features being previously attributed to multiphoton dissociation of NO_2, the rotational profile they observed is exactly what is expected for a narrow, highly rotationally excited rotational profile of NO fragments produced in coincidence with $O(^3P_J)$. When REMPI spectra are recorded at either side of the spectrum shown in Fig. 4.3(a), the peak of the rotational distribution is found to occur at excitation energies close to 5.37 eV. If one considers the transition probabilities (see Table 4.1) of the vibrational bands close to the studied wavelengths, one sees that the transition probability for the $(1)^2\Sigma^+\leftarrow(1)^2\Pi_\Omega$ (0, 1) transition is 4 times greater than the corresponding $(1)^2\Sigma^+\leftarrow(1)^2\Pi_\Omega$ (2, 3) transition probability. Were NO $(1)^2\Pi_\Omega$ fragments produced equally populating the rotationally excited v=1 levels and relatively rotationally cold v=3 levels the underlying rotational progression of the (2, 3) band would be observed in the REMPI spectrum [Fig. 4.3(a)] with a peak intensity around a quarter of that of the (0, 1) progression. The absence of such a progression and the signal-noise ratio in the recorded spectrum suggests that in fact the population of relatively rotationally cold levels of the (2, 3) band must be less than $\frac{2}{3}$ of that of the rotationally excited levels of the (0, 1) band. Considering the intensity profile of the $O(^3P_J)$ energy distributions and that the rotational profile of the (0, 1) band is spread over more than 60 rotational levels, it seems likely that the population of the NO $(1)^2\Pi_\Omega$ in v=3 is actually significantly less than $\frac{2}{3}$ that of the population of v=1.

There are a number of potential complications to the analysis of the whole (0, 1) rotational profile. Close to 5.55 eV, the photolysis energy is sufficient to produce NO $(1)^2\Pi_{\frac{1}{2}}$ in v=1 in coincidence with $O(^1D_2)$. The rovibrational profiles of the NO $(1)^2\Pi_\Omega$ fragments produced concomitantly with $O(^1D_2)$ have been probed between 5.41 and 5.71 eV (103; 216). These profiles are characterized by relatively statistical profiles with rotational temperatures between 200 and 400 K (65; 103; 216). The dissociation via the $O(^1D_2)$ channel favours the production of vibrationally inverted NO $(1)^2\Pi_\Omega$ fragments with relatively little energy partitioned into rotation [this will be discussed more fully in the following chapter and has been summarised in a recent publication (65)]. With the low rotational excitation of these NO $(1)^2\Pi_\Omega$ fragments in mind, there should be almost no population of rotational levels above N=35 in the $O(^1D_2)$

v=1 channel. These rotational levels would appear in the REMPI spectrum close to 5.28 eV, but this energy is below the threshold for the production of NO $(1)^2\Pi_\Omega$ in v=1 with $O(^1D_2)$ so they would not be observable in a single laser experiment. Furthermore, NO $(1)^2\Pi_\Omega$ produced in coincidence with $O(^1D_2)$ should not have an effect on the rest of the (0, 1) NO $(1)^2\Pi_\Omega$ with $O(^3P_J)$ rotational profile, as NO $(1)^2\Pi_\Omega$ cannot be formed in v=2 with $O(^1D_2)$ at excitation energies below 5.54466 eV. The result is that the entire (0, 1) rotational profile in the REMPI spectrum is a signature of NO $(1)^2\Pi_\Omega$ fragments formed with $O(^3P_J)$ fragments only. Despite this, however, further complications to the band structure could arise from its spectral width; the band spans a range between 5.23 to 5.44 eV. In this region signatures from NO $(1)^2\Pi_\Omega$ fragments formed with $O(^3P_J)$ in v=2, 3 and 4 could be observed. As discussed previously, the contribution to the total $O(^3P_J)$ signal from NO $(1)^2\Pi_\Omega$ fragments in v=3 must be small. On similar arguments the effect of NO $(1)^2\Pi_\Omega$ fragments in v=2 and 4 probed via the (1, 2) and (3, 4) bands can be assessed.

Analysis of the spectral region which corresponds to the rotationally cold part of the (1, 2) band in the spectrum recorded by Im and Bernstein indicates that the population of these levels is less than $\frac{3}{5}$ of the population of NO $(1)^2\Pi_\Omega$ fragments in v=1 and N~42 (216). If the (1, 2) band were assumed to have a similar rotational profile to the (0, 1) band, a primary peak in the distribution could be expected at an excitation energy of 5.42134 eV (228.697 nm). When spectra are recorded between 5.41 and 5.46 eV only very weak signals are observed. As very few of these rotational lines are above the level of the noise, the signatures of rotational profiles in this energy range are below the detection limit of the experiment. If the rotational profile of the NO $(1)^2\Pi_\Omega$ fragments in v=2 was similar to that of v=1, it is likely that these photofragments would not be able to be detected via the (1, 2) band as the transition probability for this band is almost 300 times smaller than that of the (0, 1) band. The absence of any appreciable signal close to 5.42924 eV (228.364 nm) indicates that the population of fragments produced in v=4 with little rotational excitation must be less than $\frac{3}{4}$ of the population of the rotationally excited NO $(1)^2\Pi_\Omega$ fragments in v=1. Were the v=4 fragments to display a similar rotational profile to those in v=1, a signature close to 5.54764 eV (223.490 nm) would be expected. This would overlap with the (1, 1) vibrational band, throughout which NO $(1)^2\Pi_\Omega$ can be produced in coincidence with $O(^1D_2)$. As the total $O(^1D_2)$ channel makes up ~50% of the total NO $(1)^2\Pi_\Omega$ signal

in v=0, 1 or 2 at photolysis wavelengths which could probe the NO fragments in this band, it is unlikely that the underlying signature of rotationally excited fragments in v=4 could be observed in a single laser experiment due to the low signal intensity. For similar reasons, the underlying signatures of rotationally excited NO $(1)^2\Pi_\Omega$ fragments in v=0 or 3 are unlikely to be observed in a single-laser experiment due to the large signal from rotationally cold v=2 or 0 products formed with $O(^1D_2)$ and probed via the (2, 2) and (0, 0) $(1)^2\Sigma^+ \leftarrow (1)^2\Pi_\Omega$ bands respectively.

It has been argued that rotationally excited NO $(1)^2\Pi_\Omega$ fragments produced in v=1 have a greater contribution to the total $O(^3P_J)$ signal than rotationally cold NO $(1)^2\Pi_\Omega$ fragments in v=3. This should be evident in the energy distributions of the $O(^3P_J)$ fragments. The expected kinetic energies of the $O(^3P_J)$ fragments formed in coincidence NO $(1)^2\Pi_\Omega$ fragments in v=1 and N=50 and N=65 are drawn as dotted lines on the energy distributions in Figs. 4.2(d) to (f). It is seen that this range of rotationally excited NO co-fragments span major peaks of the energy distributions of all three $O(^3P_J)$ spin-orbit components. It should be noted that the spectrum in Fig. 4.3(a) and those recorded by Im and Bernstein are primarily a reflection of the rotational profiles of the $O(^3P_2)$ channel due to the spin-orbit product ratio. It is therefore expected that there should be good agreement between the rotational distribution recorded in Fig. 4.3(a) with one of the main peaks in the $O(^3P_2)$ energy distribution. The kinetic energy expected for peak of the rotational profile (N=57) is drawn on Fig. 4.2(d)-(f) as a single dashed line. The major peak in the $O(^3P_2)$ kinetic energy distribution [Fig. 4.2(d)] matches exactly with the energy expected for the production of an O atom in coincidence with a $(1)^2\Pi_{\frac{1}{2}}$ NO co-fragment in v=1 N=57, i.e. the strongest line in the REMPI spectrum. Similarly for the shoulder of the main peak in the $O(^3P_0)$ profile [Fig. 4.2(f)].

It was previously believed that on excitation to the $(3)^2A'$ state at energies of ~5.49 eV the $O(^3P_J)$ + NO $(1)^2\Pi_\Omega$ dissociation channel led to a sharply peaked vibrational distribution with NO $(1)^2\Pi_\Omega$ fragments formed in v=4-6. In fact, the $O(^3P_2)$ distribution [the major $O(^3P_J)$ spin-orbit product] peaks in coincidence with highly rotationally excited NO $(1)^2\Pi_\Omega$ fragments in v=1 and N~57.

The other peaks in the O atom energy distributions are indicative of further structure in the rovibrational profiles of the NO $(1)^2\Pi_\Omega$ co-fragments. Provided there is no interference in the recorded $O(^3P_2)$ distribution from the photolysis of species other than NO_2 and that the absorption of a single photon led to dissociation, the peak at

kinetic energy / eV	v	~N_{max}	peak
1.47	0	24	a
1.32	1	24	b
1.19	2	20	c
1.05	0	60	d
0.95	1	57	e
0.81	2	57	f
0.71	3	54	g
0.38	?	?	h
0.25	?	?	i
0.12	?	?	j

Table 4.2: Vibrational and rotational assignments of the NO co-fragment responsible for the peaks occurring in the O($^3P_2$) kinetic energy release spectrum [Fig. 4.2(d)].

~1.47 eV [Fig. 4.2(d); peak a] must be due to O($^3P_2$) fragments formed in **v**=0 with a rotational quantum number close to **N**=24. It seems likely that the peak at 1.32 eV (Fig. 4.2(d); peak b) is then due to the production of NO $(1)^2\Pi_{\frac{1}{2}}$ in **v**=1 due to the similarity in the rotational profile of this peak ($\mathbf{N}_{max}$=24). Such a bimodal rotational profile (peaking at **N**~57 and **N**~24) is in agreement with the spectra recorded by Im and Bernstein at excitation energies between 5.25 and 5.41 eV (236 and 229 nm) (216).

With evidence for bimodality in the rotational profiles of the NO $(1)^2\Pi_\Omega$ fragments formed in low **v** and the observation that the major dissociation pathway in the O($^3P_2$) product channel produces highly rotationally excited NO $(1)^2\Pi_\Omega$ fragments in **v**=1, it would be reasonable to expect highly rotationally excited NO $(1)^2\Pi_\Omega$ products in **v**=0 and also **v**=2. Were the **v**=2 fragments to display the same bimodal rotational profile as the **v**=1 fragments with peaks at **N**~24 and 57, peaks would be expected at 1.17 and 0.81 eV in the O($^3P_2$) distribution. In fact prominent peaks are observed in the distribution at 1.19 and 0.81 eV [Fig. 4.2(d), peaks c and f], corresponding to diatomic fragments in **v**=2, **N**~20 and **v**=2, **N**~57 respectively. With a similar argument, rotationally excited fragments (**N**=57) produced in **v**=0 would be expected to occur close to 1.10 eV. A major peak is observed in Fig. 4.2(d) at 1.05 eV which would correlate with **N**~60. With this in mind, the broad peak at 0.71 eV [Fig. 4.2(d) peak g] likely correlates with NO $(1)^2\Pi_\Omega$ fragments in **v**=3 with a maximum in the rotational pro-

file occurring at **N**~54. It would seem that a dissociation mechanism which promotes rotational excitation in fragments occupying the lower vibrational levels adequately explains the major features of the $O(^3P_2)$ energy distribution. As might be expected in a mechanism favoring rotational excitation, fragments formed with vibrational excitation are generally formed with slightly less rotational excitation.

Based on the bimodal rotational profile of the NO $(1)^2\Pi_\Omega$ fragments in **v**=1, there are likely other minor peaks due to rotationally cold fragments in Fig. 4.2(d) which are somewhat masked by the more intense peaks in the $O(^3P_2)$ energy distribution. Assuming similar rotational profiles for the different vibrational states, a peak at 1.05 eV is expected for fragments in **v**=3 and **N**~20. This peak would form part of peak d. The contribution of such a peak to the distribution, however, must be very small (as is evident in Fig. 4.3(a)) and a firm assignment would require the detection of the relevant NO $(1)^2\Pi_\Omega$ co-fragments. There are no obvious features in the distribution which could be assigned to relatively rotationally cold fragments in **v**=4, 5 or 6. It seems that the two rotational modes observed in the $O(^3P_2)$ distribution share a similar vibrational profile.

The peak energies of the $O(^3P_2)$ distribution and the co-fragment assignments are summarized in Table 4.2. A similar treatment has been carried out for the $O(^3P_0)$ energy distribution [Fig. 4.2(f)]. This is summarized in Table 4.3. The main conclusion of the analysis of the energy distributions is that there appear to be two different dissociation mechanisms by which $O(^3P_J)$ atoms can be formed with kinetic energies between 1.55 and 0.5 eV. The major mechanism forms vibrationally cold but rotationally hot NO $(1)^2\Pi_{\frac{1}{2}}$ fragments with a minor mechanism forming rotationally colder diatomic products with a similar vibrational profile. The production of such highly rotationally excited products from the dissociation of the $(3)^2A'$ state has recently been predicted by Schinke and co-workers (8).

4.4.3 Translational anisotropy of the $O(^3P_{2,0})$ fragments

To support the interpretation of the $O(^3P_{2,0})$ energy distributions, the anisotropies of the (in the case of the J=2 fragments assumed) unaligned image features were analyzed using the well known formula introduced by Zare (219). The structure in the unaligned $O(^3P_{2,0})$ energy distributions allows the anisotropy of the image features to

kinetic energy / eV	v	~N_{max}	peak
1.47	0	24	a
1.32	1	24	b
1.19	2	20	c
1.05	0	60	d
0.95	1	57	e
0.81	2	57	f
0.71	3	54	g
0.38	?	?	h
0.25	?	?	i
0.12	?	?	j

Table 4.3: As Table 4.2 but for the O($^3P_0$) kinetic energy release spectrum [Fig. 4.2(f)].

be individually assessed. The spatial anisotropy of each ring obtained by fitting radially averaged profiles as a function of the kinetic energy of the fragments is plotted in Fig. 4.6. The anisotropies of the O($^3P_2$) and O($^3P_0$) images display the same trends with kinetic energy release. Fragments with high kinetic energies have the highest anisotropy parameters (1.5 and 1.2 respectively) with the anisotropy decreasing to a minimum at 0.5 eV (0.5 and 0.6). However, below kinetic energies of 0.5 eV, the O(^3P_J) anisotropy parameter rises. This change in the trend of the anisotropy parameter below 0.5 eV is a clear indication of a difference, on average, in the dissociation mechanism as NO $(1)^2\Pi_\Omega$ fragments are formed with greater internal excitation.

Focusing on the anisotropies between 1.55 and 0.5 eV, changes are expected in the anisotropy parameter due to the different dissociation mechanisms which produce relatively rotationally cold and highly rotationally excited NO fragments. Peaks a, b and c in Figs. 4.2(d) and (f) are assigned to O($^3P_{2,0}$) atoms produced in coincidence with NO $(1)^2\Pi_\Omega$ products in v=0, 1 and 2 with relatively little rotational excitation. Peaks d and e are primarily attributed to rotationally excited fragments produced via the major dissociation pathway; although there is likely underlying structure due to the minor dissociation pathway. Using a simple impulsive model of the dissociation and assuming a 36 fs dissociation timescale [as supported by the work of Tsuji *et al.* (98) and Schinke *et al.* (8)], it would be expected that peaks d and e are the result of a more

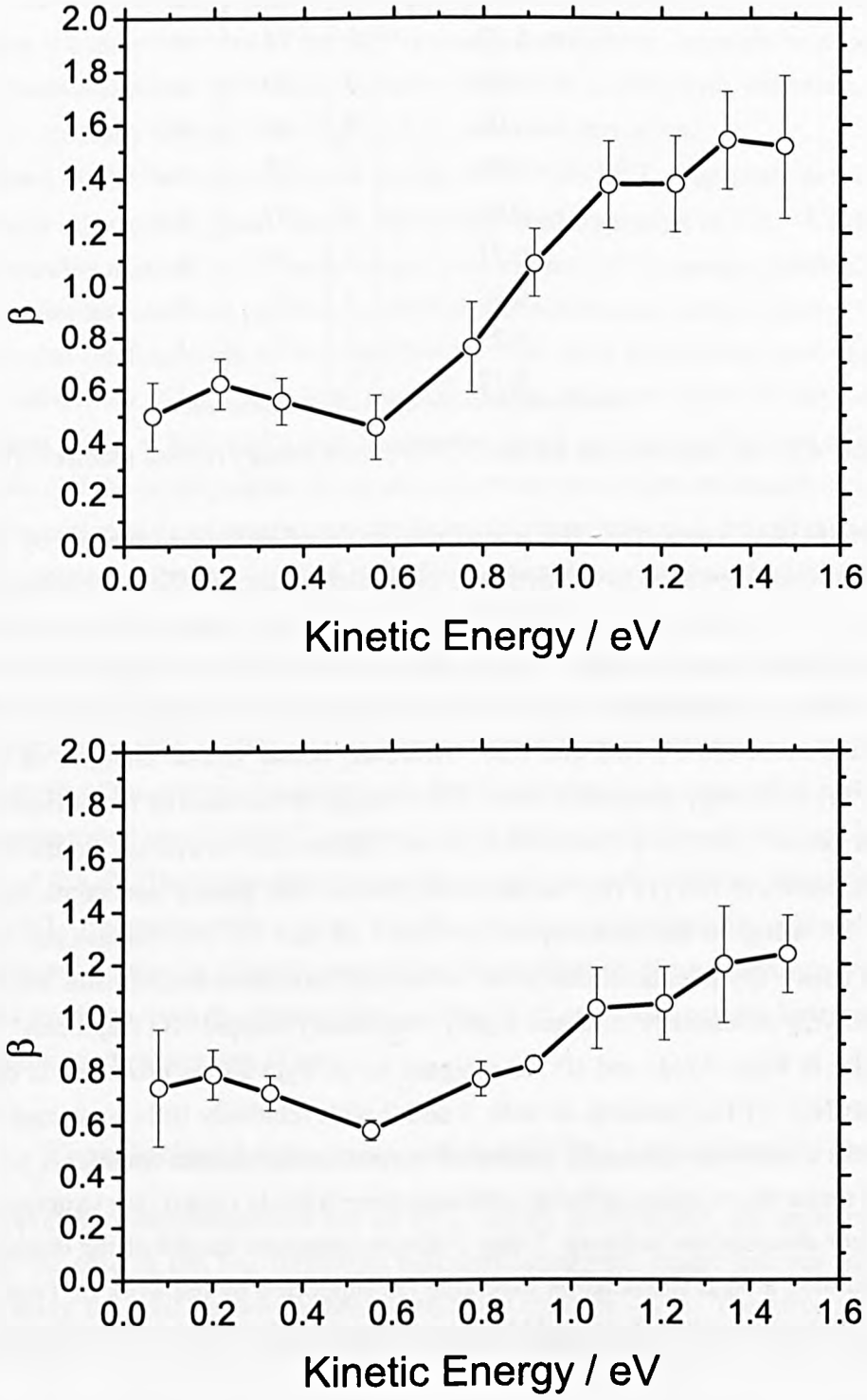

Figure 4.6: $O(^3P_2)$ (top) and $O(^3P_0)$ (bottom) translational anisotropies as a function of the kinetic energy release.

bent geometry at the point of dissociation. Conversely, peaks a, b and c should be the result of dissociation via a more linear parent geometry. It is therefore expected that the anisotropy of rings a, b and c would be greater than those of rings d and e. This is indeed observed in Fig. 4.6 for peaks a, b, d and e. The large reduction of the anisotropy of ring c is rationalized by the large contribution of the underlying high kinetic energy tail of peak d due to diatomic fragments in **v**=0 and **N**~50. At lower kinetic energies (0.50–0.90 eV) the anisotropy parameter reflects an average of the anisotropy due to rotationally cold NO $(1)^2\Pi_\Omega$ products (potentially in **v**=4, 5 and 6), the anisotropy due to rotationally excited fragments in **v**=2 and importantly the highly rotationally excited tails of the rotational profiles which form peaks d and e. The resulting anisotropy is heavily weighted by highly rotationally excited fragments produced from NO_2 dissociating with a reduced bond angle. As a result the anisotropy of the image features reduces as the kinetic energy of the fragments decreases to 0.50 eV.

The image features seen at kinetic energies below 0.50 eV appear to result from the dissociation of NO_2 producing relatively rotationally cold NO $(1)^2\Pi_\Omega$ fragments in **v**=8–11. The appearance of these minor peaks is consistent with the observations of Ahmed *et al.* who also observed a second, competitive, dissociation channel in the $O(^3P_J)$ distributions which produced internally excited NO fragments at a photolysis energy of 5.826 eV (5). Similar peaks have been observed in the $O(^3P_J)$ distributions close to 6.20 eV, where they dominate the distribution (6). It would seem that this dissociation mechanism becomes more important as the photolysis energy is increased from 5.49 to 6.20 nm. Close to 5.49 eV, the intensity of the $O(^3P_J)$ signal at kinetic energies between 0 and 0.5 eV depends on the temperature of the source (see Fig. 4.5). So one must question whether or not peaks h, i and j in Figs. 4.2(d) and (f) are due to interference from N_2O_4; it is not believed so for the following reasons.

The influence of the NO_2/N_2O_4 equilibrium

The effects of the NO_2/N_2O_4 equilibrium on the UV study of the photodissociation dynamics of NO_2 have been discussed previously in the literature (4; 126). The temperature studies reported here (see Fig. 4.5) reveal a broad unstructured underlying feature in the $O(^3P_2)$ kinetic energy profile between 0.0 and 0.5 eV at lower sample

gas temperatures. This feature was prominent in the $O(^3P_2)$ distribution with a significantly smaller contribution to the $O(^3P_1)$ distribution and no contribution to the $O(^3P_0)$ signal at a sample backing pressure of 1 bar, a NO_2 partial pressure of 2% and a sample temperature of 295 K. The maximum of the feature occurred close to 0.1 eV. This broad feature was lost as the sample temperature is raised to ~400 K [see Fig. 4.2(d) to (f)]. The feature had an overall anisotropy of 0.2±0.1 which was in qualitative agreement with the results of Brouard *et al.* who observed a similar structure in the $O(^3P_2)$ velocity profile with an anisotropy of 0.1 using a room temperature sample gas, a sample pressure of 2 bar and NO_2 partial pressures of 10%, 1% and trace quantities in He (4). Brouard and co-workers observed a decrease in the contribution of the broad unstructured component as the partial pressure of the NO_2 in their sample was reduced. Using the spin-orbit ratio of Rubahn *et al.* (203) to normalize their speed distributions it was deduced that the dissociation of N_2O_4 at 5.49 eV produces $O(^3P_2)$ atoms almost exclusively. In experiments in which the total sample pressure behind the molecular beam source is increased to 2 bar a significant increase in the contribution of the broad unstructured component in the $O(^3P_2)$ kinetic energy profile is seen, in complete agreement with the observations of Brouard *et al.* With the higher kinetic energy resolution afforded by the DC slice imaging technique, however, three peaks on top of the broad background feature are additionally observed at 0.22, 0.25 and 0.37 eV [peaks h, i and j in Figs. 4.2(d) and 4.2(f)]. The area under each of these peaks, unlike the underlying profile, is independent of temperature. This implies that these peaks are due to NO_2 photolysis and not due to the photolysis of a contaminant. In separate experiments, the kinetic energy profile of the $O(^3P_0)$ fragment distribution was recorded at 295 and 393 K. In this case the profile was found to be independent of temperature, supporting the interpretation that peaks h, i and j are due to NO_2 photolysis.

Considering the thermodynamic stabilities of the oxides of nitrogen and the sample gas conditions employed here, the only potentially important contaminant species in these experiments are NO and N_2O_4 (220). In a single laser experiment at excitation energies close to 5.49 eV the photolysis of NO to produce $O(^3P_J)$ atoms can be considered unimportant (221). At the laser fluence employed we can also discount any contribution from the dissociation of O_2 (192). As pointed out by Brouard *et al.* (4), the reduction of the NO_2 partial pressure in the reagent mixture would push the NO_2/N_2O_4 equilibrium to favour the monomer. Under the conditions employed by Brouard *et al.*

(room temperature sample, 2 bar backing pressure), NO_2 partial pressures of 10% and 1% result in 48% and 11% of the NO_2 existing in its dimeric form. Given that the N_2O_4 absorption cross-section is ten times that of NO_2 at excitation energies close to 5.49 eV, the N_2O_4 photolysis products would be expected to have a yield between 1 and 5 times those of NO_2. A partial pressure of 0.01% would be required to push the equilibrium 99.9% in favor of the monomer to bring the single photon N_2O_4 photolysis yield to the sub 1% level. It is therefore unsurprising that in the experiments of Brouard and co-workers, using trace amounts of NO_2 did not remove the broad unstructured slow component in the $O(^3P_2)$ kinetic energy profile.

An alternative way of pushing the equilibrium of the sample gas towards the monomer is to increase its temperature. With a backing pressure of 1 bar and a NO_2 partial pressure of 2%, sample temperatures of 298 and 345 K result in ~20% and ~2% of the NO_2 existing in dimeric form. It might therefore be expected that the single photon photolysis yield of N_2O_4 products would increase by a factor of 10 as the temperature is decreased from 345 to 298 K. In fact an increase of about 3.3 is observed which would be consistent, within the experimental uncertainty, with the dissociation of N_2O_4 via a two photon excitation (with an expected increase of a factor of $\sqrt{10}$). Here, the anisotropy between 0.0 and 0.5 eV would represents the average of the anisotropy of the temperature dependent feature and peaks h, i and j. The anisotropies of peaks h, i and j are shown in Fig. 4.6; β~0.5–0.8. As an average anisotropy value of 0.2 is measured between 0.0 and 0.5 eV at 298 K, the temperature dependent feature can be considered to be essentially isotropic. The kinetic energy profile and anisotropies of the slow $O(^3P_2)$ atoms suggests that they are either produced by a threshold dissociation process following two photon absorption of N_2O_4 in which the co-fragment is formed with large internal excitation or that the $O(^3P_2)$ atoms are formed from an NO_2 photoproduct produced by the one-photon dissociation of N_2O_4 in a secondary step. The dissociation mechanism cannot be definitively identified but the broad peak can be attributed to N_2O_4 photolysis by either of the above mechanisms and peaks h, i and j to a dissociation process of the monomer. It is noted that without detection of the NO co-fragments for the peaks h, i and j in Figs. 4.2(d) and (f) and Fig. 4.5, the rovibrational profiles of these peaks cannot be definitively assigned.

Dissociation mechanisms

The calculations of Schinke *et al.* reveal the mechanism for the production of vibrationally cold, highly rotationally excited NO $(1)^2\Pi_\Omega$ products (the major dissociation products at excitation energies close to 5.49 eV) (8). The Franck-Condon window to the parent $(3)^2A'$ state occurs at the repulsive wall of the potential and sets up motion in the bound symmetric stretching coordinate. At the other side of the potential the motion of the NO_2 is deflected towards the dissociative asymmetric stretching coordinate with the dissociation taking place on the timescale of a single symmetric stretch vibration (~36 fs). The vibrational excitation produced due to the position of the Franck-Condon window and the excess energy in the $(3)^2A'$ potential is retained in the dissociation, primarily producing NO $(1)^2\Pi_\Omega$ in **v**=0 or 1. The narrow, inverted rotational profiles can then be explained by the impulsive model with the torque for NO rotation increasing as the NO_2 bond angle decreases. Within the sudden recoil limit, the anisotropy of the relevant $O(^3P_2)$ image features imply that the average bond angle of the parent, as it dissociates on the adiabatic $(3)^2A'$ surface via the major pathway, lies between 118 and 129°.

At higher excitation energies the vibrational energy of this major dissociation channel increases as the initial excitation occurs higher in the $(3)^2A'$ state resulting in a greater degree of symmetric stretch excitation. The rotational energy is calculated to remain relatively constant (8). The overall change in internal energy should be approximately described by the solid line in Fig. 4.1. The major peak in the $O(^3P_1)$ distribution recorded by Ahmed *et al.* at excitation energies close to 5.83 eV (5) [at a $O(^3P_1)$ kinetic energy of 1.18 eV] could therefore be attributed to NO $(1)^2\Pi_\Omega$ fragments produced in **v**=2 and **N**~53. The secondary peak in the $O(^3P_J)$ distributions recorded by Coroiu *et al.* (6) (at total fragment kinetic energies close to 1.24 eV) could similarly be assigned to production in coincidence with NO $(1)^2\Pi_\Omega$ in **v**=5 and **N**~59. This correlates with the experiments of Hancock and Morrison at slightly higher excitation energy where the major peak in the vibrational profile occurs at **v**=5 (although the vibrational profile is convoluted with the profile of the $O(^1D_2)$ co-fragments) (7). At this excitation wavelength a rotational distribution peaking at a rotational level close to **N**=60 would be expected, as predicted by Schinke *et al.* (8)

An explanation for the production of the rotationally cold NO $(1)^2\Pi_\Omega$ fragments in low vibrational levels [peaks a, b and c in Fig. 4.2(d) and (f)] and those produced highly internally excited [peaks h, i and j in Fig. 4.2(d) and (f)] is not forthcoming from the results of Schinke *et al.* (8) When the intensities of peaks a, b and c are analyzed in the three $O(^3P_J)$ images, a spin-orbit ratio of 1.00:0.65:0.15 is measured, which is in reasonable agreement with the overall spin-orbit ratio measured for the fragments with kinetic energies between 0.50 and 1.10 eV (peaks d-g). The vibrational profile of the fragments produced by this secondary dissociation mechanism is similar to that of the major pathway (mainly v=0–2). Presumably the vibrational profile of the secondary dissociation mechanism is also determined early in the dissociation by the position of the Franck-Condon window on the $(3)^2A'$ potential. It therefore appears that there are two different pathways coupling the diabatic $(3)^2A'$ state to NO $(1)^2\Pi_\Omega$ + $O(^3P_J)$. Two different rotational profiles result with the minor profile being due to dissociation via a more linear geometry. The similarity of the spin-orbit ratios for the two dissociation mechanisms implies that the spin-orbit branching is determined late in the dissociation.

The temperature studies strongly suggest that the $O(^3P_J)$ peaks produced with highly internally excited NO $(1)^2\Pi_\Omega$ fragments were due to NO_2 photolysis at energies close to 5.49 eV. A more accurate investigation of the origin of these peaks could be carried out at higher excitation energies where they would be prominent in the photofragment distributions and thermodynamic effects should be more obvious. It is expected that the $O(^3P_J)$ distributions measured with a room temperature sample, a total gas pressure of ~1 bar and NO_2 partial pressures close to 2% at excitation energies between 5.83 eV and 6.42 eV would contain between five and ten times more signal from two photon N_2O_4 photolysis than at 5.49 eV. These effects are evident in the results of Ahmed *et al.* (5) and Coroiu *et al.* (6), who observe broad underlying features in the $O(^3P_J)$ kinetic energy distributions close to 5.83 and 6.17 eV respectively. The excitation energy dependence of the intensity ratio of the broad underlying component and the sharp features at low kinetic energies in the $O(^3P_J)$ profiles provides further evidence that these features have different origins.

A final consideration is the difference between the spin-orbit ratios measured in this study and those recorded by Rubahn *et al.* at excitation energies close to 5.49 eV (203) and Miyawaki *et al.* close to 5.83 eV (222). The overall spin-orbit ratio determined at 393 K in this study is 1.00:0.71:0.15 and is the result of the photolysis of a beam

containing ~0.1% N_2O_4. The room temperature gas mixtures used in the molecular beam studies carried out by Rubahn *et al.* and Miyawaki *et al.* resulted in different concentrations of N_2O_4 at their laser interaction regions. Based on the experimental conditions it is expected that the N_2O_4 concentration should be significantly higher in the experiments of Miyawaki *et al.* (between 19.4% and 48.5% of the total NO_2) in comparison to the studies of Rubahn *et al.* (between 8.8% and 32.4% of the total NO_2). The effect of the N_2O_4 is expected to be around five times greater in the studies of Miyawaki *et al.* due to the increase in the (single photon) N_2O_4 absorption cross-section between 5.49 and 5.83 eV. The results of Brouard *et al.* (4) and those obtained in this study suggest that the 5.49 eV photolysis of N_2O_4 produces $O(^3P_J)$ photoproducts with a spin-orbit ratio heavily weighted in favor of the $O(^3P_2)$ fragment. As all of the spin-orbit ratios are normalized with respect to the $O(^3P_2)$ fragment the affects of N_2O_4 photolysis should be observed as decreases in the relative $O(^3P_1)$ and $O(^3P_0)$ signals. This effect is most obvious in the strong $O(^3P_1)$ signal which decreases, as expected, as the N_2O_4 percentage and its absorption cross-section increase [with intensity values of 0.71, 0.50 and 0.35 for 0.1% at 5.49 eV, 8-33% at 5.49 eV (203) and 19-49% at 5.83 eV (222) respectively]. The effect is less obvious in the weak $O(^3P_0)$ signal, the intensity of which will be particularly sensitive to the probe laser power and the experimental signal to noise ratio. These results further illustrate the advantages of kinetic energy resolved detection in understanding the origins of photofragments as afforded by the VMI technique.

4.5 Conclusions

The dissociation dynamics of NO_2 to produce NO $(1)^2\Pi_\Omega$ and $O(^3P_J)$ have been studied on excitation to the $(3)^2A'$ state at excitation energies close to 5.49 eV using REMPI spectroscopy, DC slice and conventional velocity map ion imaging. It was previously believed that on excitation to the $(3)^2A'$ state at energies of ~5.49 eV the $O(^3P_J)$ + NO $(1)^2\Pi_\Omega$ dissociation channel led to a sharply peaked vibrational distribution with NO $(1)^2\Pi_\Omega$ fragments formed in v=4–6. In contrast to these previous studies, the high kinetic energy resolution achieved by DC slice imaging of $O(^3P_J)$ fragments coupled with REMPI spectroscopy and velocity map imaging of state selected NO fragments reveals that the dissociation favors the production of highly rotationally excited

NO $(1)^2\Pi_\Omega$ fragments. All three $O(^3P_J)$ spin-orbit component energy distributions are found to peak in coincidence with NO $(1)^2\Pi_\Omega$ fragments in **v**=0 and 1 and **N**~60, with a secondary rotational maxima at **N**~20. The translational anisotropy of the fragments has been examined to conclude that the dissociative geometry becomes more bent (on average) as the kinetic energy release of the $O(^3P_J)$ decreases from 1.55 to 0.5 eV. The increase in the anisotropy parameter from 0.50 to 0 eV has been attributed to another minor dissociation mechanism producing kinetically cold $O(^3P_J)$ in coincidence with internally excited NO fragments.

The spin-orbit branching ratio in the $O(^3P_J)$ photoproducts is found to be markedly non-statistical. For O fragments with a translational energy in the range 0.50 to 1.55 eV the intensities of the three channels (uncorrected for degeneracy and line-strength factors) are determined to be 1.00:0.71:0.15 for the $O(^3P_2)$, $O(^3P_1)$ and $O(^3P_0)$ states respectively. Another set of oxygen atoms with translational energies in the range 0.00 to 0.50 eV are also observed. The intensity ratio for these photoproducts is found to be 1.00:0.47:0.10. Temperature studies have highlighted that these fragments are correlated with internally excited NO $(1)^2\Pi_\Omega$ fragments produced from NO_2. The yield of these photofragments is noted to increase with excitation energy. The temperature studies also reiterated that the room temperature study of the UV NO_2 photodissociation dynamics can be biased by the photolysis of N_2O_4.

Chapter 5

Photodissociation of NO_2 in the $(3)^2A'$ State: The $O(^1D_2)$ Channel

5.1 Introduction

In the previous chapter it was demonstrated that dissociation via the predissociative $(3)^2A'$ state forms $O(^3P_J)$ atoms in coincidence with highly rotationally excited NO $(1)^2\Pi_\Omega$ fragments (64). Secondary dissociation pathways were also identified. These experiments highlighted the complexity of the dissociation dynamics above the second dissociation limit. Here the dissociation dynamics of the $O(^1D_2)$ + NO $(1)^2\Pi_\Omega$ dissociation channel are discussed.

As stated in the last chapter, the second absorption band of NO_2 is attributed to a pure parallel transition to the $(3)^2A'$ state, which carries all of the oscillator strength across this excitation range (8). The origin of this potential occurs at an excitation energy of 4.97498 eV (99) where the state is known to have a lifetime of 41.0±1.6 ps (98; 114) which reduces to, and remains, less than 100 fs after excitation above the (0 0 2) vibrational level (98; 114). Below the energetic threshold for $O(^1D_2)$ production the correlation of the adiabatic $(3)^2A'$ state with the first dissociation limit primarily results in the production of internally excited NO $(1)^2\Pi_\Omega$ concomitantly with $O(^3P_J)$ (8; 64; 205; 206). At excitation energies above 5.08291 eV (55; 91), dissociation to produce ground state NO in coincidence with electronically excited oxygen atoms can occur. The threshold for the production of NO $(1)^2\Pi_{\frac{3}{2}}$ occurs

14.856 meV (90) above this level:

$$NO_2\ (1)^2A' \rightarrow NO\ (1)^2\Pi_{\frac{1}{2}};0,0 + O(^1D_2) \qquad E \geq 5.08291\ eV$$

$$NO_2\ (1)^2A' \rightarrow NO\ (1)^2\Pi_{\frac{3}{2}};0,0 + O(^1D_2) \qquad E \geq 5.09777\ eV$$

At excitation energies between 5.1 eV and 6.4 eV, the $O(^1D_2)$ yield is found to remain relatively constant; between 0.4 and 0.5 (7; 99; 100; 101). The experiments of Tsuji *et al.* highlight that the opening of the $O(^1D_2)$ dissociation channel has no effect on the lifetime of the $(3)^2A'$ state (98). Calculations by Jackels and Davidson (105) and Schinke *et al.* (8) give an overview of the topography of the $(3)^2A'$ potential and the latter emphasise its correlation with the $O(^1D_2)$ dissociation channel in the diabatic representation. These calculations also suggest that avoided crossings and the coupling strength between the $(3)^2A'$ and $(4)^2A'$ adiabatic surfaces (also labelled $(2)^2B_2$ and $(2)^2A_1$ in C_{2v} point group notation) are responsible for determining the $O(^3P_J)$:$O(^1D_2)$ branching ratio. Both sets of calculations suggest that the crossings occur at bond angles close to 110° and extended ON-O bond lengths.

A number of previous experimental studies have been carried out to measure the rovibrational product distribution of the NO fragments produced in coincidence with $O(^1D_2)$ on excitation to the $(3)^2A'$ state (3; 5; 6; 7; 101; 103; 110; 211; 216; 223). Ahmed *et al.* used VMI (1) to photodissociate and state selectively probe the NO fragments at excitation energies between 5.49 and 5.64 eV in all three energetically accessible vibrational states with which $O(^1D_2)$ can be formed (3). By probing different rotational states of the NO $(1)^2\Pi_\Omega$ (0, 0) $(1)^2\Sigma^+ \leftarrow (1)^2\Pi_\Omega$ vibrational band using (1+1) REMPI, these investigators found that the $O(^1D_2)$:$O(^3P_J)$ branching ratio varied with rotational state. This was attributed to the production of markedly different rotational distributions via the $O(^3P_J)$ and $O(^1D_2)$ dissociation channels. A similar effect was observed in the (1, 1) and (2, 2) vibrational bands.

Im and Bernstein studied the photodissociation across a similar photolysis energy range; 5.23–5.71 eV (216). By probing the nascent NO $(1)^2\Pi_\Omega$ generated using a one-laser fragmentation/REMPI detection scheme, mass-resolved excitation spectra were recorded which were assumed to probe the $O(^1D_2)$ dissociation channel exclusively. They characterised the rotational energy distributions of the NO $(1)^2\Pi_\Omega$ produced in these vibrational bands with a rotational temperature of approximately 200 K. In an

earlier study, Bigio *et al.* measured similar mass-resolved excitation spectra at energies between 5.49 and 5.64 eV and also attributed the spectra to NO $(1)^2\Pi_\Omega$ fragments produced in coincidence with $O(^1D_2)$ (103). They found that NO $(1)^2\Pi_\Omega$ fragments produced via this dissociation channel had a propensity to populate the highest accessible vibrational level; v=2. Similar TOF measurements of the NO $(1)^2\Pi_\Omega$ and $O(^1D_2)$ fragments have been carried out at excitation energies of ~5.83 eV (211) and ~6.03 eV (223). Both studies measured diatomic fragment vibrational profiles which peaked in the highest accessible vibrational levels. Similarly inverted vibrational profiles have also been observed at higher excitation energies (7).

Coroiu *et al.* probed the $O(^1D_2)$ translational energy distribution and orbital angular momentum alignment using VMI (6). They also recorded a marked vibrational inversion. The differences in the distributions measured using single laser fragmentation and (2+1) REMPI detection schemes centred at excitation energies of 6.03 eV [via the $3p^1$ ($^1P_1$) state] and 6.09 eV [via the $3p^1$ ($^1F_3$) state] were used to assess the electronic orbital angular momentum alignment. This was found to be significant in the $O(^1D_2)$ fragment with the M_J sub-state populations varying as a function of the NO co-fragment internal energy. Analysis of the fragment polarisation also allowed the translational anisotropy of the distribution to be fitted. At these photolysis energies the translational anisotropy parameter was found to decrease as more energy was partitioned into internal modes of the NO.

Vector correlation measurements ($\mathbf{v}$, $\mathbf{J}$) in dissociation processes provide a sensitive probe of the nature of dissociative photoexcited states. In the case of molecular fragments, the correlation of the rotational angular momentum with the fragment recoil velocity gives information about the topography of the dissociative potential. For atomic fragments, the correlation of the orbital angular momentum vector with the recoil velocity of the fragment gives information about the electronic symmetry of the dissociative electronic state. These measurements are particularly useful when dissociative processes occur on optically dark potentials. Polarised photofragment distributions have been measured using a variety of techniques including Doppler (224; 225), ion TOF (226; 227) and ion imaging (6; 228; 229; 230) methods. A strength of ion imaging techniques in carrying out these measurements is that the entire photoproduct energy and angular profiles are recorded in a single experiment. However, as aligned or oriented photoproduct distributions (those with non-equivalent M_J sub-state populations)

do not necassarilly posses axes of cylindrical symmetry, the implementation of the analytic inversion techniques commonly used to construct the original 3D ion distributions from their 2D projections are not generally applicable. Although specific aligned photoproduct distributions may be studied using analytic inversion methods (214; 231) more general treatments require forward convolution techniques (159; 179; 180; 182), fitting procedures (183) or tomographic imaging techniques (40) to extract the alignment information from the raw experimental data. A strength of slice ion imaging approaches (36; 50; 187; 188) is that the central portion of the photoproduct distribution (which carries all of the photofragment radial and angular information) is measured directly. This allows photofragment alignment moments, translational anisotropies and energy distributions to be extracted from the raw images generated using different laser polarisation combinations without the need to invert or deconvolute radial profiles. The use of these methods can be particularly appealing when photofragments are produced with a range of kinetic energies. In this case a small basis set corresponding to particular sets of alignment and translational anisotropy parameters can be used to fit to the experimental anisotropies at different kinetic energies. The fitting parameters then yield the molecular-frame photofragment polarisation information and the translational anisotropy which can be used to reconstruct the kinetic energy profile of the fragments.

In this chapter experiments using the DC slice (50) and crush (1) variants of the VMI technique are described which unravel the photodissociation dynamics of the NO $(1)^2\Pi_\Omega$ + $O(^1D_2)$ dissociation channel of NO_2 at excitation energies close to 5.49 eV. By probing both the atomic and molecular fragments distinct fragmentation pathways producing NO $(1)^2\Pi_\Omega$ fragments with differing degrees of internal excitation are highlighted. Atomic fragment polarisation measurements allow us to probe indirectly the non-adiabatic dynamics responsible for these fragmentation pathways. The chapter is organised in the conventional experimental, results, discussion, and conclusions format.

5.2 Experimental

In the experiments reported here DC slice and crush velocity map imaging has been employed in conjunction with mass-resolved REMPI spectroscopy using linearly po-

larised light fields in order to probe the nitric oxide and electronically excited atomic oxygen photoproducts of nitrogen dioxide photolysis at excitation energies close to 5.49 eV (~226 nm). The experiments were carried out using the VMI spectrometer described in Chapter 3. For these experiments, reagent molecules were entrained in a pulsed supersonic expansion of 2% NO_2 (Air Products Ltd.) purified by reaction with 5% O_2 (BOC gases) in a seed gas of He (BOC gases). The supersonic expansion was created by a heated pulsed valve (General Valve) with a 500 μm orifice and a backing pressure of ~1 bar. For all of the experiments reported here the nozzle was held at 393 K in order to push the NO_2/N_2O_4 equilibrium to 99.9% in favour of the monomer. The molecular beam conditions employed resulted in an (uncalibrated) expansion chamber pressure that was maintained between $1–8\times10^{-6}$ mbar throughout the experiments. This resulted in a (uncalibrated) detection chamber pressure that remained close to 1×10^{-8} mbar. The rotational temperature of the molecular beam was determined to be ~20 K from the rotational profile of NO contaminant in the NO_2 expansion.

The frequency tripled output of a Nd:YAG laser (Continuum Surelite III-10) was used to pump a dye laser (Sirah Cobra Stretch) operating with a Coumarin 2 dye (Exciton). The fundamental output of the dye laser was frequency doubled to produce pulses with maximum energies between 2.5 and 3.0 mJ at a repetition rate of 10 Hz between 5.46 and 5.69 eV (227 and 218 nm) with a temporal profile of 4 ns (at FWHM). During the experiments, the laser energy was maintained between 50 and 300 μJ and was focused with a 250 mm fused silica lens in the centre of the molecular beam. The single laser pulse photodissociated NO_2 and ionized the nitric oxide photofragments via a (1+1) REMPI process.

$O(^1D_2)$ fragments were probed by another laser via a (2+1) REMPI process with a probe photon energy centred around 6.03410 eV (~205.473 nm). The laser was Doppler scanned to probe the entire atomic distribution via the $2p^3 3p^1$ ($^1P_1$) intermediate level that was ionised to the O^+ $2s^2 2p^3$ ($^2D_{\frac{5}{2},\frac{3}{2}}$) levels. The probe light was generated by a dye laser (Sirah Cobra Stretch) operating with an Exalite 411 dye (Exciton) and pumped by the third harmonic of another Nd:YAG laser (Continuum Surelite II-10). The fundamental output of the dye laser was frequency doubled to produce a maximum of 600 μJ of probe light with a temporal profile of 4 ns (at FWHM). In the $O(^1D_2)$ imaging experiments, the probe energy was actually maintained below 170 μJ

to prevent saturation. The probe beam was counter-propagated with respect to the pump beam and was focused by another 250 mm focal length lens a few millimetres beyond the molecular beam in an effort to uniformly probe the photoproduct distributions. A Soleil-Babinet compensator (Optics for Research, SB-10) was used to rotate the pump laser polarisation and a photoelastic modulator (Morvue Electronic Systems, MFS 3) was used to vary the polarisation of the probe.

The detector was gated to detect ions of a given mass, and for slicing experiments to detect the central part of one of the photoproduct distributions. In the slicing experiments, the detector on-time was maintained below 10 ns using a custom built power supply (Photek). Images were captured using a 640×480 pixel CCD camera (LaVision Imager 3) and were averaged and processed using the DaVis software package (LaVision GmbH) and an event counting macro. Crush velocity map images were post-processed using the Hankel/Abel transform to reconstruct the photoproduct distributions after the projection (167; 168; 175). To generate kinetic energy distributions, all velocity map images (crush and slice) were treated by multiplying the image pixels by the relevant $r\sin\theta$ Jacobian term and integrating the resulting intensity distributions with respect to angle to produce 1D functions in energy space. The 1D profiles were then calibrated in energy using NO photoionisation or O_2 photodissociation, the mechanisms and energetics of which are well understood. In the case of slice images, this treatment assumes an infinitely narrow slice of the photoproduct distribution. Although this is an approximation, the treatment has previously been used to accurately reproduce photoproduct energy and angular distributions from slice images (provided a narrow enough slice of the distribution is measured) (12; 15; 188; 212; 213; 214; 215).

5.3 Results

The rotational profiles of the NO fragments formed in coincidence with $O(^1D_2)$ and $O(^3P_J)$ were probed using a single laser and mass-resolved REMPI spectroscopy. In these experiments the wavelength of the dissociating laser was scanned in order to probe different NO rotational states. For the $O(^1D_2)$ channel the three accessible NO vibrational levels (v=0, 1 and 2) were probed (respectively) at excitation energies between 5.462 to 5.510 eV (227.0 to 225.0 nm), 5.515 to 5.575 eV (224.8 to 222.4 nm) and 5.575 to 5.623 eV (224.4 to 220.5 nm). These REMPI spectra may be affected by

rotational angular momentum alignment effects resulting in less efficient ionisation of some of the NO fragments in particular rotational states. However, assuming that these effects are small for low rotational quantum numbers and are similar across particular rotational bands, the rotational profiles should be qualitatively correct. Fig. 5.1 shows single-colour REMPI spectra spanning the (0, 0), (1, 1) and (2, 2) vibrational bands of the NO $^2\Pi_\Omega$ $(1)^2\Sigma^+ \leftarrow (1)^2\Pi_\Omega$ transition. Single-colour DC slice and crushed velocity map images of NO $(1)^2\Pi_\Omega$ fragments were also recorded at a number of different excitation energies in the (0, 0), (1, 1) and (2, 2) vibrational bands.

Fig. 5.2 shows DC slice velocity map images of the $O(^1D_2)$ fragment produced on excitation to the $(3)^2A'$ state at 5.47952 eV for different polarisation combinations. This excitation energy should allow a direct comparison with the single-colour $O(^3P_0)$ data reported in the previous chapter. In these experiments pump-probe delays were maintained at 15 ns. Probe only images are shown in Fig. 5.3; these images were normalised with respect to the two-colour images and subtracted from them in order to produce the images shown in Fig. 5.2. Obvious orbital angular momentum alignment effects are observed in Fig. 5.2 [particularly in the low energy feature of panel (a)] and it is noteworthy that the angular profiles produced by photolysis close to 5.48 eV (two-colour experiment) and 6.03 eV (probe only experiment) are very different.

5.4 Discussion

5.4.1 NO rovibrational profiles

The rotational profiles of the NO $(1)^2\Pi_\Omega$ fragments produced from NO_2 photolysis between 5.46 and 5.69 eV have previously been described by a thermal distribution using a range of rotational temperatures between 200 K and 1600 K (103; 216). Although there is no reason *a priori* that a dissociation process should produce a statistical rotational distribution, the REMPI spectrum shown in Fig. 5.1(a) can be approximately described with a rotational temperature between 300 and 400 K. As with previous experiments (103; 216), the rotational profiles in Fig. 5.1 have been recorded with a single laser. This results in an increase in the photolysis energy as higher rotational states are probed in the R branches of the distributions. Although the change in photolysis energy is relatively small across the rotational profiles [0.05, >0.06 and 0.03 eV for

Fig. 5.1(a), (b) and (c) respectively], this corresponds to a potential increase of 11–17 in the rotational quantum number. This means that it is not strictly valid to model the rotational profiles using a single rotational temperature. Nonetheless, some qualitative statements can be made.

In Fig. 5.1(a), the P_1 branch peaks at a rotational quantum number between **N**=7 and 9 [in Hund's case (b) nomenclature] at photolysis energies close to 5.480 eV with the R_1 branch peaking close to **N**=9 or 10 close to 5.485 eV. The P_2, Q_2 and R_2 branches imply similar, albeit slightly lower, peak N values in the rotational distribution produced at lower photolysis energies (close to 5.465 eV). It is noted that these branches, which are due to ionization of spin-orbit excited NO, show that the $(1)^2\Pi_{\frac{3}{2}}$ fragments are produced with a smaller yield than the ground state fragments. It is also noted that the rotational level population decays below the experimental detection limit at a rotational quantum number close to **N**=22 at the highest photolysis energies (~5.50 eV) employed in Fig. 5.1(a). In contrast to the relatively statistical rotational profiles observed in the (0, 0) band, the (1, 1) and (2, 2) rotational profiles display more non-statistical distributions. Accurate analyses of these bimodal rotational profiles [shown in Fig. 5.1(b) and (c)] are difficult due to the changes in the distributions across the branches as the photolysis and probe energy is scanned. However, it can be stated that the (1, 1) band consists of a relatively 'cold' rotational distribution (peaking close to **N**=7 for both NO spin-orbit components between 5.520 and 5.545 eV) along with a set of features associated with another 'hotter' rotational contour (peaking between **N**=21 and 25 at photolysis energies between 5.550 and 5.575 eV for the fragments in the ground spin-orbit state). The (2, 2) rotational profile shown in Fig. 5.1(c) represents a colder bimodal rotational distribution (as is expected when the majority of the available excess energy has been partitioned into the NO vibrational mode). This distribution can be approximated using two profiles; one peaking close to **N**=4 or 5 and the other close to **N**=12–14. As might be expected, the distribution, produced close to the energetic threshold, shows almost no population of the excited spin-orbit state. All three rotational profiles in Fig. 5.1 seem consistent with rotational populations which peak at higher rotational energies as the photolysis energy increases.

At excitation energies between 5.46 and 5.63 eV the $O(^3P_J)$ and the $O(^1D_2)$ product channels are open with a branching ratio which is close to 1:1 (7; 99; 100; 101). To determine the origin of the features in the REMPI spectra in Fig. 5.1, DC slice and

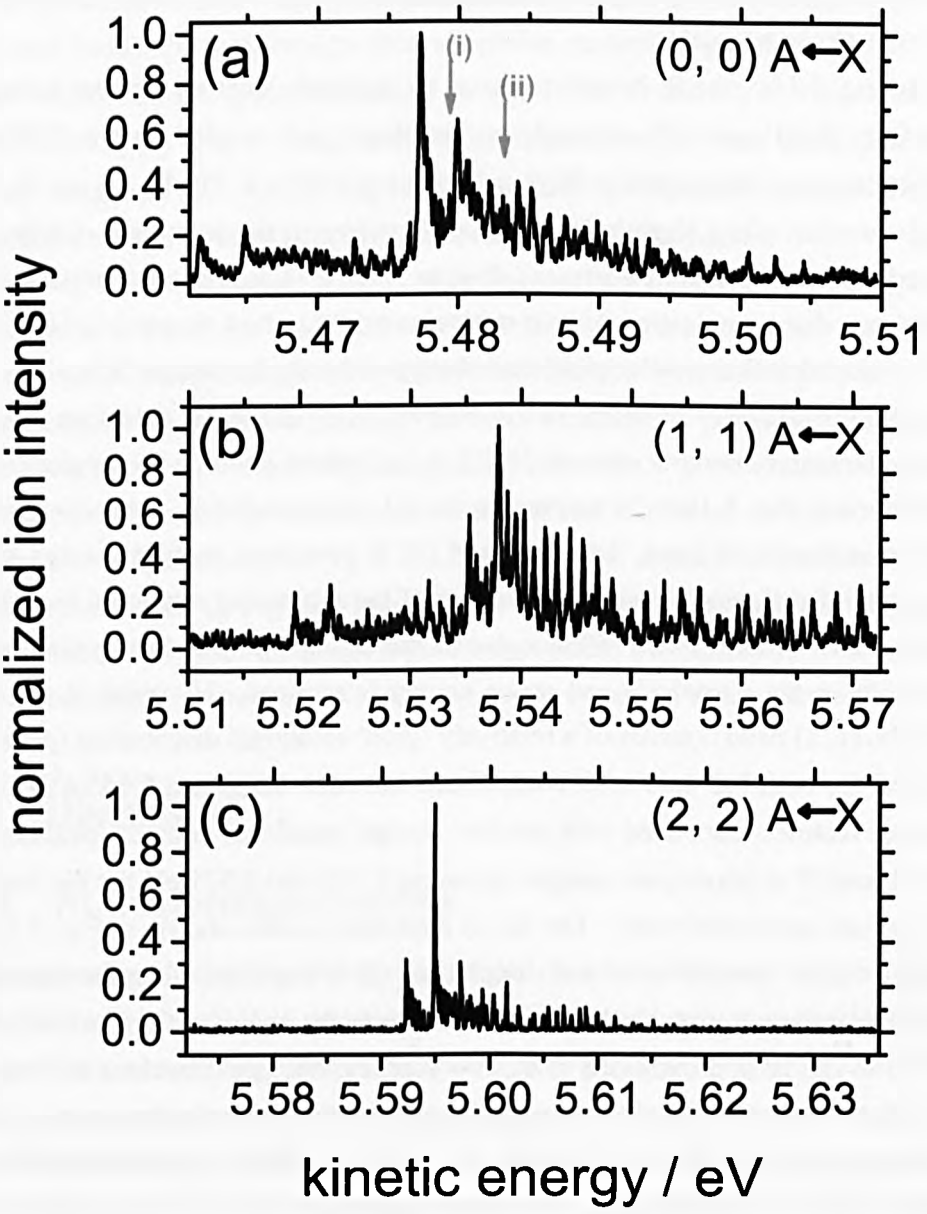

Figure 5.1: Experimental mass-resolved (1+1) REMPI spectra of the (0, 0), (1, 1) and (2, 2) $(1)^2\Sigma^+ \leftarrow (1)^2\Pi_\Omega$ or A←X bands of NO, panels (a), (b) and (c) respectively. The vertical arrows (i) and (ii) in panel (a) indicate excitation energies at which DC slice images of the NO fragments have been recorded (see text and Figs. 5.4, 5.5 and 5.6 for details).

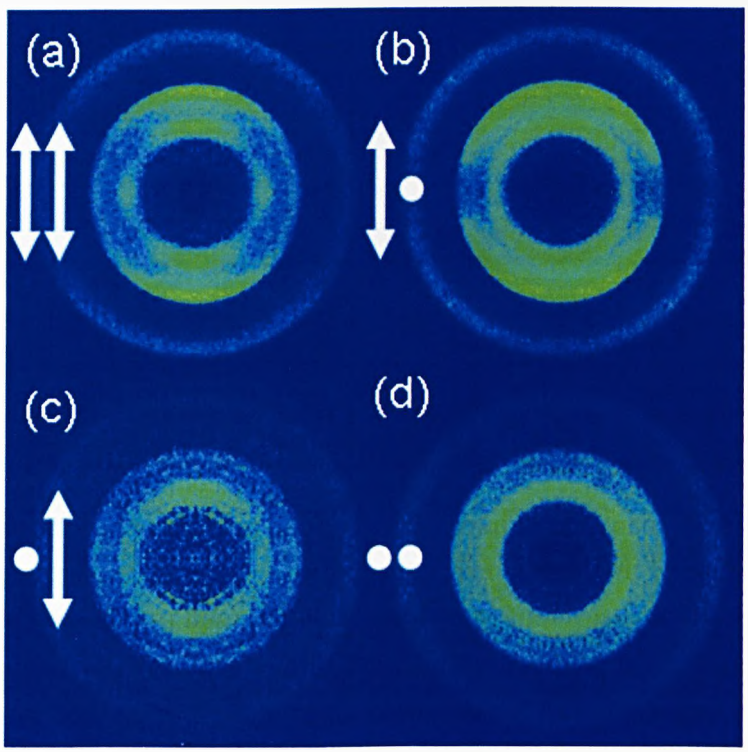

Figure 5.2: DC slice velocity map images of the $O(^1D_2)$ fragment. Panels (a)–(d) correspond to the images recorded with the pump and probe laser polarisations respectively aligned parallel-parallel, parallel-perpendicular, perpendicular-parallel and perpendicular-perpendicular to the detector face. The photolysis energy is 5.4795 eV (226.27 nm). The probe photon energy is 6.0341 eV (205.47 nm).

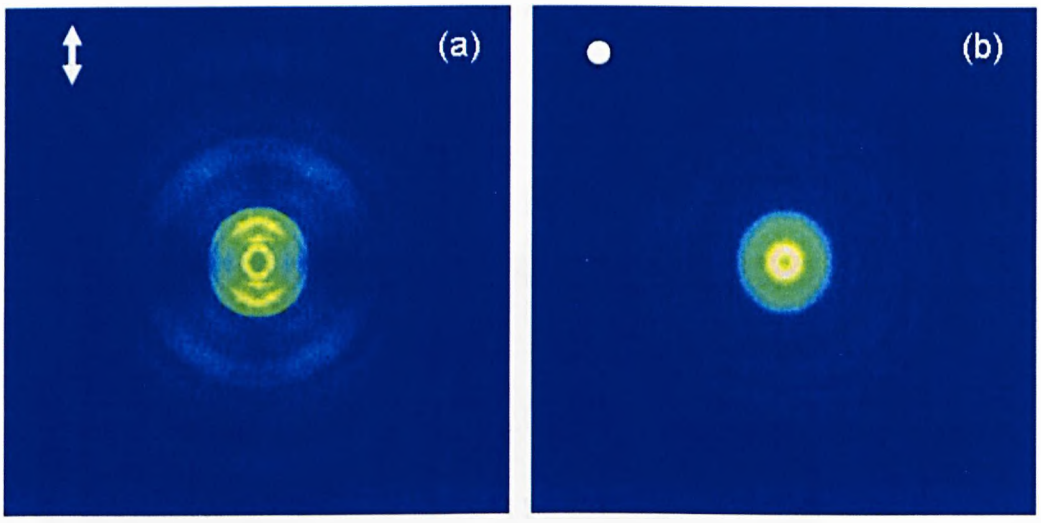

Figure 5.3: Single-colour, probe only DC slice velocity map images of the $O(^1D_2)$ fragment produced at 6.0341 eV (205.47 nm). Panels (a) and (b) correspond to probe polarisations aligned parallel and perpendicular to the detector face respectively.

crush velocity map images have been recorded on different rotational lines in the three spectra. One of the limitations of the DC slice imaging technique is that the method can result in the measurement of low resolution (and in extreme cases biased) kinetic energy profiles for fragments which are formed with low momenta (15). The ability to stretch a photoproduct ion distribution along the TOF axis of the spectrometer (and therefore detect a narrow central part of the Newton sphere) is non-linearly proportional to the fragment mass and its kinetic energy. For a given species and detection gate width, the kinetic energy resolution of the technique increases with the kinetic energy of the fragment. For this reason, under the experimental conditions employed here, DC slice imaging offers improved resolution for NO $(1)^2\Pi_\Omega$ fragments produced in v=0 with relatively little rotational excitation (N=0–22). However, in the case of fragments produced in v=1 and 2 the kinetic energy release is small enough that crush velocity map imaging offers equally good energy resolution, despite the noise introduced by the reconstruction. Figs. 5.4(a) and (b) show representative single-colour DC slice images of NO $(1)^2\Pi_\Omega$ fragments primarily produced in v=0. The kinetic energy profiles of images (a) and (b) are shown in Figs. 5.5 and 5.6.

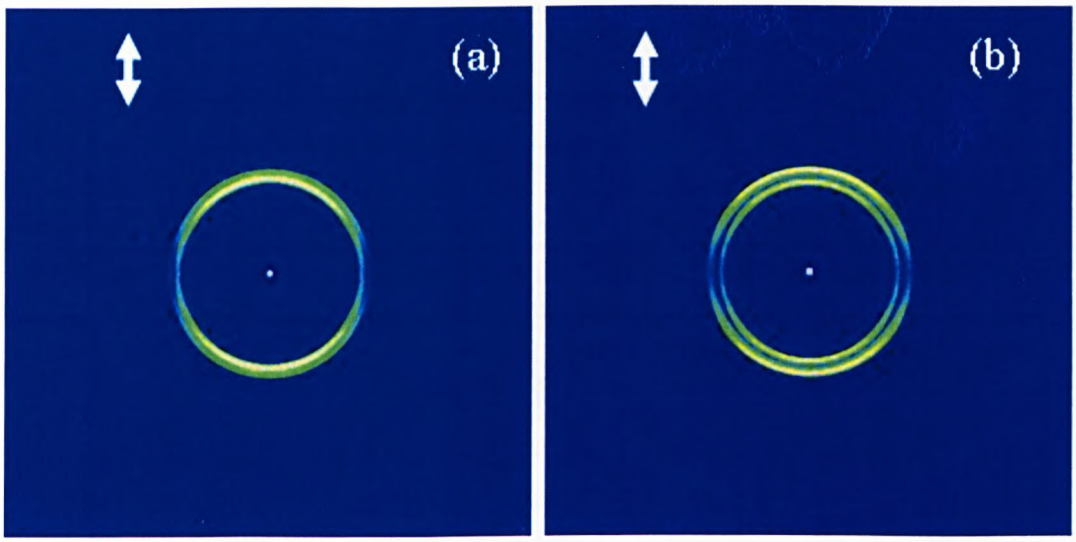

Figure 5.4: DC slice velocity map images of NO $(1)^2\Pi_\Omega$ fragments primarily produced in different rotational states of v=0. The photolysis/probe energies are 5.47941 eV and 5.48324 eV respectively for panels (a) and (b). These energies correspond to those marked above the rotational lines in the REMPI spectrum shown in Fig. 5.1(a) with grey arrows. The double headed arrows on the images show the alignment of the photolysis/probe laser polarisation vector with respect to the detector face.

The energy distribution shown in Fig. 5.5 exhibits two main peaks [(iii) and (iv)] with a number of less intense features, shown in an expanded view in the insert. At an excitation energy of 5.47941 eV, NO_2 photodissociates to give NO $(1)^2\Pi_{\frac{1}{2}}$ with $O(^1D_2)$ with an excess energy of 397 meV and NO $(1)^2\Pi_{\frac{1}{2}}$ with $O(^3P_2)$ with an excess energy of 2.364 eV. This energy is partitioned between electronic (spin-orbit), vibrational and rotational degrees of freedom to produce a rovibrational profile which is similar to the one shown in Fig. 5.1. The remaining energy is partitioned, conserving linear momentum, into the fragment translational energy. The laser energy and focus employed in these single laser experiment only allows the NO $(1)^2\Pi_\Omega$ fragments to be probed in a (1+1) REMPI process. At a photolysis energy of 5.47941 eV, the laser is quasi-resonant with the $P_1(1)$, $P_1(16)$, $R_2(12)$, $Q_2(17)$ and $O_{12}(34)$ transitions of the (0, 0) $(1)^2\Sigma^+ \leftarrow (1)^2\Pi_\Omega$ band. As only the **N**=1 and 16 and 12, 17 and 34 rotational levels of NO in v=0 and the ground and excited spin-orbit states can be probed respectively, the expected kinetic energy of the NO $(1)^2\Pi_\Omega$ products can be calculated. Some calculated

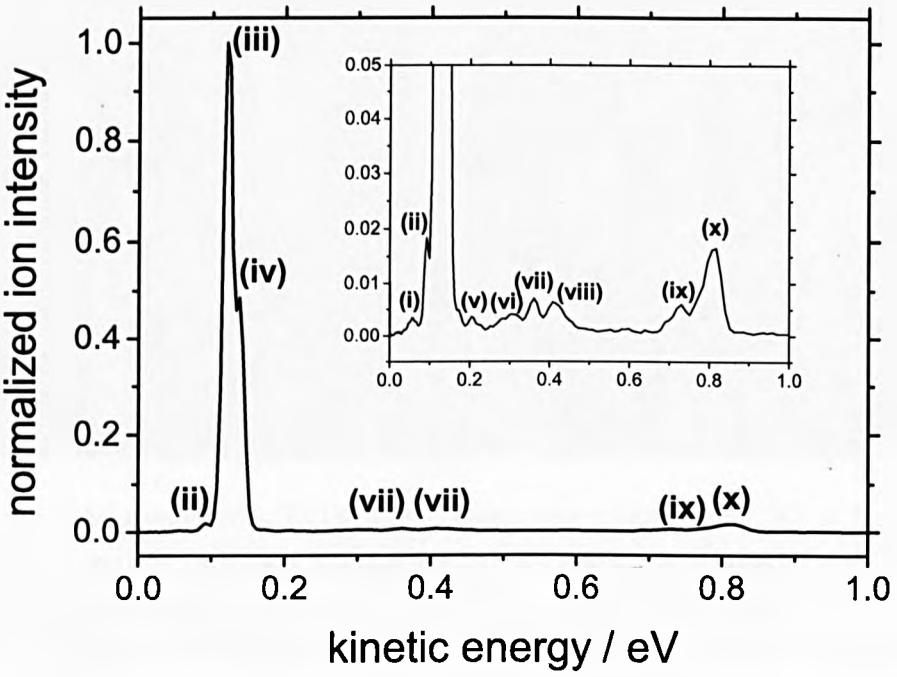

Figure 5.5: Energy distribution produced by multiplying the image pixel intensities in Fig. 5.4(a) by the appropriate Jacobian factor, integrating the resulting image with respect to angle, squaring the image radius and multiplying the result by the energy calibration factor. The inset shows an expanded intensity scale to highlight the weaker features in the energy distribution.

kinetic energies are shown in the right hand column of Table 5.1.

Based on Fig. 5.1(a) peaks associated with ground spin-orbit state fragments are expected to be most intense. Peaks (iii) and (iv) in Fig. 5.5 are therefore attributed to NO $(1)^2\Pi_{\frac{1}{2}}$ (v=0) products formed in N=16 and N=1 respectively with $O(^1D_2)$. This is in good agreement with the calculated kinetic energy release of these fragments (Table 5.1). In addition to these intense peaks, NO $(1)^2\Pi_{\frac{3}{2}}$ fragments formed in v=0 and N=12 and 17 are also expected. These fragments would be formed with kinetic energies of ~121 meV and ~110 meV respectively and are likely masked by the more intense ground spin-orbit state peak due to fragments in N=16. A weak peak is also observed at 53 meV due to the rotationally excited fragments, N=34, formed with a

Peak	Co-fragment(s)	KE / eV (obs.)	Intermediate state	v	~N	Branch	KE / eV (calc.)
(i)	$O(^1D_2)$	0.053	$(1)^2\Sigma^+$	0	34	O_{12}	0.046
(ii)	$O(^3P_J)$	0.092	$(2)^2\Sigma^+$	9	26	P_2	0.086
(iii)	$O(^1D_2)$	0.120	$(1)^2\Sigma^+$	0	16	P_1	0.118
(iv)	$O(^1D_2)$	0.138	$(1)^2\Sigma^+$	0	1	P_1	0.138
(v)	$O(^3P_J)$	0.204	$(3)^2\Pi_\Omega$	5	57	P_1	0.201
(vi)	$O(^3P_J)$	0.304	$(3)^2\Pi_\Omega$	6	33	Q_2	0.273
			$(3)^2\Pi_\Omega$	6	32	Q_1	0.282
			$(3)^2\Pi_\Omega$	6	28	R_2	0.294
			$(3)^2\Pi_\Omega$	6	25	R_1	0.310
(vii)	$O(^3P_J)$	0.358	$(1)^2\Sigma^+$	4	46	Q_1	0.354
(viii)	$O(^3P_J)$	0.415	$(2)^2\Sigma^+$	5	14	P_1	0.415
(ix)	$O(^3P_J)$	0.731	$(1)^2\Sigma^+$	0	34	O_{12}	0.730
(x)	$O(^3P_J)$	0.807	$(1)^2\Sigma^+$	0	16	P_1	0.802
			$(1)^2\Sigma^+$	0	12	R_2	0.805
			$(1)^2\Sigma^+$	0	17	Q_2	0.795

Table 5.1: Interpretation of the peaks in the NO $(1)^2\Pi_\Omega$ kinetic energy distribution shown in Fig. 5.5. The branch refers to the rotational branch via which a particular rotational state was probed, the subscript 1 indicates $\Omega=\frac{1}{2}$ and 2 that $\Omega=\frac{3}{2}$. The calculated kinetic energy refers to the expected kinetic energy of an NO fragment produced at a photolysis/probe energy of 5.47941 eV with the relevant co-fragment and in the relevant spin-orbit and rovibrational state.

low yield in the excited spin-orbit state and probed via the O_{12} band [peak (i)].

As NO $(1)^2\Pi_\Omega$ fragments are equally produced with $O(^3P_J)$ and $O(^1D_2)$ fragments intense features in Fig. 5.5 due to NO produced via the first dissociation channel might also be expected. However, as has been shown in the previous chapter, the majority of the NO fragments formed in **v**=0 concomitantly with $O(^3P_J)$ are highly rotationally excited (N_{max} ~60 at photolysis energies of ~5.494 eV). As the NO fragments produced in coincidence with $O(^3P_J)$ are likely spread over 7 or more vibrational states and in excess of 60 rotational states in the **v**=0, 1, 2 and 3 levels, their contribution to the energy distribution shown in Fig. 5.5 is likely small. Despite this weak features are observed at NO kinetic energies close to 0.4 and 0.8 eV which, on energetic grounds, can only be NO fragments produced with $O(^3P_J)$. Peak (x) is attributed to NO $(1)^2\Pi_\Omega$ fragments produced in **v**=0 and **N**~12, 16 and 17 via a secondary $O(^3P_J)$ dissociation channel (which produces vibrationally cold, relatively rotationally cold NO products). It has been demonstrated in the previous chapter that this channel produces an NO rotational profile peaking at **N**~24 (at photolysis energies of ~5.494 eV) (64) and for this reason a peak associated with NO fragments formed in **v**=0 and **N**=1 with $O(^3P_J)$ is expected to be significantly less intense. Indeed any such peak appears to be below the experimental detection limit. Peak (ix) is then attributed to NO formed in **v**=0 and **N**=34 . The lower intensity of this peak with respect to peak (x) is rationalised by the lower $(1)^2\Sigma^+\leftarrow(1)^2\Pi_\Omega$ transition strength of the O_{12} band.

Another set of weak features is observed in Fig. 5.5 with kinetic energies close to 0.4 eV [peaks (v) to (viii)]. NO fragments with similar kinetic energies are observed right across the rotational contour shown in Fig. 5.1(a) and must be due to internally excited NO produced with ground state oxygen atoms. Previous experiments have assigned these peaks to NO fragments produced in **v**=5 which are probed via the (4, 5) $(1)^2\Sigma^+\leftarrow(1)^2\Pi_\Omega$ vibrational transition (3). In addition to this ionisation pathway it is also possible to ionise rotationally excited NO $(1)^2\Pi_\Omega$ via the (2, 3) and (3, 4) $(1)^2\Sigma^+\leftarrow(1)^2\Pi_\Omega$ bands and the (0, 5) $(3)^2\Pi_\Omega\leftarrow(1)^2\Pi_\Omega$ band with similar probe energies (where states **N**~50, 35 and 20 states would be probed respectively). Furthermore the bandheads of the (1, 6) $(3)^2\Pi_\Omega\leftarrow(1)^2\Pi_\Omega$ and the (0, 5) $(2)^2\Sigma^+\leftarrow(1)^2\Pi_\Omega$ transitions occur close to the bandhead of the (0, 0) $(1)^2\Sigma^+\leftarrow(1)^2\Pi_\Omega$ transition. NO kinetic energies close to 0.4 eV could result for fragments ionised by any of these probe schemes.

The excitation energies used to produce NO images such as those in Fig. 5.4(a) and (b) and those reported by Ahmed *et al.* (3) are optimised on the total NO ion signal. As the ion signal due to NO fragments produced in v=0 with $O(^1D_2)$ dominates the energy distributions, there is no reason why these excitation energies should probe the peak of any probe transition other than those starting from v=0. For this reason, the fortuitous overlap with transitions of other NO vibrational states does not yield any information about the population of these levels. Despite this some qualitative observations can be made. Based on the $O(^3P_J)$ images reported in the previous chapter and published in a previous paper (64), a significantly greater population of NO fragments are expected in rotationally excited levels of v=3 with respect to rotationally cold v=0, 5 and 6 products. If transition probabilities for the resonant step of the ionisation is considered (see Table 5.2), it is found that the (2, 3) transition probability is roughly half that of the (0, 0) $(1)^2\Sigma^+ \leftarrow (1)^2\Pi_\Omega$ transition. However, more than 3 times the population of rotationally excited levels in v=3 is expected with respect to rotationally cold fragments in v=0. Therefore, if the probe laser overlaps with the peak of a resonance corresponding to rotationally excited NO fragments in the (2, 3) band, a peak roughly one and a half times the size of the corresponding peak for NO produced in v=0, low N and with $O(^3P_J)$ should be observed. However, it is noted that these fragments make up less than one tenth of the total NO produced with $O(^3P_J)$ and this portion of the population is spread over more than 60 rotational quanta. For this reason, it is expected that the NO fragments produced with $O(^1D_2)$ will make the dominant contribution to the REMPI spectrum. From the transition probabilities of the (3, 4) $(1)^2\Sigma^+ \leftarrow (1)^2\Pi_\Omega$ and the (0, 5) $(3)^2\Pi_\Omega \leftarrow (1)^2\Pi_\Omega$ bands these fragments are not expected to be observable above the noise level in Fig. 5.1(a) although weak signatures of $O(^3P_J)$ fragments probed via these bands are seen in the NO images (see Tables 5.1 and 5.3).

It is difficult to make an assessment of the population of rotationally cold levels of v=5 and 6 from the $O(^3P_J)$ energy distributions (due to likely overlap with rotationally excited fragments produced in v=2 and 3 respectively), although, it is expected that the population will be relatively small. Considering the transition strengths of the (4, 5) $(1)^2\Sigma^+ \leftarrow (1)^2\Pi_\Omega$ and (0, 5) $(2)^2\Sigma^+ \leftarrow (1)^2\Pi_\Omega$ bands, observation of v=5 fragments is over 5.5 times more likely via the (0, 5) transition. It is also highlighted that the (1, 6) $(3)^2\Pi_\Omega \leftarrow (1)^2\Pi_\Omega$ transition strength should result in efficient excitation to

NO excited state	Vibrational transition	Bandhead / eV	Transition probability
$(1)^2\Sigma^+$	(2, 2)	5.59478	2.624×10^{-3}
$(2)^2\Sigma^+$	(1, 6)	5.54631	1.015×10^{-2}
$(1)^2\Sigma^+$	(1, 1)	5.53765	1.610×10^{-3}
$(1)^2\Sigma^+$	(4, 5)	5.48866	9.342×10^{-4}
$(1)^2\Sigma^+$	(0, 0)	5.47989	2.389×10^{-3}
$(2)^2\Sigma^+$	(0, 5)	5.47894	5.266×10^{-3}
$(2)^2\Sigma^+$	(3, 9)	5.46894	7.541×10^{-3}
$(3)^2\Pi_\Omega$	(1, 6)	5.44113	1.153×10^{-2}
$(1)^2\Sigma^+$	(3, 4)	5.42924	1.807×10^{-3}
$(1)^2\Sigma^+$	(2, 3)	5.36918	1.178×10^{-3}
$(3)^2\Pi_\Omega$	(0, 5)	5.36499	6.526×10^{-3}
$(1)^2\Sigma^+$	(5, 7)	5.33562	1.090×10^{-3}

Table 5.2: Transition probabilities and excitation energies for selected vibrational bands in the absorption spectrum of ground state NO. The data are taken from constants published in the LIFBASE spectral simulation program. (9)

the intermediate resonance despite the expected small ground vibrational level population. It is also worthwhile noting that the ionisation efficiency of the intermediate NO $(2)^2\Sigma^+$ and $(3)^2\Pi_\Omega$ states in these routes should be essentially equivalent to that of the $(1)^2\Sigma^+$ state as the three states exhibit similar equilibrium bond lengths (106.37, 107.5 and 106.46 pm for the $(1)^2\Sigma^+$, $(3)^2\Pi_\Omega$ and $(2)^2\Sigma^+$ states respectively) and vibrational frequencies (0.2940 eV, 0.2910 eV and 0.2885 eV respectively) (111).

Based on the transition probabilities, the NO fragment kinetic energies, the expected vibrational populations and the probe photon energy, the collection of peaks marked (v)–(viii) in Fig. 5.5 are assigned to partially resonant (1+1) ionisation of NO fragments produced in coincidence with $O(^3P_J)$ in **v**=4, 5 and 6 with different degrees of rotational excitation via the (3, 4) $(1)^2\Sigma^+\leftarrow(1)^2\Pi_\Omega$, (0, 5) $(2)^2\Sigma^+\leftarrow(1)^2\Pi_\Omega$ and (1, 6) $(3)^2\Pi_\Omega\leftarrow(1)^2\Pi_\Omega$ bands respectively. Similarly we can assign peak (ii) to the ionisation of highly internally excited NO in **v**=9, in accord with the work oultined in the previous chapter which highlighted the production of translationally cold $O(^3P_J)$ atoms close to this excitation energy. The assignments of the peaks in Fig. 5.5 are summarised in Table 5.1. A similar treatment can be applied to the energy distribution shown in Fig. 5.6.

At a photolysis/probe energy of 5.48324 eV, NO $(1)^2\Pi_{\frac{1}{2}}$ is formed in coincidence with $O(^1D_2)$ with an excess energy of 400 meV and in coincidence with $O(^3P_2)$ with an excess energy 2.368 eV. At this probe energy NO in **v**=0 can be ionised via the $R_1(5)$, $P_1(21)$ and $P_2(27)$ transitions. In Fig. 5.6 two intense peaks are seen at 0.105 eV and 0.137 eV [peaks (iii) and (iv)]. These features are assigned to NO $\Omega=\frac{1}{2}$ fragments produced in **v**=0 and **N**=21 and 5 respectively; in good agreement with the calculated NO kinetic energies (Table 5.3). Peak (ii) is then attributed to NO $(1)^2\Pi_{\frac{3}{2}}$ produced in **v**=0 and **N**=27 with $O(^1D_2)$ while peak (ix) is attributed to NO **v**=0 and **N**=21 produced in coincidence with $O(^3P_J)$ atoms. The collection of weak peaks at NO kinetic energies of ~0.4 eV are then assigned to NO fragments produced in **v**=3, 5 and 6 ionised via the $(1)^2\Sigma^+\leftarrow(1)^2\Pi_\Omega$, $(2)^2\Sigma^+\leftarrow(1)^2\Pi_\Omega$ and $(3)^2\Pi_\Omega\leftarrow(1)^2\Pi_\Omega$ bands. A summary of the assignments of the peaks in Fig. 5.6(d) are given in Table 5.3.

From the energy distributions shown in Fig. 5.5 and 5.6 a number of points can be concluded. Having probed the NO $\Omega=\frac{1}{2}$ fragments produced with $O(^1D_2)$ in the **v**=0, **N**=1, 5, 16 and 21 states it is observed that the 16th rotationally excited state has a higher population than the 1st and the 5th has a higher population than the 21st. This is

Peak	Co-fragment(s)	KE / eV (obs.)	Intermediate state	v	~N	Branch	KE / eV (calc.)
(i)	$O(^3P_J)$	0.063	$(1)^2\Sigma^+$	7	56	R_1	0.065
(ii)	$O(^1D_2)$	0.081	$(1)^2\Sigma^+$	0	27	P_2	0.079
(iii)	$O(^1D_2)$	0.105	$(1)^2\Sigma^+$	0	21	P_1	0.105
(iv)	$O(^1D_2)$	0.137	$(1)^2\Sigma^+$	0	5	R_1	0.137
(v)	$O(^3P_J)$	0.258	$(3)^2\Pi_\Omega$	6	38	P_1	0.253
(vi)	$O(^3P_J)$	0.290	$(3)^2\Pi_\Omega$	6	29	R_2	0.290
(vii)	$O(^3P_J)$	0.345	$(1)^2\Sigma^+$	3	57	Q_2	0.344
(viii)	$O(^3P_J)$	0.421	$(2)^2\Sigma^+$	5	6	R_1	0.429
			$(2)^2\Sigma^+$	5	11	Q_1	0.422
			$(2)^2\Sigma^+$	5	18	P_1	0.407
(ix)	$O(^3P_J)$	0.793	$(1)^2\Sigma^+$	0	21	P_1	0.790

Table 5.3: Interpretation of the peaks in the NO $(1)^2\Pi_\Omega$ kinetic energy distribution shown in Fig. 5.6. The branch refers to the rotational branch via which a particular rotational state was probed, the subscript 1 indicates $\Omega=\frac{1}{2}$ and 2 that $\Omega=\frac{3}{2}$. The calculated kinetic energy refers to the expected kinetic energy of an NO fragment produced at a photolysis/probe energy of 5.48324 eV with the relevant co-fragment and in the relevant spin-orbit and rovibrational state.

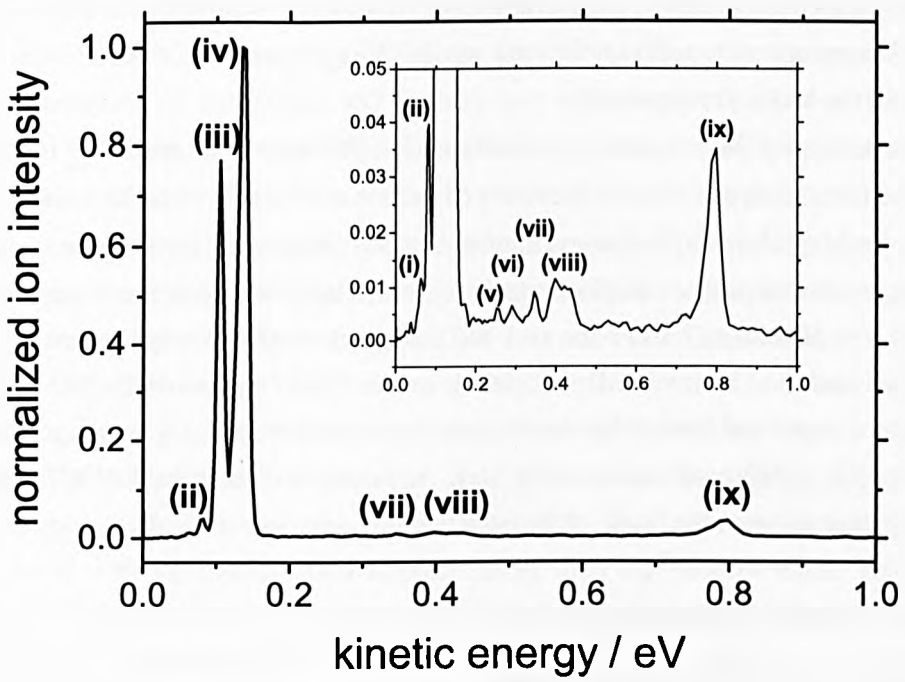

Figure 5.6: As Fig. 5.5 but for the image in Fig. 5.4(b).

in good agreement with the analysis of the entire rotational profile shown in Fig. 5.1(a). NO $\Omega=\frac{3}{2}$ fragments are also observed as minor photoproducts; as expected from the analysis of the whole rotational profile. More importantly, however, NO fragments which span the rotational state range attributed to the REMPI spectrum have been probed and it has been found that NO is produced predominantly with O($^1D_2$) rather than O(^3P_J) with a ratio in excess of 50:1. As expected from the analysis reported in the previous chapter, the contribution of vibrationally excited fragments [probed via the (3, 4) and (2, 3) $(1)^2\Sigma^+\leftarrow(1)^2\Pi_\Omega$ bands and the (0, 5) $(2)^2\Sigma^+\leftarrow(1)^2\Pi_\Omega$ band] to the distribution shown in Fig. 5.1(a) is insignificant after analysis of the images shown in Fig. 5.4. For these reasons the NO fragments produced in v=0 in coincidence with O($^1D_2$) can be confidently assigned as the carrier of the spectrum shown in Fig. 5.1(a).

Similar results are obtained from crush velocity map images recorded on different rotational lines of the (1, 1) and (2, 2) $(1)^2\Sigma^+\leftarrow(1)^2\Pi_\Omega$ vibrational bands. These images are in agreement with those of Ahmed *et al.* (3) As in the (0, 0) band, overlapping probe

transitions occur across the (1, 1) and (2, 2) absorption bands. However, with the same rationale as used to assign the carrier of Fig. 5.1(a) the NO fragments produced in **v**=1 and 2 concomitantly with $O(^1D_2)$ are assigned as the carriers of the spectra shown in Fig. 5.1(b) and (c) respectively.

In summary the rotational distributions for NO fragments produced in **v**=0, 1 and 2 have been recorded. The **v**=0 rotational profile can be described by a single progression, peaking close to **N**=8 at excitation energies close to 5.48 eV. In contrast, the **v**=1 and 2 rotational profiles display significant bimodality with one mode peaking at relatively low N values (7 and 4 for **v**=1 and 2 respectively) and another peaking at **N**=23 for **v**=1 and **N**=13 for **v**=2. By recording velocity map images of the NO fragments at different rotational lines it has been possible to attribute the rotational profiles shown in Fig. 5.1 to NO produced with $O(^1D_2)$. Any contribution from the $O(^3P_J)$ channel is interpreted to lie in the noise of the spectra.

5.4.2 $O(^1D_2)$ imaging

Treatment of aligned photoproducts

DC slice imaging has been used to record the radial and angular profile of the excited state oxygen fragments at a photolysis energy of 5.47952 eV. At this energy $O(^1D_2)$ atoms can be formed with NO $(1)^2\Pi_\Omega$ fragments in **v**=0 or 1 only. Due to the intermediate resonance used in the $O(^1D_2)$ ionisation scheme, these experiments are sensitive to orbital angular momentum alignment in the photofragments. By recording images with different probe laser polarisations the sensitivity to the distribution of aligned photoproducts changes. By monitoring these changes from different perspectives (by changing the pump laser polarisation) fragment polarisation moments can be derived which describe the photoproduct angular distributions. These moments yield the M_J substate populations and their angular dependencies as well as the translational anisotropy of the photoproduct distributions which can be related to the fragmentation mechanism. The alignment moments also allow the photofragment energy distribution to be reconstructed.

In these experiments a distribution of photoproducts created by the dissociation of unaligned parent molecules via a pure parallel transition (8) with linearly polarised

light was considered. The $O(^1D_2)$ fragment atoms were probed in a (2+1) REMPI process using a second linearly polarised light field. If the polarisation vector of the pump field is aligned so that it is perpendicular to the detector face then the angular momentum distribution of the photon will be isotropic with respect to the detector. Furthermore, so will the angular momentum distribution of the unpolarised parent molecules. Similarly a probe field which is polarised perpendicular to the detector face will also have an isotropic angular momentum distribution with respect to the detector face. In this geometry the measured photoproduct distribution must, therefore, be isotropic; we cannot create alignment from unaligned photons and parent molecules.

Fig. 5.7(a) [also Fig. 5.2(d)] shows the $O(^1D_2)$ distribution produced in an experimental geometry with the pump and probe laser polarisations aligned perpendicularly to the detector face. Contrary to arguments above, this image displays a clear anisotropy which increases with fragment velocity. The observed anisotropy must be associated with an experimental artefact rather than the photophysics. Having analysed the laser polarisations at the vacuum windows and found them to be linear, this anisotropy was attributed to non-uniform ionisation of the photoproduct distribution. Relatively low probe laser energies with relatively weak laser foci were used in these experiments to prevent the saturation of the probe transition. Using similar focal length lenses for the pump and probe lasers means that the higher energy photons of the probe beam will necessarily be more tightly focused than the pump. The faster oxygen fragments are moving at ~1700 m s^{-1} so that in the 15 ns pump-probe delay they move ~30 μm. This is comparable with the beam waist of the probe laser. This coupled to the fact that the probe volume is smaller than the pump causes the photofragments expanding perpendicularly to the probe laser propagation direction to be less efficiently probed than those expanding in the parallel direction. This is the same problem encountered in crossed-molecular beam experiments whereby the slower species are more efficiently probed than the fast species. This is corrected for with the so called number density-to-flux transformation (232). To correct the measured photoproduct distributions the anisotropies of the rings appearing in the image shown in Fig. 5.7(a) are used. By fitting to these features using an expansion of even Legendre moments the increase of the anisotropy with fragment velocity can be modeled. Using a quadratic fit to the resulting anisotropy parameters we get an expression for the image intensity with respect to angle and image radius, which can be used to produce the image correction function

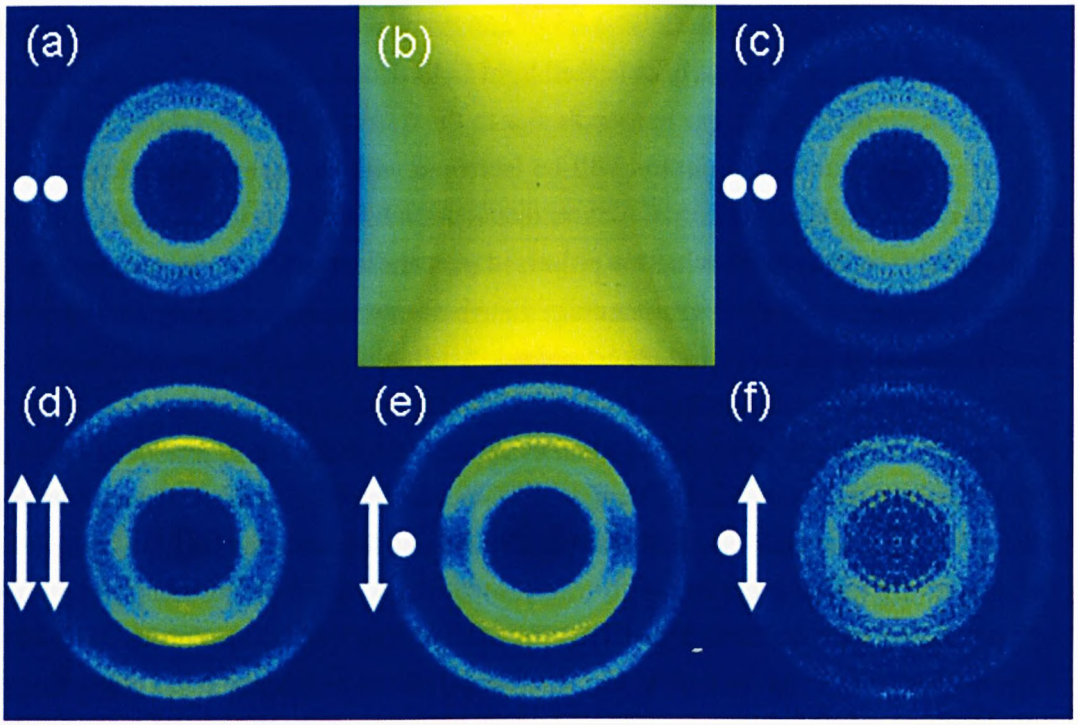

Figure 5.7: DC slice velocity map images of the $O(^1D_2)$ fragment. Panel (a) corresponds to an image recorded with both laser polarisations aligned perpendicular to the detector face and parallel to the TOF direction. Panel (b) shows the correction factor applied to the image in Panel (a) to produce an isotropic distribution (see text). Panels (c), (d), (e) and (f) show corrected DC slice images for the perpendicular-perpendicular, parallel-parallel, parallel-perpendicular and perpendicular-parallel pump and probe laser polarisations respectively.

shown in Fig. 5.7(b). Dividing the raw images by this correction factor removes the contribution of the experimental artefact from the angular distributions, only leaving the contribution due to the photophysics. The corrected images for the four laser geometries are shown in Figs. 5.7(c) to (f). Furthermore as Fig. 5.7(c) displays the central slice of a necessarily unaligned distribution, it yields the $O(^1D_2)$ photoproduct kinetic energy distribution directly. This kinetic energy distribution is shown as a solid line in Fig. 5.8 along with the distributions which are biased by orbital angular momentum effects (those obtained directly from the images shown in Figs. 5.7(d), (e) and (f)).

There are a number of different methods of extracting dynamical parameters from

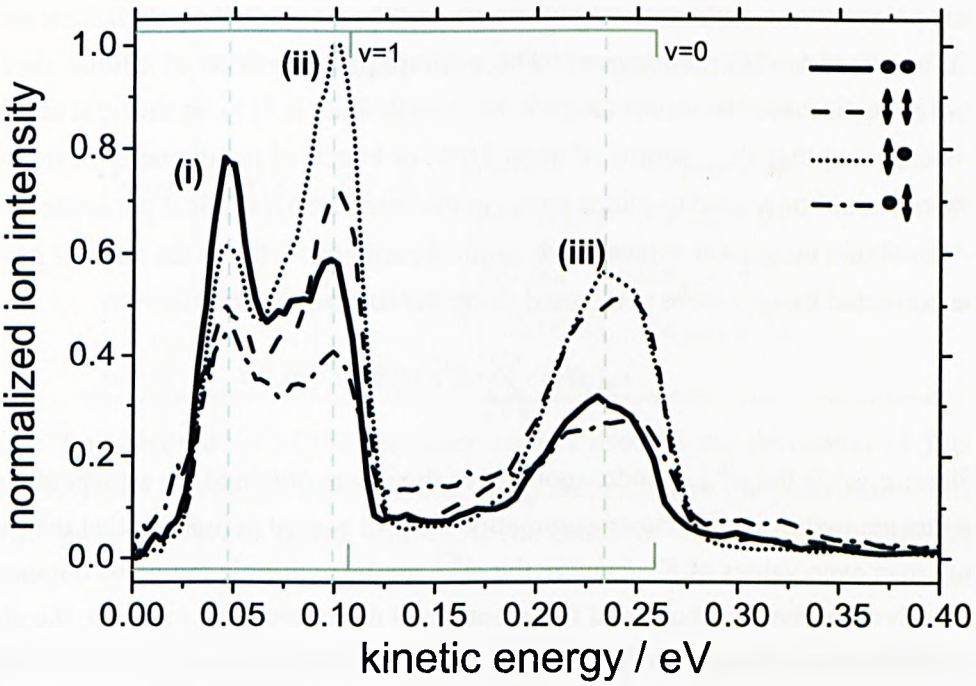

Figure 5.8: O($^1D_2$) energy distributions recorded at an excitation energy of 5.47952 eV for the four laser polarisation combinations associated with Fig. 5.7 (c) to (f). The perpendicular-perpendicular laser polarisation combination (solid line) represents the relative populations (unbiased by orbital angular momentum alignment effects) of the features labelled (i), (ii) and (iii).

velocity map images (159; 179; 180; 181; 182; 183; 229; 231; 233; 234), here a fitting procedure which is based on the previous angular momentum treatment of Mo and Suzuki (229) has been chosen. This treatment is easily implemented and was previously used to extract alignment parameters from velocity map images of the O($^1D_2$) distribution formed from NO_2 photolysis at an excitation energy close to 6.05 eV (6). The treatment used here assumes an infinitely narrow slice through the photoproduct distribution. It is therefore only applicable to crush velocity map images of cylindrically symmetric objects but in the case of slice images the distributions need not have cylindrical symmetry. However, the increase in the effective slice width as the kinetic energy of the photoproducts decreases means that slice images only approximately fit

within this treatment. Depending on the translational anisotropy of the fragments and their polarisations, different image features and their associated polarisation moments will be sliced to different degrees. The assumption and effects of a finite slice width have been discussed by others (12; 15; 50; 212; 213; 214; 215). In the light of this work it is expected that slice widths of order 10%, or better, of the diameter of the Newton sphere should only lead to minor errors in the extracted dynamical parameters.

To obtain numerical values for dynamical parameters, fits to the angular profiles of the corrected images were performed using the following formula:

$$c_n(g) = \sum_{K'kq}{}' a_0^{(K')} \rho_q^{(k)} Z_q^{nK'k}(g), \tag{5.1}$$

where: $c_n(g)$ is the n^{th} Legendre moment of the image obtained for a particular experimental geometry, g; the primed summation symbol is used to indicate that the sum runs only over even values of K', k and q; the $a_0^{(K')}$ are the multipole moments obtained from an analysis of the distribution of fragment recoil directions with regard to the direction of polarisation of the pump laser; the $\rho_q^{(k)}$ are the multipole moments of the fragment polarisation in the body-fixed, "recoil" frame to be defined below; and the $Z_q^{nK'k}(g)$ are coefficients whose values relate the dynamical parameters (the $a_0^{(K')}$ and $\rho_q^{(k)}$) and the experimental geometry to the values of the Legendre moments of the images.

In what follows: (a) the reference frames that are used in the derivation of Eq. (5.1); (b) the definition of the Legendre moments of the observed images; (c) the definitions of the dynamical parameters; (d) the derivation of Eq. (5.8), the formula used in the calculation of the "geometric" coefficients, $Z_q^{nK'k}(g)$; and (e) technical details of the fitting procedure are discussed.

Reference frames. The goal is to use the images obtained in the laboratory to obtain information about the NO_2 dissociation dynamics as seen from a body-fixed perspective. This immediately implies the need for two reference frames: the space-fixed or "lab" frame that we will represent by $X_0Y_0Z_0$ and the body-fixed or "recoil" frame that we will represent by xyz. Because the directions of (linear) polarisation of the pump and probe lasers are important for the dissociation dynamics and polarisation detection, it is useful to define two additional reference frames having their Z axes along those polarisation directions. These are the "pump" frame that we will denote by $X_1Y_1Z_1$

Frame	Axes	Definition
lab	$X_0Y_0Z_0$	X_0 perpendicular to detector face; Y_0 parallel to laser propagation directions; laser polarisation directions parallel to X_0 or Z_0.
pump	$X_1Y_1Z_1$	$X_1Y_1Z_1 \equiv \begin{cases} X_0Y_0Z_0 & \text{if } \epsilon_{\text{pump}} \parallel Z_0 \\ (-Z_0)Y_0X_0 & \text{if } \epsilon_{\text{pump}} \parallel X_0 \end{cases}$
probe	$X_2Y_2Z_2$	$X_2Y_2Z_2 \equiv \begin{cases} X_0Y_0Z_0 & \text{if } \epsilon_{\text{probe}} \parallel Z_0 \\ (-Z_0)Y_0X_0 & \text{if } \epsilon_{\text{probe}} \parallel X_0 \end{cases}$
recoil	xyz	$z \parallel \mathbf{v}_{\text{rec}}$; $y \parallel (Z_1 \times z)$.

Table 5.4: Definitions of the reference frames used in the derivation of Eqs. (5.1) and (5.8). All frames are right-handed, ϵ_{pump} and ϵ_{probe} are the polarisation directions of the pump and probe lasers, and $\mathbf{v}_{\text{rec}}$ is the center-of-mass velocity of the recoiling atom.

and the "probe" frame that we will denote by $X_2Y_2Z_2$. The explicit definitions we have used for these four reference frames are presented on Table 5.4.

Legendre moments of observed images. All of the observed images were obtained in the Y_0Z_0 plane of the lab frame. Furthermore, they are in principle symmetric under reflection on the Z_0 axis (in practice, experimental noise destroys this symmetry, but in the data treatment it was restored by taking the average of the $Y_0 \leq 0$ and $Y_0 \geq 0$ halves). Thus, for every experimental geometry the measured intensity depends only on the lab-frame polar angle, Θ_0, and can be written as a Legendre series:

$$I_{\text{obs}}(\Theta_0; g) = \sum_n \frac{2n+1}{2} c_n(g) P_n(\cos\Theta_0), \tag{5.2a}$$

where $I_{\text{obs}}(\Theta_0; g)$ is the image intensity and P_n is a Legendre polynomial. Inversion of this equation leads to

$$c_n(g) = \int_{-1}^{1} I_{\text{obs}}(\Theta_0; g) P_n(\cos\Theta_0)\, d(\cos\Theta_0), \tag{5.2b}$$

which is the formula that was used in the determination of the Legendre moments of the observed images. As the measurements involve unpolarised parent molecules

and linear laser polarisations, they are free of orientation effects; the only Legendre moments that can contribute to the observed images are those quantifying alignment — in other terms, those associated with even n. It is also noted that the observed images were normalised so that $c_0(g) = 1$.

Dynamical parameters. There is a single approximation that is made regarding the description of the NO_2 dissociation dynamics, namely that the polarisation of the atomic fragment is independent of the angle between the direction of polarisation of the pump laser ($\varepsilon_{\text{pump}}$) and the fragment recoil direction ($\mathbf{v}_{\text{rec}}$). This approximation, which was also used in earlier studies [see, *e.g.*, Refs.(6; 229)], implies that the intensity of the observed image is given by the product of two factors:

$$I_{\text{obs}} = I_{\text{rec}} I_{\text{det}}, \tag{5.3}$$

where I_{rec} is the distribution of fragment recoil directions and I_{det} is the fragment detection efficiency. Except for an unimportant proportionality factor, for a one-photon fragmentation I_{rec} is given by (235)

$$I_{\text{rec}}(\theta, \varphi) = \frac{1}{4\pi}[1 + \beta P_2(\cos\theta)], \tag{5.4}$$

where θ and φ are the polar and azimuthal angles that specify the direction of $\mathbf{v}_{\text{rec}}$ in the pump frame. This expression involves a single dynamical parameter: β, the asymmetry parameter. Note also that it can be written as a covariant multipolar expansion,

$$\begin{aligned} I_{\text{rec}}(\theta, \varphi) &= \sum_{K'Q'} \frac{2K'+1}{4\pi} a_{Q'}^{(K')} C^*_{K'Q'}(\theta, \varphi) \\ &= \sum_{K'} \frac{2K'+1}{4\pi} a_0^{(K')} P_{K'}(\cos\theta), \end{aligned} \tag{5.5}$$

where the $C_{K'Q'}$ are modified spherical harmonics (236) and in the second line the fact that the only nonvanishing multipole moments are $a_0^{(0)} = 1$ and $a_0^{(2)} = \beta/5$ and also the $C_{K'0}(\theta, \varphi) = P_{K'}(\cos\theta)$ relation has been used (236).

In the case of interest here (two-photon fragment excitation), the second factor on the right-hand side of Eq. (5.3) is given by (237)

$$I_{\text{det}} = \sum_k \rho^{(k)}_{q_2=0} \tilde{P}_k, \tag{5.6}$$

where $\rho^{(k)}_{q_2=0}$ is a zero-component multipolar polarisation moment specifying the fragment polarisation in the probe frame (hence the "q_2" notation for the index specifying the component of the polarisation moment of rank k) and $\tilde{P}_k$ is a frame-independent geometric factor given by a known formula (237). The dynamical parameter appearing in this equation, $\rho^{(k)}_{q_2=0}$, can be replaced by a set of others that are of greater interest here — the set of fragment polarisation moments in the recoil frame, $\{\rho^{(k)}_q\}$ — through a rotation of reference frame. We define the recoil-frame polarisation moments via a covariant multipolar expansion of the corresponding density matrix:

$$\langle jm_1|\rho|jm_2\rangle = \sum_{k\,q} \frac{2k+1}{2j+1}\rho^{(k)}_q \langle jm_1, kq|jm_2\rangle, \tag{5.7a}$$

$$\rho^{(k)}_q = \sum_{m_1 m_2} \langle jm_1|\rho|jm_2\rangle \langle jm_1, kq|jm_2\rangle, \tag{5.7b}$$

where $\langle jm_1, kq|jm_2\rangle$ is a Clebsch-Gordan coefficient. The normalisation is such that $\mathrm{Tr}(\rho) = \rho^{(0)}_0 = 1$.

Note that neither the pump and probe laser polarisations are restricted to be the same, nor is it assumed that the fragment polarisation is cylindrically symmetric around the fragment recoil direction. These are the main differences between the formalism employed here and the earlier applications or modifications (6; 229) of the treatment first suggested by Mo and coworkers (229; 237).

Formula for $Z^{nK'k}_q(g)$ coefficients. Other than the conventions and the approximation already mentioned, the derivation of the expression that was used to calculate the $Z^{nK'k}_q(g)$ coefficients involves only previously published expressions and standard techniques of angular momentum algebra. For this reason, it has been decided that the intermediate formulae which, although necessary for checking these results and useful for those interested in their modification (say, through use of different conventions and/or experimental geometries), would make the reading difficult will not be presented here. Instead, a diagram of how the derivation was achieved is presented , see Fig. 5.9. The details of the derivation, including the intermediate formulae, are discussed in the supplementary material (see Appendix C).

As indicated on Fig. 5.9, the starting points of the derivation were Eq. (5.4) and Eq. (5.6); respectively, they correspond to boxes #1 and #3 of the diagram. The two expressions are manipulated in different ways:

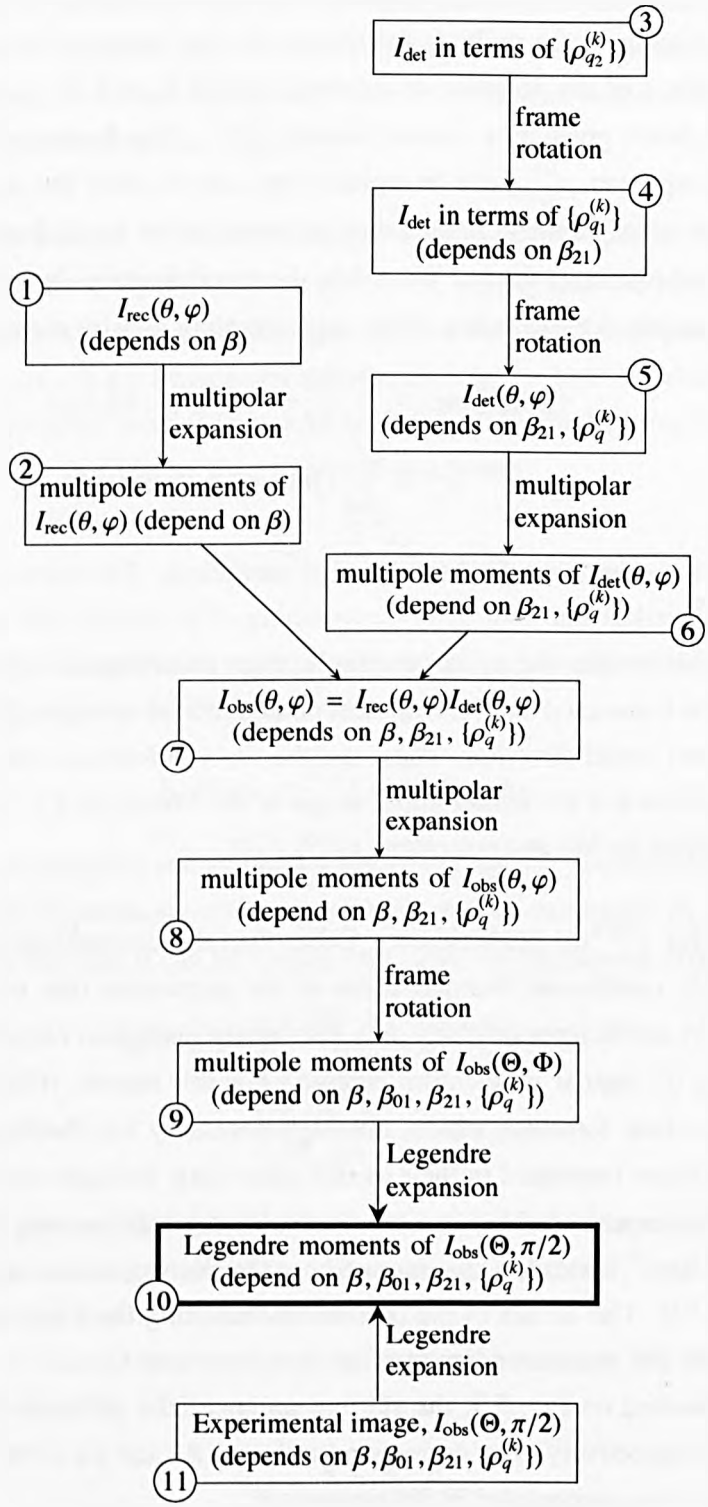

Figure 5.9: Schematic representation of the procedure used in the derivation of Eqs. (5.1) and (5.8).

- Eq. (5.4) is rewritten as a multipolar expansion [this leads to Eq. (5.5) and from box #1 to box #2 of the diagram].

- In Eq. (5.6), the probe-frame (q_2-dependent) fragment polarisation moments are rotated twice, first from the probe to the pump frame [in terms of Euler angles, the rotation is $R_{X_2Y_2Z_2\to X_1Y_1Z_1} \equiv R(0,\beta_{21},0)$] and then from the pump frame to the recoil frame [$R_{X_1Y_1Z_1\to xyz} \equiv R(\varphi,\theta,0)$]. This leads from box #3 to boxes #4 and then #5. The resulting expression is then written as a multipolar expansion, which leads to box #6.

The next step is multiplication of the multipolar expansions of I_{rec} and I_{det} as per Eq. (5.3). The result (box #7 of the diagram) is a product of two multipolar expansions, which depends on the dynamical parameters (β and $\{\rho_q^{(k)}\}$), on an experimental parameter (β_{21}, the single nonzero Euler angle of the rotation between pump and probe frames) and on the angles between the directions of fragment recoil and pump laser polarisation (θ, φ).

Because of its functional dependence on θ and ϕ, the function of box #7 can be seen as being defined on the pump frame, $X_1Y_1Z_1$. This is rewritten as a single multipolar expansion (this takes us down to box #8) and is then rotated into the lab frame; this rotation, $R_{X_1Y_1Z_1\to X_0Y_0Z_0} \equiv R(0,-\beta_{01},0)$, leads to the result of box #9: an expression for the dependence of the lab-frame image on all the dynamical and experimental parameters.

Finally, the value of the lab-frame azimuthal angle was fixed (after symmetrisation, all of the observed images are associated with $\Phi = \pi/2$) and the multipolar expansion was rewritten as a Legendre series. This gives the Legendre moments of $I_{\text{obs}}(\Theta,\pi/2)$, see box #10. As these Legendre moments can also be obtained from the experimental data [use of Eq. (5.2b) takes us from box #11 to box #10], we are now ready for the fitting of the observed images.

As shown in detail in the supplementary material, the procedure just described

leads to the following expression for the geometric coefficients appearing in Eq. (5.1):

$$Z_q^{nK'k}(g) = -\frac{5}{8\pi}(2K'+1)\sqrt{2k+1}\langle 20,k0|20\rangle \begin{Bmatrix} 2 & 2 & k \\ 2 & 2 & 1 \end{Bmatrix} \times {\sum_{\substack{T\,t_0 \\ K\,Q}}}' (-1)^{t_0/2}(2K+1) d^T_{t_0 Q}(\beta_{01}) d^k_{Q0}(\beta_{21}) I^{Tn}_{t_0 000} \times I^{kK'}_{-QqQ0}\langle K'0, KQ|TQ\rangle\langle K'0, K0|T0\rangle, \tag{5.8}$$

where the primed summation symbol again indicates that the sum only runs over even values of the dummy indices, $\{\cdots\}$ is a 6-j coefficient, $d^A_{a_1 a_2}(\xi)$ is a reduced rotation matrix element, and

$$I^{AB}_{a_1 a_2 b_1 b_2} = \int_{-1}^{1} d^A_{a_1 a_2}(\xi) d^B_{b_1 b_2}(\xi)\, d(\cos\xi). \tag{5.9}$$

Note that Eq. (5.8) also reveals to what fragment polarisation moments the measurements are sensitive. While some of the conclusions are rather obvious (*e.g.*, the vanishing of $\langle 20, k0|20\rangle$ for odd k implies that fragment orientation cannot be observed), the others (these measurements are only sensitive to the real part of fragment polarisation moments with even q) are less so. Readers interested in proofs of the latter should consult the supplementary material.

Fitting procedure. The observed Legendre moments depend nonlinearly on six dynamical parameters: β, $\rho_0^{(2)}$, $\rho_{+2}^{(2)} = \rho_{-2}^{(2)}$, $\rho_0^{(4)}$, $\rho_{+2}^{(4)} = \rho_{-2}^{(4)}$, $\rho_{+4}^{(4)} = \rho_{-4}^{(4)}$. To deal with this nonlinear, multidimensional fitting problem the downhill simplex method has been used (238; 239). Other than Eq. (5.1), all it requires is specification of seven sets of initial values for the fit parameters and of the parameter constraints.

The starting values have been chosen as combinations of (i) orthogonal polarisation states spanning the complete space of accessible fragment polarisation states with (ii) an asymmetry parameter in one of the extremes of its allowed range: $\beta = -1$ or $\beta = 2$. Once a local minimum was found, we restarted the calculation by replacing one of the combinations of β and $\{\rho_q^{(k)}\}$ (one of the simplex vertices) by the one corresponding to that minimum, and the procedure was repeated until the global minimum was reached and the fit no longer improved.

As for parameter constraints, $-1 \leq \beta \leq 2$ has been used and the fact that, for any valid set of polarisation moments, the corresponding density matrix must be positive semidefinite; by rejecting density matrices with negative eigenvalues, the fit results could be prevented from moving into physically meaningless regions of the parameter space.

The results were obtained by simultaneous fits of all experimental geometries with at least one laser polarisation not perpendicular to the detector face (as discussed above, the arrangement in which pump and probe laser polarisations are both perpendicular to the detector face is insensitive to fragment polarisation). The set of complex fragment polarisation parameters thus obtained, $\{\rho_q^{(k)}\}$, was then transformed into a set of real polarisation parameters, $\{\rho_{q\pm}^{(k)}\}$, defined according to the Hertel-Stoll convention (240), which in this case can be expressed as

$$\rho_{q+}^{(k)} = \sqrt{2}\rho_q^{(k)}, \qquad q > 0, \tag{5.10a}$$

$$\rho_{q-}^{(k)} = 0, \qquad q > 0, \tag{5.10b}$$

$$\rho_0^{(k)} = \rho_0^{(k)}. \tag{5.10c}$$

The real multipole moments have well-defined limits (241) and a more direct physical/directional significance (242).

The results of the fitting procedure for the uncorrected and corrected images shown in Figs. 5.2 and 5.7 are shown in Fig. 5.10. The differences in the angular profiles and their fits for the uncorrected and corrected data highlight the effects of the correction procedure outlined at the beginning of this section. It is noted that the experimental artefact has a substantial effect on the dynamical parameters obtained from the fits. In the remainder of the discussion the energy distributions and dynamical parameters obtained from the corrected data set are considered exclusively.

Energy distribution

The $O(^1D_2)$ energy distribution (unbiased by orbital angular momentum alignment) shown as the solid black line in Fig. 5.8 displays three broad features which peak at kinetic energies of 0.047, 0.100 and 0.238 eV [marked (i), (ii) and (iii) respectively]. At a photolysis energy of 5.47952 eV the excess energy above the second dissociation limit is ~382 meV and it is possible to produce $O(^1D_2)$ in coincidence with NO $(1)^2\Pi_{\frac{1}{2}}$

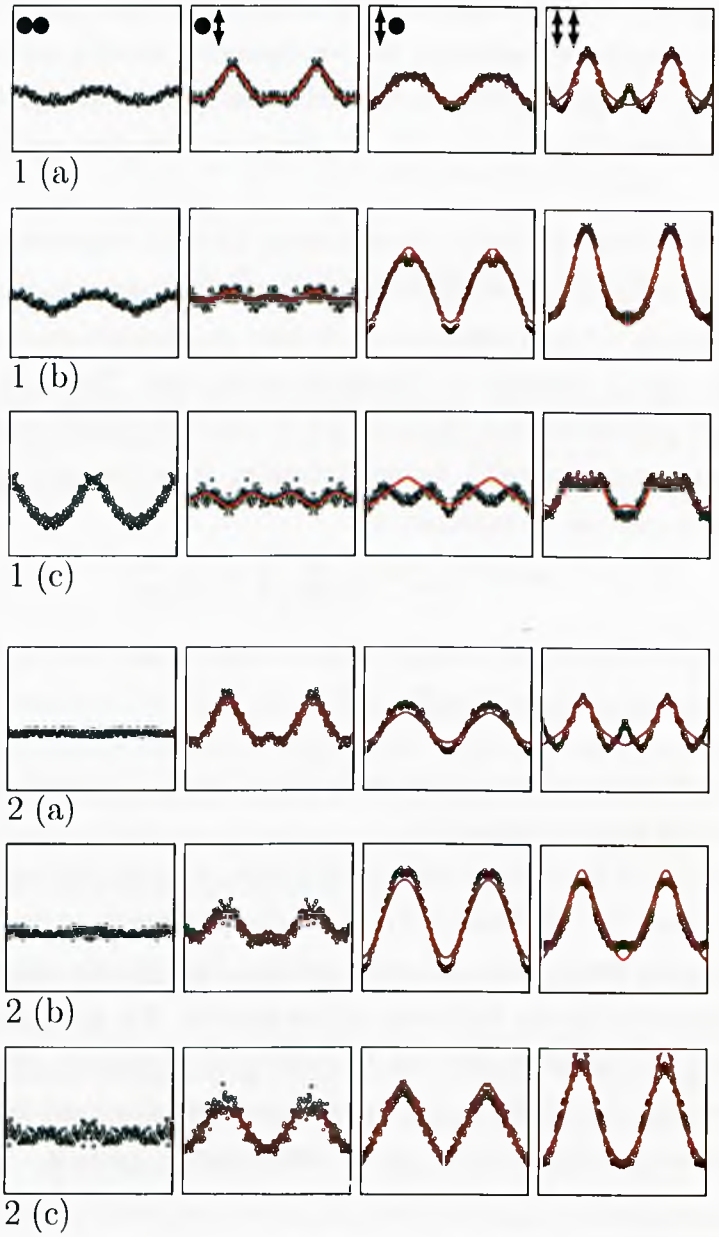

Figure 5.10: Experimental and corrected experimental anisotropies obtained by integrating the images shown in Figs. 5.2(a) to (d) and Figs. 5.7 (c) to (f) with respect to radius for each of the three features. Panel 1 (a) shows the raw anisotropy obtained from the inner ring in Fig. 5.2 for the four polarisation settings. Panel 1 (b) shows the raw anisotropy for the middle ring and Panel 1 (c) that for the outer ring. Panels 2 (a)-(c) shows the corresponding corrected anisotropies obtained from the images shown in Figs. 5.7 (c) to (f).

fragments in v=0 or 1 and N=0 to 42. Based on the conservation of linear momentum, $O(^1D_2)$ atoms can be produced with a maximum kinetic energy of 0.249 eV in coincidence with NO $(1)^2\Pi_{\frac{1}{2}}$ products in v=0 and N=0. The low kinetic energy release of the $O(^1D_2)$ fragments at this excitation energy makes it difficult to effectively slice the distribution. By carrying out experiments with relatively low repeller voltages (1000 V) the distribution could be stretched along the TOF axis so that $O(^1D_2)$ atoms formed at the peak of features (i), (ii) and (iii) had a TOF spread of ~63, 98 and 161 ns respectively. These conditions allowed a good ion signal strength to be retained while maintaining low photolysis and probe laser fluences. The high-voltage gating pulse in these experiments is estimated to have a temporal duration of 6 ns (FWHM with respect to the threshold for ion detection and the peak of the electrical pulse) but the duration of the recorded ion signal is actually narrower than this due to the exponential increase in signal with channel plate voltage. This results in slices which correspond to less than 9.5%, 6.1% and 3.7% of the photoproduct distributions for the three features respectively. In this case the error associated with assuming perfect slicing should be small (12; 15; 188). It is noted that a small fraction of $O(^1D_2)$ atoms are formed with kinetic energies in excess of the 0.249 eV kinetic energy limit. This is attributed to the error associated with calibrating the spectrometer using photoproducts with velocities significantly in excess of those measured. This leads to the estimation that the error in the measured kinetic energy release is 18 meV (FWHM) or less.

There are a number of different ways in which the excess energy could be partitioned in the NO fragments to produce the observed $O(^1D_2)$ energy distribution. The rotational profiles deduced from Fig. 5.1 are used to assign peaks (i), (ii) and (iii). As discussed in Section [5.4.1], in all of the REMPI spectra NO $(1)^2\Pi$ fragments in the $\Omega=\frac{1}{2}$ state make up more than 90% of the total NO. Therefore, the peaks in Fig. 5.8 are primarily attributed to $O(^1D_2)$ atoms formed with NO $(1)^2\Pi_{\frac{1}{2}}$. Peak (iii) can only be attributed to $O(^1D_2)$ formed with NO $(1)^2\Pi_{\frac{1}{2}}$ in v=0, therefore the peak of this feature can be assigned to $O(^1D_2)$ produced in coincidence with vibrationally cold diatomic co-fragments formed in N~12. The FWHM of this feature spans a rotational profile dominated by fragments in N=7 to 17; in good agreement with the rotational profile shown Fig. 5.1(a). Peaks (ii) and (i) could be assigned to NO $(1)^2\Pi_{\frac{1}{2}}$ fragments formed in v=0 and N~34 and 39 or v=1 and N~7 and 21. The absence of signatures of vibrationally cold, rotationally excited NO fragments in Figs. 5.1(a) and (b) and the

KE / eV	v	~N_{max}	Peak
0.047	1	19/21	(i)
0.100	1	0/7	(ii)
0.238	0	9/12	(iii)

Table 5.5: Vibrational and rotational assignments of the NO co-fragment responsible for peaks occurring in the $O(^1D_2)$ kinetic energy release spectrum (Fig. 5.8). ~N_{max} corresponds to the rotational energy at the peak of the feature for a $(1)^2\Pi_{\frac{3}{2}}/(1)^2\Pi_{\frac{1}{2}}$ co-fragment.

presence of a bimodal rotational profile in Fig. 5.1(b) allows peaks (i) and (ii) to be correlated with NO $(1)^2\Pi_{\frac{1}{2}}$ in **v**=1 and **N**~7 and 21 respectively. The assignments of the peaks in Fig. 5.8 are summarised in Table 5.5.

The yields of the $O(^1D_2)$ dissociation channels can be obtained by assessing the areas under the three features in Fig. 5.8. Using the profile recorded with both lasers polarised perpendicular to the detector, the relative yields of the processes leading to the peaks (i), (ii) and (iii) can be estimated by approximating their profiles with Gaussians and integrating these fits. Using this approach the branching ratio between the NO fragments in **v**=0 and 1 [peak (iii) to (i) plus (ii)] is estimated to be close to 1:3. As features (i) and (ii) overlap, the branching ratio for these two features cannot be unambiguously determined. Gaussian fits give a population ratio for the two rotational modes of **v**=1 which is close to 9:10. However, based on the rotational profile in Fig. 5.1(b) and the profile of peak (ii) between 0.066 eV and 0.124 eV, a Boltzmann profile would be a better reflection of the shape of the peak. This allows the (i) to (ii) branching ratio to be refined as 2:5. It is noted that these conclusions are very similar to those of Dick and co-workers who have also recently measured the rotational distribution of NO $(1)^2\Pi_\Omega$ fragments produced at excitation energies close to 5.5 eV using a novel approach to ion imaging (243).

Based on the inferred lifetime of the $(3)^2A'$ state (98), at excitation energies approximately 382 meV above the second dissociation limit the fragmentation process can be described as quasi-direct. For direct dissociation of a triatomic species, the rotational profile of the diatomic fragment can be related to the rotational and bending vibrational motion of the parent molecule prior to excitation and the topography of

the reaction coordinate. Two limiting cases for the production of rotational profiles in direct dissociation processes can be defined. If the reaction coordinate occurs across a region of an excited state potential which does not involve a change of the Jacobi angle between the atomic and diatomic moieties then a fragment rotational distribution is produced which is determined by the parent rotational and the ground electronic state bending mode excitation (244). In the case of a triatomic species excited from a supersonic expansion, this would primarily result in a rotationally cold, unimodal diatomic fragment distribution. However, if the reaction coordinate samples a region of the excited state potential where the two coordinates of the Jacobi angle and the radial separation of the two moieties are inherently coupled, the change in the Jacobi angle during the dissociation results in greater degrees of fragment rotational excitation. In this case, there is an interplay of the parent rotation, ground state bending motion and the change in Jacobi angle as the bond breaks (244). For triatomic species excited from a supersonic expansion, the fragment rotational profile would be dominated by a unimodal distribution which peaks at a rotational quantum number which is essentially determined by the gradient of the reaction coordinate along the Jacobi angle coordinate. This latter situation effectively describes the rotational profile of the peak labeled (iii) in Fig. 5.8.

Now consider an indirect dissociation process via a long-lived state or a quasi-direct dissociation occurring through a relatively narrow bottleneck. In these cases, the final rotational state distribution of the products qualitatively resembles the wavefunction at the transition state or crossing point to the dissociative adiabatic potential. The rotational profile is determined by the square of the wavefunction in the bending coordinate multiplied by the degree of coupling between the Jacobi angle and the rotational degrees of freedom (which is a reflection of the topography of the exit channel). In this situation, crossing the transition state with zero point bending motion results in a unimodal rotational profile where the peak of the distribution is determined by the coupling strength of the transition state bending motion to diatomic rotation. If the transition state is crossed with greater degrees of bending mode excitation, the nodal structure of the bending wavefunction results in a multimodal rotational profile where the number of modes is equal to the number of nodes. A single quantum of bending mode excitation can therefore result in a bimodal rotational profile (244; 245).

Alternatively, a multimodal rotational profile may be produced via two different dissociative pathways which converge to the same dissociation limit. In this case the photoexcited state effectively couples to one or more dissociative electronic states with the torque generated along each reaction coordinate producing a different unimodal rotational profile. The bimodal rotational profile observed for the NO fragments in v=1 [Fig. 5.8, peaks (i) and (ii)] is, therefore, the signature of at least two non-adiabatic crossings along the reaction coordinate or a single crossing occurring over a small region of the coordinate space with a significant degree of bending excitation in the photoexcited state. It is noteworthy that the $O(^1D_2)$ energy distribution produced ~382 meV above the second dissociation limit is qualitatively similar to the $O(^3P_J)$ distribution produced ~380 meV above the first dissociation limit via the $(2)^2A'$ state (50; 94; 158; 246; 247). Both distributions exhibit relatively statistical rotational profiles for the NO $(1)^2\Pi_\Omega$ fragments formed in v=0 which are in contrast to the bimodal rotational profiles of the vibrationally excited fragments. The energy distribution recorded ~380 meV above the first dissociation limit has previously been attributed to the production of NO $(1)^2\Pi_\Omega$ fragments in v=0 and 1 via a tight transition state [the $(2)^2A'/(1)^2A'$ conical intersection] with a degree of parent bending mode excitation (56; 96; 248).

The energy distribution of the $O(^1D_2)$ fragments formed with the probe laser alone are highly structured (see Fig. 5.11). At this photolysis energy NO $(1)^2\Pi_\Omega$ can be produced in v=0–4. The corresponding image [Fig. 5.3(a)], recorded with the laser polarisation parallel to the detector face, is comparable to that recorded by Coroiu *et al.* (6) However, in the experiments reported here the higher kinetic energy resolution highlights additional structure in the radial profiles. The structure of the photoproduct energy distribution (recorded with the laser polarisation perpendicular to the detector face) consists of more peaks than accessible vibrational states. Accurate assignment of these features is not currently possible in the absence of NO co-fragment rotational profiles. However, the energy distribution does imply that multimodal fragment rotational distributions are prevalent in the second absorption band of NO_2.

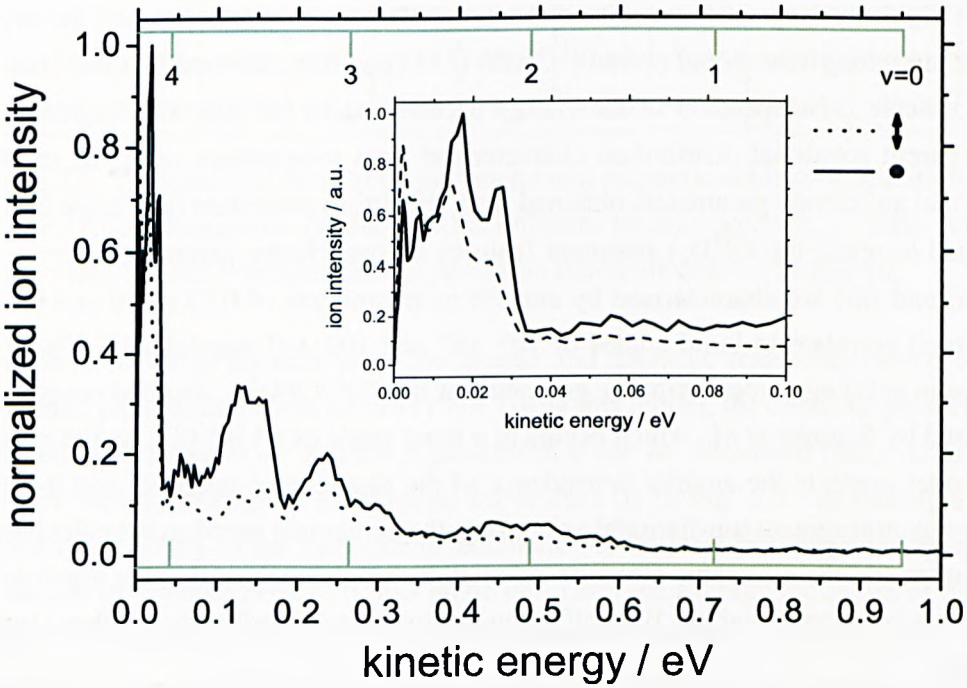

Figure 5.11: $O(^1D_2)$ energy distribution recorded in single laser experiments at excitation energies of 6.03 41 eV for laser polarisation alignments parallel or perpendicular to the detector face associated with Fig. 5.3(a) (parallel - dashed line) and (b) (perpendicular - solid line). The insert shows an expansion of the low energy portion of the kinetic energy release spectrum.

Translational anisotropy

Although the shortcomings of the axial recoil model are well known it is often applied to triatomic photodissociation. In this model the photoproduct distribution created by a single photon dissociation process can be described using the well known expression accredited to Zare (Eq. 5.4) (235). The translational anisotropy parameter can then be related to the dissociation timescale and dissociative geometry using the equally well known classical expression derived by Yang and Bersohn (249)

$$\beta = 2P_2\left[cos(\chi)\right]\left[\frac{1+\omega^2\tau^2}{1+4\omega^2\tau^2}\right] \tag{5.11}$$

where χ is related to the bond angle at the moment of dissociation.

At the level of excitation considered here, dissociation via the $(3)^2A'$ state to the $O(^1D_2)$ limit is quasi-direct. The dissociation timescale approaches half the asymmetric stretching vibrational period (~36 fs) (114) and it is assumed that the dissociation timescale is independent of the energy partitioning in the diatomic fragment. Using a parent rotational distribution characterised by a temperature of 20 K, the translational anisotropy parameters obtained from the fitting procedure (see Table 5.6) can be used to relate the $O(^1D_2)$ fragment features to dissociative parent geometries. Peaks (ii) and (iii) are characterised by anisotropy parameters of 0.87±0.10 and 0.81±0.10 which correlate to bond angles of 105 ±4° and 102 ±4° respectively. These angles are in good agreement with the geometry of the $(3)^2A'/(4)^2A'$ avoided crossing calculated by Schinke *et al.*, which occurs at a bond angle of ~110° (8). As the axial recoil model neglects the angular dependence of the dissociative potential and its effect on the photofragment translational anisotropy, the agreement between the calculated bond angles and the electronic structure calculations might suggest that the topology of the dissociative potential has little effect on the rotational distributions in these two channels.

By constrast, the photofragments labeled (i) in Fig. 5.8 are more problematic. It is noted that the alignment treatment discussed in section [5.4.2] failed to reproduce qualitatively all of the angular profiles of feature (i) [see Fig. 5.10 Panel 2(a)]. This may be due to the breakdown of the assumption that the fragment polarisation is not coupled to the translational anisotropy, although within the angular momentum treatment employed here this assumption allows a meaningful fit to the experimental data. For the remainder of the discussion it is assumed that the polarisation moments derived from feature (i) are qualitatively correct. The β parameter for this feature is 0.33 where an error of ±0.2 is estimated. Within the axial recoil limit this correlates to a bond angle of 84±8°. However, due to the high degree of rotational excitation with respect to translational energy, the axial recoil approximation (or impulsive model) will provide a poor description of the dissociation process (94; 244).

Non-axial recoil dynamics are frequently encountered in photofragment imaging experiments when the degree of rotational excitation of a photofragment is large and the relative translational energy is low (94; 212; 250). In these cases a more complicated model is required in order to relate the translational anisotropy parameter to the dissociative process. Demyanenko *et al.* have proposed a classical model to account

KE / eV	β_v	p_0	p_1	p_2	$\rho_0^{\{2\}}$	$\rho_{2+}^{\{2\}}$	$\rho_0^{\{4\}}$	$\rho_{2+}^{\{4\}}$	$\rho_{4+}^{\{4\}}$	peak
0.047	0.33	0.00	0.48	0.02	-0.24	-0.21	-0.34	+0.18	-0.19	(i)
0.100	0.87	0.00	0.39	0.11	-0.09	-0.19	-0.26	+0.16	-0.11	(ii)
0.238	0.81	0.00	0.41	0.08	-0.15	-0.20	-0.26	+0.29	+0.09	(iii)

Table 5.6: Translational anisotropy parameter and magnetic sublevel populations, $p_{|M_J|}$, of the $O(^1D_2)$ fragments produced with different kinetic energies, together with the fitted values of the 5 independent polarisation moments defined in Eq. 10.

for the short-range interaction of the atomic and diatomic fragments during a direct triatomic photodissociation process (94). Using this model, the crossing geometry calculated by Schinke *et al.* and the β parameter, it can be calculated that a deviation of ~13±4° occurs from pure axial recoil for feature (i) in Fig. 5.8. Assuming a single crossing geometry to the dissociative adiabatic $(4)^2A'$ state [as suggested by the calculations of Schinke *et al.* (8)], this angle describes the average reduction of the bond angle of the parent NO_2 as the O and NO moieties separate. This reduction of bond angle after the avoided crossing would then be responsible for the rotational excitation of the diatomic fragments associated with feature (i). The bond angle reduction is in contrast to values of ~4±2° and ~3±2° for features (ii) and (iii) respectively which are associated with less rotationally excited fragments. Although the crossing geometry of Schinke *et al.* has been used as a fitting parameter in these calculations, it is noted that the measured translational anisotropy parameters are in agreement with the diatomic fragment rotational assignments discussed in Section [5.4.1] and those shown in Table 5.5.

Alignment parameters and M_J sub-state populations

The $O(^1D_2)$ polarisation moments that have been obtained from the fitting procedure can be used to generate the probability density functions that directly illustrate how the angular momentum of the atom, and also the corresponding position vector, are polarised (251; 252). These probability densities are presented on Fig. 5.12, where the top row [panels (a.i–iii)] shows the polarisation of the position vector and the bottom row [panels (b.i–iii)] shows the polarisation of the angular momentum vector; the three

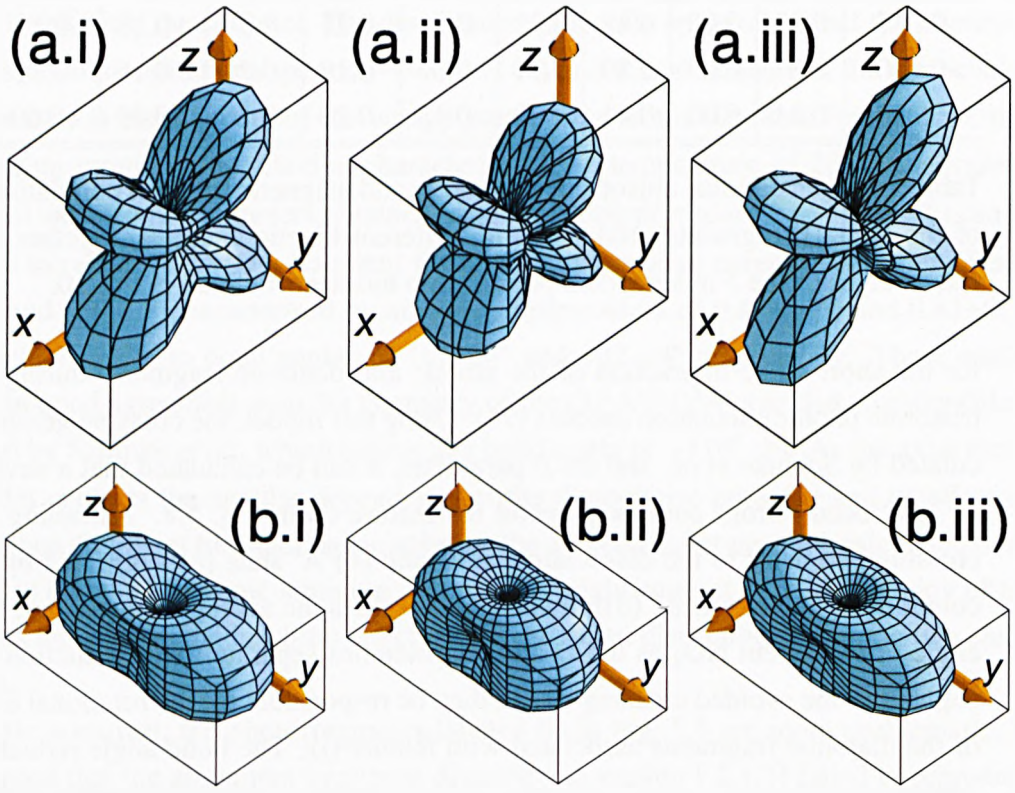

Figure 5.12: Recoil-frame polarisations of the $O(^1D_2)$ electronic position [top, panels (a.i–iii)] and angular momentum [bottom, panels (b.i–iii)] vectors. The data in the three columns correspond to the features labeled (i), (ii) and (iii) on Fig.5.8.

columns correspond to the features labelled as (i), (ii) and (iii) in Fig. 5.8, and the x, y and z axes are those of the recoil frame defined on Table 5.6.

Note that for a $^1D_2$ state the total angular momentum coincides with the electronic orbital angular momentum, but also that the position vector does not coincide with the position of any particular electron, just as the total electronic angular momentum does not coincide with the angular momentum of any particular electron. The probability densities shown on Fig. 5.12 *do not* result from one-electron orbitals, although the J=2 condition inevitably causes the position-representation orbitals to have the familiar d-orbital shapes. The probability densities of Fig. 5.12 result from incoherent superposition of five such orbitals. Comparison of the results on the three colums of

Fig. 5.12 shows that the photodissociation mechanisms underlying features (i–iii) of Fig. 5.8 lead to similarly-polarised atoms: their electronic position vector is aligned along $\pm(x+z)$ and their angular momentum along $\pm y$. This suggests dissociation via a common transition state and electronic surface.

The populations of the M_J sub-states can also be extracted from the polarisation moments; they are shown on Fig. 5.13. For all of the features (i–iii) of Fig. 5.8, it is found that the total populations of the $|M_J|=1$ substates are in excess of 75%. It is interesting to compare this result with the work of Coroiu *et al.* (6) at higher excitation energies. These workers found a similar propensity to populate the $|M_J|=1$ sub-states for oxygen atoms correlating with NO $(1)^2\Pi_\Omega$ produced in $v=1$. However, the alignment parameters differed considerably for the fragments correlating with diatomic products with greater internal excitation. The difference in the alignment moments for the internally excited fragments is tentatively attributed to the opening of another dissociation channel that is observed at higher excitation energies.

The polarisations of $O(^1D_2)$ fragments with $|M_J|=1$ can correlate with d_{xz} and d_{yz} orbitals, but Fig. 5.12 shows that the former clearly dominate. Now, remember that xz is the plane containing the fragment recoil and parent dipole moment directions. If the dipole moment lies on the plane containing the three atoms, and if the recoil direction also lies on this plane (that is what one would expect on the basis of an impulsive model), then xz is also the C_s plane of symmetry. This implies that in the dominant processes the electronic wavefunction of the atomic fragment has A′ symmetry. Assuming that the dissociation process exclusively occurs on A′ electronic potentials, this in turn implies that there should be a preference for the production of NO $(1)^2\Pi_\Omega$ in the A′ Λ-doublet state. This is yet to be probed directly.

5.4.3 NO $(1)^2\Pi_\Omega$ + $O(^1D_2)$ dissociation mechanisms

The rotational profiles shown in Fig. 5.1 and the $O(^1D_2)$ energy distribution shown in Fig. 5.8 highlight different dissociation pathways for the production of $O(^1D_2)$. Analysis of the energy partitioning for the three features in Fig. 5.8 suggest that the axial-recoil approximation is close to valid for the fragments labeled (ii) and (iii) in Fig. 5.8. In these cases the anisotropy parameters can be related to dissociative geometries which are in good agreement with the calculations of Schinke *et al.* (8) The

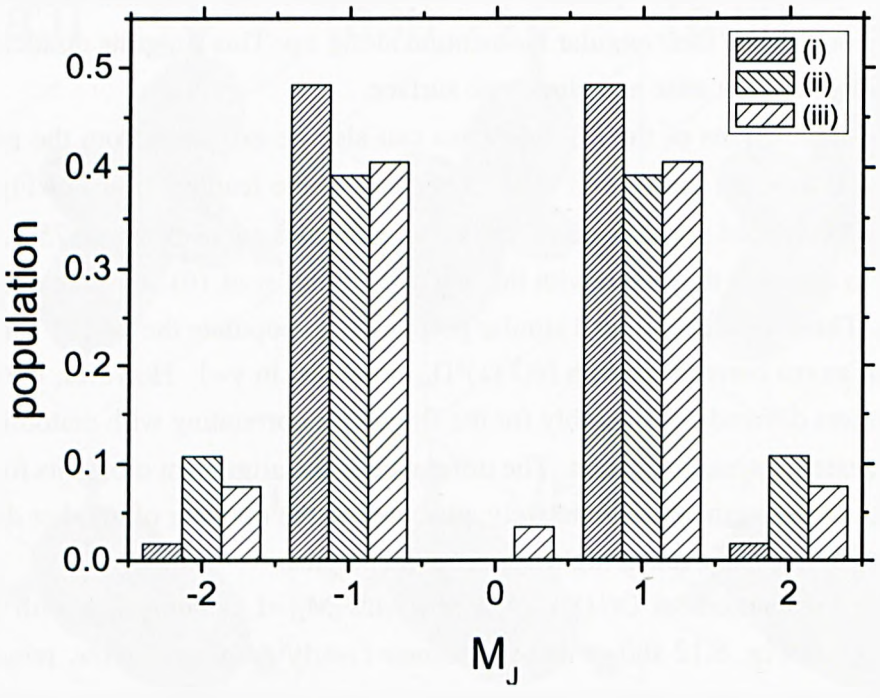

Figure 5.13: M_J sub-state populations extracted from the corrected images for the features labeled (i), (ii) and (iii) in Fig. 5.8.

results reported here suggest that this geometry results in the production of a relatively rotationally cold, vibrationally inverted diatomic fragment distribution implying that beyond the crossing point for dissociation there is little interaction between the atomic and diatomic moieties or change in Jacobi angle for these fragments.

Feature (i) in Fig. 5.8 is attributed to vibrationally and relatively rotationally excited diatomic fragments. By considering the ratio of rotational to total excess energy in this fragmentation process, it is unlikely that the dissociation can be treated within the axial recoil limit. (94) The non-axial recoil dynamics and resulting increased diatomic rotational excitation results in a significant reduction of the translational anisotropy parameter for these fragments. The rotational assignments of the NO fragments formed in coincidence with these oxygen atoms are therefore in agreement with the low translational anisotropy parameter obtained from the fitting procedure and are also consistent with this effect being exclusively observed for vibrationally excited fragments (where

the ratio of rotational to translational energy is high).

The similarity of the three multipole distributions [for features (i) to (iii)] is attributed to dissociation via a common avoided crossing and electronic state, likely the adiabatic $(4)^2A'$ state. This implies that the bimodal rotational profile of the NO fragments in v=1 is a consequence of the fragmentation of parent molecules with at least one quantum of bending mode excitation. It is noted that the peak of the diatomic vibrational profiles of the fragments produced in coincidence with both $O(^1D_2)$ and $O(^3P_J)$ occur at the same levels at this excitation energy (v=1) and at higher excitation energies in the $(3)^2A'$ adiabatic state [see Coriou *et al.* (6) and the interpretation of the higher kinetic energy mode in their $O(^3P_J)$ energy distributions at ~6.03 eV which was given in the previous chapter; v=4 or 5 (64)]. It appears that the vibrational distribution in the $O(^1D_2)$ channel is determined by the symmetric stretch motion setup by the Franck-Condon window to the $(3)^2A'$ adiabatic state in accord with the explanation of Schinke *et al.* (8) This vibrational energy is retained on crossing to the $(4)^2A'$ adiabatic state.

The bimodal rotational profiles of the NO fragments produced in coincidence with $O(^3P_J)$ (64) and the vibrationally excited NO fragments produced with $O(^1D_2)$ are intriguing. They suggest that the rotational bimodality is introduced, like the diatomic vibrational excitation, by the change in geometry (bond angle) associated with the Franck-Condon window from the $(1)^2A'$ to the $(3)^2A'$ state. This would be further supported if a bimodal rotational profile was observed for the vibrationally cold NO fragments formed concomitantly with $O(^1D_2)$. If ground vibrational state diatomic fragments were produced with rotational energies between 0.134 and 0.237 eV, these fragments would make up parts of peaks (i) or (ii) and would correspond to fragment rotational levels between N=25 and 33. It is noted that there is no evidence for such features in Figs. 5.1(a) and (b), however, due to the signal to noise levels of the experiments these fragments would only be expected to be observed if they were produced with a yield in excess of 10%. The absence of such fragments in the rotational profiles is likely due to the ineffective coupling of the bending mode excitation to fragment rotation due to the crossing geometry and/or the topography of the dissociative $(4)^2A'$ adiabatic state. This interpretation of the rotational profiles is supported by the $O(^1D_2)$ energy distribution recorded at excitation energies close to 6.03 eV (see Fig 5.9). Here

the vibrational inversion is more obvious and the rotational profile of the NO fragments which likely correlate with v=4 are observed to be made up of at least three different modes. It is suggested that this multimodal rotational profile is the result of a higher degree of parent bending mode excitation [although at this excitation energy, non-adiabatic couplings with higher energy electronic states cannot be ruled out and are suggested by the alignment results of Coroiu *et al.* (6)]. The less structured rovibrational distributions of the faster fragments in this energy distribution are consistent with the results obtained at lower excitation energies.

In the experiments reported here at excitation energies close to 5.48 eV, parent molecules are primarily excited from their ground vibrational and lowest few rotational states. It seems that the Franck-Condon factors to the $(3)^2A'$ adiabatic state result in the preferential excitation of single quanta of parent symmetric stretching and bending modes [where ν_1' ~143 meV and ν_2' ~65 meV respectively (114)] which are transferred into vibrationally excited, rotationally bimodal product distributions for the majority of the diatomic fragments. In the case of the $O(^1D_2)$ channel this is calculated to occur via two excited adiabatic states and a tight transition state (8). The $O(^1D_2)/O(^3P_J)$ branching ratio is determined by the coupling strength between the $(3)^2A'$ and $(4)^2A'$ adiabatic electronic surfaces and the profiles and branching ratios of the rotational modes sensitively depend on the topographies of these states. It is hoped that these findings will stimulate further theoretical study in order to understand the origins of these non-statistical rovibrational distributions.

5.5 Conclusions

Mass-resolved REMPI spectroscopy and velocity map imaging have been used to study the photoproduct distributions observed on excitation to the $(3)^2A'$ state of NO_2 between 5.46 and 5.64 eV. The two techniques have allowed us to unequivocally assign the single laser NO fragment rovibrational profiles to NO $(1)^2\Pi_\Omega$ fragments produced concomitantly with $O(^1D_2)$. In addition the small yet complex contribution of NO $(1)^2\Pi_\Omega$ fragments produced with $O(^3P_J)$ atoms with differing degrees of internal excitation across this excitation range has been highlighted.

By recording DC slice velocity map images of the $O(^1D_2)$ fragments produced using different pump and probe laser polarisations at an excitation energy of 5.47952 eV

the kinetic energy profile has been measured and the translational anisotropy parameters and multipole moments of the $O(^1D_2)$ fragment polarisation have been derived as a function of kinetic energy. Using the NO fragment REMPI profiles the features of the $O(^1D_2)$ energy distribution have been assigned to production in coincidence with a unimodal rotational distribution of fragments in v=0 and a bimodal rotational profile of vibrationally excited fragments in v=1. Furthermore, the $O(^1D_2)$ energy distribution highlights the vibrational inversion of the diatomic cofragments, in accord with previous work (103).

From the multipole moments obtained from the $O(^1D_2)$ images it is concluded that the majority of these fragments are formed in the $M_J \pm 1$ state and that all of the $O(^1D_2)$ fragments are produced via the same avoided crossing to the $(4)^2A'$ dissociative electronic state. The translational anisotropy parameters of the $O(^1D_2)$ fragments produced in coincidence with rotationally cold diatomic fragments are related to dissociative geometries which are found to be in good agreement with the calculations of Schinke *et al.* who highlight an avoided crossing between the $(3)^2A'$ and $(4)^2A'$ adiabatic surfaces at a bond angle close to 110°. The lower translational anisotropy of the slower $O(^1D_2)$ fragments is interpreted as a signature of production with rotationally and vibrationally excited diatomic fragments. Here the low translational energy and relatively high rotational energy is a result of non-axial recoil dynamics occurring after the avoided crossing close to 110°.

Analysis of the $O(^1D_2)$ and $O(^3P_J)$ photofragment distributions recorded at ~5.48 eV (64) and 6.03 eV (6) allows the vibrational inversion of the NO $(1)^2\Pi_\Omega$ fragments produced with $O(^1D_2)$ to be attributed to the symmetric stretch motion set up by the Franck-Condon window from the $(1)^2A'$ state to the $(3)^2A'$ state. This symmetric stretching motion is retained for the majority of the NO $(1)^2\Pi_\Omega$ fragments formed with either $O(^1D_2)$ or $O(^3P_J)$. The bimodal rotational profiles observed for the diatomic fragments formed with the majority of the $O(^3P_J)$ fragments and the vibrationally excited diatomic fragments formed with $O(^1D_2)$ are consistent with bending motion caused by the geometry change on excitation to the $(3)^2A'$ state. For the $O(^1D_2)$ channel, a single quantum of bending motion is effectively transferred via the $(3)^2A'/(4)^2A'$ avoided crossing into two rotational modes for the vibrationally excited NO $(1)^2\Pi_\Omega$ fragments produced close to the energetic threshold. In contrast this rotational structure is lost for the vibrationally cold diatomic fragments, where the motion set up by

the Franck-Condon window is presumably washed out due to the topography of the reaction coordinate.

Chapter 6

Visible/Ultraviolet Decomposition of NO_2

6.1 Introduction

A number of experiments have been carried out to probe the fragmentation dynamics of NO_2 in the time domain (14; 25; 26; 28; 59; 60; 61; 62; 63; 124; 125; 126; 253; 254). Due to the high field strengths associated with the short laser pulses employed, many of these experiments are complicated by the ease with which multiphoton transitions are induced and the difficulties associated with limiting the number of photons absorbed. Generally these experiments measure the signals associated with different competing optical pathways that contribute to the overall photodynamics to differing degrees. As many nuclear configurations can be accessed in these multiphoton experiments, it becomes increasingly difficult to isolate transient states and to elucidate dissociation mechanisms. Furthermore, in extreme cases, the intense electric fields used to drive these multiphoton processes result in non-perturbative light-matter interactions that result in intensity dependent decomposition dynamics. In the case of NO_2 the situation is further complicated due to the high density of accessible electronic states and the extensive coupling that occurs between them (as outlined in Chapter 2). Despite this a number of experiments have used temporal measurements to provide further insight into the fragmentation dynamics of this well-studied molecule. It is noted, however, that many of the decomposition processes observed in these studies are intensity dependent resulting in different decomposition pathways being measured in seemingly

similar experiments.

The threshold dissociation time scale of NO_2 has been studied in great detail; with the majority of the time domain work performed by Wittig and co-workers (59; 60; 61) and Tröe and co-workers (62; 63). These groups measured the energy dependence of the unimolecular decomposition rate finding that dissociation time scales reduced from 50 ps close to threshold to less than 80 fs 0.1 eV above this level (59; 60; 61). These results were, on average, consistent with the predictions of statistical rate laws. However, the measurements also highlighted step-like increases in the decomposition rates where the step separation was interpreted as a signature of the energy level separation at the transition state. As the excitation energy increased, so did the accessible phase space. Therefore, at threshold energies canonical reaction paths opened that facilitated jumps in the decomposition rate. Similar step-like rate increases have been indirectly observed in energy domain experiments by measuring photofragment linewidths (204) and fragment translational anisotropy parameters (58; 93). Some of these effects and the disparities between the specific findings of the different research groups have been rationalised by the theoretical work of Klippenstein and Radivoyevitch who used variational Rice-Ramsperger-Kassel-Marcus (RRKM) theory to calculate the nuclear coordinates of the transition state as a function of excitation energy (92). Here it was calculated that the transition state moved to lower ON-O bond lengths as the excess energy was increased. These findings have been important in postulating the decomposition mechanism that occurs via the $(1)^2B_2$ state (see Chapter 2) and highlight the importance of canonical reaction measurements in understanding complex decomposition processes.

Further time-resolved measurements were performed by Singhal *et al.* (253) who performed single-colour TOF MS experiments at excitation energies of 3.30603 eV using 50 fs laser pulses with an intensity of 5×10^{13} W cm^{-2}. This allowed them to investigate the MPI and dissociative multiphoton ionisation (DMI) pathways of NO_2 using ultrashort laser pulses with excitation energies above the first dissociation limit. Under these conditions NO^+ ions were primarily observed with smaller yields of NO_2^+. The researchers concluded that the observed NO^+ ion signal arose from single-photon excitation to the $(1)^2B_2$ state followed by electronic predissociation via the ground state to form NO $(1)^2\Pi_\Omega$ fragments with $O(^3P_J)$ atoms. It was claimed that the free diatomic fragments were then promoted to the ground NO^+ $(1)^1\Sigma^+$ ion state by absorbing three

more photons. Subsequent experiments by the same research group highlighted the increase in parent ion yield with laser intensity (254). At the same excitation energy Davies *et al.* carried out single-colour experiments using 100 fs laser pulses and laser intensities of $\sim 10^{12}$ W cm^{-2} to identify a DMI process using the PEPICO imaging technique pioneered by the same research group and demonstrated in this landmark study (25; 26). Using the extra information afforded by the coincidence imaging technique, these researchers attributed the primary NO^+ fragment signal to a three-photon excitation to a highly excited state of NO_2 which dissociated to NO $(2)^2\Pi_\Omega$ in coincidence with $O(^3P_J)$ atoms. The authors reported that the neutral, electronically excited diatomic fragments were subsequently ionised to the NO^+ $(1)^1\Sigma^+$ ground ion state by a single photon. This was favoured in spite of the fact that the energy of a single photon was higher than the first dissociation limit and that the combined energy of three photons was higher than the adiabatic ionisation potential of NO_2. Additionally, the experiment allowed these researchers to determine a bond-cleavage time for this process of 350–500 fs.

López-Martens *et al.* investigated the effects of laser field intensity on the multi-photon dissociation dynamics of NO_2 in more detail using two-colour LIF depletion spectroscopy (124). Using a pump field with an energy of 3.09960 eV the dissociative production of neutral NO $(1)^2\Sigma^+$ was monitored through the depletion of the NO $(1)^2\Sigma^+ \rightarrow$NO $(1)^2\Pi_\Omega$ fluorescence induced by a probe field (1.54980 eV). At pump laser intensities between $3–20\times10^{12}$ W cm^{-2}, the dominant dissociative pathway was determined to involve the absorption of three pump photons to reach a highly excited neutral state of NO_2 (close to 9.3 eV) to give NO $(1)^2\Sigma^+$ in v=0, 1 and potentially 2 with ground state oxygen atoms on a time scale no longer than 600 fs. Unlike in the experiments of Davies *et al.* (25; 26), in these experiments three pump photons were not energetic enough to produce NO fragments in the $(2)^2\Pi_\Omega$ state.

In a follow up study by the same research group the decomposition dynamics of NO_2 were studied using variable excitation energies between 2.95 and 3.14 eV with pump laser intensities of 5.3 TW cm^{-2} and probe laser intensities between 0.5 and 4.0 TW cm^{-2} (125). Again this experiment was only sensitive to fluorescent states with the probe induced depletion of the free NO $(1)^2\Sigma^+$ fluorescence used to monitor the decomposition process. Here it was observed that, where energetically feasible, NO $(1)^2\Sigma^+$ was produced in its v'=0 and 1 states only with the two vibrational states

displaying different probe intensity dependencies and temporal modulation patterns. It was also observed that, at all probe laser intensities and at time delays in excess of 500 fs, the NO $(1)^2\Sigma^+ \rightarrow$NO $(1)^2\Pi_\Omega$ fluorescence signal was constant implying that the fragmentation process was complete prior to this time delay. The researchers suggested that the NO $(1)^2\Sigma^+$ fragments were produced via valence/Rydberg state crossings at the three pump photon level which allowed direct fragmentation.

In the same experiments the effects of probe laser intensity on the time-resolved NO $(1)^2\Sigma^+$ fluorescence signal were attributed to laser-field dressed eigenstate interactions that facilitated adiabatic transfer from the Rydberg to dissociative valence diabats resulting in transient v′=0 fluorescence peaks at time delays close to 200 fs. The fluorescence spikes were then accredited to parent molecules that had been trapped in temporary light-dressed bound potentials which were present around t=0 due to the high electric field strengths. This resulted in bursts of emission as the pump-probe delay was extended beyond the cross-correlation time (~140 fs) and the bound-light dressed state disappeared. As would be expected, these effects were observed to increase with probe laser intensity. Although the intensity dependent transient maximums were observed at all excitation energies (2.95, 2.99, 3.10 and 3.14 eV), the transient signal intensity was observed at progressively lower probe laser intensities as the pump excitation energy increased. These strong-field or non-perturbative effects [that have in similar situations been referred to as alternating current Stark schemes of coherent control (39)] illustrate the significant effects that the field intensity can have on the observed photodynamics.

In the same study the NO $(1)^2\Sigma^+$ v′ = 1 fragments were found to display different probe laser intensity and pump-probe delay dependencies to the v′ = 0 fragments. The difference in the temporal fluorescence signals for the NO v′=0 and 1 products with probe laser intensity was attributed to the final vibrational levels being prepared via different intensity dependent mechanisms. In order to gain an insight into these fragmentation mechanisms the group calculated the diabatic and laser field-dressed adiabatic PES of the $(1)^2A_1$ ground state and the initially excited $(1)^2B_2$ state as well as the $3s\,\sigma\,^2\Sigma_g^+$ Rydberg states that were expected to be involved in the fragmentation. This allowed the researchers to highlight avoided crossings between the potentials and monitor the effects of laser intensity on these non-adiabatic interactions. Using this approach the researchers attributed the NO $(1)^2\Sigma^+$ v′ = 0 fragments to single-photon excitation to the $(1)^2B_2$ state with relaxation to vibrationally excited levels of the $(1)^2A_1$

state with the resulting nuclear relaxation presenting a good Franck-Condon window for two photon excitation to the $3s\,\sigma\,{}^2\Sigma_g^+$ state. The Rydberg state was then assumed to dissociate vibrationally adiabatically to give vibrationally cold NO $(1)^2\Sigma^+$. Due to the proximity of the (1 0 0) vibrational level of NO_2 with a light induced surface crossing between the $(1)^2B_2$ and the $3s\,\sigma\,{}^2\Sigma_g^+$ Rydberg state over the excitation energy range employed in these experiments, it was postulated that the NO $(1)^2\Sigma^+$ v′=1 fragments were formed after direct excitation to the Rydberg state by three pump photons [with resonant enhancement, without relaxation, via the $(1)^2B_2$ state]. It was then assumed that the vibrational excitation of the ground state of the parent was transferred to the NO $(1)^2\Sigma^+$ fragments. It was also highlighted that due to the high-field electric strengths employed, the population of the (1 0 0) levels of the parent ground electronic state could be significantly enhanced over the thermodynamic populations due to the Rabi cycling facilitated by the overlapped pump and probe fields.

Eppink *et al.* carried out VMI (126) experiments in order to separately monitor the time-dependent production of NO and NO_2 ions generated when the triatomic was irradiated with 40 fs laser pulses at excitation energies of 3.10 eV and 4.66 eV (400 nm and 266 nm respectively) (126). In these experiments the laser fields were estimated to have a typical total intensity of 5×10^{11} W cm^{-2} and a cross-correlation time of 90 fs. Crucially, in this case, the majority of the pump laser bandwidth was below the first dissociation limit. Under these conditions, the researchers observed the predominant production of NO^+ ions over NO_2^+ ions (the latter only being significantly formed when the two laser pulses were temporally overlapped or temporally reversed). The fragment ions were observed to be formed with a sub-100 fs rise-time with a number of different components. Translationally hot NO^+ fragments were preferentially formed (72% of the NO^+ signal) with a broad range of velocities where the kinetic energy distribution peaked close to 280 meV. These fragments were observed to be short-lived with a time-constant of 90±10 fs FWHM and were attributed to a (3+1′) DMI process similar to that proposed by López-Martens *et al.* (124). A smaller contribution of translationally cold, long-lived NO^+ fragments was also measured. This feature was found to exhibit an oscillatory decay with a damping time constant of 4000±400 fs and an oscillation time constant of ~600 fs. The feature was assigned as a signature of a (1+2′) DMI process where the oscillation was tentatively accredited to wavepacket motion between

the photoexcited $(1)^2B_2$ state and a subset of vibrationally excited levels of the $(1)^2A_1$ ground state.

In a subsequent publication, some of the same authors extended this research (14). By changing the conditions of the sample gas, the researchers produced a supersonic expansion seeded with NO_2 where 94% of the reagent gas was in its monomeric form with negligible amounts of nitric oxide contaminant. This reduced the short time ion signal from nascent NO and also eliminated contributions from N_2O_4 photolysis (this is in contrast to the previous paper, where 50% of the sample gas was calculated to be in its dimeric form). With the improved signal associated with concentrating the monomer, the researchers were able to separately record photoion and photoelectron images with the additional benefit of being able to collect these images over shorter time steps. A number of features were observed in the photoelectron images. At short time delays a photoelectron feature was observed at 0.420 eV, which from its time-dependence, was associated with the broad NO^+ ion peak previously observed with a kinetic energy close to 0.300 eV (126). These ionic fragments were assigned previously to free neutral NO $(1)^2\Sigma^+$ produced on absorption of three pump photons and ionised by a single probe photon. This process would be expected to produce photoelectrons with kinetic energies of ~0.880 eV, however, such features were not observed indicating that the NO^+ fragments must have been formed via a different mechanism. The ion and electron peaks were thus interpreted as arising from a (3′+1) DMI process which directly formed NO ions via the $(1)^3A_2$ excited state of the parent cation which would be expected to give photoelectrons with an energy close to 0.370 eV. This fragmentation process was interpreted to be responsible for the photoions and photoelectrons with kinetic energies of 0.310 eV and 0.420 eV respectively due to the broad agreement between the calculated and observed electron energy. Another short-lived photoelectron peak was observed with a kinetic energy close to 1.5 eV. This peak was found to be present at negative pump-probe delays and was attributed to direct ionisation of NO_2 in a (2′+1) process that was assumed to be resonantly enhanced by the 3*d* Rydberg states.

A number of long-lived photoelectron peaks were observed in the same experiments. Intriguingly the majority of the long-lived photoelectron signal was produced with very little kinetic energy and the temporal behaviour of these fragments was observed to be similar to that of the translationally cold NO^+ ions that were produced with

a picosecond decay constant and a faster oscillatory component. For this reason, the two signals were attributed to the same decomposition process, a (1+2′) DMI process which produced kinetically cold ions and electrons. As outlined in the previous paper, the oscillations were thought to be signatures of the wavepacket motion between the $(1)^2B_2$ state of NO_2 accessed on absorption of a single pump photon and vibrationally excited levels of the ground state of the parent molecule. In these experiments the combined energy of one pump and two probe photons was slightly in excess of the first dissociative ionisation limit (~12.3797 eV, see Chapter 2) and provided that an ion surface that correlated with ground state NO^+ $(1)^1\Sigma^+$ and $O(^3P_J)$ fragments could be accessed, the fragmentation process would be expected to produce kinetically cold fragments as observed in the experiment. However, it is noted that according to the results of Hirst (142) such a process could only result from population (perhaps indirectly) of an electronically excited cation state at a significantly different geometry from that associated with the ground state of the neutral as at this geometry the experimental excitation energy is below the onset of the lowest energy excited ion states. Furthermore, the 600 fs oscillation time-constant was inconsistent with the calculated adiabatic transfer time between the $(2)^2A'$ state and vibrationally excited levels of the $(1)^2A'$ potential (83).

In addition to these kinetically cold contributions to the electron yield, Form *et al.* observed weak and long-lived components due to relatively fast photoelectrons with kinetic energies of ~1 and 2 eV (14). These signals were tentatively attributed to a two-photon pump process occurring to the $(2)^2B_2$ state of NO_2. It was then proposed that these electronically excited molecules were ionised to electronically excited states of the cation on absorption of two probe photons to yield the observed photoelectron signals. However, based on the calculated topography of the $(2)^2B_2$ PES (8) it appears unlikely that excitation to this state at the energy associated with two pump photons would produce photoelectron signals with such long lifetimes.

Recently the decomposition process originally studied by Eppink *et al.* (126) and Form and co-workers (14) has been revisited by Vredenborg *et al.* (28) using a time-resolved PEPICO imaging spectrometer similar to that used by Davies and coworkers (26). With the ability to unequivocally assign photoelectron features to NO^+ or NO_2^+ ions, the visible/UV decomposition dynamics could be studied in greater detail. These experiments were carried out using a pump laser excitation energy of 3.097 eV and a

probe field with an energy of 4.645 eV with both pulses having a 160 fs duration resulting in a cross-correlation time and time resolution of ~240 fs (FWHM). Assuming a similar diameter of the focused pump and probe beams, this resulted in a maximum total laser intensity of $\sim 2\times10^{12}$ W cm^{-2} which was significantly higher than the laser intensities used in the experiments of Eppink *et al.* and Form *et al.* Under these conditions ten times more NO^+ ions were detected with respect to parent ions close to t=0. An enhancement of these signals at positive time-delays was only observed for the NO^+ fragments. Interestingly, the translationally cold photoelectrons first observed by Form *et al.* were only observed with NO^+ ions, any such features were completely absent from the photoelectron spectrum observed concomitantly with NO_2^+.

Four main photoelectron features were observed in coincidence with NO_2^+. Two of these peaks with kinetic energies of 60 meV and 400 meV were also present in the pump only photoelectron spectrum. Here, the low energy peak appeared at a time-delay of ~200 fs while the higher energy peak began to disappear on a similar time scale. By a delay of 500 fs, the 400 meV peak was completely absent whereas the 60 meV peak reached a maximum. The intensity of the low energy peak was observed to remain constant over a 2 ps period. Based on the photoelectron energies and their temporal behaviours, the 400 meV peak was assigned to a (1+2′) ionisation process which was resonantly enhanced by the $(1)^2B_2$ state and one of the 3*p* Rydberg states at the levels of the first and second photons respectively. The 60 meV peak was assigned to a similar (1+2′) process where relaxation had occurred at the level of the first photon from the initially excited $(1)^2B_2$ state to vibrationally excited levels of the $(1)^2A_1$ ground state. These levels were assumed to be subsequently ionised via a 3*p* Rydberg state to the ground $(1)^1\Sigma^+$ or $(1)^2A_1$ state of the parent cation.

Two further electron peaks were observed in the NO_2^+ photoelectron spectrum at ~1.5 and ~2.0 eV. The 1.5 eV peak disappeared on the time scale of the laser cross-correlation time, in good agreement with the results of Eppink *et al.* (126) and Form *et al.* (14) whereas the 2.0 eV peak grew to a maximum on a time scale of 500 fs, remaining at this intensity up to the probed 2 ps delay. In this case the 1.5 eV peak was attributed to a (2′+1) process with the 2.0 eV peak ascribed to a (3+1′) ionisation of the parent molecule. Similar features were observed in the experiments of Form *et al.*, although in that publication a 2.0 eV photoelectron peak (which is also present in the Vredenborg photoelectron spectrum correlating with NO^+) was attributed to a (2+2′)

ionisation process occurring via the short lived $(2)^2B_2$ state as opposed to direct (3+1′) ionisation.

The primary photoelectron signal, correlating with NO^+ ions, was made up of seven different contributions. Four of these were short-lived (0.35, 0.65, 1.4 and 1.9 eV) with a single transient peak (1.2 eV) and the remaining two peaks appearing and peaking on a 500 fs time scale with no intensity variation over the next 1.5 ps (0 and 0.9 eV). Here it is noted that the signal-to-noise level of these coincidence experiments was not high enough to measure oscillatory components in the decay of these signals. However, the authors do report that these oscillations have been detected in conventional time-resolved photoion/photoelectron imaging experiments in their laboratory. The short lived peaks at 0.35, 0.65 and 1.4 eV were ascribed to (3+1′) DMI processes directly leading to charged diatomic fragments. The structure and kinetic energy of the peaks facilitated assignment of the peaks to fast direct fragmentation via the $(1)^3A_2$ parent ion state, predissociation via the $(1)^3B_2$ state and prompt ionisation via the ground parent ion state leaving the excited ion core just above the dissociation threshold to give slow NO^+ respectively. The kinetic energy and structure of the other short-lived electron signal (1.9 eV) allowed the peak to be assigned to a (2+2′) process resulting in prompt ionisation and fast direct dissociation on the $(1)^3A_2$ NO_2^+ surface to give NO^+ $(1)^2\Sigma^+$ in coincidence with $O(^3P_J)$.

The transient 1.2 eV photoelectron peaked at a time delay of 500 fs and had disappeared at a temporal delay of 2 ps. This was attributed to a (3+1′) ionisation process where dynamics at the three pump photon level result in the production of very slow NO^+ in v=1 and the associated electrons with kinetic energies of 1.2 eV. The remaining long-lived features (0 and 0.9 eV) appeared at a delay of 200 fs and remained over the probed 2 ps temporal window. The dominant 0 eV electron was attributed to (1+2′) DMI process via the NO_2^+ ground state to yield slow NO^+ $(1)^1\Sigma^+$ with $O(^3P_J)$ atoms in accord with the results of Eppink *et al.* (126) and Form *et al.* (14). The 200 fs onset of this feature was consistent with relaxation from the photoexcited $(1)^2B_2$ state to vibrationally excited levels of the $(1)^2A_1$ ground state (83) although direct fragmentation on the ground cation state is not consistent with the MRCI calculations of Hirst (142). Finally, the long-lived 0.9 eV electron feature was attributed to a three photon pump process that produced free NO in the $(1)^2\Sigma^+$ state which was subsequently ionised by a single probe photon, in accord with the results of López-Martens *et al.* (124).

The lab-frame angular distribution of this feature was characterised by a second order anisotropy parameter of 1.2. As these features were recorded using a 3D imaging technique, the recoil-frame anisotropy parameter was also measured (1.3). It is noted that Vredenborg *et al.* (28) ruled out a (2+1′) ionisation process in this paper due to the lack of a 1.25 eV photoelectron.

In this chapter the dissociative processes that occur when gas-phase NO_2 molecules were excited with visible photons, just below the first dissociation limit, and were subsequently excited with ultraviolet laser fields is considered. Here, the previous time-resolved studies were complemented by performing similar experiments with nanosecond laser systems. In this case the time resolution is sacrificed and electric-field strength is significantly decreased. However, it was found that the wavelength tunability and the increased energy resolution of the probe laser in this approach yielded new insights into the high-energy decomposition behaviour of NO_2.

6.2 Experimental

In the experiments reported in this chapter a combination of crush (1) and DC slice (50) VMI has been employed in conjunction with mass-resolved REMPI spectroscopy in order to probe the nitric oxide and atomic oxygen photoproducts of nitrogen dioxide photolysis with linearly polarised visible and ultraviolet excitation fields. Reagent molecules were entrained in a pulsed supersonic expansion of 2% NO_2 (Air Products Ltd.) purified by reaction with 5% O_2 (BOC gases) in a seed gas of He (BOC gases). The supersonic expansion was created by a heated pulsed valve (General Valve) with a 500 μm orifice and a backing pressure of ~1 bar. For all of the experiments reported here the nozzle was held at 393 K in order to push the NO_2/N_2O_4 equilibrium to 99.9% in favour of the monomer. Experiments were performed using the imaging spectrometer described in Chapter 3 and throughout these experiments the expansion chamber was held at a (uncalibrated) pressure between $1–6\times10^{-6}$ mbar with the detection chamber held at a (uncalibrated) pressure close to 1×10^{-8} mbar. Under these conditions the rotational temperature of the molecular beam was determined to be ~20 K from the rotational profile of NO contaminant in the NO_2 expansion. The frequency tripled output of a Nd:YAG laser (Continuum Surelite II-10) was used to pump a broadband OPO (Continuum Surelite OPO) which was used to generate pump light

with energies between 2.480 and 2.987 eV (500.0 and 415.1 nm) with a bandwidth of ~9 meV (~1.1 nm), a temporal duration of 4 ns (both at FWHM) and a repetition rate of 10 Hz. Depending on the experiment pump energies between 300 and 800 μJ were implemented. The pump laser beam was focused using a 250 mm focal length lens, however, as the broadband OPO generates light at a range of positions along the laser beam propagation axis, different components of the laser pulses have different divergences. This makes the beam difficult to focus and results in a focused beam with an extended Rayleigh length. The implication of this is that there is a lower pump intensity at the laser-molecular beam interaction region than would be expected from the laser pulse energies and temporal duration and the characteristics of the focusing lens. Assuming a perfect focus the conditions employed here would result in pump laser intensities of ~3.5–7.0×10^9 W cm^{-2} but based on the difficulties associated with focusing the beam, pump laser intensities of the order of 5–10×10^8 W cm^{-2} were more likely.

For the probe radiation the frequency tripled output of another Nd:YAG laser (Continuum Surelite III-10) was used to pump a dye laser (Sirah Cobra Stretch) operating with either a Coumarin 2, Coumarin 102, Coumarin 307 or Exalite 411 laser dye (Exciton). The fundamental output of the dye laser was frequency doubled in all cases to produce pulses at a repetition rate of 10 Hz with temporal profiles of 4 ns (at FWHM). Excitation energies between 5.46 and 5.69 eV (227 and 218 nm), 5.01 and 5.39 eV (247.5 and 230 nm), 4.77 and 5.08 eV (260 and 244 nm) and 5.90 and 6.05 eV (210 and 205 nm) were generated using the three respective laser dyes and the laser beams were focused using 250 or 300 mm focal length lenses where the foci were placed 5–10 mm beyond the molecular beam in an effort to uniformly probe the photoproduct distributions. In all cases the pump and probe pulses were counter-propagated. During the experiments, the probe laser energy was maintained between 160 and 650 μJ depending on the experiment resulting in pulse intensities of 3–30×10^8 W cm^{-2} depending on the conditions employed.

Ground electronic state NO fragments could be ionised via (1+1) REMPI schemes and electronically excited NO photofragments [produced in the $(1)^2\Sigma^+$, $(3)^2\Pi_\Omega$ and $(2)^2\Sigma^+$ states] could be ionised by absorbing a single probe photon. Alternatively NO ions could be produced directly from a dissociative ionisation process occurring via excited ion states of the parent molecule. $O(^3P_J)$ fragments were probed via a

(2+1) REMPI processes by tuning the probe photon energy around 5.4944, 5.4846 and 5.4804 eV (~225.65, 226.06 and 226.23 nm) for the 2, 1 and 0 spin-orbit states respectively. The UV laser was Doppler scanned to probe the entire atomic distribution via the $2s^2 2p^3 3p^1\ ^3P_J$ two-photon resonances which were ionised to leave a $O^+(^4S_{\frac{3}{2}})$ ion following the three-photon excitation. Attempts were made to probe $O(^1D_2)$ fragments via a (2+1) REMPI process by tuning the probe photon energy around 6.03410 eV (~205.473 nm). In these experiments the laser was Doppler scanned to probe the entire atomic distribution via the $2s^2 2p^3 3p^1\ ^1P_1$ intermediate level. Absorption of another probe photon from this resonance would have ionised the excited oxygen atoms to produce $O^+(^2D_J)$ and $O^+(^2P_J)$ ions. The entire $O(^1S_0)$ fragment distribution was probed using a (2+1) REMPI process by tuning the probe laser energy around the $2s^2 2p^3 3p^1\ ^1D_2$ intermediate resonance at an excitation energy of 5.1353 eV (~241.4336 nm). Absorption of a further probe photon produced both $O^+(^2D_J)$ and $O^+(^2P_J)$ ions.

For these experiments the detector was gated to detect ions of a given mass or, in the case of slice images, the centre of the photoproduct Newton spheres using the custom built detector power supply (Photek Ltd.). Images were captured using a 640×480 pixel CCD camera (LaVision Imager 3) and were averaged and processed using the DaVis software package (LaVision GmbH) and an event counting macro. Crush velocity map images were post-processed using the Hankel/Abel transform to reconstruct the photoproduct distributions after the projection (167; 168; 175). To generate kinetic energy distributions, pixels in the velocity map images were multiplied by the appropriate Jacobian term ($r\sin\theta$) and the resulting images were integrated with respect to polar angle in order to represent them as a 1D function in energy space. The 1D profiles were then calibrated in energy using O_2 or Br_2 photodissociation depending on the probe photon energy employed. The mechanisms and energetics of these fragmentation processes are well understood (192; 193).

6.3 Results

By irradiating NO_2 at 2.951 eV (420.2 nm) and probing the photoexcited state using different probe photon energies between 4.76767 and 5.08033 eV in ~0.00977 eV steps (260.052 and 244.048 nm in 0.500 nm steps) 33 velocity map images of the NO^+ photofragments were produced. Here the experimental conditions allowed fragments

Probe Photon Energy / eV	KE Feature 1 / eV	Assignment	KE Feature 2 / eV	Assignment
5.01862	1.225	NO $(1)^2\Sigma^+$	2.170	NO $(2)^2\Sigma^+$
4.89960	1.071	NO $(1)^2\Sigma^+$	1.963	NO $(2)^2\Sigma^+$
4.78608	1.000	NO $(1)^2\Sigma^+$	1.970	NO $(2)^2\Sigma^+$

Table 6.1: Photoelectron features observed with kinetic energies between 0.1 and 4.0 eV after excitation with a pump field with an energy of 2.951 eV and a probe photon energy that was varied and is given in the first column. From the electron kinetic energies and the separation of the different features, the photoelectron signals were assigned to signatures of single photon ionisation of the NO $(1)^2\Sigma^+$ and NO $(2)^2\Sigma^+$ states.

with kinetic energies between 0 and 3.0 eV to be recorded. These images are shown in Figs. 6.1, 6.2 and 6.3. All of these images were recorded under identical conditions (E_{pump}=400 μJ pulse^{-1}, E_{probe}=600 μJ pulse^{-1}, 20000 laser shots, laser focus positioned 6 mm beyond the centre of the molecular beam) and were normalised by recording images with the same pump and probe wavelengths at the end of a day and in the morning of the following day to produce identical radial profiles. In all of the images shown in Figs. 6.1, 6.2 and 6.3 the probe only laser signal corresponded to less than 10% of the mass-resolved ion yield. By inverting the images and extracting the energy distributions of the photofragments a contour plot of the NO^+ fragment kinetic energy against the probe excitation energy was produced. The NO^+ kinetic energy contour plot is shown in Fig. 6.4. In all cases the NO photofragments were produced with kinetic energies which were less than 0.85 eV with the majority of the fragments formed with kinetic energies that were less than 0.40 eV. Some of the energy distributions that were used to produce the contour plot are shown in Fig. 6.5.

Photoelectron images were also recorded at selected probe photon energies (4.78608, 4.89960 and 5.01862 eV or 259.051, 253.050 and 247.048 nm) under the same conditions as reported for the NO^+ fragments. A summary of the peaks in the three photoelectron images are shown in Table 6.1.

In separate experiments the photoexcited state generated after excitation at photon energies of 2.818 or 2.951 eV (E_{pump}=500–600 μJ pulse^{-1}) was probed using a sec-

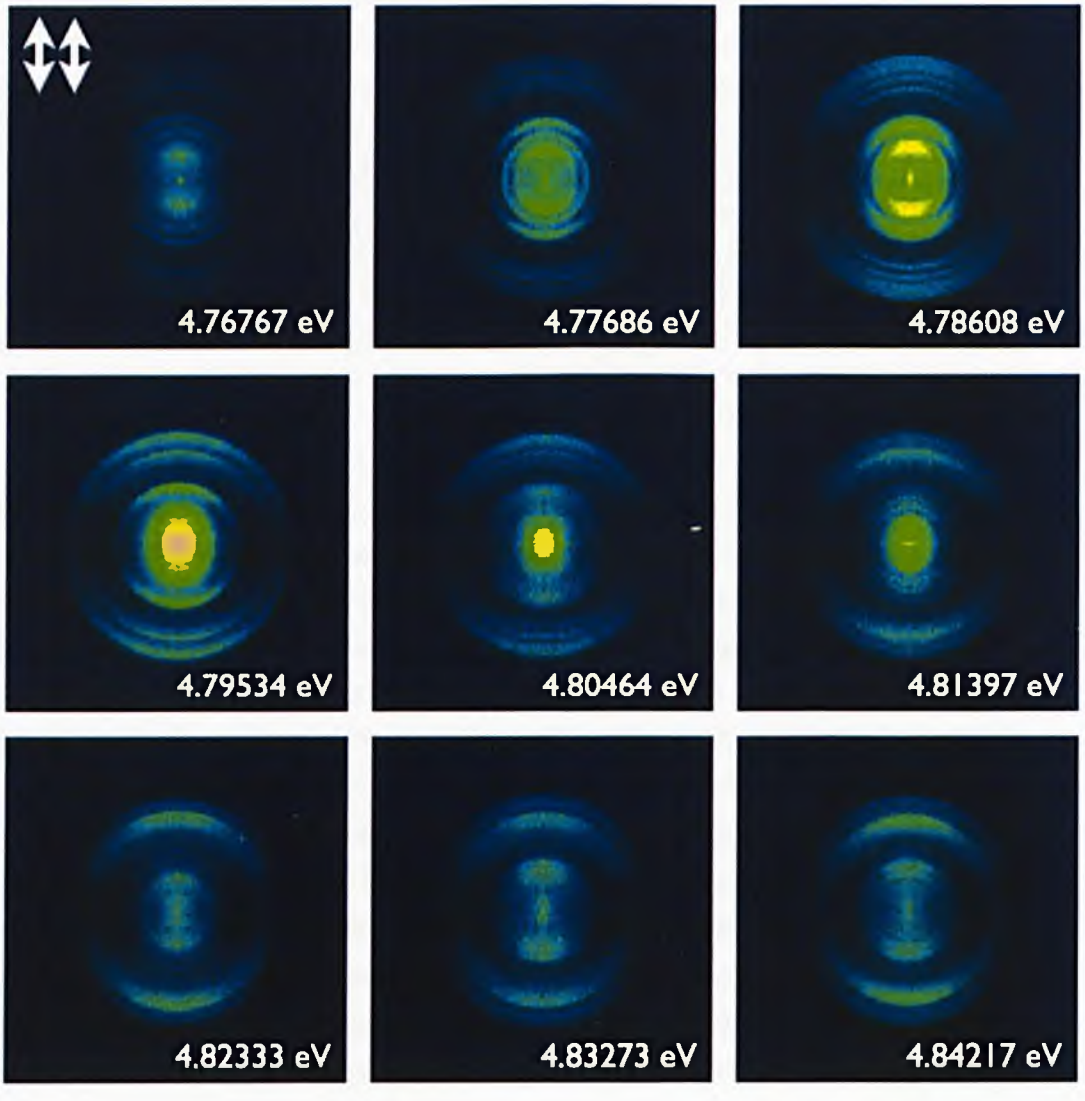

Figure 6.1: Crush velocity map images resulting from visible/UV excitation of NO_2. Here the pump photon energy was maintained at 2.951 eV and the probe photon energy varies depending on the image. The figure shows images recorded with probe laser excitation energies between 4.76767 and 4.84217 eV recorded in ~0.0977 eV steps.

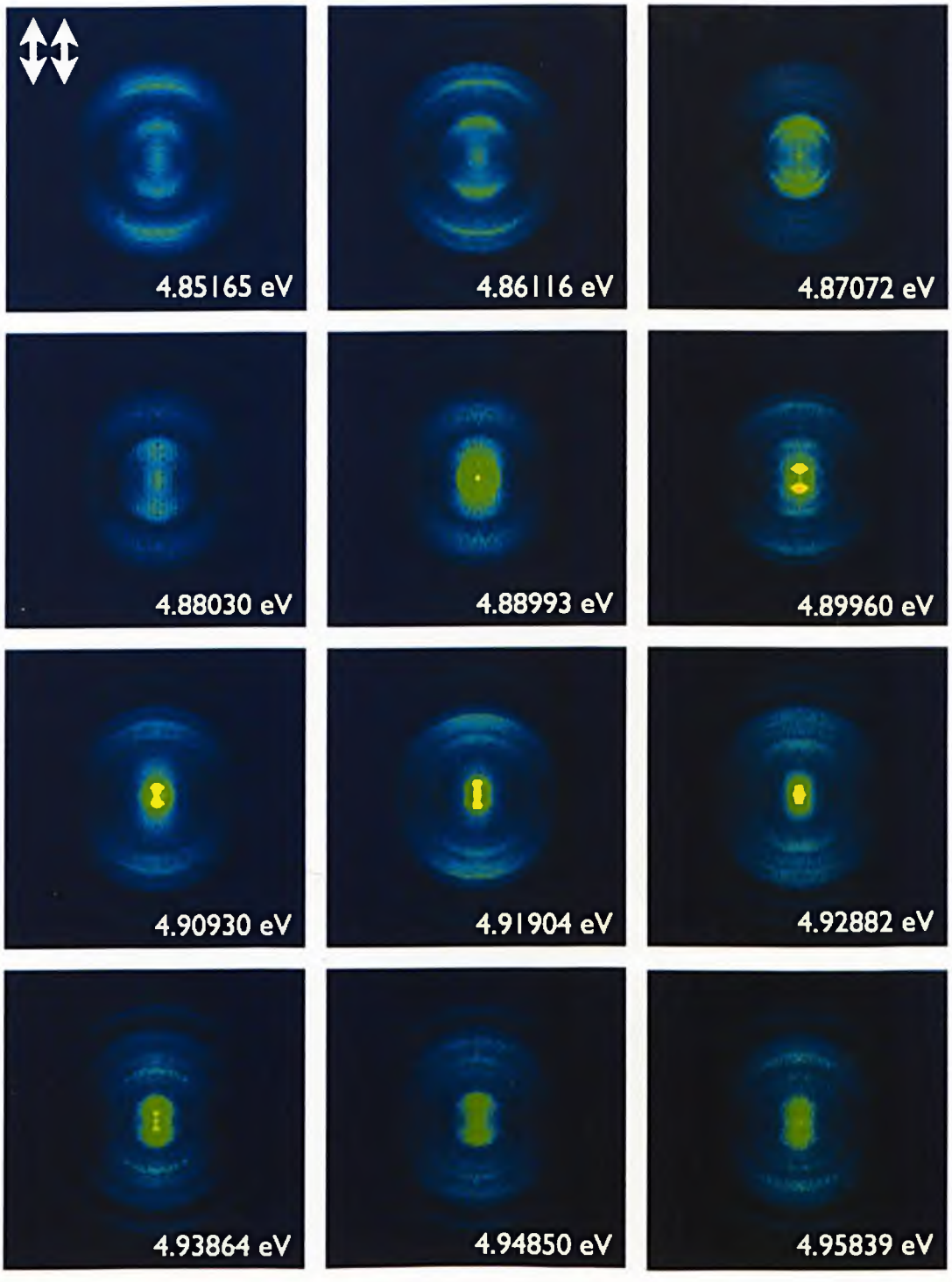

Figure 6.2: As Fig. 6.1 but with probe laser excitation energies between 4.85165 and 4.95839 eV.

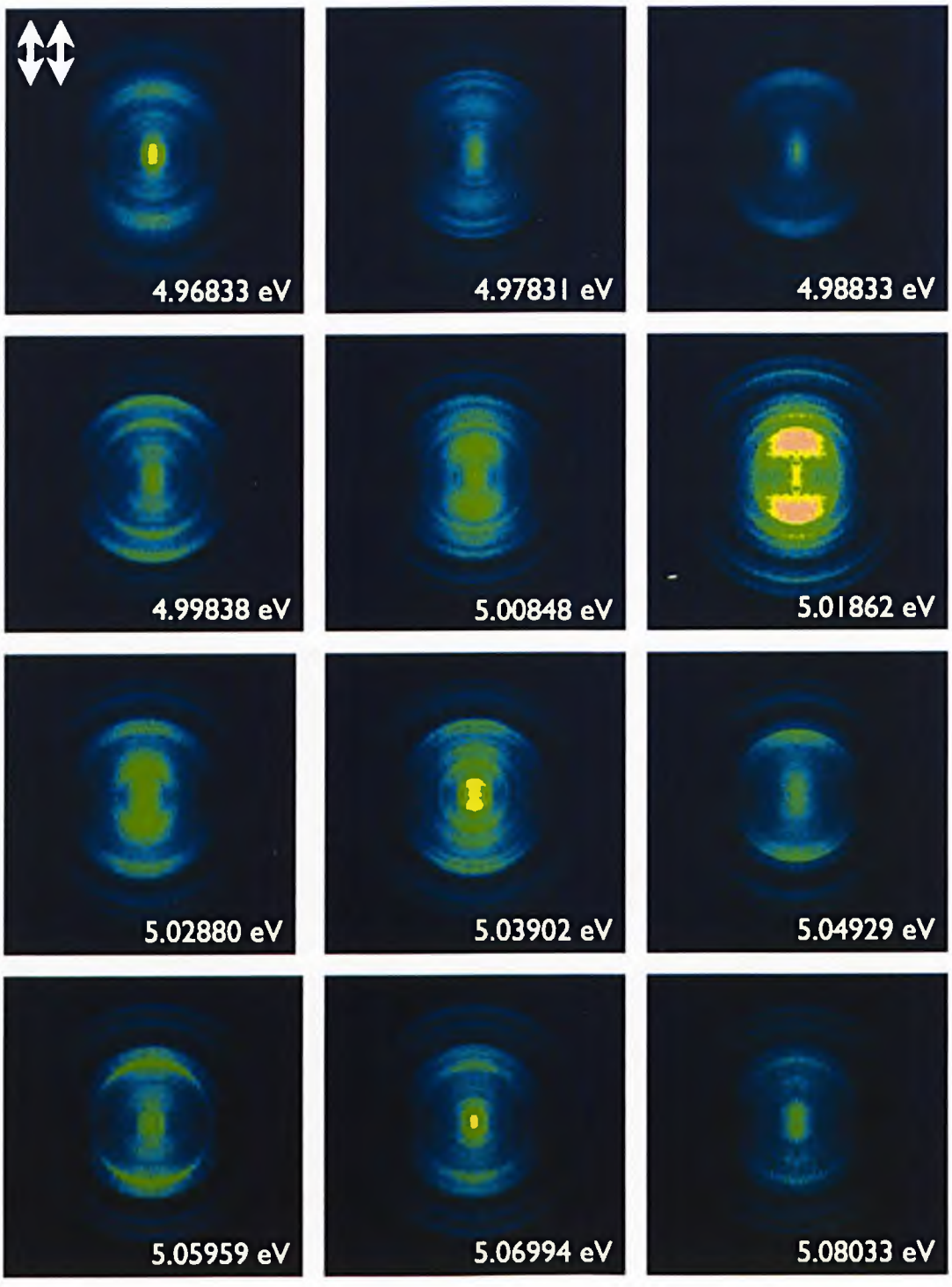

Figure 6.3: As Fig. 6.1 but with probe laser excitation energies between 4.96833 and 5.08033 eV.

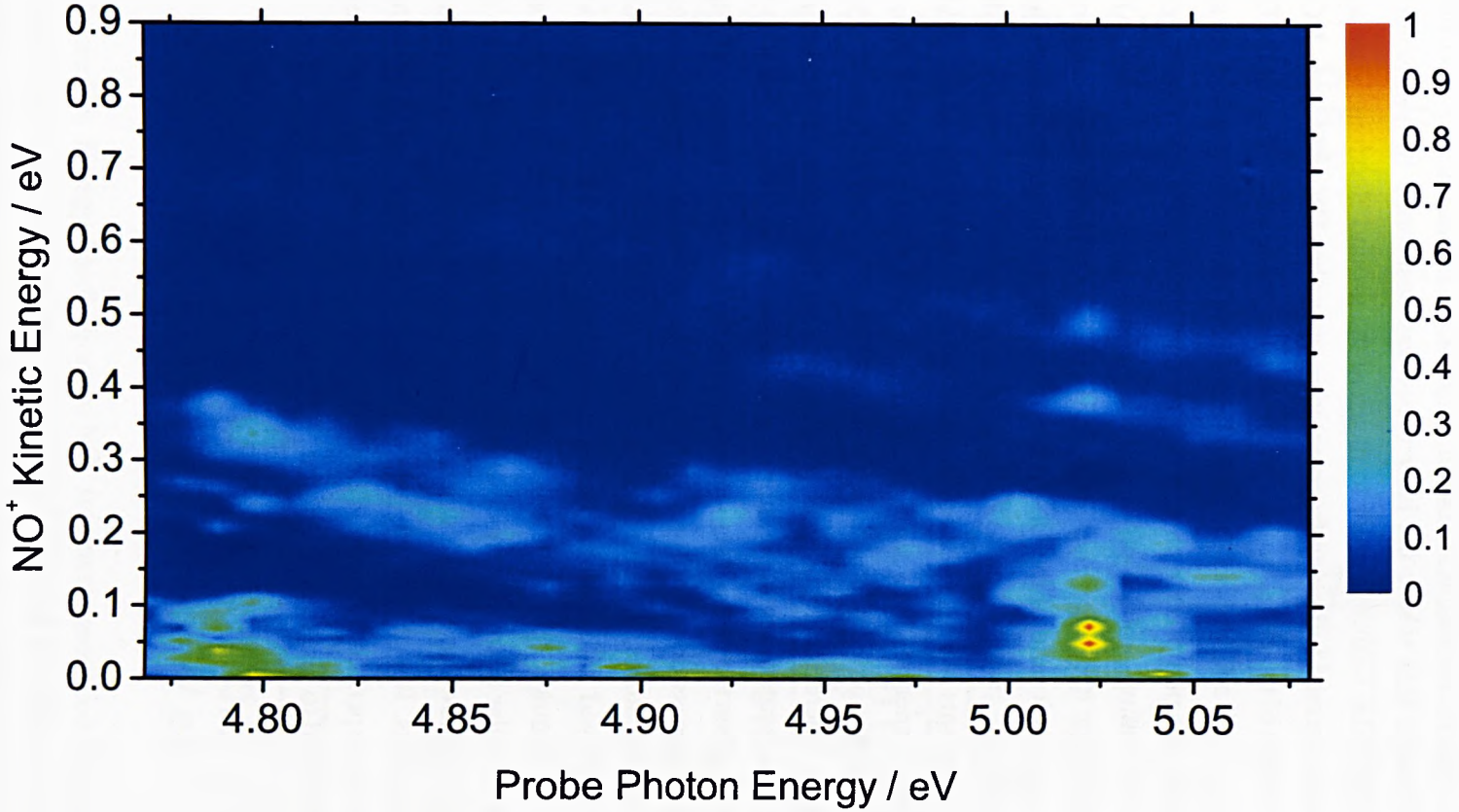

Figure 6.4: Contour plot of the energy distributions obtained from the crush velocity map images shown in Figs. 6.1, 6.2 and 6.3. The pump excitation energy was 2.951 eV. Here the energy distributions were plotted against the probe laser excitation energy. The contour plot shows that the majority of the NO^+ fragments were formed with kinetic energies that were less than 0.4 eV and that on average the kinetic energy release decreased with increased probe photon energy.

ond light field with an excitation energy of 5.49439 eV (E_{probe}=250–300 μJ pulse^{-1}, 300 mm focal length lens where the laser focus was positioned 10 mm beyond the centre of the molecular beam) in order to measure the ground electronic state atomic oxygen fragments formed following fragmentation or further UV excitation. DC slice velocity map images of the pump-probe + probe and the probe only signal of the O($^3P_2$) fragments formed with and without the pump laser field (120000 laser shots) are shown in Fig. 6.6 where the pump laser photon had an energy of 2.951 eV. Crush velocity map images of the pump-probe + probe and the probe only signal of the O($^3P_2$) fragments formed at pump excitation energies of 2.818 eV (80000 laser shots) are shown in Fig. 6.7. The spin-orbit ratio of the O(^3P_J) fragments formed at pump excitation energies of 2.818 eV (E_{pump}=400 μJ pulse^{-1}, E_{probe}=600 μJ pulse^{-1}) is shown in Table 6.2. In addition experiments were carried out in order to probe any O($^1D_2$) atoms produced with pump photon energies between 2.480 and 2.987 eV (500.0 to 415.1 nm, 500–600 μJ pulse^{-1}) with a probe photon energy of 6.03410 eV (~300 μJ pulse^{-1}, 250 mm focal length lens where the focus was ~5 mm beyond the centre of the molecular beam). Under these experimental conditions a reduction of the probe only O($^1D_2$) signal was observed when the pump laser was applied to the molecular beam implying that the pump-probe process does not form O($^1D_2$) atoms. In the experiments performed to probe any O($^1S_0$) atoms, a pump photon energy of 2.951 eV (E_{pump}=200–400 μJ pulse^{-1}) was employed with a probe photon energy close to 5.1353 eV (E_{probe}=450–600 μJ pulse^{-1}, 250 mm focal length lens where the laser focus was~8 mm beyond the centre of the molecular beam). A crush velocity map image of the pump-probe signal of O($^1S_0$) atoms is shown in Fig. 6.8 where the image corresponds to an accumulation of 120000 laser shots. It is also noted that NO_2^+ signals were observed to be extremely weak in all of the experiments reported here. At all excitation energies the parent ion signals corresponded to less than 5% of the NO^+ yield.

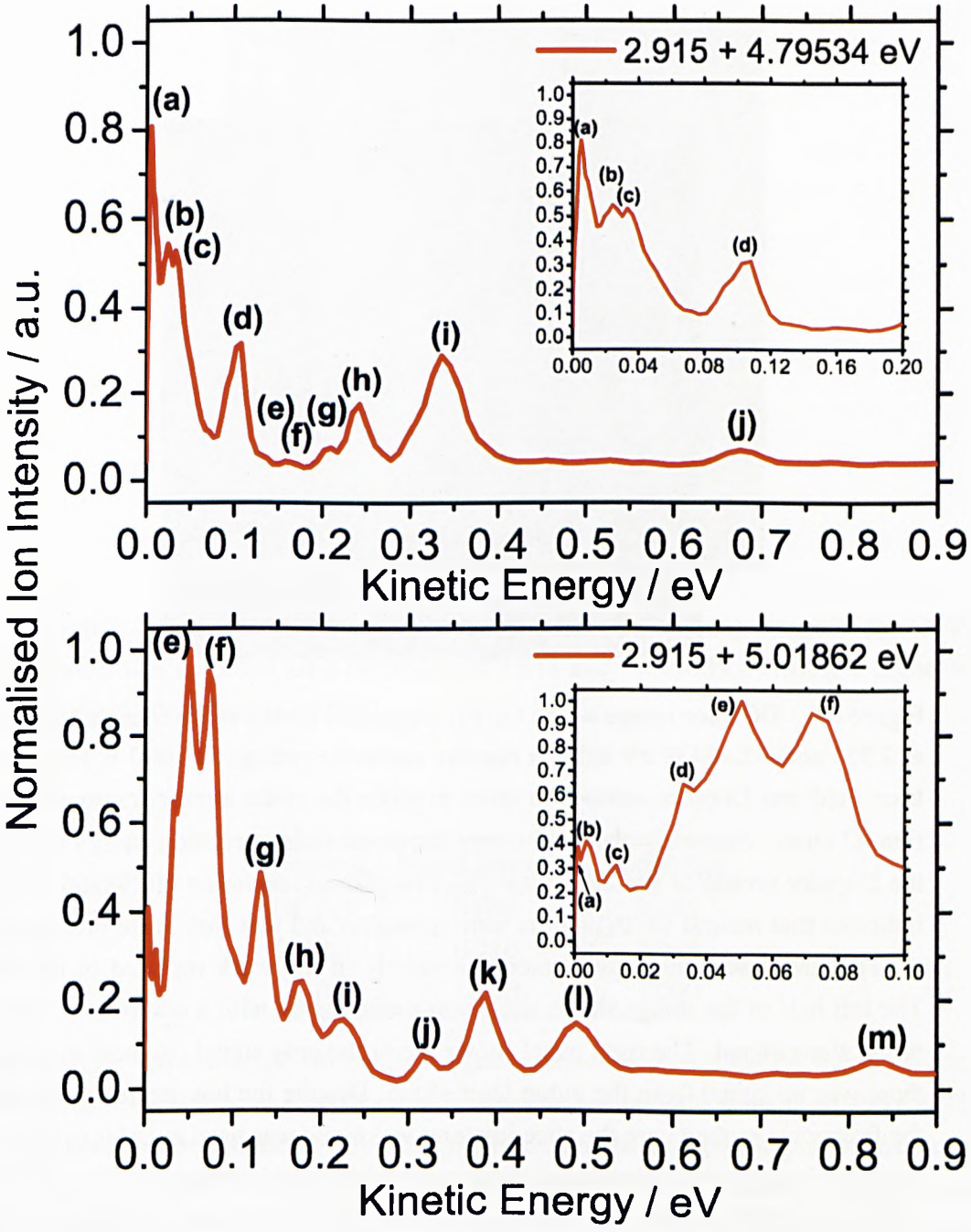

Figure 6.5: Energy distributions of NO^+ fragments produced following NO_2 excitation at 2.915 and 4.79534 eV (top panel) and 2.915 and 5.01862 eV (bottom panel). The energy distributions are vertical slices through the contour plot shown in Fig. 6.4.

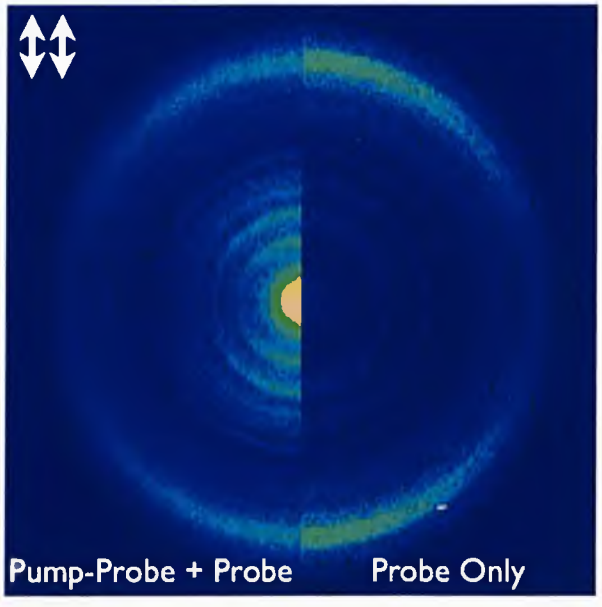

Figure 6.6: DC slice image of the $O(^3P_2)$ fragments produced after excitation of NO_2 at 2.951 and ~5.49439 eV using a repeller electrode voltage of 1000 V. Here the UV laser field was Doppler scanned in order to probe the entire atomic fragment distribution. O atoms were only observed where the probe laser excitation energy was within the Doppler profile of the $2s^2 2p^3 3p^1\ ^3P_2$ two-photon resonance (10.98886 eV). This indicates that neutral $O(^3P_2)$ atoms were produced and that they were probed via the (2+1) REMPI scheme implemented extensively in the work reported in this thesis. The left half of the image shows the pump-probe signal with a contribution from the probe alone signal. The right panel shows the probe only signal. In these experiments there was no signal from the pump laser alone. Despite the low momenta of some of the fragments probed here the slice imaging technique was used in order to accurately measure the energy separation of the pump-probe image features. In the case of the very slow fragments the slice images represent full projections of the photoproduct Newton spheres.

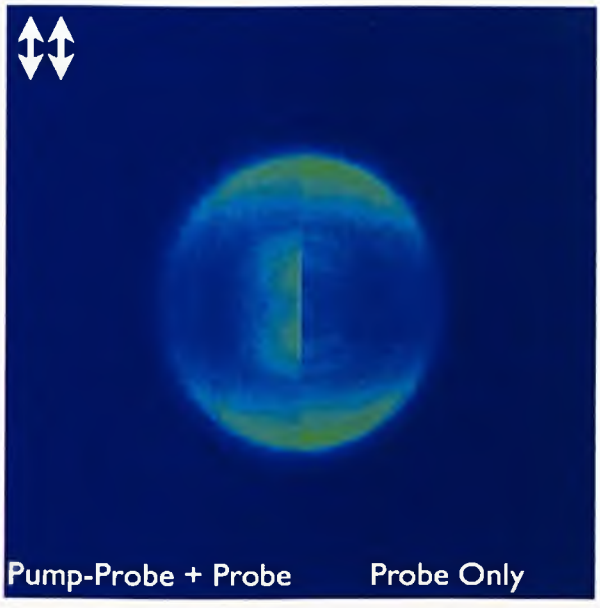

Figure 6.7: As Fig. 6.6 except in this case a crush velocity map image of the $O(^3P_2)$ fragments was recorded after excitation at 2.818 and ~5.49439 eV using a higher repeller electrode voltage (3000 V).

Fragment	Signal Intensity	Population
$O(^3P_0)$	0.004	0.205
$O(^3P_1)$	0.210	0.350
$O(^3P_2)$	1.000	1.000

Table 6.2: Line-strength normalised signal intensities of the $O(^3P_J)$ fragments produced after excitation at ~2.818 eV with possible further excitation at ~5.494 eV. The populations were obtained by dividing the line-strength corrected signal intensities by the state degeneracy. A preference for the ground spin-orbit state is observed and the population ratio is observed to be significantly different than that observed for the $O(^3P_J)$ fragments formed after single-photon excitation to the $(3)^2A'$ state (see Chapter 4).

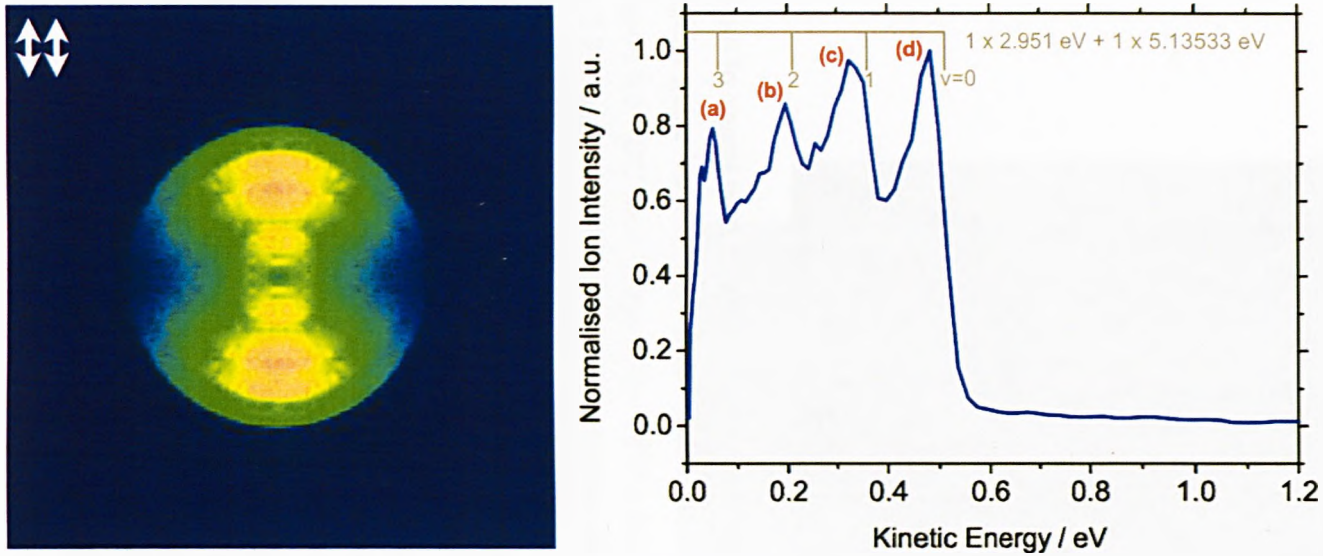

Figure 6.8: The left panel shows a crush velocity map image image (averaged over 120000 laser shots) of the $O(^1S_0)$ fragments produced after excitation of NO_2 at 2.951 and ~5.13533 eV using a repeller electrode voltage of 5000 V. Here the UV laser field was Doppler scanned in order to probe the entire atomic fragment distribution. O atoms were only observed where the probe laser excitation energy was within the Doppler profile of the $2s^2 2p^3 3p^1\ ^1D_2$ two-photon resonance (10.27066 eV). This indicates that neutral $O(^1S_0)$ atoms were produced and that they were probed via a (2+1) REMPI scheme. No signal was observed with the pump or probe lasers alone, resulting in a background free image. The right hand panel shows the corresponding energy distribution obtained from this image. The maximum kinetic energy of these fragments suggests that the majority were formed by a 1+1′ excitation process and the vibrational comb associated with the NO $(1)^2\Pi_\Omega$ co-fragments highlights that they were produced in all four of the energetically accessible vibrational states with a slight propensity for low **v**.

6.4 Discussion

6.4.1 NO^+ fragments

The data shown in Figs. 6.1, 6.2 and 6.3 might be expected to be signatures of similar decomposition processes as those outlined in the introduction to this chapter (14; 25; 26; 28; 124; 125; 126; 253; 254). At the pump excitation energy employed to produce these images, single-photon excitation principally populates the bound $(1)^2B_2$ electronic state which can couple back to the ground state via the conical intersection discussed in Chapter 2. At this excitation energy the $(1)^2B_2$ and the $(1)^2A_1$ states are bound along all nuclear co-ordinates resulting in successive crossings and re-crossings and a mixed vibronic manifold that has a lifetime on the order of tens of microseconds (85; 255; 256; 257). As a UV probe field is applied 20 ns after the pump field this allows further excitation to occur either through absorption of more pump photons (within the 4 ns OPO pulse duration) or through absorption of one or more UV probe photons after the 20 ns delay. A number of possible multiphoton excitation routes can be considered.

2→1′+1′

Two-photon excitation by the pump laser field may populate the $(2)^2B_2$ state with resonant enhancement via the $(1)^2B_2$ state as proposed by Grant and co-workers (67; 68; 69; 70). In this case the short-lived photoexcited state would be expected to decay within 100 fs and neutral NO $(1)^2\Pi_\Omega$ and $O(^3P_J)$ fragments would be produced. Here, the diatomic fragments could be formed in v=0–13 and with kinetic energies between 970 and 0 meV respectively. Diatomic fragments might also be expected to be produced in v=0–3 in coincidence with $O(^1D_2)$ via a non-adiabatic interaction. However, based on the results of Bigio *et al.*, smaller yields would be expected for this channel (67). Due to the 20 ns pump-probe delay employed in these experiments, further excitation of the parent molecule by the probe field would not be possible. In the case of the two-photon dissociation the rovibrational distribution of the diatomic fragments could be probed through a two-photon ionisation process. Provided that the probe field was intense enough, ionisation may occur through a two-photon non-resonant excitation scheme which would be expected to result in broad NO^+ kinetic

energy distributions due to the simultaneous ionisation of diatomic fragments in many quantum states. However, where the probe photon energy matched a resonance for excitation to an intermediate neutral electronic state of NO, state-selective ionisation through a (1′+1′) REMPI process would be favoured. This probe scheme could involve the $(1)^2\Sigma^+$, $(3)^2\Pi_\Omega$ and $(2)^2\Sigma^+$ states as intermediate resonances (see Table 6.3) and would be expected to produce relatively sharp features in the NO^+ images at a variety of kinetic energies that would depend on the neutral photoproduct distribution and the accessible REMPI transitions at each probe wavelength.

1+1′→(1′+1′)

Alternative excitation routes could involve the absorption of a single probe photon from the initially excited $(1)^2B_2/(1)^2A_1$ mixed manifold. Here, the combined excitation energy for this process would be between ~7.718 and 8.031 eV depending on the probe laser energy employed. This process would be expected to populate low-lying Rydberg levels that converge on the ground state of the cation (118; 119). Following excitation to these levels, absorption of more probe photons could occur or the Rydberg state(s) could decay. Considering further absorption, the electronic configuration of the Rydberg state would be expected to result in favourable ionisation to the ground electronic state of the cation. In this situation alternative excitations to doubly electronically excited neutral states or single or multiphoton (above-threshold ionisation, ATI) absorption processes to electronically excited states of the cation would be expected to be minimal due to the similarities of the nuclear and electronic structures of the Rydberg states and the ground state of the cation. As the ground cation state has been observed to be stable throughout its Franck-Condon window from the electronic ground state in single-photon experiments (143), there is little evidence to suggest that this process would produce neutral or charged photoproducts. However, the fragmentation process cannot be entirely ruled out due to the different nuclear geometries accessed on excitation to the ground cation state following multiphoton excitation schemes or isoenergetic single-photon excitation schemes.

An alternative fragmentation process could occur from the Rydberg states prepared at the 1+1′ level due to the Rydberg-valence non-adiabatic interactions discussed by Petsalakis *et al.* (122). Here NO $(1)^2\Pi_\Omega$ fragments could be produced with $O(^3P_J)$,

NO excited state	Vibrational transition	Bandhead / eV	Transition probability
$(3)^2\Pi_\Omega$	(1, 8)	5.01927	5.034×10^{-3}
$(1)^2\Sigma^+$	(0, 2)	5.01784	4.328×10^{-3}
$(1)^2\Sigma^+$	(3, 6)	5.00305	1.771×10^{-3}
$(2)^2\Sigma^+$	(2, 10)	4.99687	5.323×10^{-3}
$(1)^2\Sigma^+$	(5, 9)	4.91289	3.030×10^{-4}
$(1)^2\Sigma^+$	(1, 4)	4.86024	1.884×10^{-3}
$(2)^2\Sigma^+$	(0, 8)	4.84369	6.763×10^{-4}
$(3)^2\Pi_\Omega$	(1, 9)	4.81444	2.838×10^{-3}
$(2)^2\Sigma^+$	(2, 11)	4.79907	7.709×10^{-4}
$(1)^2\Sigma^+$	(0, 3)	4.79251	4.041×10^{-3}
$(3)^2\Pi_\Omega$	(0, 8)	4.72753	8.396×10^{-3}
$(1)^2\Sigma^+$	(5, 10)	4.72178	7.781×10^{-6}
$(2)^2\Sigma^+$	(1, 10)	4.72049	1.482×10^{-4}
$(3)^2\Pi_\Omega$	(1, 10)	4.61270	1.481×10^{-3}
$(2)^2\Sigma^+$	(4, 15)	4.57617	1.697×10^{-3}

Table 6.3: Transition probabilities and excitation energies for selected vibrational bands in the absorption spectrum of ground state NO. More than 30 vibrational bands are accessible over the probe energy range employed to produce Figs. 6.1, 6.2 and 6.3 (4.76767–5.08033 eV). However, due to the resonant enhancement of the ionisation signal, the NO $(1)^2\Pi_\Omega$ fragments were only expected to be ionised via the absorption bands detailed above when probe photon energies of 4.79534 and 5.01862 eV were implemented (see Fig. 6.5). The data are taken from constants published in the LIFBASE spectral simulation program (9).

$O(^1D_2)$ and/or $O(^1S_0)$ atoms (see Table 2.4) depending on the identity of the coupled valence state and any subsequent non-adiabatic interactions on the way to the product asymptote correlating with that adiabatic valence state. In single-photon excitation experiments, where the excitation energy was within the 1+1′ energy range discussed here, the production of highly vibrationally and rotationally excited ground state NO fragments were observed in coincidence with $O(^3P_J)$ atoms with little or no production of electronically excited atoms (110). If these highly vibrationally excited fragments could be probed in a (1′+1′) REMPI scheme at probe excitation energies between 4.76862 and 5.08132 eV and assuming the states accessed at the 1+1′ level fragment within 4 ns, the fragment distribution could be measured using a nanosecond probe field. In contrast, the time-resolved experiments described in the introduction would not be sensitive to such a fragmentation process unless it occurred on a time scale that was less than 100 fs as the probe laser beam would need to both induce fragmentation and probe the photoproduct distribution within the probe pulse length. Where resonant ionisation of the photoproducts was possible, however, this 1+1′→1′+1′ process would be expected to produce relatively sharp features in the NO^+ kinetic energy distributions that make up the contour plot shown in Fig. 6.4.

It is highlighted that within the 1+1′→1′+1′ excitation scheme the probed photoproduct distribution would be expected to change with the probe laser excitation energy. Depending on the probe laser energy employed in the experiments reported here, the 1+1′ pumping process would allow the production of NO $(1)^2\Pi_\Omega$ in different vibrational level ranges. At the lowest and highest probe excitation energies the diatomic fragments could be formed in v=0–1 or v=0–3 in coincidence with $O(^1S_0)$ atoms, v=0–12 or v=0–14 in coincidence with $O(^1D_2)$ atoms and/or v=0–23 or v=0–26 in coincidence with $O(^3P_2)$ atoms respectively.

1+2′ DMI

The time-resolved imaging studies of Eppink *et al.* (126), Form *et al.* (14) and Vredenborg and co-workers (28) assigned the principal long-lived NO^+ signal to a (1+2′) dissociative ionisation. Such an excitation scheme may also occur in the nanosecond experiments reported here. Under the conditions employed to produce the images shown in Figs. 6.1, 6.2 and 6.3 the total excitation energy for such a process would

lie between 12.486 and 13.111 eV depending on the probe laser excitation energy. Such a process would be expected to be resonantly enhanced at the level of the first and perhaps second photon by the $(1)^2B_2$ state and one or more Rydberg states respectively. If this excitation route occurs, total excess energies between 0.106 and 0.732 eV would occur permitting the formation of NO^+ $(1)^1\Sigma^+$ in v=0 or v=0–3 respectively. As outlined above, excitation to Rydberg levels converging to the ground cation state would be expected to yield stable $(1)^1A_1$ parent ions. Although the different nuclear gemoetries accessed in single and multiphoton excitation processes may permit dissociative ionisation via an avoided crossing between the ground cation state and an electronically excited cation state in multiphoton excitation schemes. It is highlighted, however, that there is little evidence for such a DMI process where the ground state of the cation has been probed in relatively low vibrational levels in multiphoton experiments (131; 132; 133; 134; 135; 136; 137; 138; 139).

An alternative mechanism for the 1+2′ DMI scheme could occur if a neutral state, most likely at the level of the second photon, allowed the $(1)^3B_2$ or $(1)^3A_2$ ion states to be accessed at extended N-O bond lengths where the threshold for excitation corresponds to the dissociative ionisation limit of 12.3797 eV (142). This excitation energy is considerably lower than the 12.815 and 13.593 eV respective thresholds observed in single-photon experiments. Furthermore, provided the probe laser field was intense enough another DMI mechanism could also occur. In this case direct two-photon excitation to the potential well of the electronically excited $(1)^3B_2$ ion state could take place from the mixed $(1)^2B_2/(1)^2A_1$ manifold at probe photon energies in excess of ~4.932 eV. At the excitation energies employed in the experiments presented in Figs. 6.1, 6.2 and 6.3, this process would be expected to lead to relatively slow fragmentation where the decomposition rate would depend on the probe photon energy employed (142).

In any of the cases outlined above the excess energy for the DMI process would be partitioned between the NO^+ $(1)^1\Sigma^+$ and $O(^3P_J)$ internal states and the kinetic energies of the electron and the two fragments. This mechanism would therefore be expected to produce relatively slow photoelectrons with slow atomic and molecular fragments. Within this excitation scheme the energy distributions of the electrons could be modulated by ionisation leading to different vibrational states of the initially populated cation state. Each cation vibrational state could then produce different photoproduct

distributions and would result in different atomic and molecular ion kinetic energy profiles. Furthermore, the initial ionisation step would be expected to be dependent on the excitation energy of the probe photon which would result in changes in the electron distribution and the resulting NO^+ kinetic energy profiles. This process would therefore be expected to yield a highly complex diatomic kinetic energy contour plot which was dominated by low kinetic energy NO^+ fragments with broad kinetic energy distributions that extended to the energetic limit associated with the DMI process.

3→1′+1′

A final consideration would be the three photon pump process that was observed in a number of time-resolved studies (14; 25; 26; 28; 124; 125; 126). In the femtosecond experiments a 3+1′ excitation scheme was advocated where parent ionisation leading to electronically excited ion states with subsequent dissociation was observed on short time scales (14; 28). These processes have been linked to the production of low kinetic energy photoelectrons and broad kinetic energy distributions of NO^+ fragments. However, in the experiments reported here these processes would not be expected to occur due to the 20 ns pump-probe delay. On longer time scales, at temporal delays in excess of ~0.5 ps, fragmentation was observed to occur at the level of three pump photons to produce neutral electronically excited NO fragments. Depending on the pump excitation energy in such a process, the probe laser pulse may be expected to ionise free neutral NO fragments that could be formed in a number of electronic states including the $(1)^2\Pi_\Omega$, $(1)^2\Sigma^+$, $(2)^2\Pi_\Omega$, $(3)^2\Pi_\Omega$ and the $(2)^2\Sigma^+$ states. In the time-resolved experiments signatures of NO $(1)^2\Sigma^+$ and $(3)^2\Pi_\Omega$ have been observed and have been attributed to three photon excitation processes that were resonantly enhanced at the levels of either the first and third or all three pump photons (14; 28; 124; 125; 126). As highlighted in Chapter 4, ionisation of the $(2)^2\Pi_\Omega$ fragments would be unlikely in any of the experiments outlined above or here (218) despite LIF signatures of these fragments being observed following single-photon excitation at energies close to 9.5 eV (123).

In the case of single-photon $(1)^2\Sigma^+$, $(3)^2\Pi_\Omega$ and $(2)^2\Sigma^+$ ionisation, broad features would be expected in the NO^+ kinetic energy profile as the entire distribution of NO photoproducts would be ionised with little state selectivity. Conversely, state-selective ionisation leading to sharp features in the diatomic energy distribution could occur

for NO $(1)^2\Pi_\Omega$ fragments that were probed via a (1'+1') REMPI process. In the experiments reported here for the NO^+ fragments, a three-photon pump process would deposit 8.851 eV of energy into the parent molecule allowing NO to be produced in the $(1)^2\Pi_\Omega$ or $(1)^2\Sigma^+$ states where the ground state diatomic fragments could be formed with $O(^3P_J)$, $O(^1D_2)$ and/or $O(^1S_0)$ atoms but the electronically excited diatomics could only be produced concomitantly with $O(^3P_J)$ atoms. Specifically this three photon pump process could produce NO $(1)^2\Pi_\Omega$ in v=0–6 in coincidence with $O(^1S_0)$ atoms, v=0–18 in coincidence with $O(^1D_2)$ atoms and/or v=0–33 in coincidence with $O(^3P_2)$ atoms. For the NO fragments that could be produced in the $(1)^2\Sigma^+$ state only the lowest vibrational state would be accessible where a maximum diatomic fragment kinetic energy of 89 meV could be observed.

Analysis of the NO^+ energy distributions

A detailed analysis of the kinetic energy distributions displayed in the contour plot shown in Fig. 6.4 reveal a number of aspects about the multiphoton fragmentation process. Firstly, the kinetic energy of the NO^+ fragments were generally observed to decrease as the probe laser energy was increased implying that the diatomic fragments were increasingly internally excited with increased probe photon energy. Furthermore, the kinetic energy distributions highlight that all of the NO^+ peaks had well defined kinetic energy spreads corresponding to less than 0.05 eV (FWHM). This suggests that the excitation process either produced NO^+ fragments in a limited number of quantum states directly or that a REMPI probe scheme was involved in the ionisation of neutral fragments. In order to assess which process was taking place an annotated version of the NO^+ contour plot is presented in Fig. 6.9. Here the probe excitation energy dependent threshold for the production of NO^+ fragments through a 1+2' DMI process (grey diagonal line) and the probe energy independent threshold for the three pump photon fragmentation to produce NO $(1)^2\Sigma^+$ fragments (black horizontal line) have been added to the contour plot. Additionally the threshold for excitation to the bottom of the potential well of the $(1)^3B_2$ excited ion state is shown as a vertical line. The figure highlights a lack of features in the energy distributions that correlate with these thresholds or other lower kinetic energy lines with the same gradients in kinetic energy space. This suggests that, under the experimental conditions employed here, the 1+2' DMI process

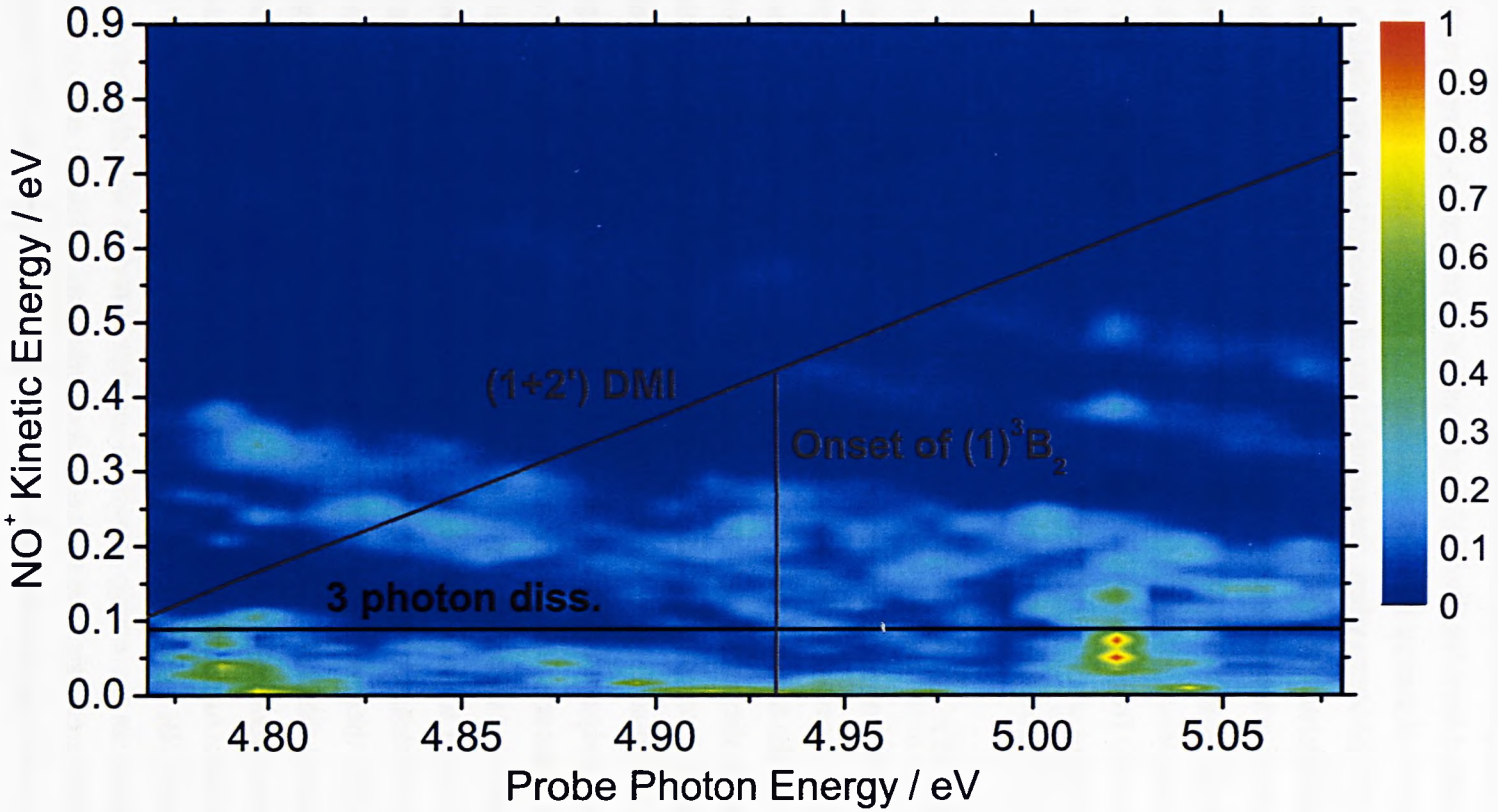

Figure 6.9: Contour plot of the energy distributions obtained from the crush velocity map images shown in Figs. 6.1, 6.2 and 6.3 where the thresholds for a 1+2′ DMI process producing NO^+ $(1)^1\Sigma^+$ and a three photon pump process producing NO $(1)^2\Sigma^+$ fragments that were ionised by a single probe photon is shown.

and the three photon pump process to produce NO $(1)^2\Sigma^+$ fragments make little or no contribution to the NO^+ signal and the observed photodynamics. Provided higher energy absorption processes (like 1+3′ or 4→1′+1′) were insignificant, this means that NO $(1)^2\Pi_\Omega$ and perhaps NO $(2)^2\Pi_\Omega$ products were predominantly formed and that the ground electronic state diatomic species must be ionised via a (1′+1′) REMPI process. Furthermore, as the accessible NO $(1)^2\Pi_\Omega$ absorption bands involved in the REMPI processes were shaded to the blue, this would be consistent with a reduction of NO^+ kinetic energy with increased probe photon energy.

The conclusions drawn from Fig. 6.9 place restrictions on the excitation schemes that could be responsible for the NO^+ kinetic energy profiles. In order to assess the contributions of the excitation schemes that incorporated resonant ionisation of neutral fragments, two of the energy distributions have been analysed in detail. These NO^+ kinetic energy distributions are shown in Fig. 6.5 and correspond to the NO^+ fragments formed following NO_2 excitation at 2.915 and 4.79534 eV (top panel) and 2.915 and 5.01862 eV (bottom panel).

At the probe photon energies employed to produce Fig. 6.5 diatomic photofragments could be probed via many different vibrational bands associated with the $(1)^2\Sigma^+\leftarrow(1)^2\Pi_\Omega$, $(3)^2\Pi_\Omega\leftarrow(1)^2\Pi_\Omega$ and $(2)^2\Sigma^+\leftarrow(1)^2\Pi_\Omega$ transitions. However, the restrictions imposed by the state-selective ionisation scheme and the narrow bandwidth probe laser pulse with known photon energy allowed the resonant probe transitions to be calculated in the majority of cases. This calculation was not possible for ground state fragments produced in vibrational levels between 22 and 33 [19–33 for fragments probed via the $(3)^2\Pi_\Omega$ intermediate state] as the available Dunham coefficients for the NO $(1)^2\Pi_\Omega$, $(1)^2\Sigma^+$, $(3)^2\Pi_\Omega$ and $(2)^2\Sigma^+$ electronic states could not reliably reproduce the absorption bands. It was therefore impossible to assess the contributions of such fragments to the contour plot shown in Fig. 6.4. It is noted however, that the single-photon results of Taherian *et al.* suggest that these fragments may dominate the photoproduct distributions (110).

By recording velocity map images of the NO^+ fragments, each photoion signal could be attributed to an initial diatomic quantum state and a particular atomic co-fragment. This assignment was achieved by calculating the expected kinetic energy for NO $(1)^2\Pi_\Omega$ fragments produced via the three proposed excitation schemes in all of the quantum states that could be probed. In the case of a 4.79534 eV probe laser

Peak	KE / eV (obs.)	Excitation scheme	v	N	Co-fragment(s)	Int. state	Branch	KE / eV (calc.)
(a)	0.005	2→1′+1′	10	55	$O(^3P_2)$	$(3)^2\Pi_\Omega$	R_2	0.009
(b)	0.024	2→1′+1′	3	18	$O(^1D_2)$	$(1)^2\Sigma^+$	Q_2/Q_{21}	0.017
		2→1′+1′	3	18	$O(^1D_2)$	$(1)^2\Sigma^+$	P_1	0.021
		1+1′→1′+1′	10	46	$O(^1D_2)$	$(1)^2\Sigma^+$	P_1	0.030
(c)	0.033	2→1′+1′	3	10	$O(^1D_2)$	$(1)^2\Sigma^+$	Q_{21}	0.033
		2→1′+1′	3	10	$O(^1D_2)$	$(1)^2\Sigma^+$	Q_1	0.038
		1+1′→1′+1′	10	46	$O(^1D_2)$	$(1)^2\Sigma^+$	P_1	0.030
(d)	0.108	2→1′+1′	11	22	$O(^3P_2)$	$(2)^2\Sigma^+$	O_{12}	0.113
(e)	0.138	2→1′+1′	10	33	$O(^3P_2)$	$(2)^2\Sigma^+$	R_{21}	0.137
		2→1′+1′	10	33	$O(^3P_2)$	$(2)^2\Sigma^+$	R_1	0.141
		2→1′+1′	11	12	$O(^3P_2)$	$(2)^2\Sigma^+$	Q_2	0.132
		2→1′+1′	11	12	$O(^3P_2)$	$(2)^2\Sigma^+$	Q_{12}	0.135
(f)	0.158	2→1′+1′	10	29	$O(^3P_2)$	$(2)^2\Sigma^+$	S_{21}	0.154
(g)	0.210	?	?	?	?	?	?	?
(h)	0.243	2→1′+1′	8	41	$O(^3P_2)$	$(3)^2\Pi_\Omega$	P_1	0.240
		1+1′→1′+1′	8	31	$O(^1D_2)$	$(3)^2\Pi_\Omega$	R_{21}	0.242
(i)	0.336	1′→1′+1′	3	10	$O(^3P_2)$	$(1)^2\Sigma^+$	Q_{21}	0.334
		1′→1′+1′	3	10	$O(^3P_2)$	$(1)^2\Sigma^+$	Q_1	0.337
(j)	0.675	2→1′+1′	3	24	$O(^1D_2)$	$(1)^2\Sigma^+$	P_2	0.684
		1+1′→1′+1′	3	10	$O(^1D_2)$	$(1)^2\Sigma^+$	Q_{21}	0.675
		1+1′→1′+1′	3	10	$O(^1D_2)$	$(1)^2\Sigma^+$	Q_1	0.679
		3→1′+1′	15	61	$O(^3P_2)$	$(2)^2\Sigma^+$	Q_{21}	0.672
		3→1′+1′	15	61	$O(^3P_2)$	$(2)^2\Sigma^+$	Q_1	0.675

Table 6.4: Possible assignments of the peaks in the NO^+ kinetic energy distribution shown in the top panel of Fig. 6.5. The energy distribution was produced from the image recorded with a pump photon energy of 2.915 eV and a probe photon energy of 4.79534 eV. The branch refers to the rotational branch via which a particular rotational state was probed. The calculated energy corresponds to that of NO $(1)^2\Pi_\Omega$ fragments produced by the relevant excitation mechanism, with the relevant co-fragment and in the relevant spin-orbit, vibrational and rotational state.

energy, the results of the calculations are summarised in Table 6.4. Here all but one of the kinetic energy peaks have been assigned to diatomic quantum states where the fragments were produced with a particular atomic partner. Here the NO fragments defined by the parameters associated with the calculated kinetic energies were taken as potential sources of the NO^+ image features if the calculated kinetic energies were within 0.010 eV of the measured kinetic energy. This was seen as a reasonable error bound for the measured kinetic energies when the inaccuracies associated with the Hankel transform and the kinetic energy calibration procedure were considered. Due to the plethora of accessible probe transitions and the different dissociation channels associated with the different excitation schemes it was, in general, impossible to uniquely assign the majority of the photoion peaks. However, the assignments shown in Table 6.4 suggest that at least two of the considered excitation schemes and at least two different atomic product asymptotes appear to be important in the production of NO^+ fragments following visible-ultraviolet excitation under these conditions.

The kinetic energy profile shown in the bottom panel of Fig. 6.5 can be analysed in a similar way to the energy distribution shown in the top panel. Possible peak assignments for the bottom energy distribution are shown in Table 6.5. Similarly to the analysis presented in Table 6.4 the majority of the peaks in the profile were assigned, albeit not uniquely. However, the analysis illustrates that at this probe photon energy (5.01862 eV) all three proposed excitation mechanisms appear to be involved in the decomposition process as do the $(1)^2\Pi_\Omega$ + $O(^1S_0)$, $(1)^2\Pi_\Omega$ + $O(^1D_2)$ and $(1)^2\Pi_\Omega$ + $O(^3P_2)$ product asymptotes.

Finally it is noted that in spite of the large amount of information presented in the NO^+ contour plot shown in Fig. 6.4, these energy distributions do not allow the overall photoproduct distributions to be extracted. The contour plot represents snapshots of the photoproduct distributions that can be probed at particular UV excitation energies. In order to fully analyse the photoproduct distribution, REMPI spectra would need to be recorded with sub-meV resolution across the probe photon energy range and velocity map images would need to be recorded at specific probe photon energies. Under the conditions employed here, however, it was impossible to record NO^+ REMPI spectra due to the large shot-to-shot fluctuations in the pump laser pulse intensity. Furthermore it was prohibitively time consuming to record and analyse velocity map images with anything like the required resolution to extract the overall photoproduct internal state

Peak	KE / eV (obs.)	Excitation scheme	v	N	Co-fragment(s)	Int. state	Branch	KE / eV (calc.)
(a)	0.001	3→1′+1′	6	31	$O(^1S_0)$	$(1)^2\Sigma^+$	P_1	0.002
		3→1′+1′	4	56	$O(^1S_0)$	$(1)^2\Sigma^+$	R_1	-0.002
(b)	0.004	3→1′+1′	6	31	$O(^1S_0)$	$(1)^2\Sigma^+$	P_1	0.002
		3→1′+1′	4	56	$O(^1S_0)$	$(1)^2\Sigma^+$	R_1	-0.002
(c)	0.013	1+1′→1′+1′	9	67	$O(^1D_2)$	$(3)^2\Pi_\Omega$	P_1	0.017
		3→1′+1′	6	28	$O(^1S_0)$	$(1)^2\Sigma^+$	Q_2	0.009
		3→1′+1′	6	28	$O(^1S_0)$	$(1)^2\Sigma^+$	Q_{12}	0.015
(d)	0.033	3→1′+1′	6	23	$O(^1S_0)$	$(1)^2\Sigma^+$	R_2	0.027
		3→1′+1′	4	51	$O(^1S_0)$	$(1)^2\Sigma^+$	S_{21}	0.030
(e)	0.051	2→1′+1′	9	59	$O(^3P_2)$	$(3)^2\Pi_\Omega$	R_1	0.050
		1+1′→1′+1′	2	17	$O(^1S_0)$	$(1)^2\Sigma^+$	Q_2	0.043
		3→1′+1′	6	15	$O(^1S_0)$	$(1)^2\Sigma^+$	S_{21}	0.049
(f)	0.072	1+1′→1′+1′	2	0	$O(^1S_0)$	$(1)^2\Sigma^+$	R_1	0.070
(g)	0.132	2→1′+1′	8	57	$O(^3P_2)$	$(2)^2\Sigma^+$	Q_1	0.134
(h)	0.180	2→1′+1′	10	21	$O(^3P_2)$	$(2)^2\Sigma^+$	Q_{21}	0.181
		2→1′+1′	10	21	$O(^3P_2)$	$(2)^2\Sigma^+$	Q_1	0.184
(i)	0.226	?	?	?	?	?	?	?
(j)	0.316	3→1′+1′	9	67	$O(^1D_2)$	$(3)^2\Pi_\Omega$	P_1	0.324
(k)	0.388	1+1′→1′+1′	8	6	$O(^1D_2)$	$(3)^2\Pi_\Omega$	P_1	0.388
		1+1′→1′+1′	8	7	$O(^1D_2)$	$(3)^2\Pi_\Omega$	P_1	0.387
		3→1′+1′	9	60	$O(^1D_2)$	$(1)^2\Sigma^+$	O_{12}	0.382
		3→1′+1′	9	59	$O(^1D_2)$	$(3)^2\Pi_\Omega$	R_1	0.391
(l)	0.491	1′→1′+1′	2	5	$O(^3P_2)$	$(1)^2\Sigma^+$	Q_{21}	0.496
		1′→1′+1′	2	5	$O(^3P_2)$	$(1)^2\Sigma^+$	Q_1	0.499
		1′→1′+1′	2	12	$O(^3P_2)$	$(1)^2\Sigma^+$	R_2	0.487
(m)	0.832	1+1′→1′+1′	2	12	$O(^1D_2)$	$(1)^2\Sigma^+$	R_2	0.832
		3→1′+1′	6	15	$O(^1D_2)$	$(1)^2\Sigma^+$	S_{21}	0.823

Table 6.5: As Table 6.4 but for a probe photon energy of 5.01862 eV.

profiles. Efforts were therefore made in order to probe the photoproduct distributions associated with the different excitation schemes and each product channel by probing the atomic fragments directly. The analysis of these experiments is reported in the following pages.

6.4.2 Photoelectron signals

By recording photoelectron images within the excitation range used to probe the NO^+ fragment distributions, signatures of parent ionisation, DMI processes and neutral fragment ionisation could be observed and distinguished. A number of time-resolved imaging experiments have measured signatures of parent ionisation and DMI processes on relatively short (<300 fs) and longer time scales. However, signatures of such processes were not identified in these nanosecond experiments. The photoelectron signals presented in Table 6.1 likely highlight signatures of neutral fragment ionisation. This is rationalised by the electron kinetic energy distributions and their probe wavelength dependences. With the implemented probe photon energies, neutral NO fragments must have either been produced directly in the $(1)^2\Sigma^+$ and $(3)^2\Pi_\Omega$ states which were ionised by a single probe photon or in the $(1)^2\Pi_\Omega$ state which was probed in a REMPI scheme via these excited electronic states. Here, it is noted that due to the similarities of the nuclear geometries of the $(1)^2\Sigma^+$ and $(3)^2\Pi_\Omega$ neutral states and the NO^+ $(1)^1\Sigma^+$ cation state (111), these experiments show no sensitivity to diatomic rovibrational populations.

Considering the analysis of the NO^+ kinetic energy distributions presented in the previous subsection it appears that the REMPI probe processes dominate within the employed excitation energy range. The intensity profiles of these image features then highlight that the fragments were predominantly probed via the $(1)^2\Sigma^+$ state as the signals associated with ionisation from this state were found to be eight or more times more intense than the corresponding $(3)^2\Pi_\Omega$ photoelectron features. It is noted that these experiments should also be sensitive to ionisation processes via the NO $(2)^2\Sigma^+$ and higher energy electronically excited states of NO. The absence of these features, therefore, highlights the minor role of ionisation through these intermediate levels at these probe photon energies and under the conditions employed in this study.

6.4.3 Atomic oxygen fragments

In an effort to probe the entire photoproduct distribution that correlated with ground state atomic oxygen atoms, neutral $O(^3P_J)$ photofragments were ionised using a (2'+1') REMPI process at photon energies close to 5.49439 eV. The kinetic energy distributions obtained from the resulting images (Figs. 6.6 and 6.7) are shown in Fig. 6.10 where the top panel shows the distribution from the slice image recorded at a pump laser excitation energy of 2.951 eV (see Fig. 6.6) and the bottom panel shows the distribution obtained by Hankel transforming the crush velocity map image recorded at a pump laser excitation energy of 2.818 eV (see Fig. 6.7). In each plot the energy distribution of the pump-probe + probe signal and the probe only signal are shown. These profiles were normalised with respect to the image features arising from the probe beam and the difference between the two profiles was taken. The resulting profile should be a fairly good representation of the pump-probe image signal and it is therefore plotted in both of the energy distributions shown in Fig. 6.10. The kinetic energies and the energy separation of the resulting pump-probe image features are shown in Table 6.6.

Depending on the excitation scheme(s) occurring to produce the different portions of the NO^+ contour plot shown in Fig. 6.4, the oxygen images may probe the same photoproduct distributions or, if the probe laser pulse was involved in the initial pumping process, a different photoproduct distribution to that responsible for the contour features. If the $O(^3P_J)$ fragments were produced in a two-photon pump process the partner fragments could be produced in v=0–11 or v=0–13 for pump photon energies of 2.818 and 2.951 eV respectively. In a three photon pump process the partner fragments could be produced in v=0–29 or v=0–33 for the two pump photon energies respectively. For a 1+1' dissociation process the partner fragments could be produced in v=0–28 or v=0–32 for the respective pump excitation energies.

By analysing the kinetic energies of the $O(^3P_2)$ image features shown in Table 6.6, the peak positions of the two energy distributions may be understood. In the images observed at both pump laser excitation energies a series of peaks were observed at low kinetic energies (0–400 meV) with a peak separation of ~0.075 eV. Considering the Dunham coefficients of NO in the $(1)^2\Pi_\Omega$ and $(1)^2\Sigma^+$ states, this spacing is too small to be attributed to diatomic fragments formed in different vibrational levels with

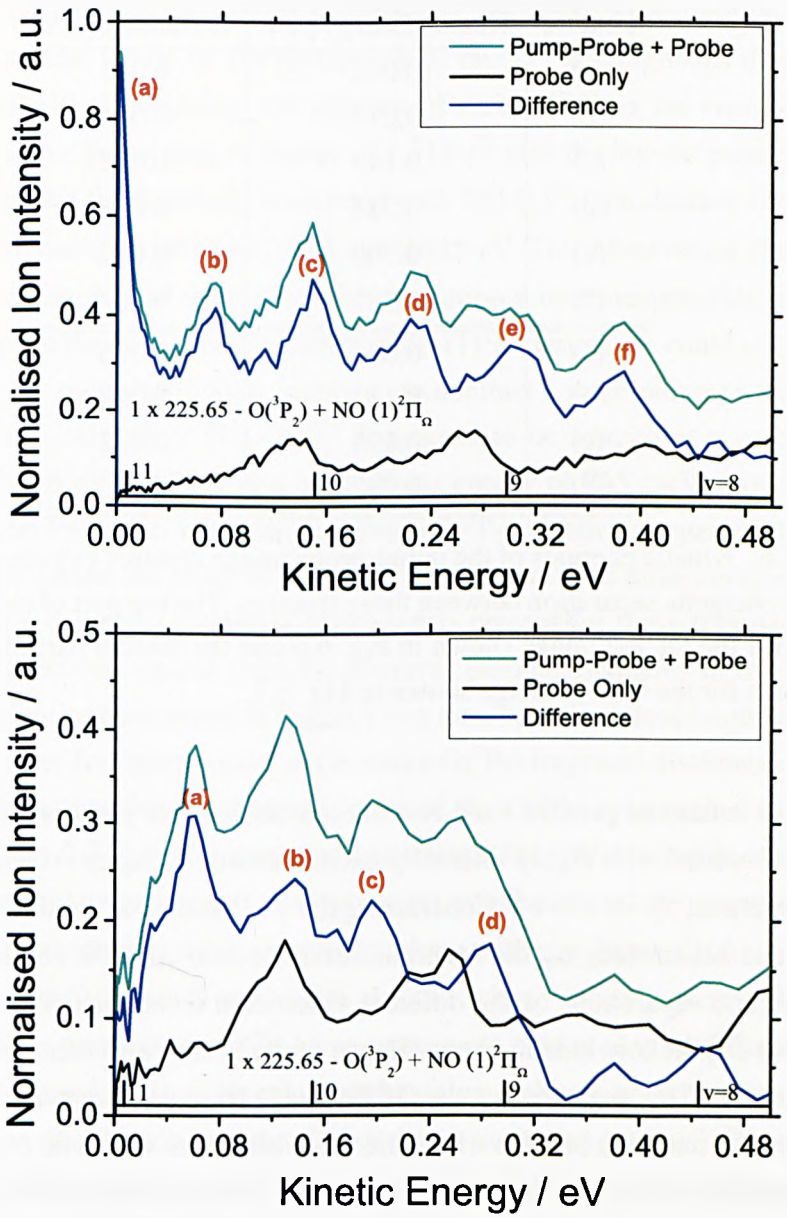

Figure 6.10: Energy distributions obtained from the images shown in Figs. 6.6 (top) and 6.7 (bottom). The panels correspond to initial pump energies of 2.951 and 2.818 eV respectively. In each panel the energy distribution associated with the pump-probe + probe signal, the probe only signal and the difference signal are plotted. The pump-probe + probe signals and probe only signals were normalised with respect to the peak of the probe only parts of each distribution before the subtraction. Different y-axis scales are used for the two panels to highlight the features in the less intense $O(^3P_J)$ distribution observed at excitation energies of 2.818 eV. The vibrational comb for the probe only fragments is shown in both panels.

Feature	Kinetic Energy / eV	Difference / eV
(a)	0.002	0.073
(b)	0.075	0.074
(c)	0.149	0.075
(d)	0.224	0.076
(e)	0.300	0.087
(f)	0.387	N/A
(a)	0.061	0.076
(b)	0.137	0.058
(c)	0.195	0.092
(d)	0.287	N/A

Table 6.6: Kinetic energies of the pump-probe image features extracted from Fig. 6.10 and the energetic separation between those features. The top part of the table shows the results for the $O(^3P_2)$ image shown in Fig. 6.6 and the bottom part of the table shows the results for the $O(^3P_2)$ image shown in Fig. 6.7.

unimodal rotational profiles via a two-photon dissociative process alone. In this case peaks associated with highly internally excited diatomic fragments would be expected to be separated by ~0.130 eV. Considering the 1+1′ and three photon dissociation processes and acknowledging the uncertainties associated with the Dunham coefficients, the energetic separations of the different vibrational levels that would have to be responsible for the low kinetic energy image features are consistent with the measured peak spacing. This suggests that the $O(^3P_J)$ image features were due to either a 1+1′ or three photon pumping process where the this assignment would be consistent with the single-photon results of Taherian and co-workers (110). However, the kinetic energies associated with the image features could not be used to make a firm assignment of the excitation scheme due to the uncertainty in the Dunham coefficients and the unknown rotational profiles of the vibrationally excited fragments.

A curious feature of the $O(^3P_2)$ image recorded with a pump photon energy of 2.918 eV is the large intensity of peak (a) (see the top panel of Fig. 6.10). Although the kinetic energy associated with this peak is consistent with what appears to be a vibrational progression of highly internally excited NO $(1)^2\Pi_\Omega$ fragments, this anoma-

lous intensity suggests that another process may also make a contribution to this peak. A good candidate would be the production of NO $(1)^2\Sigma^+$ fragments close to the energetic threshold. Considering the absence of such a peak in the energy distribution associated with a pump photon energy of 2.818 eV (see the bottom panel of Fig. 6.10) this suggests that the threshold associated with NO $(1)^2\Sigma^+$ production is reached with pump photon energies between 2.818 and 2.915 eV. This observation yields information about at least part of the dissociative excitation scheme responsible for the $O(^3P_2)$ production. For the 1+1′ pumping scheme NO $(1)^2\Sigma^+$ fragments could not be produced at either of the pump excitation energies. In contrast a three pump photon excitation process would only allow NO $(1)^2\Sigma^+$ fragments to be formed at a pump excitation energy of 2.918 eV resulting in a total excess energy of 255 meV allowing diatomic products to be formed in v=0 with maximum $O(^3P_2)$ kinetic energies of 166 meV. The peak position on the top panel of Fig. 6.10 is consistent with these energies and would suggest that a degree of rotational excitation is present for these fragments. The absence of appreciable signals from the diatomic partner fragments in the NO^+ kinetic energy distributions presented in Fig. 6.4 can then be rationalised by the small contribution that these fragments make to the entire $O(^3P_J)$ fragment distribution.

In order to consider the thermalisation of the $O(^3P_J)$ spin-orbit distribution presented in Table 6.2 and perhaps gain some insight into the electronic state via which the $O(^3P_J)$ atoms were formed, the spin-orbit populations of the pump-probe image features are presented as a Boltzmann plot along with similar results for single-photon excitation to the $(2)^2B_2$ state at energies close to 5.49 eV (see Chapter 4). These results suggest that the pump-probe $O(^3P_J)$ fragments were produced via a different electronic surface or a significantly different decomposition pathway with respect to the major single-photon distribution generated after direct excitation to the $(2)^2B_2$ state. As the spin-orbit distribution is also significantly different from the minor distribution associated with the internally excited fragments observed after single photon excitation to the $(2)^2B_2$ state an excitation process to a higher energy state appears to be favoured. The visible-UV spin-orbit distribution appears to be statistical which allows an electronic temperature of ~208 K to be extracted from the plot. This result suggests that the spin-orbit channels are highly non-adiabatic for the visible-UV fragmentation process.

For any electronically excited atomic fragments that may be produced, experiments that probed these products directly would give some information about the fragmenta-

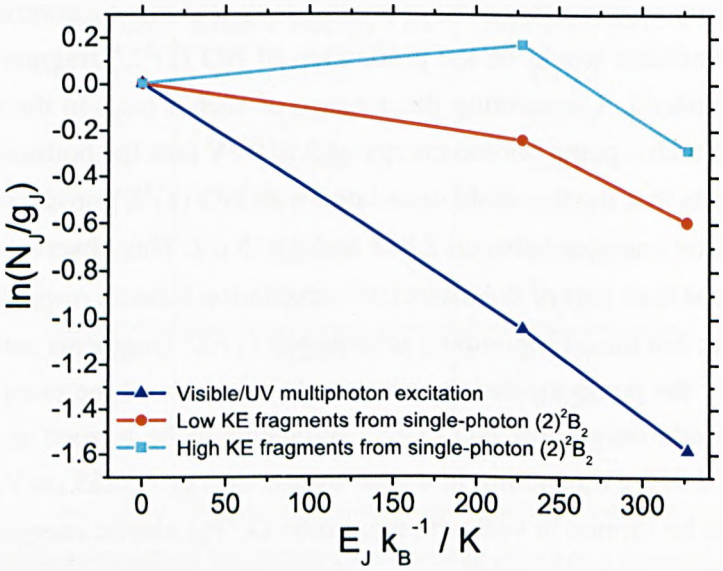

Figure 6.11: Boltzmann plots showing $O(^3P_J)$ fragment spin-orbit state populations. The square points represent the spin-orbit distribution of vibrationally cold fragments measured after single photon dissociation of NO_2 via the $(2)^2B_2$ state (see Chapter 4). The circle points show similar peaks for the $O(^3P_J)$ fragments formed in coincidence with internally excited diatomic fragments in single-photon experiments via the same electronic state (see Chapter 4). The triangular points represent the spin-orbit state distribution recorded following visible and ultraviolet excitation of NO_2. A linear fit to the latter points gives an electronic temperature of 208 K and highlights a seemingly statistical spin-orbit state distribution following the multiphoton fragmentation process.

tion process involved in their production. For the experiments that were performed to measure the pump-probe $O(^1D_2)$ signals a decrease in the $O(^1D_2)$ yield was measured with respect to probe alone signal when pump excitation energies between 2.480 and 2.987 eV were implemented. This suggests that $O(^1D_2)$ fragments were not formed to significant degrees after two or three photon excitation under these conditions. This would be in disagreement with the results of Grant and co-workers who attributed NO $(1)^2\Pi_\Omega$ fragments to a two photon pump processes to the $(2)^2B_2$ state resulting in the production of $O(^1D_2)$ atoms (67; 68; 69; 70). In this case the disparity between the results of Grant and co-workers and those discussed in this chapter may be accounted for

by differences in the pump laser intensities employed in the different measurements.

Alternatively a 1+1′ pump process may dominate under the conditions employed to probe $O(^1D_2)$ atoms. Here, the total excitation energies would lie between 8.514 and 8.531 eV. This would suggest that excitation at these energies does not result in $O(^1D_2)$ production which would be in agreement with the lower energy single-photon measurements of Taherian *et al.* (110). However, the lower energy experiments that were carried out to probe the NO^+ fragments (with 1+1′ dissociation energies between 7.7182 and 8.0308 eV) suggested that neutral NO fragments may be formed in coincidence with $O(^1D_2)$ atoms. Here the difference in the fragmentation energies may account for the seemingly different results. With this in mind conclusions cannot be made about the overall $O(^1D_2)$ photoproduct profile.

The $O(^1S_0)$ fragment distribution shown in Fig. 6.8 provides evidence that fragmentation occurs via at least two different dissociation limits when NO_2 is excited in the visible region of the spectrum and is further excited in the UV. The kinetic energy distribution of the electronically excited fragments suggests that the majority were formed via a 1+1′ pump process which resulted in the co-production of NO $(1)^2\Pi_\Omega$ fragments in all four of the energetically accessible vibrational levels (v=0–4) where there was a slight preference for the production of vibrationally 'cold' products. Interestingly, $O(^1S_0)$ atoms were not observed in the single-photon measurements that were performed by Taherian *et al.* at similar total pump-photon energies (110). This implies that the shift in the Franck-Condon window that followed visible excitation in the multiphoton experiments allowed a different region of co-ordinate space to be accessed resulting in $O(^1S_0)$ production. From the data presented here it is unclear whether the $O(^3P_J)$ and $O(^1S_0)$ atoms were produced following excitation to common electronic states or whether they were produced via very different dissociative pathways.

6.5 Conclusions

The photoproducts formed after irradiation of NO_2 with visible and UV nanosecond laser pulses have been studied in detail using the VMI technique. Where NO^+ fragments and, separately, the concomitant photoelectrons have been directly monitored, the kinetic energy profiles highlight that neutral ground electronic state NO fragments

Feature	Kinetic Energy / eV	Difference / eV
(a)	0.052	0.143
(b)	0.195	0.128
(c)	0.323	0.159
(d)	0.482	N/A

Table 6.7: Kinetic energies of the pump-probe $O(^1S_0)$ image features extracted from Fig. 6.8 and the energetic separation between those features.

were predominantly formed and that these fragments were readily ionised via two-photon REMPI schemes. In all cases reported here the NO^+ fragments have been detected with kinetic energies that were less than 0.85 eV where the majority of these photoproducts were formed with kinetic energies that were less than 0.40 eV. This highlights the large degree of internal excitation of the photoproducts that has already been observed in time-resolved imaging experiments (14; 28; 126). By studying the trends in the NO^+ fragment kinetic energy distribution, contributions from DMI processes have been found to be insignificant. Where the NO^+ fragment kinetic energy profiles have been analysed in detail, signatures of three different excitation pathways (involving two-photon, 1+1′ and three-photon dissociation) and three different product asymptotes appear to have been observed. This is in contrast to previous time-resolved studies which have attributed long time scale NO^+ signals to DMI processes and three photon production of electronically excited NO that was ionised by a single probe photon.

Additionally the $O(^3P_J)$ photoproducts have been probed directly where these measurements highlight the dominance of internally excited NO $(1)^2\Pi_\Omega$ fragments that were formed via the $O(^3P_J)$ dissociation channel. By considering the kinetic energy profiles of the features in the $O(^3P_2)$ energy distribution, the primary $O(^3P_J)$ dissociation process has been tentatively attributed to formation in coincidence with ground electronic state NO fragments in levels where $v \approx 30$. Weak signatures of vibrationally 'cold', NO $(1)^2\Sigma^+$ fragments produced in coincidence with $O(^3P_2)$ fragments via a three pump photon excitation scheme have also been tentatively assigned. Measurements of the $O(^3P_J)$ spin-orbit distribution have also been undertaken and the results

are consistent with a 1+1′ or three pump photon excitation scheme. Here, the spin-orbit population ratios highlight a thorough mixing between the spin-orbit levels in the asymptotic regions of the dissociative potentials.

Experiments that were performed in order to probe the $O(^1D_2)$ distribution following either a two or three pump photon or a single pump-single probe photon excitation process failed to detect these electronically excited oxygen atoms. These results suggest that a negligible yield of $O(^1D_2)$ fragments were produced via the three pump and single pump-single probe photon excitation schemes and that production via a two photon excitation process, as advocated by Grant and co-workers (67; 68; 69; 70), does not occur to a significant degree under the laser intensity conditions employed here. The direct observation of $O(^1S_0)$ fragments confirms the multichannel nature of NO_2 photolysis following visible-UV excitation. The observation of kinetically cold $O(^1S_0)$ and $O(^3P_J)$ photoproducts is consistent with the NO^+ imaging studies performed here and previous time-resolved measurements.

Chapter 7

Conclusions and Future Work

7.1 Conclusions

A VMI spectrometer has been constructed, optimised and applied to study the decomposition behaviour of NO_2. Through these experiments the spectrometer has been shown to produce high quality ionisation spectra and slice and crush velocity map images which have facilitated a good understanding of complex fragmentation processes.

The multi-channel dissociation dynamics of NO_2 after excitation to the $(3)^2A'$ state were investigated using REMPI spectroscopy, DC slice and conventional velocity map ion imaging. It was previously believed that after excitation to the $(3)^2A'$ state at energies close to 5.49 eV the $O(^3P_J)$ + NO $(1)^2\Pi_\Omega$ dissociation channel led to a sharply peaked vibrational distribution with NO $(1)^2\Pi_\Omega$ fragments formed in v=4–6. In contrast to the previous studies, the high kinetic energy resolution achieved by DC slice imaging the $O(^3P_J)$ fragments coupled with REMPI spectroscopy and velocity map imaging of state selected NO fragments at excitation energies between 5.30 and 5.45 eV revealed that the dissociation favors the production of highly rotationally excited NO $(1)^2\Pi_\Omega$ fragments. All three $O(^3P_J)$ spin-orbit component energy distributions were inferred to peak in coincidence with NO $(1)^2\Pi_\Omega$ fragments in v=0 and 1 and N~60, with a secondary rotational maxima at N~20. The translational anisotropy of the fragments was examined to conclude that the dissociative geometry became more bent (on average) as the kinetic energy release of the $O(^3P_J)$ decreases from 1.55 to 0.5 eV. The increase in the anisotropy parameter from 0.50 to 0 eV was attributed to

another, likely non-adiabatic and, minor dissociation mechanism producing kinetically cold $O(^3P_J)$ in coincidence with internally excited NO fragments.

The spin-orbit branching ratio in the $O(^3P_J)$ photoproducts was found to be markedly non-statistical (see Fig. 6.11). For O fragments with a translational energy in the range 0.50 to 1.55 eV the intensities of the three channels (uncorrected for degeneracy and line-strength factors) were determined to be 1.00:0.71:0.15 for the $O(^3P_2)$, $O(^3P_1)$ and $O(^3P_0)$ states respectively. For the oxygen atoms formed with translational energies in the range 0.00 to 0.50 eV the intensity ratio was found to be 1.00:0.47:0.10. Furthermore, temperature studies have highlighted that these fragments were correlated with internally excited NO $(1)^2\Pi_\Omega$ fragments produced from NO_2 and the yield of these photofragments is noted to increase with excitation energy. These temperature studies have reiterated how the room temperature study of the UV NO_2 photodissociation dynamics can be biased by the photolysis of N_2O_4.

Mass-resolved REMPI spectroscopy and velocity map imaging was also used to study the diatomic photoproduct distributions observed on excitation to the $(3)^2A'$ state between 5.46 and 5.64 eV. The two techniques have allowed the unequivocal assignment of the single laser NO fragment rovibrational profiles to NO $(1)^2\Pi_\Omega$ fragments produced concomitantly with $O(^1D_2)$. In addition the small yet complex contribution of NO $(1)^2\Pi_\Omega$ fragments produced with $O(^3P_J)$ atoms with differing degrees of internal excitation across this excitation range has been highlighted.

By recording DC slice velocity map images of the $O(^1D_2)$ fragments produced using different pump and probe laser polarisations at an excitation energy of 5.47952 eV the kinetic energy profile of these fragments has been measured and the translational anisotropy parameters and the recoil angle averaged multipole moments of the $O(^1D_2)$ fragment polarisation have been derived as a function of kinetic energy. Using the NO fragment REMPI profiles the features of the $O(^1D_2)$ energy distribution have been assigned to production in coincidence with a unimodal rotational distribution of fragments in v=0 and a bimodal rotational profile of vibrationally excited fragments in v=1. Furthermore, the $O(^1D_2)$ energy distribution highlighted the vibrational inversion of the diatomic cofragments, in accord with previous work (103).

The multipole moments obtained from the $O(^1D_2)$ images showed that the majority of these fragments were formed in the $M_J \pm 1$ state and suggested that all of the

$O(^1D_2)$ fragments were produced via the same avoided crossing to the $(4)^2A'$ dissociative electronic potential. The translational anisotropy parameters of the $O(^1D_2)$ fragments produced in coincidence with rotationally cold diatomic fragments were related to dissociative geometries which were, for the most part, found to be in good agreement with the calculations of Schinke *et al.* who highlight an avoided crossing between the $(3)^2A'$ and $(4)^2A'$ adiabatic surfaces at a bond angle close to 110° (8). It has then been suggested that the lower translational anisotropy of the slower $O(^1D_2)$ fragments was a signature of non-axial recoil dynamics occurring after this avoided crossing.

Conclusions about the overall single-photon decay dynamics of the $(3)^2A'$ state were made based on the $O(^1D_2)$ and $O(^3P_J)$ photofragment distributions recorded close to 5.49 eV (64; 65) and 6.03 eV (6; 65). Due to the vibrational inversion of the NO $(1)^2\Pi_\Omega$ fragments, where v=1 fragments were preferentially produced with $O(^1D_2)$ and the dominance of NO $(1)^2\Pi_\Omega$ fragments in v=1 produced with $O(^3P_J)$ atoms the fragment vibrational excitation was attributed to the symmetric stretch motion set up by the Franck-Condon window from the $(1)^2A'$ state to the $(3)^2A'$ state. This implies that the symmetric stretching motion of the pwerent is retained for the majority of the electronically excited NO_2 molecules as they deform towards the $O(^1D_2)$ or $O(^3P_J)$ product asymptotes. The bimodal rotational profiles observed for the diatomic fragments formed with the majority of the $O(^3P_J)$ fragments and the vibrationally excited diatomic fragments formed with $O(^1D_2)$ atoms is similarly consistent with pwerent bending motion caused by the geometry change on excitation to the $(3)^2A'$ state. For the $O(^1D_2)$ channel, a single quantum of bending motion is effectively transferred via the $(3)^2A'/(4)^2A'$ avoided crossing into two rotational modes for the vibrationally excited NO $(1)^2\Pi_\Omega$ fragments produced close to the energetic threshold. In contrast this rotational structure is lost for the vibrationally cold diatomic fragments, where the motion set up by the Franck-Condon window is presumably washed out due to the topography of the reaction coordinate. For the $O(^3P_J)$ channel the parent bending motion may be effectively transferred into two rotational modes by the configurationally restrictive photoexcited adiabatic PES which favours the production of rotationally excited fragments. Alternatively, this could be the result of a non-adiabatic interaction between the $(3)^2A'$ state and another potential that leads to the $O(^3P_J)$ asymptote.

Visible/UV multiphoton excitation experiments have also been performed to elucidate details about the high energy decomposition behaviour of NO_2 and to complement

recent time-resolved studies. By recording velocity map images of NO^+ fragments at a range of UV laser excitation energies the production of relatively slow NO^+ fragments was observed to be favoured. These results coupled with electron imaging experiments highlighted the dominant production of neutral ground electronic state NO fragments and that these fragments were readily ionised via two-photon REMPI schemes throughout the employed probe laser excitation energy range. By studying the trends in the NO^+ fragment kinetic energy distribution, contributions from DMI processes have been found to be insignificant. Where the NO^+ fragment kinetic energy profiles have been analysed in detail, signatures of two pump photon, single pump single probe photon and three pump photon dissociation have been observed. Furthermore, the analysis associated with these excitation schemes suggests that fragmentation occurs to form $O(^3P_J)$, $O(^1D_2)$ and $O(^1S_0)$ atomic fragments. These results were in contrast to the interpretation of time-resolved experiments which attributed long-lived NO^+ ion signals to DMI processes and electronically excited NO fragments that were ionised by a single probe photon where both processes resulted in $O(^3P_J)$ formation.

By probing the $O(^3P_J)$ photoproducts directly the dominance of highly internally excited NO $(1)^2\Pi_\Omega$ fragments via the $O(^3P_J)$ dissociation channel has been illustrated. By considering the kinetic energy profiles of the features in the $O(^3P_2)$ energy distribution, the primary $O(^3P_J)$ dissociation process has been tentatively attributed to formation in coincidence with ground electronic state NO fragments with ~30 vibrational quanta of excitation via a single pump-single probe or three pump photon excitation scheme. Weak signatures of vibrationally 'cold', NO $(1)^2\Sigma^+$ fragments produced in coincidence with $O(^3P_2)$ fragments via the three pump photon excitation scheme have also been tentatively assigned. By measuring the $O(^3P_J)$ spin-orbit distribution further insight about the lowest energy dissociation limit was obtained. Here, a seemingly statistical fine-structure state distribution was measured that implies a thorough mixing of spin-orbit levels towards the product asymptote.

In experiments that were performed in order to probe the $O(^1D_2)$ distribution following either a single pump-single probe, two or three visible pump photon excitation these electronically excited atoms were not observed. In fact the probe alone signal was depleted when the visible pump field was applied to the experiment. These results suggest that a negligible yield of $O(^1D_2)$ fragments were produced via single

pump-single probe photon or three pump photon excitation schemes and that production via a two pump photon excitation process, as advocated by Grant and coworkers (67; 68; 69; 70), does not occur to a significant degree under the laser intensity conditions employed here. Observation and analysis of the $O(^1S_0)$ fragment distribution allowed these fragments to be attributed to a single pump-single probe photon excitation process that resulted in the co-production of NO $(1)^2\Pi_\Omega$ in v=0–4. These measurements coupled with the $O(^3P_J)$ experiments highlight the multichannel decomposition behaviour of NO_2 following visible-UV excitation.

More generally the measurements reported in this thesis were illustrative of how a multidimensional detection technique like VMI when coupled with state-selective spectral probes of photoproduct distributions can elucidate detailed information about dynamical fragmentation processes in the energy domain.

7.2 Future Work

A number of further experiments could be performed to gain more insight into the dissociation dynamics of NO_2 after excitation to the $(3)^2A'$ state. Some interesting experiments would be to extract the angular momentum alignment of the $O(^3P_{2,1})$ fragments from velocity map images recorded with different laser polarisation combinations or probe transitions as partially investigated by Ahmed *et al.* at excitation energies close to 5.83 eV (5). Of interest here would be the differences between the polarisation moments extracted from the $O(^3P_{2,1})$ fragments formed with different kinetic energies over a range of pump photon energies. For the principle dissociation mechanism that produces $O(^3P_{2,1})$ atoms this may give some indication of whether the two rotational branches were produced via the same adiabatic PES and dissociative pathway or whether a non-adiabatic interaction plays a role in the rotational bimodality. These measurements would be worthwhile in view of the fact that the MRCI calculations of Schinke and co-workers (8) failed to reproduce the minor lower **N** rotational mode.

The single-photon excitation experiments to the $(3)^2A'$ state also highlighted a minor dissociation channel that produces internally excited NO $(1)^2\Pi_\Omega$ in coincidence with $O(^3P_J)$ at excitation energies that were close to 5.49 eV. However, it is thought that this dissociation channel becomes increasingly important at higher excitation energies and that it may dominate the $O(^3P_J)$ channel diatomic fragment distribution at

excitation energies close to 6.20 eV. Again these features were not reproduced by the MRCI calculations of Shinke *et al.* (8). A number of experiments could be performed in order to probe these fragments in more detail. Due to the increased contribution of these fragments at excitation energies between 5.8 and 6.2 eV these fragments would be best probed within this energy range but particular cwere would need to be taken at these excitation energies to remove or account for the contributions of the N_2O_4 photolysis. In order to correlate the $O(^3P_J)$ fragments from NO_2 photolysis with specific rovibrational states of NO $(1)^2\Pi_\Omega$ the diatomic fragments would need to be probed directly and state-specifically. Under the assumption that these fragments were highly vibrationally excited, which is suggested by Fig. 4.1, it should be possible to probe these fragments using (1+1) REMPI processes via the NO $(1)^2\Sigma^+\leftarrow(1)^2\Pi_\Omega$ and NO $(2)^2\Sigma^+\leftarrow(1)^2\Pi_\Omega$ bands at probe excitation energies of 4.43 to 4.85 eV and 4.86 and 5.39 eV respectively. Here the NO $(2)^2\Sigma^+\leftarrow(1)^2\Pi_\Omega$ transition strengths were considerably higher although many of these bands will overlap with different vibrational profiles. In addition to these measurements it may be possible to extract some information about the electronic state that was responsible for their production by measuring the orbital angular momentum alignment of the low kinetic energy $O(^3P_J)$ fragments produced via this mechanism so that a more complete picture of the $(3)^2A'$ state decomposition dynamics could be gained.

Considering the angular momentum alignment measurements of the $O(^1D_2)$ fragments presented in Chapter 5 and those reported by Coroiu *et al.* (6) it would be interesting to apply an extended angular momentum treatment to this data in order to extract polarisation moments from the angular profiles of the velocity map images without making the assumption that the polarisation moments do not change with recoil angle. As such treatments have been implemented with similar data (181) the application of such a treatment to the images presented in Chapter 5 should be reasonably straightforward. Similarly the finite slice width employed in the experiments reported in Chapter 5 could be accounted for in order to assess the influence of the finite slice width on the extracted dynamical parameters. A treatment incorporating these extensions would give more accurate and more extensive information about the decomposition process in the molecular reference frame and would allow the validity of the assumption that the polarisation moments of the fragments do not change as a

function of recoil angle to be assessed. This may validate or disprove the interpretation that all of the $O(^1D_2)$ fragments were formed via the same avoided crossing. A further direction of study may be to extract the polarisation moments from velocity map images of the $O(^1D_2)$ fragments as a function of pump excitation energy. Comparison of the alignments moments obtained using the approximate treatment outlined in Chapter 5 and those similarly obtained and presented by Coroiu *et al.* suggest that there is a change in the electronic character of the decomposition process associated with the $O(^1D_2)$ channel between excitation energies of ~5.49 and ~6.20 eV. The energy dependence of the polarisation moments would therefore be expected to yield a threshold for a direct excitation process to a state other than the $(3)^2A'$ state or the single-photon threshold for another vibronic interaction with the $(3)^2A'$ state in the $O(^1D_2)$ dissociation channel.

As highlighted in Chapter 2 very few experiments have been performed to probe the photoproduct distributions from NO_2 photolysis at excitation energies between 6.45 eV and the first ionisation potential. Imaging experiments carried out at different energies in this excitation range where different electronic states of the O and potentially N atomic fragments could be probed via REMPI processes would give good insights into the different optically bright (and perhaps dark) higher energy states as well as the different dissociation channels that were expected to occur. Such experiments would also be expected to provide valuable information for electronic structure studies which have yet to accurately characterise the higher energy valence electronic surfaces of NO_2.

A number of unanswered questions remain regarding the visible/UV decomposition behaviour outlined in Chapter 6. Alternative experimental approaches could be used to garner more information about the fragmentation process. One approach would be to carry out isoenergetic single-photon pump experiments with respect to the single pump-single probe and three pump photon excitation schemes using VMI and REMPI spectroscopy as probes to provide some information about at least some of the open dissociation channels and, assuming favourable selection rules, the final photoexcited PES involved in the multiphoton fragmentation processes. It is noted, however, that the photoproduct distributions measured in single-photon experiments would be unlikely to be the same as those produced through the multiphoton processes where different

selection rules may result in excitation to a different final state and assuming the final state for the two processes was the same, a different nuclear geometry of the final excited state would be expected to be excited and sampled. In order to extract more information about the decomposition process, three (narrow-linewidth) laser experiments would likely be required so that intermediate resonances could be well defined and the products independently and state-selectively probed. Alternatively a coincidence experiment could be performed using kHz nanosecond dye laser systems or modern wavelength tunable kHz time-resolved laser sources. Here the correlated measurement of electrons and photoions as a function of pump and probe wavelengths and the molecular frame anisotropies obtained would give a greater insight into the fragmentation process.

More generally the work referenced and presented in this thesis highlights a need for a systematic analysis of the effects of relative slice width on the dynamical parameters obtained from slice images. A similar analysis is also required in order to study the effects of the parameterisation of the modern image reconstruction algorithms and fitting procedures described in Chapter 3 to obtain dynamical parameters obtained from crush velocity map images. With this analysis in place a similar systematic study to that presented for some of the older inversion algorithms (175) could be performed to compwere the dynamical parameters obtained from the different reconstruction techniques. This would facilitate some interesting comparisons between state-of-the-art slice and crush imaging experiments. The slice imaging techniques that were described in Chapter 3 were originally developed to overcome the restrictions associated with the image inversion methods available at the time. Since the development of these techniques a number of substantial improvements have been made to the image reconstruction methods used to invert axially symmetric images or reconstruct axially asymmetric charged particle distributions. As outlined in Chapter 3 all of the slicing methods have limitations that effect the experimental signal strengths and, to differing degrees depending on the experimental conditions, the resulting dynamical parameter fidelity. However, considering what seems to be a fundamental velocity focusing advantage (again see Chapter 3) for the DC slice imaging technique over crush imaging experiments it is presently unclear whether there were substantial advantages to neglecting the majority of the charged particle distribution to record slice images. Furthermore, it is not clear what experimental conditions would be required in order to exceed the kinetic

energy resolution limit and/or dynamical parameter fidelity afforded by crush imaging experiments coupled with well-parameterised modern inversion techniques.

Appendix A

Published article: Photodissociation of NO_2 in the $(2)^2B_2$ state; a slice imaging study and reinterpretation of previous results

The article presented below was published in the Journal of Chemical Physics and describes the imaging studies and the interpretation of these experiments that have been presented in Chapter 4. The article was principally written by myself where I took advice about corrections to the paper from my supervisor and journal article referees. The article is very similar in structure to Chapter 4.

THE JOURNAL OF CHEMICAL PHYSICS 129, 154312 (2008)

Photodissociation of NO_2 in the $(2)^2B_2$ state: A slice imaging study and reinterpretation of previous results

Iain Wilkinson and Benjamin J. Whitaker[a)]
School of Chemistry, University of Leeds, Leeds LS2 9JT, United Kingdom

(Received 24 July 2008; accepted 15 September 2008; published online 20 October 2008)

The photodissociation dynamics of nitrogen dioxide have been probed above the second dissociation limit at photolysis wavelengths close to 226 nm. The $O(^3P_J)+NO(^2\Pi_\Omega)$ product channel has been examined using direct current slice velocity map imaging of the $O(^3P_J)$ and $NO(^2\Pi_\Omega)$ fragments. Mass-resolved resonantly enhanced multiphoton ionization spectroscopy and velocity map imaging have been used to probe directly the rovibrational population distributions of the NO fragments. We also examine possible interference from the dissociation of N_2O_4 by investigating the effect of the sample temperature on the $O(^3P_J)$ fragment energy distributions. The $O(^3P_J)+NO(^2\Pi_\Omega)$ dissociation channel has been found to favor the production of vibrationally cold, highly rotationally excited $NO(^2\Pi_\Omega)$ products with all three oxygen spin-orbit components. Other minor dissociation channels which produce $O(^3P_J)$ atoms have also been identified. We discuss the significance of these dissociation channels and present a reinterpretation of previous studies of NO_2 dissociation on excitation to the $(2)^2B_2$ state. © *2008 American Institute of Physics.*
[DOI: 10.1063/1.2994735]

I. INTRODUCTION

The photodissociation of nitrogen dioxide (NO_2) has been studied for more than half a century. The molecule has received considerable attention due to interest in fundamental questions about the nature of unimolecular decomposition dynamics and also because of its important roles in the chemistry of combustion,[1] the stratosphere,[2] and the troposphere.[2] Further interest arises from the strongly vibronically coupled nature of its low lying electronic states and subsequent nonadiabatic dynamics, which provide a significant challenge to theory due to the molecule's open shell structure.[3,4] Nitrogen dioxide also provides an experimental opportunity to study nonradiative decay processes in the small molecule limit.[5]

The absorption spectrum of NO_2 displays two broad features between 200 and 700 nm.[6–9] The first band is associated with excitation from the ground $(1)^2A_1$ state to both the $(1)^2B_1$ and $(1)^2B_2$ electronically excited states with the majority of the oscillator strength lying on the $(1)^2B_2 \leftarrow (1)^2A_1$ transition.[10] The complexity of the absorption spectrum between 700 and 250 nm is attributed to vibronic coupling of the excited $(1)^2B_2$ state to the other energetically accessible electronic manifolds [the electronically excited $(1)^2B_1$ and $(1)^2A_2$ states and the $(1)^2A_1$ ground state]. Close to the peak of the first electronic absorption feature, the first dissociation limit is reached 3.115 545(6) eV above the origin of the $(1)^2A_1$ state,[11]

$$NO_2(^2A_1) \rightarrow NO(^2\Pi_{1/2};0,0) + O(^3P_2), \quad \lambda \leq 398.0 \text{ nm}.$$

Higher energy excitation also produces NO in its $^2\Pi_{3/2}$ spin-orbit state [14.856 meV above the $NO(^2\Pi_{1/2})$ ground state][12] along with the production of NO in coincidence with $O(^3P_1)$ and $O(^3P_0)$ fragments [19.623 and 28.141 meV above the $O(^3P_2)$ ground state respectively].[13]

Since the original photofragment ion studies of Busch and Wilson in 1972,[10,14] the photodissociation of NO_2 via the $(1)^2B_2$ state has been extensively studied. Literature is too extensive to review in any detail here. The rise of the second electronic absorption band of NO_2 is assigned to the opening of the $(2)^2B_2 \leftarrow (1)^2A_1$ transition at 4.974 98 eV.[15] At these excitation energies the effect of the NO_2/N_2O_4 equilibrium becomes important. Below 250 nm, the absorption cross section of N_2O_4 rises sharply, with the N_2O_4 to NO_2 absorption cross-sectional ratio increasing from 0.01 at 400 nm to 100 close to 200 nm.[7,9] The UV photolysis of N_2O_4 has been noted to produce electronically and vibrationally excited NO_2 as well as $NO(^2\Pi_\Omega)$ and $O(^3P_J)$ products, making it difficult to separate the decomposition product channels of the two species.[16–18] The equilibrium results in ~81% of NO_2 existing in its dimeric form at room temperature and atmospheric pressure (STP). The obvious implication of this is that photodissociation studies at wavelengths below 250 nm require careful reagent preparation, N_2O_4 correction factors, and/or experimental methods which allow the NO_2 and N_2O_4 photoproducts to be distinguished.

The second electronic absorption band of NO_2 shows a much simpler vibronic structure than the visible/near UV band and was partially analyzed by Harris and King.[19] The symmetry of the excited state was later assigned as $^2B_2$ when the band was further studied by Ritchie *et al.*[20] The transition corresponds to a linear superposition of the $5a_1 \leftarrow 3b_2$ and $2b_1 \leftarrow 1a_2$ valence electron excitations and carries an average oscillator strength of 0.0068 eV^{-1}.[9,21–23] At its origin the $(2)^2B_2$ state is known to be predissociative with a lifetime of 42 ± 5 ps.[24] The $(2)^2B_2$ state is calculated to be weakly

a)Author to whom correspondence should be addressed. Electronic mail: b.j.whitaker@leeds.ac.uk.

bound with a shallow potential well in the asymmetric stretching coordinate in the adiabatic representation.[4] For an overview of the topography of the $(2)^2B_2$ surface and other relevant electronic states, the recent results of Schinke *et al.* are recommended.[4]

At higher excitation energies, 5.082 909 eV, dissociation to produce NO in coincidence with electronically excited oxygen can occur,[11,13]

$$NO_2(^2A_1) \rightarrow NO(^2\Pi_{1/2};0,0) + O(^1D_2), \quad \lambda \leq 243.9 \text{ nm}.$$

The $O(^1D_2)$ yield is found to remain relatively constant, between 40% and 50%, upon direct excitation to the $(2)^2B_2$ state above this energetic threshold.[24–28] Although full dynamical calculations on accurate potential energy surfaces are required to understand the details of the branching ratio into the two channels,[4] the significant $O(^3P_J)$ yield can be rationalized by the correlation of the $(2)^2B_2$ manifold with the $NO(^2\Pi_\Omega)+O(^3P_J)$ dissociation channel via the asymmetric stretch in the adiabatic representation. The $O(^1D_2)$ yield is then explained by the proximity of the adiabatic $(3)^2B_2$ surface which correlates with the $NO(^2\Pi_\Omega)+O(^1D_2)$ dissociation channel along the asymmetric stretch coordinate. This view is supported by the experimental results of Tsuji *et al.*[26] and Uselman and Lee[24] who observed that asymmetric stretch excitation in the $(2)^2B_2$ state promoted the predissociation and also dramatically increased the $O(^1D_2)$ yield close to the $(2)^2B_2$ origin. On excitation to the $(2)^2B_2$ state with two vibrational quanta in the asymmetric stretch, the excited state lifetime is observed to decrease below 100 fs.[24,26] No further marked decrease in lifetime is observed at higher excitation energies throughout the rest of the vibrational manifold.

A number of experiments have been carried out to measure the energy partitioning of the dissociation over a range of excitation wavelengths. The spin-orbit branching ratios (uncorrected for degeneracy and line-strength factors) of the ground state oxygen photoproducts were measured by Rubahn *et al.*[29] close to 226 nm who obtained $O(^3P_2):O(^3P_1):O(^3P_0)$ branching ratios of 1.00:0.71:0.25, 1.00:0.68:0.27, and 1.00:0.50:017 in a thermal sample, a neat supersonic expansion, and a seeded supersonic expansion of NO_2, respectively, using laser induced fluorescence (LIF). Miyawaki *et al.*[30] carried out similar measurements at 212.9 nm in a molecular beam and determined a branching ratio of 1.00:0.35:0.08, suggesting that there is a weak wavelength dependence to the measured $O(^3P_J)$ distribution between 226 and 213 nm. It is noteworthy that for excitation wavelengths longer than the $(2)^2B_2$ band origin, that is to the continuum of the $(1)^2B_2$ potential energy surface, both groups recorded similar spin-orbit ratios.

The production of $NO(^2\Pi_\Omega)$ in coincidence with $O(^3P_J)$ has been studied close to the $(2)^2B_2$ origin, below the $O(^1D_2)$ threshold, by a number of researchers. McKendrick *et al.*[31] measured NO fragments in both $v=2$ and 6 at a photolysis wavelength of 248.5 nm. Slanger *et al.*[32] later repeated this experiment but probing other vibrational levels ($v=4-8$) with a separate probe laser using LIF. They observed a marked vibrational inversion with the population distribution peaking at $v=7$. McFarlene *et al.*[33] used a resonantly enhanced multiphoton ionization (REMPI) detection scheme to probe the whole vibrational distribution at the same photolysis wavelength. These experiments observed a bimodal vibrational distribution peaking at $v=0$ with a subsidiary maximum at $v=5$ (although the peak at $v=0$ has been questioned in literature[34]). Nonstatistical NO fragment rotational profiles were also observed. More recently, Morrell *et al.*[35] carried out a further study at 248 nm using time-resolved Fourier transform infrared (TR FTIR) spectroscopy to measure the NO fragment fluorescence in $v=2-8$. The measured vibrational distribution was in qualitative agreement with McFarlene *et al.*, peaking at $v=5$.

At slightly higher excitation energies and above the threshold for $O(^1D_2)$ production the $O(^3P_J)$ product channel has been studied using the velocity map imaging (VMI) technique by Ahmed *et al.*[34] and separately by Brouard *et al.*[16] Ahmed *et al.* measured the kinetic energy distribution of the unaligned $O(^3P_0)$ fragment in a single laser experiment at 226.23 nm. Here the $O(^3P_0)$ distribution was interpreted to peak in coincidence with $NO(^2\Pi_\Omega)$ fragments in $v=4$ or 5 with an average translational anisotropy parameter of 1.32. Additionally, images of the $NO(^2\Pi_\Omega)$ fragments were recorded using REMPI to ionize the fragments via the $A \leftarrow X(0,0)$, (1,1), and (2,2) transitions. It was determined that the rotational profiles of the NO produced in coincidence with $O(^1D_2)$ and $O(^3P_J)$ were markedly different.

Brouard *et al.* imaged all three spin-orbit components of the ground state oxygen fragment in a single laser experiment close to 226 nm. The kinetic energy profiles of the oxygen fragments were found to be bimodal and to depend strongly on the partial pressure of the NO_2 in the sample mixture. The signal strength of the slow component was found to be particularly sensitive to the NO_2 partial pressure although the kinetic energy spread of the fast component was also observed to narrow as the NO_2 partial pressure was reduced. The slow component was attributed to the dissociation of N_2O_4 at 226 nm to produce NO_2 with both NO and $O(^3P_J)$.[35,36] The broadening of the fast component was attributed to the photolysis of N_2O_4 to produce translationally hot NO_2 fragments,[18,37,38] which were subsequently photolyzed to produce $O(^3P_J)$. The $O(^3P_J)$ images recorded at low NO_2 partial pressures were ascribed to the photolysis of NO_2 alone with the $O(^3P_0)$ kinetic energy distribution obtained at low partial pressure being narrower than that measured by Ahmed *et al.* It was, therefore, suggested that the distribution obtained by Ahmed *et al.* contained interference from the photolysis of N_2O_4 contaminant. Brouard *et al.* interpreted their low pressure data as being due to $O(^3P_0)$ fragments produced in coincidence with $NO(^2\Pi_\Omega)$ in $v=4-6$. The translational anisotropy of the total $O(^3P_0)$ distribution was determined to be ~1.0. The analysis of the $O(^3P_2)$ and $O(^3P_1)$ images may be affected by orbital angular momentum alignment effects and as a result the anisotropies of these images were not published. Despite the efforts of Brouard *et al.* to minimize the N_2O_4 content of their supersonic expansion, the slow component of the signal is still dominant in their $O(^3P_2)$ distribution.

At 212.8 nm the photodynamics of the dissociation were studied by Ahmed *et al.*[39] and by Richter *et al.*[40] Ahmed

et al. used VMI in order to measure the orbital angular momentum alignment of the $O(^3P_2)$ and $O(^3P_1)$ photofragments and also recorded images of the unaligned $O(^3P_0)$ fragment. At this excitation energy, the alignment of the $O(^3P_2)$ fragment was found to be negligible, in contrast, the $O(^3P_1)$ fragment was found to display appreciable orbital alignment. The $O(^3P_1)$ kinetic energy release spectrum displayed a bimodal distribution, peaking at a translational energy consistent with the coproduction of $NO(^2\Pi_\Omega)$ in $v=4$. A subsidiary maximum at low kinetic energy was assigned to the production of $O(^3P_1)$ in coincidence with $NO(^2\Pi_\Omega)$ in $v=10$ or 11. The spin-orbit branching ratios were noted to be markedly different for the fast and slow $O(^3P_J)$ fragments. The time-of-flight (TOF) mass spectrometry $O(^3P_2)$ experiments of Richter *et al.* agree qualitatively with the measurements of Ahmed *et al.*, also suggesting a bimodal fragment distribution with a peak close to the energy associated with NO molecules in $v=4$.

At higher excitation energies, Coroiu *et al.*[41] used the VMI technique to probe the $O(^3P_J)$ fragment distribution close to 200 nm in a single laser experiment. A bimodal velocity distribution was observed for all three spin-orbit components. In each case the distribution peaked at speeds consistent with the production of highly vibrationally excited NO fragments, in $v=13$ or 14. A secondary peak was interpreted to be due to $NO(^2\Pi_\Omega)$ in a vibrational level close to 7. As with the results obtained at lower excitation energies, potential angular momentum alignment of the $O(^3P_2)$ and $O(^3P_1)$ may have effected the measured kinetic energy profiles and translational anisotropies. However the fast component of the unaligned $O(^3P_0)$ fragment anisotropy was measured to be ~ 1.0, in accord with the results of Brouard *et al.* close to 226 nm. The anisotropy of the slow component was measured to be 0.55 implying dissociation taking place on a longer timescale and/or via a more bent geometry.

The TR FTIR experiments of Hancock and Morrison at 193 nm also suggested a bimodal vibrational distribution of the $O(^3P_J)$ fragments.[25] By recording the fluorescence of the NO fragments produced in coincidence with both ground and electronically excited state oxygen atoms, the overall vibrational distribution was measured. The primary peak in the distribution occurs with NO in $v=5$, which may be due to either the $O(^3P_J)$ or $O(^1D)$ dissociation channel. Above $v=6$, NO can only be formed in coincidence with $O(^3P_J)$ fragments. The vibrational populations between $v=7$ and 16 displayed bimodal structure, peaking at $v=7$ [and perhaps below with a contribution from the $O(^1D_2)$ cofragments] with an ancillary maximum at $v=14$. An interesting aspect of these experiments is that their TR nature should have identified any contributions from the dissociation of N_2O_4. The absence of these contributions seems to suggest that the $O(^3P_J)$ dissociation is genuinely vibrationally bimodal, at least at 193 nm.

In summary, literature regarding the energy partitioning in the dissociation of NO_2 from the $(2)^2B_2$ state does not paint an entirely consistent picture. At 248 nm, the $O(^3P_J)$ distribution has been measured to peak with $NO(^2\Pi_\Omega)$ in $v=0$ with a subsidiary maximum somewhere between $v=5$ and 7.[31–33,35] At 226 nm the distribution is interpreted as peaking somewhere between $v=4$ and 6.[16,34] At slightly higher excitation energies, 213 nm, a bimodal distribution is measured with a major peak at a kinetic energy consistent with the production of $NO(^2\Pi_\Omega)$ fragments in $v=4$ with an ancillary maximum consistent with production in $v=10$ or 11.[39] Close to 200 nm, the kinetic energy of the $O(^3P_J)$ fragments are consistent with production in coincidence with $NO(^2\Pi_\Omega)$ in $v=7$ and $v=13$ or 14.[41] At still shorter wavelengths, the $NO(^2\Pi_\Omega)$ distribution is found to peak at $v=7$ or less with a small peak at $v=14$ in the $NO(^2\Pi_\Omega)+O(^3P_J)$ distribution.[25] The energy partitioning determined by all of these studies is summarized in Fig. 1. The most probable internal energy of the photofragments is plotted against the initial excess energy in the $(2)^2B_2$ state for the high and low energy channels, respectively. The "error bars" represent the half width half maxima of the reported internal energy profiles in each study. In the study of Hancock and

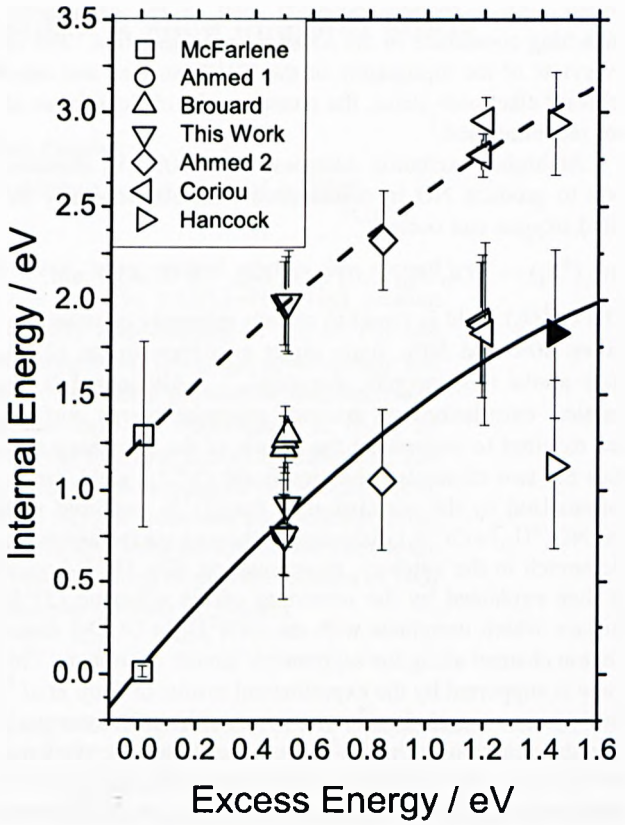

FIG. 1. Peak internal energy of the $NO(^2\Pi_\Omega)$ fragments produced in coincidence with $O(^3P_J)$ for two different dissociation channels (high and low internal energies) at different excess energies in the $(2)^2B_2$ state. The figure compares previous studies; McFarlene *et al.* (Ref. 33), Ahmed *et al.* (1) (Ref. 34), Brouard *et al.* (Ref. 16), Ahmed *et al.* (2) (Ref. 39), Coroiu *et al.* (Ref. 41), and Hancock and Morrison (Ref. 25); with this work. The error bars represent the half width half maximum of the internal energy distributions reported in these studies. In the experiments of Hancock and Morrison (Ref. 25) only vibrational profiles were recorded. In this case the rotational energy corresponding to $N\sim 57$ has been added to the most probable vibrational energy for the low internal energy channel (to give a total internal energy of ~ 1.82 eV). This point is drawn as a filled triangle. The lines drawn through the points are quadratic least-squares fits but are merely a guide to the eye and have no physical significance. The solid line links data for the channel producing fast O atoms. The dashed line links data for the channel producing slow O atoms.

Morrison[25] only a vibrational profile was reported (represented by open triangles in the figure). However the calculations of Schinke *et al.*[4] allow us to estimate the expected rotational energy in the low (internal) energy channel. Accordingly we have also reported Hancock and Morrison's datum with an additional 695 meV of internal rotational energy (solid triangle).

The dissociation dynamics close to 226 nm are particularly interesting. This is the only excitation wavelength at which a bimodal $O(^3P_J)$ energy distribution has been attributed to N_2O_4 photolysis. The two imaging studies carried out close to this excitation wavelength measured $O(^3P_J)$ distributions with similar profiles.[16,34] However, these studies differ substantially in the determined kinetic energies of the peaks of the $O(^3P_J)$ fragment distributions. In this paper we describe experiments at photolysis wavelengths close to 226 nm using the direct current (dc) slice imaging detection technique.[42] We achieve substantially higher energy resolution of the $O(^3P_J)$ kinetic energy release spectra than has been obtained previously. We couple these experiments with the detection of the NO cofragments in order to understand the energy partitioning of the dissociation and the mechanism in more detail. The results of these experiments allow us to reappraise critically previous observations and to provide a new interpretation of the photodissociation dynamics of the $(2)^2B_2$ state of NO_2 that is in accord with recent theoretical work.[4] The paper is organized in the conventional experimental, results, discussion format.

II. EXPERIMENTAL

In our experiments dc slice VMI (Ref. 42) has been employed in conjunction with mass-resolved REMPI spectroscopy in order to probe the nitric oxide and atomic oxygen photoproducts of nitrogen dioxide photolysis close to 226 nm. Reagent molecules were prepared in a pulsed supersonic expansion of 2% NO_2 (Air Products Ltd.) purified by reaction with 5% O_2 (BOC gases) in a seed gas of He (BOC gases). The supersonic expansion was created by a heated pulsed valve (General Valve) with a 500 μm orifice and a backing pressure of $\sim$1 bar. For all of the experiments other than the temperature studies, the nozzle was held at 393 K in order to push the NO_2/N_2O_4 equilibrium to 99.9% in favor of the monomer. The expansion chamber was held at a pressure between $(1-8)\times10^{-6}$ mbar throughout the experiments. The rotational temperature of the molecular beam was determined to be $\sim$20 K from the rotational profile of NO contaminant in the NO_2 expansion. This molecular beam was doubly skimmed 50 and 600 mm downstream from the orifice, using 1 and 2 mm diameter skimmers (Beam Dynamics) respectively, in order to limit its translational velocity perpendicular to the direction of travel. The second skimmer lies at the base of a set of VMI ion/electron optics based on the designs of Wrede *et al.*[43] and Yonekura *et al.*[44] The electron optics were mounted so as to project the photoion or photoelectron distributions along the axis of the molecular beam propagation and were designed to operate both in conventional VMI (Ref. 45) and dc slicing modes[42] depending on the extraction voltages employed. The detection chamber was held at a pressure close to 1×10^{-8} mbar throughout these experiments.

The frequency tripled output of a Nd:YAG (yttrium aluminum garnet) laser (Continuum Surelite III-10) was used to pump a dye laser (Sirah Cobra Stretch) operating with a Coumarin 2 (Exciton) and, separately, a Coumarin 47 dye (Exciton) to span the required excitation wavelengths. The fundamental was frequency doubled to produce pulses with maximum energies between 2.5 and 3 mJ pulses at a repetition rate of 10 Hz between 218 and 236 nm with a temporal profile of 3 ns [full width at half maximum (FWHM)]. During the experiments, the laser energy was maintained between 50 and 500 μJ and was focused 2 mm beyond the molecular beam jet with a 250 mm fused silica lens. The single laser pulse photodissociated and ionized the photofragments via (1+1) or (2+1) REMPI processes for the nitric oxide and oxygen fragments, respectively.

Photoions/photoelectrons were detected at the end of a mu-metal TOF tube by a dual microchannel plate vacuum detector in a chevron arrangement (40 mm diameter, with a P43 phosphor screen; Photek). The detector was gated to detect ions of a given mass, and for slicing experiments to detect the central part of one of the photoproduct distributions. In the slicing experiments, the detector on time was maintained below 20 ns (usually less than 10 ns) using a custom built power supply (Photek). Images were captured using a 640×480 pixel charged couple device camera (LaVision Imager 3) and were averaged and processed using the DAVIS software package (LaVision) and an event counting macro. Conventional velocity map images were postprocessed using the Hankel/Abel transform to reconstruct the photoproduct distributions after the projection.[46] The resulting velocity map images were calibrated using NO photoionization or O_2 photodissociation, the mechanisms and energetics of which are well understood.

III. RESULTS

dc slice images of the three $O(^3P_J)$ fragments were recorded using a single laser, scanning the Doppler profiles of the fragments in order to probe the entire distributions. In these experiments, the pulse energies were maintained close to 250 μJ pulse^{-1}. The resulting images are shown in Fig. 2 [panels (a)–(c)]. The corresponding calibrated kinetic energy release spectra are shown in the same figure [panels (d)–(f)]. The kinetic energy resolved spin-orbit branching ratio was determined in separate experiments in which the three images were recorded on the same day under identical conditions (nozzle temperature 393 K, backing pressure 1 bar). The relative signal intensity ratio of the $O(^3P_J)$ fragments with kinetic energies between 0.50 and 1.55 eV was determined to be 1.00:0.71:0.15 for the $O(^3P_2)$, $O(^3P_1)$, and $O(^3P_0)$ fragments, respectively. The image intensities in Fig. 2 have been normalized to this ratio. This normalization allowed the spin-orbit intensity ratio of the slower fragments to be extracted. For the fragments with kinetic energies between 0 and 0.5 eV this was determined to be 1.00:0.47:0.11.

The kinetic energy distributions of the atomic oxygen

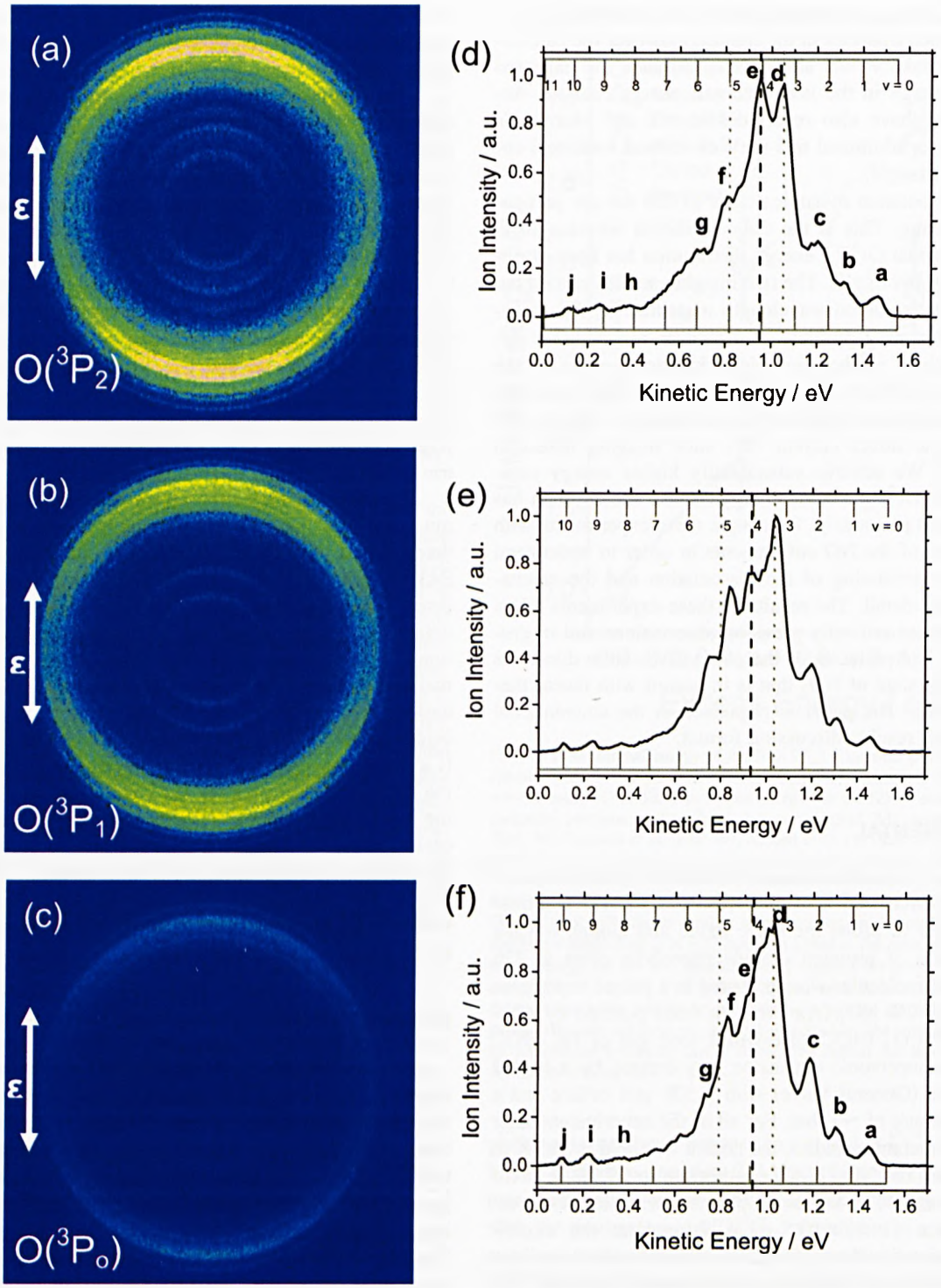

FIG. 2. (Color) dc slice velocity map images of the (a) $O(^3P_2)$, (b) $O(^3P_1)$, and (c) $O(^3P_0)$ fragments recorded using a single laser for both photolysis of the parent NO_2 molecule and photoionization of the O fragment. The laser, which is polarized vertically to the image plane, is scanned over approximately 0.016 nm around each ionization resonance in order to ensure that the entire Doppler profile of the O fragments is evenly sampled. Each image is recorded for ~150 000 laser shots. Panel (d) shows the $O(^3P_2)$ translational energy distribution produced from the photodissociation of NO_2 via the $(2)^2B_2$ state with associated peak labels as discussed in the text. The distribution is simply obtained by angular integration of the corresponding image (a), multiplication by the appropriate Jacobian, $r \sin(\vartheta)$, and calibrated against a known kinetic energy release spectrum, usually of O atoms from the ~226 nm photodissociation of O_2, recorded immediately prior or post the image acquisition with exactly the same extraction voltages and laser/molecular beam intersection point. Panels (e) and (f) show the photofragment distributions as in (d) but for the $O(^3P_1)$ and $O(^3P_0)$ fragments, respectively.

fragments are highly structured. The $O(^3P_1)$ and $O(^3P_0)$ fragment distributions peak at kinetic energies of 1.03 and 1.04 eV, respectively. The $O(^3P_2)$ distribution shows two major peaks at 0.95 and 1.05 eV.

Further experiments were performed to probe the NO $(1)^2\Pi_\Omega$ fragments directly. In these experiments, the NO fragments were probed state specifically via a (1+1) REMPI scheme on the $A \leftarrow X(1\ ^2\Pi_r^+ \leftarrow 1\ ^2\Pi_\Omega)$ transitions. These experiments probe the NO fragments produced in coincidence with $O(^3P_J)$ and $O(^1D_2)$ fragments since both product channels are open below 243.9 nm. Spectra were collected by recording the total mass-resolved (by TOF) NO^+ signal arriving at the phosphor screen while scanning the excitation/probe wavelength. The spectra of the (0,0), (1,1), and (2,2) bands so recorded were in good agreement with those obtained by Im and Bernstein[47] and Bigio *et al.*[48] Velocity map images recorded in these bands confirmed the observations of Ahmed *et al.* that the two product channels produce NO fragments with very different rotational profiles.[34] Furthermore, for all of the probed rotational lines in these bands, the $NO(^2\Pi_\Omega)$ fragments produced in coincidence with $O(^3P_J)$ are the minor photoproducts.

Mass-resolved REMPI spectra measured across the excitation region of the (2,3) band display very different rotational profiles to the (0,0), (1,1), and (2,2) bands. The REMPI profile of the NO fragments recorded close to the (2,3) band head is shown in Fig. 3(a). A progression of peaks separated by ~4.6 meV occurs for excitation energies between 5.34 and 5.41 eV in good agreement with the results of Im and Bernstein.[47] Some representative velocity map ion images recorded in different rotational states corresponding to peaks (a)–(c) in Fig. 3(a) are shown in Fig. 4.

In order to measure the effect of N_2O_4 on the $O(^3P_J)$ kinetic energy distributions, $O(^3P_J)$ images were recorded at 295, 345, and 393 K. The resulting energy distributions are shown in Fig. 5. A broad feature is observed in the $O(^3P_2)$ distributions at low temperatures which becomes less significant as the temperature is increased to 393 K. This feature was found to be most significant in the $O(^3P_2)$ distribution.

IV. DISCUSSION

A. $O(^3P_J)$ spin-orbit branching ratios

The photofragment speed distributions and velocity anisotropy will be affected by orbital angular momentum alignment effects. In a one laser one color experiment it is impossible to quantify these effects although the $O(^3P_0)$ fragment is intrinsically unaligned. A qualitative measure of the orbital alignment in the other $O(^3P)$ channels may be obtained by recording images with the laser polarization oriented perpendicular to the face of the detector. Since the photoproduct distribution created in a single laser, single photon dissociation process must be azimuthally symmetric, any anisotropy is direct evidence for alignment effects in the photoproduct distribution. From the isotropic profile of the $O(^3P_2)$ fragments recorded with the laser polarized perpendicular to the detector we conclude that the $O(^3P_2)$ products are essentially unaligned, at least for the faster more intense component. In contrast, the $O(^3P_1)$ image in the perpendicular configuration

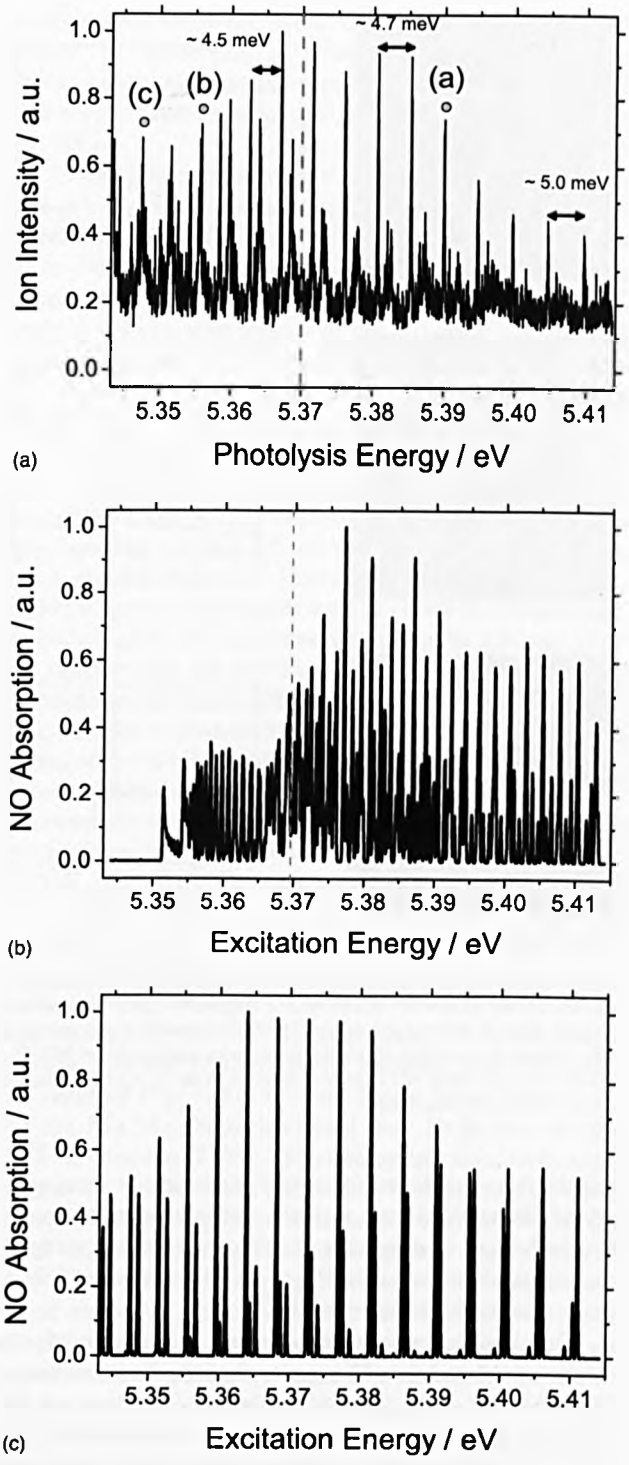

FIG. 3. Panel (a) mass-resolved (TOF) REMPI excitation spectrum of $NO(^2\Pi_\Omega)$ recorded at single photon excitation energies spanning the range of the (2,3) $A \leftarrow X$ transition. Peak separations are noted to be around 4.6 meV. The expected position of the (2,3) band head is superimposed on the spectrum as a dashed vertical line at ~5.37193 eV. The lines in the spectrum marked (a)–(c) correspond to the excitation energies used to record the images presented in Fig. 4. Panels (b) and (c) show simulated NO absorption spectra for the NO $A \leftarrow X$ transition using the LIFBASE spectral simulation software package (Ref. 50). Panel (b) shows the absorption of NO fragments produced in $v=3$ with a peak in a statistical rotational distribution at N=21, while (c) shows the absorption of NO fragments produced in $v=1$ with a sharp rotational profile peaking at N~57 with a FWHM corresponding to the energy spread of ten rotational levels.

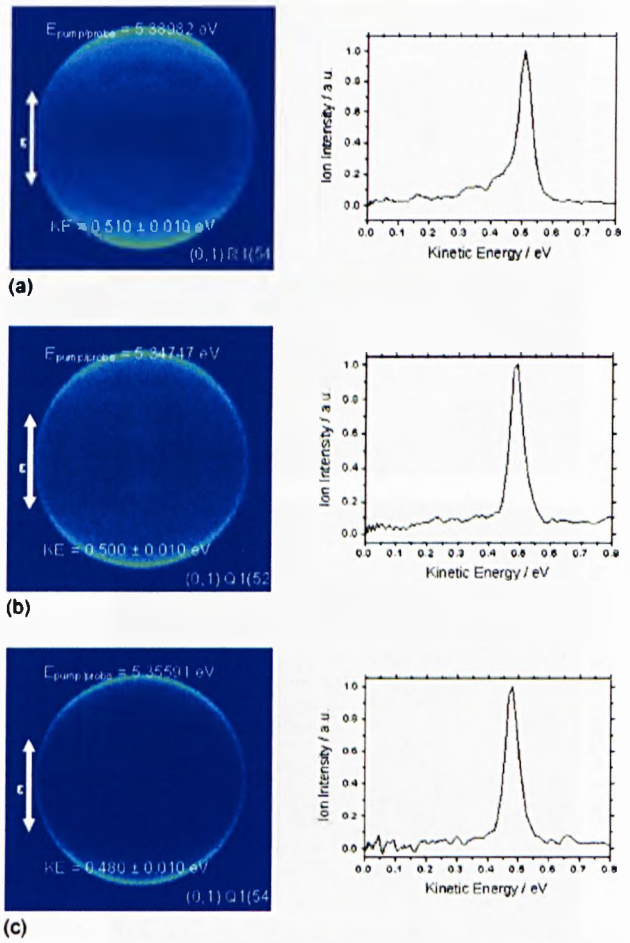

FIG. 4. (Color online) Representative velocity map images and corresponding kinetic energy release spectra of NO fragments formed at excitation energies close to 230 nm [(a)–(c) in Fig. 3]. The kinetic energy release of these fragments is too high for the fragments to be rotationally hot $NO(^2\Pi_\Omega)$ radicals in $v=3$. These NO fragments must be in the 2, 1, or 0 vibrational states. See text for discussion.

displayed a significant anisotropy indicating at least some orbital alignment. These qualitative observations are consistent with those of Ahmed *et al.* who, in a two color experiment at a photolysis wavelength of 213 nm, were able to make quantitative measurements.[39]

Our basic alignment experiments, together with the results of Ahmed *et al.*, suggest that the fast component (0.5–1.55 eV) of the $O(^3P_2)$ distribution (Fig. 3) is not significantly aligned. This means that the observed intensity ratio of the $O(^3P_2)$ to $O(^3P_0)$ images should give a good measure of the true spin-orbit branching ratio. In contrast, because the $O(^3P_1)$ photoproducts are most probably aligned their measured intensity must be considered as a lower bound. With this caveat, the spin-orbit intensity ratio of the fast $O(^3P_J)$ fragments is determined to be 1.00:0.71:0.15 at a sample temperature of 393 K; in slight disagreement with the results of Rubahn *et al.*[29] Normalizing the ratio with respect to the two photon line strengths and the state degeneracies highlights the preference of the dissociation for the production of $O(^3P_1)$ photoproducts, which is markedly nonstatistical (in agreement with the results of Rubahn *et al.*[29]). The

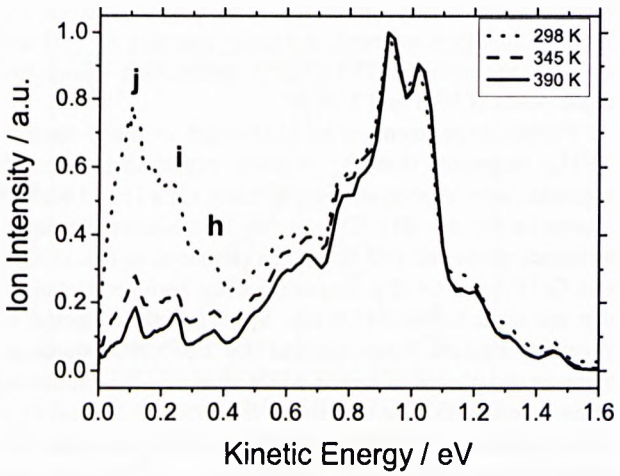

FIG. 5. $O(^3P_2)$ energy release spectra recorded at a backing pressure of 1 bar and nozzle temperatures of 295 K (dotted line), 345 K (dashed line), and 393 K (solid line).

spin-orbit intensity ratio of the slow $O(^3P_J)$ fragments (0–0.5 eV of kinetic energy) was found to be quite different; favoring dissociation to produce $O(^3P_2)$ photoproducts. We obtain a branching ratio of 1.00:0.47:0.11 (uncorrected for degeneracy and line-strength factors) at a sample temperature of 393 K, although the orbital angular momentum alignment effects mean that the $O(^3P_1)$, and possibly the $O(^3P_2)$ signals are lower bounds of the real intensities. Despite this, the difference in the spin-orbit branching ratio must reflect real differences in the dissociation dynamics of the slow and fast fragments.

B. Energy partitioning in the NO fragments

Our single laser experiments were performed with varying excitation wavelengths between 232 and 220 nm in order to probe different photolysis products. The range of excitation wavelengths populates different vibrational levels of the $(2)^2B_2$ state of the parent NO_2 molecules. However, the vibrational structure of the absorption spectrum in this region is primarily associated with the bound symmetric stretch in the $(2)^2B_2$ vibrational manifold. This stretch can be considered as orthogonal to the unbound, dissociative asymmetric stretch coordinate, and should have no appreciable effect on the $O(^1D_2)/O(^3P_J)$ branching ratio or dissociation time scale. It should also be noted that due to the change in the photolysis wavelength required to Doppler scan over each $O(^3P_J)$ ionization resonance, the structure due to individual rotational levels in the NO cofragment cannot be resolved in these single laser experiments. Despite this, the energy distributions of all three $O(^3P_J)$ spin-orbit components are highly structured [Figs. 2(d)–2(f)].

Focusing on the intrinsically unaligned $O(^3P_0)$ distribution [Fig. 2(f)], the majority of the oxygen atoms are formed with kinetic energies between 1.55 and 0.50 eV. This part of the distribution can be split into at least seven distinct peaks [labeled (a)–(g)]. The maximum of the distribution occurs at a kinetic energy consistent with the production of $O(^3P_0)$ in coincidence with $NO(^2\Pi_{1/2})$ in $v=3$ and $N\sim21$. This is in good agreement with the results of Ahmed *et al.*[34] when the

TABLE I. Transition probabilities and excitation energies for selected vibrational bands in the $A \leftarrow X$ absorption spectrum of NO. The data are taken from constants published in the LIFBASE spectral simulation program (Ref. 50).

$A \leftarrow X$ vibrational band	Bandhead / eV	Transition probability
(3,3)	5.651 47	6.186×10^{-4}
(2,2)	5.594 78	2.624×10^{-3}
(1,1)	5.537 65	1.610×10^{-3}
(0,0)	5.479 89	2.389×10^{-3}
(3,4)	5.429 24	1.807×10^{-3}
(2,3)	5.369 21	1.178×10^{-3}
(1,2)	5.308 50	1.671×10^{-5}
(0,1)	5.247 23	4.909×10^{-3}

vibrational comb in their paper was corrected so that $v=0$ was positioned at a total photofragment kinetic energy consistent with dissociation via the $NO(^2\Pi_{1/2})+O(^3P_0)$ limit (~2.379 eV). With the correction to the results of Ahmed *et al.*, the peak in their and our distributions are in slight disagreement with Brouard *et al.* who claimed that the peak of the distribution was consistent with $NO(^2\Pi_\Omega)$ production in $v=4-6$. Considering the reported high kinetic energy peaks of the $O(^3P_J)$ distributions observed at 248, 213, and 200 nm (consistent with maxima at $v=0$, $v=4$, and $v=7$, respectively) a distribution peaking at $v=3$ for a photolysis wavelength of 226 nm appears to be consistent with the majority of the previous results (see Fig. 1) and we conclude that the differences between the reported energy distributions must be due to errors in the calibration of the ion images.

If the $O(^3P_J)$ fragments do peak at an energy consistent with the production of the $NO(^2\Pi_\Omega)$ cofragments in $v=3$ (as implied by the results of Ahmed *et al.*[34] and our work), the mass-resolved REMPI spectrum recorded for excitation energies between 5.41 and 5.34 eV [229–232 nm, see Fig. 3(a)] should reveal the rotational profile of these fragments. Between 5.41 and 5.34 eV $NO(^2\Pi_\Omega)$ fragments can only be produced in coincidence with $O(^1D_2)$ in $v=0$ or 1. This means that the spectral signature of the $v=3$ fragments would be due to the $O(^3P_J)$ dissociation channel only. Rotationally cold $NO(^2\Pi_{1/2})$ in $v=3$ is expected to be observed at 5.3692 eV (230.92 nm) due to the reasonable transition probabilities for the $A \leftarrow X$ (2,3) transition (see Table I) and assumed large population of the $NO(^2\Pi_\Omega)$ $v=3$ level [based on the $O(^3P_J)$ energy distributions]. Given the $NO(^2\Pi_\Omega)$ and $NO(^2\Sigma^+)$ rotational constants (1.7049 and 1.9956 cm^{-1}, respectively) and knowing the higher order terms in the Dunham expansion,[12,49] and the origin of the $NO(^2\Sigma^+)$ A state at 5.45105 eV,[12] intense peaks in the $v=3$ rotational profile would be expected to occur at an excitation energy ~5.3838 eV (230.29 nm) with prominent rotational lines separated by ~1.5 meV. Examination of the REMPI spectrum in Fig. 3(a) reveals no such feature. Instead a broad rotational progression with average peak spacing of ~4.6 meV is visible. Clearly the observed rotational profile does not originate at 5.3692 eV [the $A \leftarrow X$ (2,3) band origin, shown as a dashed vertical line in the figure] and the NO cofragment associated with the peak of the $O(^3P_0)$ kinetic energy release spectrum cannot be in $v=3$. We confirm this remark by presenting a simulated absorption profile, obtained using the LIFBASE program,[50] of NO fragments in $v=3$ with a statistical rotational profile peaking at N ~ 21 in Fig. 3(b).

We have already noted that the recorded REMPI spectrum is in agreement with the spectrum observed by Im and Bernstein between 5.23 and 5.46 eV. They attributed the signal to a multiphoton dissociation process[47] but this is not our interpretation. Several representative single laser mass-resolved velocity map images of the NO fragment recorded between 5.34 and 5.43 eV are shown in Fig. 4. These images have been recorded for the peaks marked (a)–(c) in the REMPI spectrum [Fig. 3(a)]. The analysis of the kinetic energies of these fragments indicates that if they were from NO in $v=3$, the probed states would span rotational states between N=18 and N=33. This would result in peak separations between 1.2 and 2.5 meV in the REMPI spectrum, which are not observed. Furthermore, comparison of the photolysis/probe wavelengths used to obtain the images with the $NO(^2\Pi_\Omega)$ $A \leftarrow X$ (2,3) absorption lines in LIFBASE (Ref. 50) indicates that the NO fragments with 18–30 quanta of rotational energy could not be probed by the applied laser field. In order to produce a rotational profile with peak separations of the order of 4.6 meV fragments with significantly higher rotational energies are required, corresponding to NO fragments occupying rotational levels with quantum numbers around 57 or ~700 meV of rotational excitation.

The requirement for rotational excitation in the 700 meV range and the kinetic energy release observed in Fig. 4 is only consistent with NO fragments in the vibrational range of $v=0-2$. Considering the ionization stage of the experiment, summing the photon energy and the maximum vibrational energy of the NO $^2\Pi_\Omega$ fragments ($v=2$), an energy between 5.92 and 5.99 eV can be accessed over the excitation range of Fig. 3(a) at the one photon level. This means that the NO $^2\Pi_\Omega$ fragments could only be probed via the $(1)^2\Sigma^+$ (A) or the $(2)^2\Pi_\Omega$ (B) intermediate state (with term energies of 5.451 05 and 5.692 56 eV, respectively)[12] in a (1+1) REMPI process. It is also noted that ionization of the NO B state is forbidden within a Koopmans' type picture of the (1+1) ionization process. This is consistent with experimental studies in which the NO B state fluorescence is observed without any competition from ionization. There are no intermediate resonances at the two photon level for a (2+1) ionization process of the NO fragments. Therefore one must conclude that the carrier of the spectrum in Fig. 3(a) must be NO $(1)^2\Pi_\Omega$ (X state) fragments in $v=0$, 1, or 2 probed via a (1+1) REMPI process using the NO $(1)^2\Pi_\Omega$ (A) state as an intermediate resonance.

Because of the shorter bond length of the NO A state with respect to the X state (106.37 and 115.08 pm, respectively), the rotational bands of the $A \leftarrow X$ transitions are shaded to the blue. We therefore expect the absorption lines of rotationally excited NO fragments which are probed via the A state to occur at higher excitation energies than the vibrational band head. With the constraints on the populated vibrational levels of the $NO(^2\Pi_\Omega)$ fragments imposed by the energetics, there are only two vibrational bands which we

may be probing in Figs. 3(a) and 4; the (1,2) and (0,1) bands. The line spacing and line intensities observed in Fig. 3(a) imply a rotational profile which peaks in a rotational level close to 57. For the $A \leftarrow X$ transition, the 57th rotational level in the Q branch should occur ~113 meV to the blue of the (1,2) and (0,1) band heads. Based on the information in Table I, we expect the $Q(57)$ rotational line of the (1,2) and (0,1) vibrational bands to occur at 5.425 and 5.368 eV, respectively. We therefore attribute the spectrum shown in Fig. 3(a) to highly rotationally excited NO $(1)^2\Pi_\Omega$ fragments produced in $v=1$.

The assignment is confirmed by comparison of Fig. 3(a) with simulations of the NO $^2\Pi_\Omega$ $A \leftarrow X$ absorption spectrum using LIFBASE, as shown in Fig. 3(c). The simulated line positions match the observed positions for $NO(^2\Pi_\Omega)$ populations in $v=1$. A nonstatistical rotational distribution spanning $N=52-65$ and peaking close to $N=60$ simulates the intensity profile of the NO fragments; although exact agreement was not sought and is not expected since LIFBASE is only capable of simulating an absorption spectrum and not a REMPI spectrum. The rotational energies of the imaged NO fragments can be calculated from their kinetic energies assuming that the fragments have one quanta of vibrational excitation. The measured kinetic energies of the NO fragments (Fig. 4) are consistent with the production in $v=1$ with rotational quantum numbers between 49 and 58.

In the light of this new rovibrational assignment, the $NO(^2\Pi_\Omega)$ fragments probed by Im and Bernstein's experiment between 5.23 and 5.46 eV correspond to the entire rotational distribution of the $A \leftarrow X$ (0,1) vibrational band.[47] Despite these features being previously attributed to multiphoton dissociation of NO_2, the rotational profile they observed is exactly what is expected for a narrow, highly rotationally excited rotational profile of NO fragments produced in coincidence with $O(^3P_J)$. When REMPI spectra are recorded on either side of the spectrum shown in Fig. 3(a), we find that the peak of the rotational distribution occurs close to 231 nm. If one considers the transition probabilities (see Table I) of the vibrational bands close to the studied wavelengths, one sees that the transition probability for the $A \leftarrow X$ (0,1) transition is four times greater than the corresponding $A \leftarrow X$ (2,3) transition probability. Were $NO(^2\Pi_\Omega)$ fragments produced equally populating the rotationally excited $v=1$ levels and relatively rotationally cold $v=3$ levels the underlying rotational progression of the (2,3) band would be observed in the REMPI spectrum [Fig. 3(a)] with a peak intensity around a quarter of that of the (0,1) progression. The absence of such a progression and the signal-noise ratio in the recorded spectrum suggests that in fact the population of relatively rotationally cold levels of the (2,3) band must be less than $\frac{2}{3}$ of that of the rotationally excited levels of the (0,1) band. Considering the intensity profile of the $O(^3P_J)$ energy distributions and that the rotational profile of the (0,1) band is spread over more than 60 rotational levels, it seems likely that the population of the $NO(^2\Pi_\Omega)$ in $v=3$ is actually significantly less than $\frac{2}{3}$ that of the population of $v=1$.

There are a number of potential complications to the analysis of the whole (0,1) rotational profile. Close to 5.55 eV, the photolysis energy is sufficient to produce $NO(^2\Pi_{1/2})$ in $v=1$ in coincidence with $O(^1D_2)$. The rovibrational profiles of the $NO(^2\Pi_\Omega)$ fragments produced concomitantly with $O(^1D_2)$ have been probed between 5.41 and 5.71 eV.[47,48] These distributions are characterized by relatively statistical profiles with rotational temperatures between 200 and 400 K.[47,48,51] The dissociation via the $O(^1D_2)$ channel favors the production of vibrationally inverted $NO(^2\Pi_\Omega)$ fragments with relatively little energy partitioned into rotation (we will discuss this more fully in a subsequent publication).[51] With the low rotational excitation of these $NO(^2\Pi_\Omega)$ fragments in mind, there should be almost no population of rotational levels above $N=35$ in the $O(^1D_2)$ $v=1$ channel. These rotational levels would appear in the REMPI spectrum close to 5.28 eV, but this is below the energetic threshold for the production of $NO(^2\Pi_\Omega)$ in $v=1$ with $O(^1D_2)$ so they would not be observable in a single laser experiment. Furthermore, $NO(^2\Pi_\Omega)$ produced in coincidence with $O(^1D_2)$ should not have an effect on the rest of the (0,1) $NO(^2\Pi_\Omega)$ with $O(^3P_J)$ rotational profile, as $NO(^2\Pi_\Omega)$ cannot be formed in $v=2$ with $O(^1D_2)$ at excitation energies below 5.544 66 eV. The result of this is that the entire (0,1) rotational profile in the REMPI spectrum is due to $NO(^2\Pi_\Omega)$ fragments formed with $O(^3P_J)$ fragments only. Despite this, further complications to the band structure could arise from its spectral width; the band spans a range between 5.23 and 5.44 eV. In this region signatures from $NO(^2\Pi_\Omega)$ fragments formed with $O(^3P_J)$ in $v=2-4$ could also be observed. As we have discussed the contribution to the total $O(^3P_J)$ signal from $NO(^2\Pi_\Omega)$ fragments in $v=3$ must be small. On similar arguments the effect of $NO(^2\Pi_\Omega)$ fragments in $v=2$ and 4 probed via the (1,2) and (3,4) bands can be assessed.

The analysis of the spectral region which corresponds to the rotationally cold part of the (1,2) band in the spectrum recorded by Im and Bernstein indicates that the population of these levels is less than $\frac{3}{5}$ of the population of $NO(^2\Pi_\Omega)$ fragments in $v=1$ and $N\sim42$. If the (1,2) band were assumed to have a similar rotational profile to the (0,1) band, we would expect a primary peak in the distribution at an excitation energy of 5.421 34 eV (228.697 nm). When spectra are recorded between 5.41 and 5.46 eV only very weak signals are observed. As very few of these rotational lines are above the level of the noise, the signatures of rotational profiles in this energy range are below the detection limit of our experiment. If the rotational profile of the $NO(^2\Pi_\Omega)$ fragments in $v=2$ was similar to that of $v=1$, it is likely that we would not be able to detect these photofragments via the (1,2) band as the transition probability for this band is almost 300 times smaller than that of the (0,1) band. The absence of any appreciable signal close to 5.429 24 eV (228.364 nm) indicates that the population of fragments produced in $v=4$ with little rotational excitation must be less than $\frac{3}{4}$ of the population of the rotationally excited $NO(^2\Pi_\Omega)$ fragments in $v=1$. Were the $v=4$ fragments to display a similar rotational profile to those in $v=1$, a signature would be expected to be seen close to 5.547 64 eV (223.490 nm). This would overlap with the (1,1) vibrational band, throughout which $NO(^2\Pi_\Omega)$ can be produced in coincidence with $O(^1D_2)$. As the total $O(^1D_2)$ channel makes up ~50% of the total $NO(^2\Pi_\Omega)$ signal in $v=0$, 1 or 2 at photolysis wavelengths which could

probe the NO fragments in this band, it is unlikely that the underlying signature of rotationally excited fragments in $v=4$ could be observed in a single laser experiment due to the low signal intensity. For similar reasons, the underlying signatures of rotationally excited $NO(^2\Pi_\Omega)$ fragments in $v=0$ or 3 are unlikely to be observed in a one laser experiment due to the large signal from rotationally cold $v=2$ or 0 products formed with $O(^1D_2)$ probed via the (2,2) and (0,0) bands.

We have argued that rotationally excited $NO(^2\Pi_\Omega)$ fragments produced in $v=1$ have a greater contribution to the total $O(^3P_J)$ signal than rotationally cold $NO(^2\Pi_\Omega)$ fragments in $v=3$. This should be evident in the energy distributions of the $O(^3P_J)$ fragments. The expected kinetic energies of the $O(^3P_J)$ fragments formed in coincidence $NO(^2\Pi_\Omega)$ fragments in $v=1$ and N=50 and N=65 are drawn as dotted lines on the energy distributions in Figs. 2(d)–2(f). We see that this range of rotationally excited NO cofragments span major peaks of the energy distributions of all three $O(^3P_J)$ spin-orbit components. It should be noted that the spectrum in Fig. 3(a) and those recorded by Im and Bernstein are primarily a reflection of the rotational profiles of the $O(^3P_2)$ channel due to the spin-orbit product ratio. It is therefore expected that there should be good agreement between the rotational distributions recorded in Fig. 3(a) with one of the main peaks in the $O(^3P_2)$ energy distribution. The kinetic energy expected for the peak of the rotational profile (N =57) is drawn in Figs. 2(d)–2(f) as a single dashed line. The major peak in the $O(^3P_2)$ kinetic energy distribution [Fig. 2(d)] matches exactly with the energy expected for the production of an O atom in coincidence with a $^2\Pi_{1/2}$ NO cofragment in $v=1$ N=57, i.e., the strongest line in the REMPI spectrum, similarly for the shoulder of the main peak in the $O(^3P_0)$ profile [Fig. 2(f)]. It was previously believed that on excitation at ~226 nm to the $(2)^2B_2$ state the $O(^3P_J)$ $+NO(^2\Pi_\Omega)$ dissociation channel led to a sharply peaked vibrational distribution with $NO(^2\Pi_\Omega)$ fragments formed in v =4–6. In fact, the $O(^3P_2)$ distribution [the major $O(^3P_J)$ spin-orbit product] peaks in coincidence with highly rotationally excited $NO(^2\Pi_\Omega)$ fragments in $v=1$ and N~57.

The other peaks in the O atom energy distributions are indicative of further structure in the rovibrational profiles of the $NO(^2\Pi_\Omega)$ cofragments. Provided that there is no interference in the recorded $O(^3P_2)$ distribution from species other than NO_2 and that the absorption of a single photon led to dissociation, the peak at ~1.47 eV [Fig. 2(d); peak (a)] must be due to $O(^3P_2)$ fragments formed in $v=0$ with a rotational quantum number close to N=24. It seems likely that the peak at 1.32 eV [Fig. 2(d); peak (b)] is then due to the production of $NO(^2\Pi_{1/2})$ in $v=1$ due to the similarity in the rotational profile of this peak ($N_{max}=24$). A bimodal rotational profile (peaking at N~57 and N~24) is in agreement with the spectra recorded by Im and Bernstein between 229 and 236 nm.

With evidence for bimodality in the rotational profiles of the $NO(^2\Pi_\Omega)$ fragments formed in low v and the observation that the major dissociation pathway in the $O(^3P_2)$ product channel produces highly rotationally excited $NO(^2\Pi_\Omega)$ fragments in $v=1$, it would be reasonable to expect highly rotationally excited $NO(^2\Pi_\Omega)$ products in $v=0$ and also $v=2$. Were the $v=2$ fragments to display the same bimodal rotational profile as the $v=1$ fragments with peaks at N~24 and 57, peaks would be expected at 1.17 and 0.81 eV in the $O(^3P_2)$ distribution. In fact prominent peaks are observed in the distribution at 1.19 and 0.81 eV [Fig. 2(d), peaks (c) and (f)], corresponding to diatomic fragments in $v=2$, N~20 and $v=2$, N~57, respectively. With a similar argument, rotationally excited fragments (N=57) produced in $v=0$ would be expected to occur close to 1.10 eV. A major peak is observed in Fig. 2(d) at 1.05 eV which would correlate with N~60. With this in mind, the broad peak at 0.71 eV [Fig. 2(d) peak (g)] likely correlates with $NO(^2\Pi_\Omega)$ fragments in $v=3$ with a maximum in the rotational profile occurring at N~54. It would seem that a dissociation mechanism which promotes rotational excitation in fragments occupying the lower vibrational levels adequately explains the major features of the $O(^3P_2)$ energy distribution. As might be expected in a mechanism favoring rotational excitation, fragments formed with vibrational excitation are generally formed with slightly less rotational excitation.[52]

Based on the bimodal rotational profile of the $NO(^2\Pi_\Omega)$ fragments in $v=1$, there are likely other minor peaks due to rotationally cold fragments in Fig. 2(d) which are somewhat masked by the more intense peaks in the $O(^3P_2)$ energy distribution. Assuming similar rotational profiles for the different vibrational states, we expect a peak at 1.05 eV for fragments in $v=3$ and N~20. This peak would form part of peak (d). The contribution of such a peak to the distribution, however, must be very small [as is evident in Fig. 3(a)] and a firm assignment would require the detection of the relevant $NO(^2\Pi_\Omega)$ cofragments. There are no obvious features in the distribution which could be assigned to relatively rotationally cold fragments in $v=4$, 5, or 6. It seems that the two rotational modes observed in the $O(^3P_2)$ distribution share a similar vibrational profile.

The peak energies of the $O(^3P_2)$ distribution and the cofragment assignments are summarized in Table II. A similar treatment has been carried out for the $O(^3P_0)$ energy distribution [Fig. 2(f)]. This is summarized in Table III. The main conclusion of the analysis of the energy distributions is that there appear to be two different dissociation mechanisms by which $O(^3P_J)$ atoms can be formed with kinetic energies

TABLE II. Vibrational and rotational assignments of the NO cofragment responsible for the peaks occurring in the $O(^3P_2)$ kinetic energy release spectrum [Fig. 2(d)].

Kinetic energy / eV	v	$\sim N_{max}$	Peak
1.47	0	24	a
1.32	1	24	b
1.19	2	20	c
1.05	0	60	d
0.95	1	57	e
0.81	2	57	f
0.71	3	54	g
0.38	?	?	h
0.25	?	?	i
0.12	?	?	j

TABLE III. As Table II but for the $O(^3P_0)$ kinetic energy release spectrum [Fig. 2(f)].

Kinetic energy / eV	v	N_{max}	Peak
1.44	0	26	a
1.30	1	26	b
1.19	2	20	c
1.03	0	61	d
0.92	1	58	e
0.83	2	55	f
0.73	3	52	g
0.37	?	?	h
0.25	?	?	i
0.11	?	?	j

between 1.55 and 0.5 eV. The major mechanism forms vibrationally cold but rotationally hot $NO(^2\Pi_{1/2})$ fragments with a minor mechanism forming rotationally colder diatomic products with a similar vibrational profile. The production of such highly rotationally excited products from the dissociation of the $(2)^2B_2$ state was recently predicted by Schinke *et al.*[4]

C. Translational anisotropy of the $O(^3P_{2,0})$ fragments

To support the interpretation of the $O(^3P_{2,0})$ energy distributions, the anisotropies of the unaligned image features were analyzed using the well known formula introduced by Zare.[53] The structure in the unaligned $O(^3P_{2,0})$ energy distributions allows the anisotropy of the image features to be individually assessed. The spatial anisotropy of each ring obtained by fitting radially averaged profiles as a function of the kinetic energy of the fragments is plotted in Fig. 6. The anisotropies of the $O(^3P_2)$ and $O(^3P_0)$ images display the same trends with kinetic energy release. Fragments with high kinetic energies have the highest anisotropy parameters (1.5 and 1.2, respectively) with the anisotropy decreasing to a minimum at 0.5 eV (0.5 and 0.6). However, below kinetic energies of 0.5 eV, the $O(^3P_J)$ anisotropy parameter rises. This change in the trend of the anisotropy parameter below 0.5 eV is a clear indication of a difference, on average, in the dissociation mechanism as $NO(^2\Pi_\Omega)$ fragments are formed with greater internal excitation.

Focusing on the anisotropies between 1.55 and 0.5 eV, we expect changes in the anisotropy parameter due to the different dissociation mechanisms which produce relatively rotationally cold and highly rotationally excited NO fragments. Peaks a, b, and c in Figs. 2(d) and 2(f) are assigned to $O(^3P_{2,0})$ atoms produced in coincidence with $NO(^2\Pi_\Omega)$ products in $v=0$, 1, and 2, respectively, with relatively little rotational excitation. Peaks (d) and (e) are primarily attributed to rotationally excited fragments produced via the major dissociation pathway; although there is likely underlying structure due to the minor dissociation pathway. Using a simple impulsive model of the dissociation and assuming a 36 fs dissociation time scale (as supported by the work of Tsuji *et al.*[26] and Schinke *et al.*[4]), it would be expected that peaks (d) and (e) are the result of a more bent geometry at the point of dissociation. Conversely, peaks (a)–(c) should be the result of dissociation via a more linear parent geometry.

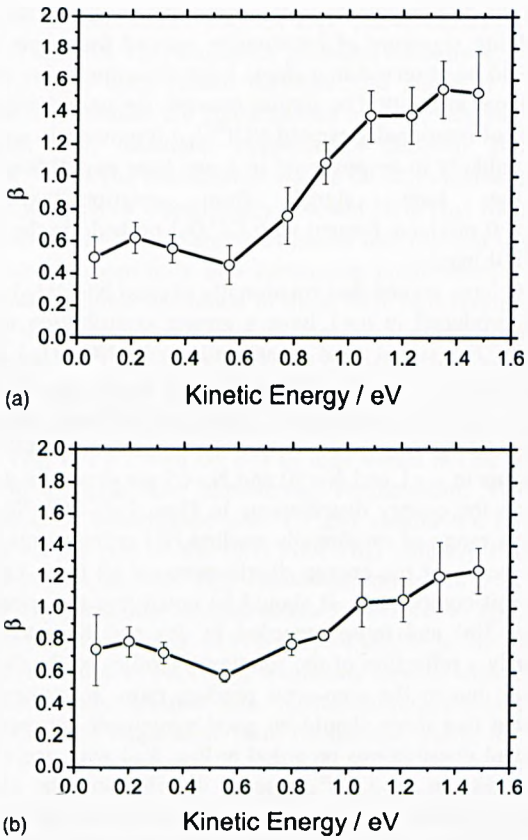

FIG. 6. $O(^3P_2)$ and $O(^3P_0)$ translational anisotropies as a function of the kinetic energy release.

We therefore expect that the anisotropy of rings (a)–(c) would be more anisotropic than rings (d) and (e). This is indeed observed in Fig. 6 for peaks (a), (b), (d), and (e). The large reduction in the anisotropy of ring (c) is rationalized by the large contribution of the underlying high kinetic energy tail of peak (d) due to diatomic fragments in $v=0$ and $N\sim 50$. At lower kinetic energies (0.50–0.90 eV) the anisotropy parameter reflects an average of the anisotropy due to rotationally cold $NO(^2\Pi_\Omega)$ products (potentially in $v=4-6$), the anisotropy due to rotationally excited fragments in $v=2$ and importantly the highly rotationally excited tails of the rotational profiles which form peaks (d) and (e). The resulting anisotropy is heavily weighted by highly rotationally excited fragments produced from NO_2 dissociating with a reduced bond angle. As a result the anisotropy of the image features reduces as the kinetic energy of the fragments decreases to 0.50 eV.

The image features seen at kinetic energies below 0.50 eV appear to result from the dissociation of NO_2 producing relatively rotationally cold $NO(^2\Pi_\Omega)$ fragments in $v=8-11$. The appearance of these minor peaks is consistent with the observations of Ahmed *et al.* who also observed a second, competitive, dissociation channel in the $O(^3P_J)$ distributions which produced internally excited NO fragments at a photolysis wavelength of 212.8 nm.[39] Similar peaks have been observed in the $O(^3P_J)$ distributions close to 200 nm, where they dominate the distribution.[41] It would seem that this dissociation mechanism becomes more important as the pho-

tolysis wavelength is reduced from 226 to 200 nm. Close to 226 nm, the intensity of the $O(^3P_J)$ signal at kinetic energies between 0 and 0.5 eV depends on the temperature of the source (see Fig. 5). So one must question whether or not peaks (h)–(j) in Figs. 2(d) and 2(f) are due to interference from N_2O_4; we do not believe so for the following reasons.

D. The influence of the NO_2/N_2O_4 equilibrium

The effects of the NO_2/N_2O_4 equilibrium on the UV study of the photodissociation dynamics of NO_2 have previously been discussed in literature.[16,54] In our experiments, temperature studies (Fig. 5) reveal a broad unstructured underlying feature in the $O(^3P_2)$ kinetic energy profile at lower sample gas temperatures between 0 and 0.5 eV. This feature was prominent in the $O(^3P_2)$ distribution with a significantly smaller contribution to the $O(^3P_1)$ distribution and no contribution to the $O(^3P_0)$ with a sample backing pressure of 1 bar, a NO_2 partial pressure of 2%, and a sample temperature of 295 K. The maximum of the feature occurs close to 0.1 eV. This broad feature is lost as the sample temperature is raised to ~400 K [see Figs. 2(d)–2(f)]. The feature has an overall anisotropy of 0.2 ± 0.1, which is in qualitative agreement with the results of Brouard *et al.* who observed a similar structure in the $O(^3P_2)$ velocity profile with an anisotropy of 0.1 using a room temperature sample gas, a sample pressure of 2 bar, and NO_2 partial pressures of 10%, 1%, and "trace quantities" in He.[16] Brouard *et al.* observed a decrease in the contribution of the broad unstructured component as the partial pressure of the NO_2 in their sample was reduced.. They used the spin-orbit ratio of Rubahn *et al.*[29] to normalize their speed distributions and hence to deduce that the 226 nm dissociation of N_2O_4 produces almost exclusively $O(^3P_2)$ atoms. In experiments in which we increase the total sample pressure behind our molecular beam source to 2 bar we also see a significant increase in the contribution of the broad unstructured component in the $O(^3P_2)$ kinetic energy profile, in complete agreement with the observations of Brouard *et al.* With the higher resolution afforded by the dc slice imaging technique, however, we additionally observe three peaks on top of the broad background feature at 0.22, 0.25, and 0.37 eV [peaks (h), (i), and (j) in Figs. 2(d) and 2(f), respectively]. The area under each of these peaks, unlike the underlying profile, is independent of temperature. This implies that these peaks are due to NO_2 photolysis and not due to the photolysis of a contaminant. In separate experiments, the kinetic energy profile of the $O(^3P_0)$ fragment distribution was recorded at 295 and 393 K. In this case the profile was found to be independent of temperature, supporting the interpretation that peaks (h)–(j) are due to NO_2 photolysis.

In the presence of oxygen and helium and based on the thermodynamic stabilities of the oxides of nitrogen, the only important species in these experiments are NO and N_2O_4.[55] Furthermore, in a single laser experiment close to 226 nm the photolysis of NO to produce $O(^3P_J)$ atoms can be considered unimportant.[56] At the laser fluence employed we can also discount any contribution from the dissociation of O_2.[57] As pointed out by Brouard *et al.*,[16] the reduction in the NO_2 partial pressure in the reagent mixture would push the NO_2/N_2O_4 equilibrium to favor the monomer. Under the conditions employed by Brouard *et al.* (room temperature sample, 2 bar backing pressure), NO_2 partial pressures of 10% and 1% result in 48% and 11% of the NO_2 existing in its dimeric form. Given that the N_2O_4 absorption cross section is ten times that of NO_2 close to 226 nm, we would expect the N_2O_4 photolysis products to have a yield between one and five times those of NO_2. A partial pressure of 0.01% would be required to push the equilibrium 99.9% in favor of the monomer to bring the single photon N_2O_4 photolysis yield to the sub-1% level. It is therefore unsurprising that in the experiments of Brouard *et al.*, using "trace amounts" of NO_2 did not remove the broad unstructured slow component in the $O(^3P_2)$ kinetic energy profile.

An alternative way of pushing the equilibrium of the sample gas toward the monomer is to increase its temperature. With a backing pressure of 1 bar and a NO_2 partial pressure of 2% sample temperatures of 298 and 345 K result in ~20% and ~2% of the NO_2 existing in dimeric form, respectively. We might therefore expect the single photon photolysis yield of N_2O_4 products to increase by a factor of 10 as the temperature is decreased from 345 to 298 K. In fact we observe an increase of about 3.3 which would be consistent, within the experimental uncertainty, with the dissociation of N_2O_4 via a two photon excitation (with an expected increase of $\sqrt{10}$). The anisotropy between 0 and 0.5 eV represents the average of the anisotropy of the temperature dependent feature and peaks (h)–(j). The anisotropies of peaks (h)–(j) are shown in Fig. 6; $\beta \sim 0.5$–0.8. As we measure an average anisotropy value of 0.2 between 0 and 0.5 eV at 298 K, we can consider the temperature dependent feature to be essentially isotropic. The kinetic energy profile and anisotropies of the slow $O(^3P_2)$ atoms suggest that they are either produced by a threshold dissociation process following two photon absorption of N_2O_4 in which the cofragment is formed with large internal excitation or that the $O(^3P_2)$ atoms are formed from a NO_2 photoproduct produced by the one photon dissociation of N_2O_4 in a secondary step. We cannot definitively identify the dissociation mechanism. We therefore assign the broad peak to N_2O_4 photolysis by either of the above mechanisms and peaks (h)–(j) to a dissociation process of the monomer. Without detection of the NO cofragments for the peaks (h), (i), and (j) in Figs. 2(d) and 2(f) the rovibrational profiles of these peaks cannot be definitively assigned.

E. Dissociation mechanisms

The calculations of Schinke *et al.* revealed the mechanism for the production of vibrationally cold, highly rotationally excited $NO(^2\Pi_\Omega)$ products (the major dissociation products close to 226 nm).[4] The Franck–Condon window to the parent $(2)^2B_2$ state occurs at the repulsive wall of the potential and sets up motion in the bound symmetric stretching coordinate. At the other side of the potential the motion of the NO_2 is deflected toward the dissociative asymmetric stretching coordinate with the dissociation taking place on the time scale of a single symmetric stretch vibration (~35 fs). The vibrational excitation produced due to the po-

sition of the Franck–Condon window and the excess energy in the $(2)^2B_2$ potential is retained in the dissociation, primarily producing $NO(^2\Pi_\Omega)$ in $v=0$ or 1. The narrow, inverted rotational profiles are then explained by the impulsive model with the torque for NO rotation increasing as the NO_2 bond angle decreases along the bending coordinate. The anisotropy of the relevant $O(^3P_2)$ image features implies that the average bond angle of the NO_2 as it dissociates on the adiabatic $(2)^2B_2$ surface via the major pathway lies between 118° and 129°.

At higher excitation energies the vibrational energy of this major dissociation channel increases as the initial excitation occurs higher in the $(2)^2B_2$ state resulting in a greater degree of symmetric stretch excitation. The rotational energy is calculated to remain relatively constant.[4] The overall change in internal energy should be approximately described by the solid line in Fig. 1. The major peak in the $O(^3P_1)$ distribution recorded by Ahmed *et al.*[39] close to 213 nm [at a $O(^3P_1)$ kinetic energy of 1.18 eV] can therefore be attributed to $NO(^2\Pi_\Omega)$ fragments produced in $v=2$ and $N\sim53$. The secondary peak in the $O(^3P_J)$ distributions recorded by Coroiu *et al.*[41] (at total fragment kinetic energies close to 1.24 eV) can similarly be assigned to production in coincidence with $NO(^2\Pi_\Omega)$ in $v=5$ and $N\sim59$. This correlates with the experiments of Hancock and Morrison at slightly higher excitation energy where the major peak in the vibrational profile occurs at $v=5$ [although the vibrational profile is convoluted with the profile of the $O(^1D_2)$ cofragments].[25] At this excitation wavelength we would expect a rotational distribution peaking at a rotational level close to $N=60$, as predicted by Schinke *et al.*[4]

An explanation for the production of the rotationally cold $NO(^2\Pi_\Omega)$ fragments in low vibrational levels [peaks (a)–(c) in Figs. 2(d) and 2(f)] and those produced highly internally excited [peaks (h)–(j) in Figs. 2(d) and 2(f)] is not forthcoming from the results of Schinke *et al.*[4] When the intensities of peaks (a)–(c) are analyzed in the three $O(^3P_J)$ images we measure a spin-orbit ratio of 1.00:0.65:0.15, which is in good agreement with the overall spin-orbit ratio measured for the fragments with kinetic energies between 0.50 and 1.10 eV [peaks (d)–(g)]. The vibrational profile of the fragments produced by this secondary dissociation mechanism is similar to that of the major pathway (mainly $v=0-2$). Presumably the vibrational profile of the secondary dissociation mechanism is also determined early in the dissociation by the position of the Franck–Condon window on the $(2)^2B_2$ potential. It therefore appears that there are two different pathways coupling the diabatic $(2)^2B_2$ state to $NO(^2\Pi_\Omega)+O(^3P_J)$. Two different rotational profiles result with the minor profile being due to dissociation via a more linear geometry. The similarity of the spin-orbit ratios for the two dissociation mechanisms implies that the spin-orbit branching is determined late in the dissociation.

The temperature studies strongly suggest that the $O(^3P_J)$ peaks produced with highly internally excited $NO(^2\Pi_\Omega)$ fragments are due to NO_2 photolysis at 226 nm. A more accurate investigation of the origin of these peaks could be carried out at higher excitation energies where they are prominent in the photofragment distributions and thermodynamic effects should be more obvious. It is expected that the $O(^3P_J)$ distributions measured with a room temperature sample, a total gas pressure of ~1 bar and NO_2 partial pressures close to 2% between 213 and 193 nm would contain between five and ten times more signal from two photon N_2O_4 photolysis than at 226 nm. These effects are evident in the results of Ahmed *et al.*[39] and Coroiu *et al.*,[41] who observed broad underlying features in the $O(^3P_J)$ kinetic energy distributions close to 213 and 201 nm, respectively. The wavelength dependence of the intensity ratio of the broad underlying component and the sharp features at low kinetic energies in the $O(^3P_J)$ profiles provides further evidence that these features have different origins.

A final consideration is the difference between the spin-orbit ratios measured in this study and those recorded by Rubahn *et al.*[29] close to 226 nm and Miyawaki *et al.*[58] close to 213 nm. The overall spin-orbit ratio determined at 393 K in this study is 1.00:0.71:0.15 and is the result of the photolysis of a beam containing ~0.1% N_2O_4. The room temperature gas mixtures used in the molecular beam studies carried out by Rubahn *et al.* and Miyawaki *et al.* resulted in different concentrations of N_2O_4 at their laser interaction regions. Based on the experimental conditions it is expected that the N_2O_4 concentration should be significantly higher in the experiments of Miyawaki *et al.* (between 19.4% and 48.5% of the total NO_2) in comparison to the studies of Rubahn *et al.* (between 8.8% and 32.4% of the total NO_2). The effect of the N_2O_4 is expected to be around five times greater in the studies of Miyawaki *et al.* due to the increase in the (single photon) N_2O_4 absorption cross section between 226 and 213 nm. The results of Brouard *et al.*[16] and those obtained in this study suggest that the 226 nm photolysis of N_2O_4 produces $O(^3P_J)$ photoproducts with a spin-orbit ratio heavily weighted in favor of the $O(^3P_2)$ fragment. As all of the spin-orbit ratios are normalized with respect to the $O(^3P_2)$ fragment the effects of N_2O_4 photolysis should be observed as decreases in the relative $O(^3P_1)$ and $O(^3P_0)$ signals. This effect is most obvious in the strong $O(^3P_1)$ signal which decreases, as expected, as the N_2O_4 percentage and its absorption cross section increase (0.71, 0.50, and 0.35 for 0.1% at 226 nm, 8%–33% at 226 nm, and 19%–49% at 213 nm, respectively). The effect is less obvious in the weak $O(^3P_0)$ signal, the intensity of which will be particularly sensitive to the probe laser power and the experimental signal to noise ratio. These results further illustrate the advantages of kinetic energy resolved detection of photofragments as afforded by the VMI technique.

V. CONCLUSIONS

The dissociation dynamics of NO_2 to produce $NO(^2\Pi_\Omega)$ and $O(^3P_J)$ have been studied on excitation to the $(2)^2B_2$ state close to 226 nm using REMPI spectroscopy, dc slice, and conventional velocity map ion imaging. It was previously believed that on excitation at ~226 nm to the $(2)^2B_2$ state the $O(^3P_J)+NO(^2\Pi_\Omega)$ dissociation channel led to a sharply peaked vibrational distribution with $NO(^2\Pi_\Omega)$ fragments formed in $v=4-6$. In contrast to these previous studies, the high resolution achieved by dc slice imaging of

$O(^3P_J)$ fragments coupled with REMPI spectroscopy and VMI of state selected NO fragments reveals that the dissociation favors the production of highly rotationally excited $NO(^2\Pi_\Omega)$ fragments. All three $O(^3P_J)$ spin-orbit component energy distributions are found to peak in coincidence with $NO(^2\Pi_\Omega)$ fragments in $v=0$ and 1 and $N\sim60$, with a secondary rotational maxima at $N\sim20$. The translational anisotropy of the fragments has been examined to conclude that the dissociative geometry becomes more bent (on average) as the kinetic energy release of the $O(^3P_J)$ decreases from 1.55 to 0.5 eV. The increase in the anisotropy parameter from 0.50 to 0 eV has been attributed to another minor dissociation mechanism producing kinetically cold $O(^3P_J)$ in coincidence with internally excited NO fragments.

The spin-orbit branching ratio in the $O(^3P_J)$ photoproducts is found to be markedly nonstatistical. For O fragments with a translational energy in the range of 0.50–1.55 eV the intensities of the three channels (uncorrected for degeneracy and line-strength factors) are determined to be 1.00:0.71:0.15 for the $O(^3P_2)$, $O(^3P_1)$, and $O(^3P_0)$ states, respectively. Another set of oxygen atoms with translational energies in the range of 0.00–0.50 eV are also observed. The intensity ratio for these photoproducts is found to be 1.00:0.47:0.1. Temperature studies have highlighted that these fragments are correlated with internally excited $NO(^2\Pi_\Omega)$ fragments produced from NO_2. The yield of these photofragments is noted to increase with excitation energy. Temperature studies have also demonstrated that the room temperature study of the UV NO_2 photodissociation dynamics can be biased by the photolysis of N_2O_4.

ACKNOWLEDGMENTS

I.W. is grateful to the Engineering and Physical Sciences Research Council (U.K.) (EPSRC) for a research studentship. We are also indebted to Mr. Panagiotis Kapatanopoulos for the design and construction of the high speed pulser unit used to gate the microchannel plates and to Dr. Ivan Anton-Garcia for assistance in constructing the VMI spectrometer. This work has been supported by the EPSRC Grant No. EP/G000360/1.

[1] W. C. Gardiner, Jr., *Gas-Phase Combustion Chemistry* (Springer, New York, 1999).
[2] B. J. Finlayson-Pitts and J. N. Pitts, *Chemistry of the Upper and Lower Atmosphere: Theory, Experiments, and Applications* (Academic, New York, 1999).
[3] J. Rolke, N. Cann, Y. Zheng, B. P. Hollebone, C. E. Brion, Y. A. Wang, and E. R. Davidson, Chem. Phys. **201**, 1 (1995).
[4] R. Schinke, S. Y. Grebenshchikov, and H. Zhu, Chem. Phys. **346**, 99 (2008).
[5] R. Jost, M. Joyeux, and M. Jacon, Chem. Phys. **283**, 17 (2002).
[6] W. Schneider, G. K. Moortgat, G. S. Tyndall, and J. P. Burrows, J. Photochem. Photobiol., A **40**, 195 (1987).
[7] A. C. Vandaele, C. Hermans, P. C. Simon, M. Carleer, R. Colin, S. Fally, M. F. Merienne, A. Jenouvrier, and B. Coquart, J. Quant. Spectrosc. Radiat. Transf. **59**, 171 (1998).
[8] M. F. Merienne, A. Jenouvrier, B. Coquart, and J. P. Lux, J. Atmos. Chem. **27**, 219 (1997).
[9] J. W. Au and C. E. Brion, Chem. Phys. **218**, 109 (1997).
[10] G. E. Busch and K. R. Wilson, J. Chem. Phys. **56**, 3638 (1972).
[11] R. Jost, J. Nygard, A. Pasinski, and A. Delon, J. Chem. Phys. **105**, 1287 (1996).
[12] K. P. Huber and G. Herzberg, *Molecular Spectra and Molecular Structure: Constants of Diatomic Molecules* (Van Nostrand Reinhold, New York, 1979), Vol. IV.
[13] Y. Ralchenko, A. E. Kramida, J. Reader, and N. A. Team, National Institute of Standards and Technology, 2008.
[14] G. E. Busch and K. R. Wilson, J. Chem. Phys. **56**, 3626 (1972).
[15] G. Herzberg, *Molecular Spectra and Molecular Structure: Electronic Spectra and Electronic Structure of Polyatomic Molecules* (Krieger, Malabar, FL, 1966), Vol. III.
[16] M. Brouard, R. Cireasa, A. P. Clark, T. J. Preston, and C. Vallance, J. Chem. Phys. **124**, 064309 (2006).
[17] G. Inoue, Y. Nakata, Y. Usui, H. Akimoto, and M. Okuda, J. Chem. Phys. **70**, 3689 (1979).
[18] J. A. Mueller, M. L. Morton, S. L. Curry, J. P. D. Abbatt, and L. J. Butler, J. Phys. Chem. A **104**, 4825 (2000).
[19] L. Harris and G. W. King, J. Chem. Phys. **8**, 775 (1940).
[20] R. K. Ritchie, A. D. Walsh, and P. A. Warsop, Proc. R. Soc. London, Ser. A **266**, 257 (1962).
[21] R. S. Mulliken, Rev. Mod. Phys. **14**, 204 (1942).
[22] T. Nakayama, M. Y. Kitamura, and K. Watanabe, J. Chem. Phys. **30**, 1180 (1959).
[23] A. D. Walsh, J. Chem. Soc. **1953**, 2260 (1953).
[24] W. M. Uselman and E. K. C. Lee, J. Chem. Phys. **65**, 1948 (1976).
[25] G. Hancock and M. Morrison, Mol. Phys. **103**, 1727 (2005).
[26] K. Tsuji, M. Ikeda, J. Awamura, A. Kawai, and K. Shibuya, Chem. Phys. Lett. **374**, 601 (2003).
[27] K. F. Preston and R. J. Cvetanovic, J. Chem. Phys. **45**, 2888 (1966).
[28] F. Sun, G. P. Glass, and R. F. Curl, Chem. Phys. Lett. **337**, 72 (2001).
[29] H. G. Rubahn, W. J. Van Der Zande, R. Zhang, M. J. Bronikowski, and R. N. Zare, Chem. Phys. Lett. **186**, 154 (1991).
[30] J. Miyawaki, K. Yamanouchi, and S. Tsuchiya, J. Chem. Phys. **99**, 254 (1993).
[31] C. B. Mckendrick, C. Fotakis, and R. J. Donovan, J. Photochem. **20**, 175 (1982).
[32] T. G. Slanger, W. K. Bischel, and M. J. Dyer, J. Chem. Phys. **79**, 2231 (1983).
[33] J. Mcfarlane, J. C. Polanyi, and J. G. Shapter, J. Photochem. Photobiol., A **58**, 139 (1991).
[34] M. Ahmed, D. S. Peterka, and A. G. Suits, in *Atomic and Molecular Beams*, edited by R. Campargue (Springer-Verlag, Berlin, 2001), p. 343.
[35] C. Morrell, C. Breheny, V. Haverd, A. Cawley, and G. Hancock, J. Chem. Phys. **117**, 11121 (2002).
[36] B. F. Parsons, S. L. Curry, J. A. Mueller, P. C. Ray, and L. J. Butler, J. Chem. Phys. **111**, 8486 (1999).
[37] M. Kawasaki, H. Sato, A. Fukuroda, T. Kikuchi, S. Kobayashi, and T. Arikawa, J. Chem. Phys. **86**, 4431 (1987).
[38] W. N. Sisk, C. E. Miller, and H. S. Johnston, J. Phys. Chem. **97**, 9916 (1993).
[39] M. Ahmed, D. S. Peterka, A. S. Bracker, O. S. Vasyutinskii, and A. G. Suits, J. Chem. Phys. **110**, 4115 (1999).
[40] R. C. Richter, V. I. Khamaganov, and A. J. Hynes, Chem. Phys. Lett. **319**, 341 (2000).
[41] A. M. Coroiu, D. H. Parker, G. C. Groenenboom, J. Barr, I. T. Novalbos, and B. J. Whitaker, Eur. Phys. J. D **38**, 151 (2006).
[42] D. Townsend, M. P. Minitti, and A. G. Suits, Rev. Sci. Instrum. **74**, 2530 (2003).
[43] E. Wrede, S. Laubach, S. Schulenburg, A. Brown, E. R. Wouters, A. J. Orr-Ewing, and M. N. R. Ashfold, J. Chem. Phys. **114**, 2629 (2001).
[44] N. Yonekura, C. Gebauer, H. Kohguchi, and T. Suzuki, Rev. Sci. Instrum. **70**, 3265 (1999).
[45] A. T. J. B. Eppink and D. H. Parker, Rev. Sci. Instrum. **68**, 3477 (1997).
[46] *Imaging in Molecular Dynamics: Technology and Applications*, edited by B. J. Whitaker (Cambridge University Press, Cambridge, 2003).
[47] H. S. Im and E. R. Bernstein, J. Phys. Chem. A **106**, 7565 (2002).
[48] L. Bigio, R. S. Tapper, and E. R. Grant, J. Phys. Chem. **88**, 1271 (1984).
[49] C. Amiot, J. Mol. Spectrosc. **94**, 150 (1982).
[50] J. Luque and D. R. Crosley, LIFBASE: Database and Spectral Simulation Program, (Version 1.5), SRI International Report MP 99–009 (1999).
[51] I. Wilkinson and B. J. Whitaker (unpublished).
[52] R. Schinke, *Photodissociation Dynamics* (Cambridge University Press, Cambridge, 1993).

[53] R. N. Zare, *Angular Momentum, Understanding Spatial Aspects in Chemistry and Physics* (Wiley, New York, 1988).
[54] A. T. J. B. Eppink, B. J. Whitaker, E. Gloaguen, B. Soep, A. M. Coroiu, and D. H. Parker, J. Chem. Phys. **121**, 7776 (2004).
[55] N. N. Greenwood and A. Earnshaw, *Chemistry of the Elements* (Butterworth-Heinemann, London, 1995).
[56] B. L. G. Bakker, A. T. J. B. Eppink, D. H. Parker, M. L. Costen, G. Hancock, and G. A. D. Ritchie, Chem. Phys. Lett. **283**, 319 (1998).
[57] B. Buijsse, W. J. Van Der Zande, A. T. J. B. Eppink, D. H. Parker, B. R. Lewis, and S. T. Gibson, J. Chem. Phys. **108**, 7229 (1998).
[58] J. Miyawaki, T. Tsuchizawa, K. Yamanouchi, and S. Tsuchiya, Chem. Phys. Lett. **165**, 168 (1990).

Appendix B

Published article: Photodissociation of NO_2 in the $(2)^2B_2$ state; the $O(^1D_2)$ dissociation channel

The article presented below was published in the Journal of Chemical Physics and describes the imaging studies and the interpretation of those experiments that have been presented in Chapter 5. The article was principally written by myself where I took advice about corrections to the paper from my supervisor, Dr Marcelo de Miranda and the journal article referees. However, the angular momentum theory presented in the paper was almost exclusively written by Dr de Miranda. The article is very similar in structure to Chapter 5.

Photodissociation of NO_2 in the (2) $^2B_2$ state: The $O(^1D_2)$ dissociation channel

Iain Wilkinson, Marcelo P. de Miranda, and Benjamin J. Whitaker[a)]
School of Chemistry, University of Leeds, Leeds LS2 9JT, United Kingdom

(Received 27 March 2009; accepted 14 July 2009; published online 6 August 2009)

Direct current slice and crush velocity map imaging has been used to probe the photodissociation dynamics of nitrogen dioxide above the second dissociation limit. The paper is a companion to a previous publication [J. Chem. Phys. **128**, 164318 (2008)] in which we reported results for the $O(^3P_J)+NO(^2\Pi_\Omega)$ adiabatic product channel. Here we examine the $O(^1D_2)+NO(^2\Pi_\Omega)$ diabatic product channel at similar excitation energies. Using one- and two-color imaging experiments to observe the velocity distributions of state selected NO fragments and O atoms, respectively, we are able to build a detailed picture of the dissociation dynamics. We show that by combining the information obtained from velocity map imaging studies with mass-resolved resonantly enhanced multiphoton ionization spectroscopy it is possible to interpret and fully assign the NO images. By recording two-color images of the $O(^1D_2)$ photofragments with different polarization combinations of the pump and probe laser fields we also measure the orbital angular momentum alignment in the atomic fragment. We find that the entire $O(^1D_2)$ photofragment distribution is similarly aligned with most of the population in the $M_J=\pm 1$ magnetic sublevels. The similarity of the fragment polarizations is interpreted as a signature of all of the $O(^1D_2)$ atoms being formed via the same avoided crossing. At the photolysis energy of 5.479 52 eV we find that the NO fragments are preferentially formed in $v=1$ and that the vibrationally excited fragments exhibit a bimodal rotational distribution. This is in contrast to the unimodal rotational profile of the NO fragments in $v=0$. We discuss these observations in terms of the calculated topology of the adiabatic potential energy surfaces and attribute the vibrational inversion and rotational bimodality of the $v=1$ fragments to the symmetric stretch and bending motion generated on excitation to the (2) $^2B_2$ state. © *2009 American Institute of Physics*. [DOI: 10.1063/1.3194286]

I. INTRODUCTION

The photodissociation of nitrogen dioxide (NO_2) has been studied for more than half a century. The deceptively complex triatomic plays critical roles in the chemistry of combustion,[1] the stratosphere, and the troposphere.[2] Nitrogen dioxide has also been an important subject of study in the development of reaction dynamics.[3,4] The nature of the strongly vibronically coupled low-lying electronic states and subsequent nonadiabatic dynamics has been vital to our understanding of dynamically driven (nonstatistical) fragmentation and energy partitioning. Due to the wavelength filtering of the stratospheric ozone layer and the accessibility of near ultraviolet wavelengths in the laboratory, the majority of previous photodissociation studies have focused on excitation to the (2) $^2A'$ state [also labeled (1) $^2B_2$ in C_{2v} symmetry or the $\tilde{B}$ state in C_s or C_{2v}]. At excitation energies in excess of 3.115 546(6) eV,[5] ground state oxygen atoms are produced in coincidence with $NO(^2\Pi_\Omega)$ fragments via this photoexcited state. In this paper we focus on the second dissociation limit associated with excitation to the (3) $^2A'$ [(2) $^2B_2$ or $\tilde{D}$] state to produce $O(^1D_2)$ and $O(^3P_J)$ in coincidence with $NO(^2\Pi_\Omega)$.

In a previous paper we gave an overview of the photophysics of NO_2 and demonstrated that dissociation via the predissociative (3) $^2A'$ state forms $O(^3P_J)$ atoms in coincidence with highly rotationally excited $NO(^2\Pi_\Omega)$ fragments.[6] Secondary dissociation pathways were also identified. These experiments highlighted the complexity of the dissociation dynamics above the second dissociation limit. Here we will discuss the dissociation dynamics of the $O(^1D_2)+NO(^2\Pi_\Omega)$ dissociation channel.

The second absorption band of NO_2 (248–193 nm)[7] is attributed to a pure parallel transition to the (3) $^2A'$ state, which carries all of the oscillator strength across this excitation range.[8] The origin of this potential occurs at an excitation energy of 4.974 98 eV,[9] where the state is known to have a lifetime of 41.0 ± 1.6 ps.[10,11] At this energy the potential is calculated to be weakly bound with a shallow well in the asymmetric stretching coordinate in the adiabatic representation.[8] Predissociation rates of specific vibrational levels are found to increase sharply with increasing vibrational excitation below the second dissociation limit. The lifetime is observed to reduce to the sub-100-fs regime above the (0, 0, 2) level, with no marked decrease observed at higher excitation energies.[8,11,12] Below the energetic threshold for $O(^1D_2)$ production the correlation of the adiabatic (3) $^2A'$ state with the first dissociation limit primarily results in the production of internally excited $NO(^2\Pi_\Omega)$ concomitantly with $O(^3P_J)$.[6,8,13,14] At excitation energies above

a)Electronic mail: b.j.whitaker@leeds.ac.uk.

5.082 91 eV, dissociation to produce ground state NO in coincidence with electronically excited oxygen atoms can occur. The threshold for the production of NO $^2\Pi_{3/2}$ occurs 14.856 meV above this level:

$$NO_2(1\ ^2A') \rightarrow NO(^2\Pi_{1/2};0,0) + O(^1D_2) \times \hbar\omega \geq 5.082\ 91\ \text{eV},$$

$$NO_2(1\ ^2A') \rightarrow NO(^2\Pi_{3/2};0,0) + O(^1D_2) \times \hbar\omega \geq 5.097\ 77\ \text{eV}.$$

At excitation energies between 5.1 and 6.4 eV, the $O(^1D_2)$ yield is found to remain relatively constant, between 0.4 and 0.5.[15–18] The experiments of Tsuji *et al.* highlight that the opening of the $O(^1D_2)$ dissociation channel has no effect on the lifetime of the (3) $^2A'$ state.[11] Recent calculations by Schinke *et al.* give an overview of the topography of the (3) $^2A'$ potential and emphasize its correlation with the $O(^1D_2)$ dissociation channel in the diabatic representation.[8] These calculations also suggest that avoided crossings between the (3) $^2A'$ and (4) $^2A'$ adiabatic surfaces (which occur at bond angles close to 110° and extended ON–O bond lengths) are responsible for determining the $O(^3P_J)$:$O(^1D_2)$ branching ratio.

A number of previous experimental studies have been carried out to measure the rovibrational product distribution of the NO fragments produced in coincidence with $O(^1D_2)$ on excitation to the (3) $^2A'$ state.[17–26] Ahmed *et al.* used velocity map imaging[27] (VMI) to photodissociate and state selectively probe the NO fragments at excitation energies between 5.49 and 5.64 eV in all three energetically accessible vibrational states with which $O(^1D_2)$ can be formed.[25] By probing different rotational states of the $NO(^2\Pi_\Omega)(0,0)$ $A \leftarrow X$ vibrational band using (1+1) REMPI (resonantly enhanced multiphoton ionization), these investigators found that the $O(^1D_2)$:$O(^3P_J)$ branching ratio varied with rotational state. This was attributed to the production of markedly different rotational distributions via the $O(^3P_J)$ and $O(^1D_2)$ dissociation channels. A similar effect was observed in the (1, 1) and (2, 2) vibrational bands.

Im and Bernstein studied the photodissociation across a similar photolysis energy range, 5.23–5.71 eV.[19] By probing the nascent $NO(^2\Pi_\Omega)$ generated using a one-laser fragmentation/REMPI detection scheme, mass-resolved excitation spectra were recorded which were assumed to probe the $O(^1D_2)$ dissociation channel exclusively. They characterized the rotational energy distributions of the $NO(^2\Pi_\Omega)$ produced in these vibrational bands with a rotational temperature of approximately 200 K. In an earlier study, Bigio *et al.* measured similar mass-resolved excitation spectra at energies between 5.49 and 5.64 eV and also attributed the spectra to $NO(^2\Pi_\Omega)$ fragments produced in coincidence with $O(^1D_2)$.[26] They found that $NO(^2\Pi_\Omega)$ fragments produced via this dissociation channel had a propensity to populate the highest accessible vibrational level, $v=2$. Similar time-of-flight (TOF) measurements of the $NO(^2\Pi_\Omega)$ and $O(^1D_2)$ fragments have been carried out at excitation energies of ~5.83 eV (Ref. 21) and ~6.03 eV.[22] Both studies measured diatomic fragment vibrational profiles which peaked in the highest accessible vibrational levels. Similarly inverted vibrational profiles have also been observed at higher excitation energies.[17]

Coroiu *et al.* probed the $O(^1D_2)$ translational energy distribution and orbital angular momentum alignment using VMI.[23] They also recorded a marked vibrational inversion. The differences in the distributions measured using single-laser fragmentation and (2+1) REMPI detection schemes centered at excitation energies of 6.03 eV [via the $3p^1$ ($^1P_1$) state] and 6.09 eV [via the $3p^1$ ($^1F_3$) state] were used to assess the electronic orbital angular momentum alignment. This was found to be significant in the $O(^1D_2)$ fragment with the M_J substate populations varying as a function of the NO cofragment internal energy. Analysis of the fragment polarization also allowed the translational anisotropy of the distribution to be fitted. At these photolysis energies the translational anisotropy parameter was found to decrease as more energy was partitioned into internal modes of the NO.

Vector correlation measurements (**v**,**J**) in dissociation processes provide a sensitive probe of the nature of dissociative photoexcited states. In the case of molecular fragments, the correlation of the rotational angular momentum with the fragment recoil velocity gives information about the topography of the dissociative potential. For atomic fragments, the correlation of the orbital angular momentum vector with the recoil velocity of the fragment gives information about the electronic symmetry of the dissociative electronic state. These measurements are particularly useful when dissociative processes occur on optically dark potentials. Polarized photofragment distributions have been measured using a variety of techniques including Doppler,[28,29] ion TOF,[30,31] and ion imaging[23,32–34] methods. A strength of ion imaging techniques in carrying out these measurements is that the entire photoproduct energy and angular profiles are recorded in a single experiment. However, as aligned or oriented photoproduct distributions (those with nonequivalent M_J substate populations) do not necessarily posses axes of cylindrical symmetry, the implementation of the analytic inversion techniques commonly used to construct the original three-dimensional ion distributions from their two-dimensional projections are not generally applicable.[35] Although specific aligned photoproduct distributions may be studied using inversion methods[36,37] more general treatments require complex forward convolution techniques[38–41] or fitting procedures[42] to extract the alignment information from the raw experimental data. A strength of slice ion imaging approaches[43–46] is that the central portion of the photoproduct distribution (which carries all of the photofragment radial and angular information) is measured directly. This allows photofragment alignment moments, translational anisotropies, and energy distributions to be extracted from the raw images generated using different laser polarization combinations without the need to invert or deconvolute radial profiles if the slice is sufficiently narrow. The use of these methods is particularly appealing when photofragments are produced with a range of kinetic energies. In this case a small basis set corresponding to particular sets of alignment and translational anisotropy parameters can be used to fit to the experimental anisotropies at different kinetic energies. The fitting

parameters then yield the molecular-frame photofragment polarization information and the translational anisotropy which can be used to reconstruct the kinetic energy profile of the fragments.

In this paper we describe experiments using the direct current (dc) slice[43] and crush[27] variants of the VMI technique to unravel the photodissociation dynamics of the $NO(^2\Pi_\Omega)$ $+O(^1D_2)$ dissociation channel of NO_2 at excitation energies close to 5.49 eV. By probing both the atomic and molecular fragments we highlight distinct fragmentation pathways producing $NO(^2\Pi_\Omega)$ fragments with differing degrees of internal excitation. Atomic fragment polarization measurements allow us to indirectly probe the nonadiabatic dynamics responsible for these fragmentation pathways. The paper is organized in the conventional experimental, results, discussion, and conclusions format.

II. EXPERIMENTAL

In our experiments dc slice and crush VMI has been employed in conjunction with mass-resolved REMPI spectroscopy using linearly polarized light fields in order to probe the nitric oxide and electronically excited atomic oxygen photoproducts of nitrogen dioxide photolysis at excitation energies close to 5.49 eV (~226 nm). Reagent molecules were entrained in a pulsed supersonic expansion of 2% NO_2 (Air Products Ltd.) purified by reaction with 5% O_2 (BOC gases) in a seed gas of He (BOC gases). The supersonic expansion was created by a heated pulsed valve (General Valve) with a 500 μm orifice and a backing pressure of ~1 bar. For all of the experiments reported here the nozzle was held at 393 K in order to push the NO_2/N_2O_4 equilibrium to 99.9% in favor of the monomer. The expansion chamber was held at a pressure between 1×10^{-6} and 8×10^{-6} mbar throughout the experiments. The rotational temperature of the molecular beam was determined to be ~20 K from the rotational profile of NO contaminant in the NO_2 expansion. This molecular beam was doubly skimmed 50 and 600 mm downstream from the orifice using 1 and 2 mm diameter skimmers (Beam Dynamics), respectively, in order to limit its translational velocity perpendicular to the direction of travel. The second skimmer lies at the base of a set of VMI ion/electron optics based on the designs of Wrede *et al.*[47] and Yonekua *et al.*[48] The ion/electron optics were mounted so as to project the photoion or photoelectron distributions along the axis of the molecular beam propagation and were designed to operate both in crush VMI (Ref. 27) and dc slicing modes[43] depending on the extraction voltages employed. The detection chamber was held at a pressure close to 1×10^{-8} mbar throughout these experiments. The frequency tripled output of a neodymium doped yttrium aluminum garnet (Nd:YAG) laser (Continuum Surelite III-10) was used to pump a dye laser (Sirah Cobra Stretch) operating with a Coumarin 2 dye (Exciton). The fundamental output of the dye laser was frequency doubled to produce pulses with maximum energies between 2.5 and 3.0 mJ at a repetition rate of 10 Hz between 5.46 and 5.69 eV (227 and 218 nm) with a temporal profile of 4 ns [at full width at half maximum (FWHM)]. During the experiments, the laser energy was maintained between 50 and 300 μJ and was focused with a 250 mm fused silica lens in the center of the molecular beam. The single-laser pulse photodissociated NO_2 and ionized the nitric oxide photofragments via a (1+1) REMPI process.

$O(^1D_2)$ fragments were probed by another laser via a (2+1) REMPI process with a probe photon energy centered around 6.034 10 eV (~205.473 nm). The laser was Doppler scanned to probe the entire atomic distribution via the $2p^33p^1$ ($^1P_1$) intermediate level. The probe light was generated by a dye laser (Sirah Cobra Stretch) operating with an Exalite 411 dye (Exciton) and pumped by the third harmonic of another Nd:YAG laser (Continuum Surelite II-10). The fundamental output of the dye laser was frequency doubled to produce a maximum of 600 μJ of probe light with a temporal profile of 4 ns (FWHM). In the $O(^1D_2)$ imaging experiments, the probe energy was actually maintained below 170 μJ to prevent saturation. The probe beam was counterpropagated with respect to the pump beam and was focused by another 250 mm focal length lens a few millimeters beyond the molecular beam in an effort to uniformly probe the photoproduct distributions. A Soleil–Babinet compensator (Optics for Research, SB-10) was used to rotate the pump laser polarization and a photoelastic modulator (Morvue Electronic Systems, MFS 3) was used to vary the polarization of the probe.

Photoions/photoelectrons were detected at the end of a 310 mm mu-metal shielded field-free TOF tube by a dual microchannel plate vacuum detector in a chevron arrangement (40 mm diameter, with a P43 phosphor screen; Photek). The detector was gated to detect ions of a given mass and for slicing experiments to detect the central part of one of the photoproduct distributions. In the slicing experiments, the detector on time was maintained below 10 ns using a custom built power supply (Photek). Images were captured using a 640×480 pixel charged couple device camera (LaVision Imager 3) and were averaged and processed using the DAVIS software package (LaVision) and an event counting macro. Crush velocity map images were postprocessed using the Hankel/Abel transform to reconstruct the photoproduct distributions after the projection.[35] To generate kinetic energy distributions, all velocity map images (crush and slice) were integrated with respect to angle and the resulting intensity profiles were multiplied by the appropriate Jacobian $[r\sin(\theta)]$ in order to represent them as a one-dimensional (1D) function. The 1D profiles were then calibrated in energy using NO photoionization or O_2 photodissociation, the mechanisms and energetics of which are well understood. In the case of slice images, this treatment assumes an infinitely narrow slice of the photoproduct distribution. Although this is an approximation, the treatment has previously been used to accurately reproduce photoproduct energy and angular distributions from slice images (provided a narrow enough slice of the distribution is measured).[37,45,49–53]

III. RESULTS

The rotational profiles of the NO fragments formed in coincidence with $O(^1D_2)$ and $O(^3P_J)$ were probed using a

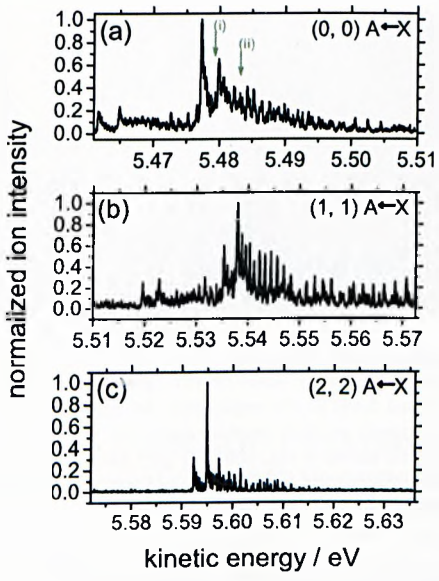

FIG. 1. Experimental mass-resolved (1+1) REMPI spectra of the (0, 0), (1, 1), and (2, 2) $A \leftarrow X$ bands of NO($^2\Pi_\Omega$), panels (a), (b), and (c) respectively. The vertical arrows (i) and (ii) in panel (a) indicate excitation energies at which dc slice images of the NO fragments have been recorded (see text and Figs. 4–6 for details).

single-laser and mass-resolved REMPI spectroscopy. In these experiments the wavelength of the dissociating laser was scanned in order to probe different NO rotational states. For the O($^1D_2$) channel the three accessible NO vibrational levels (v=0–2) were probed (respectively) between 5.462 and 5.510 eV (227.0 and 225.0 nm), 5.515 and 5.575 eV (224.8 and 222.4 nm), and 5.575 and 5.623 eV (224.4 and 220.5 nm). These REMPI spectra may be affected by rotational angular momentum alignment effects resulting in less efficient ionization of certain NO fragments, in particular, rotational states. However, assuming that these effects are small for low rotational quantum numbers and are similar across particular rotational bands, the rotational profiles should be qualitatively correct. Figure 1 shows single-color REMPI spectra spanning the (0, 0), (1, 1), and (2, 2) vibrational bands of the NO $^2\Pi_\Omega$ $A \leftarrow X$ transition. Single-color dc slice and crushed velocity map images of NO($^2\Pi_\Omega$) fragments were also recorded at a number of different excitation energies in the (0, 0), (1, 1), and (2, 2) vibrational bands. Figure 2 shows dc slice velocity map images of the O($^1D_2$) fragment produced on excitation to the (3) $^2A'$ state at 5.479 52 eV for different polarization combinations. This excitation energy should allow a direct comparison with the single-color O($^3P_0$) data recorded in our previous publication.[6] In these experiments pump-probe delays were maintained at 15 ns. Probe only images are shown in Fig. 3; these images were normalized with respect to the two-color images and subtracted from them in order to produce the images shown in Fig. 2. Obvious orbital angular momentum alignment effects are observed in Fig. 2 [particularly in the low energy feature of panel (a)] and it is noteworthy that the angular profiles produced by photolysis close to 5.48 eV (two-color experiment) and 6.03 eV (probe only experiment) shown in Fig. 3 are very different.

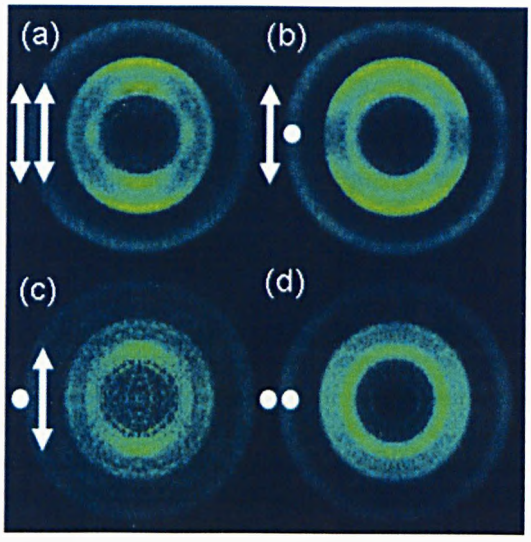

FIG. 2. dc slice velocity map images of the O($^1D_2$) fragment. Panels (a)–(d) correspond to the images recorded with the pump and probe laser polarizations respectively aligned parallel-parallel, parallel-perpendicular, perpendicular-parallel, and perpendicular-perpendicular to the detector face. The photolysis energy is 5.4795 eV (226.27 nm). The probe photon energy is 6.0341 eV (205.47 nm).

IV. DISCUSSION

A. NO rovibrational profiles

The rotational profiles of the NO $^2\Pi_\Omega$ fragments produced from NO_2 photolysis between 5.46 and 5.69 eV have previously been described by a thermal distribution using a range of rotational temperatures between 200 and 1600 K.[19,26] Although there is no reason *a priori* that a dissociation process should produce a statistical rotational distribution, we can approximately describe the REMPI spectrum shown in Fig. 1(a) with a rotational temperature between 300 and 400 K. As with previous experiments,[19,26] the rotational profiles in Fig. 1 have been recorded with a single laser. This results in an increase in the photolysis energy as higher rotational states are probed in the R branches of the distributions. Although the change in photolysis energy is relatively small across the rotational profiles [0.05, >0.06, and 0.03 eV for Figs. 1(a)–1(c), respectively], this corresponds to a potential increase of 11–17 in the rotational quantum number. This means that it is not strictly valid to

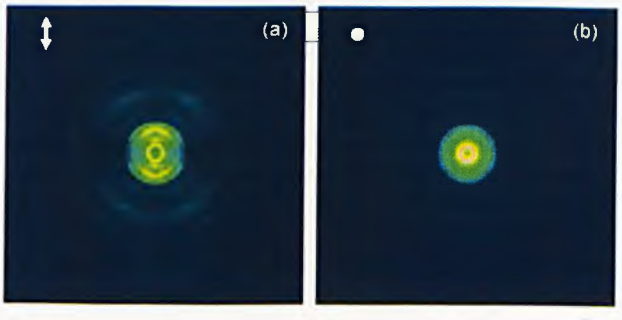

FIG. 3. Single-color, probe only dc slice velocity map images of the O($^1D_2$) fragment produced at 6.03 eV (205.47 nm). Panels (a) and (b) correspond to probe polarizations aligned parallel and perpendicular to the detector face, respectively.

model the rotational profiles using a single rotational temperature. Nonetheless, we can make some qualitative statements. In Fig. 1(a), the P_1 branch peaks at a rotational quantum number between $N=7$ and 9 [in Hund's case (b) nomenclature] at photolysis energies close to 5.480 eV with the R_1 branch peaking close to $N=9$ or 10 close to 5.485 eV. The P_2, Q_2, and R_2 branches imply similar, albeit slightly lower, peak N values in the rotational distribution at lower photolysis energies (close to 5.465 eV). We note that these branches, which are due to ionization of spin-orbit excited NO, show that the $^2\Pi_{3/2}$ fragments are produced with a smaller yield than the ground state fragments. We also note that the rotational level population decays below our detection limit at a rotational quantum number close to $N=22$ at the highest photolysis energies (~5.50 eV) employed in Fig. 1(a). In contrast to the unimodal rotational profiles observed in the (0, 0) band, the (1, 1) and (2, 2) rotational profiles display bimodal distributions. Accurate analyses of these rotational profiles [shown in Figs. 1(b) and 1(c)] are difficult due to the changes in the distributions across the branches as the photolysis and probe energy is scanned. We can, however, say that the (1, 1) band consists of a relatively "cold" rotational distribution (peaking close to $N=7$ for both NO spin-orbit components between 5.520 and 5.545 eV) along with a set of features associated with another "hotter" rotational contour (peaking between $N=21$ and 25 at photolysis energies between 5.550 and 5.575 eV for the fragments in the ground spin-orbit state). The (2, 2) rotational profile shown in Fig. 1(c) represents a colder bimodal rotational distribution (as is expected when the majority of the available excess energy has been partitioned into the NO vibrational mode). We can approximately describe this distribution using two profiles, one peaking close to $N=4$ or 5 and the other close to $N=12-14$. As might be expected the distribution, produced close to the energetic threshold, shows almost no population of the excited spin-orbit state. All three rotational profiles in Fig. 1 seem consistent with rotational populations which peak at higher rotational energies as the photolysis energy increases.

At excitation energies between 5.46 and 5.63 eV the $O(^3P_J)$ and the $O(^1D_2)$ product channels are open with a branching ratio which is close to 1:1.[15–18] To determine the origin of the features in the REMPI spectra in Fig. 1, dc slice and crush velocity map images have been recorded on different rotational lines in the three spectra. One of the limitations of the dc slice imaging technique is that the method can result in the measurement of low resolution (and in extreme cases biased) kinetic energy profiles for fragments which are formed with low momenta.[19] The ability to stretch a photoproduct ion distribution along the TOF axis of the spectrometer (and therefore detect a narrow central part of the Newton sphere) is nonlinearly proportional to the fragment mass and its kinetic energy. For a given species and detection gate width, the kinetic energy resolution of the technique increases with the kinetic energy of the fragment. For this reason, under our experimental conditions dc slice imaging offers improved resolution for $NO(^2\Pi_\Omega)$ fragments produced in $v=0$ with relatively little rotational excitation ($N=0-22$). However, in the case of fragments produced in $v=1$ and 2 the kinetic energy release is small enough that crush VMI offers equally good energy resolution despite the noise introduced by the reconstruction. Figures 4(a) and 4(b) show representative single-color dc slice images of $NO(^2\Pi_\Omega)$ fragments primarily produced in $v=0$. The kinetic energy profiles of images (a) and (b) are shown in Figs. 5 and 6.

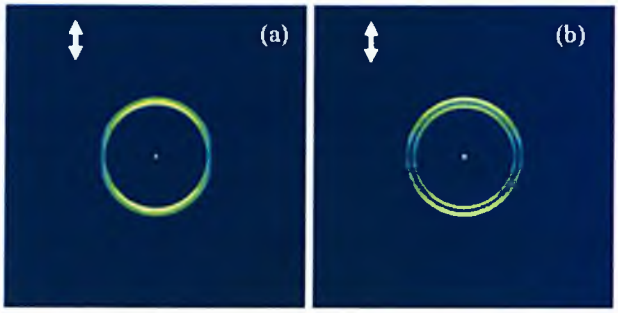

FIG. 4. dc slice velocity map images of $NO(^2\Pi_\Omega)$ fragments primarily produced in different rotational states of $v=0$. The photolysis/probe energies are 5.479 41 and 5.483 24 eV, respectively, for panels (a) and (b). These energies correspond to those marked above the rotational lines in the REMPI spectrum shown in Fig. 1(a) with gray arrows. The double headed arrows on the images show the alignment of the photolysis/probe laser polarization vector with respect to the detector face.

The energy distribution shown in Fig. 5 exhibits two main peaks [(iii) and (iv)] with a number of less intense features, shown in an expanded view in the insert. At an excitation energy of 5.479 41 eV, NO_2 photodissociates to give NO $^2\Pi_{1/2}$ with $O(^1D_2)$ with an excess energy of 397 meV and NO $^2\Pi_{1/2}$ with $O(^3P_2)$ with an excess energy of 2.364 eV. This energy is partitioned between electronic (spin-orbit), vibrational, and rotational degrees of freedom to produce a rovibrational profile which is similar to the one shown in Fig. 1. The remaining energy is partitioned, conserving linear momentum, into the fragment translational energy. The laser energy and focus employed in our single-laser experiment only allows us to probe NO $^2\Pi_\Omega$ fragments in a (1+1) REMPI process. At a photolysis energy of 5.479 41 eV we are quasiresonant with the $P_1(1)$, $P_1(16)$, $R_2(12)$, $Q_2(17)$, and $O_{12}(34)$ transitions of the (0,0) $A \leftarrow X$

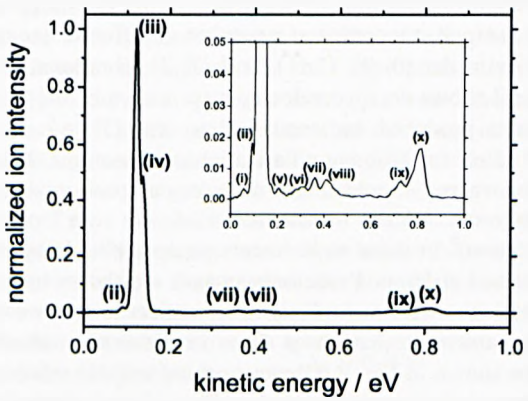

FIG. 5. Energy distribution produced by integrating the image in Fig. 4(a) with respect to angle, multiplying the resultant intensity profile by the appropriate Jacobian, squaring the image radius, and multiplying the result by the energy calibration factor. The inset shows an expanded intensity scale to highlight the weaker features in the energy distribution.

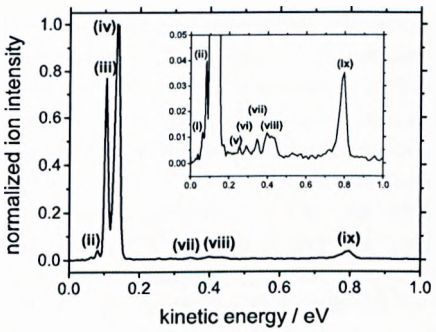

FIG. 6. As Fig. 5 but for the image in Fig. 4(b).

band. As we can only probe the $N=1$ and 16 and 12, 17, and 34 rotational levels of NO in $v=0$ for the ground and excited spin-orbit states, respectively, we can calculate the expected kinetic energy of the NO $^2\Pi_\Omega$ product. Some calculated kinetic energies are shown in the right-hand column of Table I.

Based on Fig. 1(a) we expect peaks associated with ground spin-orbit state fragments to be most intense. We therefore attribute peaks (iii) and (iv) in Fig. 5 to NO $^2\Pi_{1/2}$ ($v=0$) products formed in $N=16$ and $N=1$, respectively, with $O(^1D_2)$. This is in good agreement with the calculated kinetic energy release of these fragments (Table I). In addition to these intense peaks we also expect to see NO $^2\Pi_{3/2}$ fragments formed in $v=0$ and $N=12$ and 17. These fragments would be formed with kinetic energies of ~121 and ~110 meV, respectively, and are likely masked by the more intense ground spin-orbit state peak due to fragments in $N=16$. A weak peak is also observed at 53 meV due to the rotationally excited fragments, $N=34$, formed with a low yield in the excited spin-orbit state and probed via the O_{12} band [peak (i)].

As NO $^2\Pi_\Omega$ fragments are equally produced with $O(^3P_J)$ and $O(^1D_2)$ fragments we might also expect to see intense features in Fig. 5 due to NO produced via the first dissociation channel. However, as has been shown in our previous paper,[6] the majority of the NO fragments formed in $v=0$ concomitantly with $O(^3P_J)$ are highly rotationally excited ($N_{max}\sim 60$ at photolysis energies of ~5.494 eV). As the NO fragments produced in coincidence with $O(^3P_J)$ are likely spread over 7 or more vibrational states and in excess of 60 rotational states in the $v=0$–3 levels, their contribution to the energy distribution shown in Fig. 5 is likely small. Despite this we do see weak features at NO kinetic energies close to 0.4 and 0.8 eV which, on energetic grounds, can only be NO fragments produced with $O(^3P_J)$. Peak (x) is attributed to NO($^2\Pi_\Omega$) fragments produced in $v=0$ and $N\sim 12$–17 via a secondary $O(^3P_J)$ dissociation channel (which produces vibrationally cold relatively rotationally cold NO products). We showed elsewhere that this channel produces an NO rotational profile peaking at $N\sim 24$ (at photolysis energies of ~5.494 eV),[6] and for this reason we expect a peak associated with NO fragments formed in $v=0$ and $N=1$ with $O(^3P_J)$ to be significantly less intense. Indeed any such peak appears to be below our detection limit. Peak (ix) is then attributed to NO formed in $v=0$ and $N=34$. The lower intensity of this peak with respect to peak (x) is rationalized by the lower $A\leftarrow X$ transition strength of the O_{12} band.

Another set of weak features is observed in Fig. 5 with kinetic energies close to 0.4 eV [peaks (v)–(viii)]. NO fragments with similar kinetic energies are observed right across the rotational contour shown in Fig. 1(a) and must be due to internally excited NO produced with ground state oxygen atoms. Previous experiments have assigned these peaks to NO fragments produced in $v=5$ which are probed via the (4, 5) $A\leftarrow X$ vibrational transition.[25] In addition to this ionization pathway it is also possible to ionize rotationally excited NO $^2\Pi_\Omega$ via the (2, 3) and (3, 4) $A\leftarrow X$ bands and the (0, 5) $C\leftarrow X$ band with similar probe energies ($N\sim 50$, 35, and 20 respectively). Furthermore the bandheads of the (1, 6) $C\leftarrow X$ and the (0, 5) $D\leftarrow X$ transitions occur close to the band-

TABLE I. Interpretation of the peaks in the NO($^2\Pi_\Omega$) kinetic energy distribution shown in Fig. 5. The branch refers to the rotational branch via which a particular rotational state was probed, the subscript 1 indicates $\Omega=\frac{1}{2}$, 2 that $\Omega=\frac{3}{2}$, and 12 a transition from $\Omega=\frac{3}{2}$ in the ground state to $\frac{1}{2}$ in the intermediate state. The calculated kinetic energy refers to the expected kinetic energy of an NO fragment produced at a photolysis/probe energy of 5.479 41 eV with the relevant cofragment and in the relevant spin orbit and rovibrational state.

Peak	Cofragment(s)	KE/eV (obs.)	Intermediate state	v	~N	Branch	KE/eV (calc.)
(i)	$O(^1D_2)$	0.053	A	0	34	O_{12}	0.046
(ii)	$O(^3P_J)$	0.092	D	9	26	P_2	0.086
(iii)	$O(^1D_2)$	0.120	A	0	16	P_1	0.118
(iv)	$O(^1D_2)$	0.138	A	0	1	P_1	0.138
(v)	$O(^3P_J)$	0.204	C	5	57	P_1	0.201
(vi)	$O(^3P_J)$	0.304	C	6	33	Q_2	0.273
			C	6	32	Q_1	0.282
			C	6	28	R_2	0.294
			C	6	25	R_1	0.310
(vii)	$O(^3P_J)$	0.358	A	4	46	Q_1	0.354
(viii)	$O(^3P_J)$	0.415	D	5	14	P_1	0.415
(ix)	$O(^3P_J)$	0.731	A	0	34	O_{12}	0.730
(x)	$O(^3P_J)$	0.807	A	0	16	P_1	0.802
			A	0	12	R_2	0.805
			A	0	17	Q_2	0.795

TABLE II. Transition probabilities and excitation energies for selected vibrational bands in the absorption spectrum of ground state NO. The data are taken from constants published in the LIFBASE spectral simulation program (Ref. 54).

NO excited state	Vibrational transition	Bandhead/eV	Transition probability
A	(2, 2)	5.594 78	2.624×10^{-3}
D	(1, 6)	5.546 31	1.015×10^{-2}
A	(1, 1)	5.537 65	1.610×10^{-3}
A	(4, 5)	5.488 66	9.342×10^{-4}
A	(0, 0)	5.479 89	2.389×10^{-3}
D	(0, 5)	5.478 94	5.266×10^{-3}
D	(3, 9)	5.468 94	7.541×10^{-3}
C	(1, 6)	5.441 13	1.153×10^{-2}
A	(3, 4)	5.429 24	1.807×10^{-3}
A	(2, 3)	5.369 18	1.178×10^{-3}
C	(0, 5)	5.364 99	6.526×10^{-3}
A	(5, 7)	5.335 62	1.090×10^{-3}

head of the (0, 0) $A\leftarrow X$ transition. NO kinetic energies close to 0.4 eV could result for fragments ionized by any of these probe schemes.

The excitation energies used to produce NO images such as those in Figs. 4(a) and 4(b) and those reported by Ahmed *et al.*[25] are optimized on the total NO ion signal. As the ion signal due to NO fragments produced in $v=0$ with $O(^1D_2)$ dominates the energy distributions, there is no reason why these excitation energies should probe the peak of any probe transition other than those starting from $v=0$. For this reason, the fortuitous overlap with transitions of other NO vibrational states does not yield any information about the population of these levels. Despite this we can make some qualitative observations. From the $O(^3P_J)$ images published in our previous paper,[6] we expect a significantly greater population of NO fragments in rotationally excited levels of $v=3$ with respect to rotationally cold $v=0$, 5, and 6 products. If we consider the transition probabilities for the resonant step of the ionization (see Table II), we find that the (2, 3) transition probability is roughly half that of the (0, 0) $A\leftarrow X$ transition. We do, however, expect more than three times the population of rotationally excited levels in $v=3$ with respect to rotationally cold fragments in $v=0$. It is therefore expected that if the probe laser overlaps with the peak of a resonance corresponding to rotationally excited NO fragments in the (2, 3) band, a peak roughly one and a half times the size of the corresponding peak for NO produced in $v=0$ and low N with $O(^3P_J)$ should be observed. However, we note that these fragments make up less than one-tenth of the total NO produced with $O(^3P_J)$ and this portion of the population is spread over more than 60 rotational quanta. For this reason, we expect that the NO fragments produced with $O(^1D_2)$ will make the dominant contribution to the REMPI spectrum. From the transition probabilities of the (3, 4) $A\leftarrow X$ and the (0, 5) $C\leftarrow X$ bands we do not expect these fragments to be observable above the noise level in Fig. 1(a). Despite this we do see signatures of the $O(^3P_J)$ fragments in the NO images (see Tables I and III).

It is difficult to make an assessment of the population of rotationally cold levels of $v=5$ and 6 from the $O(^3P_J)$ energy distributions (due to likely overlap with rotationally excited fragments produced in $v=2$ and 3, respectively), although we do expect the population to be relatively small. Considering the relative transition strengths of the (4, 5) $A\leftarrow X$ and (0, 5) $D\leftarrow X$ bands, observation of $v=5$ fragments is over 5.5 times more likely via the (0, 5) transition. We also highlight the (1, 6) $C\leftarrow X$ transition strength which should result in efficient excitation to the intermediate resonance despite the expected small ground vibrational level population. It is also worthwhile noting that the ionization efficiency of the intermediate NO *D* and *C* states in these routes should be essentially equivalent to that of the *A* state as the three states exhibit similar equilibrium bond lengths (106.37, 107.5, and 106.46 pm for the *A*, *C*, and *D* states, respectively) and vibrational frequencies (2371, 2347, and 2327 cm^{-1}, respectively).[55]

Based on the transition probabilities, the NO fragment kinetic energies, the expected vibrational populations, and the probe photon energy, we assign the collection of peaks

TABLE III. Interpretation of the peaks in the $NO(^2\Pi_{\Omega})$ kinetic energy distribution shown in Fig. 6. The branch refers to the rotational branch via which a particular rotational state was probed, the subscript 1 indicates $\Omega=\frac{1}{2}$, 2 that $\Omega=\frac{3}{2}$, and 12 a transition from $\Omega=\frac{3}{2}$ in the ground state to $\frac{1}{2}$ in the intermediate state. The calculated kinetic energy refers to the expected kinetic energy of an NO fragment produced at a photolysis/probe energy of 5.483 24 eV with the relevant cofragment and in the relevant spin orbit and rovibrational state.

Peak	Cofragment(s)	KE/eV (obs.)	Intermediate state	v	$\sim N$	Branch	KE/eV (calc.)
(i)	$O(^3P_J)$	0.063	*A*	7	56	R_1	0.065
(ii)	$O(^1D_2)$	0.081	*A*	0	27	P_2	0.079
(iii)	$O(^1D_2)$	0.105	*A*	0	21	P_1	0.105
(iv)	$O(^1D_2)$	0.137	*A*	0	5	R_1	0.137
(v)	$O(^3P_J)$	0.258	*C*	6	38	P_1	0.253
(vi)	$O(^3P_J)$	0.290	*C*	6	29	R_2	0.290
(vii)	$O(^3P_J)$	0.345	*A*	3	57	Q_2	0.344
(viii)	$O(^3P_J)$	0.421	*D*	5	6	R_1	0.429
			D	5	11	Q_1	0.422
			D	5	18	P_1	0.407
(ix)	$O(^3P_J)$	0.793	*A*	0	21	P_1	0.790

marked (v)–(viii) in Fig. 5 to partially resonant (1+1) ionization of NO fragments produced in coincidence with $O(^3P_J)$ in $v=4-6$ with different degrees of rotational excitation via the (3, 4) $A\leftarrow X$, (0, 5) $D\leftarrow X$, and (1, 6) $C\leftarrow X$ bands, respectively. Similarly we can assign peak (ii) to the ionization of highly internally excited NO in $v=9$, in accord with our previous work which highlighted the production of translationally cold $O(^3P_J)$ atoms close to this excitation energy. The assignments of the peaks in Fig. 5 are summarized in Table I. A similar treatment can be applied to the energy distribution shown in Fig. 6.

At a photolysis/probe energy of 5.483 24 eV, NO $^2\Pi_{1/2}$ is formed in coincidence with $O(^1D_2)$ with an excess energy of 400 meV and in coincidence with $O(^3P_2)$ with an excess energy 2.368 eV. At this probe energy we can ionize NO in $v=0$ via the $R_1(5)$, $P_1(21)$, and $P_2(27)$ transitions. In Fig. 6 we see two intense peaks at 0.105 and 0.137 eV [peaks (iii) and (iv)]. We assign these peaks to NO $\Omega=\frac{1}{2}$ fragments produced in $v=0$ and $N=21$ and 5, respectively, in good agreement with the calculated NO kinetic energies (Table III). Peak (ii) is then attributed to NO $^2\Pi_{3/2}$ produced in $v=0$ and $N=27$ while peak (ix) is attributed to NO $v=0$ and $N=21$ produced in coincidence with $O(^3P_J)$ atoms. The collection of weak peaks at NO kinetic energies of ~0.4 eV are then assigned to NO fragments produced in $v=3$, 5, and 6 ionized via the $A\leftarrow X$, $D\leftarrow X$, and $C\leftarrow X$ bands. A summary of the assignments of the peaks in Fig. 6 is given in Table III.

From the energy distributions shown in Figs. 5 and 6 we can conclude a number of points. Having probed the NO $\Omega=\frac{1}{2}$ fragments produced with $O(^1D_2)$ in the $v=0$ and $N=1$, 5, 16, and 21 states we see that the 16th rotationally excited state has a higher population than the 1st and the 5th has a higher population than the 21st. This is in good agreement with the analysis of the entire rotational profile shown in Fig. 1(a). We also observe NO $\Omega=\frac{3}{2}$ fragments as minor photoproducts, as expected from the analysis of the whole rotational profile. More importantly, however, we have probed NO fragments which span the rotational state range attributed to the REMPI spectrum and have found that NO is produced predominantly with $O(^1D_2)$ rather than $O(^3P_J)$ with a ratio in excess of 50:1. As expected from the analysis reported in our previous paper,[6] the contribution of vibrationally excited fragments [probed via the (3, 4) and (2, 3) $A\leftarrow X$ bands and the (0, 5) $D\leftarrow X$ band] to the distribution shown in Fig. 1(a) is insignificant after analysis of the images shown in Fig. 4. For these reasons we can confidently assign NO fragments produced in $v=0$ in coincidence with $O(^1D_2)$ as the carrier of the spectrum shown in Fig. 1(a).

Similar results are obtained from crush velocity map images recorded on different rotational lines of the (1, 1) and (2, 2) $A\leftarrow X$ vibrational bands. These images are in agreement with those of Ahmed *et al.*[25] As in the (0, 0) band, overlapping probe transitions occur across the (1, 1) and (2, 2) absorption bands. However, with the same rationale as we used to assign the carrier of Fig. 1(a) we assign NO fragments in $v=1$ and 2 produced concomitantly with $O(^1D_2)$ as the carriers of the spectra shown in Figs. 1(b) and 1(c), respectively.

In summary we have recorded rotational distributions for NO fragments produced in $v=0-2$ and found that the $v=0$ rotational profile can be described by a single progression, peaking close to $N=8$ at excitation energies close to 5.48 eV. In contrast, the $v=1$ and 2 rotational profiles display significant bimodality with one mode peaking at relatively low N values (7 and 4 for $v=1$ and 2, respectively) and another peaking at $N=23$ for $v=1$ and $N=13$ for $v=2$. By recording velocity map images of the NO fragments at different rotational lines we are able to attribute the rotational profiles shown in Fig. 1 to NO produced with $O(^1D_2)$. Any contribution from the $O(^3P_J)$ channel is interpreted to lie in the noise of the spectra.

B. $O(^1D_2)$ imaging

1. Treatment of aligned photoproducts

We have used dc slice imaging to record the radial and angular profile of the excited state oxygen fragments at a photolysis energy of 5.479 52 eV. At this energy $O(^1D_2)$ atoms can be formed with NO $^2\Pi_\Omega$ fragments in $v=0$ or 1 only. Due to the intermediate resonance used in the $O(^1D_2)$ ionization scheme, these experiments are sensitive to orbital angular momentum alignment in the photofragments. By recording images with different probe laser polarizations the sensitivity to the distribution of aligned photoproducts changes. By monitoring these changes from different perspectives (by changing the pump laser polarization) we can derive fragment polarization moments which describe the photoproduct angular distributions. These moments yield the M_J substate populations and their angular dependencies as well as the translational anisotropy of the photoproduct distributions which can be related to the fragmentation mechanism. The alignment moments also allow us to reconstruct the photofragment energy distribution.

In our experiments we consider a distribution of photoproducts created by the dissociation of unaligned parent molecules via a pure parallel transition[8] with linearly polarized light. We probe the $O(^1D_2)$ fragment atoms in a (2+1) REMPI process using a second linearly polarized light field. If we align the polarization vector of the pump field so that it is perpendicular to the detector face then the angular momentum distribution of the photon will be isotropic with respect to the detector. Furthermore, so will the angular momentum distribution of the unpolarized parent molecules. Similarly a probe field which is polarized perpendicular to the detector face will also have an isotropic angular momentum distribution with respect to the detector face. In this geometry the measured photoproduct distribution must, therefore, be isotropic; we cannot create alignment from unaligned photons and parent molecules.

Figure 7(a) [also Fig. 2(d)] shows the $O(^1D_2)$ distribution produced in an experimental geometry with the pump and probe laser polarizations aligned perpendicularly to the detector face. Contrary to arguments above, this image displays a clear anisotropy which increases with fragment velocity. The observed anisotropy must be associated with an experimental artifact rather than the photophysics. Having analyzed the laser polarizations at the vacuum windows and found them to be linear, we attribute this anisotropy to non-

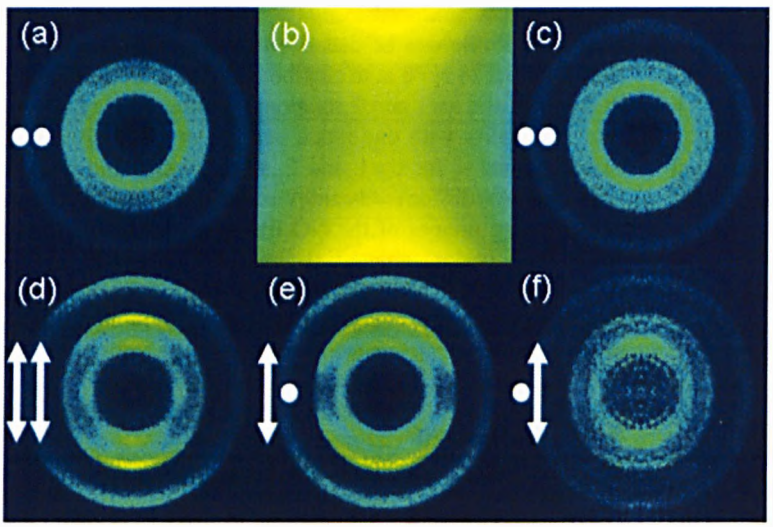

FIG. 7. dc slice velocity map images of the $O(^1D_2)$ fragment. Panel (a) corresponds to an image recorded with both laser polarizations aligned perpendicular to the detector face and parallel to the TOF direction. Panel (b) shows the correction factor applied to the image in panel (a) to produce an isotropic distribution (see text). Panels (c), (d), (e), and (f) show corrected dc slice images for the perpendicular-perpendicular, parallel-parallel, parallel-perpendicular, and perpendicular-parallel pump and probe laser polarizations, respectively.

uniform ionization of the photoproduct distribution. We choose to use relatively low probe laser energies with relatively weak laser foci to prevent the saturation of the probe transition. Using similar focal length lenses for the pump and probe lasers means that the higher energy photons of the probe beam will necessarily be more tightly focused than the pump. The faster oxygen fragments are moving at ~ 1700 m s^{-1} so that in the 15 ns pump-probe delay they move ~ 30 μm. This is comparable to the beam waist of the probe laser. This coupled to the fact that the probe volume is smaller than the pump causes the photofragments expanding perpendicularly to the probe laser propagation direction to be less efficiently probed than those expanding in the parallel direction. This is the same problem encountered in crossed-molecular beam experiments whereby the slower species are more efficiently probed than the fast species. This is corrected for with the so called number density-to-flux transformation.[56] To correct our photoproduct distributions we use the anisotropies of the rings appearing in the image shown in Fig. 7(a). By fitting to these features using an expansion of even Legendre moments we can model how the anisotropy increases with fragment velocity. Using a quadratic fit to the resulting anisotropy parameters we get an expression for the image intensity with respect to angle and image radius, which can be used to produce the image correction function shown in Fig. 7(b). Dividing the raw images by this correction factor we remove this contribution to the angular distributions, only leaving the contribution due to the photophysics. The corrected images for the four laser geometries are shown in Figs. 7(c)–7(f). Furthermore as Fig. 7(c) displays the central slice of a necessarily unaligned distribution, it yields the $O(^1D_2)$ photoproduct kinetic energy distribution. This kinetic energy distribution is shown as a solid line in Fig. 8 along with the distributions which are biased by orbital angular momentum effects [those obtained directly from the images shown in Figs. 7(d)–7(f)].

There are a number of different methods of extracting dynamical parameters from velocity map images;[33,36,38–42,57–59] we choose to use a fitting procedure which is based on the previous angular momentum treatment of Mo *et al.*[33] This treatment is easily implemented and was previously used to extract alignment parameters from velocity map images of the $O(^1D_2)$ distribution formed from NO_2 photolysis close to 205 nm.[23] Our treatment assumes an infinitely narrow slice through the photoproduct distribution. It is therefore applicable to crush velocity map images of cylindrically symmetric objects but in the case of slice images the distributions need not have cylindrical symmetry. However, the increase in the effective slice width as the kinetic energy of the photoproducts decreases means that slice images only approximately fit within this treatment. Depending on the translational anisotropy of the fragments and their polarizations, different image features and their associated polarization moments will be sliced to different degrees. The assumption and effects of a finite slice width have been discussed by others.[37,49–53] In the light of this work we expect that slice widths of order 10%, or better, of the diameter of the Newton sphere should only lead to minor errors in the extracted dynamical parameters.

To obtain numerical values for dynamical parameters, we fit to the angular profiles of the corrected images using the following formula:

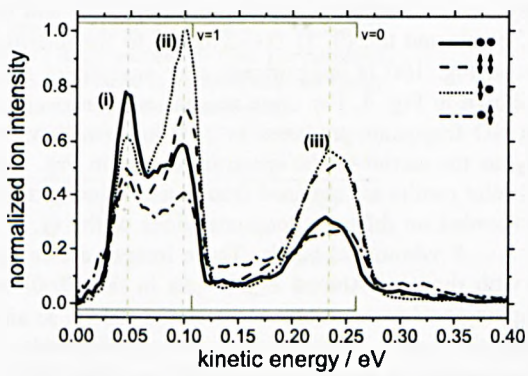

FIG. 8. $O(^1D_2)$ energy distributions recorded at an excitation energy of 5.479 52 eV for the four laser polarization combinations associated with Figs. 7(c)–7(f). The perpendicular-perpendicular laser polarization combination (solid line) represents the relative populations (unbiased by orbital angular momentum alignment effects) of the features labeled (i)–(iii).

TABLE IV. Definitions of the reference frames used in the derivation of Eqs. (1) and (8). All frames are right handed, $\varepsilon_{\text{pump}}$ and $\varepsilon_{\text{probe}}$ are the polarization directions of the pump and probe lasers, and $\mathbf{v}_{\text{rec}}$ is the center-of-mass velocity of the recoiling atom.

Frame	Axes	Definition
Laboratory	$X_0Y_0Z_0$	X_0 perpendicular to detector face; Y_0 parallel to laser propagation directions; laser polarization directions parallel to X_0 or Z_0
Pump	$X_1Y_1Z_1$	$X_1Y_1Z_1 \equiv \begin{cases} X_0Y_0Z_0 & \text{if } \varepsilon_{\text{pump}} \parallel Z_0 \\ (-Z_0)Y_0X_0 & \text{if } \varepsilon_{\text{pump}} \parallel X_0 \end{cases}$
Probe	$X_2Y_2Z_2$	$X_2Y_2Z_2 \equiv \begin{cases} X_0Y_0Z_0 & \text{if } \varepsilon_{\text{probe}} \parallel Z_0 \\ (-Z_0)Y_0X_0 & \text{if } \varepsilon_{\text{probe}} \parallel X_0 \end{cases}$
Recoil	xyz	$z \parallel \mathbf{v}_{\text{rec}}$; $y \parallel (Z_1 \times z)$.

$$c_n(g) = {\sum_{K'kq}}' a_0^{(K')} \rho_q^{(k)} Z_q^{nK'k}(g), \tag{1}$$

where $c_n(g)$ is the nth Legendre moment of the image obtained for a particular experimental geometry g, the primed summation symbol is used to indicate that the sum runs only over even values of K', k, and q, the $a_0^{(K')}$ are the multipole moments obtained from an analysis of the distribution of fragment recoil directions with regard to the direction of polarization of the pump laser, the $\rho_q^{(k)}$ are the multipole moments of the fragment polarization in the body-fixed, "recoil" frame to be defined below, and the $Z_q^{nK'k}(g)$ are coefficients whose values relate the dynamical parameters (the $a_0^{(K')}$ and $\rho_q^{(k)}$) and the experimental geometry to the values of the Legendre moments of the images.

In what follows we will discuss (a) the reference frames that are used in the derivation of Eq. (1), (b) the definition of the Legendre moments of the observed images, (c) the definitions of the dynamical parameters, (d) the derivation of Eq. (8), the formula used in the calculation of the "geometric" coefficients, $Z_q^{nK'k}(g)$, and (e) technical details of our fitting procedure.

a. Reference frames Our goal is to use the images obtained in the laboratory to obtain information about the NO_2 dissociation dynamics as seen from a body-fixed perspective. This immediately implies the need for two reference frames: The space-fixed or "lab" frame that we will represent by $X_0Y_0Z_0$ and the body-fixed or "recoil" frame that we will represent by xyz. Because the directions of (linear) polarization of the pump and probe lasers are important for the dissociation dynamics and polarization detection, it is useful to define two additional reference frames having their Z axes along those polarization directions. These are the "pump" frame that we will denote by $X_1Y_1Z_1$ and the "probe" frame that we will denote by $X_2Y_2Z_2$. The explicit definitions we have used for these four reference frames are presented in Table IV.

b. Legendre moments of observed images All our observed images were obtained in the Y_0Z_0 plane of the laboratory frame. Furthermore, they are in principle symmetric under reflection on the Z_0 axis (in practice, experimental noise destroys this symmetry, but in our data treatment we restored it by taking the average of the $Y_0 \leq 0$ and $Y_0 \geq 0$ halves). Thus, for every experimental geometry the measured intensity depends only on the lab-frame polar angle Θ_0 and can be written as a Legendre series:

$$I_{\text{obs}}(\Theta_0; g) = \sum_n \frac{2n+1}{2} c_n(g) P_n(\cos\Theta_0), \tag{2a}$$

where $I_{\text{obs}}(\Theta_0; g)$ is the image intensity and P_n is a Legendre polynomial. Inversion of this equation leads to

$$c_n(g) = \int_{-1}^{1} I_{\text{obs}}(\Theta_0; g) P_n(\cos\Theta_0) d(\cos\Theta_0), \tag{2b}$$

which is the formula we have used in the determination of the Legendre moments of the observed images. As our measurements involve unpolarized parent molecules and linear laser polarizations, they are free of orientation effects; the only Legendre moments that can contribute to the observed images are those quantifying alignment—in other terms, those associated with even n. We should also note that our observed images were normalized so that $c_0(g) = 1$.

c. Dynamical parameters There is a single approximation that we make regarding the description of the NO_2 dissociation dynamics, namely, that the polarization of the atomic fragment is independent of the angle between the direction of polarization of the pump laser ($\varepsilon_{\text{pump}}$) and the fragment recoil direction ($\mathbf{v}_{\text{rec}}$). This approximation, which was also used in earlier studies (see, e.g., Refs. 23 and 33), implies that the intensity of the observed image is given by the product of two factors:

$$I_{\text{obs}} = I_{\text{rec}} I_{\text{det}}, \tag{3}$$

where I_{rec} is the distribution of fragment recoil directions and I_{det} is the fragment detection efficiency. Except for an unimportant proportionality factor, for a one-photon fragmentation I_{rec} is given by[60]

$$I_{\text{rec}}(\theta, \varphi) = \frac{1}{4\pi}[1 + \beta P_2(\cos\theta)], \tag{4}$$

where θ and φ are the polar and azimuthal angles that specify the direction of $\mathbf{v}_{\text{rec}}$ in the pump frame. This expression involves a single dynamical parameter: β, the asymmetry parameter. Note also that it can be written as a covariant multipolar expansion,

$$\begin{aligned} I_{\text{rec}}(\theta, \varphi) &= \sum_{K'Q'} \frac{2K'+1}{4\pi} a_{Q'}^{(K')} C_{K'Q'}^{*}(\theta, \varphi) \\ &= \sum_{K'} \frac{2K'+1}{4\pi} a_0^{(K')} P_{K'}(\cos\theta), \end{aligned} \tag{5}$$

where the $C_{K'Q'}$ are modified spherical harmonics[61] and in the second line we have used the fact that the only nonvanishing multipole moments are $a_0^{(0)} = 1$ and $a_0^{(2)} = \beta/5$ and also the $C_{K'0}(\theta, \varphi) = P_{K'}(\cos\theta)$ relation.[61]

In the case of interest to us (two-photon fragment excitation), the second factor on the right-hand side of Eq. (3) is given by[62]

$$I_{\text{det}} = \sum_k \rho^{(k)}_{q_2=0} \tilde{P}_k, \tag{6}$$

where $\rho^{(k)}_{q_2=0}$ is a zero-component multipolar polarization moment specifying the fragment polarization in the probe frame (hence the q_2 notation for the index specifying the component of the polarization moment of rank k) and $\tilde{P}_k$ is a frame-independent geometric factor given by a known formula.[62] The dynamical parameter appearing in this equation, $\rho^{(k)}_{q_2=0}$, can be replaced by a set of others that are of greater interest for us—the set of fragment polarization moments in the recoil frame, $\{\rho^{(k)}_q\}$—through a rotation of reference frame. We define the recoil-frame polarization moments via a covariant multipolar expansion of the corresponding density matrix:

$$\langle jm_1|\rho|jm_2\rangle = \sum_{kq} \frac{2k+1}{2j+1} \rho^{(k)}_q \langle jm_1, kq|jm_2\rangle, \tag{7a}$$

$$\rho^{(k)}_q = \sum_{m_1 m_2} \langle jm_1|\rho|jm_2\rangle \langle jm_1, kq|jm_2\rangle, \tag{7b}$$

where $\langle jm_1, kq|jm_2\rangle$ is a Clebsch–Gordan coefficient. The normalization is such that $\text{Tr}(\rho) = \rho^{(0)}_0 = 1$.

Note that we neither restrict the pump and probe laser polarizations to be the same nor do we assume that the fragment polarization is cylindrically symmetric around the fragment recoil direction. These are the main differences between our formalism and the earlier applications or modifications[23,33] of the treatment first suggested by Mo *et al.*[33,62]

d. Formula for $Z^{nK'k}_q(g)$ coefficients Other than the conventions and approximation we have already mentioned, the derivation of the expression we used to calculate the $Z^{nK'k}_q(g)$ coefficients involves only previously published expressions and standard techniques of angular momentum algebra. For this reason, we decided against presentation here of all the intermediate formulas which, although necessary for checking our results and useful for those interested in their modification (say, through use of different conventions and/or experimental geometries), would make the reading difficult. Instead, we present a diagram of how we achieved the derivation, see Fig. 9. The details of the derivation, including the intermediate formulas, are discussed in the supplementary material.[63]

As indicated in Fig. 9, the starting points of our derivation were Eqs. (4) and (6); respectively, they correspond to boxes 1 and 3 of the diagram. We manipulate the two expressions in different ways:

- Equation (4) is rewritten as a multipolar expansion [this leads to Eq. (5) and from box 1 to box 2 of the diagram].
- In Eq. (6), the probe-frame (q_2-dependent) fragment polarization moments are rotated twice, first from the probe to the pump frame [in terms of Euler angles, the rotation is $R_{X_2Y_2Z_2 \to X_1Y_1Z_1} \equiv R(0, \beta_{21}, 0)$] and then from the pump frame to the recoil frame [$R_{X_1Y_1Z_1 \to xyz} \equiv R(\varphi, \theta, 0)$]. This leads from box 3 to box 4 and then 5. The resulting expression is then written as a multipolar expansion, which leads to box 6.

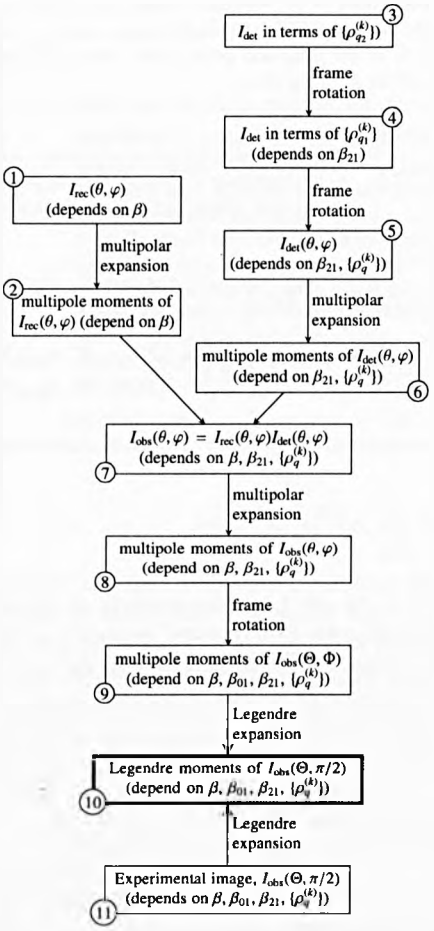

FIG. 9. Schematic representation of the procedure used in the derivation of Eqs. (1) and (8).

The next step is multiplication of the multipolar expansions of I_{rec} and I_{det} as per Eq. (3). The result (box 7 of the diagram) is a product of two multipolar expansions, which depends on the dynamical parameters (β and $\{\rho^{(k)}_q\}$), on an experimental parameter (β_{21}, the single nonzero Euler angle of the rotation between pump and probe frames), and on the angles between the directions of fragment recoil and pump laser polarization (θ, φ).

Because of its functional dependence on θ and ϕ, the function of box 7 can be seen as being defined on the pump frame, $X_1Y_1Z_1$. We rewrite it as a single multipolar expansion (this takes us down to box 8) and then rotate it to the laboratory frame; this rotation, $R_{X_1Y_1Z_1 \to X_0Y_0Z_0} \equiv R(0, -\beta_{01}, 0)$, leads to the result of box 9, an expression for the dependence of the lab-frame image on all the dynamical and experimental parameters.

Finally, we fix the value of the lab-frame azimuthal angle (after symmetrization, all our observed images are associated with $\Phi = \pi/2$) and rewrite the multipolar expansion as a Legendre series. This gives us the Legendre moments of $I_{\text{obs}}(\Theta, \pi/2)$, see box 10. As these Legendre moments can

also be obtained from the experimental data [use of Eq. (2b) takes us from box 11 to box 10], we are now ready for the fitting of the observed images.

As shown in detail in the supplementary material,[63] the procedure we have just described leads to the following expression for the geometric coefficients appearing in Eq. (1):

$$Z_q^{nK'k}(g) = -\frac{5}{8\pi}(2K'+1)\sqrt{2k+1}\langle 20,k0|20\rangle \begin{Bmatrix} 2 & 2 & k \\ 2 & 2 & 1 \end{Bmatrix} \times \sum_{\substack{Tt_0 \\ KQ}}{}' (-1)^{t_0/2}(2K+1) d^T_{t_0Q}(\beta_{01}) d^k_{Q0}(\beta_{21}) I^{Tn}_{t_0000} \times I^{kK}_{-QqQ0}\langle K'0,KQ|TQ\rangle\langle K'0,K0|T0\rangle, \quad (8)$$

where the primed summation symbol again indicates that the sum only runs over even values of the dummy indices, $\{\cdots\}$ is a $6-j$ coefficient, $d^A_{a_1a_2}(\xi)$ is a reduced rotation matrix element, and

$$I^{AB}_{a_1a_2b_1b_2} = \int_{-1}^{1} d^A_{a_1a_2}(\xi) d^B_{b_1b_2}(\xi) d(\cos\xi) \quad (9)$$

are integrals that appear because of our calculation procedure (see Fig. 9); as explained in the supplementary material, they carry no special physical meaning.

Note that Eq. (8) also reveals to what fragment polarization moments our measurements are sensitive. While some of the conclusions are rather obvious (e.g., the vanishing of $\langle 20,k0|20\rangle$ for odd k implies that we cannot observe fragment orientation), the others (our measurements are only sensitive to the real part of fragment polarization moments with even q) are less so. Readers interested in proofs of the latter should consult the supplementary material.[63]

e. Fitting procedure The observed Legendre moments depend nonlinearly on six dynamical parameters: β, $\rho_0^{(2)}$, $\rho_{+2}^{(2)}=\rho_{-2}^{(2)}$, $\rho_0^{(4)}$, $\rho_{+2}^{(4)}=\rho_{-2}^{(4)}$, and $\rho_{+4}^{(4)}=\rho_{-4}^{(4)}$. To deal with this nonlinear, multidimensional fitting problem we have used the downhill simplex method.[64,65] Other than Eq. (1), all it requires is specification of seven sets of initial values for the fit parameters and of the parameter constraints.

We have chosen the starting values as combinations of (i) orthogonal polarization states spanning the complete space of accessible fragment polarization states with (ii) an asymmetry parameter in one of the extremes of its allowed range: $\beta=-1$ or $\beta=2$. Once a local minimum was found, we restarted the calculation by replacing one of the combinations of β and $\{\rho_q^{(k)}\}$ (one of the simplex vertices) by the one corresponding to that minimum, and the procedure was repeated until the global minimum was reached and the fit no longer improved.

As for parameter constraints, we have used $-1 \le \beta \le 2$ and the fact that, for any valid set of polarization moments, the corresponding density matrix must be positive semidefinite; by rejecting density matrices with negative eigenvalues, we could then prevent the fit results from moving into physically meaningless regions of the parameter space.

The results were obtained by simultaneous fits of all experimental geometries with at least one laser polarization not perpendicular to the detector face (as discussed above, the arrangement in which pump and probe laser polarizations are both perpendicular to the detector face is insensitive to fragment polarization). The set of complex fragment polarization parameters thus obtained, $\{\rho_q^{(k)}\}$, was then transformed into a set of real polarization parameters, $\{\rho_{q\pm}^{(k)}\}$, defined according to the Hertel–Stoll convention,[66] which in our case can be expressed as

$$\rho_{q+}^{(k)} = \sqrt{2}\rho_q^{(k)}, \quad q>0, \quad (10a)$$

$$\rho_{q-}^{(k)} = 0, \quad q>0, \quad (10b)$$

$$\rho_0^{(k)} = \rho_0^{(k)}. \quad (10c)$$

The real multipole moments have well-defined limits[67] and a more direct physical/directional significance.[68]

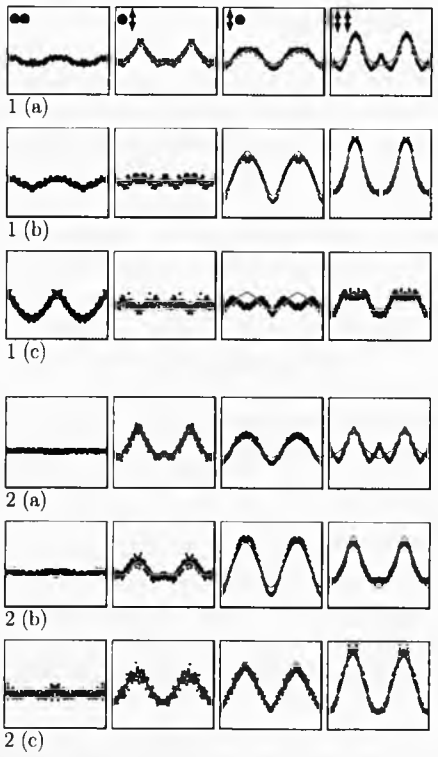

FIG. 10. Experimental and corrected experimental anisotropies obtained by integrating the images shown in Figs. 2(a)–2(d) and Figs. 7(c)–7(f) over each of the three features with respect to radius. Panel 1 (a) shows the raw anisotropy obtained from the inner ring in Fig. 2 for the four polarization settings. Panel 1 (b) shows the raw anisotropy for the middle ring and panel 1 (c) that for the outer ring. Panels 2 (a)– 2 (c) shows the corresponding corrected anisotropies obtained from the images shown in Figs. 7(c)–7(f).

The results of the fitting procedure for the uncorrected and corrected images shown in Figs. 2 and 7 are shown in Fig. 10. The differences in the angular profiles and their fits for the uncorrected and corrected data highlight the effects of the correction procedure outlined at the beginning of this section. We note that the experimental artifact has a substantial effect on the dynamical parameters obtained from the fits. In the remainder of the discussion we exclusively consider the energy distributions and dynamical parameters obtained from the corrected data set.

2. Energy distribution

The $O(^1D_2)$ energy distribution (unbiased by orbital angular momentum alignment) shown as the solid black line in Fig. 8 displays three broad features which peak at kinetic energies of 0.047, 0.100, and 0.238 eV [marked (i), (ii), and (iii), respectively]. At a photolysis energy of 5.479 52 eV the excess energy above the second dissociation limit is ~382 meV and it is possible to produce $O(^1D_2)$ in coincidence with $NO(^2\Pi_{1/2})$ fragments in $v=0$ or 1 and $N=0-42$. Based on the conservation of linear momentum, we can produce $O(^1D_2)$ atoms with a maximum kinetic energy of 0.249 eV in coincidence with $NO(^2\Pi_{1/2})$ products in $v=0$ and $N=0$. The low kinetic energy release of the $O(^1D_2)$ fragments at this excitation energy makes it difficult to effectively slice the distribution. By carrying out experiments with relatively low repeller voltages (1000 V) we were able to stretch the distribution along the TOF axis so that $O(^1D_2)$ atoms formed at the peak of features (i), (ii), and (iii) had TOF spreads of ~63, 98, and 161 ns, respectively. These conditions allowed us to retain a good ion signal strength while maintaining low photolysis and probe laser fluences. The high-voltage gating pulse in these experiments is estimated to have a temporal duration of 6 ns (FWHM with respect to the threshold for ion detection and the peak of the electrical pulse) but the duration of the recorded ion signal is actually narrower than this due to the exponential increase in signal with channel plate voltage. This results in slices which correspond to less than 9.5%, 6.1%, and 3.7% of the photoproduct distributions for the three features, respectively. In this case the error associated with assuming perfect slicing should be small.[45,49,53] It is noted that a small fraction of $O(^1D_2)$ atoms are formed with kinetic energies in excess of the 0.249 eV kinetic energy limit. We attribute this to the error associated with calibrating the spectrometer using photoproducts with velocities significantly in excess of those measured. This leads to the estimation that the error in the measured kinetic energy release is 18 meV (FWHM) or less.

There are a number of different ways in which the excess energy could be partitioned in the NO fragments to produce the observed $O(^1D_2)$ energy distribution. We use the rotational profiles deduced from Fig. 1 to assign peaks (i–(iii). As discussed in Sec. IV A, in all of the REMPI spectra NO $^2\Pi$ fragments in the $\Omega=\frac{1}{2}$ state make up more than 90% of the total NO. We therefore, primarily attribute the peaks in Fig. 8 to $O(^1D_2)$ atoms formed with $NO(^2\Pi_{1/2})$. Peak (iii) can only be attributed to $O(^1D_2)$ formed with $NO(^2\Pi_{1/2})$ in $v=0$; therefore we assign the peak of this feature to $O(^1D_2)$ produced in coincidence with vibrationally cold diatomic cofragments formed in $N\sim12$. The FWHM of this feature spans a rotational profile dominated by fragments in $N=7-17$, in good agreement with the rotational profile shown Fig. 1(a). Peaks (ii) and (i) could be assigned to $NO(^2\Pi_{1/2})$ fragments formed in $v=0$ and $N\sim34$ and 39 or $v=1$ and $N\sim7$ and 21. The absence of signatures of vibrationally cold, rotationally excited NO fragments in Figs. 1(a) and 1(b) and the presence of a bimodal rotational profile in Fig. 1(b) allows us to assign peaks (i) and (ii) to $NO(^2\Pi_{1/2})$ in $v=1$ and $N\sim7$ and 21, respectively. The assignments of the peaks in Fig. 8 are summarized in Table V. The yields of the $O(^1D_2)$ dissociation channels can be obtained by assessing the areas under the three features in Fig. 8. Using the profile recorded with both lasers polarized perpendicular to the detector, we can estimate the relative yields of the processes leading to peaks (i)–(iii) by approximating their profiles with Gaussians and integrating these fits. Using this approach we estimate that the branching ratio between the NO fragments in $v=0$ and 1 [peak (iii) to (i) plus (ii)] is close to 1:3. As features (i) and (ii) overlap, we cannot unambiguously determine the branching ratio for these two features. Gaussian fits give a population ratio for the two rotational modes of $v=1$ which is close to 9:10. However, based on the rotational profile in Fig. 1(b) and the profile of peak (ii) between 0.066 and 0.124 eV, a Boltzmann profile would be a better reflection of the shape of the peak. This allows us to refine the (i) to (ii) branching ratio as 2:5. We note that these conclusions are very similar to those of Schmaunz *et al.* who also recently measured the rotational distribution of $NO(^2\Pi_\Omega)$ fragments produced at excitation energies close to 5.5 eV using a novel approach to ion imaging.[69]

TABLE V. Vibrational and rotational assignments of the NO cofragment responsible for peaks occurring in the $O(^1D_2)$ kinetic energy release spectrum (Fig. 8). $\sim N_{max}$ corresponds to the rotational energy at the peak of the feature for the $^2\Pi_{3/2}/^2\Pi_{1/2}$ cofragment.

KE/eV	v	$\sim N_{max}$	Peak
0.047	1	19/21	(i)
0.100	1	0/7	(ii)
0.238	0	9/12	(iii)

Based on the inferred lifetime of the (3) $^2A'$ state,[11] at excitation energies ~382 meV above the second dissociation limit the fragmentation process can be described as quasidirect. For direct dissociation of a triatomic species, the rotational profile of the diatomic fragment can be related to the rotational and bending vibrational motion of the parent molecule prior to excitation and the topography of the reaction coordinate. We can define two limiting cases for the production of rotational profiles in direct dissociation processes. If the reaction coordinate occurs across a region of an excited state potential which does not involve a change in the Jacobi angle between the atomic and diatomic moieties then a fragment rotational distribution is produced which is determined by the parent rotational and the ground electronic state bending mode excitation.[70] In the case of a triatomic species excited from a supersonic expansion, this would primarily result in a rotationally cold, unimodal diatomic fragment distribution. However, if the reaction coordinate samples a region of the excited state potential where the two coordinates of the Jacobi angle and the radial separation of the two moieties are inherently coupled, the change in the Jacobi angle during the dissociation results in greater degrees of fragment rotational excitation. In this case, there is an interplay of the parent rotation, the ground state bending motion, and the change in Jacobi angle as the bond breaks.[70] For triatomic species excited from a supersonic expansion, the fragment rotational profile would be dominated by a unimodal distribution which peaks at a rotational quantum number which is

essentially determined by the gradient of the reaction coordinate along the Jacobi angle coordinate. This latter situation effectively describes the rotational profile of the peak labeled (iii) in Fig. 8.

Now consider an indirect dissociation process via a long-lived state or a quasidirect dissociation occurring through a relatively narrow bottleneck. In these cases, the final rotational state distribution of the products qualitatively resembles the wave function at the transition state or crossing point to the dissociative adiabatic potential. The rotational profile is determined by the square of the wave function in the bending coordinate multiplied by the degree of coupling between the Jacobi angle and the rotational degrees of freedom (which is a reflection of the topography of the exit channel). In this situation, crossing the transition state with zero point bending motion results in a unimodal rotational profile where the peak of the distribution is determined by the coupling strength of the transition state bending motion to diatomic rotation. If the transition state is crossed with greater degrees of bending mode excitation, the nodal structure of the bending wave function results in a multimodal rotational profile where the number of modes is equal to the number of nodes. A single quantum of bending mode excitation can therefore result in a bimodal rotational profile.[70,71]

Alternatively, a multimodal rotational profile may be produced via two different dissociative pathways which converge to the same dissociation limit. In this case the photoexcited state effectively couples to one or more dissociative electronic states with the torque generated along each reaction coordinate producing a different unimodal rotational profile. The bimodal rotational profile observed for the NO fragments in $v=1$ [Fig. 8, peaks (i) and (ii)] is, therefore, the signature of at least two nonadiabatic crossings along the reaction coordinate or a single crossing occurring over a small region of the coordinate space with a significant degree of bending excitation in the photoexcited state. It is noteworthy that the $O(^1D_2)$ energy distribution produced ~382 meV above the second dissociation limit is qualitatively similar to the $O(^3P_J)$ distribution produced ~380 meV above the first dissociation limit via the (2) $^2A'$ state.[43,72–75] Both distributions exhibit unimodal rotational profiles for the $NO(^2\Pi_\Omega)$ fragments formed in $v=0$ which are in contrast to the bimodal rotational profiles of the vibrationally excited fragments. The energy distribution recorded ~380 meV above the first dissociation limit has previously been attributed to the production of $NO(^2\Pi_\Omega)$ fragments in $v=0$ and 1 via a tight transition state [the (2) $^2A'/(1)$ $^2A'$ conical intersection] with a degree of parent bending mode excitation.[76–78]

The energy distribution of the $O(^1D_2)$ fragments formed with the probe laser alone are highly structured (see Fig. 11). At this photolysis energy $NO(^2\Pi_\Omega)$ can be produced in $v=0-4$. The corresponding image [Fig. 3(a)], recorded with the laser polarization parallel to the detector face, is comparable to that recorded by Coroiu *et al.*,[23] but in our experiments our higher resolution highlights additional structure in the radial profiles. The structure of the photoproduct energy distribution (recorded with the laser polarization perpendicular to the detector face) consists of more peaks than accessible vibrational states. Accurate assignment of these features

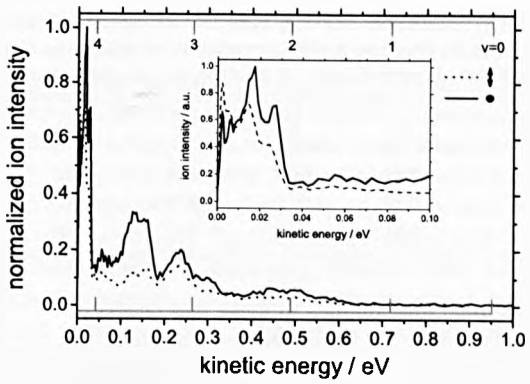

FIG. 11. $O(^1D_2)$ energy distribution recorded in single-laser experiments at 6.0341 eV (205.47 nm) for laser polarization alignments parallel or perpendicular to the detector face associated with Fig. 3(a) (parallel, dashed line) and (b) (perpendicular, solid line). The insert shows an expansion of the low energy portion of the kinetic energy release spectrum.

is not currently possible in the absence of NO cofragment rotational profiles. However, the energy distribution does imply that multimodal fragment rotational distributions are prevalent in the second absorption band of NO_2.

3. Translational anisotropy

Although the shortcomings of the axial recoil model are well known it is often applied to triatomic photodissociation. In this model we can describe the photoproduct distribution created by a single photon dissociation process using the well known expression accredited to Zare [Eq. (4)].[60] We can then relate the translational anisotropy parameter to the dissociation timescale and dissociative geometry using the equally well known classical expression derived by Yang and Bersohn,[79]

$$\beta = 2P_2(\cos(\chi))\left[\frac{1+\omega^2\tau^2}{1+4\omega^2\tau^2}\right], \tag{11}$$

where χ is related to the bond angle at the moment of dissociation. At the level of excitation considered here, dissociation via the (3) $^2A'$ state to the $O(^1D_2)$ limit is quasidirect. The dissociation timescale approaches half the asymmetric stretching vibrational period (~50 fs),[10] and we will assume that the dissociation timescale is independent of the energy partitioning in the diatomic fragment. Using a parent rotational distribution characterized by a temperature of 20 K, the translational anisotropy parameters obtained from the fitting procedure (see Table VI) can be used to relate the $O(^1D_2)$ fragment features to dissociative parent geometries. Peaks (ii) and (iii) are characterized by anisotropy parameters of 0.87 ± 0.10 and 0.81 ± 0.10 which correlate to bond angles of $105°\pm4°$ and $102°\pm4°$, respectively. These angles are in good agreement with the geometry of the (3) $^2A'/(4)$ $^2A'$ avoided crossing calculated by Schinke *et al.*, which occurs at a bond angle of ~110°.[8] As the axial recoil model neglects the angular dependence of the dissociative potential and its effect on the photofragment translational anisotropy, the agreement between the calculated bond angles and the electronic structure calculations suggests that the topology of the dissociative potential has little effect on

TABLE VI. Translational anisotropy parameter and magnetic sublevel populations, $p_{|M_J|}$, of the $O(^1D_2)$ fragments produced with different kinetic energies, together with the fitted values of the five independent polarization moments defined in Eq. (10). For easy comparsion with other work, conversion factors that relate our stereodynamical factors to the dynamical functions introduced by Siebbeles *et al.* (Ref. 57) can be found in the Appendix.

KE/eV	β_v	p_0	p_1	p_2	$\rho_0^{(2)}$	$\rho_{2+}^{(2)}$	$\rho_0^{(4)}$	$\rho_{2+}^{(4)}$	$\rho_{4+}^{(4)}$	Peak
0.047	0.33	0.00	0.48	0.02	−0.24	−0.21	−0.34	+0.18	−0.19	(i)
0.100	0.87	0.00	0.39	0.11	−0.09	−0.19	−0.26	+0.16	−0.11	(ii)
0.238	0.81	0.00	0.41	0.08	−0.15	−0.20	−0.26	+0.29	+0.09	(iii)

the rotational distributions in these two channels.

By constrast, the photofragments labeled (i) in Fig. 8 are more problematic. We note that the alignment treatment discussed in Sec. IV B 1 fails to reproduce qualitatively all of the angular profiles of feature (i) [see Fig. 10 panel 2(a)]. This may be due to the breakdown of our assumption that the fragment polarization is not coupled to the translational anisotropy, although within the angular momentum treatment employed here this assumption allows us to meaningfully fit to the experimental data. For the remainder of the discussion we assume that the polarization moments derived from feature (i) are qualitatively correct. The β parameter for this feature is 0.33 where we estimate an error of ± 0.2. Within the axial recoil limit this correlates to a bond angle of $84° \pm 8°$. However, due to the high degree of rotational excitation with respect to translational energy, the axial recoil approximation (or impulsive model) will provide a poor description of the dissociation process.[70,74]

Nonaxial recoil dynamics are frequently encountered in photofragment imaging experiments when the degree of rotational excitation of a photofragment is large and the relative translational energy is low.[50,74,80] In these cases a more complicated model is required in order to relate the translational anisotropy parameter to the dissociative process. Demyanenko *et al.* proposed a classical model to account for the short-range interaction of the atomic and diatomic fragments during a direct triatomic photodissociation process.[74] Using this model, the crossing geometry calculated by Schinke *et al.* and our β parameter we calculate that a deviation of $\sim 13° \pm 4°$ occurs from pure axial recoil for feature (i) in Fig. 8. Assuming a single crossing geometry to the dissociative adiabatic (4) $^2A'$ state (as suggested by the calculations of Schinke *et al.*[8]), this angle describes the average reduction in the bond angle of the parent NO_2 as the O and NO moieties separate. This reduction in bond angle after the avoided crossing would then be responsible for the rotational excitation of the diatomic fragments associated with feature (i). The bond angle reduction is in contrast to values of $\sim 4° \pm 2°$ and $\sim 3° \pm 2°$ for features (ii) and (iii), respectively, which are associated with less rotationally excited fragments. Although the crossing geometry of Schinke *et al.* has been used as a fitting parameter in these calculations, we note that the measured translational anisotropy parameters are in agreement with the diatomic fragment rotational assignments discussed in Sec. IV A and those shown in Table V.

4. Alignment parameters and M_J substate populations

The $O(^1D_2)$ polarization moments we have obtained from the fitting procedure can be used to generate the probability density functions that directly illustrate how the angular momentum of the atom and also the corresponding position vector are polarized.[81,82] These probability densities are presented in Fig. 12, where the top row [panels (a.i)–(a.iii)] shows the polarization of the position vector and the bottom row [panels (b.i)–(b.iii)] shows the polarization of the angular momentum vector; the three columns correspond to the features labeled as (i)–(iii) in Fig. 8, and the x, y, and z axes are those of the recoil frame defined in Table VI.

Note that for a $^1D_2$ state the total angular momentum coincides with the electronic orbital angular momentum, but also that the position vector does not coincide with the position of any particular electron, just as the total electronic angular momentum does not coincide with the angular momentum of any particular electron. The probability densities shown in Fig. 12 *do not* result from one-electron orbitals, although the $J=2$ condition inevitably causes the position-representation orbitals to have the familiar d-orbital shapes. The probability densities in Fig. 12 result from incoherent superposition of five such orbitals. Comparison of the results on the three columns of Fig. 12 shows that the photodissociation mechanisms underlying features (i)–(iii) of Fig. 8 lead to similarly polarized atoms: Their electronic position vector is aligned along $\pm(x+z)$ and their angular momentum along $\pm y$. This suggests dissociation via a common transition state and electronic surface.

We can also extract the populations of the M_J substates from the polarization moments; they are shown in Fig. 13. For all of the features (i)–(iii) of Fig. 8, we find that the total populations of the $|M_J|=1$ substates are in excess of 75%. It

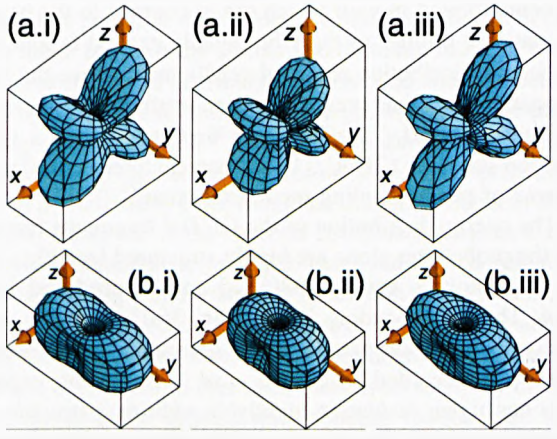

FIG. 12. Recoil-frame polarizations of the $O(^1D_2)$ electronic position [top, panels (a.i)–(a.iii)] and angular momentum [bottom, panels (b.i)–(b.iii)] vectors. The data in the three columns correspond to the features labeled (i)–(iii) in Fig. 8.

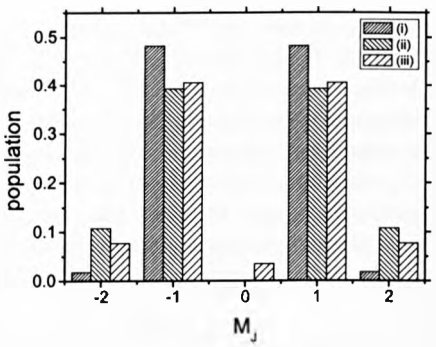

FIG. 13. M_J substate populations extracted from the corrected images for the features labeled (i)–(iii) in Fig. 8.

is interesting to compare this result with the work of Coroiu *et al.*[23] at higher excitation energies. These workers found a similar propensity to populate the $|M_J|=1$ substates for oxygen atoms correlating with $NO(^2\Pi_\Omega)$ produced in $v=1$. Significantly lower alignment was found in the fragments correlating with diatomic fragments exhibiting greater internal excitation. This is attributed to the opening of another dissociation channel at higher excitation energies.

The polarizations of $O(^1D_2)$ fragments with $|M_J|=1$ can correlate with d_{xz} and d_{yz} orbitals, but Fig. 12 shows that the former clearly dominate. Now, remember that xz is the plane containing the fragment recoil and parent dipole moment directions. If the dipole moment lies on the plane containing the three atoms, and if the recoil direction also lies on this plane (that is what one would expect on the basis of an impulsive model), then xz is also the C_s plane of symmetry. This implies that in the dominant processes the electronic wave function of the atomic fragment has A' symmetry. Assuming that the dissociation process exclusively occurs on A' electronic potentials, this in turn implies that there should be a preference for the production of $NO(^2\Pi_\Omega)$ in the A' Λ-doublet state. Unfortunately, as we scan both the photolysis and the probe laser to record the REMPI profiles, we cannot resolve the Λ-doublet components for rotational states below $N\sim20$ so we have not been able to confirm this prediction experimentally.

C. $NO(^2\Pi_\Omega)+O(^1D_2)$ dissociation mechanisms

The rotational profiles shown in Fig. 1 and the $O(^1D_2)$ energy distribution shown in Fig. 8 highlight different dissociation pathways for the production of $O(^1D_2)$. Analysis of the energy partitioning for the three features in Fig. 8 suggest that the axial recoil approximation is close to valid for the fragments labeled (ii) and (iii) in Fig. 8. In these cases the anisotropy parameters can be related to dissociative geometries which are in good agreement with the calculations of Schinke *et al.*[8] Our results suggest that this geometry results in the production of a relatively rotationally cold, vibrationally inverted diatomic fragment distribution implying that beyond the crossing point for dissociation there is little interaction between the atomic and diatomic moieties or change in Jacobi angle for these fragments.

Feature (i) in Fig. 8 is attributed to vibrationally and relatively rotationally excited diatomic fragments. By considering the ratio of rotational to total excess energy in this fragmentation process, it is unlikely that the dissociation can be treated within the axial recoil limit.[74] The nonaxial recoil dynamics and resulting increased diatomic rotational excitation results in a significant reduction in the translational anisotropy parameter for these fragments. The rotational assignments of the NO fragments formed in coincidence with these oxygen atoms are therefore in agreement with the low translational anisotropy parameter obtained from the fitting procedure and are also consistent with this effect being exclusively observed for vibrationally excited fragments (where the ratio of rotational to translational energy is high).

We attribute the similarity of the three multipole distributions [for features (i)–(iii)] to dissociation via a common avoided crossing and dissociative electronic state, likely the adiabatic (4) $^2A'$ state. This implies that the bimodal rotational profile of the NO fragments in $v=1$ is a consequence of the fragmentation of parent molecules with at least one quantum of bending mode excitation. It is noted that the peaks of the diatomic vibrational profiles of the fragments produced in coincidence with both $O(^1D_2)$ and $O(^3P_J)$ occur at the same levels at this excitation energy ($v=1$) and at higher excitation energies in the (3) $^2A'$ adiabatic state [see Ref. 23 and our interpretation of the higher kinetic energy mode in their $O(^3P_J)$ energy distributions at ~6.03 eV; $v=4$ (Ref. 6)]. It appears that the vibrational distribution in the $O(^1D_2)$ channel is determined by the symmetric stretch motion set up by the Franck–Condon window to the (3) $^2A'$ adiabatic state in accord with the explanation of Schinke *et al.*[8] This vibrational energy is retained on crossing to the (4) $^2A'$ adiabatic state.

The bimodal rotational profiles of the NO fragments produced in coincidence with $O(^3P_J)$ (Ref. 6) and the vibrationally excited NO fragments produced with $O(^1D_2)$ are intriguing. They suggest that the rotational bimodality is introduced, like the diatomic vibrational excitation, by the change in geometry (bond angle) associated with the Franck–Condon window from the (1) $^2A'$ to the (3) $^2A'$ state. This would be further supported if a bimodal rotational profile was observed for the vibrationally cold NO fragments formed concomitantly with $O(^1D_2)$. If ground vibrational state diatomic fragments were produced with rotational energies between 0.134 and 0.237 eV, these fragments would make up parts of peak (i) or (ii) and would correspond to fragment rotational levels between $N=25$ and 33. We note that there is no evidence for such features in Figs. 1(a) and 1(b); however, due to the signal to noise levels of the experiments we would only expect to see these fragments if they were produced with a yield in excess of 10%. The absence of such fragments in the rotational profiles is likely due to the ineffective coupling of the bending mode excitation to fragment rotation due to the crossing geometry and/or the topography of the dissociative (4) $^2A'$ adiabatic state. This interpretation of the rotational profiles is supported by the $O(^1D_2)$ energy distribution recorded at excitation energies close to 6.03 eV (see Fig. 9). Here the vibrational inversion is more obvious and the rotational profile of the NO fragments which likely correlate with $v=4$ is observed to be made up of at least three different modes. We suggest that this multimodal

rotational profile is the result of a higher degree of parent bending mode excitation (although at this excitation energy, nonadiabatic couplings with higher energy electronic states cannot be ruled out and are suggested by the alignment results of Coroiu *et al.*[23]). The less structured rovibrational distributions of the faster fragments in this energy distribution is consistent with the results obtained at lower excitation energies.

In our experiments at excitation energies close to 5.48 eV, NO_2 molecules are primarily excited from their ground vibrational and lowest few rotational states. It seems that the Franck–Condon factors to the (3) $^2A'$ adiabatic state result in the preferential excitation of single quanta of parent symmetric stretching and bending modes (where $\nu_1' \sim 143$ meV and $\nu_2' \sim 65$ meV, respectively[10]) which are transferred into vibrationally excited, rotationally bimodal product distributions for the majority of the diatomic fragments. In the case of the $O(^1D_2)$ channel this is calculated to occur via two excited adiabatic states and a tight transition state.[8] The $O(^1D_2)/O(^3P_J)$ branching ratio is determined by the coupling strength between the (3) $^2A'$ and (4) $^2A'$ adiabatic electronic surfaces and the profiles and branching ratios of the rotational modes sensitively depend on the topographies of these states. We hope that our findings will stimulate further theoretical study in order to understand the origins of these multimodal rovibrational distributions.

V. CONCLUSIONS

Mass-resolved REMPI spectroscopy and VMI have been used to study the photoproduct distributions observed on excitation to the (3) $^2A'$ state of NO_2 between 5.46 and 5.64 eV. The two techniques have allowed us to unequivocally assign the single-laser NO fragment rovibrational profiles to $NO(^2\Pi_\Omega)$ fragments produced concomitantly with $O(^1D_2)$. In addition we have highlighted the small yet complex contribution of $NO(^2\Pi_\Omega)$ fragments produced with $O(^3P_J)$ atoms with differing degrees of internal excitation across this excitation range.

By recording dc slice velocity map images of the $O(^1D_2)$ fragments produced using different pump and probe laser polarizations at an excitation energy of 5.479 52 eV we have measured the kinetic energy profile and derived the translational anisotropy parameters and multipole moments of the $O(^1D_2)$ fragment polarization as a function of kinetic energy. Using the NO fragment REMPI profiles we have assigned the features of the $O(^1D_2)$ energy distribution to production in coincidence with a unimodal rotational distribution of fragments in $v=0$ and a bimodal rotational profile of vibrationally excited fragments in $v=1$. Furthermore, the $O(^1D_2)$ energy distribution highlights the vibrational inversion of the diatomic cofragments, in accord with other work.[26,69]

From the multipole moments obtained from the $O(^1D_2)$ images we conclude that the majority of these fragments are formed in the $M_J \pm 1$ state and that all of the $O(^1D_2)$ fragments are produced via the same avoided crossing to the (4) $^2A'$ dissociative electronic state. The translational anisotropy parameters of the $O(^1D_2)$ fragments produced in coincidence with rotationally cold diatomic fragments are related to dissociative geometries which are found to be in good agreement with the calculations of Schinke *et al.* who highlighted an avoided crossing between the (3) $^2A'$ and (4) $^2A'$ adiabatic surfaces at a bond angle close to 110°. The lower translational anisotropy of the slower $O(^1D_2)$ fragments is a signature of production with rotationally and vibrationally excited diatomic fragments. Here the low translational energy and relatively high rotational energy are results of nonaxial recoil dynamics occurring after the avoided crossing close to 110°.

Analysis of the $O(^1D_2)$ and $O(^3P_J)$ photofragment distributions recorded at ~5.48 eV (Ref. 6) and 6.03 eV (Ref. 23) allows us to attribute the vibrational inversion of the $NO(^2\Pi_\Omega)$ fragments produced with $O(^1D_2)$ to the symmetric stretch motion set up by the Franck–Condon window from the (1) $^2A'$ state to the (3) $^2A'$ state. This symmetric stretching motion is retained for the majority of the $NO(^2\Pi_\Omega)$ fragments formed with either $O(^1D_2)$ or $O(^3P_J)$. The bimodal rotational profiles observed for the diatomic fragments formed with the majority of the $O(^3P_J)$ fragments and the vibrationally excited diatomic fragments formed with $O(^1D_2)$ are consistent with bending motion caused by the geometry change in excitation to the (3) $^2A'$ state. For the $O(^1D_2)$ channel, a single quantum of bending motion is effectively transferred via the (3) $^2A'/(4)$ $^2A'$ avoided crossing into two rotational modes for the vibrationally excited $NO(^2\Pi_\Omega)$ fragments produced close to the energetic threshold. In contrast this rotational structure is lost for the vibrationally cold diatomic fragments, where the motion set up by the Franck–Condon window is presumably washed out due to the topography of the reaction coordinate.

ACKNOWLEDGMENTS

I.W. is grateful to the Engineering and Physical Sciences Research Council (EPSRC) for a research studentship. We are also indebted to Mr. P. Kapetanopoulos for the design and construction of the high speed pulser unit used to gate the microchannel plates and to Dr. I. Anton-Garcia for assistance in constructing the VMI spectrometer. We thank Professor A. J McCaffrey, Sussex University, for the loan of a photoelastic modulator and Dr. M. Blitz and the School of Chemistry for the loan of a dye laser. This work has been supported by EPSRC Grant No. EP/G000360/1. We are also grateful to the British Council Alliance Fronco-British partnership program for partial support.

APPENDIX: CONVERSION FACTORS FOR DYNAMICAL FUNCTIONS

For ease of comparison between the results of Table VI and results by other authors, we present in this appendix the equations that relate our stereodynamical parameters to the "dynamical functions" introduced by Siebbeles *et al.*[57] These dynamical functions, $f_k(q,q')$, have been explicitly related to the stereodynamical parameters used in various works, and comprehensive compilations of transformation formulas are available.[59,83–85]

The definition of the dynamical functions reads[57]

$$f_k(q,q') = \sum_{\Omega'\Omega} \frac{(-1)^{q'-q}}{\sqrt{2j+1}} \langle j\Omega', k(q-q') | j\Omega \rangle \rho_{\Omega'\Omega}, \quad \text{(A1)}$$

where j is the angular momentum quantum number of the fragment under study, Ω its helicity quantum number (that is, the quantum number specifying the projection of **j** on the recoil direction), $\langle \cdots, \cdots | \cdots \rangle$ is a Clebsch–Gordan coefficient, and the $\rho_{\Omega'\Omega}$ are the elements of the density matrix of the fragment, normalized so that

$$\mathrm{Tr}(\rho) = \sum_{\Omega} \rho_{\Omega'\Omega} = \sigma(\theta,\varphi)\sqrt{2j+1}, \quad \text{(A2)}$$

where $\sigma(\theta,\varphi)$ is the differential cross section.

In terms of the definitions used in this work (see supplementary material), the density matrix elements just mentioned are given by

$$\rho_{\Omega'\Omega} = \frac{\sigma}{4\pi}[1 + \beta P_2(\cos\theta)] \sum_{KQ} \frac{2K+1}{\sqrt{2j+1}} \langle j\Omega', KQ | j\Omega \rangle \rho_Q^{(K)}, \quad \text{(A3)}$$

where σ is the integral cross section, $P_2(x)$ is the Legendre polynomial of second degree, and the $\rho_Q^{(K)}$ are our complex polarization moments. Insertion of this formula in Eq. (A1) leads to

$$f_k(q,q') = (-1)^{q'-q} \frac{\sigma}{4\pi}[1 + \beta P_2(\cos\theta)] \rho_{q-q'}^{(k)}, \quad \text{(A4)}$$

which is the expression relating the dynamical functions to the asymmetry parameter, β, and to our complex polarization moments. The latter can be easily obtained from the real polarization moments of Table VI:

$$\rho_0^{(k)} = \rho_0^{\{k\}}, \quad \text{(A5a)}$$

$$\rho_q^{(k)} = \frac{(-1)^q}{\sqrt{2}} (\rho_{q+}^{\{k\}} + i\rho_{q-}^{\{k\}}), \quad 1 \le q \le k, \quad \text{(A5b)}$$

$$\rho_{-q}^{(k)} = \frac{1}{\sqrt{2}} (\rho_{q+}^{\{k\}} - i\rho_{q-}^{\{k\}}), \quad 1 \le q \le k. \quad \text{(A5c)}$$

Note that the values of the polarization moments not listed on Table VI should be taken to be zero either because the symmetry of the problem makes them vanish or else because our measurements were not sensitive to them.

[1] W. C. Gardiner, Jr., *Gas-Phase Combustion Chemistry*, 2nd ed. (Springer, New York, 1999), Vol. 1.
[2] B. J. Finlayson-Pitts and J. N. Pitts, *Chemistry of the Upper and Lower Atmosphere: Theory, Experiments, and Applications*, 1st ed. (Academic, New York, 1999), Vol. 1.
[3] G. E. Busch and K. R. Wilson, J. Chem. Phys. **56**, 3638 (1972).
[4] G. E. Busch and K. R. Wilson, J. Chem. Phys. **56**, 3626 (1972).
[5] R. Jost, J. Nygard, A. Pasinski, and A. Delon, J. Chem. Phys. **105**, 1287 (1996).
[6] I. Wilkinson and B. J. Whitaker, J. Chem. Phys. **129**, 154312 (2008).
[7] J. W. Au and C. E. Brion, Chem. Phys. **218**, 109 (1997).
[8] R. Schinke, S. Y. Grebenshchikov, and H. Zhu, Chem. Phys. **346**, 99 (2008).
[9] G. Herzberg, *Molecular Spectra and Molecular Structure Volume III—Electronic Spectra and Electronic Structure of Polyatomic Molecules*, 2nd ed. (Krieger, Malabar, FL, 1991).
[10] K. E. J. Hallin and A. J. Merer, Can. J. Phys. **54**, 1157 (1976).
[11] K. Tsuji, M. Ikeda, J. Awamura, A. Kawai, and K. Shibuya, Chem. Phys. Lett. **374**, 601 (2003).
[12] R. Fan and L. D. Ziegler, J. Raman Spectrosc. **25**, 497 (1994).
[13] C. B. McKendrick, C. Fotakis, and R. J. Donovan, J. Photochem. **20**, 175 (1982).
[14] T. G. Slanger, W. K. Bischel, and M. J. Dyer, J. Chem. Phys. **79**, 2231 (1983).
[15] K. F. Preston and R. J. Cvetanovic, J. Chem. Phys. **45**, 2888 (1966).
[16] W. M. Uselman and E. K. C. Lee, J. Chem. Phys. **65**, 1948 (1976).
[17] G. Hancock and M. Morrison, Mol. Phys. **103**, 1727 (2005).
[18] F. Sun, G. P. Glass, and R. F. Curl, Chem. Phys. Lett. **337**, 72 (2001).
[19] H. S. Im and E. R. Bernstein, J. Phys. Chem. A **106**, 7565 (2002).
[20] M. Ahmed, D. S. Peterka, A. S. Bracker, O. S. Vasyutinskii, and A. G. Suits, J. Chem. Phys. **110**, 4115 (1999).
[21] R. C. Richter, V. I. Khamaganov, and A. J. Hynes, Chem. Phys. Lett. **319**, 341 (2000).
[22] N. Shafer, K. Tonokura, Y. Matsumi, S. Tasaki, and M. Kawasaki, J. Chem. Phys. **95**, 6218 (1991).
[23] A. M. Coroiu, D. H. Parker, G. C. Groenenboom, J. Barr, I. T. Novalbos, and B. J. Whitaker, Eur. Phys. J. D **38**, 151 (2006).
[24] M. R. Taherian, P. C. Cosby, and T. G. Slanger, J. Phys. Chem. **91**, 2304 (1987).
[25] R. Compargue, *Atomic and Molecular Beams: The State of The Art 2000*, 1st ed. (Springer-Verlag, Berlin, 2001), Vol. 1.
[26] L. Bigio, R. S. Tapper, and E. R. Grant, J. Phys. Chem. **88**, 1271 (1984).
[27] A. T. J. B. Eppink and D. H. Parker, Rev. Sci. Instrum. **68**, 3477 (1997).
[28] B. V. Picheyev, A. G. Smolin, and O. S. Vasyutinskii, J. Phys. Chem. A **101**, 7614 (1997).
[29] R. N. Dixon and H. Rieley, Chem. Phys. **137**, 307 (1989).
[30] Y. Wang, H.-P. Loock, J. Cao, and C. X. W. Qian, J. Chem. Phys. **102**, 808 (1995).
[31] T. P. Rakitzis, S. A. Kandel, and R. N. Zare, J. Chem. Phys. **108**, 8291 (1998).
[32] T. Suzuki, H. Katayanagi, Y. Mo, and K. Tonokura, Chem. Phys. Lett. **256**, 90 (1996).
[33] Y. Mo, H. Katayanagi, M. C. Heaven, and S. Toshinori, Phys. Rev. Lett. **77**, 830 (1996).
[34] A. T. J. B. Eppink, D. H. Parker, M. H. M. Janssen, B. Buijsse, and W. J. van der Zande, J. Chem. Phys. **108**, 1305 (1998).
[35] *Imaging in Molecular Dynamics: Technology and Applications*, edited by B. J. Whitaker (Cambridge University Press, Cambridge, 2003).
[36] T. P. Rakitzis, Chem. Phys. Lett. **342**, 121 (2001).
[37] T. P. Rakitzis, P. C. Samartzis, and T. N. Kitsopoulos, Phys. Rev. Lett. **87**, 123001 (2001).
[38] A. G. Suits, R. L. Miller, L. S. Bontuyan, and P. L. Houston, J. Chem. Soc., Faraday Trans. **89**, 1443 (1993).
[39] V. K. Nestorov and J. I. Cline, J. Chem. Phys. **111**, 5287 (1999).
[40] Y. Mo, H. Katayanagi, and T. Suzuki, J. Chem. Phys. **110**, 2029 (1999).
[41] V. K. Nestorov, R. D. Hinchliffe, R. Uberna, J. I. Cline, K. T. Lorenz, and D. W. Chandler, J. Chem. Phys. **115**, 7881 (2001).
[42] M. J. Bass, M. Brouard, A. P. Clark, and C. Vallance, J. Chem. Phys. **117**, 8723 (2002).
[43] D. Townsend, M. P. Minitti, and A. G. Suits, Rev. Sci. Instrum. **74**, 2530 (2003).
[44] K. Tonokura and T. Suzuki, Chem. Phys. Lett. **224**, 1 (1994).
[45] C. R. Gebhardt, T. P. Rakitzis, P. C. Samartzis, V. Ladopoulos, and T. N. Kitsopoulos, Rev. Sci. Instrum. **72**, 3848 (2001).
[46] J. J. Lin, J. Zhou, W. Shiu, and K. Liu, Rev. Sci. Instrum. **74**, 2495 (2003).
[47] E. Wrede, S. Laubach, S. Schulenburg, A. Brown, E. R. Wouters, A. J. Orr-Ewing, and M. N. R. Ashfold, J. Chem. Phys. **114**, 2629 (2001).
[48] N. Yonekura, C. Gebauer, H. Kohguchi, and T. Suzuki, Rev. Sci. Instrum. **70**, 3265 (1999).
[49] A. V. Komissarov, M. P. Minitti, A. G. Suits, and G. E. Hall, J. Chem. Phys. **124**, 014303 (2006).
[50] S. K. Lee, R. Silva, S. Thamanna, O. S. Vasyutinskii, and A. G. Suits, J. Chem. Phys. **125**, 144318 (2006).
[51] T. P. Rakitzis and T. N. Kitsopoulos, J. Chem. Phys. **116**, 9228 (2002).
[52] T. P. Rakitzis, P. C. Samartzis, R. L. Toomes, and T. N. Kitsopoulos, J. Chem. Phys. **121**, 7222 (2004).

[53] D. Townsend, S. K. Lee, and A. G. Suits, Chem. Phys. **301**, 197 (2004).
[54] J. Luque and D. R. Crosley, "LIFBASE: Database and spectral simulation program (version 1.5)," SRI International Report No. MP 99-009, 1999.
[55] G. Herzberg, *Molecular Spectra and Molecular Structure Volume I—Spectra of Diatomic Molecules*, 2nd ed. (Krieger, Malabar, FL, 1989).
[56] D. M. Sonnenfroh and K. Liu, Chem. Phys. Lett. **176**, 183 (1991).
[57] L. D. A. Siebbeles, M. Glass-Maujean, O. S. Vasyutinskii, J. A. Beswick, and O. Roncero, J. Chem. Phys. **100**, 3610 (1994).
[58] A. S. Bracker, E. R. Wouters, A. G. Suits, and O. S. Vasyutinskii, J. Chem. Phys. **110**, 6749 (1999).
[59] T. P. Rakitzis and R. N. Zare, J. Chem. Phys. **110**, 3341 (1999).
[60] R. N. Zare, Mol. Photochem. **4**, 1 (1972).
[61] D. A. Varshalovich, A. N. Moskalev, and V. K. Khersonskii, *Quantum Theory of Angular Momentum*, 1st ed. (World Scientific, Singapore, 1988), Vol. 1.
[62] Y. Mo and T. Suzuki, J. Chem. Phys. **109**, 4691 (1998).
[63] See EPAPS supplementary material at http://dx.doi.org/10.1063/1.3194286 for the derivation of Eq. (8) of the article, which gives the expression for the geometric coefficients appearing in Eq. (1) of the article, presented in table format.
[64] J. A. Nelder and R. Mead, Comput. J. **7**, 308 (1965).
[65] W. H. Press, S. A. Teukolslky, W. T. Vetterling, and B. P. Flannery, *Numerical Recipes*, 2nd ed. (Cambridge University Press, Cambridge, 2001), Vol. 1.
[66] I. V. Hertel and W. Stoll, Adv. At. Mol. Phys. **13**, 113 (1978).
[67] J. Aldegunde, F. J. Aoiz, and M. P. de Miranda, Phys. Chem. Chem. Phys. **10**, 1139 (2008).
[68] M. P. de Miranda, F. J. Aoiz, L. Banares, and V. S. Rabanos, J. Chem. Phys. **111**, 5368 (1999).
[69] A. Schmaunz, U. Kensy, A. Slenczka, and B. Dick, Phys. Chem. Chem. Phys. DOI:10.1039/b909037a (2009).
[70] R. Schinke, *Photodissociation Dynamics*, 1st ed. (Cambridge University Press, Cambridge, 1993).
[71] R. Schinke, A. Untch, H. U. Suter, and J. R. Huber, J. Chem. Phys. **94**, 7929 (1991).
[72] V. P. Hradil, T. Suzuki, S. A. Hewitt, P. L. Houston, and B. J. Whitaker, J. Chem. Phys. **99**, 4455 (1993).
[73] C. H. Hsieh, Y. S. Lee, A. Fujii, S. H. Lee, and K. P. Liu, Chem. Phys. Lett. **277**, 33 (1997).
[74] A. V. Demyanenko, V. Dribinski, H. Reisler, H. Meyer, and C. X. W. Qian, J. Chem. Phys. **111**, 7383 (1999).
[75] J. A. Harrison, X. Yang, M. Rosslein, P. Felder, and J. R. Huber, J. Phys. Chem. **98**, 12260 (1994).
[76] S. A. Reid and H. Reisler, J. Chem. Phys. **101**, 5683 (1994).
[77] S. A. Reid, A. Sanov, and H. Reisler, Faraday Discuss. **102**, 129 (1995).
[78] S. A. Reid and H. Reisler, J. Phys. Chem. **100**, 474 (1996).
[79] S.-C. Yang and R. Bersohn, J. Chem. Phys. **61**, 4400 (1974).
[80] A. V. Demyanenko, A. B. Potter, V. Dribinski, and H. Reisler, J. Chem. Phys. **117**, 2568 (2002).
[81] M. P. de Miranda and F. J. Aoiz, Phys. Rev. Lett. **93**, 083201 (2004).
[82] M. P. de Miranda, F. J. Aoiz, V. Sáez-Rábanos, and M. Brouard, J. Chem. Phys. **121**, 9830 (2004).
[83] A. G. Suits and O. S. Vasyutinskii, Chem. Rev. (Washington, D.C.) **108**, 3706 (2008).
[84] M. L. Costen and G. E. Hall, Phys. Chem. Chem. Phys. **9**, 272 (2007).
[85] A. J. Alexander, J. Chem. Phys. **118**, 6234 (2003).

Appendix C

Supplementary material to Chapter 5

C.1 Preface

This supplement was written by Dr Marcelo de Miranda in order to provide details about the angular momentum treatment that was used in Chapter 5 to extract recoil frame polaristation moments from the $O(^1D_2)$ velocity map images. Although this supplement is not my own work it is included as an appendix to this thesis to provide further details about the derivation of the formulas used in Chapter 5 for the interested reader. The document is also available on-line as supplementary material to were presented in Appendix 2 (65).

C.2 Supplement

This supplement serves two purposes. First, to present the derivation of Eq. (8) of Chapter 5, which gives the expression for the geometric coefficients appearing on the formula [Eq. (1) of Chapter 5] used for the fitting of dynamical parameters to the experimentally observed images. Second, to establish what dynamical parameters the measurements are sensitive to.

An outline of the derivation was presented in Sec. 5.4.2, and in Fig. 5.9 in particular. In what follows we will consider the various steps of the derivation using that figure as a guide. We will also use the various reference frames defined on Table IV of Chapter 5.

We start with the derivation of a general expression that is valid also for experimental geometries and laser polarisations differing from the ones we have used; this is done in Sec. C.2.1. Next, we use specific details of the experimental arrangements to explicitly obtain Eqs. (1) and (8) of Chapter 5 and also to determine the $O(^1D_2)$ polarisation moments that the measurements are sensitive to; this is done in Sec. C.2.2.

C.2.1 General formula

From box #1 to box #2

This step has been described in Chapter 5, see Eqs. (4) and (5). The expression corresponding to box #2 is Eq. (5), which we repeat here:

$$I_{\mathrm{rec}}(\theta,\varphi) = \sum_{K'Q'} \frac{2K'+1}{4\pi} a_{Q'}^{(K')} C^*_{K'Q'}(\theta,\varphi) = \sum_{K'} \frac{2K'+1}{4\pi} a_0^{(K')} P_{K'}(\cos\theta), \qquad \text{(C.1)}$$

where:

- θ and φ are the polar and azimuthal angles that specify the direction of recoil in the $X_1Y_1Z_1$ frame.
- $I_{\mathrm{rec}}(\theta,\varphi)$ is the distribution of fragment recoil directions.
- The $a_{Q'}^{(K')}$ are multipole moments of I_{rec} in the pump, $X_1Y_1Z_1$ frame. Note:
  - The multipolar expansion is covariant and normalised so that $a_0^{(0)} = 1$.
  - The only nonvanishing multipole moments are $a_0^{(0)} = 1$ and $a_0^{(2)} = \beta/5$, where β is the asymmetry parameter.
- $C^*_{K'Q'}(\theta,\varphi)$ and $P_{K'}(\cos\theta)$ are, respectively, (complex conjugates of) modified spherical harmonics and Legendre polynomials. They are related by $C_{K'Q'}(\theta,\varphi) = P_{K'}(\cos\theta)$, see Ref. (236, left=,right=).

From box #3 to box #5

The expression corresponding to box #3 is the relation between the detector response and the fragment polarisation in a two-photon excitation process. It has been derived

by Mo and Suzuki and reads (237)

$$I_{\text{det}} = \sum_k \rho^{(k)}_{q_2=0} \tilde{P}_k, \tag{C.2a}$$

$$\tilde{P}_k = (-1)^{J_i+J_f} \sqrt{5(2k+1)(2J_i+1)} \langle 2(2s), k0|2(2s)\rangle \begin{Bmatrix} J_i & J_i & k \\ 2 & 2 & J_f \end{Bmatrix}, \tag{C.2b}$$

where:

- The $\rho^{(k)}_{q_2=0}$ are the zero-component polarisation moments of the fragment in the probe, $X_2Y_2Z_2$ frame. They are normalised so that $\rho^{(0)}_0 = 1$.
- J_i and J_f are the initial and final angular momentum quantum numbers of the fragment in the two-photon transition.
- $s = 0$ for linearly polarised light, or $s = \pm 1$ for right- or left-handed circularly polarised light.
- $\langle \cdot\cdot, \cdot\cdot|\cdot\cdot\rangle$ and $\{ \vdots \}$ are Clebsch-Gordan and 6-j coefficients, respectively.

For linearly polarised light, Eq. (C.2b) is valid only when $J_i \neq J_f$. We also note that only $q_2 = 0$ moments appear on Eq. (C.2a); that expression is therefore valid for both covariant and contravariant expansions of the fragment density matrix. As throughout this work, we choose to use a covariant expansion, see Eq. (7) of Chapter 5 for its general form.

We now need to express the probe-frame polarisation moments appearing on Eq. (C.2a) in terms of the recoil-frame polarisation moments that are of interest to us. We do this via two rotations of reference frame:

- First we rotate from the probe to the pump frame. In terms of Euler angles this rotation is

$$R_{X_2Y_2Z_2 \to X_1Y_1Z_1} \equiv R(\alpha_{21}, \beta_{21}, \gamma_{21}); \tag{C.3}$$

  we stress that the three Euler angles are defined as those that take $X_2Y_2Z_2$ into $X_1Y_1Z_1$, not the other way around.

- Next we rotate from the pump to the recoil frame. In terms of Euler angles this rotation is

$$R_{X_1Y_1Z_1 \to xyz} \equiv R(\varphi, \theta, 0); \tag{C.4}$$

the three Euler angles are defined as those that take $X_1Y_1Z_1$ into xyz, not the other way around.

Since the polarisation moments used here are associated with covariant expansions, these two rotations lead to

$$\rho^{(k)}_{q_2} = \sum_{q_1} D^{k*}_{q_2q_1}(\alpha_{21},\beta_{21},\gamma_{21})\rho^{(k)}_{q_1} = \sum_{q_1} D^{k*}_{q_2q_1}(\alpha_{21},\beta_{21},\gamma_{21})\left(\sum_{q} D^{k*}_{q_1q}(\varphi,\theta,0)\rho^{(k)}_{q}\right)$$
$$= \sum_{q_1q} \rho^{(k)}_{q} D^{k*}_{q_2q_1}(\alpha_{21},\beta_{21},\gamma_{21}) D^{k*}_{q_1q}(\varphi,\theta,0), \tag{C.5}$$

where the $D^{k}_{q_aq_b}(R)$ are rotation matrix elements defined as in Refs. (219; 236; 258; 259; 260, left=,right=). Inserting this result in Eq. (C.2a) and using the formula (236)

$$D^{k}_{0q_1}(\alpha_{21},\beta_{21},\gamma_{21}) = C_{k(-q_1)}(\beta_{21},\gamma_{21}) \tag{C.6}$$

one gets

$$I_{\text{det}}(\theta,\varphi) = \sum_{kq_1q} \rho^{(k)}_{q} D^{k*}_{0q_1}(\alpha_{21},\beta_{21},\gamma_{21}) D^{k*}_{q_1q}(\varphi,\theta,0)\tilde{P}_k \tag{C.7}$$
$$= \sum_{kq_1q} \rho^{(k)}_{q} \tilde{P}_k C^{*}_{k(-q_1)}(\beta_{21},\gamma_{21}) D^{k*}_{q_1q}(\varphi,\theta,0), \tag{C.8}$$

which is the expression corresponding to box #5, except that on Fig. 5.9 we have not indicated that $I_{\text{det}}(\theta,\varphi)$ depends on γ_{21}. The reason is that all the experimental geometries we have used imply $\gamma_{21} = 0$. For the sake of generality, here we will only make use of data specific to the measurements after determination of the final expression for the geometric coefficients.

From box #5 to box #6

Further manipulation of Eq. (C.8) is made easier if we rewrite it as a multipolar expansion. We again use an expansion that is covariant and normalised so that the zero-rank polarisation moment is unity:

$$I_{\text{det}}(\theta,\varphi) = \sum_{KQ} \frac{2K+1}{4\pi} p^{(K)}_{Q} C^{*}_{KQ}(\theta,\varphi), \tag{C.9a}$$

$$p^{(K)}_{Q} = \int_0^{2\pi}\int_0^{\pi} I_{\text{det}}(\theta,\varphi) C_{KQ}(\theta,\varphi)\sin\theta\, d\theta\, d\varphi. \tag{C.9b}$$

Inserting Eq. (C.8) in Eq. (C.9b) one gets

$$\begin{aligned} p_Q^{(K)} &= \int_0^{2\pi}\int_0^{\pi}\left(\sum_{kq_1q}\rho_q^{(k)}\tilde{P}_k C^*_{k(-q_1)}(\beta_{21},\gamma_{21})D^{k*}_{q_1q}(\varphi,\theta,0)\right)C_{KQ}(\theta,\varphi)\sin\theta\,d\theta\,d\varphi \\ &= \sum_{kqq_1}\rho_q^{(k)}\tilde{P}_k C^*_{k(-q_1)}(\beta_{21},\gamma_{21})\int_0^{2\pi}\int_0^{\pi}D^{k*}_{q_1q}(\varphi,\theta,0)C_{KQ}(\theta,\varphi)\sin\theta\,d\theta\,d\varphi \\ &= \sum_{kqq_1}\rho_q^{(k)}\tilde{P}_k C^*_{k(-q_1)}(\beta_{21},\gamma_{21})\int_0^{2\pi}\int_0^{\pi}D^{k*}_{q_1q}(\varphi,\theta,0)D^{K*}_{Q0}(\varphi,\theta,0)\sin\theta\,d\theta\,d\varphi, \end{aligned} \tag{C.10}$$

where in the last line we have used the formula (236)

$$C_{KQ}(\theta,\varphi) = D^{K*}_{Q0}(\varphi,\theta,0). \tag{C.11}$$

Using the relation between the elements of rotation matrices and reduced rotation matrices, (236)

$$D^K_{Q_1Q_2}(\varphi,\theta,\chi) = e^{-iQ_1\varphi}d^K_{Q_1Q_2}(\theta)e^{-iQ_2\chi}, \tag{C.12}$$

and noting that the elements of the reduced rotation matrix are real, one finds that the integral on the right-hand term of Eq. (C.10) is given by

$$\begin{aligned} \int_0^{2\pi}\int_0^{\pi}D^{k*}_{q_1q}(\varphi,\theta,0)D^{K*}_{Q0}(\varphi,\theta,0)\sin\theta\,d\theta\,d\varphi &= \int_0^{2\pi}\int_0^{\pi}e^{iq_1\varphi}d^k_{q_1q}(\theta)e^0e^{iQ\varphi}d^K_{Q0}(\theta)e^0\sin\theta\,d\theta\,d\varphi \\ &= \left(\int_0^{2\pi}e^{i(q_1+Q)\varphi}\,d\varphi\right)\left(\int_0^{\pi}d^k_{q_1q}(\theta)d^K_{Q0}(\theta)\sin\theta\,d\theta\right) \\ &= 2\pi\delta_{q_1(-Q)}\int_0^{\pi}d^k_{q_1q}(\theta)d^K_{Q0}(\theta)\sin\theta\,d\theta \\ &= 2\pi\delta_{q_1(-Q)}\int_0^{\pi}d^k_{(-Q)q}(\theta)d^K_{Q0}(\theta)\sin\theta\,d\theta. \end{aligned} \tag{C.13}$$

This implies that Eq. (C.10) can be written as

$$\begin{aligned} p_Q^{(K)} &= \sum_{kqq_1}\rho_q^{(k)}\tilde{P}_k C^*_{k(-q_1)}(\beta_{21},\gamma_{21})2\pi\delta_{q_1(-Q)}\int_0^{\pi}d^k_{(-Q)q}(\theta)d^K_{Q0}(\theta)\sin\theta\,d\theta \\ &= 2\pi\sum_{kq}\rho_q^{(k)}\tilde{P}_k C^*_{kQ}(\beta_{21},\gamma_{21})\int_0^{\pi}d^k_{(-Q)q}(\theta)d^K_{Q0}(\theta)\sin\theta\,d\theta \\ &= 2\pi\sum_{kq}\rho_q^{(k)}\tilde{P}_k C^*_{kQ}(\beta_{21},\gamma_{21})I^{kK}_{(-Q)qQ0} \\ &= \sum_{kq}\rho_q^{(k)}\tilde{P}_k W_{kqKQ}, \end{aligned} \tag{C.14}$$

where in the last two lines line we have introduced some shorthand notation, namely

$$I^{AB}_{a_1a_2b_1b_2} = \int_0^\pi d^A_{a_1a_2}(\xi) d^B_{b_1b_2}(\xi) \sin\xi \, d\xi \tag{C.15}$$

(apart from a slight change in notation, this is Eq. (9) of Chapter 5) and

$$W_{kqKQ} = 2\pi C^*_{kQ}(\beta_{21}, \gamma_{21}) I^{kK}_{(-Q)qQ0}. \tag{C.16}$$

Equation (C.14) is the expression for the multipole moments referred to in box #6 of Fig. 5.9. The corresponding multipolar expansion is that of Eq. (C.9a).

From boxes #2 and #6 to box #8

Multiplication of the expressions for $I_{\rm rec}(\theta,\varphi)$ and $I_{\rm det}(\theta,\varphi)$ — respectively, Eqs. (C.1) and (C.9a), corresponding to boxes #2 and #6 of Fig. 5.9 — leads to the expression corresponding to box #7:

$$\begin{aligned}
I_{\rm obs}(\theta,\varphi) &= I_{\rm rec}(\theta,\varphi) I_{\rm det}(\theta,\varphi) \\
&= \left(\sum_{K'} \frac{2K'+1}{4\pi} a_0^{(K')} P_{K'}(\cos\theta) \right) \left(\sum_{KQ} \frac{2K+1}{4\pi} p_Q^{(K)} C^*_{KQ}(\theta,\varphi) \right) \\
&= \sum_{K'KQ} \frac{(2K'+1)(2K+1)}{16\pi^2} a_0^{(K')} p_Q^{(K)} P_{K'}(\cos\theta) C^*_{KQ}(\theta,\varphi) \\
&= \sum_{K'KQ} \frac{(2K'+1)(2K+1)}{16\pi^2} a_0^{(K')} p_Q^{(K)} D^{K'}_{00}(\varphi,\theta,0) D^K_{Q0}(\varphi,\theta,0) \\
&= \sum_{K'KQ} \frac{(2K'+1)(2K+1)}{16\pi^2} a_0^{(K')} p_Q^{(K)} \sum_{T'} \langle K'0, KQ|T'Q\rangle \langle K'0, K0|T'0\rangle D^{T'}_{Q0}(\varphi,\theta,0) \\
&= \sum_{K'KQ} \frac{(2K'+1)(2K+1)}{16\pi^2} a_0^{(K')} p_Q^{(K)} \sum_{T'} \langle K'0, KQ|T'Q\rangle \langle K'0, K0|T'0\rangle C^*_{T'Q}(\theta,\varphi),
\end{aligned} \tag{C.17}$$

where in the last three lines we have used the relations among Legendre polynomials, modified spherical harmonics and rotation matrix elements, and also the Clebsch-Gordan series. (236)

As before, further manipulation is made easier if we rewrite $I_{\rm obs}(\theta,\varphi)$ as a multipolar expansion. We do this using the same covariance and normalisation conventions as

before:

$$I_{\text{obs}}(\theta,\varphi) = \sum_{Tt_1} \frac{2T+1}{4\pi} \tau_{t_1}^{(T)} C_{Tt_1}^*(\theta,\varphi), \tag{C.18a}$$

$$\tau_{t_1}^{(T)} = \int_0^{2\pi}\int_0^{\pi} I_{\text{obs}}(\theta,\varphi) C_{Tt_1}(\theta,\varphi)\sin\theta\, d\theta\, d\varphi. \tag{C.18b}$$

Inserting Eq. (C.17) in Eq. (C.18b) one gets

$$\begin{aligned}
\tau_{t_1}^{(T)} &= \int_0^{2\pi}\int_0^{\pi}\left(\sum_{K'KQ} \frac{(2K'+1)(2K+1)}{16\pi^2} a_0^{(K')} p_Q^{(K)} \right.\\
&\qquad \left. \times \sum_{T'} \langle K'0, KQ|T'Q\rangle\langle K'0, K0|T'0\rangle C_{T'Q}^*(\theta,\varphi)\right) C_{Tt_1}(\theta,\varphi)\sin\theta\, d\theta\, d\varphi\\
&= \sum_{\substack{K'K\\T'Q}} \frac{(2K'+1)(2K+1)}{16\pi^2} a_0^{(K')} p_Q^{(K)} \langle K'0, KQ|T'Q\rangle\langle K'0, K0|T'0\rangle\\
&\qquad \times \int_0^{2\pi}\int_0^{\pi} C_{T'Q}^*(\theta,\varphi) C_{Tt_1}(\theta,\varphi)\sin\theta\, d\theta\, d\varphi\\
&= \sum_{\substack{K'K\\T'Q}} \frac{(2K'+1)(2K+1)}{16\pi^2} a_0^{(K')} p_Q^{(K)} \langle K'0, KQ|T'Q\rangle\langle K'0, K0|T'0\rangle \frac{4\pi}{2T+1}\delta_{T'T}\delta_{t_1Q}\\
&= \sum_{K'K} \frac{(2K'+1)(2K+1)}{4\pi(2T+1)} a_0^{(K')} p_{t_1}^{(K)} \langle K'0, Kt_1|Tt_1\rangle\langle K'0, K0|T0\rangle,
\end{aligned} \tag{C.19}$$

where in the third line we have used the orthogonality of the modified spherical harmonics. (236)

Equation (C.19) is the expression for the multipole moments referred to in box #8 of Fig. 5.9. The corresponding multipolar expansion is that of Eq. (C.18a).

From box #8 to box #9

As implicitly indicated in the notation (specifically, by the use of the symbol "t_1" to identify the components of multipole moments), the multipolar expansion of Eq. (C.18a) is defined by reference to the pump, $X_1Y_1Z_1$ frame. The easiest way to see this is by consideration of the angles upon which $I_{\text{obs}}(\theta,\varphi)$ and its multipolar expansion depend. These angles are defined in the $X_1Y_1Z_1$ frame and serve two purposes:

- They specify the direction of fragment recoil in $X_1Y_1Z_1$.

- They are the Euler angles that take $X_1Y_1Z_1$ into the recoil frame (not the other way around): $R_{X_1Y_1Z_1\to xyz} \equiv R(\varphi,\theta,0)$.

Therefore, to obtain an expression for $I_{\text{obs}}(\Theta,\Phi)$ (this is the observed intensity in the lab, $X_0Y_0Z_0$ frame) we need to rotate the reference frame used in Eqs. (C.18). This leads to the lab-frame multipolar expansion of the observed intensity,

$$I_{\text{obs}}(\Theta,\Phi) = \sum_{Tt_0} \frac{2T+1}{4\pi} \tau_{t_0}^{(T)} C_{Tt_0}^{*}(\Theta,\Phi), \tag{C.20a}$$

$$\tau_{t_0}^{(T)} = \int_0^{2\pi}\int_0^{\pi} I_{\text{obs}}(\Theta,\Phi) C_{Tt_0}(\Theta,\Phi)\sin\theta\, d\theta\, d\varphi. \tag{C.20b}$$

The pump-to-lab rotation is $R_{X_1Y_1Z_1\to X_0Y_0Z_0} \equiv R(\alpha_{10},\beta_{10},\gamma_{10})$. Therefore, the lab-frame multipole moments are related to their probe-frame counterparts by

$$\tau_{t_1}^{(T)} = \sum_{t_0} D_{t_1t_0}^{T*}(\alpha_{10},\beta_{10},\gamma_{10})\tau_{t_0}^{(T)}, \tag{C.21}$$

an equation whose inverse can be written as

$$\begin{aligned}\tau_{t_0}^{(T)} &= \sum_{t_1} D_{t_1t_0}^{T}(\alpha_{10},\beta_{10},\gamma_{10})\tau_{t_1}^{(T)} = \sum_{t_1} D_{t_1t_0}^{T}(-\gamma_{01},-\beta_{01},-\alpha_{01})\tau_{t_1}^{(T)} \\ &= \sum_{t_1} D_{t_0t_1}^{T*}(\alpha_{01},\beta_{01},\gamma_{01})\tau_{t_1}^{(T)},\end{aligned} \tag{C.22}$$

where we have used a symmetry property of the rotation matrices (236) and $\alpha_{01} = -\gamma_{10}$, $\beta_{01} = -\beta_{10}$ and $\gamma_{01} = -\alpha_{10}$ are the Euler angles that specify the lab-to-pump rotation: $R_{X_0Y_0Z_0\to X_1Y_1Z_1} \equiv R(\alpha_{01},\beta_{01},\gamma_{01})$.

Inserting Eq. (C.19) in Eq. (C.22) and the using Eq. (C.14) one gets

$$\begin{aligned}
\tau_{t_0}^{(T)} &= \sum_{t_1} D_{t_0 t_1}^{T*}(\alpha_{01},\beta_{01},\gamma_{01}) \\
&\quad \times \left(\sum_{K'K} \frac{(2K'+1)(2K+1)}{4\pi(2T+1)} a_0^{(K')} p_{t_1}^{(K)} \langle K'0, Kt_1 | Tt_1 \rangle \langle K'0, K0 | T0 \rangle \right) \\
&= \sum_{K'K} \frac{(2K'+1)(2K+1)}{4\pi(2T+1)} a_0^{(K')} \langle K'0, K0 | T0 \rangle \\
&\quad \times \left(\sum_{t_1} \langle K'0, Kt_1 | Tt_1 \rangle D_{t_0 t_1}^{T*}(\alpha_{01},\beta_{01},\gamma_{01}) p_{t_1}^{(K)} \right) \\
&= \sum_{K'K} \frac{(2K'+1)(2K+1)}{4\pi(2T+1)} a_0^{(K')} \langle K'0, K0 | T0 \rangle \\
&\quad \times \left[\sum_{t_1} \langle K'0, Kt_1 | Tt_1 \rangle D_{t_0 t_1}^{T*}(\alpha_{01},\beta_{01},\gamma_{01}) \left(\sum_{kq} \rho_q^{(k)} \tilde{P}_k W_{kqKt_1} \right) \right] \\
&= \sum_{K'kq} a_0^{(K')} \rho_q^{(k)} X_{t_0}^{K'kT}, \qquad \text{(C.23)}
\end{aligned}$$

where

$$X_{t_0}^{K'kT} = \frac{\tilde{P}_k}{4\pi} \frac{(2K'+1)}{(2T+1)} \sum_{Kt_1} (2K+1) \langle K'0, K0 | T0 \rangle \langle K'0, Kt_1 | Tt_1 \rangle D_{t_0 t_1}^{T*}(\alpha_{01},\beta_{01},\gamma_{01}) W_{kqKt_1}. \qquad \text{(C.24)}$$

Equation (C.23) is the expression for the multipole moments referred to in box #9 of Fig. 5.9. The corresponding multipolar expansion is that of Eq. (C.20a).

From box #9 to box #10

What is observed in the experiments presented in Chapter 5 is the $\Phi = \pi/2$ slice of the three-dimensional function of Eq. (C.20a) — that is, $I_{\text{obs}}(\Theta, \pi/2)$. This function can be rewritten as a Legendre series,

$$I_{\text{obs}}(\Theta, \pi/2) = \sum_n \frac{2n+1}{2} c_n P_n(\cos\theta), \qquad \text{(C.25a)}$$

$$c_n = \int_{-1}^{1} I_{\text{obs}}(\Theta, \pi/2) P_n(\cos\Theta) d(\cos\Theta). \qquad \text{(C.25b)}$$

Using Eq. (C.20a) one finds that the Legendre moments are given by

$$\begin{aligned} c_n &= \int_{-1}^{1} \left(\sum_{Tt_0} \frac{2T+1}{4\pi} \tau_{t_0}^{(T)} C_{Tt_0}^{*}(\Theta, \pi/2) \right) P_n(\cos\Theta) d(\cos\Theta) \\ &= \sum_{Tt_0} \frac{2T+1}{4\pi} \tau_{t_0}^{(T)} e^{-it_0\pi/2} \int_0^{\pi} d_{t_0 0}^{T}(\Theta) d_{00}^{n}(\Theta) \sin\Theta \, d\Theta \\ &= \sum_{Tt_0} \frac{2T+1}{4\pi} \tau_{t_0}^{(T)} e^{-it_0\pi/2} I_{t_0 000}^{Tn}, \end{aligned} \tag{C.26}$$

where we have again used the relations among Legendre polynomials, modified spherical harmonics and rotation matrix elements (236). Considering Eq. (C.23) we can recast this result as

$$\begin{aligned} c_n &= \sum_{Tt_0} \frac{2T+1}{4\pi} \left(\sum_{K'kq} a_0^{(K')} \rho_q^{(k)} X_{t_0}^{K'kT} \right) e^{-it_0\pi/2} I_{t_0 000}^{Tn} \\ &= \sum_{K'kq} a_0^{(K')} \rho_q^{(k)} \left(\sum_{Tt_0} \frac{2T+1}{4\pi} X_{t_0}^{K'kT} e^{-it_0\pi/2} I_{t_0 000}^{Tn} \right) \\ &= \sum_{K'kq} a_0^{(K')} \rho_q^{(k)} Z_q^{nK'k}, \end{aligned} \tag{C.27}$$

where

$$Z_q^{nK'k} = \sum_{Tt_0} \frac{2T+1}{4\pi} X_{t_0}^{K'kT} e^{-it_0\pi/2} I_{t_0 000}^{Tn}. \tag{C.28}$$

Inserting Eqs. (C.24), (C.16) and (C.2b) into Eq. (C.28) one gets

$$
\begin{aligned}
Z_q^{nK'k} &= \sum_{Tt_0} \frac{2T+1}{4\pi} e^{-it_0\pi/2} I^{Tn}_{t_0000} \frac{\tilde{P}_k}{4\pi} \frac{(2K'+1)}{(2T+1)} \\
&\quad \times \left(\sum_{Kt_1} (2K+1)\langle K'0, K0|T0\rangle \langle K'0, Kt_1|Tt_1\rangle D^{T*}_{t_0t_1}(\alpha_{01},\beta_{01},\gamma_{01}) W_{kqKt_1} \right) \\
&= \frac{\tilde{P}_k}{16\pi^2}(2K'+1) \sum_{\substack{Tt_0 \\ Kt_1}} e^{-it_0\pi/2}(2K+1) D^{T*}_{t_0t_1}(\alpha_{01},\beta_{01},\gamma_{01}) I^{Tn}_{t_0000} \\
&\qquad \times \langle K'0, K0|T0\rangle \langle K'0, Kt_1|Tt_1\rangle W_{kqKt_1} \\
&= \frac{\tilde{P}_k}{16\pi^2}(2K'+1) \sum_{\substack{Tt_0 \\ Kt_1}} e^{-it_0\pi/2}(2K+1) D^{T*}_{t_0t_1}(\alpha_{01},\beta_{01},\gamma_{01}) I^{Tn}_{t_0000} \\
&\qquad \times \langle K'0, K0|T0\rangle \langle K'0, Kt_1|Tt_1\rangle \left(2\pi C^*_{kt_1}(\beta_{21},\gamma_{21}) I^{kK}_{(-t_1)qt_10} \right) \\
&= \frac{\tilde{P}_k}{8\pi}(2K'+1) \sum_{\substack{Tt_0 \\ Kt_1}} e^{-it_0\pi/2}(2K+1) D^{T*}_{t_0t_1}(\alpha_{01},\beta_{01},\gamma_{01}) C^*_{kt_1}(\beta_{21},\gamma_{21}) \\
&\qquad \times I^{Tn}_{t_0000} I^{kK}_{(-t_1)qt_10} \langle K'0, K0|T0\rangle \langle K'0, Kt_1|Tt_1\rangle \\
&= \frac{(-1)^{J_i+J_f}}{8\pi}(2K'+1)\sqrt{5(2k+1)(2J_i+1)}\langle 2(2s), k0|2(2s)\rangle \begin{Bmatrix} J_i & J_i & k \\ 2 & 2 & J_f \end{Bmatrix} \\
&\times \sum_{\substack{Tt_0 \\ Kt_1}} e^{-it_0\pi/2}(2K+1) D^{T*}_{t_0t_1}(\alpha_{01},\beta_{01},\gamma_{01}) C^*_{kt_1}(\beta_{21},\gamma_{21}) \\
&\qquad \times I^{Tn}_{t_0000} I^{kK}_{(-t_1)qt_10} \langle K'0, K0|T0\rangle \langle K'0, Kt_1|Tt_1\rangle, \qquad \text{(C.29)}
\end{aligned}
$$

which completes the derivation of the general expression for the dependence of the observed Legendre moments on the dynamical and experimental parameters. In the notation used in Chapter 5, Eqs. (C.27) and (C.29) are

$$
c_n(g) = \sum_{K'kq} a_0^{(K')} \rho_q^{(k)} Z_q^{nK'k}(g), \qquad \text{(C.30)}
$$

and

$$Z_q^{nK'k}(g) = \frac{(-1)^{J_i+J_f}}{8\pi}(2K'+1)\sqrt{5(2k+1)(2J_i+1)}\langle 2(2s),k0|2(2s)\rangle \begin{Bmatrix} J_i & J_i & k \\ 2 & 2 & J_f \end{Bmatrix}$$
$$\times \sum_{\substack{Tt_0 \\ KQ}} e^{-it_0\pi/2}(2K+1)D^{T*}_{t_0Q}(\alpha_{01},\beta_{01},\gamma_{01})C^*_{kQ}(\beta_{21},\gamma_{21})$$
$$\times I^{Tn}_{t_0000} I^{kK}_{(-Q)qQ0}\langle K'0,K0|T0\rangle\langle K'0,KQ|TQ\rangle, \tag{C.31}$$

C.2.2 Specialisation to the conditions of the experiments

In the experiments reported in Chapter 5 the $O(^1D_2)$ fragments were probed using a linearly polarised laser to excite it to a $^1P_1$ state. This implies $s = 0$, $J_i = 2$ and $J_f = 1$. Furthermore, the experimental geometries were such that we invariably had $\alpha_{01} = \gamma_{01} = \alpha_{21} = \gamma_{21} = 0$. Inserting these experimental parameter values in Eq. (C.31) one gets

$$\begin{aligned} Z_q^{nK'k}(g) &= \frac{(-1)^3}{8\pi}(2K'+1)5\sqrt{2k+1}\langle 20,k0|20\rangle \begin{Bmatrix} 2 & 2 & k \\ 2 & 2 & 1 \end{Bmatrix} \\ &\times \sum_{\substack{Tt_0 \\ KQ}} e^{-it_0\pi/2}(2K+1)D^{T*}_{t_0Q}(0,\beta_{01},0)C^*_{kQ}(\beta_{21},0) \\ &\times I^{Tn}_{t_0000} I^{kK}_{(-Q)qQ0}\langle K'0,K0|T0\rangle\langle K'0,KQ|TQ\rangle, \\ &= -\frac{5}{8\pi}(2K'+1)\sqrt{2k+1}\langle 20,k0|20\rangle \begin{Bmatrix} 2 & 2 & k \\ 2 & 2 & 1 \end{Bmatrix} \\ &\times \sum_{\substack{Tt_0 \\ KQ}} e^{-it_0\pi/2}(2K+1)d^T_{t_0Q}(\beta_{01})d^k_{Q0}(\beta_{21})I^{Tn}_{t_0000} I^{kK}_{(-Q)qQ0}\langle K'0,K0|T0\rangle\langle K'0,KQ|TQ\rangle, \end{aligned} \tag{C.32}$$

where we have used the relations among modified spherical harmonics, rotation matrix elements and reduced rotation matrix elements (236). Now, note the following:

- The measurements involve photodissociation of unpolarised molecules with linearly polarised photons and fragment detection also with linearly polarised photons. As linearly polarised photons are aligned but not oriented, the results are free of orientation effects. This implies the following:
  - ▹ Only even-n Legendre moments and even-T multipole moments can contribute to the observed images.

▹ We can neither produce nor detect oriented O(^{1}D$_2$) fragments; only even k values contribute to the observed images.

- Clebsch-Gordan coefficients satisfy (236)

$$\langle j_1 m_1, j_2 m_2 | j_3 m_3 \rangle = (-1)^{j_1+j_2-j_3} \langle j_1 -m_1, j_2 -m_2 | j_3 -m_3 \rangle, \tag{C.33}$$

which implies that $\langle K'0, K0|T0\rangle$ vanishes unless $K' + K - T$ is even. As the summation of Eq. (C.30) only involves $K' = 0$ or 2, and T must be even, this implies that K must also be even.

- The reduced rotation matrix elements satisfy (236)

$$d^j_{m_1 m_2}(0) = \delta_{m_1 m_2}, \tag{C.34}$$

$$d^j_{m0}(\pm\pi/2) = (-1)^{j+m} d^j_{m0}(\pm\pi/2). \tag{C.35}$$

Because k must be even and the experimental geometries involve $\beta_{21} = 0, \beta_{21} = \pi/2$ or $\beta_{21} = -\pi/2$, this implies that $d^k_{Q0}(\beta_{21})$ vanishes unless Q is also even.

- The first integral on Eq. (C.32) can be written as

$$I^{Tn}_{t_0 000} = \int_{-1}^{1} d^T_{t_0 0}(\xi) d^n_{00}(\xi) d(\cos\theta). \tag{C.36}$$

As the reduced rotation matrices satisfy (236)

$$d^j_{m0}(\pi - \xi) = (-1)^{j+m} d^j_{m0}(\xi), \tag{C.37}$$

the first and second reduced rotation matrix elements appearing in the integral of Eq. (C.36) have definite parities: $(-1)^{T+t_0}$ and $(-1)^n$, respectively. As n and T are even and the integral vanishes unless the two parities are the same, t_0 must also be even. Note that this implies that

$$e^{-it_0\pi/2} = (-1)^{t_0/2} \tag{C.38}$$

is real and similarly for the $Z^{nK'k}_q(g)$ coefficients, for all the other quantities appearing on Eq. (C.32) are real.

- The photodissociation process involved unpolarised parent molecules and a single linearly-polarised pump photon. Furthermore, the recoil frame was defined so that the photon polarisation direction (the Z_1 axis) lies in the xz plane. These conditions imply that the polarisation of the $O(^1D_2)$ fragment must be invariant under reflection on the xz plane and also under rotation by π around the z axis. In terms of the recoil-frame density matrix elements, the requirements are that we must have (236)

$$\langle jm_1|\rho|jm_2\rangle = (-1)^{m_2-m_1}\langle jm_1|\rho|jm_2\rangle, \tag{C.39}$$

$$= (-1)^{m_2-m_1}\langle j-m_1|\rho|j-m_2\rangle \tag{C.40}$$

  (note that these symmetries also imply complete absence of fragment orientation, $\langle jm_1|\rho|jm_2\rangle = \langle j-m_1|\rho|j-m_2\rangle$). Using Eq. (7) of Chapter 5, the symmetries of the Clebsch-Gordan coefficients (236), and the fact that density matrices are Hermitean, one can easily show that the symmetry properties just discussed imply (i) that the only recoil-frame polarisation moments of the $O(^1D_2)$ fragment that can be nonzero are those with even q, and (ii) that these nonvanishing polarisation moments are necessarily real.

Taking into account the observations above we can rewrite Eqs. (C.30) and (C.32) as

$$c_n(g) = \sum_{K'kq}{}' a_0^{(K')}\rho_q^{(k)}Z_q^{nK'k}(g), \tag{C.41}$$

$$Z_q^{nK'k}(g) = -\frac{5}{8\pi}(2K'+1)\sqrt{2k+1}\langle 20,k0|20\rangle \begin{Bmatrix} 2 & 2 & k \\ 2 & 2 & 1 \end{Bmatrix} \times \sum_{\substack{T\,t_0 \\ KQ}}{}' (-1)^{t_0/2}(2K+1)d^T_{t_0Q}(\beta_{01})d^k_{Q0}(\beta_{21})I^{Tn}_{t_0000}I^{kK}_{(-Q)qQ0}\langle K'0,K0|T0\rangle\langle K'0,KQ|TQ\rangle, \tag{C.42}$$

where the primed summation symbols indicate that the sums run only over even values of the summation indices and the $\rho_q^{(k)}$ are real.

This completes the derivation. Equations (C.41) and (C.42) are Eqs. (5.1) and (5.8) from Chapter 5.

Appendix D

Published article: Time-dependent photoionisation of azulene; competition between ionisation and relaxation in excited states

The article presented below was published in the Journal of Chemical Physics and describes a range of experiments which were performed to understand the relaxation and ionisation dynamics of azulene after excitation to its S_2, S_3 and S_4 states and the influence of the relaxation processes on its ionisation behaviour. The majority of the work presented in this article was performed by Dr Valérie Blanchet, Dr Kevin Raffael, Dr Giorgio Turri, Dr Béatrice Chatel and Professor Bertrand Girard with my supervisor Professor Benjamin J. Whitaker at the Laboratoire Collisions Agrégats Réactivité at the Université Paul Sabatier in Toulouse. However, some complimentary experiments were performed in Leeds by Dr Ivan Anton Garcia and me using an earlier version of the spectrometer described in Chapter 3. My contribution to the work was to record single-colour velocity map images of the photoelectrons ejected by azulene on irradiation with nanosecond and femtosecond laser pulses at excitation energies of ~3.10 eV and ~4.66 eV and ~3.20 eV and ~4.81 eV respectively with Dr Anton Garcia. We also measured ~100 ps pump-probe ion and electron decay transients and selected electron images with 180 fs femtosecond resolution after azulene excitation at an energy of ~4.81 eV.

Time-dependent photoionization of azulene: Competition between ionization and relaxation in highly excited states

Valérie Blanchet,[1,a)] Kevin Raffael,[1] Giorgio Turri,[1] Béatrice Chatel,[1] Bertrand Girard,[1] Ivan Anton Garcia,[2] Iain Wilkinson,[2] and Benjamin J. Whitaker[2]
[1]*Laboratoire Collisions Agrégats Réactivité, UMR 5589, CNRS, Institut de Recherches sur les Systèmes Atomiques et Moléculaires Complexes, UPS Toulouse, 31062 Toulouse Cedex 04, France*
[2]*School of Chemistry, University of Leeds, Leeds LS2 9JT, United Kingdom*

(Received 1 October 2007; accepted 1 April 2008; published online 30 April 2008)

Pump-probe photoionization has been used to map the relaxation processes taking place from highly vibrationally excited levels of the S_2 state of azulene, populated directly or via internal conversion from the S_4 state. Photoelectron spectra obtained by $1+2'$ two-color time-resolved photoelectron imaging are invariant (apart from in intensity) to the pump-probe time delay and to the pump wavelength. This reveals a photoionization process which is driven by an unstable electronic state (e.g., doubly excited state) lying below the ionization potential. This state is postulated to be populated by a probe transition from S_2 and to rapidly relax via an Auger-like process onto highly vibrationally excited Rydberg states. This accounts for the time invariance of the photoelectron spectrum. The intensity of the photoelectron spectrum is proportional to the population in S_2. An exponential energy gap law is used to describe the internal conversion rate from S_2 to S_0. The vibronic coupling strength is found to be larger than 60 ± 5 μeV. © *2008 American Institute of Physics*. [DOI: 10.1063/1.2913167]

I. INTRODUCTION

The electronic structure of azulene is noteworthy due to the atypical fluorescence which occurs from the second excited $S_2(^2A_1)$ state, instead of the lower $S_1(^1B_2)$ excited state. As such, it is well known as the textbook exception to Kasha's rule that "the emitting level of a given multiplicity is the lowest excited level of that multiplicity."[1] Little is known about the higher electronic valence states,[2–4] other than their use as stepping stones through which to prepare highly excited molecules in order to observe the unimolecular dynamics of the molecule.[5,6]

Azulene is a planar asymmetric top molecule that belongs to the C_{2v} point group (see Fig. 1). There are four distinct regions in the absorption spectrum of the molecule: 700–500 nm, 350–310 nm, 290–260 nm, and 240–200 nm with relative oscillator strengths of 0.01, 0.06, 1, and 0.4 (see Table I). The $S_2(^2A_1) \leftarrow S_0(^1A_1)$ and the $S_4(^3A_1) \leftarrow S_0(^1A_1)$ absorptions are optically allowed with an electric dipole transition moment along the z axis. The $S_1(^1B_2) \leftarrow S_0(^1A_1)$ and $S_3(^2B_2) \leftarrow S_0(^1A_1)$ transitions are y polarized. Like the $S_1(^1B_2) \leftarrow S_0(^1A_1)$ transition the $S_2(^2A_1) \leftarrow S_0(^1A_1)$ transition is characterized by the creation of a double bond type character on the transannular connection. Early fluorescence quantum yield experiments suggested long lifetimes[7] for single vibrational levels in S_2 and subpicosecond ones for the S_3 and S_4 levels.[2] The 2–3 ns lifetimes of the S_2 vibrational levels were later confirmed by picosecond-resolved quantum beat experiments.[8,9] Intriguingly, Diau *et al.*[10] observed an additional fast exponential component in the ion time profile in two-color photoionization experiments, with a 350 fs decay on top of the long decay component when exciting the S_2 state with 470 meV excess vibrational energy. We have performed time-resolved pump-probe photoionization and photoelectron spectroscopy via the electronically excited states (S_2–S_4) of azulene. At all the wavelengths studied here, the transient signals exhibit two distinct and well-defined behaviors: (i) short-term (on the order of a picosecond) polarization dependent transients[11] and (ii) longer (10 ps–1 ns) timescale decays. The present paper will consider the longer term behavior, which will be explained as the result of internal conversion from S_2 to S_0 and treated via a statistical model; and focus principally on the photoionization processes occurring within the electronically excited states of azulene.

Although for most of our experiments a $1+1'$ photoionization process is energetically allowed we will present a series of converging arguments to conclude that the photoionization actually proceeds via a complex ($1+2'$) mechanism with fast internal conversion taking place within the probe pulse. To elucidate this photoionization mechanism, we have measured pump-probe (263–295 nm/400 nm) signals on the parent photoion and also recorded photoelectron spectra; with both one-color (258 and 266 nm) and two-color (268–335 nm/400 nm) ionization schemes. Although the ionization mechanism is indubitably complicated, we will present evidence suggesting that the phenomena we are observing may be quite generic in polycyclic molecules.

Figure 1 provides a framework for the forthcoming discussion. It depicts a number of possible excitation and ionization paths. Figure 1(1) is a schematic of the one-color two photon ionization process and Figs. 1(2) and 1(3) are those of the two-color photoionization processes. Each electroni-

a)Author to whom correspondence should be addressed. Electronic mail: val@irsamc.ups-tlse.fr.

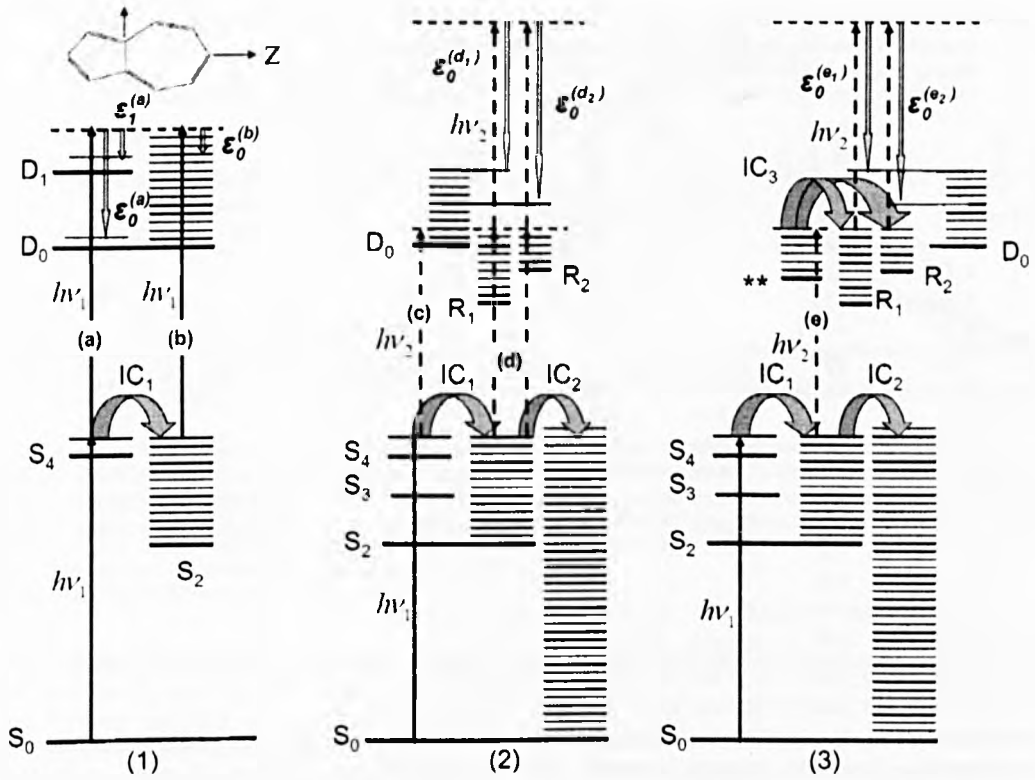

FIG. 1. (1) One-color photoionization onto the cation states D_0 and D_1 via one-photon resonance with S_4 [path (a)]. Within the pulse duration, internal conversion to the S_2 state (IC_1) can take place [path (b)]. $\varepsilon_0^{(a)}(\varepsilon_0^{(b)})$ is the photoelectron kinetic energy expected from photoionization taking place onto D_0 from path (a) [respectively from the path (b)], assuming approximate conservation of the vibrational energy. See Fig. 3 for the recorded photoelectron spectra. [(2) and (3)] Two-color pump-probe (1+1′ or 1+2′) photoionization with (c) a direct one-photon probe transition from the initially prepared state (S_4 in this example) or (d) a two-photon photoionization enhanced via resonances with Rydberg states R_1 and R_2. During the pump-probe delay internal conversion onto the $S_2(IC_1)$ and $S_0(IC_2)$ states can take place. (e) Two-photon photoionization via a doubly excited state (**) that decays within the probe pulse duration onto Rydberg states (IC_3).

cally excited state can be either directly excited/ionized [paths (a) and (c)] or each can first decay to a lower electronic state by vibronic coupling before being ionized [paths (b) and (d)–(e)]. In this latter case, two probe photons are necessary to ionize the molecule due to the large amount of vibrational energy in the lower lying states. In the two-color photoionization schemes, at least one (resonant or nonresonant) intermediate state mediates the transition. In the resonant case, this intermediate state can be directly ionized [path (d)] or it can relax toward another electronic state if its lifetime is shorter than the probe pulse duration [path (e)].

In this paper, we will successively examine Koopmans' type correlations in the S_2 and S_4 electronic states[12] via the one-color photoelectron spectrum, the evidence for the presence of a doubly excited electronic state involved in the photoionization via the two-color time-resolved photoelectron spectroscopy, and its relaxation onto Rydberg states. Finally, we complete this study with a statistical approach to describe the long decay component and the coupling between the S_2 and S_0 states.

II. EXPERIMENTAL DETAILS

Experiments were performed in our two laboratories using similar instruments. Here, we describe the experiment in Toulouse in detail and then point out any significant differences between the two setups. We employ pump-probe time-of-flight mass spectrometry to detect the photoions and velocity map imaging to record the photoelectrons spectra.[13]

Both pump and probe pulses were generated from a master 1 kHz 2.5 mJ regenerative amplifier centered at ~805 nm and delivering a pulse with a Fourier limited full width at half maximum (FWHM) of ~60 fs (Amplitude Systems). A home-made noncollinear optical parametric amplifier[14] (NOPA) pumped with a fraction of the frequency doubled output of the Ti:sapphire amplifier, with subsequent second harmonic generation (SHG), provided the ultraviolet (UV) pump pulse. The NOPA output was partly recompressed by a prism pair. The typical FWHM of the pump pulse in energy was 30–50 meV, corresponding to a Fourier limit of 35–60 fs. For most of the experiments reported here, the probe pulse at ~403 nm was obtained by SHG of the fundamental output of the regenerative amplifier. The cross correlation between the pump and probe pulses, recorded by off-resonant multiphoton ionization of nitric oxide, had a typical 120 fs FWHM. Pump and probe beams were combined at a small angle (~1°) and focused onto the molecular beam by a 750 mm focal length spherical aluminum mirror. In order to reduce multiphoton effects, such as dissociative ionization, the typical energies used were <1 μJ for the pump pulse and ~15 μJ for the probe pulse. The pulse-to-pulse stability was better than 85% for both pump and probe

TABLE I. Band origins of the main electronic states of azulene and its cation. The orientation of the dipolar momenta of transition from S_0 are added in parenthesis. The Rydberg states are listed as a function of their binding energies and compared to various listed in literature. All energies are in eV.

	Electronic energy	Electronic energy converging onto D_0	Binding energy	Binding energy converging onto D_0 (Ref. 30)	Binding energy converging onto D_0 (Ref. 31)	Binding energy (Ref. 26)	Binding energy (Ref. 27)
S_1 (y)	1.77						
S_2 (z)	3.56						
S_3 (y)	4.23						
S_4 (z)	4.40						
R_A		4.72	2.69		2.70 ($3p_x$)		
R_B		5.19	2.22		2.51 ($3p_y$)		2.16($3p$)
R_C		5.64	1.77		1.63($3d_{xy}$)		1.62($3d$)
R_D		5.92	1.49	1.40($4s$)	1.42($3d_{xz}$)		1.36($4s$)
R_E		6.15	1.26			1.16($4p$)	1.14($4p$)
R_F		6.33	1.08	1.03($4p$)		1.06($4d$)	1.06($4d$)
D_0	7.41						
D_1	8.50						
D_2	10.07						
D_3	10.85						

beams. The dimensions of the two beams were measured at their spatial overlap, from which we deduce intensities of $\sim 3.0 \times 10^{10}$ W/cm^2 for the pump pulse and $\sim 2.0 \times 10^{11}$ W/cm^2 for the probe pulse. These intensities correspond to an insignificant ponderomotive potential of a few meV. We are therefore confident that multiphoton ionization takes place in an unperturbed energy scheme.[15]

The setup in Leeds is very similar except that the regenerative amplifier (Clark MXR 2010) is seeded with a frequency doubled Er fiber laser and, consequently, the central wavelengths of the harmonics that are used for the probe and pump fields are slightly shifted from those used in Toulouse: 387 and 258 nm (Leeds), 403 and 269 nm (Toulouse). In addition, a Nd:YAG yttrium aluminum garnet pumped dye laser (Continuum Surelite/Sirah) was used in the Leeds' apparatus to obtain photoelectron images on the nanosecond time scale. For this experiment, the third harmonic of one Nd:YAG laser was used to pump a dye (Exalite 404) to generate tunable light close to 400 nm. The linewidth of the dye laser was 0.1 cm^{-1} with a typical pulse energy kept below 3 mJ to avoid fragmentation. In all of the experiments reported below, every signal has been recorded with parallel laser polarization.

Azulene molecules (Aldrich, 99% without further purification) were sublimed continuously at 340 K with 150 Torr of nitrogen and then expanded through a 200 μm diameter nozzle. The resulting molecular beam was collimated by a 1 mm diameter skimmer before it intersected, perpendicularly, the focused laser beams. The resulting ions and photoelectrons were subsequently detected at the output of a 40 cm TOF velocity map imaging spectrometer, whose axis is perpendicular to the plane defined by the lasers and molecular beam.[13] The azulene sublimed cleanly without evidence of decomposition in the ion mass spectrum observed with either pump or probe laser alone. We were unable to detect any trace of van der Waals clusters such as azulene-N_2 or (azulene)$_n$ in the mass spectrum under these expansion conditions.[16,17]

For each pump-probe delay, the ion signal was averaged over ~ 2000 laser pulses and the photoelectron image over $\sim 4 \times 10^5$ laser pulses. The images were calibrated by recording photoelectron signals from nitric oxide, acetylene, and oxygen at various accelerating and focusing voltages. Typically, the detection window spanned from 0.1 to 3.5 eV with a resolution of 65 meV at 1.4 eV [for a repeller voltage of -3 kV and an extractor to repeller voltage ratio of 0.735 (Ref. 13)]. The 5% energy resolution achieved corresponds to the laser bandwidth.

III. RESULTS AND DISCUSSION

A. Pump-probe signals

Figure 2 shows the typical monoexponential decay of the parent $C_{10}H_8^+$ ion recorded for two pump wavelengths respectively falling within the S_0–S_4 (λ_{pump}=268 nm) and S_0–S_3 (λ_{pump}=293 nm) absorption bands. A monoexponential picosecond decay has been observed for all the pump wavelengths investigated between 258 and 293 nm. In these experiments, the probe pulse is the second harmonic of the laser chain, namely, 403 nm, for all pump wavelengths except 258 nm, where the probe wavelength was 387 nm. This detection scheme corresponds to paths (c)–(e) in Fig. 1.

The pump photon energy in these data spans the absorption range of the S_3 and S_4 electronic states (see Table I)[2] but is always below the photodissociation threshold[18] or the isomerization barrier to naphtalene.[5,19] The decay time decreases with increasing excitation energy but is greater than 30 ps even for the highest energy studied, ~ 5 eV. These would be remarkably long lifetimes for such high lying electronic states and would not be consistent with the broad features observed in the jet-cooled fluorescence excitation spec-

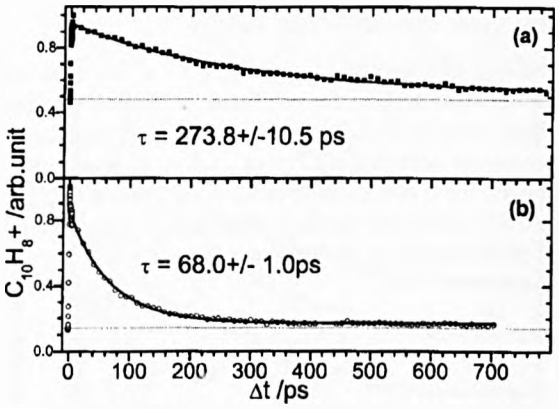

FIG. 2. Time transients recorded on the parent ion $C_{10}H_8^+$ with $\Delta t=0$ determined by a cross correlation recorded by photoionization of NO. A single exponential fit (full line) gives a time constant of (a) 273.8 ± 10.5 ps for an excitation taking place at the origin band of the S_3 state, namely, λ_{pump} =293 nm and (b) 68 ± 1 ps at 223 meV above the origin band of the S_4 state, namely, λ_{pump}=268 nm. For both measurement, the probe pulse is the second harmonic generation of the fundamental output (~400 nm).

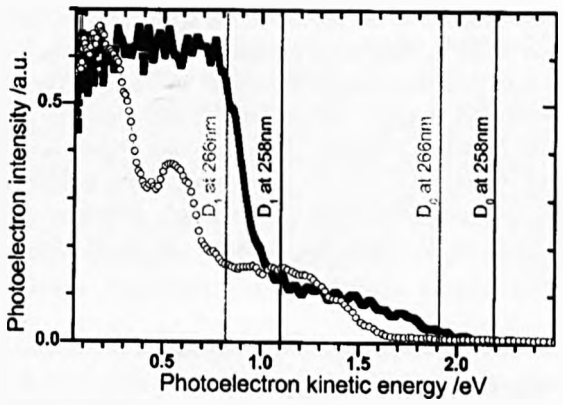

FIG. 3. One-color photoelectron spectra recorded with a femtosecond-pulse centered at 266 nm (empty circle) or 258 nm (full square). For both wavelengths, vertical lines indicate the maximum kinetic energy that might be released for ionization taking place to the cation ground state D_0 or the first excited state D_1.

tra of the S_3 and S_4 states.[2] From the spectral profiles, Fujii *et al.*[2] suggested that the S_3 and S_4 states were efficiently coupled to the S_2 state and this was later confirmed by Lawrance and Knight by pump-probe spectroscopy.[20]

In order to assign the nonradiative processes related to the decay times shown in Fig. 2 and, in particular, to evaluate the relative contributions from paths (c) and (d) to the observed ion transients, we investigated photoelectron spectra, as described below.

B. One-color photoelectron spectra

The signature of the S_4 or S_3 states via photoionization has never been detected. Indeed, the $1+1$ photoelectron spectrum recorded at the origin of the S_4 band with an 8 ps pulse results in a single photoelectron peak from the S_2 electronic state, and is correlated to the cation ground state via a $\Delta v \approx 0$ propensity rule.[21] This is indicative of efficient internal conversion from the initially pumped vibrationless level of the S_4 state onto S_2, as depicted by path (b) in Fig. 1. A similar propensity to preserve the vibrational quantum state upon photoionization from S_2 was observed in the $1+1'$ zero kinetic energy photoelectron spectra recorded on resonance via the first few vibrational levels of S_2.[17] These experiments show that, on the picosecond time scale, the prevailing contribution to the molecular eigenstates underlying the electronic absorption spectrum around the S_4 electronic origin comes from S_2. The same conclusion can be drawn from similar experiments performed close to the origin of the S_3 state.[21] On the picosecond time scale, no clear signature of photoionization to D_1 is observed, even though this photoionization route is energetically allowed. The observation of a $\Delta v \approx 0$ propensity rule suggests that the S_2 and cation ground states should have a similar geometry.

In order to detect the S_4 signature via photoionization, we performed the same experiment but with 120 fs pulses. The photoelectron spectrum was recorded for two different wavelengths (258 and 266 nm) in which the total two-photon energy (9.61 and 9.32 eV, respectively) was sufficient to photoionize azulene to the cationic ground state, D_0 (7.41 eV), or the first excited state of the ion, D_1 (8.50 eV) but not to the second excited state D_2 (10.07 eV) (see Table I).[17,22]

Figure 3 shows that there are at least two thresholds on the photoelectron spectrum at both wavelengths. The vibrational energies in S_2 are 1.24 eV at 258 nm and 1.10 eV at 266 nm. Assuming the same $\Delta v \approx 0$ propensity rule onto D_0 observed by Weber and Thantu,[21] the photoelectron spectra would be anticipated to peak at 0.96 and 0.81 eV for the two excitation wavelengths respectively. However, as can be seen in Fig. 3, there are no obvious discrete peaks appearing at these energies. Instead, the large rising features around 1.11 and 0.82 eV exactly fit the ionization threshold onto the D_1 ion state. It seems that on the time scale of a few tens of femtoseconds ionization to D_1 is favored, in marked contrast to what is observed on the picosecond time scale. The vibrational energies in the S_4 state are respectively 0.26 eV at 266 nm and 0.4 eV for a pulse centred at 258 nm.[2] For 266 nm excitation, the photoelectron spectrum peaks at 0.55 eV, corresponds to a vibrational energy in D_1 of 0.27 eV. This perfectly agrees with photoionization onto D_1 governed by a $\Delta v \approx 0$ propensity rule, but this time occurring out of the S_4 electronic state. The same $\Delta v \approx 0$ propensity rule applied at 258 nm should lead to a photoelectron spectrum peaking at 0.71 eV, at which we observe the onset of a plateau. The fraction observed in the D_0 channel (lying from 1.9 to 0.9 eV on Fig. 3 for the 266 nm photoionization case) is formed with very little vibrational selectivity; the tail spreads over more than 1 eV. This can be tentatively assigned to a growing contribution of the S_2 electronic state in the one-photon resonance over the 120 fs pulse duration. For both wavelengths, the very low energy components could correspond to an autoionization process.

On a time scale of 8 ps, the population created in S_4 has completely relaxed to S_2. Consequently, photoionization to D_0 with a $\Delta v \sim 0$ propensity rule is the only signature observed in the photoelectron spectrum. In contrast, when the experiment is performed on the femtosecond scale, a signifi-

cant contribution of the photoelectron signal arises from ionization of the S_4 state since photoionization takes place on a time scale commensurate with internal conversion. These observations set an upper limit certainly lower than 8 ps for the S_3 and S_4 states lifetimes. The two-color experiment discussed in Sec. III C will fix a new upper limit to 120 fs. In conclusion, photoionization can be simply driven by $\Delta v \approx 0$ transitions to D_1 from the S_4 state and to D_0 from the S_2 state.

C. Two-color photoelectron spectra

Having identified the S_4 contribution to the total photoionization cross section, the nonradiative processes related to the decay times of Fig. 2 might be assigned by time-resolved photoelectron spectroscopy. Note that in the two-color experiments, the probe pulse is centered at around 400 nm, so it is useful to compare the $\Delta v \approx 0$ propensity rule observed in 1+1 photoionization (at 266 nm) to the 1+1′ or 1+2′ schemes:

One-color photoionization 1+1

$$S_0 \xrightarrow{h\nu_{266\ \mathrm{nm}}} S_4(v=0)+E_{\mathrm{vib}}(0.26\ \mathrm{eV}) \xrightarrow{h\nu_{266\ \mathrm{nm}}} D_1(v=0)+0.82\ \mathrm{eV}] \Rightarrow \Delta v=0 \text{ allowed},$$

$$D_0(v=0)+1.92\ \mathrm{eV}] \Rightarrow \Delta v=0 \text{ allowed},$$

$$\downarrow \mathrm{IC}$$

$$S_2(v=0)+E_{\mathrm{vib}}(1.1\ \mathrm{eV}) \xrightarrow{h\nu_{266\ \mathrm{nm}}} D_0(v=0)+1.92\ \mathrm{eV}] \Rightarrow \Delta v=0 \text{ allowed}.$$

Two-color photoionization 1+1′

$$S_0 \xrightarrow{h\nu_{266\ \mathrm{nm}}} S_4(v=0)+E_{\mathrm{vib}}(0.26\ \mathrm{eV}) \xrightarrow{h\nu_{400\ \mathrm{nm}}} D_1(v=0)-0.74\ \mathrm{eV}] \Rightarrow \text{ionization not allowed},$$

$$D_0(v=0)+0.35\ \mathrm{eV}] \Rightarrow \Delta v=0 \text{ allowed},$$

$$\downarrow \mathrm{IC}$$

$$S_2(v=0)+E_{\mathrm{vib}}(1.1\ \mathrm{eV}) \xrightarrow{h\nu_{400\ \mathrm{nm}}} D_0(v=0)+0.35\ \mathrm{eV}] \Rightarrow \Delta v=0 \text{ not allowed},$$

$$S_0 \xrightarrow{h\nu_{335\ \mathrm{nm}}} S_2(v=0)+E_{\mathrm{vib}}(0.14\ \mathrm{eV}) \xrightarrow{h\nu_{400\ \mathrm{nm}}} D_0(v=0)-0.61\ \mathrm{eV}] \Rightarrow \text{ionization not allowed}.$$

Two-color photoionization 1+2′

$$S_0 \xrightarrow{h\nu_{266\ \mathrm{nm}}} S_4(v=0)+E_{\mathrm{vib}}(0.26\ \mathrm{eV}) \xrightarrow{2h\nu_{400\ \mathrm{nm}}} D_1(v=0)+2.36\ \mathrm{eV}] \Rightarrow \Delta v=0 \text{ allowed},$$

$$\downarrow \mathrm{IC}$$

$$S_2(v=0)+E_{\mathrm{vib}}(1.1\ \mathrm{eV}) \xrightarrow{2h\nu_{400\ \mathrm{nm}}} D_0(v=0)+3.45\ \mathrm{eV}] \Rightarrow \Delta v=0 \text{ allowed},$$

$$S_0 \xrightarrow{h\nu_{335\ \mathrm{nm}}} S_2(v=0)+E_{\mathrm{vib}}(0.14\ \mathrm{eV}) \xrightarrow{2h\nu_{400\ \mathrm{nm}}} D_0(v=0)+2.49\ \mathrm{eV}] \Rightarrow \Delta v=0 \text{ allowed}.$$

With a 400 nm probe, 1+1′ photoionization onto D_0 is energetically only allowed for pump wavelengths shorter than 287.5 nm. Photoionization onto D_1 or D_2 requires two probe photons for all the pump wavelengths studied. Taking into account the pump wavelength range and the resulting vibrational energy in the S_2 state, one-photon ionization at 400 nm can never satisfy the $\Delta v \approx 0$ propensity rule. Consequently, two-photon ionization is expected to compete very efficiently with one-photon ionization.

Figure 4(a) shows the photoelectron spectra recorded at a 1 ps delay for various pump wavelengths. Surprisingly, the photoelectron spectrum does not depend on the excitation wavelength; only the integrated photoelectron intensity varies as a function of the delay time. The very slow photoelectron (<200 meV) contribution assigned to the 1+1′ route is significantly reduced at 335 nm, where photoionization can only take place via a 1+2′ scheme. As expected, photoionization is strongly dominated by the two-photon transition. This is further supported by the laser power dependence of the parent ion signal, which was found to be linear in the pump intensity and quadratic in the probe intensity. If the same $\Delta v \approx 0$ propensity rule, as observed in Fig. 3, is applied for two-photon ionization at 400 nm, the photoelectron correlated with D_1 from S_4 on excitation at 266 nm should appear at a kinetic energy around 2.1 eV. There is no component at any delay that appears around this kinetic energy. Indeed, the most striking feature is the similarity between the photoelectron spectra for excitation to various internal ener-

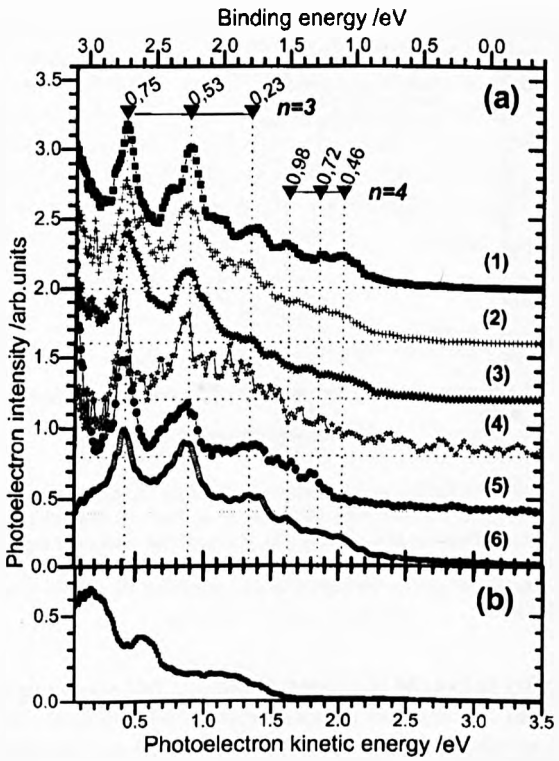

FIG. 4. Photoelectron spectra recorded with a probe pulse centered at (a) 400 nm and pump excitation at (1) 268 nm, (2) 275.5 nm, (3) 283 nm, and (4) 335 nm. For comparison, one-color photoionization at 400 nm obtained (5) in the femtosecond regime or (6) nanosecond regime are plotted, as well as (b) the 266 nm femtosecond-one color experiment presented in Fig. 3. Each $1+2'$ photoelectron spectra has been recorded at $\Delta t \sim 1$ ps after subtraction of the background spectra (one-color experiment recorded with the pump alone or the probe alone). The vertical shifts introduced to compare the spectra are indicated by horizontal dot lines. The different Rydberg states are identified as a function of their binding energy [top axis of (a)], their principal quantum number n, and a quantum defect δ assuming that these ones are in the 0–1 range.

gies in S_4 (λ_{pump}=268, 275.5, and 283 nm) and the one recorded from the S_2 (λ_{pump}=335 nm) state. The invariance of the photoelectron spectra to excitation energy and pump-probe delay can only be rationalized if the two-photon probe ionization occurs out of the same electronic state for *all* of the pump energies studied. The obvious candidate is the S_2 state since it is the only state to have a sufficiently long radiative lifetime to be compatible with the long decay times shown in Fig. 2.

Our time resolution is evidently not sufficient to detect the transition between ionization from S_4 and from S_2 via any variation of the photoelectron spectrum, therefore, we can conclude that the internal conversion between S_4 and S_2 is faster than 120 fs. Once in the S_2 state, the population can convert further to highly vibrationally excited levels in S_1 and S_0. We will examine this internal conversion, which occurs over a time scale of more than 60 ps in Sec. III D. The two-color photoionization takes place via path (d) and/or (e) of Fig. 1.

As we have noted, apart from its relative intensity, the photoelectron energy spectrum is invariant to the pump photon excitation energy. The photoelectron spectra in Fig. 4(a) are also highly structured. At first sight, it is tempting to identify this structure as a signature of the vibrational structure of the ion but this hypothesis must be immediately rejected. Indeed, this pattern spreads over more than 1.5 eV with a splitting varying around 500 meV. Given the large variation of vibrational energy in S_2 [see Eq. (1)] as well as the typical vibrational quanta of azulene cation (smaller than 0.2 eV),[23] it is difficult to assign the photoelectron pattern of Fig. 4(a) to a vibrational progression. In fact, we will now show that this photoelectron spectrum is the signature of two-photon transitions via vibrationally excited Rydberg states.

Consider a Rydberg state lying at an electronic energy R_n, reached after absorption of one probe photon. Energy conservation gives

$$\hbar\omega_{pump} + \hbar\omega_{probe} = R_n + E_{vib}^{R_n}, \tag{1}$$

where E_{vib}^{R} is the vibrational energy in the Rydberg state. If the molecule absorbs a second probe photon and ionizes, the ejected photoelectron will have a kinetic energy given by[24]

$$E_{kin}^{e} = (\hbar\omega_{pump} + \hbar\omega_{probe}) + \hbar\omega_{probe} - E_{vib}^{ion} - IP. \tag{2}$$

Introducing the binding energy E_b^n=IP$-R_n$ of the Rydberg state relative to the IP to which it converges, and assuming the propensity rule $\Delta v \approx 0$ in the ionization step (on Franck–Condon arguments and the structural similarity between the Rydberg states and the cation) so that $E_{vib}^{R_n} \approx E_{vib}^{ion}$, we get

$$E_{kin}^{e} = \hbar\omega_{probe} - E_b^n, \tag{3}$$

which demonstrates that, within such an ionization scheme, the kinetic energy distribution of the photoelectron spectrum does not depend on the pump wavelength but only on the Rydberg state binding energy and on the probe wavelength. This invariance is mainly due to the conservation of vibrational energy in the Rydberg states through the photoionization, as represented on Fig. 1(2 and 3).

Such behavior has been previously observed in the photoelectron spectra of other aromatic systems obtained with short optical pulses.[25,26] The bandwidth of the observed photoelectron bands is relatively narrow (around 200 meV) compared to the few eV of vibrational excitation in these Rydberg states. This is another signature of photoionization taking place via a vibrational propensity rule $\Delta v \approx 0$, and further supports the assignment of the intermediate levels to Rydberg states in the resonantly induced two-photon ionization. The binding energy with respect to D_0 is used to define the top axis of Fig. 4(a). These Rydberg states have previously been observed by Weber *et al.* via one color three-photon ionization with femtosecond pulses at 265 nm [multiphoton ionization (MPI)].[27] In this paper, the authors suggest that the Rydberg states are optically dark states populated by an ultrafast internal conversion from an optically bright superexcited state (SES) of short lifetime.[28,29] A few of the Rydberg states of azulene have been directly detected by absorption spectroscopy[30,31] and by multiphoton ionization.[26,27] In the MPI studies by Weber *et al.*,[26,27] no assumption was made as to which limit the Rydberg states were converging to. Therefore, in order to compare our results to these previous data, the Rydberg states are listed in Table I as a function of their binding energies; their absolute

electronic energies are obtained by assuming a common convergence limit to D_0. Weber *et al.* deduce the electronic symmetry of the Rydberg states on the basis of the quantum defect value extracted from their analysis (close to 1 for a *s* orbitals, 0.3–0.5 for *p* orbitals, and <0.1 for higher angular momentum states). Using the same arguments, the calculated quantum defects are listed on top of each contribution in Fig. 4(a). The binding energies extracted from Fig. 4(a) are in good agreement with the known spectroscopy of the Rydberg states in azulene.[26,27,30,31] Based on the relative agreement with the absorption spectroscopy by Lewis *et al.*,[31] we cautiously conclude that most of the Rydberg states observed in Fig. 4(a) converge onto D_0 but this statement is amenable to further confirmation.

The remaining question is does the photoionization from S_2 take place via an optical resonance with the Rydberg states [path (d) in Fig. 1] or via some other state that relaxes to Rydberg states [path (e)] as proposed by Weber? The general concept of a "superexcited state" defines a neutral state higher than the ionization potential with two-electron holes or an inner-shell electron.[32] Detailed experimental and theoretical data on the ionization of azulene are scarce,[21,22,33,34] but the onset of shake-up ion states has been calculated by Deleuze to lie at quite low excitation energies, around 9.6 eV with a dominant configuration corresponding to $\ldots(1b_1)^2(2b_1)^2(1a_2)^2(3b_1)^2(2a_2)^0(4b_1)^0(3a_2)^1$.[33] Any neutral state converging to this cation state is likely to be a SES. The presence of a doubly excited state lying at an energy as low as 4.95 eV has been detected by magnetic circular dichroism (MCD) on different derivatives of azulene.[24] This kind of state is not strictly speaking a SES since it lies below the IP but some of the properties of such a state are very similar to a SES. Now, we will demonstrate why the photoelectron spectra of Fig. 4(a) lead us to propose a photoionization scheme corresponding to path (e) in Fig. 1.

If a progression of the Rydberg states involved in the time-resolved photoionization scheme [presented in Fig. 4(a)] converge to D_0, they will share the geometry of the cationic state. Consequently, transitions from S_2 to this subset of Rydberg states should also follow the $\Delta v \approx 0$ propensity since S_2 is also parallel to D_0.[17,21] At a fixed probe energy, such a propensity rule might be satisfied for one of the Rydberg states but it is very unlikely to be satisfied for all of them over the implemented pump energy range. The invariance of the Rydberg features observed in the photoelectron spectra to the pump wavelength therefore implies that D_0 Rydberg states must be populated via an intermediate state with a different geometry to S_2 and D_0. Furthermore, this intermediate state must couple to such a D_0 Rydberg progression via internal conversion on the time scale of the probe pulse. Once populated, the Rydberg states are photoionized by a subsequent probe photon. Since the combined energy of one pump and one probe photon for $\lambda_{pump} > 287.5$ nm is below the ionization threshold to D_0, the excited state in question is most likely an unstable double hole state with very diffuse electronic orbitals. The natural decay should then occur by an Auger-like process, namely, by filling the unoccupied lower molecular orbital with the resulting excess energy balanced by the ejection of an electron. Since this excited

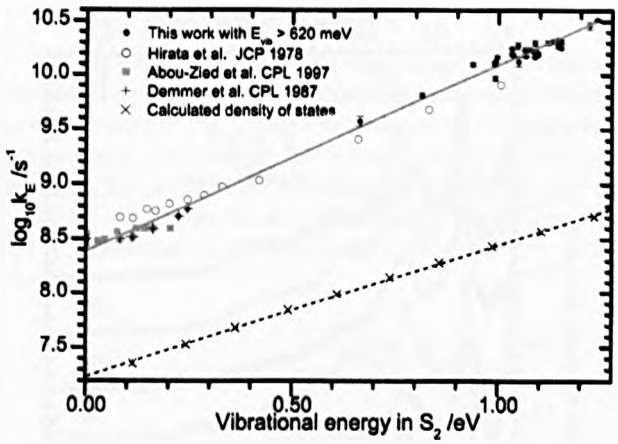

FIG. 5. Plot of $\log(k_E)$ vs vibrational energy in the S_2 state. Our data are compared to the previous work by Hirata *et al.* (Ref. 7) Abou-Zield *et al.* (Ref. 9), and Demmer *et al.* (Ref. 8), as well as to the calculated density of states taking into account only the vibrational modes of A_1 symmetry. Linear fits are done on our data (straight line) and calculated the density of states (dashed line).

state lies below the ionization threshold, the energy required to expel the electron is not available. Nevertheless, states with an appropriate electronic configuration and an equivalent energy are present, the states being the Rydberg series converging to D_0. The instability of a doubly excited state would result in efficient and extremely fast internal conversion with respect to the probe pulse duration. Note that this process would be independent of the vibrational energy in this double hole state, and this would rationalize the independence of the Rydberg fingerprint to the vibrational energy in the S_2 manifold. This two-photon ionization channel [path (e)] would also be strongly favored because of inefficient Franck–Condon factors from S_2 onto D_0 [path (d)] as a result of insufficient energy to achieve vibrational energy conservation [as shown in Eq. (1)]. Another interesting feature in the photoelectron spectra [Fig. 4(a)] is the prominent contribution of the Rydberg states with larger binding energy whatever the vibrational energy of the S_2 state. This unexpected invariance over the studied 1 eV pump energy range[28,35] might be rationalized by an intermediate excited state originating at low electronic energy but populated with a large vibrational energy. This would be consistent with the doubly excited state revealed in MCD around 4.95 eV.[24] In such a case, internal conversion would be expected to favor population transfer to Rydberg states with a large binding energy. We can tentatively assign the electronic configuration of this doubly excited state. The S_2 state is a superposition of two one electron excitations: HOMO (highest occupied molecular orbital) to HOMO+2 and HOMO−1 to lowest unoccupied molecular orbital (LUMO).[36] The ion shake-up state calculated by Deleuze[33] corresponds to the excitation HOMO to HOMO+2. The doubly excited state could easily involve the double excitation of the HOMO+2 orbital. This configuration would be in agreement with Deleuze's calculation and be of A_1 symmetry, as required for the observed optical anisotropy.[11]

Photoelectron spectra 5 and 6 of Fig. 4(a) are one-color profiles recorded at 400 nm (5) in the femtosecond regime or

(6) nanosecond regime. Remarkably, the intensity distribution of the photoelectron spectra at 400 nm is the same regardless of whether the MPI takes place in the nanosecond or femtosecond regime. It is useful here to comment on the difference between one-color photoionization at 400 nm [Fig. 4(a)] and at 266 nm [Fig. 4(b)]. Photoelectron spectra recorded at 400 nm show the Rydberg fingerprint, while those recorded at 266 nm display the electronic character of the S_4 state and the S_2 states. A two-photon excitation at 400 nm can reach an excited state, as already observed in the liquid phase,[3] whose population would then rapidly decay to the S_2 state. In that case, photoionization at 266 nm via $\Delta v \approx 0$ transitions are energetically allowed, while these channels are closed for photoionization at 400 nm:

$$S_0 \xrightarrow{h\nu_{266\ \mathrm{nm}}} S_4(v=0)+E_{\mathrm{vib}}(0.26\ \mathrm{eV}) \xrightarrow{h\nu_{266\ \mathrm{nm}}} D_1(v=0)+0.82\ \mathrm{eV}\Rightarrow \Delta v=0 \text{ allowed},$$

$$\downarrow \mathrm{IC}$$

$$S_2(v=0)+E_{\mathrm{vib}}(1.1\ \mathrm{eV}) \xrightarrow{h\nu_{266\ \mathrm{nm}}} D_0(v=0)+1.92\ \mathrm{eV}\Rightarrow \Delta v=0 \text{ allowed}.$$

$$S_0 \xrightarrow{2h\nu_{400\ \mathrm{nm}}} S_{??} \xrightarrow{h\nu_{400\ \mathrm{nm}}} D_0(v=0)+1.92\ \mathrm{eV}\Rightarrow \Delta v=0 \text{ not allowed}.$$

$$\downarrow \mathrm{IC}$$

$$S_2(v=0)+E_{\mathrm{vib}}(2.64\ \mathrm{eV})$$

Consequently, at 400 nm the transition to the intermediate double hole state competes efficiently with direct photoionization, in contrast to the 266 nm scheme.

Doubly excited states are quite difficult to investigate spectroscopically mainly due to their markedly different geometry to the valence states as well as their short lifetimes. It is mainly through their relaxation process that they are detectable. Despite the difficulty, we hope our observations might inspire theorists to take up the challenge to calculate the geometry and electronic configuration of the doubly excited states on polyaromatic systems, such as azulene. Indeed, these curious states are of potential importance in a variety of interesting processes since these states might coexist with the ion states as well as dissociative neutral states. The dynamics of such states are thus likely to play a crucial role in Rydberg fingerprint spectroscopy, which is used, for instance, to differentiate charge distributions in isomeric aromatic molecules,[35] as well as conformational dynamics.[37]

D. Nonradiative relaxation from vibrationally excited S_2 state

The time transients recorded in Fig. 2 map the relaxation from the S_2 state. This is revealed by the persistence of the intensity distribution of the time-resolved photoelectron spectrum as a function of the pump-probe delay as well as the same sensitivity to the rotational coherence (not presented here).[11] We now examine the variation of the decay rate as a function of the excitation energy using a statistical approach.

Nonradiative relaxation in azulene is largely governed by internal conversion (IC) rather than intersystem crossing (ISC). If we ignore ISC, the decay time τ_e is simply a function of the radiative rate k_r and the nonradiative relaxation rate k_{IC},

$$\frac{1}{\tau_e}=k_e=\frac{k_r}{\phi_r}=k_{\mathrm{IC}}+k_r, \tag{4}$$

where ϕ_r is the fluorescence quantum yield. In Fig. 5, we plot the decay rates measured for different vibrational energies in S_2 state, together with lifetime measurements[9] obtained for low E_{vib} and data deduced from quantum yield measurements.[7,8] The fluorescence rate is usually supposed independent of the vibrational mode,[38] such that any variation in the decay time simply stems from a dependency of the IC rate with the excess energy. At the origin of S_2, the weak coupling between the S_2–S_1 state[39] can be described by an electronic energy gap law.[40] At larger excess vibrational energies, the relaxation becomes dominated by the S_2–S_0 internal conversion.[7]

With increasing vibrational energy, the internal conversion rate is expected to slightly increase before tailing off at yet higher energy.[38,41] The overall trend of exponentially increasing k_{IC} versus vibrational energy in S_2 has already been observed[7–9,41] for an excess vibrational energy greater than 0.24 eV.[2,8] In the framework of Fermi's golden rule, the internal conversion rate can be approximated as[38]

$$k_{\mathrm{IC}}(E_i)=\frac{2\pi}{\hbar}|V_i|^2\rho(E_i), \tag{5}$$

where $\rho(E_i)$ is the vibrational level density in S_0 at the energy $E_i=E_{S_2}(0)+E_{\mathrm{vib}}(S_2)$ with $E_{S_2}(0)$ defining the vibrational zero point energy of S_2 and $|V_i|^2$ the mean-square value of the S_2–S_0 coupling at the energy E_i. The vibrational level density at high excess energy can be roughly estimated by an exponential function of vibrational energy[38]

$$\rho(E_i) \propto \exp\left(\frac{E_i}{\varepsilon_{S_0}}\right) \tag{6}$$

where ε_{S_0} is the typical energy scale of increase in level density as a function of the vibrational energy in S_0. In a crude approximation, one can assume a weak variation of coupling $|V_i|^2$ as a function of E_i, such that

$$\alpha = \frac{\delta \ln(k_e)}{\delta E_{\text{vib}}(S_2)} = \frac{k_{\text{IC}}}{k_r + k_{\text{IC}}} \frac{1}{\varepsilon_{S_0}} \sim \frac{1}{\varepsilon_{S_0}}. \tag{7}$$

This simple calculation overestimates α by not taking into account the vibrational modes promoting the IC that will lead to a reduced state density; however, it explains the linear dependency observed in Fig. 5.

Figure 5 compares the rate k_e measured at high excess energy in the present work with earlier gas-phase measurements at lower excess vibrational energy.[7–9,41] The value of $\alpha = 1.70 \pm 0.05$ eV^{-1} is the result of a linear fit taking into account our data together with two measurements obtained by picosecond resolved fluorescence and a jet-cooled molecular beam at excess energy $\geqslant$236 meV.[8]

In order to detect the importance of promoting modes, a calculation of the state density in S_0 at the different vibrational energies of S_2 has been carried out using the generating function for the number of states of a given energy[42]

$$f(z) = \prod_{i=0}^{n_{A_1}} \frac{1}{1 - z^{\varepsilon_i}}, \tag{8}$$

where n_{A_1} is the total number of in-plane vibrational modes of A_1 symmetry (17 for azulene) and ε_i are the vibrational energies in S_0.[23] The number of possible combinations at the total vibrational energy E in the S_0 state is calculated by numerical integration of the Cauchy residue formula which inverts the generating function,[43]

$$N(E) = \frac{1}{2\pi i} \int_c \frac{dz}{z^{E+1}} f(z). \tag{9}$$

This contour integral is done with a resolution of $\Delta E = 10$ meV, fixed by the convergence of the calculation, leading to a density of states,

$$\rho(E) = \frac{N(E)}{\Delta E}. \tag{10}$$

Here, the anharmonicities of the vibrational modes are not taken into account nor are all the mode combinations, but the good agreement with the experimental data (slope $\alpha = 1.21 \pm 0.02$ eV^{-1}—dashed plot on Fig. 5) leads us to conclude that the internal conversion S_2–S_0 is not limited by a promoting mode process. Note that, for instance, if the six out-of-plane A_2 vibrational modes[23] are added in the calculation, the slope increases to $\alpha = 2.27 \pm 0.02$ eV^{-1}.

At high excitation energy, the internal conversion rate might simply depend on the difference in entropy between the initial and the final electronic states. Indeed, the entropy of the initial state has to be taken into account to reflect the dissipative character of the intramolecular vibrational relaxation. When the vibrational energy in S_2 becomes significant, the entropy of S_2 increases at the same rate $\varepsilon = \varepsilon_{S_0}$ as the entropy in S_0 and the internal conversion rate will reach its converging limit defined by[38]

$$k_{\text{IC}} = \frac{2\pi}{\hbar} \frac{|V_i|^2}{\varepsilon} \exp\left(\frac{E_{S_2}(0) - E_{S_0}(0)}{\varepsilon}\right). \tag{11}$$

Although we have not yet observed this fall-off behavior in the IC rate between the S_2 and S_0 states, we can still estimate a lower limit for the vibronic coupling V_i from the k_{IC} measured at the maximum excess vibrational energy investigated here 1.24 eV s^{-1} and $\varepsilon \propto 1/\alpha = 586 \pm 17$ meV. The lower limit for V_i is 60 ± 5 μeV. Note that the S_2–S_4 vibronic coupling is estimated to 99.2 meV.[20] A more definitive statement concerning the magnitude of the coupling must await the determination of the fall-off region of k_{IC} via pump-probe experiments done at higher energy: The slope, α, for excess energy in S_1 from 0 to 250 meV, is found to be very close to the one observed here with $\alpha = 1.50 \pm 0.53$ eV^{-1}.[39]

IV. CONCLUSION

We have performed time-resolved studies on the S_2–S_4 excited states of azulene. Our pump-probe experiments reveal an internal conversion process onto the S_2 state, followed by an internal conversion onto S_0. The S_2–S_0 decay rate follows an exponential energy gap law as a function of the vibrational energy in the S_2 state. The vibronic coupling strength is anticipated to be larger than 60 μeV based on a statistical description of the internal conversion. These experiments also reveal an uncommon ionization pathway involving a common set of Rydberg states that are populated on an ultrafast time scale from a doubly excited state, or possibly several such states. Experimental evidence suggests that this probe transition becomes efficient when the excess energy in the ion continuum is not high enough to reach the Franck–Condon window. Above the IP, doubly excited states can autoionize or undergo dissociative ionization in addition to relaxing by an Auger-like process to vibrationally excited Rydberg states whose origins lie below the IP. However, if the doubly excited state itself lies below the IP, only this last decay route is open. In fact, these processes may be quite general in aromatic systems in which doubly excited states below the IP are likely to be ubiquitous.

ACKNOWLEDGMENTS

The authors would like to thank D. S. Dean for his help in calculating the density of states and A. Beswick for helpful references on statistical theories applied to relaxation dynamics. This work was supported by CNRS, le Ministère de la Recherche, Région Midi-Pyrénées through "Plan état-Région Spectroscopies Optiques Ultimes," ANR COCOMOUV and the British Council Alliance programme. B.J.W. thanks the CNRS and the UPS for his invited position in the LCAR. K.R. thanks the CNRS for his postdoc fellowship. G.T. thanks the European network COCOMO for his postdoc fellowship. I.W. and B.J.W. are also grateful to the EPSRC for partial support of this work through GR/S47656/01 and for a research studentship.

[1] M. Kasha, Discuss. Faraday Soc. **9**, 14 (1950).
[2] M. Fujii, T. Ebata, N. Mikami, and M. Ito, Chem. Phys. **77**, 191 (1983).
[3] P. Foggi and F. V. R. Neuwahl, J. Phys. Chem. A **107**, 1689 (2003).
[4] J. R. Cable and A. C. Albrecht, J. Chem. Phys. **84**, 1969 (1986); L. Ciano, P. Foggi, and P. Remigio Salvi, J. Photochem. Photobiol., B **105**, 129 (1997).
[5] M. Damm, F. Deckert, H. Hippler, and J. Troe, J. Phys. Chem. **95**, 2005 (1991).
[6] U. Hold, T. Lenzer, K. Luther, and A. C. Symonds, J. Chem. Phys. **119**, 11192 (2003); H. Hippler, L. Lindemann, and J. Troe, J. Chem. Phys. **83**, 3906 (1985).
[7] Y. Hirata and E. C. Lim, J. Chem. Phys. **69**, 3292 (1978).
[8] D. R. Demmer, J. W. Hager, G. W. Leach, and S. C. Wallace, Chem. Phys. Lett. **136**, 329 (1987).
[9] O. K. Abou-Zied, D. R. M. Demmer, S. C. Wallace, and R. P. Steer, Chem. Phys. Lett. **266**, 75 (1997).
[10] E.-G. Diau, S. De Feyter, and A. H. Zewail, J. Chem. Phys. **110**, 9785 (1999).
[11] K. Raffael, V. Blanchet, B. Chatel, G. Turri, B. Girard, I. Garcia, I. Wilkinson, and B. J. Whitaker, "Time-dependent photoionization of azulene: Optically induced anistropy on the femtosecond scale," Chem. Phys. Lett. (submitted).
[12] A. Stolow, A. E. Bragg, and D. M. Neumark, Chem. Rev. (Washington, D.C.) **104**, 1719 (2004).
[13] A. T. J. B. Eppink and D. H. Parker, Rev. Sci. Instrum. **68**, 3477 (1997).
[14] G. Cerullo and S. De Silvestri, Rev. Sci. Instrum. **74**, 1 (2003); A. Monmayrant, A. Arbouet, B. Girard, B. Chatel, B. J. Whitaker, A. Barman, and D. Kaplan, Appl. Phys. B: Lasers Opt. **81**, 177 (2005).
[15] N. Nakashima, S. Shimizu, T. Yatsuhashi, S. Sakabe, and Y. Izawa, J. Photochem. Photobiol. C **1**, 131 (2000).
[16] H. C. Hsu, C.-L. Liu, J.-J. Lyu, and C.-K. Ni, J. Chem. Phys. **124**, 134303 (2006).
[17] D. Tanaka, S. Sato, and K. Kimura, Chem. Phys. **239**, 437 (1998).
[18] S. Hassoon, D. L. Snavely, and I. Oref, J. Chem. Phys. **97**, 9081 (1992).
[19] M. F. Lin, C. L. Huang, Y. T. Lee, and C. K. Ni, J. Chem. Phys. **119**, 2032 (2003); Y. A. Dyakov, C. K. Ni, S. H. Lin, Y. T. Lee, and A. M. Mebel, J. Phys. Chem. A **109**, 8774 (2005).
[20] W. D. Lawrance and A. E. W. Knight, J. Phys. Chem. **94**, 1249 (1990).
[21] P. M. Weber and N. Thantu, Chem. Phys. Lett. **197**, 556 (1992).
[22] R. Boschi, E. Clar, and W. Schmidt, J. Chem. Phys. **60**, 4406 (1974).
[23] P. M. Kozlowski, G. Rauhut, and P. Pulay, J. Chem. Phys. **103**, 5650 (1995).
[24] W. Gerhartz and J. Michl, J. Am. Chem. Soc. **100**, 6877 (1978).
[25] M. Tsubouchi, B. J. Whitaker, L. Wang, H. Kohguchi, and T. Suzuki, Phys. Rev. Lett. **86**(20), 4500 (2001).
[26] N. Kuthirummal and P. M. Weber, Chem. Phys. Lett. **378**, 647 (2003).
[27] N. Kuthirummal and P. M. Weber, J. Mol. Struct. **787**, 163 (2006).
[28] C. P. Schick and P. M. Weber, J. Phys. Chem. A **105**, 3725 (2001).
[29] C. P. Schick and P. M. Weber, J. Phys. Chem. A **105**, 3735 (2001).
[30] T. Kitagawa, Y. Harada, H. Inokuchi, and K. Kodera, J. Mol. Spectrosc. **19**, 1 (1966).
[31] J. W. Lewis, R. V. Nauman, D. B. Bouler, and S. P. McGlynn, J. Phys. Chem. **87**, 3611 (1983).
[32] S. T. Pratt, Annu. Rev. Phys. Chem. **56**, 281 (2005).
[33] M. S. Deleuze, J. Chem. Phys. **116**, 7012 (2002).
[34] S. Hirata, M. Head-Gordon, J. Szczepanski, and M. Vala, J. Phys. Chem. A **107**, 4940 (2003).
[35] J. L. Gosselin and P. M. Weber, J. Phys. Chem. A **109**, 4899 (2005).
[36] A. Murakami, T. Kobayashi, A. Goldberg, and S. Nakamura, J. Chem. Phys. **120**, 1245 (2004).
[37] M. P. Minitti and P. M. Weber, Phys. Rev. Lett. **98**, 253004 (2007).
[38] B. A. Jacobson, J. A. Guest, F. A. Novak, and S. A. Rice, J. Chem. Phys. **87**, 269 (1987).
[39] B. D. Wagner, D. Tittelbach-Helmrich, and R. P. Steer, J. Phys. Chem. **96**, 7904 (1992); N. Tetreault, R. S. Muthyala, R. S. H. Liu, and R. P. Steer, J. Phys. Chem. A **103**, 2524 (1999); A. A. Ruth, E. K. Kim, and A. Hese, Phys. Chem. Chem. Phys. **1**, 5121 (1999).
[40] R. Englman and J. Jortner, Mol. Phys. **18**, 145 (1970).
[41] T. M. Woudenberg, S. K. Kulkarni, and J. E. Kenny, J. Chem. Phys. **89**, 2789 (1988).
[42] S. H. Lin and H. Eyring, J. Chem. Phys. **39**, 1577 (1963).
[43] S.-H. Lin and H. Eyring, J. Chem. Phys. **43**, 2153 (1965).

Appendix E

Published article: Time-dependent photoionisation of azulene; optically induced anisotropy on the femtosecond scale

The article presented below was published in Chemical Physics Letters and describes experiments that were performed in order to understand the short-time transient ion signals after azulene was excited to its S_2, S_3 and S_4 states using ultrashort laser pulses and is subsequently ionised by a second ultrashort light field. By recording pump-probe transient ion decay traces using parallel and perpendicular laser polarisation combinations the short-time decay transient signal was attributed to the rotational coherence of the excited state molecules that was generated by the pump transition. The majority of the work presented in this article was performed by Dr Valérie Blanchet, Dr Kevin Raffael, Dr Giorgio Turri, Dr Béatrice Chatel and Professor Bertrand Girard with my supervisor Professor Benjamin J. Whitaker at the Laboratoire Collisions Agrégats Racuteeactivité at the Université Paul Sabatier in Toulouse. However, some complimentary experiments were performed in Leeds using an earlier version of the spectrometer described in Chapter 3. Specifically, Dr Ivan Anton Garcia and I recorded short timescale pump-probe decay transients using different pump and probe laser polarisations at excitation energies close to 4.81 eV. This allowed the anisotropy of the ion yield to be measured as a function of pump-probe delay.

Chemical Physics Letters 460 (2008) 59–63

Contents lists available at ScienceDirect

Chemical Physics Letters

journal homepage: www.elsevier.com/locate/cplett

Time-dependent photoionization of azulene: Optically induced anistropy on the femtosecond scale

Kevin Raffael [a], Valérie Blanchet [a,*], Béatrice Chatel [a], Giorgio Turri [a], Bertrand Girard [a], Ivan Anton Garcia [b], Iain Wilkinson [b], Benjamin J Whitaker [b]

[a] Laboratoire Collisions Agrégats Réactivité (UMR 5589, CNRS -Université de Toulouse, UPS), Institut de Recherches sur les Systèmes Atomiques et Moléculaires Complexes, France
[b] School of Chemistry, University of Leeds, Leeds, LS2 9JT, UK

ARTICLE INFO

Article history:
Received 31 March 2008
In final form 4 June 2008
Available online 11 June 2008

ABSTRACT

We measure the photoionization cross-section of vibrationally excited levels in the S_2 state of azulene by femtosecond pump–probe spectroscopy. At the wavelengths studied (349–265 nm in the pump) the transient signals exhibit two distinct and well-defined behaviours: (i) short-term (on the order of a picosecond) polarization dependent transients and (ii) longer (10 ps–1 ns) timescale decays. This Letter focuses on the short-time transient. In contrast to an earlier study by Diau et al. [E.G. Diau, S. De Feyter, A.H. Zewail, J. Chem. Phys. 110 (1999) 9785.] we unambiguously assign the fast initial decay signal to rotational dephasing of the initial alignment created by the pump transition.

1. Introduction

The photochemistry of azulene has been the subject of extensive experimental and theoretical studies due to its second electronically excited singlet state S_2 exhibiting a much stronger fluorescence than the lower lying first electronically excited singlet state S_1 [2–4]. As such, the molecule is well known as the textbook exception to Kasha's rule that 'the emitting level of a given multiplicity is the lowest excited level of that multiplicity' [5]. Azulene has subsequently become a model compound with which to study intramolecular dynamics and energy transfer processes [6]. Intriguingly, sometime ago Diau et al. [1] observed a fast exponential component in the ion time-profile with a 350 fs decay on the top of a long decay component, when exciting the S_2 state with 471 meV excess vibrational energy. They suggested that the appearance of the fast 350 fs signal was a direct manifestation of a non-radiative process occurring in S_2. However, this is surprising when one considers the ns lifetime time of the S_2 state obtained by fluorescence quantum yield experiments [4] and other time-resolved experiments [2,3,7]. This contradiction prompted us to reinvestigate the short-time dynamics in S_2 state by time-resolved photoelectron/photoion imaging spectroscopy. These experiments have been performed as a function of the pump wavelength, the relative polarization of the pump and probe pulses and the carrier gas pressure. Our results lead us to conclude that the short decay first observed by Diau et al. [1] in fact corresponds to anisotropy in the rotational distribution of the pumped S_2 levels.

2. Experimental details

We employ pump–probe time-of-flight (TOF) mass-spectrometry to detect either photoions or photoelectrons resulting from the absorption of one pump photon to populate an excited state of the neutral which is then ionized at a controlled time delay by two or more probe photons. As more fully described elsewhere [7] both pump and probe pulses are generated from a 1 kHz–2.5 mJ chirped pulse amplifier (CPA) centered at ~805 nm delivering a fundamental pulse with a Fourier limited full-width at half maximum (FWHM) of ~60 fs (Amplitude Systems). A non-collinear optical parametric amplifier (NOPA) [8,9] with subsequent sum frequency mixing or second harmonic generation (SHG) produces the ultraviolet pump pulse. The NOPA output is partly recompressed by a prism pair. The tunability of the NOPA allows the pump central wavelength to be varied from 370 to 265 nm. The typical spectral width of the pump pulse is 250–450 cm^{-1}, corresponding to a Fourier limited pulse of 35–60 fs at FWHM in intensity. For all of the experiments reported here the probe pulse is obtained by SHG of the fundamental output of the CPA. The cross-correlation time, recorded by off-resonant multiphoton ionization of nitric oxide, has a typical 120–320 fs FWHM depending on the pump wavelength. At the pulse energies employed (<1 μJ for the pump and ~15–25 μJ for the probe) we are confident that multiphoton ionization takes place in an unperturbed energy scheme [10].

The focused laser beams intersect, perpendicularly, a skimmed continuous molecular beam containing azulene diluted in nitrogen. This yields photoions and photoelectrons which are subsequently detected, depending on the sign of the applied accelerating voltage, at the output of a 40 cm time-of-flight velocity map imaging spectrometer whose axis is perpendicular to the

* Corresponding author. Fax: +33 561 558 317.
E-mail address: val@irsamc.ups-tlse.fr (V. Blanchet).

0009-2614/$ - see front matter © 2008 Elsevier B.V. All rights reserved.
doi:10.1016/j.cplett.2008.06.009

plane defined by the laser and molecular beams [11]. The translational speed of the molecular beam was estimated from the length of the azulene ion image and its distance from the centre of the background gas spot due to azulene at rest in the laboratory frame. The distribution of this translational speed corresponds to a temperature of 25 K, and we assume that the rotational temperature is similar. We also performed some experiments in an unseeded beam of pure azulene vapour. Under these expansion conditions we estimate a rotational temperature close to 170 K. We were unable to detect any trace of van der Waals clusters such as azulene-N_2 or $(azulene)_n$ in the mass spectrum under either expansion condition [12,13].

For each pump–probe delay, controlled by a programmable translation stage placed in the pump beam path, an average over ~2000 laser pulses was made to record the transients on the ion signal. Photoelectron spectra were obtained by velocity map imaging over $\sim 4 \times 10^5$ laser pulses [14].

3. Results and discussion

3.1. A-time-resolved photoionization

Fig. 1 shows time profiles of the photoion signal of the parent azulene ion, $C_{10}H_8^+$, recorded for different pump wavelengths (265–367 nm) with a 400 nm probe pulse over a 4 ps delay range. All the decay traces were recorded with parallel pump and probe polarisations. The pump excitations span an energy range of over 1 eV from the band origin of S_2 ($2A_1$) (**Fig. 1**c–e) to vibrationally excited levels in S_4($3A_1$) (**Fig. 1**a and b) [15]. The off-resonance cross-correlation signal (**Fig. 1**f) gives a FWHM of 320 fs. This cross-correlation time is reduced to 120 fs when using SHG instead of frequency mixing to produce the pump pulse. Whatever the pump excitation, a fast component is evident in all the time profiles (**Fig. 1**a–e). It can be fitted by a single exponential decay of 465 fs as illustrated by the solid line in **Fig. 1**a. This decay is the same for all pump wavelengths investigated and is in reasonable agreement with the 350 fs decay reported previously by Diau et al. [1]. Taking into account the difference in electronic character between the S_2 and S_4 states and the change of vibrational density over the 1 eV energy window scanned here it now seems unlikely that the recurrent fast transient signal can be due to fast internal conversion from S_2 or S_4 or to dissipative intramolecular vibrational-energy redistribution, as originally suggested by Diau et al. [1] (from their ion transient signal obtained at a single excitation energy).

In order to further investigate the physical origin of the photoion time profiles, the transients were recorded with the pump and probe polarizations parallel and perpendicular to one another. **Fig. 2** shows a comparison of the time profiles recorded at 335 nm for the two polarization configurations for the azulene cation (top panel) and the fragment $C_8H_6^+$ (lower panel). At this pump energy, the vibrational excitation in S_2 is 1093 cm^{-1}, slightly lower than the 3800 cm^{-1} investigated by Diau et al. [1]. The $C_8H_6^+$ fragment ion is produced by dissociative ionization and appears as the intensity of the 400 nm probe is increased to ~25 μJ $pulse^{-1}$. The appearance potential of the $C_8H_6^+$ ion is known to be around 14 eV [16], and consequently the $C_8H_6^+$ signal must be a product of at least three photon absorption of the probe pulse. As previously demonstrated [7], power dependency studies on the parent ion support a $1+2'$ ionization scheme over all the pump wavelength range presented here. The result we wish to draw attention to is that both pump–probe transient signals show a marked and similar difference for the two polarization configurations, with the main change being the apparent suppression of the fast component when the laser polarisations are perpendicular to each other. Experiments were also performed for a relative polarisation angle of 54.7°, the magic angle, which cancels any anisotropic dependency induced by the pump on the pump–probe signal. These confirmed the polarisation dependence of the fast signal.

Such polarization dependent transients are expected for an optically induced anisotropy investigated by time-resolved polarisation sensitive spectroscopy [17–22]. The effect can be described classically as the dephasing of an ensemble of molecular rotors (whose initial population is defined by the statistical distribution at the rotational temperature of the molecular beam, the Höln-London factors and the selection rules $\Delta J = 0, \pm 1$). Photons polarised with respect to the laboratory frame excite only those molecules in the sample (in our case a 'rotationally warm' molecular beam) whose transition dipoles are favourably aligned with respect to the laboratory frame. This results in a macroscopic polarization of the sample. Because the population of initial states is determined by Boltzmann energy partitioning, the excited ensemble is made up of molecules with a range of rotational states whose classical rotational frequencies are not the same and consequently the macroscopic polarization of the ensemble rapidly becomes misaligned. The initial coherence between the rotational states in the ensemble is then lost.

Rotational coherence spectroscopy (RCS) may be performed in a variety of ways, for example, by fluorescence [17–19], multiphoton ionization or photoelectron imaging [22]. However, it is most easily observed in linear and symmetric top molecules because in asymmetric rotors the revival structures are more complicated and the signals consequently weaker. Despite this a number of observations of rotational revivals in asymmetric molecules have been made using emission and ionization techniques [23]. Enhanced sensitivity of RCS in asymmetric rotors can, also, be achieved by using degenerate four wave mixing as a detection scheme [24–26]. Azulene is an asymmetric rotor (I_x = 2841.951839(193), I_y = 1254.843135(66), I_z = 870.712723(64) MHz) [27] and although we have not been able to observe rotational revival structures in the photoion/phototoelectron decay traces we can infer the contribution of the initially induced orientational coherence from the short-time behaviour of the pump–probe decay traces.

By rotating the polarization of the probe pulse relative to the pump pulse, the anisotropy of the ensemble can be investigated by polarization sensitive photoionization. Both the S_2 and S_4 states of azulene have A_1 electronic symmetry, and consequently both states have an electric dipole transition moment with the ground electronic state aligned along the z-axis (long axis in the molecular plane, see **Fig. 1**). The fast relaxation from S_4 to S_2 within a 120 fs timescale has been discussed elsewhere [7], and would not perturb this initial alignment. The polarization sensitivity to ionization by the probe pulse is therefore expected to be the same regardless of whether the S_4 or the S_2 state is populated. The anisotropy function $r(\tau)$ is defined as

$$r(\tau) = \frac{I_{\parallel}(\tau) - I_{\perp}(\tau)}{I_{\parallel}(\tau) + 2I_{\perp}(\tau)} \tag{1}$$

where $I_{\parallel}(\tau)$ and $I_{\perp}(\tau)$ refer to the photoionization intensities at a time delay τ for parallel and perpendicular polarization configurations, respectively. Since the rotational dephasing time of the excited ensemble depends on the width of the state distribution in the initial rotational wavepacket, $r(\tau)$ relaxes faster with increasing molecular beam rotational temperature. This is clearly illustrated in **Fig. 3** for a pump pulse irradiating at 335 nm. The minimum of the anisotropy function for a rigid asymmetric top molecule due to free molecular rotation occurs around $\tau_{min} = \sqrt{I_y/kT_{rot}}$ [28]. From the observed values of τ_{min} = 1.7 ps and τ_{min} = 4.5 ps, the rotational temperatures are calculated to be around 25 K for the seeded beam

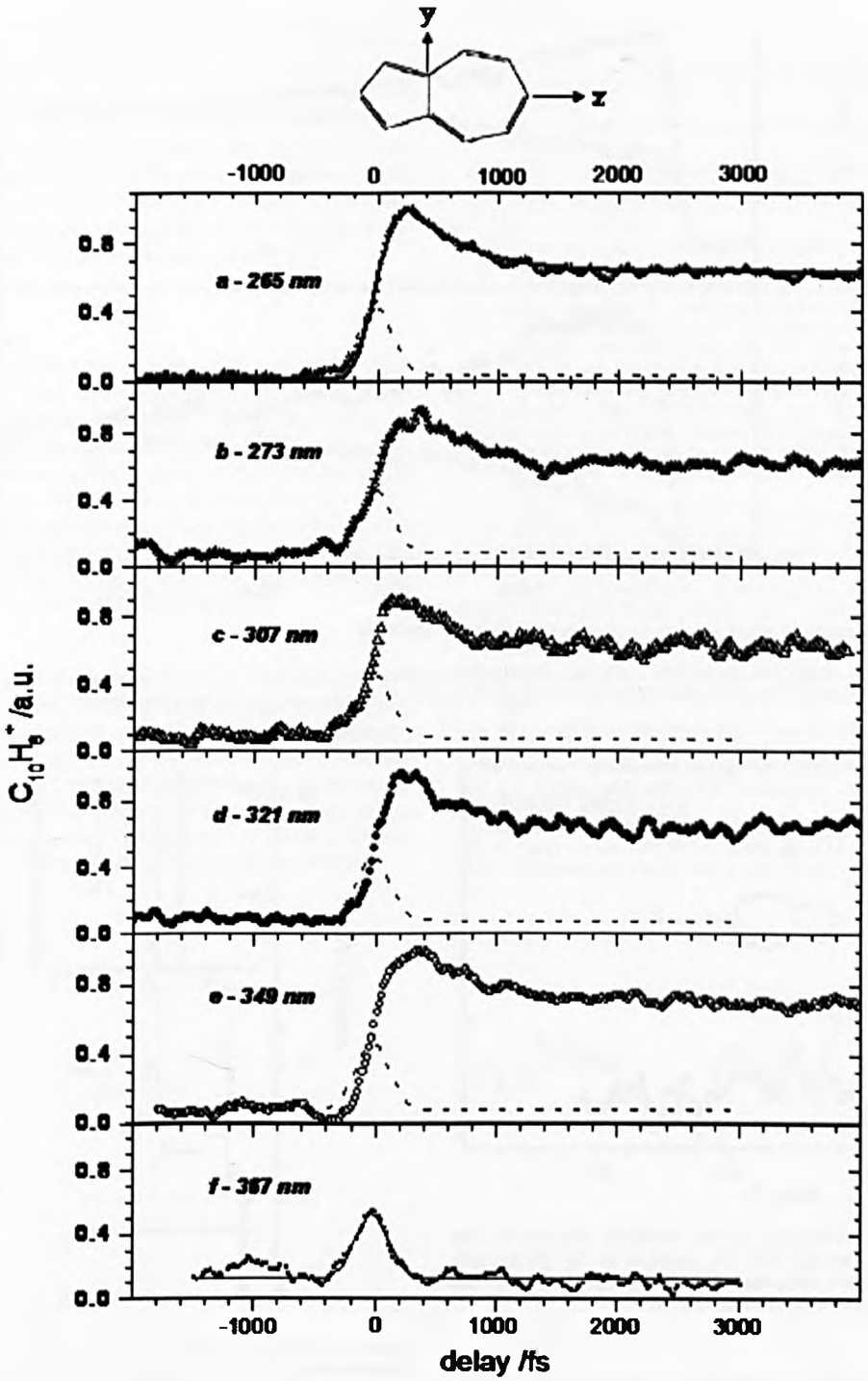

Fig. 1. Pump–probe photoionization transients of $C_{10}H_8$ for different pump wavelengths and a probe pulse centered at 400 nm. The pump and probe polarizations are parallel. Signals a–b correspond to excitation into the S_4 electronically excited state, whilst signals c–e involve the S_2 state. The cross-correlation time measured off-resonance, trace f, is 320 ± 14 fs. These cross-correlation fit is reported in dot lines in each panel. All the transients exhibit two exponentially decaying components. The faster of the two can be fitted by an exponential decay with a time constant of 465 fs. The convolution of the two decays with the cross-correlation signal is shown as the solid line in trace a.

and 170 K for a pure azulene beam, in very good agreement with our time of flight measurements of the translational temperature of the molecular beam.

The time-dependent ionization of electronically excited azulene studied as a function of the polarization and rotational temperature demonstrates that the short transient observed corresponds to optically induced anisotropy rather than electronic relaxation via internal conversion. Nevertheless, the question arises as to exactly how this sensitivity via the probe photoionization is achieved. Indeed, we record essentially identical pump–probe transients regardless of the excitation energy over a wide spectral window that spans at least two electronic states (S_2 and S_4). We have

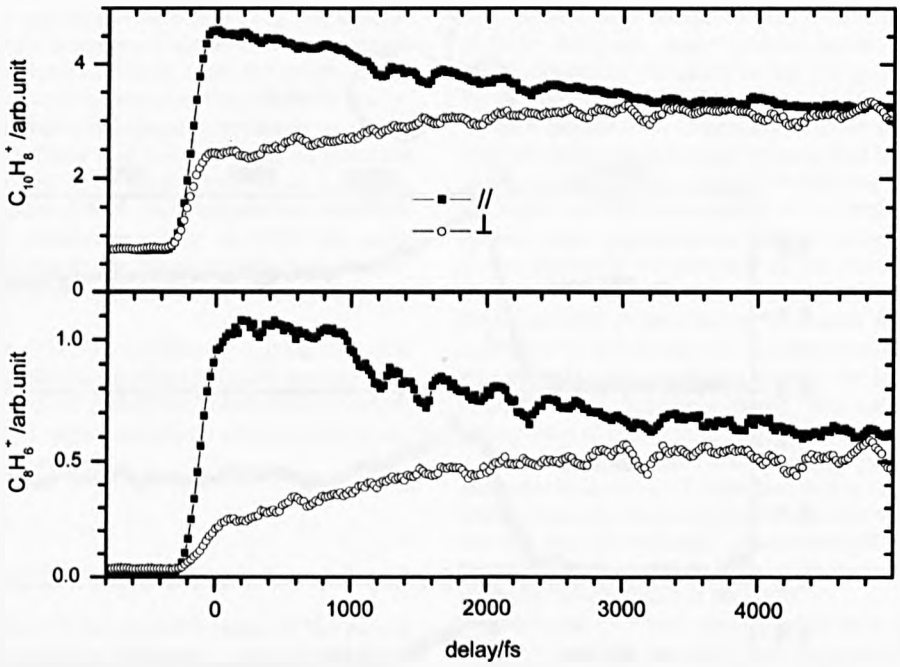

Fig. 2. Comparison of the time-resolved photoionization signals for parallel and perpendicular configurations of the laser polarisations. The pump and probe are centred at 335 nm and 400 nm respectively. The transients are recorded on both the parent ion, $C_{10}H_8^+$, (top panel) and the main fragment ion, $C_8H_6^+$, (bottom panel).

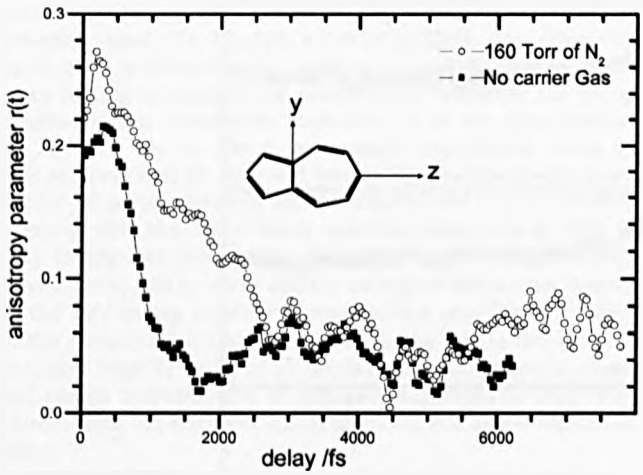

Fig. 3. Effect of rotational temperature on the anisotropy function $r(t)$. The rotational temperature is estimated from the minimum of the $r(t)$ function: $\tau_r = \sqrt{\frac{I_z}{kT_{rot}}}$. This leads rotational temperature around 25 K for the 160 Torr N_2 beam seeded with azulene and 170 K for the pure azulene jet.

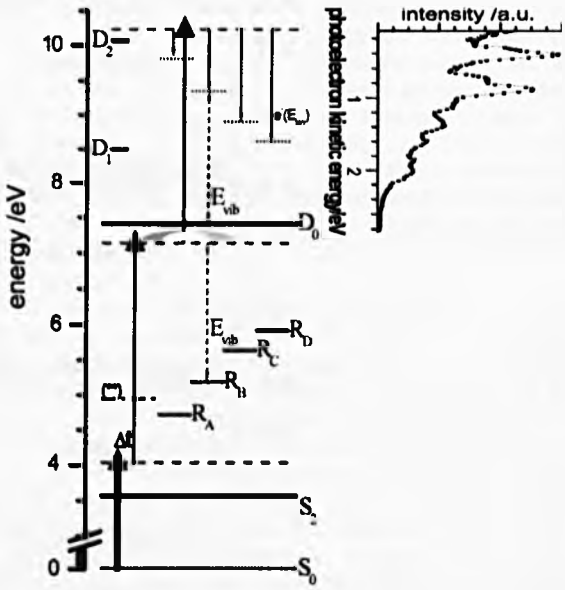

Fig. 4. Pump–probe ionization scheme involving a doubly excited (**) state. The one photon pump transition is indicated by the thick black arrow. The transient photoelectron and the azulene ion signals are produced by a subsequent two-photon probe transition, indicated by the two thin arrows. The first probe photon is postulated to be degenerate with a doubly excited state (most probably vibrationally highly excited) which rapidly decays, within the duration of the probe pulse, to high lying vibrational levels of a set of Rydberg states converging onto the ground state of the cation, D_0, giving the photoelectron spectrum shown on the right hand side of the figure. See Ref. [7] for full details.

previously demonstrated [7] (i) that the S_4 state decays very rapidly towards the S_2 state within less than the pump pulse duration (120 fs), and (ii) that whatever the pump wavelength the photoionization is driven by a sequential two photon transition from the S_2 state. This explains why the same behaviour and contrast is observed for data recorded above and below the S_4 threshold. The scenario is summarized in **Fig. 4** for the case of a direct S_2 excitation. This two photon transition involves a resonance with an intermediate doubly excited state that decays within the duration of the probe pulse to a set of Rydberg states that are subsequently ionized by the second probe photon. This doubly excited state has been detected by magnetic circular dichroism on different derivatives of azulene around 4.95 eV [29]. The photoelectron images show the fingerprint of the Rydberg states [30,31], which is manifest by the observation that the photoelectron spectrum is invariant to the pump wavelength [7]. The characteristic spectrum is depicted on the right hand side of **Fig. 4**. The invariance to the pump wavelength arises because the vibrational excess energy in the Rydberg state is conserved in the cation from Franck–Condon arguments. The overall transition moment from S_2 to the doubly

excited state must lie along the z-axis in order to explain the larger ionization probability for parallel polarized pump and probe fields.

To summarize, at all the wavelengths studied the transient photoionization signals exhibit two distinct and well-defined behaviours: (i) short-term (on the order of a picosecond) polarization dependent transients which are due to optically induced anisotropy where the sensitivity is achieved by photoionizing via a doubly excited state as sketched in **Fig. 4**, (ii) longer (10 ps–1 ns) timescale decays corresponding to the internal conversion of S_2–S_0. The latter can be described by a statistical model [7].

4. Conclusions

We have investigated the time-profiles of pump–probe transients in azulene in which the pump photon excites the electronically excited singlet states S_2–S_4 and the subsequent dynamics are probed via photoionization. On the contrary to what has been suggested previously [1], the short-term decay behaviour that is observed on the timescale of ~400 fs when the polarizations of the pump and probe laser fields are parallel is associated with an optically induced anisotropy of the molecular axes in the S_2 state. This is observed via two-photon ionization that involves a doubly excited state relaxing onto a set of Rydberg states [7].

Acknowledgments

This work was supported by CNRS, le Ministère de la Recherche, Région Midi-Pyrénées through 'Plan état-Région Spectroscopies Optiques Ultimes', ANR COCOMOUV and the British Council Alliance programme. BJW thanks the CNRS and the UPS for his invited positions in the LCAR. KR thanks the CNRS for his postdoc fellowship. GT thanks the European network COCOMO for his postdoc fellowship. IW is grateful to the UK's EPSRC for a research studentship.

References

[1] E.-G. Diau, S. De Feyter, A.H. Zewail, J. Chem. Phys. 110 (1999) 9785.
[2] D.R. Demmer, J.W. Hager, G.W. Leach, S.C. Wallace, Chem. Phys. Lett. 136 (1987) 329.
[3] O.K. Abou-Zied, D.R.M. Demmer, S.C. Wallace, R.P. Steer, Chem. Phys. Lett. 266 (1997) 75.
[4] Y. Hirata, E.C. Lim, J. Chem. Phys. 69 (1978) 3292.
[5] M. Kasha, Discuss. Faraday Soc. 9 (1950).
[6] T. Makinoshima, M. Fujitsuka, M. Sasaki, Y. Araki, O. Ito, S. Ito, N. Morita, J. Phys. Chem. A (2004).
[7] V. Blanchet et al., J. Chem. Phys. 128 (2008) 164318.
[8] G. Cerullo, S. De Silvestri, Rev. Sci. Instrum. 74 (2003) 1.
[9] A. Monmayrant, A. Arbouet, B. Girard, B. Chatel, B.J. Whitaker, A. Barman, D. Kaplan, Appl. Phys. B: Lasers and Optics 81 (2005) 177.
[10] N. Nakashima, S. Shimizu, T. Yatsuhashi, S. Sakabe, Y. Izawa, J. Photochem. Photobiol. C: Photochem. Rev. 1 (2000) 131.
[11] A.T.J.B. Eppink, D.H. Parker, Rev. Sci. Instrum. 68 (1997) 3477.
[12] H.C. Hsu, C.L. Liu, J.J. Lyu, C.K. Ni, J. Chem. Phys. 124 (2006) 134303.
[13] D. Tanaka, S. Sato, K. Kimura, Chem. Phys. 239 (1998) 437.
[14] T. Suzuki, B.J. Whitaker, Int. Rev. Phys. Chem. 3 (2001) 313.
[15] M. Fujii, T. Ebata, N. Mikami, M. Ito, Chem. Phys. 77 (1983) 191.
[16] H.W. Jochims, H. Rasekh, E. Ruhl, H. Baumgartel, S. Leach, Chem. Phys. 168 (1992) 159.
[17] J.S. Baskin, P.M. Felker, A.H. Zewail, J. Chem. Phys. 86 (1987) 2483.
[18] P.M. Felker, A.H. Zewail, J. Chem. Phys. 86 (1987) 2460.
[19] J.S. Baskin, P.M. Felker, A.H. Zewail, J. Chem. Phys. 84 (1986) 4708.
[20] N.A. Borisevich, E.V. Khoroshilov, I.V. Kryukov, P.G. Kryukov, A.V. Sharkov, A.P. Blokhin, G.B. Tolstorozhev, Chem. Phys. Lett. 191 (1992) 225.
[21] J.S. Baskin, A.H. Zewail, J. Phys. Chem. A 105 (2001) 3680.
[22] M. Tsubouchi, B.J. Whitaker, L. Wang, H. Kohguchi, T. Suzuki, Phys. Rev. Lett. 86 (2001) 4500.
[23] P.M. Felker, J. Phys. Chem. A 96 (1992) 7844.
[24] W. Jarzeba, V.V. Matylitsky, C. Riehn, B. Brutschy, Chem. Phys. Lett. 368 (2003) 680.
[25] M. Dantus, Annu. Rev. Phys. Chem. 52 (2001) 639.
[26] C. Riehn, V.V. Matylitsky, M.F. Gelin, B. Brutschy, Mol. Phys. 103 (2005) 1615.
[27] F.J. Lovas, R.D. Suenram, J. Phys. Chem. Ref. Data 18 (1989) 1245.
[28] A.P. Blokhin, M.F. Gelin, E.V. Khoroshilov, I.V. Kryukov, A.V. Sharkov, Opt. Spectrosc. 95 (2003) 346.
[29] W. Gerhartz, J. Michl, J. Am. Chem. Soc. 100 (1978) 6877.
[30] N. Kuthirummal, P.M. Weber, Chem. Phys. Lett. 378 (2003) 647.
[31] N. Kuthirummal, P.M. Weber, J. Mol. Struct. 787 (2006) 163.

References

[1] A. T. J. B. Eppink and D. H. Parker, *Rev. Sci. Instrum.*, 1997, **68**(9), 3477–3484. xvi, 1, 45, 46, 48, 54, 57, 89, 97, 125, 127, 180

[2] J. McFarlane, J. C. Polanyi, and J. G. Shapter, *Journal of Photochemistry and Photobiology A: Chemistry*, 1991, **58**(2), 139–172. xxi, 94, 96, 98

[3] R. Compargue, *Atomic and Molecular Beams: The State of The Art 2000*, Vol. 1, Springer-Verlag, Berlin, 1st ed., 2001. xxi, 94, 96, 97, 98, 102, 106, 107, 125, 138, 139, 143

[4] M. Brouard, R. Cireasa, A. P. Clark, T. J. Preston, and C. Vallance, *J. Chem. Phys.*, 2006, **124**(6), 064309/1–064309/15. xxi, 5, 10, 92, 94, 96, 97, 98, 117, 118, 122

[5] M. Ahmed, D. S. Peterka, A. S. Bracker, O. S. Vasyutinskii, and A. G. Suits, *J. Chem. Phys.*, 1999, **110**(9), 4115–4118. xxi, 5, 10, 95, 96, 98, 102, 117, 120, 121, 125, 218

[6] A. M. Coroiu, D. H. Parker, G. C. Groenenboom, J. Barr, I. T. Novalbos, and B. J. Whitaker, *Eur. Phys. J. D: At. Mol. Opt. Phys.*, 2006, **38**(1), 151–162. xxi, 10, 95, 96, 98, 117, 120, 121, 125, 126, 147, 150, 151, 160, 165, 167, 168, 169, 216, 219

[7] G. Hancock and M. Morrison, *Mol. Phys.*, 2005, **103**(13), 1727–1733. xxi, 5, 10, 93, 96, 97, 98, 120, 125, 126, 131

[8] R. Schinke, S. Y. Grebenshchikov, and H. Zhu, *Chem. Phys.*, 2008, **346**(1-3), 99–114. xxi, 5, 9, 10, 13, 14, 92, 93, 97, 98, 114, 115, 120, 121, 124, 125, 144, 162, 163, 165, 167, 168, 177, 216, 218, 219

[9] J. Luque and D. R. Crosley, LIFBASE: Database and spectral simulation program (version 1.5): SRI international report: MP 99-009, 1999. xxii, 103, 107, 108, 140, 195

[10] M. T. Zanni, T. R. Taylor, B. J. Greenblatt, B. Soep, and D. M. Neumark, *J. Chem. Phys.*, 1997, **107**(19), 7613–7619. 1

[11] A. G. Smolin, O. S. Vasyutinskii, E. R. Wouters, and A. G. Suits, *J. Chem. Phys.*, 2004, **121**(14), 6759–6770. 1

[12] D. Townsend, S. K. Lee, and A. G. Suits, *Chem. Phys.*, 2004, **301**(2-3), 197–208. 1, 100, 129, 148, 157

[13] M. Tsubouchi, B. J. Whitaker, and T. Suzuki, *J. Phys. Chem. A*, 2004, **108**(33), 6823–6835. 1

[14] N. T. Form, B. J. Whitaker, L. Poisson, and B. Soep, *Phys. Chem. Chem. Phys.*, 2006, **8**(25), 2925–2932. 1, 19, 171, 176, 177, 178, 179, 193, 196, 198, 212

[15] A. V. Komissarov, M. P. Minitti, A. G. Suits, and G. E. Hall, *J. Chem. Phys.*, 2006, **124**(1), 014303/1–014303/12. 1, 56, 100, 129, 134, 148, 157

[16] A. D. Webb, N. H. Nahler, R. N. Dixon, and M. N. R. Ashfold, *J. Chem. Phys.*, 2006, **125**(20), 204312. 1

[17] M. Brouard, A. V. Green, F. Quadrini, and C. Vallance, *J. Chem. Phys.*, 2007, **127**(8), 084304. 1

[18] M. Brouard, F. Quadrini, and C. Vallance, *J. Chem. Phys.*, 2007, **127**(8), 084305. 1

[19] A. G. Suits, S. D. Chambreau, and S. A. Lahankar, *Int. Rev. Phys. Chem.*, 2007, **26**(4), 585–607. 1

[20] S. J. Cavanagh, S. T. Gibson, M. N. Gale, C. J. Dedman, E. H. Roberts, and B. R. Lewis, *Phys. Rev. A*, 2007, **76**(5), 052708. 1

[21] R. de Nalda, J. Dura, A. Garcia-Vela, J. G. Izquierdo, J. Gonzalez-Vazquez, and L. Banares, *J. Phys. Chem.*, 2008, **128**(24), 244309. 1

[22] D. M. Neumark, *J. Phys. Chem. A*, 2008, **112**(51), 13287–13301. 1

[23] G. A. Garcia, L. Nahon, C. J. Harding, and I. Powis, *Phys. Chem. Chem. Phys.*, 2008, **10**(12), 1628–1639. 1

[24] P. Hockett, M. Staniforth, K. L. Reid, and D. Townsend, *Phys. Rev. Lett.*, 2009, **102**(25), 253002. 1

[25] J. A. Davies, J. E. LeClaire, R. E. Continetti, and C. C. Hayden, *J. Chem. Phys.*, 1999, **111**(1), 1–4. 1, 19, 171, 173, 193, 198

[26] J. A. Davies, R. E. Continetti, D. W. Chandler, and C. C. Hayden, *Phys. Rev. Lett.*, 2000, **84**(26), 5983–5986. 1, 171, 173, 177, 193, 198

[27] O. Gessner, A. M. D. Lee, J. P. Shaffer, H. Reisler, S. V. Levchenko, A. I. Krylov, J. G. Underwood, H. Shi, A. L. L. East, D. M. Wardlaw, E. T. H. Chrysostom, C. C. Hayden, and A. Stolow, *Science*, 2006, **311**(5758), 219–222. 1

[28] A. Vredenborg, W. G. Roeterdink, and M. H. M. Janssen, *J. Chem. Phys.*, 2008, **128**(20), 204311. 1, 5, 19, 35, 171, 177, 180, 193, 196, 198, 212

[29] A. G. Suits, L. S. Bontuyan, P. L. Houston, and B. J. Whitaker, *J. Chem. Phys.*, 1992, **96**(11), 8618–8620. 1, 52

[30] L. S. Bontuyan, A. G. Suits, P. L. Houston, and B. J. Whitaker, 05 , 1993, **97**(24), 6342–6350. 1, 52

[31] N. Yonekura, C. Gebauer, H. Kohguchi, and T. Suzuki, *Rev. Sci. Instrum.*, 1999, **70**(8), 3265–3270. 1, 52, 57

[32] K. T. Lorenz, M. S., and D. W. Chandler, *Phys. Chem. Chem. Phys.*, 2000, **2**(4), 481–494. 1, 52

[33] M. S. Westley, K. T. Lorenz, D. W. Chandler, and P. L. Houston, *J. Chem. Phys.*, 2001, **114**(6), 2669–2680. 1, 52

[34] H. Kohguchi, T. Suzuki, and M. H. Alexander, *Science*, 2001, **294**(5543), 832–834. 1

[35] T. N. Kitsopoulos, M. A. Buntine, D. P. Baldwin, R. N. Zare, and D. W. Chandler, *Science*, 1993, **260**(5114), 1605–1610. 1

[36] J. J. Lin, J. Zhou, W. Shiu, and K. Liu, *Rev. Sci. Instrum.*, 2003, **74**(4), 2495–2500. 1, 2, 55, 127

[37] J. Mikosch, U. Fruhling, S. Trippel, D. Schwalm, M. Weidemuller, and R. Wester, *Phys. Chem. Chem. Phys.*, 2006, **8**(25), 2990–2999. 1

[38] H. Kawamata, S. Tauro, and K. Liu, *Phys. Chem. Chem. Phys.*, 2008, **10**(30), 4378–4382. 1

[39] B. J. Sussman, D. Townsend, M. Y. Ivanov, and A. Stolow, *Science*, 2006, **314**(5797), 278–281. 1, 174

[40] M. Wollenhaupt, M. Krug, J. Köhler, T. Bayer, C. Sarpe-Tudoran, and T. Baumert, 06 , 2009, **95**(4), 647–651. 1, 52, 127

[41] M. Wollenhaupt, M. Krug, J. Köhler, T. Bayer, C. Sarpe-Tudoran, and T. Baumert, 05 , 2009, **95**(2), 245–259. 1

[42] I. Znakovskaya, P. von den Hoff, S. Zherebtsov, A. Wirth, O. Herrwerth, M. J. J. Vrakking, R. de Vivie-Riedle, and M. F. Kling, *Phys. Rev. Lett.*, 2009, **103**(10), 103002. 1

[43] J. R. R. Verlet, A. Kammrath, G. B. Griffin, and D. M. Neumark, *J. Chem. Phys.*, 2005, **123**(23), 231102. 2

[44] A. Kammrath, J. R. R. Verlet, A. E. Bragg, G. B. Griffin, and D. M. Neumark, *J. Phys. Chem. A*, 2005, **109**(50), 11475–11483. 2

[45] A. Kammrath, J. R. R. Verlet, G. B. Griffin, and D. M. Neumark, *J. Chem. Phys.*, 2006, **125**(7), 076101. 2

[46] A. Kammrath, J. R. R. Verlet, G. B. Griffin, and D. M. Neumark, *J. Chem. Phys.*, 2006, **125**(17), 171102. 2

[47] A. Kammrath, G. B. Griffin, J. R. R. Verlet, R. M. Young, and D. M. Neumark, *J. Chem. Phys.*, 2007, **126**(24), 244306. 2

[48] L. Poisson, E. Gloaguen, J.-M. Mestdagh, B. Soep, A. Gonzalez, and M. Chergui, *J. Phys. Chem. A*, 2008, **112**(39), 9200–9210. 2

[49] S. P. K. Koehler, Y. Ji, D. J. Auerbach, and A. M. Wodtke, *Phys. Chem. Chem. Phys.*, 2009, **11**(35), 7540–7544. 2

[50] D. Townsend, M. P. Minitti, and A. G. Suits, *Rev. Sci. Instrum.*, 2003, **74**(4), 2530–2539. 2, 54, 55, 62, 97, 127, 148, 160, 180

[51] W. C. Gardiner Jnr., *Gas-Phase Combustion Chemistry*, Vol. 1, Springer, 2nd ed., 1999. 5

[52] B. J. Finlayson-Pitts and J. N. Pitts, *Chemistry of the Upper and Lower Atmosphere: Theory, Experiments, and Applications*, Vol. 1, Academic Press, 1st ed., 1999. 5

[53] G. E. Busch and K. R. Wilson, *J. Chem. Phys.*, 1972, **56**(7), 3638–54. 5, 91

[54] G. E. Busch and K. R. Wilson, *J. Chem. Phys.*, 1972, **56**(7), 3626–38. 5, 7, 91

[55] R. Jost, J. Nygard, A. Pasinski, and A. Delon, *J. Chem. Phys.*, 1996, **105**(3), 1287–1290. 5, 9, 14, 17, 18, 19, 30, 34, 91, 92, 124

[56] S. A. Reid, D. C. Robie, and H. Reisler, *J. Chem. Phys.*, 1994, **100**(6), 4256–4271. 5, 9, 160

[57] A. Sanov, C. R. Bieler, and H. Reisler, *J. Phys. Chem.*, 1995, **99**(37), 13637–46. 5

[58] S. J. Matthews, S. Willitsch, and T. P. Softley, *Phys. Chem. Chem. Phys.*, 2007, **9**(42), 5656–5663. 5, 9, 172

[59] I. Bezel, P. Ionov, and C. Wittig, *J. Chem. Phys.*, 1999, **111**(20), 9267–9279. 5, 9, 171, 172

[60] I. Bezel, D. Stolyarov, and C. Wittig, *J. Phys. Chem. A*, 1999, **103**(49), 10268–10273. 5, 9, 171, 172

[61] S. I. Ionov, G. A. Brucker, C. Jaques, Y. Chen, and C. Wittig, *J. Chem. Phys.*, 1993, **99**(5), 3420–35. 5, 9, 171, 172

[62] B. Abel, B. Kirmse, J. Troe, and D. Schwarzer, *J. Chem. Phys.*, 2001, **115**(14), 6522–6530. 5, 171, 172

[63] B. Abel, N. Lange, and J. Troe, *J. Chem. Phys.*, 2001, **115**(14), 6531–6537. 5, 171, 172

[64] I. Wilkinson and B. J. Whitaker, *J. Chem. Phys.*, 2008, **129**(15), 154312/1–154312/15. 5, 10, 124, 138, 139, 167, 169, 216

[65] I. Wilkinson, M. P. de Miranda, and B. J. Whitaker, *J. Chem. Phys.*, 2009, **131**(5), 054308. 5, 10, 110, 216, 259

[66] D. Toffoli, R. R. Lucchese, M. Lebech, J. C. Houver, and D. Dowek, *J. Chem. Phys.*, 2007, **126**(5), 054307. 5

[67] L. Bigio and E. R. Grant, *J. Chem. Phys.*, 1987, **87**(1), 360–369. 5, 10, 11, 193, 210, 213, 218

[68] L. Bigio and E. R. Grant, *J. Chem. Phys.*, 1987, **87**(10), 5589–5597. 5, 10, 13, 193, 210, 213, 218

[69] R. J. S. Morrison and E. R. Grant, *J. Chem. Phys.*, 1982, **77**(12), 5994–6004. 5, 10, 11, 193, 210, 213, 218

[70] R. J. S. Morrison, B. H. Rockney, and E. R. Grant, *J. Chem. Phys.*, 1981, **75**(6), 2643–2651. 5, 10, 193, 210, 213, 218

[71] G. K. Jarvis, Y. Song, C. Y. Ng, and E. R. Grant, *J. Chem. Phys.*, 1999, **111**(21), 9568–9573. 5, 23, 24, 25, 26, 29, 30, 31, 32, 33

[72] R. S. Mulliken, *Rev. Mod. Phys.*, 1942, **14**(2-3), 204. 5, 92

[73] A. D. Walsh, *J. Chem. Soc.*, 1953, pp. 2266–2288. 5, 16, 92

[74] M. W. Schmidt, K. K. Baldridge, J. A. Boatz, E. S. T., M. S. Gordon, J. H. Jensen, S. Koseki, N. Matsunaga, K. A. Nguyen, S. Su, T. L. Windus, M. Dupuis, and J. A. Montgomery Jr., *J. Comp. Chem.*, 1993, **14**(11), 1347–1363. 6, 27

[75] G. Herzberg, *Molecular Spectra and Molecular Structure Volume III - Electronic Spectra and Electronic Structure of Polyatomic Molecules*, Krieger, Malabar, Florida, 2nd ed., 1991. 7, 9, 13, 15

[76] A. C. Vandaele, C. Hermans, P. C. Simon, M. Carleer, R. Colin, S. Fally, M. F. Merienne, A. Jenouvrier, and B. Coquart, *J. Quant. Spectros. Radiat. Transfer*, 1998, **59**(3-5), 171–184. 7, 9, 91, 92

[77] J. W. Au and C. E. Brion, *Chem. Phys.*, 1997, **218**(1,2), 109–126. 7, 9, 13, 14, 16, 17, 20, 21, 22, 23, 24, 26, 29, 30, 33, 34, 91, 92

[78] R. A. Gangi and L. Burnelle, *J. Chem. Phys.*, 1971, **55**(2), 843–850. 7, 9

[79] C. G. Stevens and R. N. Zare, *J. Mol. Spectrosc.*, 1975, **56**(2), 167 – 187. 7, 15

[80] C. Stevens, M. Swagel, R. Wallace, and R. Zare, *Chem. Phys. Lett.*, 1973, **18**(4), 465 – 469. 7

[81] C. F. Jackels and E. R. Davidson, *J. Chem. Phys.*, 1976, **64**(7), 2908–17. 7

[82] M. Sanrey and M. Joyeux, *J. Chem. Phys.*, 2006, **125**(1), 014304/1–014304/8. 7, 9

[83] Y. Arasaki and K. Takatsuka, *Chem. Phys.*, 2007, **338**(2-3), 175 – 185. 7, 9, 177, 179

[84] A. Delon, R. Jost, and M. Lombardi, *J. Chem. Phys.*, 1991, **95**(8), 5701–5718. 7, 15

[85] A. Delon and R. Jost, *J. Chem. Phys.*, 1999, **110**(9), 4300–4308. 7, 193

[86] V. Kurkal, P. Fleurat-Lessard, and R. Schinke, *J. Chem. Phys.*, 2003, **119**(3), 1489–1501. 7

[87] E. Leonardi and C. Petrongolo, *J. Chem. Phys.*, 1997, **106**(24), 10066–10071. 7

[88] K. Aoki, K.-n. Hoshina, and K. Shibuya, *J. Chem. Phys.*, 1996, **105**(6), 2228–2235. 9, 15

[89] K. Shibuya, C. Terauchi, M. Sugawara, K. Aoki, K. Tsuji, and S. Tsuchiya, *J. Mol. Struct.*, 1997, **413-414**, 501 – 509. 9, 15

[90] K. P. Huber and G. Herzberg, *Molecular Spectra and Molecular Structure IV. Constants of Diatomic Molecules*, Vol. 4, Van Nostrand Reinhold Company Inc., New York, 1st ed., 1979. 9, 17, 18, 19, 30, 34, 88, 107, 108, 109, 125

[91] Y. Ralchenko, A. E. Kramida, J. Reader, and N. A. Team, *NIST Atomic Spectra Database (version 3.1.5)*, National Institute of Standards and Technology, September 2009. 9, 17, 18, 34, 88, 92, 124

[92] S. J. Klippenstein and T. Radivoyevitch, *J. Chem. Phys.*, 1993, **99**(5), 3644–53. 9, 172

[93] O. L. A. Monti, H. Dickinson, S. R. Mackenzie, and T. P. Softley, *J. Chem. Phys.*, 2000, **112**(8), 3699–3709. 9, 172

[94] A. V. Demyanenko, V. Dribinski, H. Reisler, H. Meyer, and C. X. W. Qian, *J. Chem. Phys.*, 1999, **111**(16), 7383–7396. 9, 160, 162, 163, 166

[95] S. A. Reid, A. Sanov, and H. Reisler, *Faraday Disc.*, 1995, **102**, 129 – 146. 9

[96] S. A. Reid and H. Reisler, *J. Phys. Chem.*, 1996, **100**(2), 474–87. 9, 160

[97] T. Nakayama, M. Y. Kitamura, and K. Watanabe, *J. Chem. Phys.*, 1959, **30**(5), 1180–1186. 9, 13, 14, 17, 20, 23, 24, 26, 30, 92

[98] K. Tsuji, M. Ikeda, J. Awamura, A. Kawai, and K. Shibuya, *Chem. Phys. Lett.*, 2003, **374**(5,6), 601–607. 10, 13, 92, 93, 115, 124, 125, 158

[99] W. M. Uselman and E. K. C. Lee, *J. Chem. Phys.*, 1976, **65**(5), 1948–55. 10, 13, 15, 92, 93, 124, 125, 131

[100] K. F. Preston and R. J. Cvetanovic, *J. Chem. Phys.*, 1966, **45**(8), 2888–93. 10, 93, 125, 131

[101] F. Sun, G. P. Glass, and R. F. Curl, *Chem. Phys. Lett.*, 2001, **337**(1,2,3), 72–78. 10, 93, 125, 131

[102] K. Tsukiyama, K. Shibuya, K. Obi, and I. Tanaka, *J. Chem. Phys.*, 1985, **82**(3), 1147–1152. 10

[103] L. Bigio, R. S. Tapper, and E. R. Grant, *J. Phys. Chem.*, 1984, **88**(7), 1271–3. 11, 16, 102, 110, 125, 126, 130, 169, 215

[104] S. Katsumata, H. Shiromaru, K. Mitani, S. Iwata, and K. Kimura, *Chem. Phys.*, 1982, **69**(3), 423 – 431. 13, 26

[105] C. F. Jackels and E. R. Davidson, *J. Chem. Phys.*, 1976, **65**(8), 2941–2957. 13, 92, 125

[106] O. Edqvist, E. Lindholm, L. E. Selin, L. Asbrink, C. E. Kuyatt, S. R. Mielczarek, J. A. Simpson, and I. Fischer-Hjalmars, *Phys. Scr.*, 1970, **1**(4), 172–178. 13, 16, 20, 21, 22, 23, 24, 26, 29, 31

[107] Y. Morioka, H. Masuko, M. Nakamura, E. Ishiguro, and M. Sasanuma, *J. Phys. B: At. Mol. Phys.*, 1976, **9**(13), 2321–2330. 13, 20, 21, 22, 23, 29

[108] K. L. McEwen, *J. Chem. Phys.*, 1960, **32**(6), 1801–1814. 14

[109] R. Schinke, *J. Chem. Phys.*, 2008, **129**(12), 124303. 14, 15

[110] M. R. Taherian, P. C. Cosby, and T. G. Slanger, *J. Phys. Chem.*, 1987, **91**(9), 2304–9. 14, 125, 196, 201, 208, 211

[111] G. Herzberg, *Molecular Spectra and Molecular Structure Volume I - Spectra of Diatomic Molecules*, Krieger, Malabar, Florida, 2nd ed., 1989. 14, 141, 205

[112] R. Jost, M. Joyeux, and M. Jacon, *Chem. Phys.*, 2002, **283**(1-2), 17–28. 15

[113] J. Hardwick and J. Brand, *Chem. Phys. Lett.*, 1973, **21**(3), 458 – 461. 15

[114] K. E. J. Hallin and A. J. Merer, *Can. J. Phys.*, 1976, **54**(11), 1157–71. 15, 124, 162, 168

[115] J. B. Coon, F. A. Cesani, and F. P. Huberman, *J. Chem. Phys.*, 1970, **52**(4), 1647–1654. 15

[116] W. C. Bowman and F. C. D. Lucia, *J. Chem. Phys.*, 1982, **77**(1), 92–107. 15

[117] K. S. Haber, J. W. Zwanziger, F. X. Campos, R. T. Wiedmann, and E. R. Grant, *Chem. Phys. Lett.*, 1988, **144**(1), 58 – 64. 16, 23

[118] R. S. Tapper, R. L. Whetten, G. S. Ezra, and E. R. Grant, *J. Phys. Chem.*, 1984, **88**(7), 1273–1275. 16, 20, 194

[119] H. Matsui, J. M. Behm, and E. R. Grant, *Int. J. Mass Spectrom. Ion Proc.*, 1996, **159**(1-3), 37 – 48. 16, 20, 194

[120] M. B. Knickelbein, K. S. Haber, L. Bigio, and E. R. Grant, *Chem. Phys. Lett.*, 1986, **131**(1-2), 51 – 55. 16

[121] ed. P. Linstrom and W. Mallard, *NIST Chemistry WebBook, NIST Standard Reference Database Number 69*, National Institute of Standards and Technology, September 2009. 17, 18, 34

[122] I. D. Petsalakis, G. Theodorakopoulos, and M. S. Child, *J. Chem. Phys.*, 2001, **115**(22), 10394–10403. 17, 194

[123] K. H. Welge, *J. Chem. Phys.*, 1966, **45**(4), 1113–17. 19, 198

[124] R. B. Lopez-Martens, T. W. Schmidt, and G. Roberts, *J. Chem. Phys.*, 1999, **111**(16), 7183–7186. 19, 171, 173, 175, 179, 193, 198

[125] T. W. Schmidt, R. B. Lopez-Martens, and G. Roberts, *J. Chem. Phys.*, 2004, **121**(9), 4133–4142. 19, 171, 173, 193, 198

[126] A. T. J. B. Eppink, B. J. Whitaker, E. Gloaguen, B. Soep, A. M. Coroiu, and D. H. Parker, *J. Chem. Phys.*, 2004, **121**(16), 7776–7783. 19, 117, 171, 175, 176, 177, 178, 179, 193, 196, 198, 212

[127] P. Baltzer, L. Karlsson, B. Wannberg, D. M. P. Holland, M. A. MacDonald, M. A. Hayes, and J. H. D. Eland, *Chem. Phys.*, 1998, **237**(3), 451 – 470. 20, 23, 24, 25, 26, 27, 29, 30, 31, 32, 33

[128] W. C. Price, D. M. Simpson, and R. G. W. Norrish, *Trans. Farad. Soc.*, 1941, **37**, 106 – 113. 20, 24, 26

[129] Y. Tanaka and A. S. Jursa, *J. Chem. Phys.*, 1962, **36**(9), 2493–2497. 20, 21, 24, 26, 29

[130] D. E. Clemmer and P. B. Armentrout, *J. Chem. Phys.*, 1992, **97**(4), 2451–2458. 23

[131] F. X. Campos, Y. Jiang, and E. R. Grant, *J. Chem. Phys.*, 1990, **93**(4), 2308–2327. 23, 197

[132] F. X. Campos, Y. Jiang, and E. R. Grant, *J. Chem. Phys.*, 1990, **93**(11), 7731–7739. 23, 197

[133] F. X. Campos, Y. Jiang, and E. R. Grant, *J. Chem. Phys.*, 1991, **94**(9), 5897–5906. 23, 197

[134] G. P. Bryant, Y. Jiang, and E. R. Grant, *J. Chem. Phys.*, 1992, **96**(7), 4827–4840. 23, 197

[135] G. P. Bryant, Y. Jiang, M. Martin, and E. R. Grant, *J. Chem. Phys.*, 1994, **101**(9), 7199–7210. 23, 197

[136] H. Matsui and E. R. Grant, *J. Chem. Phys.*, 1996, **104**(1), 42–47. 23, 197

[137] H. Matsui, E. E. Mayer, and E. R. Grant, *J. Mol. Spectrosc.*, 1996, **175**(1), 203 – 214. 23, 197

[138] H. Matsui, J. M. Behm, and E. R. Grant, *J. Phys. Chem. A*, 1997, **101**(36), 6717–6722. 23, 197

[139] P. Bell, F. Aguirre, E. R. Grant, and S. T. Pratt, *J. Phys. Chem. A*, 2004, **108**(45), 9645–9651. 23, 197

[140] C. R. Brundle, D. Neumann, W. C. Price, D. Evans, A. W. Potts, and D. G. Streets, *J. Chem. Phys.*, 1970, **53**(2), 705–715. 24, 26, 29, 31, 33

[141] J. Schirmer, L. S. Cederbaum, and W. V. Niessen, *Chem. Phys.*, 1981, **56**(3), 285 – 302. 25, 32

[142] D. M. Hirst, *J. Chem. Phys.*, 2001, **115**(20), 9320–9330. 25, 27, 30, 31, 32, 177, 179, 197

[143] J. H. D. Eland and L. Karlsson, *Chem. Phys.*, 1998, **237**(1-2), 139 – 148. 30, 31, 32, 33, 34, 194

[144] C. Blondel, W. Chaibi, C. Delsart, C. Drag, F. Goldfarb, and S. Kröger, *Eur. Phys. J. D*, 2005, **33**(3), 335–342. 30

[145] K. Shibuya, S. Suzuki, T. Imamura, and I. Koyano, *J. Phys. Chem. A*, 1997, **101**(4), 685–689. 34

[146] D. Strickland and G. Mourou, *Opt. Comm.*, 1985, **56**(3), 219 – 221. 40

[147] K. Tamura, H. Haus, and E. Ippen, *Electronics Lett.*, 1992, **28**(24), 2226–2228. 41

[148] T. Wilhelm, J. Piel, and E. Riedle, *Opt. Lett.*, 1997, **22**(19), 1494–1496. 41

[149] E. Riedle, M. Beutter, S. Lochbrunner, J. Piel, S. Schenkl, S. Spörlein, and W. Zinth, *Appl. Phys. B*, 2000, **71**(3), 457–465. 41

[150] D. P. de Bruijn and J. Los, *Rev. Sci. Instrum.*, 1982, **53**(7), 1020–1026. 42

[151] D. W. Chandler and P. L. Houston, *J. Chem. Phys.*, 1987, **87**(2), 1445–7. 44

[152] H. Helm, N. Bjerre, M. J. Dyer, D. L. Huestis, and M. Saeed, *Phys. Rev. Lett.*, 1993, **70**(21), 3221–3224. 44, 76

[153] T. Bergmann, T. P. Martin, and H. Schaber, *Rev. Sci. Instrum.*, 1989, **60**(3), 347–349. 44

[154] W. C. Wiley and I. H. McLaren, *Rev. Sci. Instrum.*, 1955, **26**(12), 1150–1157. 44, 49

[155] D. W. Chandler, J. W. T. Jr., M. H. Janssen, and D. H. Parker, *Chem. Phys. Lett.*, 1989, **156**(2-3), 151 – 158. 45

[156] D. P. Baldwin, M. A. Buntine, and D. W. Chandler, *J. Chem. Phys.*, 1990, **93**(9), 6578–6584. 45

[157] M. A. Buntine, D. P. Baldwin, and D. W. Chandler, *J. Chem. Phys.*, 1992, **96**(8), 5843–5856. 45

[158] V. P. Hradil, T. Suzuki, S. A. Hewitt, P. L. Houston, and B. J. Whitaker, *J. Chem. Phys.*, 1993, **99**(6), 4455–63. 45, 160

[159] A. G. Suits, R. L. Miller, L. S. Bontuyan, and P. L. Houston, *J. Chem. Soc., Faraday Trans.*, 1993, **89**(10), 1443–1447. 45, 127, 147

[160] J. W. G. Mastenbroek, C. A. Taatjes, K. Nauta, M. H. M. Janssen, and S. Stolte, *J. Phys. Chem.*, 1995, **99**(13), 4360–4363. 45

[161] Y. Sato, Y. Matsumi, M. Kawasaki, K. Tsukiyama, and R. Bersohn, *J. Phys. Chem.*, 1995, **99**(44), 16307–16314. 45

[162] H. Katayanagi, Y. Mo, and T. Suzuki, *Chem. Phys. Lett.*, 1995, **247**(4-6), 571 – 576. 45

[163] L. J. Rogers, M. N. R. Ashfold, Y. Matsumi, M. Kawasaki, and B. J. Whitaker, *J. Chem. Soc. Farad. Trans.*, 1992, **92**(24), 5181–5183. 45

[164] L. J. Rogers, M. N. R. Ashfold, Y. Matsumi, M. Kawasaki, and B. J. Whitaker, *Chem. Phys. Lett.*, 1996, **258**(1-2), 159 – 163. 45

[165] T. Shibata and T. Suzuki, *Chem. Phys. Lett.*, 1996, **262**(1-2), 115 – 119. 45

[166] B. D. Leskiw, M. H. Kim, G. E. Hall, and A. G. Suits, *Rev. Sci. Instrum.*, 2005, **76**(10), 104101. 48

[167] L. M. Smith, D. R. Keefer, and S. I. Sudharsanan, *J. Quant. Spectrosc. Radiat. Transfer*, 1988, **39**(5), 367 – 373. 49, 87, 99, 129, 182

[168] C. J. Dasch, *Appl. Opt.*, 1992, **31**(8), 1146–1152. 49, 99, 129, 182

[169] C. Bordas, F. Paulig, H. Helm, and D. L. Huestis, *Rev. Sci. Instrum.*, 1996, **67**(6), 2257–2268. 49

[170] J. Winterhalter, D. Maier, J. Honerkamp, V. Schyja, and H. Helm, *J. Chem. Phys.*, 1999, **110**(23), 11187–11196. 49, 52

[171] S. Manzhos and H.-P. Loock, *Comput. Phys. Commun.*, 2003, **154**(1), 76 – 87. 49

[172] G. A. Garcia, L. Nahon, and I. Powis, *Rev. Sci. Instrum.*, 2004, **75**(11), 4989–4996. 49, 50, 52

[173] M. J. J. Vrakking, *Rev. Sci. Instrum.*, 2001, **72**(11), 4084–4089. 49

[174] V. Dribinski, A. Ossadtchi, V. A. Mandelshtam, and H. Reisler, *Rev. Sci. Instrum.*, 2002, **73**(7), 2634–2642. 50

[175] ed. B. J. Whitaker, *Imaging in Molecular Dynamics: Technology and Applications*, Cambridge University Press, 2003. 50, 91, 99, 129, 182, 221

[176] K. Zhao, T. Colvin, W. T. H. III, and G. Zhang, *Rev. Sci. Instrum.*, 2002, **73**(8), 3044–3050. 50

[177] G. M. Roberts, J. L. Nixon, J. Lecointre, E. Wrede, and J. R. R. Verlet, *Rev. Sci. Instrum.*, 2009, **80**(5), 053104. 50

[178] F. Renth, J. Riedel, and F. Temps, *Rev.Sci. Instrum.*, 2006, **77**(3), 033103. 50

[179] V. K. Nestorov and J. I. Cline, *J. Chem. Phys.*, 1999, **111**(12), 5287–5290. 52, 127, 147

[180] V. K. Nestorov, R. D. Hinchliffe, R. Uberna, J. I. Cline, K. T. Lorenz, and D. W. Chandler, *J. Chem. Phys.*, 2001, **115**(17), 7881–7891. 52, 127, 147

[181] A. S. Bracker, E. R. Wouters, A. G. Suits, and O. S. Vasyutinskii, *J. Chem. Phys.*, 1999, **110**(14), 6749–6765. 52, 147, 219

[182] Y. Mo, H. Katayanagi, and T. Suzuki, *J. Chem. Phys.*, 1999, **110**(4), 2029–2041. 52, 127, 147

[183] M. J. Bass, M. Brouard, A. P. Clark, and C. Vallance, *J. Chem. Phys.*, 2002, **117**(19), 8723–8735. 52, 127, 147

[184] D. A. Chestakov, S.-M. Wu, G. Wu, D. H. Parker, A. T. J. B. Eppink, and T. N. Kitsopoulos, *J. Phys. Chem. A*, 2004, **108**(39), 8100–8105. 53, 54

[185] W. Li, S. D. Chambreau, S. A. Lahankar, and A. G. Suits, *Rev.Sci. Instrum.*, 2005, **76**(6), 063106. 53, 55

[186] M. L. Lipciuc, J. B. Buijs, and M. H. M. Janssen, *Phys. Chem. Chem. Phys.*, 2006, **8**(2), 219–223. 53

[187] K. Tonokura and T. Suzuki, *Chem. Phys. Lett.*, 1994, **224**(1-2), 1–6. 53, 127

[188] C. R. Gebhardt, T. P. Rakitzis, P. C. Samartzis, V. Ladopoulos, and T. N. Kitsopoulos, *Rev. Sci. Instrum.*, 2001, **72**(10), 3848–3853. 54, 100, 127, 129, 157

[189] H. A. Cruse and T. P. Softley, *J. Chem. Phys.*, 2004, **121**(9), 4089–4096. 54

[190] E. Wrede, S. Laubach, S. Schulenburg, A. Brown, E. R. Wouters, A. J. Orr-Ewing, and M. N. R. Ashfold, *J. Chem. Phys.*, 2001, **114**(6), 2629–2646. 57

[191] B.-Y. Chang, R. C. Hoetzlein, J. A. Mueller, J. D. Geiser, and P. L. Houston, *Rev. Sci. Instrum.*, 1998, **69**(4), 1665–1670. 84

[192] B. Buijsse, W. J. van der Zande, A. T. J. B. Eppink, D. H. Parker, B. R. Lewis, and S. T. Gibson, *J. Chem. Phys.*, 1998, **108**(17), 7229–7243. 88, 118, 182

[193] M. J. Cooper, E. Wrede, A. J. Orr-Ewing, and M. N. R. Ashfold, *J. Chem. Soc., Faraday Trans.*, 1998, **94**, 2901–2907. 88, 182

[194] G. Reiser, W. Habenicht, K. Mller-Dethlefs, and E. W. Schlag, *Chem. Phys. Lett.*, 1988, **152**(2-3), 119 – 123. 88

[195] M. Sander, L. A. Chewter, K. Müller-Dethlefs, and E. W. Schlag, *Phys. Rev. A*, 1987, **36**(9), 4543–4546. 88

[196] W. Schneider, G. K. Moortgat, G. S. Tyndall, and J. P. Burrows, *J. Photochem. Photobiol. A*, 1987, **40**(2-3), 195–217. 91

[197] M. F. Merienne, A. Jenouvrier, B. Coquart, and J. P. Lux, *J. Atmos. Chem.*, 1997, **27**(3), 219–232. 91

[198] J. T. C. Hall and F. E. Blacet, *J. Chem. Phys.*, 1952, **20**(11), 1745–1749. 92

[199] G. Inoue, Y. Nakata, Y. Usui, H. Akimoto, and M. Okuda, *J. Chem. Phys.*, 1979, **70**(8), 3689–3693. 92

[200] J. A. Mueller, M. L. Morton, S. L. Curry, J. P. D. Abbatt, and L. J. Butler, *J. Phys. Chem. A*, 2000, **104**(21), 4825–4832. 92, 94

[201] L. Harris and G. W. King, *J. Chem. Phys.*, 1940, **8**, 775–84. 92

[202] R. K. Ritchie and A. D. Walsh, *Proc. Roy. Soc. (London) Ser. A*, 1962, **267**, 395–407. 92

[203] H. G. Rubahn, W. J. Van der Zande, R. Zhang, M. J. Bronikowski, and R. N. Zare, *Chem. Phys. Lett.*, 1991, **186**(2-3), 154–60. 93, 105, 118, 121, 122

[204] J. Miyawaki, K. Yamanouchi, and S. Tsuchiya, *J. Chem. Phys.*, 1993, **99**(1), 254–64. 93, 172

[205] C. B. McKendrick, C. Fotakis, and R. J. Donovan, *J. Photochem.*, 1982, **20**(2), 175–8. 93, 96, 124

[206] T. G. Slanger, W. K. Bischel, and M. J. Dyer, *J. Chem. Phys.*, 1983, **79**(5), 2231–40. 93, 96, 124

[207] C. Morrell, C. Breheny, V. Haverd, A. Cawley, and G. Hancock, *J. Chem. Phys.*, 2002, **117**(24), 11121–11130. 94, 96

[208] B. F. Parsons, S. L. Curry, J. A. Mueller, P. C. Ray, and L. J. Butler, *J. Chem. Phys.*, 1999, **111**(18), 8486–8495. 94

[209] M. Kawasaki, H. Sato, A. Fukuroda, T. Kikuchi, S. Kobayashi, and T. Arikawa, *J. Chem. Phys.*, 1987, **86**(8), 4431–7. 94

[210] W. N. Sisk, C. E. Miller, and H. S. Johnston, *J. Phys. Chem.*, 1993, **97**(39), 9916–23. 94

[211] R. C. Richter, V. I. Khamaganov, and A. J. Hynes, *Chem. Phys. Lett.*, 2000, **319**(3,4), 341–348. 95, 125, 126

[212] S. K. Lee, R. Silva, S. Thamanna, O. S. Vasyutinskii, and A. G. Suits, *J. Chem. Phys.*, 2006, **125**(14), 144318/1–144318/12. 100, 129, 148, 162

[213] T. P. Rakitzis and T. N. Kitsopoulos, *J. Chem. Phys.*, 2002, **116**(21), 9228–9231. 100, 129, 148

[214] T. P. Rakitzis, P. C. Samartzis, and T. N. Kitsopoulos, *Phys. Rev. Lett.*, 2001, **87**(12), 123001/1–123001/4. 100, 127, 129, 148

[215] T. P. Rakitzis, P. C. Samartzis, R. L. Toomes, and T. N. Kitsopoulos, *J. Chem. Phys.*, 2004, **121**(15), 7222–7227. 100, 129, 148

[216] H. S. Im and E. R. Bernstein, *J. Phys. Chem. A*, 2002, **106**(33), 7565–7572. 100, 102, 107, 110, 111, 113, 125, 130

[217] C. Amiot, *J. Mol. Spectrosc.*, 1982, **94**(1), 150–72. 107

[218] H. Zacharias, F. de Rougemont, T. F. Heinz, and M. M. T. Loy, *J. Chem. Phys.*, 1996, **105**(1), 111–117. 108, 198

[219] R. N. Zare, *Angular Momentum, understanding spatial aspects in chemistry and physics*, Vol. 1, John Wiley & Sons, Inc., New York, 1st ed., 1988. 114, 262

[220] N. N. Greenwood and A. Earnshaw, *Chemistry of the Elements*, Vol. 1, Butterworth-Heinemann, 3rd ed., 1995. 118

[221] B. L. G. Bakker, A. T. J. B. Eppink, D. H. Parker, M. L. Costen, G. Hancock, and G. A. D. Ritchie, *Chem. Phys. Lett.*, 1998, **283**(5,6), 319–325. 118

[222] J. Miyawaki, T. Tsuchizawa, K. Yamanouchi, and S. Tsuchiya, *Chem. Phys. Lett.*, 1990, **165**(2-3), 168–70. 121, 122

[223] N. Shafer, K. Tonokura, Y. Matsumi, S. Tasaki, and M. Kawasaki, *J. Chem. Phys.*, 1991, **95**(9), 6218–23. 125, 126

[224] B. V. Picheyev, A. G. Smolin, and O. S. Vasyutinskii, *J. Phys. Chem. A*, 1997, **101**(41), 7614–7626. 126

[225] R. N. Dixon and H. Rieley, *Chem. Phys.*, 1989, **137**(1-2-3), 307–21. 126

[226] Y. Wang, H.-P. Loock, J. Cao, and C. X. W. Qian, *J. Chem. Phys.*, 1995, **102**(2), 808–14. 126

[227] T. P. Rakitzis, S. A. Kandel, and R. N. Zare, *J. Chem. Phys.*, 1998, **108**(20), 8291–8294. 126

[228] T. Suzuki, H. Katayanagi, Y. Mo, and K. Tonokura, *Chem. Phys. Lett.*, 1996, **256**(1,2), 90–95. 126

[229] Y. Mo, H. Katayanagi, M. C. Heaven, and S. Toshinori, *Phys. Rev. Lett.*, 1996, **77**(5), 830–833. 126, 147, 150, 151

[230] A. T. J. B. Eppink, D. H. Parker, M. H. M. Janssen, B. Buijsse, and W. J. van der Zande, *J. Chem. Phys.*, 1998, **108**(4), 1305–1308. 126

[231] P. T. Rakitzis, *Chem. Phys. Lett.*, 2001, **342**(1,2), 121–126. 127, 147

[232] D. M. Sonnenfroh and K. Liu, *Chem. Phys. Lett.*, 1991, **176**(2), 183–190. 145

[233] L. D. A. Siebbeles, M. Glass-Maujean, O. S. Vasyutinskii, J. A. Beswick, and O. Roncero, *J. Chem. Phys.*, 1994, **100**(5), 3610–23. 147

[234] T. P. Rakitzis and R. N. Zare, *J. Chem. Phys.*, 1999, **110**(7), 3341–3350. 147

[235] R. N. Zare, *Mol. Photochem.*, 1972, **4**(1), 1–37. 150, 161

[236] D. A. Varshalovich, A. N. Moskalev, and V. K. Khersonskii, *Quantum Theory of Angular Momentum*, Vol. 1, World Scientific, Singapore, 1st ed., 1988. 150, 260, 262, 263, 264, 265, 266, 268, 270, 271, 272

[237] Y. Mo and T. Suzuki, *J. Chem. Phys.*, 1998, **109**(11), 4691–4692. 150, 151, 261

[238] J. A. Nelder and R. Mead, *Comp. J.*, 1965, **7**(4), 308–313. 154

[239] W. H. Press, S. A. Teukolsky, W. T. Vetterling, and B. P. Flannery, *Numerical Recipes*, Vol. 1, Cambridge University Press, Cambridge, 2nd ed., 2001. 154

[240] I. V. Hertel and W. Stoll, *Adv. At. Mol. Phys.*, 1978, **13**, 113. 155

[241] J. Aldegunde, F. J. Aoiz, and M. P. de Miranda, *Phys. Chem. Chem. Phys.*, 2008, **10**(8), 1139–1150. 155

[242] M. P. de Miranda, F. J. Aoiz, L. Banares, and V. S. Rabanos, *J. Chem. Phys.*, 1999, **111**(12), 5368–5383. 155

[243] A. Schmaunz, U. Kensy, A. Slenczka, and B. Dick, *Phys. Chem. Chem. Phys.*, 2009, **11**(33), 7115–7119. 158

[244] R. Schinke, *Photodissociation Dynamics*, Cambridge University Press, 1st ed., 1993. 159, 162

[245] R. Schinke, A. Untch, H. U. Suter, and J. R. Huber, *J. Chem. Phys.*, 1991, **94**(12), 7929–36. 159

[246] C. H. Hsieh, Y. S. Lee, A. Fujii, S. H. Lee, and K. P. Liu, *Chem. Phys. Lett.*, 1997, **277**(1-3), 33–38. 160

[247] J. A. Harrison, X. Yang, M. Rosslein, P. Felder, and J. R. Huber, *J. Phys. Chem.*, 1994, **98**(47), 12260–12269. 160

[248] S. A. Reid, A. Sanov, and H. Reisler, *Faraday Disc.*, 1996, **102**, 129–146. 160

[249] S.-C. Yang and R. Bersohn, *J. Chem. Phys.*, 1974, **61**(11), 4400–7. 161

[250] A. V. Demyanenko, A. B. Potter, V. Dribinski, and H. Reisler, *J. Chem. Phys.*, 2002, **117**(6), 2568–2577. 162

[251] M. P. de Miranda and F. J. Aoiz, *Phys. Rev. Lett.*, 2004, **93**. 163

[252] M. P. de Miranda, F. J. Aoiz, V. Sáez-Rábanos, and M. Brouard, *J. Chem. Phys.*, 2004, **121**, 9830. 163

[253] R. P. Singhal, H. S. Kilic, K. W. D. Ledingham, C. Kosmidis, T. McCanny, A. J. Langley, and W. Shaikh, *Chem. Phys. Lett.*, 1996, **253**(1-2), 81 – 86. 171, 172, 193

[254] R. P. Singhal, H. S. Kilic, K. W. D. Ledingham, T. McCanny, W. X. Peng, D. J. Smith, C. Kosmidis, A. J. Langley, and P. F. Taday, *Chem. Phys. Lett.*, 1998, **292**(4-6), 643 – 646. 171, 173, 193

[255] D. Neuberger and A. B. F. Duncan, *J. Chem. Phys.*, 1954, **22**(10), 1693–1696. 193

[256] O. Chesnovsky and A. Amirav, *Chem. Phys. Lett.*, 1984, **109**(4), 368 – 373. 193

[257] F. Santoro and C. Petrongolo, *J. Chem. Phys.*, 1999, **111**(21), 9651–9657. 193

[258] A. R. Edmonds, *Angular Momentum in Quantum Mechanics*, Princeton University Press, Princeton, 1957. 262

[259] M. E. Rose, *Elementary Theory of Angular Momentum*, John Wiley & Sons, Inc., New York, 1957. 262

[260] D. M. Brink, *Angular Momentum*, Clarendon Press, Oxford, 1968. 262